NASA SP-236

RESEARCH ON URANIUM PLASMAS AND THEIR TECHNOLOGICAL APPLICATIONS

A symposium held at
UNIVERSITY OF FLORIDA
Gainesville, Florida
January 7-8, 1970

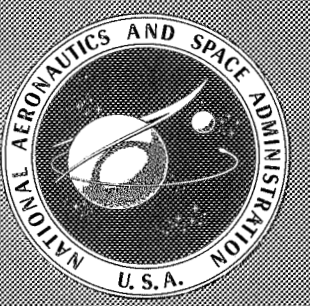

NATIONAL AERONAUTICS AND SPACE ADMINISTRATION

NASA SP-236

RESEARCH ON URANIUM PLASMAS AND THEIR TECHNOLOGICAL APPLICATIONS

The proceedings of a symposium held January 7–8, 1970 in Gainesville, Florida, and sponsored by the National Aeronautics and Space Administration and the University of Florida

Edited by

Karlheinz Thom and Richard T. Schneider

Scientific and Technical Information Office 1971
NATIONAL AERONAUTICS AND SPACE ADMINISTRATION
Washington, D.C.

Page intentionally left blank

Foreword

The Symposium covered in this volume was the first of its kind, bringing together experts in nuclear gaseous-core reactor development, plasma physicists, and nuclear engineering scientists. The intention of the meeting, to stimulate uranium plasma research by exposing the various ideas, points of view, and approaches to possible applications in this field, was met with full success. With pleasure we acknowledge the enthusiastic response and the valuable contributions of all the participants and authors.

The General Chairman was Richard T. Schneider, University of Florida; the Program Chairman was Karlheinz Thom, NASA Office of Advanced Research and Technology; and the Arrangements Chairman was M. Jack Ohanian, University of Florida. The Program Committee members were: Charles E. Franklin, NASA Space Nuclear Propulsion Office; Robert G. Ragsdale, NASA Lewis Research Center; and Richard T. Schneider.

K.T.
R.T.S.

Page intentionally left blank

Contents

SESSION IV

NUCLEONICS AND RADIATION

Chairman: M. J. Ohanian

SESSION V

NUCLEAR LIGHT BULB ENGINE

Chairman: C. E. Franklin

SESSION VI

MHD POWER GENERATION

Chairman: H. Hassan

SESSION VII

NUCLEAR LASERS

Chairman: A. Javan

PANEL DISCUSSION: DIRECTION AND NEEDS FOR FUTURE RESEARCH

Chairman: R. E. Uhrig

Introduction

KARLHEINZ THOM

Atomic Energy Commission and
National Aeronautics and Space Administration

The Symposium on Research on Uranium Plasmas and Their Technological Applications was held in order to bring together scientists and engineers who are involved in the different phases of nuclear propulsion research for the exchange of information and ideas. The meeting was initiated and organized jointly by the NASA Office of Advanced Research and Technology and the University of Florida, with the cooperation of the NASA Space Nuclear Propulsion Office and the NASA Lewis Research Center. In addition to the usual objectives of professional meetings, the organizers expected contributions from the participants to the question of priorities in future research and development. As expected, the participants' philosophies diverged, but their principal interest appeared to be centered in the idea of a fissioning uranium plasma-core reactor.

Studies of controlled nuclear energy release in a gaseous-core reactor at very high temperatures furnish the motivation for much uranium plasma research. Much work has been done to investigate gas-core-reactor schemes, particularly for rocket propulsion in space at high thrust and at a specific impulse several times that of chemical propulsion. According to spaceflight principles, large payload fractions and short trip times should result from use of this method of propulsion. More instructive comparison results from specific mission analysis, because trajectory opportunities, such as swingbys, may in some cases obscure the gains of advanced propulsion if those are figured solely from elementary rocket equations.

In figure 1 principal modes of propulsion considered for a specific manned Mars mission are compared. The payload and the staytime at destination are the same for each mode of propulsion. The curves show the advantages to be expected from advanced propulsion design. For example, at a mission time of 400 days, chemical cryogenic propulsion requires an original mass of 4×10^6 kg in Earth orbit, whereas nuclear plasma propulsion would require less than 5 percent of that.

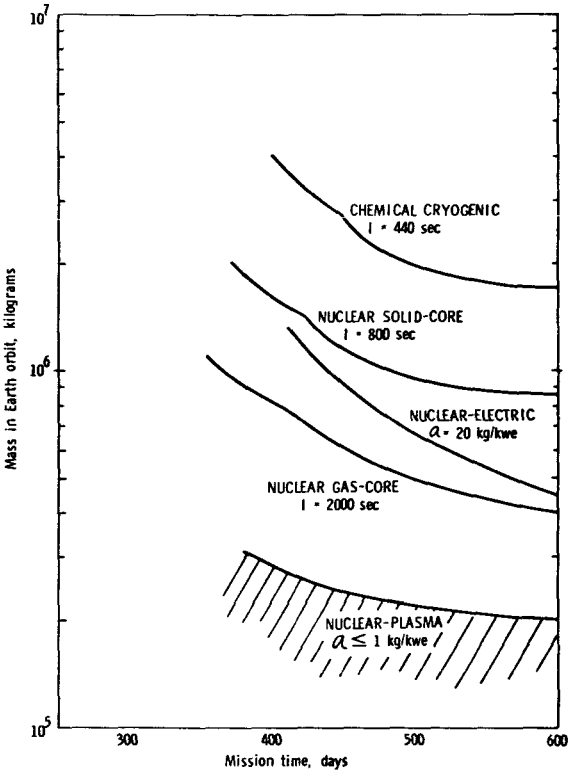

FIGURE 1.—*Principal modes of propulsion considered for manned Mars landing missions. 1980 opportunity; staytime, 40 days; eight men; mass for mission module (includes life-support and Earth entry vehicle), 50 000 kg; mass for excursion module (to be left in Mars orbit), 50 000 kg.*

For propulsion at relatively low specific impulse and high thrust to engine weight ratios, the propellant is the largest fraction of the original mass, and specific impulse is a sufficiently descriptive figure of merit. At high specific impulse, the deadweights of powerplant and thruster become dominant. The figure of merit is then more appropriately expressed by relating the mass of such deadweights to the jet power of the system. This figure of merit is the specific mass a measured in kilograms per kilowatt. Jet power is the product of thrust and exhaust velocity (or specific impulse $\times g$), but, when the parameter a is used, it is always assumed that the exhaust velocity, or the specific impulse, is large.

The nuclear-electric curve represents prospective propulsion systems involving nuclear energy sources at temperatures of contemporary solid-core reactors with ion or plasma engines for thrust. The specific mass at 20 kg/kW is a goal of present development efforts.

The nuclear-gas-core curve shows the characteristics of presently adopted schemes of conceptual gas-core rockets.

The nuclear-plasma region indicates the regime of operation of hypothetical plasma systems in which nuclear energy is generated and converted into thrust in the plasma state. The feasibility of such a system is examined, for instance, in the paper by Sherman (p. 47).

The figure shows the variation with each of these modes of propulsion of the initial mass in Earth orbit. This initial mass can be interpreted as the price tag for the mission!

Because of substantial reductions of efforts and cost that could result from advanced propulsion concepts, the National Aeronautics and Space Administration has conducted investigations of gas-core nuclear rocket schemes through the AEC–NASA Space Nuclear Propulsion Office (SNPO). Nuclear electric propulsion systems were investigated under programs of the NASA Space Power and Electric Propulsion Division. Fundamental principles of plasma acceleration and deceleration were investigated under the plasmadynamics research program in the NASA Office of Advanced Research and Technology.

The plasmadynamics research has contributed significantly to the development of plasma thrusters and power converters. Beyond that, it has produced a broad knowledge of fundamental processes occurring in plasma devices, such as ionization, excitation, and recombination rates; instabilities; and boundary-layer interactions. Until recently, however, nuclear reactions were not included in this plasmadynamics research.

Because of critical mass requirements, it appears to be impossible to build a small-scale prototype engine. It is estimated that a gas-core reactor for rocket propulsion would operate at a thermal power of up to 100 000 MW, while the volume of its cavity is projected to be 1, or a few, meters.[3]

Pressure is calculated at hundreds of atmospheres. Obviously, the construction of such a machine would stress our technological capabilities, and its cost would by far exceed the limits of present NASA research program budgets.

As the program chairman of this meeting, I tried to provoke relevant discussions by means of an introductory speech in which I took a position for a program of basic research. The question of basic research versus "engineering approach" was vividly discussed, although a true controversy does not exist! What appears to be such is rather a different determination of technical priorities by people with different professional backgrounds. Their judgments, based on their expertise, were the contributions we had hoped for.

There were several informal discussion periods.[1] One followed the panel discussion at the end of the symposium and others came about rather occasionally when, after the formal adjournment of the meeting, a large number of participants remained for additional discourse. The discussions were tape recorded and subsequently transcribed by University of Florida personnel. Such a method of conference reporting is far from perfect, but informal discussions unimpeded by requirements of form were recorded subject to the obvious limitations. Such discussions are included in the following section entitled "Review" which contains both specific and general opinions on the subject, including the need for basic research.

[1] Technical discussions that followed the presentation of papers are printed in this proceedings at the end of each of such papers.

Review

KARLHEINZ THOM

In NASA it is now recognized that plasma physics should also be applied to gas-core reactor problems, especially to supplement current Space Nuclear Propulsion Office programs. However, beyond that and in a broader perspective, the "fissioning uranium plasma" appears as a new scientific research objective in its own right. Applications in addition to that of the gas-core rocket can be envisioned. Session I of this Symposium is an attempt to survey various possible applications, such as closed-loop magnetohydrodynamic power generation and nuclear-powered lasers.

Investigations of uranium plasma reactors seem to be limited to theoretical studies and simulation experiments. For example, in a gas-core rocket reactor, the uranium plasma must be separated from a bypassing propellant before the latter is expanded through a nozzle. This is necessary so as not to lose too much of the costly uranium fuel and to obtain high specific impulse. Such separation, however, is not easily achieved under the requirements of efficient heat transfer from the uranium plasma to the propellant and of effective protection of structures against large heat fluxes. Much effort has been spent to solve the fuel-propellant separation problem by fluid mechanics means. Various flow-field configurations have been tried theoretically and in experiments in which the uranium plasma and hydrogen combination in a reactor was simulated, for instance, by an iodine-air mixture. Almost all the papers in Session II of this Symposium are concerned with recent research on the separation problem.

An obvious solution to the separation problem is to avoid contact of fuel and propellant in the first place. In the nuclear light bulb engine concept, the uranium plasma is contained in transparent vessels, so that its radiation can heat a bypassing propellant. This concept is extensively described in Session V. Studies on radiative heat transfer and emission spectra applicable to both concepts are presented in Sessions IIIA and IV.

From the standpoint of basic research, one can presently even disregard the separation problem and question whether a fissioning uranium plasma can stably exist and, if so, what its predominant characteristics will be. The fuel-propellant separation problem could then emerge as a second-order problem merely imposed by the specific boundary conditions of specific intuitively conceived engineering schemes. Novel means of separation may present themselves during the growth of scientific understanding.

In the plasma physicist's point of view, a fissioning uranium plasma appears as a multicomponent plasma in a state of extreme nonequilibrium. There is the fission fragment component, consisting of completely ionized atoms at an energy of roughly a hundred million electron volts. Uranium atoms and ions exist at an energy of the order of a few electron volts, while the neutron component is essentially thermalized at moderator temperature. The electrons should essentially be equilibrated with the uranium gas, but on a microscale that may not be so. Finally, there is the photon component, expected to be the principal carrier of energy from the fissioning plasma to a station of useful power extraction. Nonequilibria and large temperature and density gradients may drive instabilities. In the paper by Monsler and Kerrebrock (p. 135) and that by Becker (p. 231) examples of such instabilities are described. The energy levels of excited atoms and ions will hardly exist everywhere and at all times in thermal equilibrium. Population inversion should therefore be expected to be a rather common feature of fissioning uranium plasmas. Possibilities of laser excitation involving nuclear reactions are analyzed in the papers by Russell

(p. 53), by Guyot et al. (p. 357), by Thiess and Miley (p. 369), and by Allario et al. (p. 397).

In such a program of basic research, in contrast to investigating conceptual schemes of technological application, one concentrates, for instance, on samples of uranium plasma, produced in the laboratory, for spectroscopic analysis. One exposes ^{235}U plasma samples to neutron irradiation to study the mechanisms by which fission fragments deposit their energy while traversing the plasma. Experiments of this kind are described in papers presented in Session IIIB. Parallel to such small-scale experimentation, theoretical analysis of basic phenomena should be conducted; this should include analysis on instabilities and on reaction rates involving non-Maxwellian distribution functions of the uranium plasma components.

For emphasis, I have called uranium plasma research a "new frontier of science," which involves plasma physics, nucleonics, and the nuclear engineering sciences. Each of these disciplines expands into new dimensions when applied to the uranium plasma, and a multitude of rewarding scientific problems emerge in addition to the problem of ultimate technological utilization.

Yet, I still favor basic research. The uranium plasma should have a place in more of the academic research institutions because of its own scientific value and because of additional talent that may become engaged in our common effort.

A synthesis of the informal discussions which followed the regular sessions will now be presented. The participants are listed in the "Attendees" section at the end of this volume.

Leading into the informal discussions, R. Ragsdale raised the question whether new ideas could, perhaps, result in novel gas-core reactor schemes more accessible to experimentation for the determination of priorities. In response, G. McLafferty pointed out that the gas-core reactor work is a relatively mature technology. As is the case in many technological developments, he said, ideas are numerous at the beginning, but as the art progresses many of them are proven unfeasible. He did not rule out the possibility of new ideas; however, he saw little chance for them at this advanced stage. J. Kerrebrock added to this that much knowledge and experience have been gained so that the expert can examine his ideas much more thoroughly. In his view, the apparent lack of new ideas reflects, in the first place, the difficulty of the problem.

A new idea was forwarded, however, by F. Rom [1] when he suggested the construction of an underground cavity reactor, which, he thinks, could be built for a few million dollars, for *in situ* observation of fissioning uranium plasmas. In Rom's experiment one is apparently not concerned with the fuel-propellant separation problem nor with other difficulties of engineering application requirements; such an experiment would therefore appear to belong in the category of fundamental research. Yet its magnitude is beyond that of usual laboratory experimentation. J. Williams, who had presented a paper on the use of uranium plasmas for terrestrial power generation (p. 343), suggested that Rom's experiment could also serve as a demonstration of the feasibility of uranium plasma reactors to the public. In conjunction with the recent awareness of the various useful applications of uranium plasmas, he thought such a demonstration could raise more technical interest as well as more public support for the entire research area. J. Kerrebrock, however, doubted that such a possibility could exist at present. F. Rom pointed out that his underground experiment is not just a wild idea, but that it is based on long experience in the gas-core reactor field. With the feeling that the cost of such an experiment is comparable to or even higher than that of all other uranium plasma research combined, it was argued that, as an alternative, a broad, well-funded fundamental research program would be preferable.

An alternative such as the foregoing rarely exists, however, in long-range research and development. Over longer periods of time the level of public support varies with the response with which the scientific community reacts to important technological goals. F. Moore elaborated on this by pointing toward the general usefulness of high-temperature technology, particularly with respect to terrestrial power generation at increased efficiency and subsequently reduced thermal pollution. If, as it is necessary, an entire thermodynamic cycle could be operated at very high temperatures, he said, sufficient incentive should result to justify sup-

[1] Compare F. Rom's presentation in the Panel Discussion (p. 401).

port for an appropriate long-range research and development program.

G. McLafferty cautioned at this point that the benefits of high-temperature technology had been cited many times, but potential customers of such high-temperature technology must be seriously concerned with endurance and reliability. In his estimate, we are still hundreds of millions of dollars' worth of development work away from any machinery that could be operated at uranium plasma temperatures for thousands of hours between overhauls. McLafferty thought that, at present, the only serious motivation for plasma reactor work exists in achieving high specific impulse rocket propulsion, in which there is no alternative for the high temperature. He concluded that the only other applications of uranium plasma reactors which could seriously support the cause are those for which very high temperatures are similarly a fundamental condition. He did not see any such prospects.

McLafferty's reasonable judgment was not generally accepted, mainly because of the different meanings of "temperature" to the various scientists and engineers, particularly where nonequilibria are considered. For example, plasma thrusters have been operated at kinetic temperatures in excess of 100 000° K for hundreds of hours. Electric arcs have been run at steady state at similar temperatures, and in pulsed plasma experiments even much higher temperatures have been produced. In the paper by Winterberg (p. 37), for example, the feasibility of a pulsed uranium plasma reactor is described. It was recognized that matter at very high temperatures exhibits new phenomena, the analysis of which should be the objective of basic uranium plasma research.

J. Keyes emphasized the need for power extraction from the fissioning plasma by plasmadynamic means—for instance, by coupling plasma motion with external magnetic fields. Magnetohydrodynamics of fissioning uranium plasmas appears then as another area of new research. Keyes thought that such a system could not operate on principles different from those of a heat engine. Thus, mechanisms for heat rejection should be considered, but they need not be the same as for the heat transfer problems in a gas-core rocket.

R. T. Schneider promoted an idea of energy extraction from the nonequilibrium states of the plasma. He stated that in contemporary nuclear engineering the many megavolts of fission fragment energy are quickly reduced to a temperature not higher than that used to heat the steam vessel for a conventional steam engine. In a uranium plasma, in which the fission fragments have a long mean free path, however, there should be ways to drain the high energies of the fragments before thermalization. For example, because of inelastic collisions, energy conversion may be possible via coherent light emission. This would leave the bulk of the plasma relatively cool, while such radiation could represent an equivalent of very high working temperatures. Detailed research on reaction rates in uranium plasmas and on the velocity distribution functions of its various components would be required.

Looking again at nonequilibrium characteristics of uranium plasmas and their various kinds of free energy, C. Franklin questioned the significance of possible instabilities. Specifically, he wondered whether neglecting this problem area could lead to a situation in which a uranium plasma reactor would eventually be built but would not work, or would blow up, because of unexpected instabilities. G. McLafferty's position regarding this problem was that the nonoccurrence of such instabilities in small-scale model tests and under various experimental conditions would be reasonable evidence that they would not occur in a full-scale engine. The experiments should involve actual fissioning uranium plasmas in order to be meaningful, and the question of scaling can obviously not be answered before the kind of instability is defined. Plasma physicists have developed an expertise in instability analysis, and it did appear to be a logical first approach to have their skill applied to the problem, particularly to surveying theoretically the classes of instabilities that could exist.

In a private communication at the meeting, D. Tidman mentioned three classes of instabilities that he could see immediately. T. Wilkerson referred to the atomic bomb, the only fissioning uranium plasma yet produced, which exhibits a "drastic $m=0$ radial expansion instability" which obscures perhaps 50 other instabilities that could develop if the predominant one were suppressed.

An acoustic instability, driven by thermal radiation in a gas-core rocket, was, however, not con-

sidered as a serious problem by A. Kascak on the basis of various gas dynamics calculations that he has examined. This was supported by J. Williams, who pointed out that a thermal driven instability could occur only if the opacity of the propellant varied more strongly than with the fourth power of the temperature, whereas available data indicate that in the case of a hydrogen propellant the temperature dependence of opacity is more nearly linear, and certainly not to the fourth power. M. Monsler, who had presented a paper on acoustic instabilities in Session II, remained a skeptic. He thought that the absorption coefficient may not show such a clear-cut distinction as that proposed. Furthermore, an instability approaching a critical state need not necessarily involve growth to infinite amplitude. For example, in the nuclear light bulb scheme, as he pointed out, a propellant pressure fluctuation in the order of a few percent could be destructive because of the sensitive structure of the transparent plasma containment vessels.

It appears, then, not only that the classes of possible instabilities should be established, but also that their dispersion relations should be established and their nonlinear behavior be examined.

Concern about radiation absorption in a propellant and about the emission spectra of a fissioning uranium plasma prompted C. Franklin's question as to whether such information could be obtained accurately enough within a time period of perhaps a few years. G. McLafferty said that the radio-frequency light source described in the paper by Roman (p. 301) will contribute significantly to obtaining this information, because at the present time heat fluxes corresponding to 10 000° R can be produced, and even larger ones are anticipated in the near future. R. T. Schneider, who has presented a spectroscopic study of uranium arcs (p. 181), explained that an accurate determination of absorption coefficients and emission spectra is by all means possible, although it may involve considerable effort and work.

A. Kascak pointed out the need to know the ultraviolet spectrum of radiation coming from the core because this radiation, in a gas-core rocket, could be larger than that predicted by the blackbody radiation at the edge temperature. Spectroscopic research on uranium plasmas at increasingly high temperatures, possibly produced in a pulsed electrical discharge, could lead the way to an exact determination of ultraviolet emission spectra.

The protection of walls against the fluxes of heat from the high-temperature uranium plasma is a problem area that was again mentioned by J. Williams. He described current work on seeding propellants or wall jets with particles in order to increase their opacity vastly and thereby to shield the walls against thermal radiation. He said that this is applicable to rocket nozzles and also to MHD generators in a closed-loop, uranium plasma, power generation system. Similar work, he pointed out, was previously done in conjunction with reentry problems. Williams thought that seeded boundary layers could control thermal radiation as well as conduction and convection. E. Soehngen warned against too optimistic expectations from transpiration cooling. At large rates of coolant influx, turbulent mixing of the coolant with the plasma can occur, thus defeating the purpose. Such an effect occurred in experiments with constricted arcs. A suggestion similar to established ablation techniques for reentry heat protection was made by M. Miller. He recalled a method by which an organic material is forced, under pressure, through porous walls. In contact with the hot core flow, such material would undergo transitions that could absorb sufficient heat for wall protection.

Uranium plasma research thus involves boundary-layer analysis, including the aforementioned sophistications, in addition to plasmadynamics complications. The latter were touched briefly by J. Keyes in response to R. Rosa's statement that in combustion-driven MHD generators operating at 3500° K no serious boundary-layer problems exist and that one could double the temperature in the case of atomic gases. Keyes' question was, then, how a large temperature drop through the boundary layer would influence the electrical conductivity profile. R. Rosa estimated that a voltage drop of approximately 200 volts across the boundary layer could result; he did not consider this serious if the generator were operated at an output of several thousand volts.

Work on principles of using nuclear energy to pump lasers, described in the paper by Russell (p. 53) and in the last three papers of the Symposium, appeared to some participants as a kind of "shotgun marriage." It was pointed out that ener-

getic charged particles for laser excitation could be obtained from existing particle accelerators more easily than from uranium plasmas. In the light of quantum electronics analysis, this may be a good argument. However, the aforementioned papers are concerned with direct laser excitation by corpuscular radiation from nuclear reactions. In fissioning uranium plasmas, then, there exists the possibility of coherent light generation directly from nuclear power (admixtures of other gases may be required).

Achievement of the technological goals of uranium plasma research seems to require significant advances in science and solutions of complex engineering problems. The Symposium has considerably deepened this impression, yet it has resulted more in optimism than in skepticism. None of the participants has speculated on technological lead times, but it was generally felt that those would be long. I cannot resist presenting figures 2 and 3. Figure 2 shows Dr. R. Goddard with his, the world's first, liquid-fueled rocket. One can say that spaceflight technology began with Goddard's experiments. Before, through hundreds of generations, mankind had been only dreaming of spaceflight. It took not much more than one generation, however, to move from Goddard to Apollo 11, the triumph of which is shown in figure 3. The step from Goddard's miniature rockets to the enormous and enormously complicated Apollo system appears to me to be a much larger step than that of moving from present technology to uranium plasma technology. From figure 1 in the Introduction, one can conclude that uranium plasma propulsion may lead to a second-generation spaceflight technology in which expeditions throughout the solar system will not be of a larger relative magnitude than that of previous expeditions to explore the planet Earth.

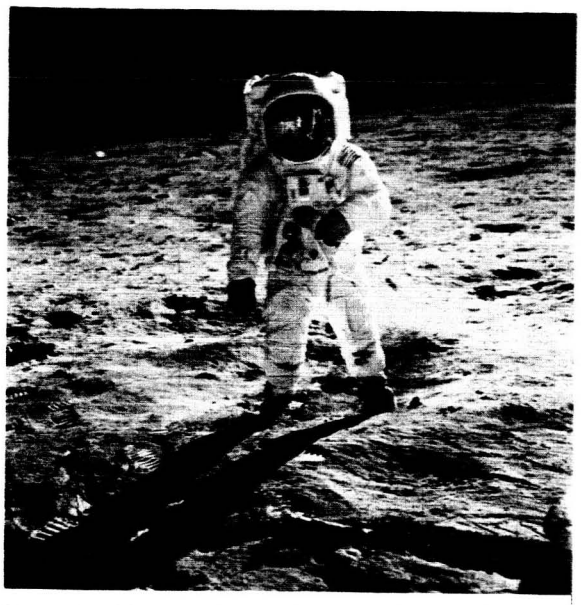

FIGURE 3.—*Enormously complicated rocket for the Apollo system led to the depicted success of the Apollo 11 mission.*

FIGURE 2.—*World's first liquid-fuel rocket with its designer, Dr. R. Goddard.*

Page intentionally left blank

SESSION 1

CONCEPTS

Chairman: K. THOM

Comparison of Closed- and Open-Cycle Systems

F. C. SCHWENK AND C. E. FRANKLIN
U.S. Atomic Energy Commission

The National Aeronautics and Space Administration (NASA), through the Space Nuclear Propulsion Office (SNPO), is currently supporting research on two gaseous-core reactor concepts, the open-cycle coaxial-flow system which is being followed and supported by the Lewis Research Center (LeRC) and the closed-cycle nuclear light bulb system being supported directly by SNPO. I would like to give you a brief comparison between the two systems in order to provide some sort of overview for subsequent papers. Before I do so, however, I think it appropriate to mention briefly the motivation behind the support for gas-core research.

The emphasis in space in the past has been toward more and more ambitious missions. As a result, propulsion systems have evolved from the fairly low performance but relatively easy to handle LO_2-kerosene engines through the LO_2-LH_2 engines of today to the proposed solid-core nuclear rockets of the late 1970's. Although the NASA missions to date have been concentrated on the near-Earth roles in space (the Moon is arbitrarily included in the near-Earth category), it is expected that there will be future missions for deep-space research and for manned planetary exploration which will require more efficient propulsion systems. Thus, we have turned to the gas-core nuclear rocket as a potential propulsion system for the future. Let me stress that word "potential," because, as this symposium progresses, I think that you will realize that today the gas core is still just a potential and not a reality in a usable form. Our early studies said that the gaseous-core nuclear reactors' potential could be as high as a 3000-sec specific impulse or approximately 3½ times the performance expected from the first general solid-core and 3 times the performance of the advanced solid-core systems. This lofty expectation has declined somewhat but there still appears to be a significant potential improvement over the solid-core nuclear reactors and at the end of this presentation I will give you my opinion as to where the maximum performance levels lie.

GENERAL DESCRIPTION

The gaseous-core nuclear reactor (GNR), whether open or closed cycle, has certain general characteristics which do not change with detail. The energy source in the GNR is a fissioning plasma of partly ionized uranium ranging in average temperature from 40 000° to 140 000° R but radiating thermal energy as does a blackbody at a lower temperature to a surrounding propellant (hydrogen) stream which has been seeded in order to make it opaque to the thermal radiation. The pressures in such a scheme may range from 100 to 1000 atm or greater depending on the system's critical mass requirements. However, it has more or less been arbitrarily assumed that pressures exceeding 1000 atm are not realistic for the time being and design considerations have been restricted to systems of 1000 atm or less, and preferably less. Once the propellant is heated, it is expanded through a nozzle to produce thrust.

The open-cycle, coaxial-flow reactor depends entirely on fluid mechanics to minimize the mixing of the fuel and propellant streams for preferential retention of the fuel. Fuel losses are accepted in this system but it is desirable to maintain them as low as possible. The closed-cycle system, however, operates on the premise that the fuel should be completely contained with no fuel being exhausted. To achieve this end, a physical barrier as well as fluid dynamic techniques are used to separate the

fuel physically from the propellant stream with the radiant energy being transferred through the barrier to the propellant.

Coaxial-Flow System

The coaxial-flow system is the current reference system for research on the open-cycle concept (fig. 1). The reference design for this concept is an

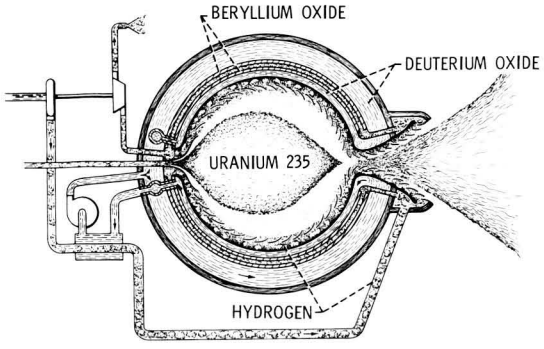

FIGURE 1.—*Coaxial-flow gas-core nuclear rocket.*

essentially spherical reactor which has an outer circulating region with deuterium oxide (D_2O), a regeneratively cooled beryllium oxide (BeO) region, a second-pass D_2O circulating region, a curved porous wall, the propellant zone, and finally the fuel region, all of which is surrounded by a pressure vessel with a nozzle. After cooling the moderator-reflector region, the hydrogen propellant is seeded and injected continuously along the curved porous cavity wall where it is heated primarily by thermal radiation from the fissioning fuel which has been injected at the upstream end of the cavity. The latest engine configuration might have the following characteristics:

(1) A single 12-ft-diam cavity
(2) A moderator thickness of $2\frac{1}{2}$ ft
(3) An engine thrust of 500 000 lb
(4) A fuel volume fraction of 0.3
(5) A specific impulse of 1800 sec
(6) A cavity pressure of 1000 atm

Nuclear Light Bulb

The nuclear light bulb is the working system for the closed-cycle research (fig. 2). The reference engine consists of seven unit cavities with a moderator-reflector material separating each cavity and

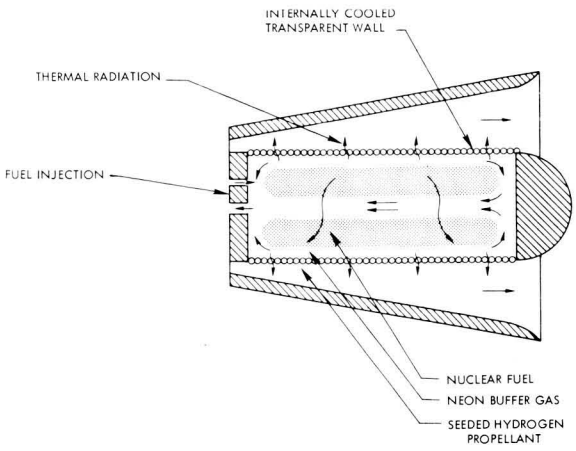

FIGURE 2.—*Concept of nuclear light bulb engine.*

running the length of same. Gaseous nuclear fuel is suspended in each cavity in a neon-driven vortex which is contained within a transparent material through which thermal radiation is transferred to a seeded hydrogen propellant stream which flows in an annulus between the moderator and the transparent wall. The present first-generation light bulb engine has the following characteristics:

(1) Seven cavities having a length of 6 ft each and a total overall volume of 170 ft^3
(2) Cavity pressure, 500 atm
(3) Propellant flow rate, approximately 50 lb/sec
(4) Engine thrust, 92 000 lb
(5) Engine power, 4600 MW
(6) Fuel radiating temperature/blackbody equivalent, 15 000° R
(7) Specific impulse, 1800 to 1900 sec
(8) Fuel volume fraction, 0.25

NEUTRONICS

Calculated critical masses for both the open-cycle and closed-cycle systems have been the subject of controversy because, for one reason or another, the validity of these calculations was suspected. It is important to get some realistic idea of the neutronic requirements and characteristics in order to determine the interrelations between critical masses and fuel volume fractions because these items set the reactor operating pressure and establish the criteria for the fluid mechanics program. As a result of this concern, critical experiments were

conducted at the National Reactor Testing Site of the Atomic Energy Commission by the Idaho Nuclear Corp. (formerly General Electric Co.) to verify calculational procedures on a cylindrical cavity configuration. These experiments showed that the critical mass was strongly dependent on both the fuel and support material locations within the core region as well as on the specific geometry of the fueled region. Some of the results of these experiments are shown in figure 3 where the critical

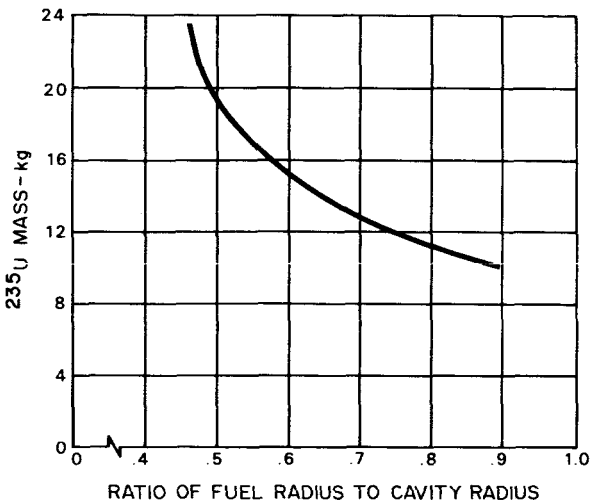

FIGURE 3.—*Results of cavity critical experiment.*

mass of ^{235}U is plotted as a function of the ratio of fuel radius to cavity radius. Using the results from such experiments, attempts were made to predict the critical masses for subsequent experiments in the single-cavity configurations. In general, these attempts were unsuccessful. However, the case for multiple-cavity configurations, i.e., the closed-cycle configurations, was somewhat better in that the predicted critical masses were within ± 10 percent of the experimental results for the analyzed cases. It is important to note from figure 3 that the required critical mass increased rapidly when the ratio of fuel to cavity radius was decreased below approximately 0.5 and essentially blew up at a radius ratio of 0.46. Therefore, it appears that the minimum desired ratio of fuel to cavity volume or fuel volume fraction is approximately 0.25 and ought to be larger in order to keep the critical mass requirements and, therefore, the pressure requirements to a reasonable level. As noted earlier, this means a reactor pressure of 1000 atm or less.

In addition to setting the operating pressure when the critical mass is known, the fuel volume fraction is important to the open- and closed-cycle engines for other reasons, some common and some not. For the moment I shall mention only one other facet of the importance of the fuel volume fraction, but I shall attempt to bring other facets in later in this paper.

For a given engine size and geometry, the operating fuel volume fraction determines the fuel radiating area and, therefore, the required energy release per unit area for a given reactor power. While this is not particularly important for the coaxial-flow reactor, it is extremely important for the nuclear light bulb because it determines a minimum equivalent blackbody radiating temperature, which in turn implies some energy spectrum. As the required radiating temperature is increased, the percentage of the energy radiated in the ultraviolet range also increases, and thus the spectrum is moved toward the transmission cutoff in the transparent material. Therefore, a minimum fuel volume fraction is established in order to provide a radiating temperature consistent with the transmission characteristics of the transparent material. Latham (ref. 1) indicates that for the reference light bulb engine the required fuel volume fraction based on radiating area and an equivalent blackbody temperature of 15 000° R will be approximately 0.25. The corresponding critical mass is approximately 16 kg of ^{233}U at a reactor pressure of approximately 500 atm. On the basis of the close correlation between the predicted and the actual experimental critical masses for the multiple-cavity configurations in the Idaho tests, it is appropriate to assume that the 16-kg critical mass is reasonable.

Although it was noted above that there are uncertainties involved in the critical masses of the open-cycle system, it is useful to review what have generally been considered to be the mass requirements for the open cycle and what the latest best guesses would be. Ragsdale (ref. 2) noted that for an engine with a cavity 10 ft in diameter and 8 ft long the best guess for the critical mass using ^{235}U would be nominally 40 kg, and he showed that a fuel volume fraction of at least 0.2 was required if the reactor pressure was

to be maintained below 1000 atm. Rom (ref. 3) modified the system to have a reflected cavity 8 ft in diameter and 8 ft long with a fuel region 6 ft in diameter, i.e., a fuel volume fraction of approximately 0.56, and, through a more rigorous procedure than that followed by Ragsdale, Rom calculated a critical mass of 47.8 kg of ^{235}U for this reference engine with the reactor pressure ranging from 595 to 1190 atm depending on the severity of mixing between the hydrogen and the uranium. Hyland, also of LeRC, has recently made as yet unpublished calculations to determine the critical mass of the spherical coaxial-flow engine. These calculations were made using real material characteristics for each region of the engine and should be the most accurate critical mass numbers to date for the open-cycle system. With an essentially spherical cavity 10 ft in diameter and with a fuel volume fraction of approximately 0.3, the required reactor pressures exceeded the 1000-atm limit. In order to bring the pressures to an allowable level it was necessary to increase the reactor size to a 12-ft diameter with a fuel diameter of 8 ft, a fuel volume fraction of 0.3. The new calculations on this larger engine resulted in ^{235}U critical masses which exceeded 100 kg if all of the hydrogen propellant flowed through the cavity. However, if 90 percent of the propellant bypasses the cavity and is assumed to be injected downstream into the nozzle, the hydrogen absorption and scattering are reduced and the ^{235}U critical mass is only 75 kg. Furthermore, when ^{233}U is substituted for the ^{235}U and 90 percent of the hydrogen bypasses the cavity, a minimum critical mass of approximately 45 kg is achieved at a nominal reactor pressure of 1000 atm. This probably represents the very minimum critical mass and, if propellant and fuel mixing is taken into account, either the mass required or the pressure will have to increase.

TRANSPARENT WALL

Since the transparent wall in the nuclear light bulb is such an important part of the closed-cycle engine and since it has such a significant effect on the fluid mechanics of the light bulb engine, it is appropriate to talk briefly about the wall and its characteristics before comparing the flow systems. The primary function of the transparent wall is to provide a physical separation between the fuel and the propellant in the engine and yet be transparent to the thermal energy radiated from the fissioning region. At least two materials are considered as prime candidates for this function: High-purity fused silica and BeO, with the fused silica receiving the most attention at the present time because of the unavailability of high-purity single-crystal BeO. The requirements on these materials are that they be transparent in the primary wavelength ranges of the thermal radiation, that they have a relatively high operating temperature (fused silica can be used at temperatures of approximately 960° C), that they be formable and fabricable, and that if they experience radiation damage which results in the formation of color centers then these centers will anneal at the wall operating temperature at a rate sufficiently fast to preclude wall destruction.

A typical absorption spectrum for Corning 7940 fused silica (fig. 4) has a transmission band from

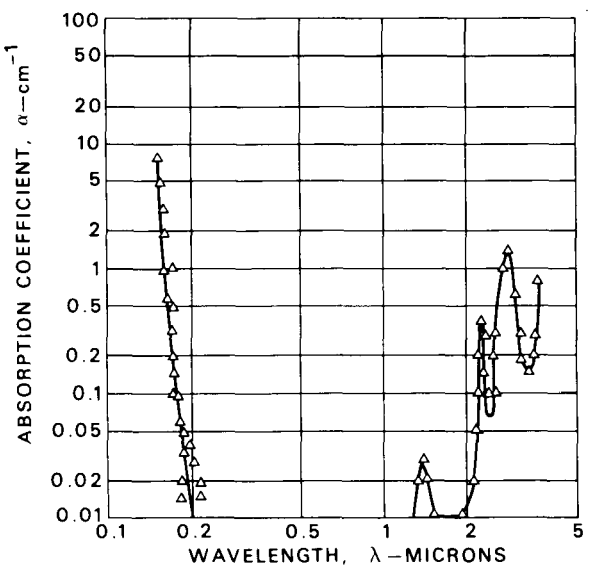

FIGURE 4.—*Typical absorption spectra for Corning 7940 fused silica measured at 22° C.*

approximately 0.2 to 2.5 μ with an ultraviolet (uv) cutoff occurring around 0.18 μ. Therefore, for the thermal energy to be radiated through the fused silica the spectrum from the plasma must be predominantly inside this transmission band. This implies that there is an equivalent blackbody radiating temperature limit for the nuclear light bulb

using fused silica and thus a performance limit. It was originally assumed that the radiant energy spectrum at a flux equivalent to a 15 000° R radiating blackbody would be essentially the same as a blackbody spectrum; thus at an equivalent 15 000° R blackbody temperature approximately 2.5 percent of the total energy would be radiated at wavelengths below 0.2 μ, a level which is completely acceptable in terms of energy deposition into the transparent wall. However, recent calculations by Krascella (ref. 4) indicate that the actual spectrum from a fissioning plasma radiating at an equivalent 15 000° R blackbody flux will probably have a much larger percentage of its spectrum at wavelengths below 0.2 μ than was originally anticipated (potentially 20 percent or greater). If the spectrum is essentially that which has been calculated by Krascella instead of that from a 15 000° R blackbody, then either a seed material such as oxygen must be injected between the plasma and the transparent wall in order to absorb radiant energy below approximately 0.2 μ or the operating temperature must be reduced to a level where the radiant energy spectrum is compatible with the transparent wall's transmission characteristics. At the moment it has not been determined which case will exist.

In addition, the presence of the transparent wall places an operational requirement on the light bulb engine which is not present in the open-cycle system, i.e., that the pressures in both the fueled region and propellant region must be brought to operating conditions together and that throughout the engine's operation these pressures must be equal to each other within a tolerance of approximately $\pm 2/3$ atm based on an assumed wall thickness of 0.005 in. and a radiating temperature of 15 000° R. Therefore, the rate at which the reactor can be brought to power is probably slower than the open-cycle engine's rate and some form of pressure control must be available which will maintain the two cavity pressures at essentially equal levels.

FLUID MECHANICS

The purpose of the fluid mechanics in both systems is to provide desired flow characteristics to the fuel and the propellant. This means the desired containment characteristics as well as the desired placement or locating of the fluids within the cavities. If all of the requirements on the fluid dynamic system are not met, then the flow scheme is either inadequate or marginal. With this in mind, it can be stated that at the present time the flow schemes for both the open- and closed-cycle engines would appear to be marginal. The reasons for this statement are included in the following discussion.

Open Cycle

The requirements placed on the fluid mechanics of the open-cycle system are such that at least two diverging sets of requirements must be made compatible. On the one hand, the engine performance and economic criteria dictate that the ratio of the propellant mass flow rate to fuel flow rate be as high as possible and probably at least 100 to 1; while, on the other hand, flow stability and fuel volume fraction criteria would have this ratio go toward unity. However, experiments by Johnson (ref. 5) at the United Aircraft Research Laboratories on a cylindrical-wall coaxial-flow test rig and two-dimensional experiments by Lanzo (ref. 6) at LeRC on curved porous-wall coaxial-flow systems show that high mass flow ratios, with their correspondingly high velocity ratios, act to reduce both the flow stability and the fuel volume fraction. Therefore, as the mass flow ratio is increased both the stability of the stream and the fuel volume fraction decrease. This trend is directly opposed to that which would be favored for the neutronics requirements which, as noted earlier, at least for the open-cycle system, would have the fuel volume fraction be 0.25 or greater.

Open-cycle flow experiments have been conducted by Johnson (ref. 5) using a 10-in.-diam coaxial-flow test rig (fig. 5) to attempt to maximize the ratios of propellant to fuel mass flow in stable flow configurations. By reducing the turbulence intensity just downstream of the inlet and by eliminating the velocity steps between the fuel and propellant streams, Johnson has demonstrated fuel volume fractions of 0.23 at absolute stream velocities up to 80 ft/sec and at mass flow ratios of approximately 100 to 1. However, Johnson indicates that at mass flow ratios of as little as 80 to 1 recirculation was present and the fuel volume fractions should be somewhat lower than indicated.

In a parallel effort at LeRC, Lanzo (ref. 6) had conducted experiments using a two-dimensional mockup of a spherical cavity. The test cavity was

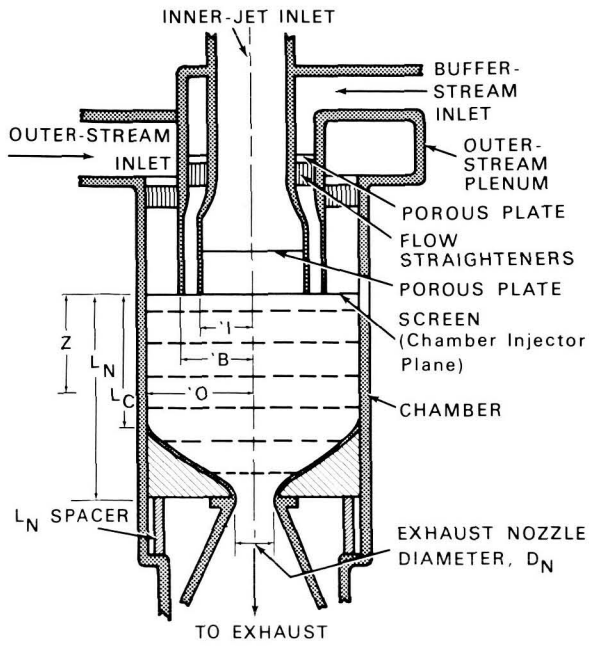

FIGURE 5.—*Schematic of coaxial-flow test apparatus.*

made up of two parallel side walls 6 in. apart connected by an almost circular porous wall 9 in. in diameter through which the simulated propellant was injected (fig. 6). Using air with smoke as the simulated fuel and air as the simulated propellant, Lanzo conducted flow experiments at mass flow ratios from 25 to 1 up to 100 to 1 and obtained, through densitometer measurements, fuel volume fractions of 0.5 to 0.3, respectively. At first glance these fuel volume fractions appear to be quite attractive; however, if it is assumed that, in a three-dimensional spherical flow geometry which also uses sidewall propellant injection, the flow pattern is three-dimensionally symmetrical, then the fuel volume fractions corresponding to the above mass flow ratios would only be 0.35 and 0.16, respectively. In addition, these experiments were conducted at very low absolute stream velocities and a Reynolds number of only 1100. Therefore, the flow pattern in the spherical cavity still has to be determined for flow velocities and Reynolds numbers which more accurately simulate real engine flows.

The work to date by both Johnson and Lanzo indicates that although ratios of propellant to fuel mass flow rates of at least 100 to 1 are possible they are not consistent with the fuel volume fractions of approximately 0.25 required by neutronic

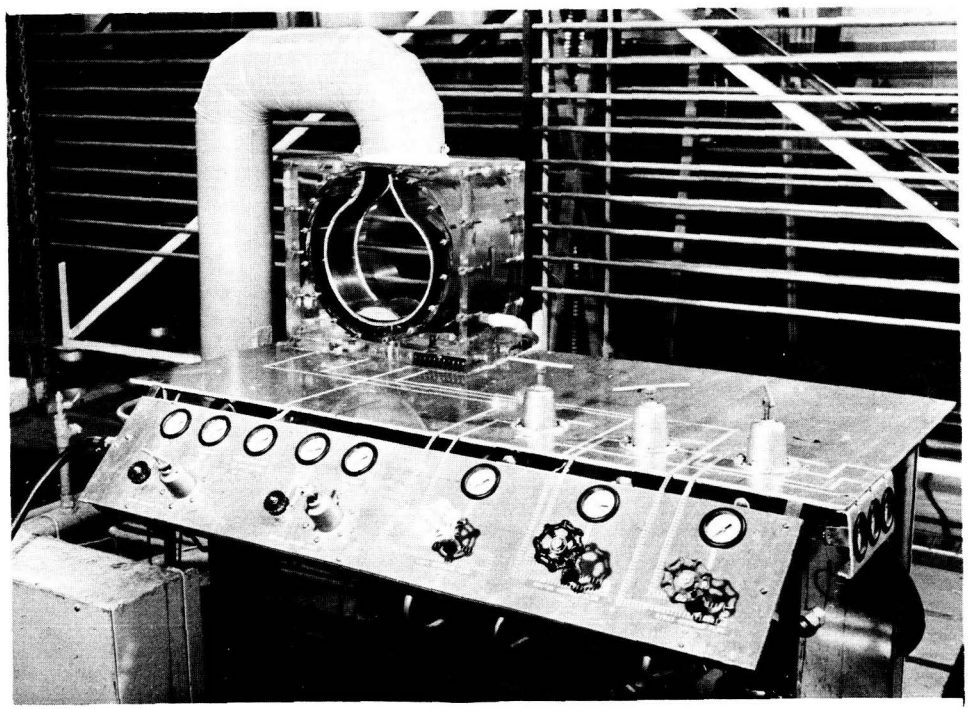

FIGURE 6.—*Two-dimensional experimental mockup of LeRC gas-core engine concept.*

considerations. Therefore, further improvements must be made in the containment characteristics with increasing mass flow ratios of the open-cycle system or it will be restricted to mass flow ratios of approximately 50 to 1 or less.

Closed Cycle

The previous discussion on the transparent walls could lead to the conclusion that their presence completely detracts from the performance of the engine; however, from the fluid mechanics standpoint, the presence of the transparent wall is a bonus since it isolates the fuel containment techniques from the engine performance. This means that the fluid mechanics for the fueled region can be specifically tailored to suit the requirements for stable vortices of the desired size. The same is true for the propellant region.

It was previously noted that calculations by Latham (ref. 1) indicated a fuel volume fraction of 0.25 was required in the light bulb engine to meet the radiating surface area requirements. Since this fuel volume fraction was also consistent with the neutronic requirements, it seems to represent a good baseline from which to evaluate the fluid mechanics research on the light bulb.

In early research on vortex fluid mechanics related to the light bulb concept, Travers (ref. 7), using a water vortex tube, found that a radial stagnation surface, i.e., a surface across which there was no flow, could be established, and the maximum radius at which this stagnation surface could be obtained using concepts consistent with a real light bulb engine was 0.7 of the cavity radius. Therefore, a practical upper limit of approximately 0.5 appears to be established for the light bulb system, a limit which, according to Travers, was set by the turbulence near the peripheral wall.

Building upon and expanding the Travers research to gaseous vortex studies, Jaminet and Mensing at the United Aircraft Research Laboratories have attained fuel volume fractions up to 0.44 in isothermal tests on the nuclear light bulb configuration, thus far exceeding the 0.25 requirement. Two things, however, detract from this accomplishment. The first is that high bypass flows were required in order to achieve such a high volume ratio and the second is that the simulated fuel concentration at the wall was on the order of 5 percent. The high bypass flow is undesirable because it increases the load on the ducting and on the fuel recycle system, a situation which potentially detracts from the engine's performance but which does not affect its feasibility. The fuel concentration at the wall, however, is completely unacceptable and must be eliminated since fuel in such a location would plate out on the cooled wall, thereby increasing the wall absorption and affecting burnout.

Just as it is important to keep the uranium plasma off the transparent wall, it is equally important to keep the propellant seed off the wall, thus necessitating either preferential or zone seeding in the propellant stream and/or some form of transpiration cooling. Recent experiments by Johnson (ref. 5), which will be reported in detail later in this symposium, indicate that a stable buffer layer of unseeded hydrogen can be achieved along the transparent wall, and seeding experiments by Klein (ref. 8), also to be reported later, have shown that the seed material can be fed into a central seeded zone and be made to stay in that zone for appreciable lengths.

SEEDING

Both gas-core concepts depend on radiant energy transfer from the fissioning plasma to the propellant. Since the hydrogen is not sufficiently ionized to be opaque to the thermal radiation at temperatures and pressures below approximately 15 000° R and 500 atm (ref. 9), seeding of the propellant with either a gas having a low ionization potential or with submicron-sized particles of a highly absorbing material is necessary to heat the hydrogen and to attenuate the radiant energy which would normally see the structural wall. The submicron-sized particles are preferred for seeding since they absorb over a broad wavelength range up to the time of vaporization instead of exhibiting the predominately line absorption characteristics common to most gases. It is desired that, once it is vaporized, the seed material will exhibit sufficiently broad line absorption characteristics to absorb the radiant energy and heat the hydrogen; however, selection of a seed material is not possible at this time since little information is available on the absorption characteristics of vaporized seeds, nor has it been

clearly demonstrated that a satisfactory seed material exists.

When a satisfactory seed material is found it should be suitable for use in both engine systems since the basic requirements for each are quite similar and vary only in detail. The primary difference between the systems is the seed density required to heat the propellant and at the same time to keep the radiant energy on the outer wall to an acceptable level. McLafferty (ref. 10) indicates that at a normal optical depth of 3.0, 95 percent of the incident energy would be absorbed by the seeds and that 98 percent would be absorbed if scattering is taken into account. On the basis of the light bulb dimensions, a seed density of approximately 4 percent of the inlet propellant density would then be required for an average seed absorption parameter of 5000 cm^2/g. Since the propellant region of the coaxial-flow system is physically much larger than that of the light bulb (feet versus inches), the required seed density will be lower. In either case, however, the quantity of seed required will have a minor effect on the engine performance when compared with other limiting factors.

CONCLUSIONS

In conclusion, the research to date on the nuclear light bulb and the coaxial-flow gaseous-core reactors indicates that either system may be practical, but there are insufficient data to say whether either system can be built in useful form. Assuming that the feasibility of both systems can be shown, the following observations can be made:

(1) Neutronics will require that the coaxial-flow reactors be physically large and performance requirements will dictate that these large reactors operate at thrust levels of 500 000 lb or greater in order to provide ratios of engine thrust to weight greater than one.

(2) The nuclear light bulb appears to be feasible neutronically in much smaller sizes than those of the coaxial-flow systems with a 100 000-lb thrust possible.

(3) The wall heating problems in either system appear to be well within engineering solution for the first-generation engines.

(4) The performance of the nuclear light bulb will be limited by the transparent wall. If selective spectrum seeding is shown to be feasible, fuel radiating temperatures up to approximately 20 000° R may be possible. However, if such seeding is not effective, the maximum fuel radiating temperature will be less than 15 000° R and, therefore, the maximum specific impulse will be less than 1800 sec.

(5) The performance of the coaxial-flow system will be limited by moderator and nozzle cooling but should have a specific impulse potential of 2500 to 3000 sec.

(6) Although ratios of propellant to fuel mass flow rates of several hundred are desirable in the open-cycle system, the data from the isothermal fluid mechanics experiments indicate that the maximum achievable flow ratios, consistent with fuel volume fraction requirements, will be on the order of 50 to 1.

REFERENCES

1. LATHAM, T. S.: Nuclear Studies of the Nuclear Light Bulb Rocket Engine. (Rept. G–910375–3, United Aircraft Res. Lab., Sept. 1968.) NASA CR–1315, 1968.
2. RAGSDALE, R. G.: Are Gas Core Nuclear Rockets Attainable? NASA TM X–5245, 1968.
3. ROM, F. E.: Nuclear Rocket Propulsion. NASA TM X–1685, 1968.
4. KRASCELLA, N. L.: Theoretical Investigation of the Radiant Emission Spectrum From the Fuel Region of a Nuclear Light Bulb Engine. Rept. H–910092–12, United Aircraft Res. Lab., Oct. 1969.
5. JOHNSON, B. V.: Exploratory Experimental Study of the Effects of Inlet Conditions on the Flow and Containment Characteristics of Coaxial Flows. Rept. H–910091–21, United Aircraft Res. Lab., Sept. 1969.
6. LANZO, C. D.: A Flow Experiment on a Curved-Porous-Wall Gas Core Reactor Geometry. NASA TM X–1852, 1969.
7. TRAVERS, A.: Experimental Investigation of Radial-Inflow Vortexes in Jet-Injection and Rotating-Peripheral-Wall Water Vortex Tubes. Rept. F–910091–14, United Aircraft Res. Lab., Sept. 1967.
8. ROMAN, W. C.; KLEIN, J. F.; AND VOGT, P. G.: Experimental Investigations to Simulate the Internal Environment, Transparent Walls, and Propellant Heating in a Nuclear Light Bulb Engine. Rept. H–910091–19, United Aircraft Res. Lab., Sept. 1969.
9. KRASCELLA, N. L.: Tables of the Composition, Opacity

and Thermodynamic Properties of Hydrogen at High Temperatures. (Rept. B-910168-1, United Aircraft Res. Lab., Sept. 1963.) NASA SP-3005, 1963.

10. McLafferty, G. H.; and Bauer, H. E.: Studies of Specific Nuclear Light Bulb and Open-Cycle Vortex-Stabilized Gaseous Nuclear Rocket Engines. (Rept. F-910093-37, United Aircraft Res. Lab., Sept. 1967.) NASA CR-1030, 1968.

DISCUSSION

Thom: A 1000-atm pressure in the reactor is very high. It is in the pressure range of heavy artillery. Could a machine work continuously and reliably under such stresses?

Franklin: Chemical systems, for example, were designed 5 years ago to operate at 500 psi.

Winterberg: This is correct. Ammonia synthesis uses a pressure of about 1000 atm.

Thom: How about thermal stresses?

Franklin: Most of the energy will be deposited in the moderator over a substantial width of material and it appears that the thermal stresses will therefore be within acceptable levels.

Williams: What happens to the 20 percent of the thermal radiation which is absorbed in the oxygen and is not transmitted to the hydrogen?

Franklin: Either there will be high oxygen flow rates because the heated oxygen will put a load on the recycle system or the oxygen will reradiate back into the plasma. The flow rates will probably be high, so there would be a limit on the recycle system.

Page intentionally left blank

Relationship Between Engine Parameters and the Fuel Mass Contained in An Open-Cycle Gas-Core Reactor

ROBERT G. RAGSDALE

NASA Lewis Research Center

The major features of an open-cycle gaseous-fueled nuclear rocket engine are that it provides high specific impulse and high thrust but loses some uranium fuel during operation. An analysis is carried out to relate the amount of uranium that would be contained in such an engine to engine performance parameters. The parameters considered are: Cavity diameter, reactor pressure, engine thrust, specific impulse, and the hydrogen-to-uranium flow rate ratio.

Several auxiliary equations are developed as a part of the analysis. Recent fluid mechanics experimental data are used to show that the fraction of the reactor cavity filled with uranium is inversely proportional to the approximate cube root of the hydrogen-to-fuel flow rate ratio. Equations are also developed that give the uranium density and opacity as a function of reactor pressure and fuel temperature. These equations are incorporated into a simplified radiant heat transfer equation.

The major results of this study are:

(1) The mass of uranium contained in the reactor cavity M_F is given by

$$M_F = 0.14 \frac{D_c^{3.3} P^{0.7}}{F^{0.29} I_{sp}^{0.26} \left(\frac{\dot{w}_{H_2}}{\dot{w}_F} \right)^{0.36}}$$

where D_c is the reactor cavity diameter in feet, P is the pressure in atmospheres, F is the thrust in pounds, I_{sp} is the specific impluse in seconds, and $\left(\frac{\dot{w}_{H_2}}{\dot{w}_F} \right)$ is the hydrogen-to-fuel flow rate ratio.

(2) The uranium loss rate can be decreased by a factor of 4 by decreasing the thrust by a factor of 6.

(3) The engine thrust can be increased by a factor of 12 if the critical mass can be decreased by a factor of 2.

(4) The uranium loss rate can be reduced by a factor of 7 if the critical mass can be reduced by a factor of 2.

The feasibility of using gaseous uranium to power a nuclear rocket engine has been under investigation for over 10 years. The advantage of such an engine is the combination of high specific impulse (1500 to 3000 sec) and high thrust (10^5 to 10^6 lb). The disadvantage of a gas-core engine is that it would be a heavy (250 000 to 500 000 lb), high-pressure (1000 atm) device. In addition, either some uranium would be exhausted along with the hydrogen propellant or the uranium would be encapsulated within a transparent fuel element. An open-cycle engine is one that allows direct contact between the fuel and the propellant. A closed-cycle engine employs some solid but transparent barrier between the fuel and the propellant. The objective of the research studies has been to determine if the good of this system outweighs the bad. Reference 1 presents a review of some early vortex open-cycle work and the current closed-cycle work and has a bibliography of 225 papers. Reference 2 reviews some recent open-cycle work and has a bibliography of 78 papers.

The present study is concerned with the uranium containment characteristics of an open-cycle gas-core engine. Figure 1 depicts the essential features of such an engine. The amount of uranium con-

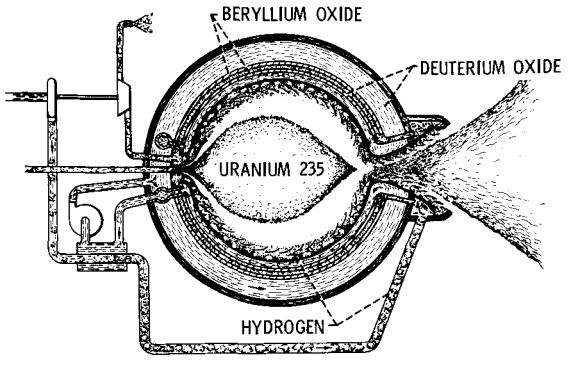

FIGURE 1.—*Conceptual gas-core nuclear rocket engine.*

tained in an engine would be influenced by a number of factors such as the hydrogen flow rate, uranium flow rate, and reactor pressure. Though it is perhaps not so obvious, engine thrust level, engine specific impulse, and cavity diameter also play a role. It is the purpose of the present study to tie all of these parameters together. One would hope to produce equations, tables, or graphs that would display the interrelationships and tradeoffs available between the uranium mass that would reside in an engine and all of the engine parameters that are involved.

It is important to realize that the uranium mass content of any given engine would not actually be a variable. For a specific engine cavity size surrounded by a given thickness and distribution of moderator materials, there is but one mass of uranium—the critical mass—that will maintain a controlled chain reaction. At least, that is true so long as the gaseous uranium fuel occupies most or all of the cavity volume. Thus the results of this study will disclose what combinations of thrust, pressure, uranium flow rate, etc. one could employ to meet the critical mass requirement of a given engine configuration.

The importance of this study resides more in the trends and the forms of the relationships developed than in the absolute numbers. Obviously, an attempt has been made to use the best information available and to center the calculations in the regions of most probable interest. However, research is still underway on gas-core problems and it will probably produce new and better numbers than some used in this study.

Therefore it will be more important, and probably more accurate, to find that an increase in thrust by a factor of 12 decreases the uranium mass contained in the engine by a factor of 2 than it will be to determine the actual value in kilograms for a particular case. However, some specific cases are presented in order to illustrate the kinds of tradeoffs between parameters that are available.

SYMBOLS

D	diameter, ft
F	thrust, lb
H	propellant exit enthalpy, Btu/lb
I_{sp}	specific impulse, sec
k	fuel wavelength-averaged absorption coefficient, ft^{-1}
M	mass, kg
n	temperature exponent in eq. (4)
P	reactor pressure, atm
Q	reactor power level, MW
$\overline{R}$	radial position in fuel normalized to fuel edge radius
T	temperature, °R
V	volume, ft^3
$\dot{w}$	flow rate, lb/sec
ρ	density, lb/ft^3

Subscripts:

c	cavity
F	uranium fuel
H_2	hydrogen propellant

ANALYSIS

Basically the analysis is quite simple. The mass of uranium fuel in the engine cavity is given simply by the uranium density times the volume occupied by the fuel. That is,

$$M_F = \rho_F V_F \tag{1}$$

The analysis consists of relating the fuel density and volume to the engine parameters that determine them. Roughly speaking, the fuel volume is determined by the fluid mechanics phenomena in the cavity, and the fuel density, by the radiant heat transfer process. That is not precisely so, but it does give a good idea of the relationships.

The specific pieces of information required are as follows: (1) The fuel volume as a function of cavity size, cavity shape, and hydrogen and ura-

nium flow rates; (2) the fuel equation of state; (3) the fuel opacity; and (4) a radiant heat transfer relation. These equations are developed in the following sections. They are then substituted into equation (1) to obtain the final result.

Fuel Volume

Although the gaseous uranium fuel would not really reside in a central volume undiluted with hydrogen as shown in figure 1, it is convenient to say that it does. Such an assumption is not grossly in error, so long as the smaller "effective" fuel volume is defined such that the total amount of uranium in this volume is the same as that when it is distributed in the entire cavity volume and diluted with hydrogen. Thus, the effective volume is the volume that would be occupied by the uranium in an engine if it were all gathered together in a central volume of pure fuel. It would still be at its original temperature, and the reactor pressure would also be unchanged. Therefore, the total mass of uranium in the engine would be the same as that in the original situation. It was shown in reference 3 that the idea of an effective fuel volume is useful when comparing various gas-core fluid flow experimental results with each other and with engine requirements.

To get away from absolute numbers, it is convenient to express the fuel volume as a fraction of the cavity volume. In a similar manner, the hydrogen and uranium flow rates are expressed as a ratio. These two parameters, the fuel volume fraction and the hydrogen-to-uranium flow rate ratio, can be used to describe both engine performance and fluid mechanics experimental results (ref. 3).

The results of two recent gas-core fluid mechanics experiments are shown in figure 2 on these coordinates. The tests were conducted at or near room temperature and pressure. Air was used to simulate the propellant and either air or freon was used to simulate the uranium fuel. These gases give fuel-to-propellant density ratios of 1 to 1 for air-air and 4.7 to 1 for air-freon. This range should encompass density ratio conditions expected in an engine (ref. 3).

The broken line through the upper set of data shows that a slope of about $-\frac{1}{2}$ represents these data pretty well. The lower set of data is a better fit with a slope of $-\frac{1}{6}$. For the present calculations the solid line shown was used to represent some kind of average of both sets of data. The line has a slope of $-\frac{1}{3}$. The equation used is:

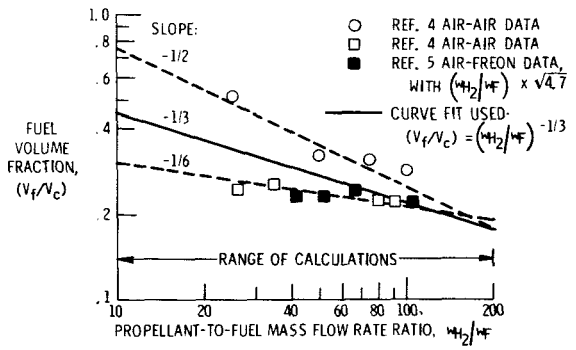

FIGURE 2.—*Curve fit of fuel volume fraction from flow experiments.*

$$\left(\frac{V_F}{V_c}\right)=\left(\frac{\dot{w}_{H_2}}{\dot{w}_F}\right)^{-1/3} \tag{2}$$

This equation is used in the present analysis to determine the fuel volume V_F as a function of hydrogen-to-uranium flow rate ratio and of the cavity size.

The two sets of data shown in figure 2 were obtained from experimental rigs that had significantly different geometries. It is therefore not surprising that the data do not coincide. The upper set of data represents air-air flow through a curved, porous-wall test section. These tests were conducted at a relatively low Reynolds number of about 1100 and are described in reference 4. The lower data were obtained in a section with straight coaxial-flow cylindrical geometry. These tests are described in reference 5. Results from both air-air and air-freon are shown in figure 2. Both sets of data fall together if the freon mass flow rate ratio $\dot{w}_{H_2}/\dot{w}_F$ is multiplied by the square root of the freon-to-air density ratio, a procedure suggested in reference 6. These tests were conducted at jet Reynolds numbers from 4000 to 40 000 corresponding to those anticipated in an engine. The results of these tests showed that there was no significant effect of Reynolds number.

Fuel Density

The present calculations require an expression for fuel density as a function of pressure and temperature. Uranium density calculations have been

reported in reference 7 at gas-core reactor conditions.

The results of these computer calculations are shown as solid lines in figure 3. The broken curves

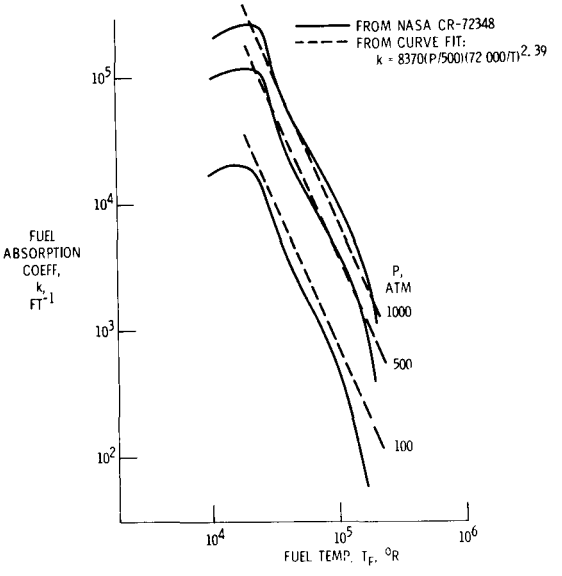

FIGURE 3.—*Curve fit of fuel density.*

are from the curve fit equation used in this study

$$\rho_F = 0.76\left(\frac{P}{500}\right)\left(\frac{72\,000}{T}\right)^{1.77} \qquad (3)$$

where the density is in pounds per cubic foot, the pressure is in atmospheres and the temperature is in degrees Reaumur. This relatively simple equation represents the fuel density variation quite well in the range of interest pressure from 100 to 1000 atm and temperature from 20 000° to 200 000° R.

Fuel Opacity

Fuel opacity information is required to determine the fuel temperature as a function of reactor power and fuel region size. Uranium absorption coefficients are reported in reference 7. They are shown in figure 4 as a function of pressure and temperature. The solid curves are from the computer calculations of reference 7. The broken curves are from the curve fit equation used in the present study

$$k = 8370\left(\frac{P}{500}\right)\left(\frac{72\,000}{T}\right)^{2.39} \qquad (4)$$

where the wavelength-averaged absorption coefficient k is in inverse feet, pressure is in atmospheres, and temperature is in degrees Reaumur. As with density, this simple equation is of adequate accuracy over the range of interest.

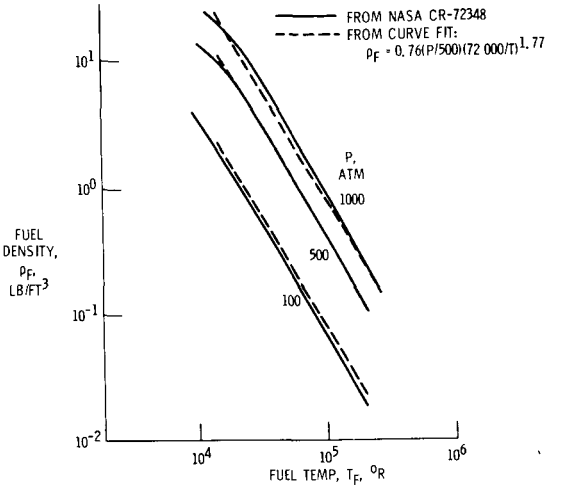

FIGURE 4.—*Curve fit of fuel absorption coefficient.*

Radiant Heat Transfer

Approximate equations for gaseous radiant heat transfer presented in reference 8 were modified for use in the present analysis. Equation (30) of reference 8 gives the gas temperature as a function of radius, edge heat flux, and optical diameter τ, which is the product of the absorption coefficient and the diameter. This equation is for an absorption coefficient that is given by cT^n. For uranium, n is -2.39 as given by equation (4).

It was necessary to simplify the form of equation (30) in order to obtain an analytic expression for the average fuel temperature. For values of τ greater than 1000, equation (30) of reference 8 simplifies to:

$$\frac{T}{T_e} = \left[\frac{3(4-n)}{32}\,\tau_e\left(\frac{q_e}{\sigma T_e^4}\right)(1-\bar{R}^2)\right]^{1/4-n} \qquad (5)$$

For all conditions of the present calculations τ is greater than 1000, so this approximation can be used. Figure 5 shows a comparison of equation (5) with equation (30) of reference 8 for conditions typical of the present calculation range. The two equations give nearly identical results.

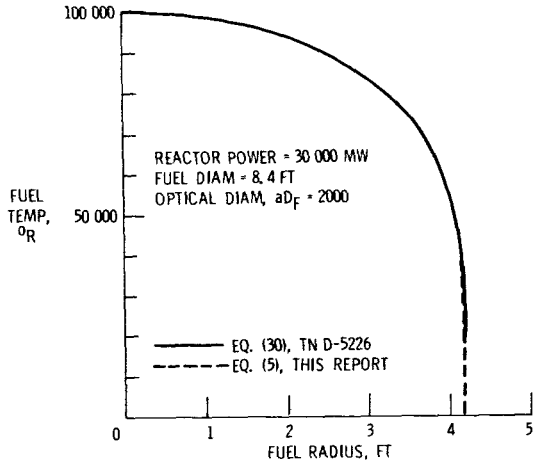

FIGURE 5.—*Fuel temperature distribution.*

The radial temperature distribution, given by equation (5), and the fuel density, given by equation (3), were used to obtain a mass-weighted average fuel temperature. Some appropriate manipulations produce the equation for the average fuel temperature in degrees Reaumur.

$$T_F = 14\,000\left(\frac{PQ_r}{D_F}\right)^{0.16} \tag{6}$$

where P is the reactor pressure in atmospheres, Q_r is the reactor power in megawatts, and D_F is the fuel diameter in feet.

Equation (6) can be rewritten in terms of engine parameters of interest by using the following relations. Engine thrust in pounds is given by

$$F = \dot{w}_{H_2} I_{sp} \tag{7}$$

where $\dot{w}_{H_2}$ is in pounds per second and I_{sp} is in seconds. The reactor power in megawatts is given by

$$Q_r = \left(\frac{(\dot{w}_{H_2} H)}{950}\right) \tag{8}$$

where $\dot{w}_{H_2}$ is in pounds per second and the propellant chamber exit enthalpy H is in British thermal units per pound. Specific impulse in seconds is related to the propellant chamber exit enthalpy H in British thermal units per pound by an overall nozzle efficiency, which was taken as 0.85 in this study:

$$I_{sp} = 0.85\sqrt{\frac{2JH}{g}} \tag{9}$$

Finally, reference 9 has shown that the average fuel temperature of a pure uranium region would be reduced by about 12 percent due to dilution by the surrounding hydrogen.

Taking this into account and combining equations (6) through (9) and (2) give:

$$T_F = 2450\left(\frac{PFI_{sp}}{D_c}\right)^{0.16}\left(\frac{\dot{w}_{H_2}}{\dot{w}_F}\right)^{0.017} \tag{10}$$

Equation (10) gives the average fuel temperature in degrees Reaumur as a function of engine parameters.

Uranium Fuel Mass in Engine

Equations (3) to (10) can be used to rewrite equation (2) for the fuel mass in the engine. Doing so gives:

$$M_F = 0.14\frac{D_c^{3.3}P^{0.72}}{F^{0.28}I_{sp}^{0.28}\left(\frac{\dot{w}_{H_2}}{\dot{w}_F}\right)^{0.36}} \tag{11}$$

This equation gives the fuel mass in kilograms as a function of engine parameters. The cavity diameter D_c is in feet; the engine pressure P is in atmospheres; engine thrust F is in pounds; specific impulse I_{sp} is in seconds; and the hydrogen-to-fuel flow rate ratio $(\dot{w}_{H_2}/\dot{w}_F)$ is dimensionless. Equation (11) was used to examine the effect on uranium mass of the various parameters and to illustrate some of the tradeoffs available between them.

RESULTS AND DISCUSSION

There are a near-endless number of forms into which equation (11) can be cast. They are all easy to obtain. For that reason, only some of the more important or interesting relationships are presented and discussed. The following effects are shown and discussed:

(1) The effect of thrust on fuel temperature
(2) The effect of reactor pressure on fuel mass in the engine
(3) The tradeoff between thrust and uranium loss rate
(4) The relationship between thrust and fuel mass present in the engine
(5) The relationship between fuel loss rate and fuel mass present in the engine

In addition to these specific variations, table I gives the mass of uranium fuel that would be in an engine for various values of the variables in equa-

TABLE I.—*Fuel Mass in Engine for* I_{sp}*=1500 Sec*

$\frac{\dot{w}_{H_2}}{\dot{w}_F}$	Fuel mass in engine, kg, for reactor pressure, atm, of—								
	100			500			1000		
	Engine cavity diameter, ft								
	8	12	16	8	12	16	8	12	16
Engine thrust = 100 000 lb									
10	8.4	32	81	27	101	260	44	167	429
50	4.7	18	46	15	57	146	25	94	241
100	3.7	14	36	12	44	114	19	73	188
200	2.9	11	28	9.1	35	89	15	57	147
Engine thrust = 500 000 lb									
10	5.3	20	52	17	65	166	28	107	275
50	3.0	11	29	9.6	36	94	16	60	154
100	2.3	8.9	23	7.5	28	73	12	47	120
200	1.8	6.9	18	5.9	22	57	10	37	94
Engine thrust = 1 000 000 lb									
10	4.4	17	43	14	53	137	23	88	227
50	2.5	9.4	24	8	30	77	13	50	127
100	1.9	7.3	19	6.2	23	60	10	39	99
200	1.5	5.7	15	4.8	18	47	8.0	30	78

tion (11). The entire table is for an arbitrary value of I_{sp} of 1500 sec. The entire table can be converted easily to correspond to any other desired specific impulse since, according to equation (11), uranium mass varies as specific impulse to the 0.28 power. Thus, for an impulse of 1000 sec, the values in table I should be multiplied by 0.89; and, for an impulse of 2000 sec, they should be multiplied by 1.12. For a given cavity diameter and moderator materials and thicknesses, one might determine that a critical mass of 50 kg would be required. Table I would then show what combinations of thrust, reactor pressure, and hydrogen-to-uranium flow rate ratio correspond to this requirement.

Average Fuel Temperature

Higher engine thrust requires higher reactor power. This in turn requires a higher fuel temperature to radiate the increased power to the surrounding hydrogen propellant. This effect is illustrated in figure 6. The curves shown are for a cavity of 12 ft, a specific impulse of 1800 sec, and a hydrogen-to-fuel flow rate ratio of 100. All of these values are in the range of interest.

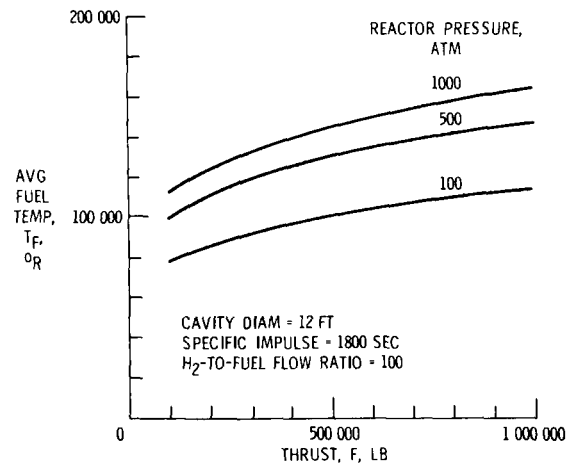

FIGURE 6.—*Average fuel temperature.*

Fuel temperature is relatively insensitive to engine thrust level. For example, consider a reactor

pressure of 500 atm. As thrust level increases from 100 000 to 1 000 000 lb, the average fuel temperature increases from 100 000° to 146 000° R. Higher reactor pressure causes higher fuel temperature because the fuel opacity increases in proportion to the pressure. But again the increase is slight.

Reactor Pressure

Although reactor pressure affects the fuel opacity which in turn affects the fuel temperature, the effect is not a major one. The important effect of reactor pressure is that it changes the fuel density. Thus an increase in reactor pressure results in more uranium in the engine cavity.

This is illustrated in figure 7. The curve shown

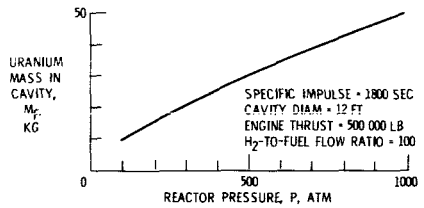

FIGURE 7.—*Effect of reactor pressure on mass of uranium in cavity.*

is for values of specific impulse, cavity diameter, engine thrust, and hydrogen-to-uranium flow rate ratio that are centered in the range of interest. Fuel mass is almost linearly proportional to reactor pressure. A pressure increase from 100 to 1000 atm increases the fuel mass from 10 to 50 kg.

This is about the range of critical masses that is likely to be required in an engine (ref. 9). On the basis of experiments in a 6-ft-diam cavity, a critical mass between 20 and 30 kg might be expected. If critical mass increases as does the diameter, then the critical mass should be between 40 and 60 kg for a 12-ft-diam cavity. If critical mass increases as does the diameter squared, then 80 to 120 kg might be required. The critical mass will probably be affected by about a factor of 2 depending upon whether ^{235}U or ^{233}U is used and also upon how much hot hydrogen propellant is in the cavity between the fuel and the surrounding moderator (ref. 9). The exact cavity reactor neutronics remain to be worked out. About the best that can be said now is that a reasonable guess at a critical mass in a 12-ft-diam cavity is 50 kg; there may be some possibility of reducing this value to 25 kg, and also some possibility that 100 kg might be required.

Engine Thrust and Uranium Loss Rate

With all other parameters fixed, a tradeoff exists between engine thrust level and the uranium loss rate. This is illustrated in figure 8 for a specific

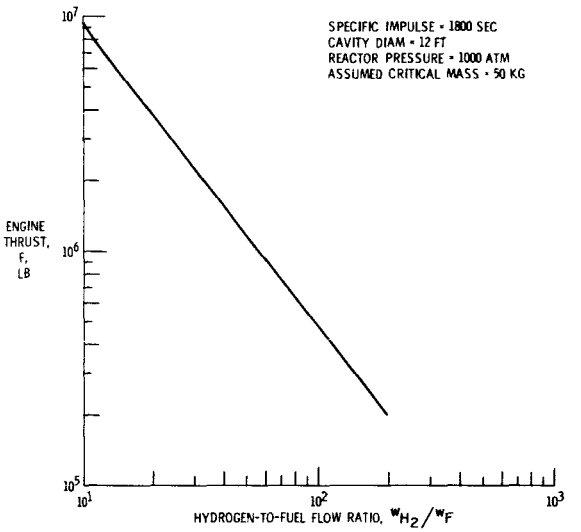

FIGURE 8.—*Tradeoff between thrust and uranium loss rate.*

impulse of 1800 sec, a cavity diameter of 12 ft, a reactor pressure of 1000 atm, and a uranium mass of 50 kg. Thus, for these values of the other parameters, if the uranium flow rate were decreased from $\frac{1}{50}$ of the hydrogen flow rate to $\frac{1}{200}$ of it, the thrust would have to be decreased from 1.2 million down to 200 000 lb. That is, decreasing the uranium loss rate by a factor of 4 was accomplished by decreasing the thrust by a factor of 6.

Engine Thrust and Fuel Mass

An increase in engine thrust causes a decrease in fuel mass present in the engine when the other parameters are held constant. The relationship is illustrated in figure 9. This particular curve is for a specific impulse of 1800 sec, a cavity diameter of 12 ft, a reactor pressure of 1000 atm, and a hydrogen-to-fuel flow rate ratio of 100.

This curve shows that a significant increase in engine thrust causes only a moderate decrease in the amount of fuel present in the engine. Specifically, a

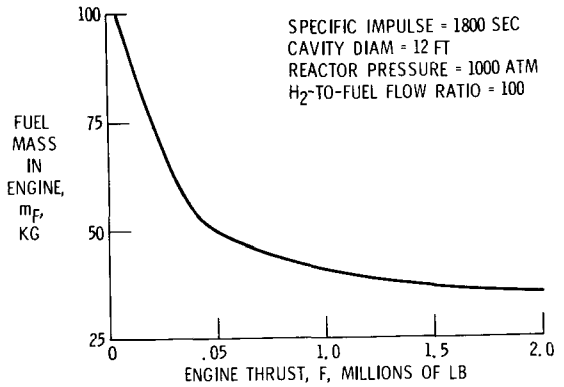

FIGURE 9.—*Effect of thrust level on uranium mass in engine.*

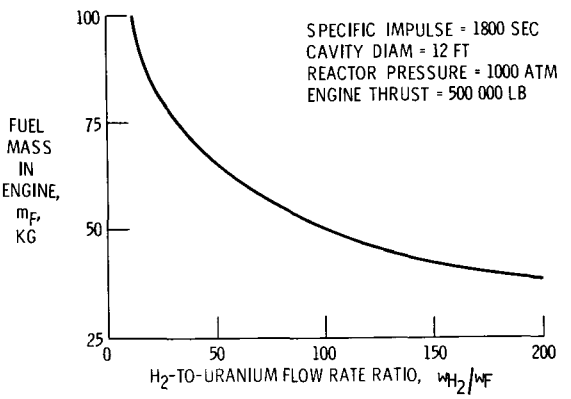

FIGURE 10.—*Effect of uranium loss rate on uranium mass in engine.*

factor of 12 increase in thrust decreases the fuel mass present in the engine by a factor of 2. The mathematical reason for this relationship is simply that fuel mass varies inversely as thrust to the 0.28 power, as given by equation (1), and 12 to the 0.28 power is 2.

The physical reason for the relationship is as follows. An increase in thrust at a constant specific impulse is achieved by increasing both the hydrogen flow rate and the reactor power. In order to transfer the increased power, the fuel temperature rises. However, the required fuel temperature has to increase as the thrust only to the 0.16 power, as given by equation (10). The higher fuel temperature causes a lower fuel density, according to equation (3). It is the decreased fuel density that causes less fuel to be present.

This curve shows how important the critical mass requirement of an engine is. A reduction in critical mass by a factor of 2 would allow the engine thrust to be increased by a factor of 12.

Uranium Loss Rate and Fuel Mass

If one could contrive to reduce the critical mass requirement of a given engine configuration, the resulting dividend would not necessarily be collected in the form of increased thrust. For example, one could choose instead to decrease the uranium loss rate. This option is depicted in figure 10. The curve shown is for a specific impulse of 1800 sec, a cavity diameter of 12 ft, a reactor pressure of 1000 atm, and an engine thrust of 500 000 lb.

This curve again shows the potential gain available if critical mass reductions can be realized. A reduction in critical mass by a factor of 2 could be translated into a reduction in the uranium loss rate by a factor of 7. The mathematical reason for this relationship is that fuel mass varies inversely as the hydrogen-to-fuel flow ratio to the 0.36 power. The physical reason is that a decrease of the uranium flow rate, at constant hydrogen flow rate, decreases the fuel volume and therefore the fuel mass in the engine.

The main point of figure 10, as with figure 9, is that the critical mass requirement of a gas-core engine is an important parameter. Any way that can be found to reduce the critical mass requirement of a gas-core engine will produce significant gains. There are many choices as to how to use such an advantage. Increased thrust or decreased uranium loss rate were the two ways illustrated. Reduced reactor size or pressure are two other possible ways to use the advantage. The choice among these options in an actual case would be determined by many factors not considered here, such as mission requirements and engine reliability. The main point here is that equation (11) gives the interrelation among the various engine parameters, so that subsequent choices can be made.

SUMMARY OF RESULTS

An analysis was carried out to determine how the amount of gaseous uranium fuel contained in an open-cycle gas-core rocket reactor is affected by various engine parameters. The latest results from gas-core fluid mechanics experiments and from

uranium plasma composition and opacity theory are incorporated. The engine parameters considered were cavity diameter, reactor pressure, engine thrust, engine specific impulse, and the hydrogen-to-uranium flow rate ratio.

Recent fluid mechanics data are used to show that the fraction of the reactor cavity filled with fuel varies inversely as the approximate cube root of the hydrogen-to-uranium flow rate ratio. Equations are also developed for uranium density and uranium opacity as a function of fuel temperature and reactor pressure. These equations are then combined with a simple equation for radiant heat transfer in the fuel region.

The major results of this study are as follows:

(1) The mass of uranium in kilograms M_F is given in terms of the cavity diameter in feet D_c, the reactor pressure in atmospheres P, the thrust in pounds F, the specific impulse in seconds I_{sp}, and the hydrogen-to-uranium flow rate ratio $(\dot{w}_{H_2}/\dot{w}_F)$ by:

$$M_F = 0.14 \frac{D_c^{3.3} P^{0.7}}{F^{0.28} I_{sp}^{0.28} \left(\frac{\dot{w}_{H_2}}{\dot{w}_F}\right)^{0.36}}$$

(2) The uranium loss rate can be decreased by a factor of 4 by decreasing the thrust by a factor of 6.

(3) The engine thrust can be increased by a factor of 12 if the critical mass can be reduced by a factor of 2.

(4) The uranium loss rate can be reduced by a factor of 7 if the critical mass can be reduced by a factor of 2.

REFERENCES

1. McLafferty, George H.: Investigation of Gaseous Nuclear Rocket Technology—Summary Technical Report. Rept. H-910093-46, United Aircraft Res. Lab., Nov. 1969.
2. Rom, Frank E.: Comments on the Feasibility of Developing Gas Core Nuclear Reactors. Paper presented at Frontiers of Power Technol. Conf., Okla. State Univ. (Stillwater, Okla., Oct. 23–24, 1969), 1969.
3. Ragsdale, Robert G.: Are Gas-Core Nuclear Rockets Attainable? Paper 68-570, AIAA, June 1968.
4. Lanzo, Chester D.: A Flow Experiment on a Curved-Porous-Wall Gas-Core Reactor Geometry. NASA TM X-1852, 1969.
5. Johnson, Bruce V.: Exploratory Experimental Study of the Effects of Inlet Conditions on the Flow and Containment Characteristics of Coaxial Flows. Rept. H-910091-21, United Aircraft Res. Lab., Sept. 1969.
6. Johnson, Bruce V.: Experimental Study of Multi-Component Coaxial-Flow Jets in Short Chambers. NASA CR-1190, 1968.
7. Parks, D. E.; Lane, G.; Stewart, J. C.; and Peyton, S.: Optical Constants of Uranium Plasma. (Rept. GA-8244, Gulf Gen. Atomic, Inc.) NASA CR-72348, 1968.
8. Ragsdale, Robert G.; and Kascak, Albert F.: Simple Equations for Calculating Temperature Distributions in Radiating Gray Gases. NASA TN D-5226, 1969.
9. Kunze, J. F.; Pincock, G. D.; and Hyland, R. E.: Cavity Reactor Critical Experiments. Nucl. Appl., vol. 6, no. 2, Feb. 1969, pp. 104–115.

DISCUSSION

Schneider: What is the temperature of uranium plasma at a 12-atm pressure?

Ragsdale: The temperature is a function of power, but generally it is around 100 000° R. On the edge of the fuel there is a relatively steep temperature gradient. The model of the fuel is very much like that of the Sun: It is optically thick, the heat is generated inside, and the internal temperature might get as high as 150 000° R. The edge temperature might be as low as 30 000° R, but the average is about 100 000° R.

Schneider: What is the lowest temperature that will still result in an interesting performance?

Ragsdale: I would say 20 000° R.

Schneider: This is very interesting because we can achieve these temperatures in experiments. Also, what is the lowest pressure less than 100 atm if you lower the temperature?

Ragsdale: Usually one would want the pressure to be as high as possible in order to reduce uranium losses.

Schneider: Yes, I am aware of this. What is the lowest pressure possible for a meaningful experiment?

Ragsdale: With an experiment at, say, 10, 50, or 100 atm, one can expect to observe essential features of the plasma.

Chang Ho: The critical mass seems to depend a great deal on the diffusion of the fuel within the cavity. Would you comment about stability and control?

Ragsdale: The control problem has been only slightly investigated. It involves nucleonics, fluid mechanics, and heat transfer and is quite complicated. There are competing mechanisms at work. For example, fuel may move into a higher neutron flux region and form a region of higher power which would tend to increase temperature and pressure and might also tend to move the fuel out. But at the

same time, the fuel is moving into a much faster moving gas stream which tends to either push it back in or carry it out of the cavity. There are some papers in Sessions II and IV that discuss part of the stability problem.

Stratton: The mass of the pressure vessel depends on the square of the radius, principally because of the neutronics. Are there scaling laws that relate optimum size, thrust, and power?

Ragsdale: First, one has to define the parameter with respect to which the engine is optimum. One can minimize the engine weight by varying the moderator thickness. If one makes the moderator thinner, a higher critical mass is required and a higher pressure is necessary, which necessitates a thicker and heavier pressure shell. So, by varying the moderator thickness, a minimum in engine weight could be obtained.

Summary of Research on the Nuclear Light Bulb Reactor[1]

JAMES W. CLARK AND GEORGE H. MCLAFFERTY
United Aircraft Research Laboratories

The objectives of this paper are to outline the overall nuclear light bulb research program and to summarize the progress that has been made in the major areas. In addition, those factors that have limited progress to date will be discussed; these are the research areas that are receiving major emphasis at the present time. There are five other detailed papers on the nuclear light bulb in the present symposium proceedings. Further details are presented in references 1 through 6.

ENGINE CONCEPT

Figure 1 is a schematic of a unit cell of a nuclear light bulb engine. Gaseous nuclear fuel (uranium-233) is contained in a vortex flow in the central region of the cavity. Hydrogen propellant, seeded with tungsten particles to increase its opacity, flows axially in an annular propellant duct. A thin, internally cooled, fused silica transparent wall is located between the fuel and propellant. The energy from the fissioning fuel is transmitted by thermal radiation through the wall to the propellant. The fuel is kept away from the wall by neon buffer gas that is injected from the wall to drive the vortex. Fuel is injected through the end wall as a liquid or as particles with a carrier gas. Flow consisting of buffer gas, fuel, and fission products is withdrawn at one or both end walls and enters a fuel recycle system.

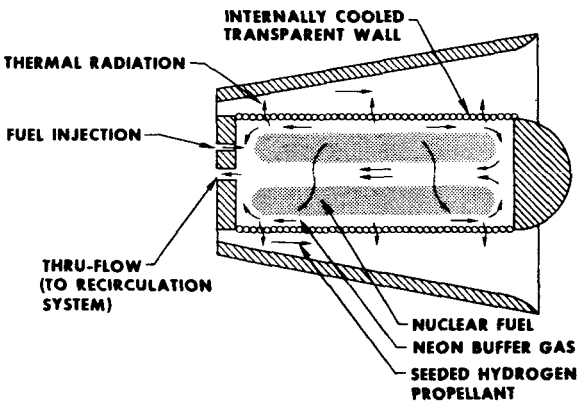

FIGURE 1.—*Concept of nuclear light bulb engine.*

In the full-scale engine, this unit cavity would be about 6 ft long, and the diameter of the transparent wall would be about 16 in. Seven unit cavities would be clustered in a hexagonal array with an internal moderator.

The major performance characteristics of the reference full-scale engine design are: Power, 4600 MW; specific impulse, 1870 sec; thrust, 92 000 lb; weight, 70 000 lb; and pressure, 500 atm. The important parameters to note are the specific impulse (1800 to 1900 sec) and the engine weight and thrust levels (on the order of 100 000 lb). This reference engine would operate at 500 atm and the total radiant heat flux from the fuel would correspond to that of a blackbody at 15 000° R. It is the standard engine used for planning the nuclear light bulb research program.

NUCLEAR LIGHT BULB RESEARCH PROGRAM

Some research has been conducted on all aspects of the engine concept, either as part of the NASA program or under the United Aircraft internal research program. The basic approach, however, has been to single out and concentrate on those funda-

[1] This research was supported by the joint AEC–NASA Space Nuclear Propulsion Office under contracts NASw–847 and SNPC–70.

mental problem areas necessary for determining the feasibility of the concept.

The current nuclear light bulb research program can be outlined as follows:

(1) Simulation of thermal environment:
  (*a*) Radiant energy source research
  (*b*) Transparent-wall model research
  (*c*) Propellant heating research
  (*d*) Supporting research
(2) Engine dynamics and startup analyses
(3) Radiation heat transfer analyses
(4) Optical absorption in fused silica

Most of the current research effort is in these four main areas. The major effort is concerned with simulating the thermal environment in the engine. The ultimate objective is to conduct a nonnuclear experiment which demonstrates the principle of operation of the engine while as many of the important factors as possible are simulated. As stated in the outline, the four areas of research involved are: Development of a radiofrequency (rf) plasma radiant energy source, development and testing of transparent-wall models, radiant heating of propellant streams seeded with particles, and supporting vortex fluid mechanics and rf plasma studies. The most important features of this work are discussed in the next section.

SIMULATION OF THERMAL ENVIRONMENT

The basic components used in the rf experiments are shown schematically in figure 2. A pair of

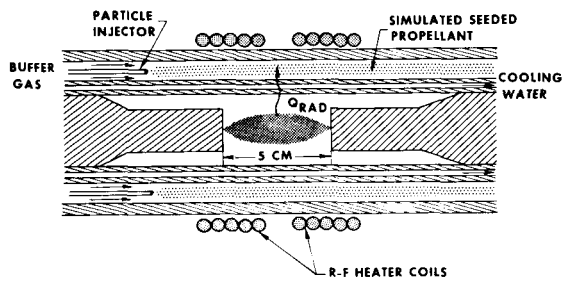

FIGURE 2.—*Geometry of radiant energy source.*

cylindrical, copper, water-cooled end walls are located along the centerline of the assembly. The faces of these end walls are 5 cm apart. Argon is injected from the end walls or from the peripheral wall (injection geometry not shown) to form a vortex. Flow is withdrawn at through-flow ports at the centers of the end walls. The plasma shape is similar to that shown in figure 2; it is from 0.6 to about 0.9 in. in diameter and is approximately ellipsoidal in shape. The diameter, shape, and stability of the plasma are strongly dependent upon three parameters: The argon mass flow, the pressure in the test chamber, and the power deposited in the plasma by the rf system.

Fused silica models of the transparent walls are located concentric with, and adjacent to, the plasma (fig. 2). The simulated propellant stream (argon seeded with carbon particles in experiments to date) is injected through the annulus outside of the transparent-wall model. There are unseeded buffer streams on the inside and outside of the seeded stream to help keep the carbon particles off the transparent-wall model and outer wall. A larger diameter fused silica tube forms a pressure vessel, and the 3-in.-i.d. rf work coils surround this tube. Further details are given in reference 2.

Three types of tests are conducted using the components shown in figure 2. Radiant energy source tests are conducted without the transparent-wall model and without the propellant stream. Transparent-wall model tests are conducted with this wall but without the propellant stream. Finally, for propellant heating tests, the complete geometry is used.

Radiant Energy Source Tests

Figure 3 summarizes the results of the radiant energy source tests. The left-hand ordinate indicates the radiant heat flux at the edge of the plasma and the right-hand ordinate indicates the corresponding equivalent (same total flux) blackbody radiating temperature. The abscissa indicates the power deposited in the plasma. The major result is that a flux of 36.7 kW/in.^{2}, which corresponds to a blackbody temperature of 10 200° R, has been attained. This is less than the 15 000° R of the reference engine, but it is nevertheless a useful flux level. To increase the flux further it is necessary to increase the power deposited in the plasma and also the chamber pressure; the highest values attained to date are 216 kW deposited (of which 156 kW were radiated) and 16 atm. Details of these tests are given in reference 2. The vacuum capacitor cooling

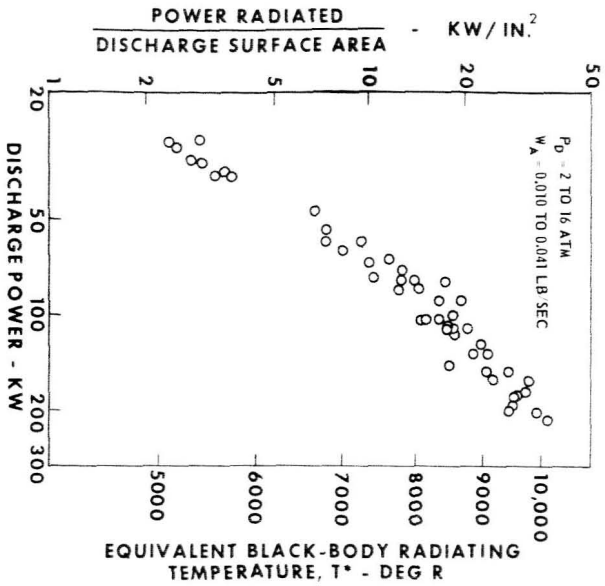

FIGURE 3.—*Performance of radiant energy source.*

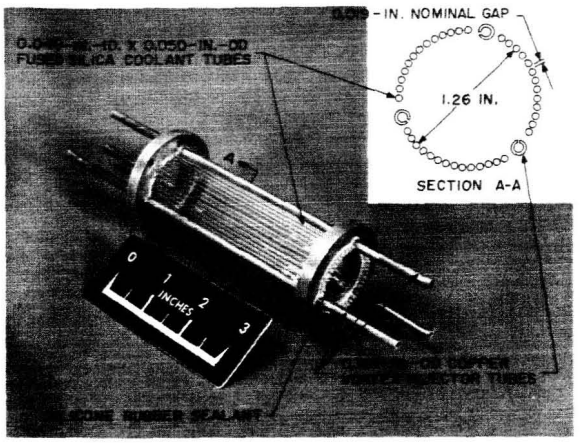

FIGURE 4.—*Photograph of transparent-wall model.*

capability in the rf resonator has been increased to allow tests in which the flux is increased by about 25 percent. The emphasis has now shifted, however, from attempts at major additional increases to efforts in the transparent-wall model and propellant-heating areas.

Transparent-Wall Model Tests

A photograph of a transparent-wall model is shown in figure 4. It consists of 39 fused silica tubes each having an i.d. of 0.050 in. and an o.d. of 0.060 in.; thus, the wall thickness of the tubes is 0.005 in., the thickness required in the reference engine design. The diameter of the circle of tubes is 1.26 in. The tubes are potted into the end manifolds using silicone rubber. There are three copper injectors from which argon is injected through a series of small holes to drive the vortex. From experiments with a variety of fabrication methods, the point has been reached where models such as this can be made routinely using the thin 0.005-in. tubing. Consideration is now being given to models using even thinner tubing.

In tests with these models around the rf radiant energy source, the model has been successfully cooled at the full-scale heat flux (ref. 2). However, unlike with the full-scale reference engine, most of the heat was deposited by convection and conduction, rather than by radiation. This was primarily due to relatively poor flow conditions in the vortex chamber; the flow was turbulent, so the diameter of the plasma was large and the plasma was close to the wall. As the power was increased, the uncooled copper vortex injectors buckled in such a manner that the injection angles varied widely and, in some tests, adjacent fused silica tubes began to flutter. In addition, the tubes were far enough apart that there were substantial flows between the vortex region and the surrounding annulus. Since the most recent series of model tests with rf plasma during the summer of 1969, several sets of copper injectors with water cooling have been built and bench tested. Also, the tubes are now potted differently so that the intertube gaps have been essentially eliminated. These new models have been tested using water instead of argon in the vortex; by injecting fluorescent dye, the flow patterns have been observed to be improved. Therefore, it is expected that the flow will also be improved when testing is resumed with rf plasmas.

Propellant Heating Experiments

Propellant heating experiments were initiated in the spring of 1969 (ref. 2). These first attempts at UARL to use thermal radiation to heat argon seeded with carbon particles did not result in large temperature rises; the maximum temperature rise achieved was only about 200° F. It was determined, however, that there were three reasons for this. First, because of poor vortex flow conditions within

the transparent-wall model, the plasma power was limited to conditions with less than about 3 kW of radiation. Second, the mass attenuation parameter of the particle-seeded stream (a measure of the amount of energy absorbed) was less than about 2000 cm^2/g. In other experiments at UARL and elsewhere, where the ducting between the particle feeder and the test section was not so complicated, values of 5000 to 10 000 cm^2/g (and even higher) have been obtained. This indicates that, in the present experiments, the particles were not sufficiently deagglomerated in the ducting between the particle feeder and the propellant duct. The third reason was the occurrence of coating of the particles on the transparent-wall model. Recent results have shown that thicker buffer layers and the use of a foam material at the inlet of the propellant duct to reduce turbulence should greatly reduce the amount of wall coating.

As a result of the initial experience, major emphasis is now placed on these three areas individually. It is estimated conservatively that an improvement by a factor of at least 20 in the propellant temperature rise should result from these recent efforts. Thus, a temperature rise of at least 4000° R, and probably more, should be possible in the near future.

Supporting Research

The supporting research noted earlier consists primarily of unheated and rf-heated two-component gas vortex tests (ref. 3). These tests are directed toward attainment of a high partial pressure of simulated fuel in the cavity with no fuel near the transparent wall. To date, simulated-fuel partial pressures well in excess of that required for the engine have been obtained (ratios of fuel partial pressure to total cavity pressure as high as 0.44 were obtained, compared with the 0.25 required). In these unheated tests, the radial distribution of simulated fuel has been similar to that desired for the engine except that a small amount of fuel was present near the outer wall. The results of the tests with rf heating have shown, as expected, that the presence of a radial gradient of temperature helps reduce turbulence near the wall and thereby decreases the amount of fuel present in the vicinity of the wall.

ENGINE DYNAMICS AND STARTUP ANALYSES

In the second portion of the nuclear light bulb research program the major effort has been to construct a UNIVAC 1108 digital computer simulation of the dynamics of the engine. The simulation includes all of the coolant loops and their associated time constants, the hydrogen turbopump dynamics, the fuel injection and recycle system, the nuclear kinetics, etc. The major conclusion to date from these studies is that the basic uncontrolled engine has neutrally stable or slightly damped characteristics. Moreover, control of the fuel flow rate appears to offer a very satisfactory method for obtaining good closed-loop control of the engine (ref. 5).

Analyses of possible startup procedures have also been made (ref. 5) using a simplified analytical model of the basic engine. Linear power ramps were used and the general engine response, auxiliary power requirements, and thermal stress levels were investigated. The results obtained to date indicate that no major problems exist with engine control or with thermal stresses during startup, even during ramps as short as 6 sec.

RADIATION HEAT TRANSFER

The primary current effort in the area of radiation heat transfer involves calculations of the thermal radiation spectrum incident upon the transparent wall. Recent calculations of the spectrum emanating from the fuel region in the reference engine have indicated that a substantial amount of energy is radiated in the ultraviolet portion of the spectrum. Below 0.2 μ, the calculated spectrum has about 4 to 5 times as much energy as does a blackbody spectrum for a 15 000° R source. Consideration is being given to adding small amounts of different seed gases—particularly oxygen—in the buffer gas and fuel regions to prevent much of this ultraviolet energy from reaching the wall (ref. 4).

OPTICAL ABSORPTION IN FUSED SILICA

The final research area noted is optical absorption in fused silica. Basically, there are several phenomena occurring as the nuclear radiation (par-

ticularly neutrons and gamma rays) passes through the transparent wall. This radiation tends to discolor the wall, thereby locally decreasing the transmissivity to thermal radiation. However, there are two alleviating processes: If the wall is maintained at a high enough temperature, thermal annealing of the coloration takes place; also, under intense illumination, optical or photon bleaching takes place to remove the radiation-induced opacity.

Several experimental programs have been conducted in which measurements have been made of the transmissivity of high-quality fused silica samples before, during, and after irradiation, at room temperature, and at elevated temperatures (ref. 6). The major effect of the radiation is to induce an absorption band in the fused silica centered at about 0.21 μ. On the basis of recent tests at elevated temperatures, and with the beneficial effect of optical bleaching omitted, it is estimated that the wall coloration and the resulting increase in the absorption of thermal radiation would require a decrease in the thickness of the transparent-wall tubing from 0.005 in. to about 0.003 or 0.004 in. In the near future, experiments will be conducted to determine the effectiveness of optical bleaching in removing induced coloration in the fused silica.

REFERENCES

1. McLafferty, G. H.: Investigation of Gaseous Nuclear Rocket Technology—Summary Technical Report. Rept. H-910093-46, United Aircraft Res. Lab., Nov. 1969.
2. Roman, W. C.; Klein, J. F., and Vogt, P. G.: Experimental Investigations to Simulate the Thermal Environment, Transparent Walls, and Propellant Heating in a Nuclear Light Bulb Engine. Rept. H-910091-19, United Aircraft Res. Lab., Sept. 1969.
3. Mensing, A. E.; and Jaminet, J. F.: Experimental Investigations of Heavy-Gas Containment in R-F Heated and Unheated Two-Component Vortexes. Rept. H-910091-20, United Aircraft Res. Lab., Sept. 1969.
4. Krascella, N. L.: Theoretical Investigation of the Radiant Emission Spectrum From the Fuel Region of a Nuclear Light Bulb Engine. Rept. H-910092-12, United Aircraft Res. Lab., Oct. 1969.
5. Latham, T. S.; Bauer, H. E.; and Rodgers, R. J.: Studies of Nuclear Light Bulb Start-Up Conditions and Engine Dynamics. Rept. H-910375-4, United Aircraft Res. Lab., Sept. 1969.
6. Palma, G. E.; and Gacosz, R. M.: Measurement of Optical Transmission During Reactor Irradiation. Rept. H-930709-1, United Aircraft Res. Lab., Oct. 1969.

DISCUSSION

Anonymous: Is the spectral distribution of your rf sources the same as that of a blackbody radiator?

Clark: No. The spectral distribution of the rf source contains many lines. However, we define a blackbody temperature which is equivalent to the total heat flux.

Anonymous: Isn't spectral distribution very important for your wall transmission? Thus, can you really simulate the radiation of uranium?

Clark: At the present time we do not know much about the uv radiation reaching the wall. It depends upon how much is absorbed by the oxygen.

Ragsdale: What are the chances that a materials research program would suggest another wall material?

Clark: Other materials which we have considered are alumina, which is Al_2O_3, and single-crystal beryllium oxide drawn into tubes. At the present time we think only the BeO would be suitable. This is not available at the present time so we are trying silicon.

Bostick: What gases were used in your experiment and how did you initiate the discharge?

Clark: In these experiments argon was used and we started the discharge by using a retracting electrode that comes in from the end walls. Since we were interested in high pressures, we started at 2 or 3 atm. In other experiments, which Arthur Mensing will discuss, we mixed argon with xenon. The objective is to probe the plasma by spectroscopy. We want to see how much of the xenon, which simulates the fuel component, will actually stay in the plasma region.

Monsler: What pressure difference can such walls withstand?

Clark: There are two pressure drops that one has to be concerned with. The drop connected with the need to flow coolant through the transparent tubing in order to remove the heat that is deposited in the wall doesn't seem to be a problem. The pressure difference between the region inside the wall and the outside is a more serious problem. We expect a pressure drop of approximately $\frac{2}{3}$ atm across the wall. A good pressure control system is needed.

Page intentionally left blank

The Colloid-Core Concept—A Possible Forerunner for the Gaseous Core[1]

Y. S. Tang, J. S. Stefanko, and P. W. Dickson

Astronuclear Laboratory
Westinghouse Electric Corp.

A concept using a colloid-fuel, vortex chamber cavity is described. Theoretical analysis of the system characteristics and a conceptual design of a ground test reactor are included. The reactor uses particulate fuel with a composition (1U-10Zr)C. The uranium is ^{233}U, and the fuel is fed to the cavity by hydrogen gas. The cavity, a compressed vortex chamber developed by the Aerospace Research Laboratory, has an L/D ratio of 0.15 in the fuel-bearing zone. Beryllium is used as the reflector material. The reflector, as well as the other core components, is cooled by hydrogen passages and is contained in a titanium alloy (T-Al-V) pressure vessel. The engine would generate a 100 000-lb thrust with a specific impulse of 1200 lb_f-sec/lb_m.

Compared with the open-cycle or closed-cycle gaseous-core reactor concept, the relative simplicity of the colloid-core reactor may suggest itself as a logical extension of the solid-core reactor technology and thus be a possible forerunner for the gaseous-core reactor.

The nuclear rocket engine promises to outperform the best conceivable chemical propulsion system by a wide margin. Basis for this promise lies in the extremely high exhaust velocities possible with the nuclear engine. This is indicated by the specific impulse I_{sp} of different systems, which is proportional to the exhaust velocity. The latter is proportional to the square root of gas temperature divided by the average molecular weight of the exhaust gas. The solid-core reactor concept, representing the state of the art in nuclear propulsion systems, offers a specific impulse greater than that of the chemical propulsion system by more than a factor of 2. The gaseous-core concept can theoretically provide a value of I_{sp} on the order of five to nine times that of chemical systems (ref. 1). Unfortunately, in the coaxial-flow gaseous-core concept some of the mobile fuel is carried out of the engine by the propellant (hydrogen). It must be replaced by continuous injection so as to maintain a constant critical mass in the reactor. Furthermore, the engine size, weight, and internal pressure are extremely large because of the high critical mass requirement of the gaseous fuel. Both the fuel loss rate and the engine weight have been the major considerations for determining the feasibility of the gaseous-core concept.

A concept using colloid fuel was first conceived by the Aerospace Research Laboratory (ARL) of Wright-Patterson Air Force Base. The fuel-bearing material may be in a particulate form which has a density several orders of magnitude greater than that of gaseous fuel. The capability of retaining the fissionable material in the reactor cavity is therefore enhanced through the utilization of a large density difference between the fuel particles and the propellant. At the same time, the high-density fuel reduces the volume requirement of the cavity in comparison with that of gaseous-core engines. The cavity is a vortex chamber where fuel particles are suspended through the vortex flow generated by tangentially injected propellant at the periphery (ref. 2).

This concept is different from the rotating-bed reactor concept (ref. 3) and the liquid-core reactor

[1] The work described in this paper was done under an Air Force contract with the Aerospace Research Laboratory at the Wright-Patterson Air Force Base.

concept (ref. 4). The rotating-bed concept utilizes a fluidized-bed configuration, and particles are not necessarily completely suspended. Consequently, the physical contact of fuel with reactor wall cannot be avoided. The liquid-core reactor concept uses gas bubbles passing through a liquid film along the reactor wall; this presents flow distribution problems that have been shown to be insurmountable. The colloid-core concept utilizes the known fluid mechanics principle to separate the fuel from the propellant in the exhaust stream, and the fuel is suspended in a confined fuel zone to satisfy the criticality requirement, as depicted schematically in figure 1.

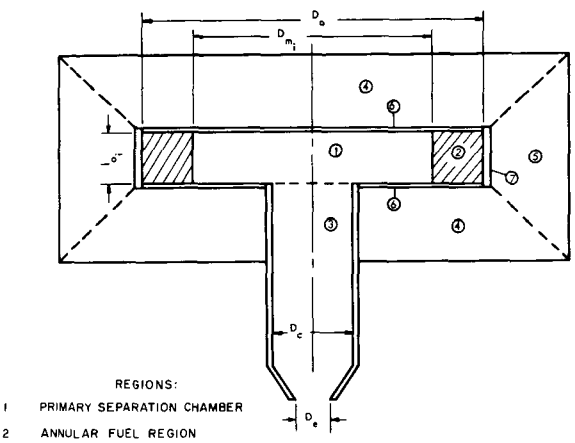

FIGURE 1.—*Schematic of reactor configuration with cylindrical cavity having low* L/D.

This paper describes the design study, conducted under ARL sponsorship, for the colloid-core concept. This includes a theoretical analysis of the system characteristics and a conceptual design of a ground test reactor.

SYSTEM CHARACTERISTICS

A thermodynamic analysis was made to evaluate the effect on engine performance of the fuel composition, the pressure-temperature conditions at the exhaust, and the vapor losses. The selection of a particular fuel composition for the reactor was made from these considerations. In spite of the extremely high efficiency for solid separation obtainable by a vortex chamber,[2] the fuel loss due to vaporization in the form of uranium vapor was found to be significant, if it is assumed that no separation of gaseous molecular species was realized in the vortex flow. The required pressure-temperature conditions at the exhaust also specify the propellant conditions at stations in the propellant cycle upstream of the exhaust. For instance, the pressure at the propellant injection ports at the periphery can be determined from the pressure at the exhaust and the pressure differential between the peripheral propellant injection port and the centerline of the reactor[3] as determined by the requirement of fuel suspension. The pumping requirement can be determined from the various pressure drops through the propellant passages. As will be shown in the conceptual design section, the pressure inside the reactor is about one-half of the pressure indicated by gas-core design estimations (ref. 6).

For the fuel losses in the form of uranium vapor carried out by the propellant, different possible fuel compositions of pure U, UC, and UC_2 with ZrC and NbC as diluents were examined. ZrC and NbC are low vapor pressure carbides and thereby mitigate fuel vaporization. They are nuclearly compatible because of their relatively low neutron capture cross sections. It was concluded that a fuel composition of (1U-10Zr)C would yield acceptable results at moderate pressures and temperatures. Nuclear analyses (ref. 7) also indicated that the critical masses with the above fuel form were within the load-carrying capacity of the cavity.

The vapor pressure data of the ternary system involving U-C-Zr or U-C-Nb are based on the thermodynamic formulation of free energy, as suggested by Kaufman and Peters (ref. 8), expressed in terms of partial pressures and vapor pressure of each element. The vapor composition in equilibrium with the solid fuel can thus be computed at a given static pressure and temperature at

[2] The capability of separating fine particles from a gas stream in a vortex chamber was demonstrated in ref. 5.

[3] Equations evaluating this pressure differential are shown in the appendix.

the exhaust. This yields the molecular weight of the vapor mixture

$$M_T = \frac{\Sigma_i M_i P_i}{P_T}$$

The degradation of the specific impulse of the rocket exhaust is evaluated from the expression

$$I_{sp} = \left(\frac{M_H}{M}\right)^{1/2} I_{spH}$$

where the specific impulse of hydrogen I_{spH} and the molecular weight for pure hydrogen M_H are obtained as a function of P_{sc} and T_s from King's real-gas nozzle calculations (ref. 9). The variation of specific impulse with the equilibrium static temperature at the nozzle inlet T_s for various dilution ratios ZrC/UC_2 or ZrC/UC is shown in figure 2

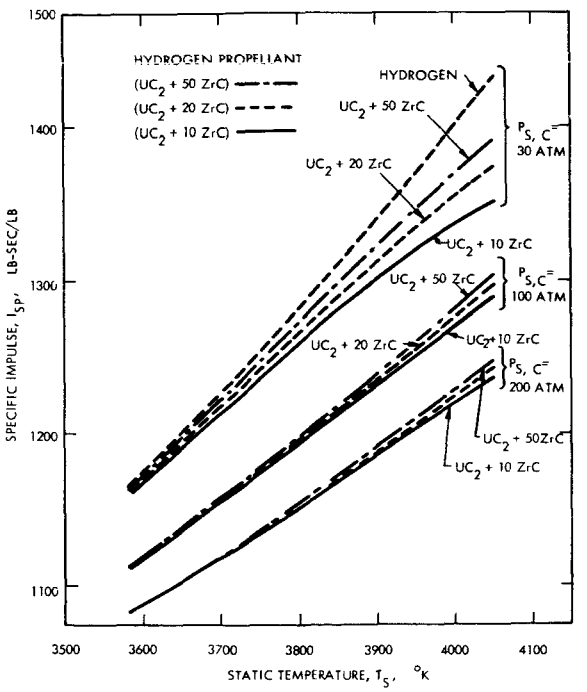

FIGURE 2.—*Specific impulse against temperature for various fuel compositions at specified static pressures.*

for a specified pressure. Figure 2 also shows the variations of specific impulse at different static pressures and for different ZrC/UC ratios. The fuel loss rates can be evaluated directly from the partial pressures at exhaust conditions and are presented in figure 3. It should be noted that actual values of

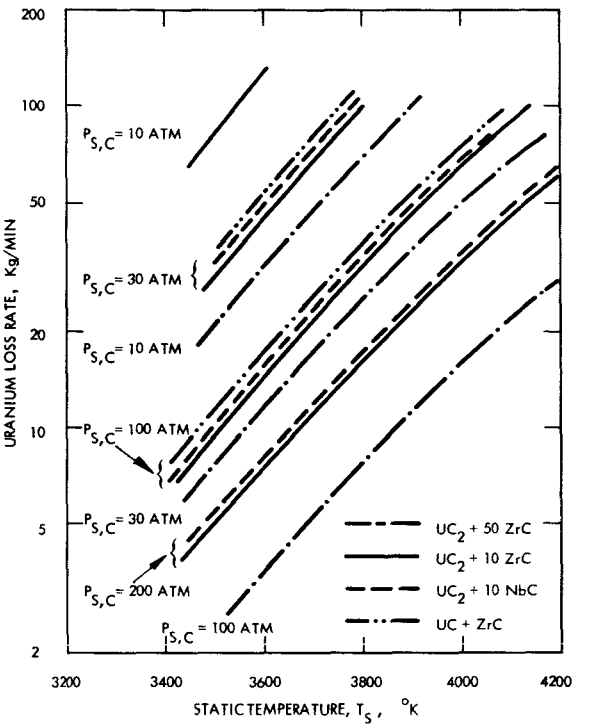

FIGURE 3.—*Loss rates of fissionable materials against static temperature for various fuel compositions and pressures.*

thrust or specific impulse are lower than the ideal values shown in the figures, which can be obtained by a nozzle discharge coefficient to take into account the heat and frictional losses. Figure 4 is a composite plot of the specific impulse and the fuel loss rates on a pressure-temperature map. As shown in the figure, at a centerline static pressure of 76 atm and static temperature of 3620° K, as represented by point *A*, the specific impulse would be 1150 $lb_f sec/lb_m$ and the uranium loss rate would be 20 kg/min. For a higher I_{sp}, at 1200 $lb_f sec/lb_m$ the static temperature must be increased, thereby increasing the fuel loss rate. To keep this loss rate at a minimum, the static pressure must be raised to 200 atm, or point *B*, which corresponds to a fuel loss rate of 28 kg/min. In this case, the ratio of the hydrogen to uranium flow approaches 100 to 1. Since these fuel loss rates were evaluated from calculated vapor pressure data of the system, these values should be considered as estimates and experimental determinations of the vapor pressure are needed.

Both bleed and topping cycles were considered

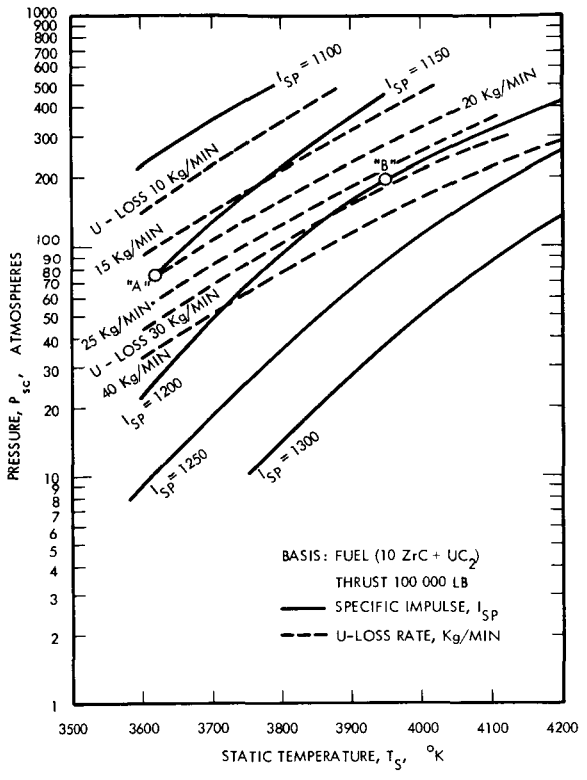

FIGURE 4.—*Specific impulses and fuel loss rates on a pressure-temperature grid.*

for propellant pump power. The bleed cycle was found undesirable because of the high bleed flow (over 15 percent) required; this corresponds to a pump discharge pressure of 9000 to 9500 psia at an assumed pump efficiency, turbine work per stage, and a pump pressure rise. A topping cycle utilizing the total propellant flow was therefore selected.

CONCEPTUAL DESIGN OF THE TEST REACTOR

Design studies of a colloid-core reactor were made to define some practical solutions for development problems. The goal was to establish a state-of-the-art concept with a feasible design approach from the structural support and heat transfer standpoints. To simulate the flight engine operating principles, a ground test reactor (GTR) was conceptually designed. The configuration of the cavity, as shown in figure 1, is primarily determined by the requirements of fuel containment and the solid loading factor, i.e., the ratio of the solid mass to the hydrogen mass in the fuel zone of the cavity, which was a result of fluid mechanical experiments conducted by ARL.

The model of fuel distribution shown in the chamber is simplified but is considered realistic. The primary function of the vortex chamber is to separate and retain fuel particles in the chamber with the solid-free gas exhaust at the exit end with dimension D_e. Clearly, the portion of the chamber with diameter D_c will experience the peak tangential velocity and serve the function of a final cleanout stage of the exhaust gas. The finest size particles in the gas stream may thus be centrifuged to the wall in region 3 where they will be carried to the closed end of the chamber. The density of fuel particles in region 3 would be negligibly small, however, and can be assumed to be solid-free. The characteristics of vortex flow are usually expressed in the form

$$rv^n = \text{Constant}$$

where n is a constant with a value between 1 and 2. The tangential velocity v will diminish as the radius is increased. Thus, the separation effectiveness is controlled by the peak tangential velocity near the central core and the solid will be built up in the outer diameter region (region 2). The thickness of the fuel zone, i.e., the dimensions of D_m, will vary as the size distribution of fuel particles is changed.

The second consideration of the cavity configuration is the tendency of particles to impinge on the peripheral wall. Because the centrifugal force acting on the particles varies with (V^2/r), increasing r, with the accompanying effect of a reduction in the tangential velocity V, will reduce the centrifugal force rapidly. Consequently, the tendency of particle impingement on the wall can be reduced by means of large-diameter (D_o) cavities.

The axial length L_o of the cavity represents the dimension where liner material of appreciable nuclear absorption cross section will be used. It would be desirable to keep L_o small as long as the boundary-layer effect on the vortex flow does not become critical. On the other hand, the solid loading factor depends on the volume containing the fuel particles. For a given critical mass, the larger L_o will correspondingly lower the solid loading factor.

The selection of the reactor size and related di-

mensions was largely based on the results of the nuclear criticality analysis. The critical mass requirement of ^{233}U versus the outer diameter D_o is presented in figure 5 for various L_o/D_o ratios. By

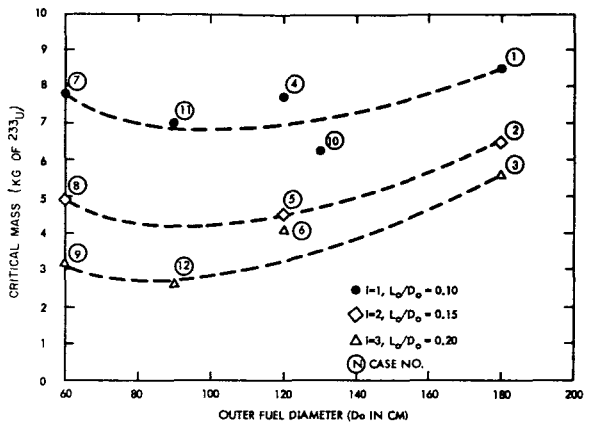

FIGURE 5.—*Critical mass of ^{233}U versus outer diameter D_o parametric results with no nozzle.*

using a fuel composition of (1U-10Zr)C, the resultant solid loading factors at various conditions are shown in figure 6.

From figure 5, one can conclude that the optimum geometry neutronically, i.e., low critical mass, is a configuration with a small outer fuel diameter, or $D_o = 60$ to 100 cm, and the highest cavity length-to-diameter ratio of the range considered, or $L_o/D_o = 0.20$. On the other hand, the solid loading factors corresponding to the required critical mass as shown in figure 6 tend to be smallest for the larger systems. Specifically, the geometry with an outside fuel diameter D_o of 180 cm and L_o/D_o ratio of 0.2 has the lowest solid loading factor, approximately five, of all cases investigated. From the fluid mechanics point of view, however, the configurations with lowest L_o/D_o ratios would be able to sustain the highest loading factors.

Considering all the above factors, the geometry represented by case 5 in figure 5 appeared to be the reasonable selection. The following dimensions describe the selected configuration and design parameters as shown in figure 1:

$D_o = 120$ cm ($\approx$47 in.)
$L_o = 18$ cm ($\approx$7 in.)
$D_m = 90$ cm ($\approx$36 in.)

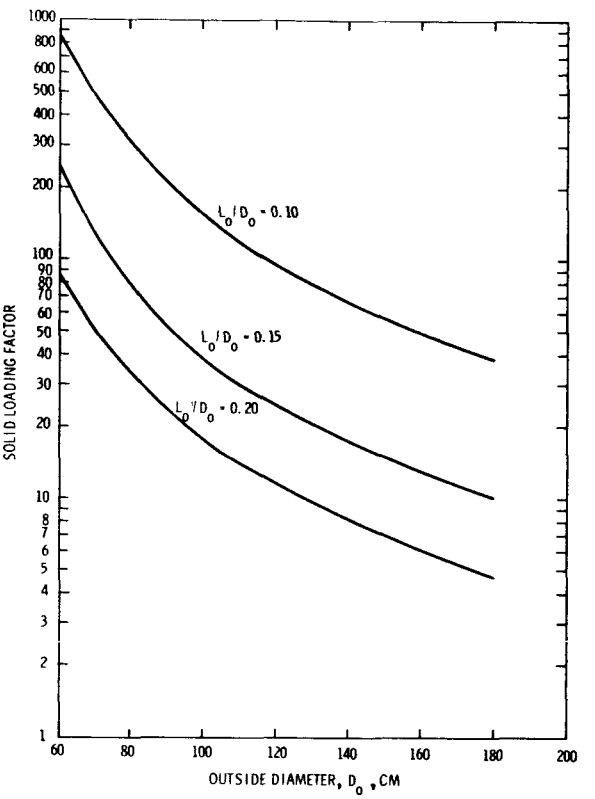

FIGURE 6.—*Solid loading factor as a function of the outside diameter (basic geometry with no nozzle).*

$D_c = 30$ cm ($\approx$11.8 in.)
Radial reflector thickness, 45 cm ($\approx$18 in.)
Axial length of reflector, 108 cm ($\approx$42.5 in.)
Thrust capability, 100 000 lb
Specific impulse, 1200 lb_f-sec/lb_m
Exhaust pressure upstream of the nozzle, 100 to 200 atm
Static temperature upstream of the nozzle, 3700° to 3900° K

The GTR is depicted in figure 7. The major part of the reflector is a beryllium reflector, which includes a fueled zone that has an annulus of 15-cm ($\approx$6 in.) thickness extending the full axial length of the reflector. Control drums containing poison plate material are located in the reflector region to provide criticality control.

Solid particulate fuel (1U-10Zr)C containing isotope ^{233}U is fed to the cavity by hydrogen gas. Depending on the further development in the effects of the agglomeration and the fission fragmentation

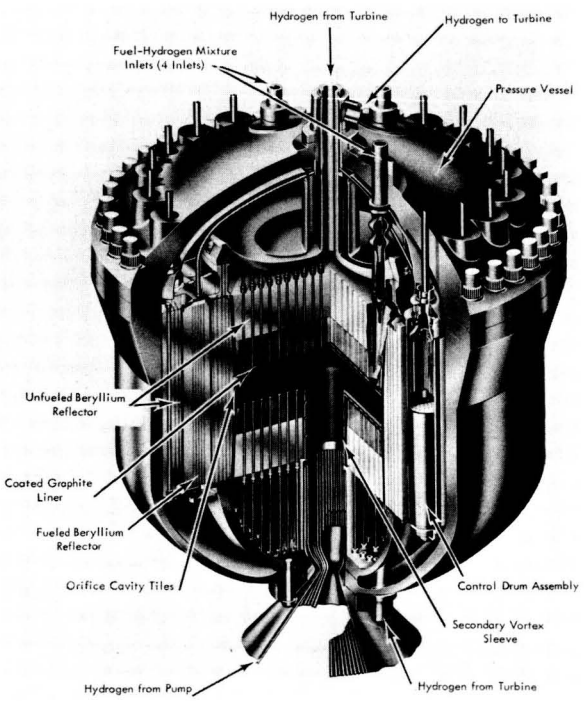

FIGURE 7.—*Ground test reactor.*

phenomena, a preliminary selection of the particle size in the range of 0.5 to 5 μ was made. The beryllium reflector material is cooled by hydrogen passages and is contained in a titanium alloy (Ti-Al-V) pressure vessel. The overall dimensions are a diameter of approximately 240 cm ($\approx$95 in.) in the cylindrical portion and a length of 240 cm flange-to-flange excluding the exhaust nozzle.

The preliminary design of the GTR reported here indicated that for a thrust capability of 100 000 lb the reactor engine would weigh about 40 000 lb. No attempt was made to optimize the weight of this system. Since the weight of the pressure vessel in his design accounts for 63 percent of the total engine weight (excluding storages), the lower operating pressure results in a considerably lighter weight than that of a gaseous-core reactor of similar thrust as reported elsewhere in this symposium.

CONCLUSIONS

In light of the study made for the colloid-core concept, it may be concluded that from the standpoint of reactor design the colloid-core concept is feasible. With a solid particulate fuel a specific impulse of 1200 lb_f-sec/lb_m is obtainable. The relative simplicity of the colloid-core reactor may suggest itself to be a logical extension of the solid-core reactor technology and thus a possible forerunner for the gaseous-core reactor.

APPENDIX

PRESSURE LOSS DUE TO DRAG IN THE VORTEX CHAMBER

In a colloid-core reactor, the injection pressure required at the periphery is a function of the static pressure differential between the cavity periphery and the center core. The latter is defined as the core which exists in a vortex flow where the gas is free from solid particles. This pressure differential depends on the particle concentration, expressed in terms of the density ρ_m of the gas particulate system and the tangential velocities V_p and V_c at the periphery of the cavity and at the center core, respectively, as shown by the relationship

$$\Delta P = -\frac{\bar{\rho}_m (V_p^2 - V_c^2)}{2g_c}$$

The particulate system in the cavity is assumed to have uniform density between the center core and the periphery, and the tangential velocities of the particles and gas within this zone are assumed to be equal. In other words, there is no slip between the solid and gas in the tangential velocity direction. If the velocity field is further assumed to follow the potential flow equation, then the pressure differential can be determined by the following equation:

$$\Delta P = \frac{\bar{\rho}_m V_p^2}{2g_c}\left[\left(\frac{r_p}{r_c}\right)^2 - 1\right]$$

where r_p and r_c are radii of the cavity and the center core, respectively. The periphery tangential velocity V_p is dictated by the required separation effectiveness which depends on the size of fuel particles. Since the separation is caused by the centrifugal field, the tangential velocity can be determined by drag in the radial direction as evaluated from Stoke's law. For very small size particles, a Cunningham correction factor may be included, as

$$\rho_s\left(\frac{\pi d^3}{6}\right)\frac{V^2}{r} = 3\pi d\mu U\left(1 + k\frac{\lambda}{d}\right)$$

where

d particle diameter
ρ_s density of the solid
k approximately constant = 2.5 to 2.8
λ mean free path of gas
U relative radial velocity

Because the smallest particles are being separated at the center core (peak tangential velocity), the diameter of a particle which has a radial velocity at this location equal to its terminal velocity is the minimum size that can be separated and is called the critical diameter. By using this diameter as a parameter, the pressure loss ΔP or the required periphery pressure P_D as a function of centerline P_F is shown in figure 8.

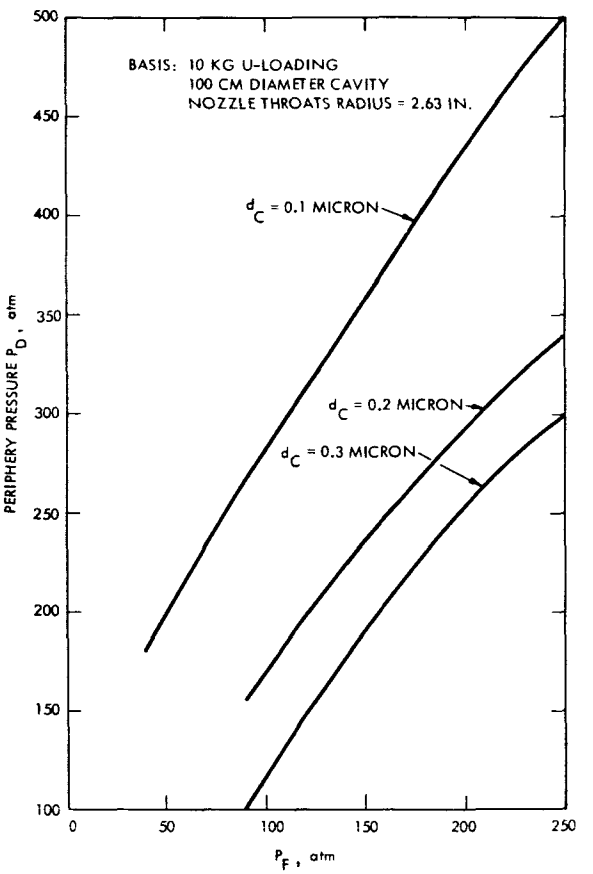

FIGURE 8.—*Cavity peripheral static pressure vs central-core static pressure. 10-kg U loading; 100-cm-diam cavity; nozzle throat radius, 2.63 in.*

REFERENCES

1. RAGSDALE, R. G.; AND ROM, F. E.: Gas-Core Reactor Work at NASA/Lewis. Paper No. 67–499, Third Propulsion Joint Specialist Conf., 1967.
2. ANON.: Engineering Study of Colloid Fueled Nuclear Rocket. Final Prog. Rept. (USAF Contract AF-33(615)-3596), Westinghouse Astronucl. Lab., 1969.
3. LINDANER, G. C.; TICKLER, P.; AND HATCH, L. P.: Experimental Studies on High-Gravity Rotating Fluidized Beds. BNL Rept. 50013(T-435), 1966.
4. GREY, J.: The Liquid-Core Nuclear Rocket. LASL–3229–MS, Proc. Advanced Nucl. Propulsion Symp., Los Alamos Sci. Lab., 1965.
5. PINCHAK, A. C.; AND POPLAWSKI, R.: On the Attainment of Extremely High Rotational Velocities in a Confined Vortex Flow. Paper No. 65–400, AIAA, 1965.
6. MCLAFFERTY, G. H.; AND BAUER, H. E.: Studies of Specific Nuclear Light Bulb and Open Cycle Vortex-Stabilized Gaseous Nuclear Rocket Engine. NASA CR–1030, 1968.
7. STEFANKO, J. S.: Nuclear Analysis of a Colloid Fueled Cavity Reactor. Am. Nucl. Soc. Ann. Meeting Paper (Toronto, Canada), 1968.
8. KAUFMAN, L.; AND PETERS, E. T.: Analysis of Vaporization in Liquid Bearing Systems at Very High Temperatures. NASA CR–353, 1965.
9. KING, C. R.: Compilation of Thermodynamic Properties and Theoretical Rocket Performance of Gaseous Hydrogen. NASA TN D–275, 1960.

DISCUSSION

J. Keyes: I have two questions. The first has to do with the flux patterns in the cavity. I think bypass inwall flows would be significant. Did you bring any of the fluids in tangentially to try to reduce this bypassing flow? My second question is: In your first sketch you showed the fuel zone as being in contact with the wall while in the last it appears that the fuel is contained somewhere away from the wall. Is it away from the wall or is it actually pushed up against the wall, which would severely limit the operating temperature?

Tang: Let me answer the second question first. As expected, some particles impinge on the wall but, because a propellant is injected at the periphery, a major part of the fuel is kept away from the wall. This is related to the first question with respect to the flow field for a vortex chamber with a particular L/D. Perhaps I should say that the work on this concept has two phases. One is that underway at Westinghouse in the study of the reactor design. The other, the in-house study at ARL, started quite some time ago with respect to this particular vortex chamber configuration, the solid carrying capacity, and also the separation efficiency. This ARL work will be reported in AIAA paper 70–1222.

Pulsed Plasma-Core Rocket Reactors[1]

F. WINTERBERG

University of Nevada

It is shown that the two principal problems of gas-core reactors, i.e., fuel-propellant separation and material problems resulting from the high operating temperatures, can be greatly reduced in a pulsed operation to very high temperatures by a fast-growing chain reaction. An expression for the reactor economy (for the fuel burnup) is derived which shows that with increasing maximum temperature in the pulsed reactor operation the same fuel burnup is possible with a smaller fuel-propellant separation. In the limiting case of temperatures above 10^7 °K, represented by the bomb propulsion concept, no separation is needed. The other limiting case, that of complete separation realized in the solid-core rocket reactor, can also be recovered from the general formula. The pulsed operation will not only reduce the material problems connected with continuous operation at high temperatures but also lead to a higher specific impulse not attainable under continuous operation. Another advantage of the pulsed operation is the possibility of a dynamic system for fuel-propellant separation.

It is widely accepted that manned interplanetary trips to Mars and Venus will take place in the foreseeable future. The presently contemplated minimum round-trip times are of the order of a year. Obviously, a reduction of this time would be highly desirable. This estimate of 1 year is based on the combined use of two already available nuclear propulsion systems, the solid-core nuclear rocket reactor, like the NERVA engine, and the electrostatic propulsion system with a nuclear powerplant. For manned trips to Jupiter and beyond, a more powerful propulsion system becomes an even greater necessity if excessive staging of rocket vehicles is to be avoided. A reduction in the trip time through higher vehicle velocities requires increased exhaust velocities; and although electric propulsion systems can attain sufficiently high exhaust velocities, their thrust is limited to rather low values. As a result, a vehicle velocity high enough for improved performance cannot be reached within a reasonable length of time and hence cannot reduce the trip time from the contemplated 1-year level.

Because of these well-known limitations, great hopes are held for the development of a gaseous-core nuclear rocket engine. It is generally conceded that such a system of propulsion would prove to be a significant step toward achieving the desired goal. All proposed schemes based on the concept of the gaseous-core nuclear rocket engine have in common the heating of a propellant (hydrogen) to high temperatures by passing it through a hot fissioning uranium gas. Because ^{235}U is expensive, all these systems attempt to minimize the loss of the hot uranium gas dragged through the nozzle by the propellant. No completely satisfactory solution for this problem has been found, and it might well turn out that no practical solution exists. We shall, however, show in this paper that there may be a way out of this difficulty. For this we look at the fuel burnup relation derived later in this paper (eq. (18)), $\Delta N_u/N_u=\sigma_f\phi\tau$, where $\Delta N_u/N_u$ is the relative amount of uranium atoms with atomic number density N_u which have undergone fission, σ_f is the fission neutron cross section, ϕ is the neutron flux, and τ is the fuel confinement time or fuel lifetime in the reactor. For continuous reactor operation with $\sigma_f \cong 10^{-22}$ cm^2, $\phi \cong 10^{15}$, and a burnup ratio $\Delta N_u/N_u \gtrsim 10^{-4}$, it follows that the fuel confinement

[1] Supported by the National Aeronautics and Space Administration under grant NGR 29-001-016.

time τ must be $\gtrsim 10^3$ sec. From the fuel burnup relation, of course, it also follows that the same fuel economy $\Delta N_u/N_u$ would be achieved with a much smaller fuel confinement time by raising the neutron flux to higher values. However, raising the neutron flux will result in a higher reactor temperature. It is therefore clear that this can be achieved only in a pulsed mode of reactor operation. In the limiting case this system would be represented by the bomb propulsion system.

In the bomb propulsion system no fuel retainment is needed because sufficiently high fuel consumption takes place during the fast-growing chain reaction. The reason for this is, of course, the very high neutron flux level attained during the short period of the nuclear explosion. Apart from political considerations, there are, however, obvious serious problems connected with this system resulting from the high energy released per explosion. From the point of view of reactor physics, there is no basic difference between nuclear reactors and nuclear bombs; the only differentiation is with regard to the neutron spectrum and time behavior. It is, therefore, appropriate to ask if a significant improvement in the gas-core rocket reactor performance can be achieved by a pulsed operation to very high levels of neutron flux and temperature, thus reducing the requirement for a large fuel retainment factor. The system would have some resemblance to the bomb propulsion concept, as well as to the original gas-core rocket reactor concept. The chain reaction would be started with a dense solid or liquid uranium-propellant mixture rapidly expanding into a hot plasma. Some system for separating the fuel from the propellant might still be needed, but since a much smaller fuel retainment is required, systems already under consideration, such as the vortex or magnetic-field separation method, may be sufficient. A different fuel retainment scheme based on a dynamic fuel-propellant separation is actually more suitable for the pulsed mode of reactor operation. This will be discussed later in the paper.

For the proposed purpose of propulsion, a chain of such "soft" nuclear explosions would take place inside a reactor vessel, and each pulse will produce a jet of hot plasma to be ejected through a nozzle. Such a hybrid system has a number of distinct advantages:

(1) The high neutron flux in the pulsed operation will lead to an increased fuel burnup rate, and thus the requirement for fuel retainment will be reduced.

(2) The high temperatures attainable in the pulsed reactor operation will result in an increased specific impulse.

(3) The material problems resulting from the high temperatures are less severe in a pulsed operation.

(4) The pulsed operation permits starting of the chain reaction from a uranium-propellant mixture at high densities with a small critical mass, thus reducing the otherwise contemplated size of a cavity reactor.

(5) The pulsed reactor operation permits employment of a dynamic system of fuel-propellant separation not possible with continuous reactor operation.

References to some previous work on nuclear rocket propulsion and gas-core rocket reactors can be found in the literature (refs. 1 and 2).

THE BASIC FUEL CONSUMPTION RELATION

Consider a cylindrical cavity reactor of radius R, length L, and volume $V=\pi R^2 L$. If N_u is the number of uranium atoms per cubic centimeter, σ_f the neutron cross section for fission, ϵ_o the energy released per fission ($\epsilon_o''=180$ MeV), and ϕ the neutron flux, we have for the reactor power P the expression

$$\begin{aligned} P &= VN_u\sigma_f\phi\epsilon_o \\ &= \pi R^2 L N_u \sigma_f \phi \epsilon_o \end{aligned} \tag{1}$$

The power of a rocket engine, on the other hand, is given by

$$P = v^2\dot{m}/2 \tag{2}$$

where v is the exhaust velocity and $\dot{m}$ is the mass flow in grams per second. The exhaust velocity as a function of the combustion chamber temperature T, which in our case is equivalent to the uranium reactor temperature, is given by

$$v^2 = 2c_pT \tag{3}$$

where c_p is the specific heat under constant pressure.

Equating equations (2) and (1) and substituting for v^2 from equation (3) result in

$$\pi R^2 L N_u \sigma_f \phi \epsilon_o = c_p T m \tag{4}$$

We shall assume that the uranium fuel and hydrogen propellant inside the reactor core are flowing axially with velocities given by v_u and v_h. If m_u and m_h are the masses of the uranium and hydrogen atoms and N_h is the atomic number density of the hydrogen, we have

$$\dot{m}=(m_uN_uv_u+m_hN_hv_h)\pi R^2 \tag{5}$$

We furthermore define the fuel retainment factor by putting

$$v_h=Sv_u \tag{6}$$

so that $S=1$ represents the case of no, and $S=\infty$, that of complete fuel retainment. In this simplified analysis we shall neglect contributions resulting from multiple ionization and excitation to the specific heat of the propellant-fuel mixture in the exhaust jet. This simplifying assumption at least will give us some qualitative insight, which is sufficient for this first exploratory study.

If we define N_u^* and N_h^* as the number densities of uranium and hydrogen atoms in the exhaust jet, assuming both fuel and propellant to be monatomic and singly ionized, we have for the specific heat c_p of the fuel-propellant mixture (k is the Boltzmann constant)

$$c_p=\frac{N_u^*+N_h^*}{N_u^*m_u+N_h^*m_h}5k \tag{7}$$

where we have neglected the electron masses as compared with the ion masses. From the requirement of fluid flow continuity we furthermore have

$$N_uv_u=N_u^*v_u^* \tag{8}$$

$$N_hv_h=N_h^*v_h^* \tag{9}$$

where v_u^* and v_h^* are the velocities of the uranium fuel and hydrogen propellant in the exhaust nozzle flow, for which

$$v_u^*=v_h^*=v \tag{10}$$

holds. Hence

$$\frac{N_h^*}{N_u^*}=\frac{N_h}{N_u}S \tag{11}$$

and

$$c_p=5k(1+\alpha S)/(m_u+m_h\alpha S) \tag{12}$$

where we have defined $\alpha=N_h/N_u$. From equations (4), (5), (6), and (12), we thus obtain

$$L\sigma_f\phi\epsilon_0=5kT(1+\alpha S)v_u \tag{13}$$

The lifetime τ of a fuel particle in the reactor is given by

$$\tau=L/v_u \tag{14}$$

With the help of equation (14), equation (13) assumes the form

$$\tau\sigma_f\phi=5kT\epsilon_0^{-1}(1+\alpha S) \tag{15}$$

This is the first form of what we shall call the basic relation. A second form is obtained from the equation for fuel burnup due to fission

$$\frac{dN_u}{dt}=-N_u\sigma_f\phi \tag{16}$$

with the solution

$$N_u=N_u(0)\ \exp\ (-\sigma_f\phi t) \tag{17}$$

From equation (16), with solution (17), there follows for small values of τ the fuel burnup ratio

$$\frac{\Delta N_u}{N_u}\cong\sigma_f\phi\tau \tag{18}$$

The left side of equation (15) is the fuel burnup ratio given by this last equation. We thus can also write

$$\frac{\Delta N_u}{N_u}=5kT\epsilon_0^{-1}(1+\alpha S) \tag{19}$$

The effect of neglecting the contributions of multiple ionization, excitation, etc. to the specific heat now becomes clear. Since the right side of both equations (15) and (19) is proportional to the specific heat, the same burnup ratio will be reached at a lower temperature if these contributions are taken into account. This is especially true for temperatures above 10^7 °K, where radiation becomes very important. The important general conclusion, however, that a higher fuel burnup is achieved at an increased temperature is unchanged in any case.

For large values of αS, equation (19) can be approximated by

$$\frac{\Delta N_u}{N_u}=5k\epsilon_0^{-1}\alpha ST \tag{20}$$

Inserting numerical values, we have

$$\frac{\Delta N_u}{N_u}=2.4\times10^{-12}T(1+\alpha S)$$

$$\cong2.4\times10^{-12}\alpha ST$$

From equation (20) it follows that the same fuel

burnup, and hence the same economy, can be obtained by either a small T and large S or a large T and small S. If, for example, $T=2\times10^4$ °K, it is well known that values of S in excess of 5×10^2 are economical. If, for example, $a=5\times10^2$, this would correspond to a fuel burnup of $\Delta N_u/N_u\cong 0.01$. A rise in the temperature T to 10^6 °K under the same fuel economy would require a value of S in excess of only 5. On the other hand, the exhaust speed and thus the specific impulse would be increased by a factor of 10.

The basic formula contains the two limiting cases of no fuel retainment (bomb propulsion) and complete fuel retainment (solid-core rocket reactor). The bomb propulsion mode would correspond to the case for which $a=S=1$. The other limiting case of complete fuel retainment can be obtained by letting $S\rightarrow\infty$ in equation (12), with the result that $c_p\rightarrow 5k/m_h$ and the exhaust speed $v\rightarrow(10\ kT/m_h)^{1/2}$, which is the adiabatic exhaust speed for ionized monatomic hydrogen. Except for the fact that the hydrogen is diatomic, this limiting case is realized in the solid-core nuclear rocket engine.

The basic relation (19) was derived under the assumption of a very special model. Its validity, however, is much more general. We define by M_u and M_h the total time-integrated uranium and hydrogen masses to be ejected in the exhaust jet. If the energy per unit mass of uranium to be imparted into the exhaust is ϵ, we have

$$(M_u+M_h)\,v^2/2=\epsilon M_u \tag{21}$$

We furthermore have

$$\epsilon=\frac{\Delta N_u}{N_u}\frac{\epsilon_o}{m_u} \tag{22}$$

and

$$\frac{M_h}{M_u}=\frac{N_h^*}{N_u^*}\frac{m_h}{m_u}=\frac{m_h}{m_u}aS \tag{23}$$

With the help of equations (3) and (12), we therefore immediately have

$$\frac{\Delta N_u}{N_u}=5kT\epsilon_o^{-1}(1+aS) \tag{24}$$

which is the same result as before. The importance of this result is that it applies to much more general modes of reactor operation, e.g., a fast pulsed system, and is independent of the chosen reactor geometry and propellant flow pattern.

We can draw two other general conclusions from the basic relations (15) and (19). Rewriting equation (19) in the form

$$T=\frac{\epsilon_o}{5k}\frac{\Delta N_u}{N_u}(1+aS)^{-1} \tag{25}$$

indicates how high the reactor temperature will be for a given fuel retainment factor S and fuel burnup value $\Delta N_u/N_u$. More important is a relation which gives the exhaust velocity v as a function of the basic parameters. With the help of equations (12) and (25), the exhaust velocity given by equation (3) can be expressed as

$$v=\left[\frac{(2\epsilon_o\Delta N_u/N_u)}{(m_u+m_haS)}\right]^{1/2} \tag{26}$$

from which it follows that, with decreasing values of S, higher exhaust velocities result for the same fuel burnup economy $\Delta N_u/N_u$. For example, the exhaust speed would be increased by a factor of 10 for the previously given values. This increased specific impulse with smaller fuel retainment requirement is very fortunate.

NEUTRON FLUX AND MAXIMUM REACTOR TEMPERATURE

We can approximate the fuel transit time τ at high temperatures by

$$\tau=L/v_u=LS/v_h\cong 2LS/v \tag{27}$$

where τ is computed for acceleration to the adiabatic velocity $v=(2c_pT)^{1/2}$. Hence

$$\tau=(2/c_pT)^{1/2}LS \tag{28}$$

Inserting this value for τ into equation (15), substituting for c_p from equation (12), and solving for the neutron flux ϕ, we have

$$\phi=\frac{(5kT)^{3/2}(1+aS)^{3/2}}{2^{1/2}\epsilon_o\sigma_f(m_u+m_haS)^{1/2}LS} \tag{29}$$

Inserting numerical values, we have for ^{235}U fuel

$$\phi=3.4\times10^{-8}\frac{T^{3/2}(1+aS)^{3/2}}{(235+aS)^{1/2}\sigma_fLS}$$

Let us put, for example, $T=10^6$ °K, $a=S=10$, $\sigma_f=5\times10^{-23}$ cm^2, and $L=300$ cm, with the result $\phi=1.2\times10^{22}$/cm^2 sec. This value is seven orders of magnitude above the most powerful steady-state reactors. From this fact it is rather obvious that such a high neutron flux can be achieved only in

a pulsed operation, as outlined in the introduction.

With the help of equation (19) we can also bring relation (29) to the form

$$\phi=\left(\frac{\Delta N_u}{N_u}\right)^{3/2}\frac{\epsilon_o^{1/2}}{\sqrt{2}\,\sigma_f(m_u+m_h\alpha S)^{1/2}LS} \tag{30}$$

which, after inserting numerical values, yields

$$\phi=\frac{9.2\times10^9\left(\frac{\Delta N_u}{N_u}\right)^{3/2}}{(235+\alpha S)^{1/2}\sigma_f LS} \tag{31}$$

HIGH NEUTRON FLUXES BY PULSED OPERATION

From the previous considerations it is apparent that the very high neutron fluxes required can be obtained only in a pulsed operation. It is therefore proposed to let the reactor start inside a combustion cavity as a prompt critical assembly of uranium and hydrogen injected into the cavity. In this regard it is not necessary, and, for reasons of neutron dynamics and possible fuel-propellant separation, even undesirable, to have a homogeneous fuel-propellant mixture. In essence the scheme will resemble a nuclear bomb, with the important difference that there will be a smaller fuel burnup ratio and a much smaller explosive power. A subcritical assembly is injected inside the reactor cavity, after which the condition for the prompt critical state must be reached very quickly. This can be done by standard chemical gun methods of injecting a piece of uranium into a subcritical assembly, making it suddenly critical. The rise time in the neutron flux to the contemplated level of $10^{22}/\text{cm}^2$ sec must take place in a time shorter than the time for thermal expansion of the plasma fireball. The chain reaction is most properly started in a critical assembly in the solid state, giving a fast rise time for the neutron flux and small critical masses. For the required fast rise time a sufficiently high initial neutron flux is needed. This may be achieved by surrounding the reactor cavity with a conventional reactor to be pulsed for a short time to a high neutron flux level (e.g., $\phi_o=10^{14}/\text{cm}^2$ sec) just at the moment when the fissionable assembly inside the reactor cavity is made prompt critical.

If we neglect neutron losses through the surface of the prompt critical reactor assembly, the neutron flux rises according to

$$\phi=\phi_o\exp\left(\frac{\eta-1}{l_o}t\right) \tag{32}$$

where η is the multiplication factor for the chain reaction and the time constant is given by

$$l_o=1/N_u\sigma_f v \tag{33}$$

The value of η is approximately 2.5; v is the average neutron velocity. For fast reactors we have $v=1.95\times10^9$ cm/sec and $\sigma_f=1.3\times10^{-24}$ cm^2; hence

$$\phi=\phi_o\exp(3.8\times10^{-15}N_u t) \tag{34}$$

For thermal reactors the neutron velocity is determined by the thermal neutron velocity. For a temperature of $T=10^7$ °K, for example, $v=4.36\times10^7$ cm/sec and $\sigma_f=5\times10^{-23}$ cm^2. For the feasible conditions to be contemplated around 10^6 °K, the neutron spectrum might more likely be intermediate, so an assumed neutron temperature of 10^7 °K does not seem to be an unreasonable guess. In any case, for the given numerical values of v and σ_f we have

$$\phi=\phi_o\exp(3.3\times10^{-15}N_u t) \tag{35}$$

which is about the same as for the fast reactor. We therefore may conclude that unless the temperature is rather low the conditions for the growth of the neutron flux do not depend too much on the neutron spectrum; this means that $\sigma_f(v)\cdot v$ is nearly constant over a wide range of energies.

Assuming for the initial neutron flux $\phi_o=10^{14}/\text{cm}^2$ sec and taking the values of equation (34), we then obtain for the required ^{235}U density

$$N_u\cong(6\times10^{14}/t)\log_{10}(10^{-14}\phi) \tag{36}$$

The time must be shorter than or at most equal to the characteristic time τ, which in our case is the expansion time of the plasma ball. If the plasma ball, for example, expands with a speed $v\cong10^7$ cm/sec, it follows that

$$t<10^{-7}R \tag{37}$$

where R is the initial radius of the prompt critical assembly inside the reactor cavity. A critical assembly with $R\cong10$ cm seems to be feasible; hence $t\lesssim10^{-6}$ sec. If the neutron flux were to rise to $\phi\cong10^{22}/\text{cm}^2$ sec, this would then require $N_u>1.6\times10^{21}$ cm^{-3}. Metallic uranium has an atomic number density $N_u^{(0)}=4.6\times10^{22}$ cm^{-3}. Thus the

required minimum densities would be 30 times smaller than those in metallic uranium.

DYNAMIC FUEL-PROPELLANT SEPARATION

The amount of energy delivered can be roughly estimated as follows: The minimum critical mass of fissionable material will be at least 1 kg. The total fission energy of 1 kg of ^{235}U is 0.74×10^{21} ergs. If a fuel burnup of $\Delta N_u/N_u=10^{-3}$ or $\Delta N_u/N_u=10^{-2}$ is achieved, this implies an explosive energy of 0.74×10^{18} or 0.74×10^{19} ergs. This corresponds to an explosive charge of approximately 10 or 100 tons of TNT. Fortunately, this energy does not have to be delivered in one single explosion if a fuel retainment factor $S>1$ can be achieved. To obtain the yield y per miniexplosion we have to multiply this energy by the mean lifetime ratio τ_h/τ_u of propellant and fuel atoms in the reactor vessel. If the maximum fission energy contained in the critical mass is E_o, the yield is given by

$$y=\frac{\Delta N_u}{N_u}\frac{E_o}{S} \tag{38}$$

where we have observed that $\tau_h/\tau_u=v_u/v_h=S^{-1}$. Since the total energy is given for $S=1$, the number S is equal to the number of miniexplosions needed to set free the energy $y_o=(\Delta N_u/N_u)E_o$, which for $\Delta N_u/N_u=10^{-3}$ is of the order of 10 tons of TNT.

If the propellant is placed toward the exhaust nozzle in front of the expanding uranium plasma, it will reach the nozzle before the uranium plasma. A possible mechanism for attaining a sufficiently high fuel-propellant separation may be an exhaust nozzle which rapidly closes in order to prevent the uranium plasma from escaping with the propellant. By the nature of the explosive process occurring, the hydrogen propellant can be shock heated up to high temperatures without being mixed up with the uranium plasma. The rapid plugging of the exhaust nozzle may even lead to increased values of fuel-propellant separation not attainable in the steady-state systems. According to equation (19), this would imply an increase in general reactor economy not only through increased temperature but also through an increased fuel retainment factor. To be retained within the reactor vessel, the hot uranium plasma would have to be solidified in order to be reusable for a new critical assembly in the proposed chainlike scheme of operation. This, of course, would add additional weight to the vehicle mass, mainly for discharging thermal waste energy. The dynamic fuel-propellant separation may be very efficient because of the large ratio of sound velocities for hydrogen and uranium at some given temperature, which is $(235)^{1/2}=15.3$. This indicates that large separation ratios can be achieved because the plug can be closed before the expanding uranium plasma reaches the nozzle. It does not seem unlikely that in this way values of $S\cong100$ are attainable, and thus the energy per explosion will be reduced from 10 tons of TNT to 100 kg of TNT.

The speed with which the nozzle would have to be closed is given by

$$v_p\cong v_uD/L \tag{39}$$

where D is the nozzle diameter and L is the length of the reactor vessel. Assume, for example, $v_u=10^5$ cm/sec and $D/L=0.1$; it follows that $v_p\cong10^4$ cm/sec. A speed of this value can be easily reached with a plug driven by pressurized gas.

In the case where the system is operated without fuel retainment, the energy output would be of the order of 10 tons of TNT, too large to be confined in a reactor vessel. In this case the reactor vessel would have to be replaced by the pusher plate, as in the Orion propulsion concept, although the energies contemplated would still be smaller than those in this latter concept.

Because of its lower critical mass and its lower boiling and melting points (an important factor for the fuel reprocessing), it may be advantageous to use plutonium. To shield the reactor vessel from the thermal radiation of the expanding fireball of fissionable material, the latter has to be completely imbedded in hydrogen. To obtain a large flow of hydrogen out of the reactor nozzle, it is obvious that much more hydrogen is placed between the critical mass and the nozzle than in other directions. This geometry will then always lead to trapped hydrogen after the nozzle is plugged. This hydrogen would have to be separated from the fissionable material in the fuel reprocessing assembly. The principle of this idea is shown in figure 1. In figure 2, a block diagram shows the interconnection of the different system components.

One important problem also occurring in the bomb propulsion system is the ablation of the con-

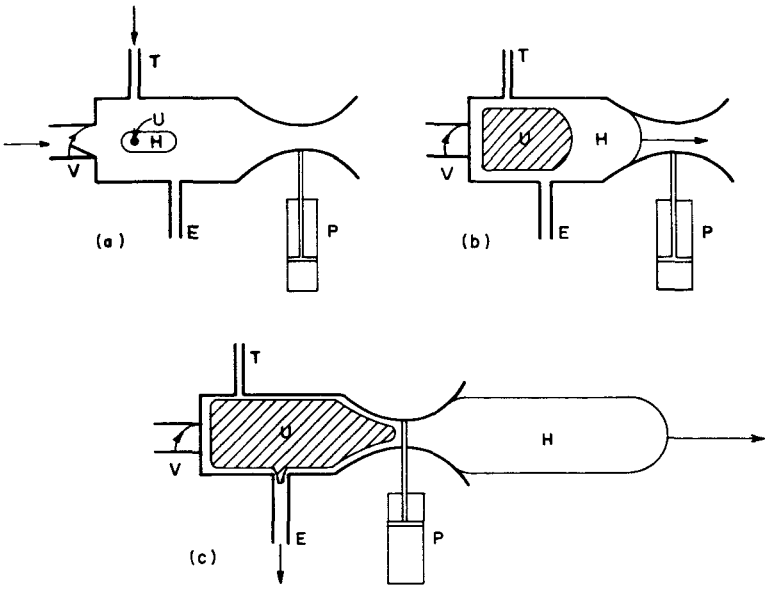

FIGURE 1.—*Operational cycle of pulsed nuclear rocket reactor.* (a) *Subcritical assembly of fuel and propellant is injected into reactor vessel and valve* V *is closed.* (b) *Subcritical assembly is made prompt critical by injection of trigger through channel* T. *The uranium plasma expands rapidly by fast-rising chain reaction and pushes hydrogen toward exhaust nozzle. Hydrogen between uranium fireball and container wall protects the latter from direct exposure to thermal radiation.* (c) *Most of the hydrogen has left reactor vessel and uranium in reactor vessel is trapped by closing nozzle plug* P *driven by a piston. Uranium-hydrogen mixture trapped inside the reactor vessel is removed via exhaust channel E, which leads to radiator and fuel-propellant reprocessing plant.*

tainer wall by the rapidly expanding hot fireball. In the case of the smaller explosion being envisaged in our case, this problem can be greatly alleviated by using a strong static magnetic field to reflect the completely ionized plasma of the fireball. In order to withstand a maximum pressure of 10^9 dyn/cm^2, a magnetic field of 1.6×10^5 G is required. A field of this strength can be produced by superconducting coils. The magnetic field not only will reflect the fireball from the wall of the reactor vessel but also will serve as a cushion to soften the impact of the shock absorbed in the wall.

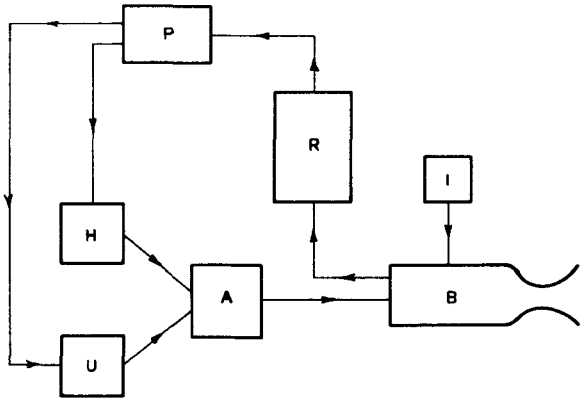

FIGURE 2.—*Flow diagram for pulsed nuclear rocket reactor.* A, *storage for fuel-propellant subcritical assembly;* B, *reactor vessel;* I, *storage for trigger to make subcritical assembly prompt critical;* R, *radiator;* P, *fuel-propellant separation and reprocessing plant;* U, *fuel storage;* H, *propellant storage.*

We would like to add that a dynamic fuel separation process is not new in engineering science and is, for example, practically realized in the two-cycle internal combustion engine and in the Schmid-Argus (V–1) jet propulsion system. Also, the advantage of a pulsed operation is utilized in internal combustion engines, where the temperatures in excess of 2000° K would be unacceptably high under continuous operation for reasons of material problems.

FUEL-PROPELLANT OPTIMIZATION

For electric propulsion systems it has been shown by Stuhlinger (ref. 3) that there exists an optimal

exhaust velocity which depends on the specific power of the energy production system and on the mission, the latter defined in terms of a certain terminal velocity and the propulsion time. For the optimal exhaust velocity, the mass ratio M_o/M_L of the initial to the final (load) vehicle mass will be a minimum.

In the case of a plasma-core rocket reactor it is not so important to minimize the mass ratio M_o/M_L as it is to minimize the amount of consumed fissionable fuel, a condition which is dictated by its high cost. The question to be answered is, therefore, which fuel-propellant ratio to be ejected in the exhaust will minimize the total amount of required fuel mass per payload mass. This minimum will require a higher mass ratio than the minimum possible mass ratio, which, however, is of minor importance because of the high fuel cost.

In order to derive the condition for optimization, we start from the basic rocket equation

$$\exp(u/v) = M_o/M_L = (M_u + M_h + M_L)/M_L \tag{40}$$

where u is the terminal rocket vehicle velocity, v is the exhaust velocity, and M_u, M_h, and M_L are the masses of the fuel, propellant, and the load, respectively. We furthermore use equations (21) and (22) to obtain

$$(M_u + M_h)\, v^2/2 = (\Delta N_u/N_u)\,(\epsilon_o\, M_u/M_u) \tag{41}$$

Defining a characteristic velocity v_o by

$$v_o^2 = 2(\Delta N_u/N_u)\,(\epsilon_o/M_u) \tag{42}$$

we obtain after inserting it into equation (41)

$$M_h/M_u = (v_o/v)^2 - 1 \tag{43}$$

This then leads to

$$\exp(u/v) = 1 + (v_o/v)^2 (M_u/M_L) \tag{44}$$

from which we obtain

$$M_u/M_L = (v/v_o)^2 [\exp(u/v) - 1] \tag{45}$$

This gives the ratio of the fuel to load mass as a function of the exhaust velocity for a given terminal velocity u. The characteristic velocity v_o is to be considered a fixed parameter. Putting

$$(u/v) = x \qquad (M_u/M_L) = (u/v_o)^2 y \tag{46}$$

we obtain from equation (45)

$$y = x^{-2}[\exp(x) - 1] \tag{47}$$

The minimum of this equation is determined by the solution of

$$\exp(-x) = 1 - (x/2) \tag{48}$$

with $x \cong 1.6$ and $y \cong 1.56$. We therefore have under optimal conditions

$$(M_u/M_L) = 1.56(u/v_o)^2 \tag{49}$$

Furthermore, because of equation (43),

$$(M_h/M_u) = 2.55(v_o/u)^2 - 1 \tag{50}$$

By inserting the numerical values into equation (42) we have

$$v_o^2 = 1.5 \times 10^{18} (\Delta N_u/N_u) \tag{51}$$

and hence

$$(M_u/M_L) = 10^{-18}\, u^2 (\Delta N_u/N_u)^{-1} \tag{52}$$

and

$$(M_h/M_u) = 3.8 \times 10^{18}\, u^{-2}\, (\Delta N_u/N_u) - 1 \tag{53}$$

Because of equation (23), one has

$$a\, S = 2.35 \times 10^2\, [3.8 \times 10^{18}\, u^{-2} (\Delta N_u/N_u) - 1] \tag{54}$$

The temperature at optimal operational condition, according to equation (25), is given by

$$T = 4.2 \times 10^{11} \{1 + 2.35 \times 10^2 [3.8 \times 10^{18}\, u^{-2}\, (\Delta N_u/N_u) - 1]\}^{-1} \frac{\Delta N_u}{N_u} \tag{55}$$

for which we can write approximately

$$T \cong 4.7 \times 10^{-10}\, u^2 \tag{56}$$

The optimal exhaust velocity, according to equations (46) and (48), is given by

$$v = u/1.6 = 0.62\, u \tag{57}$$

Let us take, for example, $\Delta N_u/N_u = 10^{-3}$ and $u = 10^7$ cm/sec. It follows that $M_u/M_L = 0.1$, $M_h/M_u = 37$, $a\, S \cong 0.9 \times 10^4$, $T = 4.7 \times 10^4$ °K, and $v = 6.2 \times 10^6$ cm/sec. If the vehicle has a payload mass of $M_L =$ 100 tons, it follows that $M_u = 10$ tons and $M_h = 370$ tons. For the initial vehicle mass one has $M_o = 480$ tons.

The required rapid growth rate in the chain reaction requires that $N_u \gtrapprox 10^{20}$ cm^{-3}. A homogeneous hydrogen-uranium mixture would therefore yield a value $a \cong 100$. This, then, would require $S \cong 100$. However, larger effective values of a can be achieved by a heterogeneous arrangement of the uranium and

hydrogen, as, e.g., by surrounding the uranium with hydrogen. This requires some additional remarks. As we stated above, good fuel economy in a pulsed reactor operation is possible even with a small fuel retainment factor by going up to high temperatures; e.g., as high as 10^6 °K. This seems to contradict the rather low temperature of 4.7×10^4 °K for the computed example. From the basic fuel consumption, it would follow that a good fuel economy can also be achieved by raising the value for α, since only the product αS enters. However, a substantial rise in α may lead to a noncritical assembly of the uranium-hydrogen mixture. This, of course, is bypassed in a heterogeneous arrangement of fissionable material and the hydrogen by a spatial separation of both substances. This would then locally imply a smaller value of α and a much higher temperature corresponding to the same fuel economy. This hot plasma then will heat up the hydrogen from which it is originally separated, and as a result the average temperature goes down and α increases correspondingly. If, for example, $S=1$, it would require an effective value of $\alpha = 0.9\times10^4$, because in the critical region $N_u > 10^{20}$ cm^{-3}, $N_h \cong 10^{22}$ cm^{-3}, and $\alpha \lesssim 100$, which is required for a fast-growing chain reaction. Therefore, a critical region with $\alpha<100$ would have to be surrounded by a sufficient amount of hydrogen to lead to an effective $\alpha=0.9\times10^4$ if $S=1$. If in the critical region, for example, $\alpha=0.9\times10^2$, this would lead to a temperature for this region of $T=4.7\times10^6$ °K. This hot fireball during its rapid expansion heats the surrounding hydrogen to an average temperature of $T=4.7\times10^4$ °K, which corresponds to the effective value of $\alpha=0.9\times10^4$.

ACKNOWLEDGMENTS

The author would like to express his sincere thanks to the NASA Space Nuclear Propulsion Office for support of this project and to Dr. L. Spight of the University of Nevada, Las Vegas, for his critical reading of the manuscript.

REFERENCES

1. Bussard, R. W.: Advances in Astronautical Propulsion. Pergamon Press (New York, N.Y.), 1962, p. 165.
2. Rom, F. E.: Nuclear Rocket Propulsion. NASA TM X-1685, 1968.
3. Stuhlinger, E.: Proc. Fifth Internat. Astronaut. Congr., Julius Springer (Vienna, Austria), 1954, p. 100.

Page intentionally left blank

Gaseous Fission Closed-Loop MHD Generator

ARTHUR SHERMAN

Computer and Applied Sciences, Inc.

The objective of the present paper is to consider the question of achieving a very low specific weight (1 kg/kW) for a nuclear electric space powerplant in order that an electrical propulsion system could prove very attractive for spaceflight. In particular, we would like to consider the feasibility of using a new concept to achieve this goal. That is, we would like to suggest the study of a gaseous fission reactor operating at moderate temperatures in a closed-loop powerplant with an MHD generator as the energy converter. By way of introduction let us review a number of pertinent facts about very distant spaceflight.

It is very clear that distant spaceflight with large payloads will require, in some way, the use of nuclear power in order to avoid the enormous size and cost of chemical rockets. At the present time two approaches are being pursued. The first is the nuclear rocket, and the second is the electric rocket with a nuclear electric powerplant. As far as the nuclear rocket is concerned there are two approaches, the solid core and the gas core. Much development work has been done on the solid-core nuclear rocket which is gas cooled. Present experience suggests that it should be operable at reasonably high temperatures, but because of material limitations it will be difficult to get any value of specific impulse higher than perhaps 10^3 sec. As far as the gas-core rocket is concerned, there is no limitation on the temperature of the nuclear fuel. In other words, it could operate at temperatures as high as 30 000° K, and so its specific impulse will be much higher. Technical problems here will be quite severe, including the question of radiant heat-transfer energy from the gas core to the containing walls and the separation of fissionable material from the rocket exhaust. Unless extremely good methods of separation are found someday, this gas-core rocket concept will be difficult to achieve because of the expense of the fissionable material lost and the concern about the contamination of the environment by this material.

The use of an electric rocket rather than one heated by either chemical or nuclear energy should be feasible also. Experimental work in recent years has shown that such rockets work reasonably well in a desirable range of specific impulse and at acceptable efficiences. However, in order to make the electric rocket concept feasible one must have a low-specific-weight nuclear electric powerplant.

Most of the work on the nuclear electric powerplant has been carried out with the assumption of a solid-core reactor as the heat source. The reactor could either be gas cooled, yielding a Brayton cyele, or liquid metal cooled, yielding a Rankine cycle. In either case turbomachinery has been considered as the conversion equipment. Because of the inherent limitations on temperature caused by the turbomachinery, such solid-core reactor systems have been found to be rather heavy. Some study has been given to the development of a nuclear electric powerplant system with a solid-core reactor and MHD generator as the conversion device. In this case, it would be possible to work with much higher temperatures than in the prior case and there would be correspondingly better system efficiencies and lower weight. However, because of the physical limitations of the solid-core reactor it is still not possible to operate such a system at a temperature high enough to produce a sufficiently highly electrically conducting plasma under thermal conditions. For this reason, much work has been done and continues to be done on the question of nonequilibrium ionization in a moderate-pressure plasma. An

alternate and novel approach to a nuclear electric space powerplant would be to use a gas-core reactor in a closed loop, but with much more moderate temperatures than in the comparable rocket application. In this case several advantages are obtained. First, one avoids completely the difficult problem that exists in the rocket system. Also, since the temperatures are not so severely high as, say, 30 000° K, radiation heat flux from the gaseous core to the solid walls should be a less severe problem. Of course the moderate but quite high cycle temperature would give rise to an extremely low radiator weight and correspondingly low powerplant weight. Finally, an MHD generator for such a high-temperature gaseous system would not only clearly work, but be efficient and compact as well.

The major objective of this paper will be to review an order-of-magnitude analysis which we have made of one possible gaseous fission closed-loop cycle making use of an MHD generator for conversion. By such analysis we hope to show that an attractive specific weight is possible when this concept is used and that more detailed studies would be justified.

GASEOUS FISSION CYCLE

The cycle we have chosen to study to illustrate the concept of using a gaseous-core reactor within a closed loop is a pure uranium vapor system. This system is shown in figure 1. Here we show on a hypothetical temperature-entropy diagram the heating of the uranium liquid in a reactor, its boiling, and its being superheated to a very high temperature at 30-atm pressure. The peak temperature for this study was chosen to be 10 000° K total temperature. The superheated highly ionized uranium vapor would then expand through an MHD generator, lose energy, and thereby drop in temperature and pressure. It was assumed that the radiator would operate at 3000° K so that the vapor pressure of the uranium when it begins to condense would be 0.01 atm. The liquid uranium when it has been fully cooled off is returned to the reactor through an electromagnetic pump.

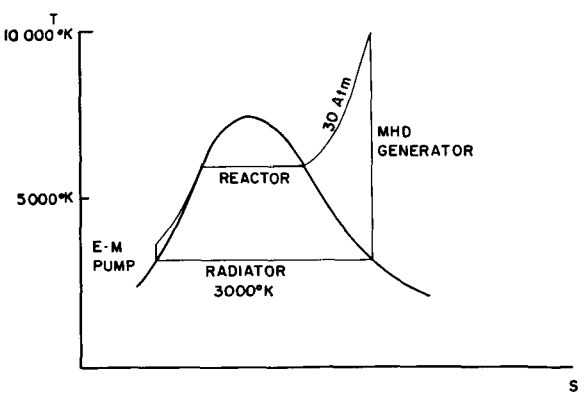

FIGURE 1.—*Temperature-entropy diagram of uranium vapor system.*

GASEOUS-CORE REACTOR

In order to make some estimate of the system weight and performance we will assume a spherical gaseous reactor operating with pure uranium vapor at a total temperature of 10 000° K and a total pressure of 30 atm (ref. 1). In this case, the sphere of uranium vapor would have a diameter of 84 cm, and the D_2O moderator would be in a spherical shell 50-cm thick. The critical mass for this quantity of uranium would be 2.6 kg, yielding a uranium vapor number density of approximately 2.2×10^{19} particles/cm^3. The mass of the moderator would be quite substantial and would be approximately 2970 kg. If we include the necessary structure for this reactor, a very rough estimate for the entire reactor system would be perhaps 3500 kg. It might be noted that in the usual gaseous-core rocket concept, the total pressure is far higher than 30 atm because in those systems the bulk of the gas in the reactor volume is the propellant; in our case there is no propellant and we are dealing entirely with uranium vapor. Accordingly, the overall pressure is substantially lower.

MHD GENERATOR

If we give some thought to the type of conditions that will exist in the channel in which we wish to have our MHD generator, then we immediately realize that it will not be feasible to use electrodes. The reason for this is that we have to deal with a gaseous vapor at 10 000° K total temperature and must cool the walls to at least 3000° K. Now uranium vapor at the pressures under consideration and 3000° K will condense to a liquid, and such condensate will collect on solid surfaces. Therefore, we will have to have some form of film cooling with a noncondensible gas. When we do this, however, we

create a layer of nonconducting gas between the solid wall and the electrically conducting uranium vapor, and this open circuit will prevent any electrode system from being feasible. There is no reason, however, that we cannot think seriously of an ac MHD generator. Such a system will be discussed briefly.

Let us assume that the uranium vapor is accelerated from a plenum chamber to a Mach number of 2 at the entrance to the MHD generator. If we assume a cross-sectional area for the entrance of the MHD generator of 400 cm², then the total energy available can be estimated in the following way:

$$\dot{m}h^o = (\rho u A)\left(\frac{5}{2}RT^o\right) \cong 134 \text{ MW}$$

Now if we assume that the MHD generator will extract only 10 percent of this total energy available, the MHD generator will produce a net of 13.4 MW.

In order to see if such a system would work and to get some idea of the generator's length it is essential that we get a reasonably good estimate of the electrical conductivity of the pure uranium vapor. We do this in the following way: Assume that the uranium vapor expands up to Mach 1 in a quasi-equilibrium state, and then above Mach 1 up to Mach 2 in a frozen state. In this case, one can calculate the electron density in pure uranium vapor at a static temperature of 7400° K and a static pressure of 15 atm. Then if we assume an ionization potential of 6 eV, we calculate an electron density approximately equal to 8.7×10^{16} electrons/cm³. Now we know that in plasmas in the density range under consideration here one finds the phenomenon of overlapping wave functions. The net effect is to yield a reduction in the apparent ionization potential. Again, in order to make a rough estimate, we shall assume that the increase in the electron density due to this effect is by a factor of 5, so that the electron density will be estimated as approximately 4.4×10^{17} electron/cm³. For this electron density and the other conditions being assumed, we obtain an approximate figure for electrical conductivity of 2300 mhos/m.

Next we wish to make an estimate of ac generator performance with a plasma of this type. From a simplified model of an MHD generator we can develop the following two relationships for power density and magnetic Reynolds number:

$$P = \frac{\pi B_o^2 U_B R_m}{\mu_o \Lambda (1+R_m^2)}$$

$$R_m = \mu_o \sigma U\left[\frac{\Lambda(1-S)}{2\pi}\right]$$

where

B_o magnetic induction
U_B traveling magnetic field velocity
$\mu_o = 4\pi\times10^{-7}$
Λ wave length of traveling field
U flow velocity
S slip velocity factor, U_B/U

Next, let us assume a slip velocity factor of 0.7, a wavelength of 50 cm, and a magnetic induction of 8500 G. With these assumptions and the electrical conductivity already calculated we find a magnetic Reynolds number of approximately 0.1 and a power density of approximately 0.335 kW/cm³.

Accordingly, in order to generate 13.4 MW with this power density, we will need approximately 0.04 m³ of volume. If the initial area is 400 cm², then the length of the generator will be approximately 100 cm.

Because of the reasonably small generator size we have estimated here and the relatively modest magnetic field requirements, we would make a rough estimate that the weight of the generator system will be approximately 500 kg.

RADIATOR

The condensing radiator that would be necessary in the system that we are considering would admittedly have to operate under extreme conditions. However, if we assume this radiator to be made of a refractory metal such as tungsten, it may be possible to operate it at the high temperature of 3000° K. At this temperature the emissivity of tungsten will be 0.9 and we obtain a rough estimate of the energy that can be radiated away per unit area as 2.76 MW/m². Now since we have chosen to assume that we are generating only 10 percent of the available power, the remaining 90 percent must be rejected through the radiator. Therefore the radiator must reject 120 MW of energy. For the radiating power per unit area just described one would need a surface area of 43 m². Then if we assume that a tungsten sheet 5 mm thick would be adequate for the radiator material and the uranium vapor

would flow between two such sheets, we know the weight of such a tungsten sheet to be 8 lb/ft^2. The radiator then would have an area of 21.5 m^2 and would radiate from both of its flat surfaces. Again a very rough estimate of the radiator mass that would be involved is approximately 1500 kg.

SYSTEM WEIGHT

When use is made of the figures calculated in the previous discussion, it is possible to come up with a rough estimate of the system weight for the gas-core closed-cycle system operating at moderately high temperatures. In the table below, we list the various weights estimated:

	Kg
Reactor	3500
Generator	500
Radiator	1500
Total	5500

The specific weight of such a powerplant is defined as the system weight divided by the system power generated. In this case, since we are generating 13 400 kW, specific weight comes out to be approximately 0.4 kg/kW. If one were to add in to the above a cooling system to keep the reactor moderator cool, then the overall system weight would be on the order of 1 kg/kW. Nonetheless, this kind of very modest specific weight would be an enormous achievement compared with the specific weights being considered for solid-core reactor and turbomachinery systems today.

CONCLUDING REMARKS

In summary, then, we have shown one possible closed cycle using a moderate-temperature gaseous fission reactor along with an ac MHD generator which could possibly yield a system with a specific weight on the order of 1 kg/kW. If it were indeed possible to develop such a powerplant with such a low specific weight then electric propulsion for very distant space missions with very large payloads would be an extremely attractive approach. In fact, many new missions in spaceflight would probably be explored if the spaceflight preliminary designers could allow themselves to plan on such a lightweight powerplant system.

The possibility of such attractive spaceflight systems based on the low specific weight systems that may be possible should warrant further more detailed study of this and similar concepts.

REFERENCES

1. Ragsdale, Robert G.; and Hyland, Robert E.: Some Nuclear Calculations of U^{235}-D_2O Gaseous Core Cavity Reactors. NASA TN D-475, 1961.

2. Sutton, George W.; and Sherman, Arthur: Engineering Magnetohydrodynamics. McGraw-Hill Book Co., Inc., 1965.

DISCUSSION

Winterberg: Several years ago, Colgate et al. proposed a similar system involving a uranium plasma. Colgate told me that the problem was an enormous optical radiation. How large is that in your case?

Sherman: There is a great deal of radiation in any plasma at 10 000° K, and at that temperature it starts to become significant to heat flux. The difficulty in the generator and in the reactor is to keep the walls cool. One would have to find some cooling method, such as film cooling. I think, on the basis of our experience with temperatures this high for very long periods of time, that this is feasible.

Rom: There is 8 or 10 percent of gamma neutron heating deposited in the moderator which has to be dissipated through another radiator. That radiator will have to be heavier than the present one because of the low temperature.

Sherman: Low-temperature radiators can be very small if there is not too much heat to be rejected, say only 10 percent.

Rom: 10 percent is a large amount of heat considering the low temperature at which the heat has to be radiated away. That has to be looked into. Another point is that if uranium gas of 10 000° K is contained within a wall the wall obviously has to be at a lower temperature than 10 000° K. You have mentioned the possibility of film cooling, but if there were no film cooling most of the uranium would condense on the wall.

Sherman: I think there would have to be film cooling.

Rom: A separator would operate at low temperatures. In addition, you will have a large amount of the heat which has to be rejected by a low-temperature radiator. This will greatly affect the weight of the whole system.

Sherman: I agree.

Hoechlin: We have spent about 18 months studying coupling MHD and the gaseous-core reactor. We believe the problem can be solved. We ran into two problems on which we are now working. The first is, as Mr. Rom said, the neutron and gamma radiation. The second is, how do you

accommodate the pressure coupling between the gaseous-core reactor and the MHD? When do you operate at very high pressure and when at low pressure?

Sherman: The gas-core reactor operates at 30 atm.

Kascak: It appears that there would be liquid uranium in the condenser; how would you remove it?

Sherman: One would proceed in very much the same way as with potassium. There is no difference under such extreme temperatures.

Winterberg: I think that plutonium has a boiling point much lower than that of uranium. That would alleviate the problem that has been mentioned.

Page intentionally left blank

Feasibility of a Nuclear Laser Excited By Fission Fragments Produced in a Pulsed Nuclear Reactor[1]

G. R. RUSSELL

Jet Propulsion Laboratory

Several analyses of nuclear pumped gas lasers (refs. 1 to 4) have been carried out recently. In most cases attention has been focused on the role that high-energy particles play in the direct excitation of laser excited states. The formation of excited states due to the recombination of thermal electrons and the associated radiative and collisional decay of these states has not been considered. In this paper we present an analysis in which the effects of low-energy thermal electrons and high-energy particles are included simultaneously in the determination of the populations of the excited states of atomic argon irradiated by fission fragments produced in a nuclear reactor.

PLASMA KINETICS

In the plasma considered in this analysis the degree of ionization is of the order of 10^{-4} and the electron temperature does not exceed 2000° K. In a recombining plasma at these conditions the total number of excited atoms normalized with the number of ground-state atoms does not exceed about 10^{-6}. Thus, the atomic ion production rate can be determined by using data obtained previously with initially un-ionized and unexcited gases. The relevant continuity equations describing the electron balance in the plasma are

$$\frac{d(X^+)}{dt}=S\phi n_a-Mn_a{}^2X^+-D_1\frac{X^+}{n_a\Lambda^2}-n_e\sum_{p=1}^{\infty}\{n_e[K(c,p)+\beta(p)]-n(p)K(p,c)\} \tag{1}$$

$$\frac{dX_2{}^+}{dt}=Mn_a{}^2X^+-\alpha_DX_2{}^+n_e-D_2\frac{X_2{}^+}{n_a\Lambda^2} \tag{2}$$

and

$$n_e=X^++X_2{}^+ \tag{3}$$

where S is a normalized volume source rate and is the rate per neutral atom per unit neutron flux rate with a dimension of square centimeters and ϕ is the neutron flux rate in neutrons per square centimeter per second. The source rate is derived from the emission of fission fragments from a thin uranium coating on the end walls of an optical cavity placed in a nuclear reactor (fig. 1). The value of S for argon (6.29×10^{-16} cm^2) is taken from the work of Leffert et al. (ref. 5). It is assumed that the length of the cavity is equal to the fission fragment range

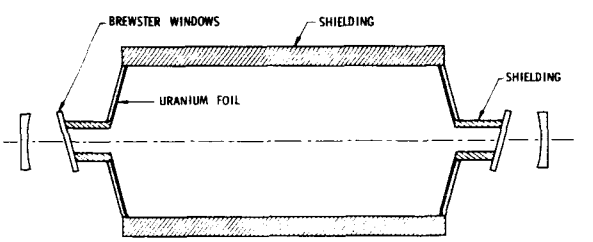

FIGURE 1.—*Reactor optical cavity. Neutron flux is admitted only at cavity end walls and cavity length is set equal to fission fragment stopping distance.*

[1] This work presents the results of one phase of research carried out in the Propulsion Research and Advanced Concepts Section of the Jet Propulsion Laboratory, California Institute of Technology, under contract NAS7-100 sponsored by the National Aeronautics and Space Administration.

in the plasma, and that S is an average source rate and is constant throughout the cavity volume; M is the rate coefficient from the production of diatomic ions by the process

$$X^+ + 2n_a \rightarrow X_2^+ + n_a \qquad (4)$$

where X^+ and X_2^+ are, respectively, the argon atomic and diatomic ion densities. A value of M equal to 2.5×10^{-31} cm^6 sec^{-1} is taken from reference 6. The diffusion rates in equations (1) and (2) are approximated with the use of a characteristic diffusion length Λ, and Λ is equal to $0.416R$, where R is the radius of the optical cavity (ref. 6). Argon mobilities used in the determination of D_1 and D_2 are 1.6 and 1.9 cm^2/V sec, respectively (ref. 7). This approximation is most accurate when diffusion dominates in equations (1) and (2), but since the diffusion rates never exceed about 4 percent of the total electron loss rate from the plasma, the inaccuracy inherent in the approximation is not important. The last term in equation (1) is the net capture rate by atomic ions of low-energy thermal electrons. The symbols $K(c,p)$ and $\beta(p)$ are, respectively, the collisional and radiative coefficients for electron capture from the continuum into level p, and $K(p,c)$ is the ionization coefficient for a transition from level p to the continuum. The dissociative recombination coefficient $\alpha_D=6.7\times10^{-7}$ cm^3 sec^{-1} (ref. 8). Because of the very low concentration of X_2^+ (of the order of 10^{-8}) in the plasma compared with the density of the ground-state atoms, the rate of destruction of X_2^+ diatomic ions by primary fission fragments and high-energy secondary electrons is always small compared with the three-body conversion rate of diatomic ions, so that this destruction rate is neglected in equation (2).

THERMAL ELECTRON ENERGY BALANCE

It has been shown by Platzman (ref. 9) for the case of helium irradiated with alpha particles that the subexcitation electrons that are produced in a series of inelastic collisions by the alpha particles and secondary high-energy electrons retain an amount of energy equal to a fraction ϵ of the helium ionization potential. Because the mean energy expended to form an ion pair normalized with the ionization potential is almost a constant for the noble gases, and since all the noble gases have very similar electronic structure, it is assumed that the value of ϵ for argon is the same as that for helium where $\epsilon=0.31$.

For a large enough degree of ionization (in this case, of the order of 10^{-1}), the subexcitation electrons are quickly thermalized by electron-electron collisions at an electron temperature T_e. These thermal electrons either are captured by atomic ions, gain or lose energy in inelastic collisions with excited neutral atoms, or lose energy in elastic collisions with atomic ions and neutral atoms. The equation governing the electron energy is

$$\frac{d\left(\frac{3}{2}n_e kT_e\right)}{dt} = -4\frac{m_e}{m_a}kn_e\sqrt{\frac{8}{\pi}\frac{kT_e}{m_e}}(n_e q_{ei} + n_a q_{ea})(T_e - T_a) + Q_{rec} - Q_{rad} + S\phi n_a E_{se} \qquad (5)$$

The first term in equation (5) is the elastic energy loss where q_{ei} and q_{ea} are the elastic electron-ion and electron-atom cross sections averaged over a Maxwellian distribution at a temperature T_e. The net gain Q_{rec} in the thermal electron energy due to inelastic electron-atom collisions associated with the radiative three-body recombination of thermal electrons with atomic ions is

$$Q_{rec} = \sum_{p=1}^{\infty} K(c,p)\, n_e^2 I_p - \sum_{p=1}^{\infty} K(p,c)\, n(p)\, n_e I_p + \sum_{p=1}^{\infty}\sum_{q<p}^{\infty} K(p,q)\, n(p)\, n_e (I_q - I_p) - \sum_{p=1}^{\infty}\sum_{q>p}^{\infty} K(q,p)\, n(q)\, n_e (I_q - I_p) \qquad (6)$$

where I_p and I_q are the binding energies of the p and q levels, respectively. The line and continuum radiation loss Q_{rad} is

$$Q_{rad} = \sum_{p=1}^{\infty}\sum_{q<p}^{\infty} G(p,q)\, A(p,q)\, n(p)\, (I_q - I_p) + \sum_{p=1}^{\infty} \beta(p)\, n_e^2 \left(I_p + \frac{3}{2}kT_e\right) \qquad (7)$$

where $K(c,p)$, $K(p,c)$, $K(p,q)$, and $K(q,p)$ are obtained by averaging Gryzinski cross sections (ref. 10) over a Maxwellian electron distribution at the temperature T_e. The radiative recombination coefficient $\beta(p)$ is obtained by using the theory of Biberman et al. (ref. 11).

The last term in equation (5) is an electron

energy source term due to subexcitation electrons created with a thermal energy E_{se} (4.87 eV) in the formation of electron-ion pairs by fission fragments.

DETERMINATION OF THE POPULATION OF ATOMIC EXCITED STATES

Atomic excited states are formed principally by five processes: (1) Recombination of thermal electrons with atomic ions, (2) inelastic collisions between excited atoms and thermal electrons, (3) radiative transitions, (4) direct excitation due to fission fragments and high-energy secondary electrons, and (5) the formation of excited states in the products of dissociative recombination of diatomic ions.

Following the theory of Bates et al. (ref. 12), the time rate of increase of $n(p)$ is given by

$$n(p) = -n(p)\left\{n_e\left[\mathrm{K}(p,c) + \sum_{q\neq p}^{\infty} K(p,q)\right] + \sum_{q<p}^{\infty} G(p,q)\,A(p,q)\right\} + n_e \sum_{q\neq p}^{\infty} n(q)K(q,p) + \sum_{q>p}^{\infty} n(q)G(q,p)A(q,p) + n_e^2[K(c,p) + \beta(p)] + S\phi n_a \eta \Psi(p) + S_D \qquad (8)$$

The first four terms in equation (8), taking into account processes (1) to (3), are included in reference 12 with the exception of the expressions $G(p,q)$ and $G(q,p)$, which are loss factors (ref. 13) varying between zero and one which take into account optical trapping in the resonant transitions. The K coefficients have been defined previously and $A(p,q)$ and $A(q,p)$ are radiative transition probabilities. For the case of argon, level p represents an array which includes all the energy levels with the same principal quantum number. Correspondingly, the individual lines within the array are assumed to be populated in proportion to their degeneracies. Similarly, the radiative transition probabilities are computed for an entire array by using the theory of Bates and Damgaard (ref. 14).

The fifth term $S\phi n_a \eta \Psi(p)$ is due to excitation of level p by fission fragments and high-energy electrons and, analogous to the atomic ion production rate, is assumed to be constant throughout the volume of the optical cavity. Platzman (ref. 9) has shown that for the case of helium irradiated by alpha particles the ratio η of the total excitation rate to the atomic ion production rate is about 0.40. It will be assumed that the same total excitation ratio is valid for argon. However, following the work of Rees et al. (ref. 15), this ratio will be increased to 0.53 to account for the differences between alpha particle and fission fragment excitation. The Ψ values for each array are determined in the following way. Because of the large energy of the primary fission fragments (100 MeV), most of the excitation will occur well past the maximum in the cross section for both heavy particles and electron-atom collisions. Because of the similarity in cross sections at high energies it is assumed that both heavy-particle and electron-atom total excitation rates can be approximated with the use of electron-atom cross sections. The theory of Gryzinski is used to calculate the ratio of the excitation cross section for an array p normalized with the cross section for the first excited state of argon (the 4s array) for optically allowed transitions from the neutral atom ground state. The excitation rate between excited-state levels due to high-energy particles is always negligible compared with the excitation from the ground state because of the exceedingly small excited-state population. The cross section ratio q^*, which is nearly constant over a large range of electron energies, is plotted in figure 2 as a function of quantum number for an electron energy of $10^3\,E_{\mathrm{ion}}$. The Ψ term in equation (8) is evaluated using the cross-section ratios q^* for argon where

$$\sum_{p=2}^{\infty} \Psi(p) = 1.0 \qquad (9)$$

Note that, unlike hydrogen, the argon cross sections tend to oscillate at small quantum numbers. This is a direct consequence of the selection rules for allowed transitions in argon applied to the classical theory of Gryzinski in the determination of the cross sections. It will be shown later that, with the proper plasma conditions, this oscillation of the cross sections can contribute to the formation of population inversions.

The last term S_D in equation (8) is due to the formation of excited states in the process of dissociative recombination. Very little is known about the distribution of excited states in the products of the dissociation of a molecular ion. For the case of argon it is likely that only one of the product atoms will be excited because the energy of the

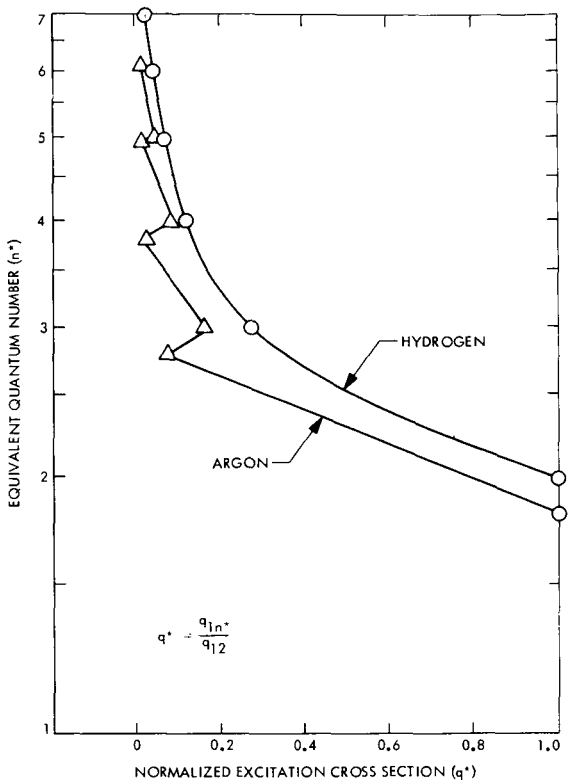

FIGURE 2.—*Normalized excitation cross section as a function of equivalent quantum number.*

first excited state is only about 4 eV below the continuum and the ionization energy is 15.7 eV. If it is assumed that only one of the products is excited, then it must be excited to an energy roughly equal to the ionization energy minus the binding energy of the molecular ion which for argon is 1.1 eV. This corresponds to the production of excited states only above the 4*d* array which is the highest level predicted for population inversions to occur in argon. Thus, inclusion of the production of excited states due to dissociative recombination would only tend to increase the population of the upper laser level. Because of the uncertainty in the specification of the distribution of the values S_D, and because the dissociative recombination rate does not exceed about 20 percent of the radiative three-body rate for the plasmas analyzed, S_D is neglected. It should be pointed out, however, that, for the case where dissociative recombination is the dominate loss mechanism for electrons in the plasma, a precise knowledge of the distribution of the products of recombination could lead to a prediction of population inversions caused principally by this process.

Only electron-atom collisions have been considered in equation (8) because it can be shown by making a comparison of atom-atom cross sections, using the theory of Drawin (ref. 16) and Russell (ref. 17), with electron-atom cross sections, using the theory of Gryzinski (ref. 10), that for a degree of ionization of 10^{-4} or greater the atom-atom collisions can be neglected.

METHOD OF SOLUTION

The reactor neutron flux is assumed to be in the form of a pulse where the flux rate is constant for about 10^{-2} sec. The elastic transfer of energy from the thermal electrons to the ion and neutral particles during this time is not fast enough to change appreciably the heavy-particle temperature, so that the heavy-particle temperature T_a is assumed to be constant throughout the period of the neutron pulse. The plasma kinetics, however, are extremely rapid compared with the neutron pulse time, so that quasi-steady solutions can be obtained from equations (1), (2), (3), (5), and (8) where the time rates of change of X^+, X_2^+, n_e, T_e, and $n(p)$ are set equal to zero.

Equation (8) represents an infinite set of rate equations for the atomic excited states of argon. Depending on the values of the electron temperature and density, a level exists adjacent to the continuum which is in Saha equilibrium at the electron temperature. For the plasma conditions studied here, where $4\times10^{12}<n_e<6\times10^{12}$ cm^{-3} and $1300<T<1800°$ K, all levels above the 6*p* level are assumed to be in Saha equilibrium at the electron temperature. There are 10 levels, including the ground state below the 6*p* level, for which equation (8) is applicable. Thus, equations (1), (2), (3), and (5) and the 9 equations for the first 9 excited states of atomic argon must be solved simultaneously for the 13 variables n_e, X^+, X_2^+, T_e, and $n(p)$ where $2\leqq p\leqq 10$. The 13 simultaneous equations are solved by iteration with the Univac 1180 computer. The results are presented in the next section.

RESULTS AND DISCUSSION

Solutions have been obtained for a range of neutron flux rates $1.8\times10^{14}<\phi<3.0\times10^{14}$ and

atom densities $2\times10^{16}<n_a<7\times10^{16}$ cm^{-3} for a heavy-particle temperature equal to 300° K. The diffusion length (cavity radius R) has been set equal to 10 cm.

The three electron loss mechanisms, collisional-radiative recombination, dissociative recombination, and diffusion, are shown as a function of the neutron flux rate in figure 3. The diatomic ion

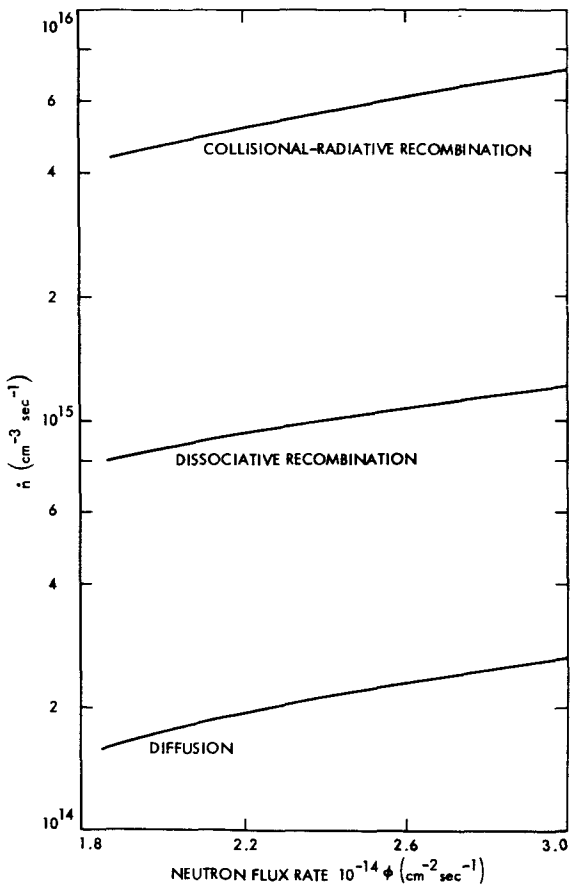

FIGURE 3.—*Electron loss mechanisms as a function of neutron flux rate.* $n_a = 3\times10^{16}$ *cm*$^{-3}$; $T = 300°$ *K; and* $R_{diff} = 10$ *cm.*

formation rate limits the dissociative recombination rate to a value of about 20 percent of the three-body recombination rate, relatively independently of the neutron flux rate. The ratio of the diatomic ion density to the atomic ion density is about 10^{-4} so that the diffusion rate is almost entirely due to atomic ions.

The recombination, radiation, and subexcitation terms in the electron energy equations have been normalized with the elastic energy loss and plotted in figure 4 as a function of the neutron flux rate.

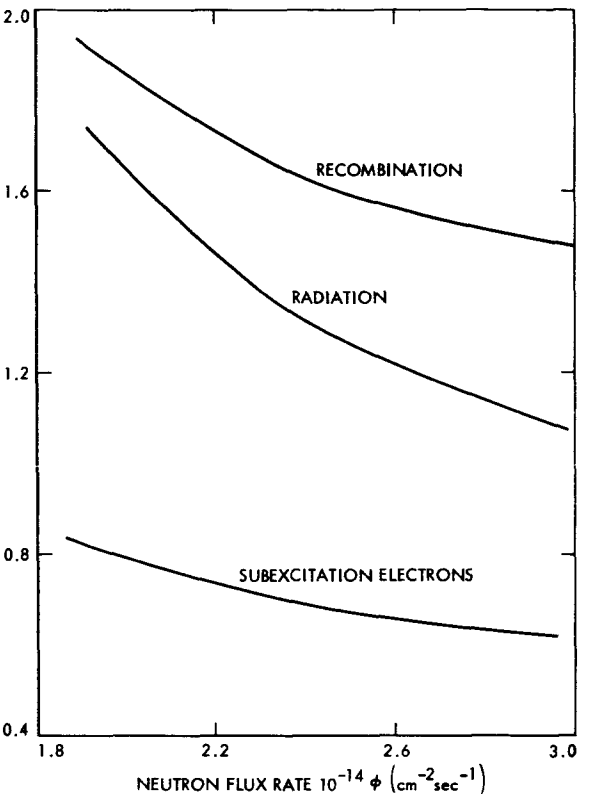

FIGURE 4.—*Terms in the electron energy equation normalized with the elastic energy loss as a function of the neutron flux rate.* $n_a = 3\times10^{16}$ *cm*$^{-3}$; $T_a = 300°$ *K; and* $R_{diff} = 10$ *cm.*

Note that all of the terms are of the same order of magnitude, and that, as the neutron flux rate is reduced, the recombination and radiation tend to become dominant in the determination of the electron temperature.

For the plasma conditions specified above, population inversions were obtained for both the $4d$–$5p$ and $5s$–$4p$ transition arrays. The results are shown in figure 5.

The inversion of the $5s$–$4p$ transition is due to the effects of both thermal electrons and high-energy particles. For the same electron temperatures and degrees of ionization as shown in figure 5, if the excitation due to high-energy particles is set equal

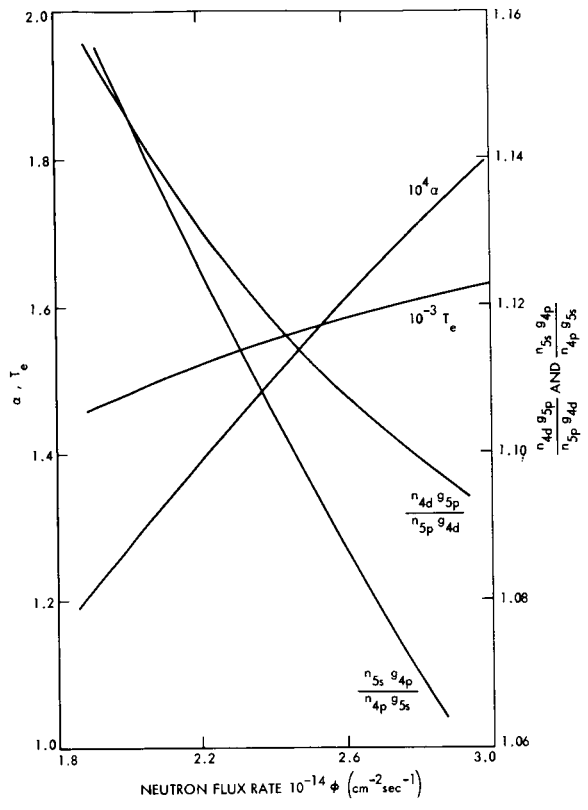

FIGURE 5.—*The degree of ionization* α, *electron temperature* T_e, *and population ratios* 4d–5p *and* 5s–4p *as a function of neutron flux rate.* $n_a = 3 \times 10^{16}$; $T_a = 300°$ *K; and* $R_{diff} = 10$ *cm.*

to zero, solutions of the rate equations governing the excited-state populations show that, although the $5s$–$4p$ population ratio is near unity, it does not exceed 1, and there are no inversions. Thus direct high-energy-particle excitation is required to produce this inversion. Transitions from the ground state to the lower $4p$ level of this inversion are forbidden whereas, as shown in figure 2, the cross section for excitation to the $5s$ level ($n^* = 3$) is larger than that for the $3d$ level ($n^* = 2.86$) which can populate the $4p$ level by an allowed $3d$–$4p$ transition. As the neutron flux is increased, both the electron density and temperature are also increased. Thus the effect of increasing both the atomic ion production rate and the direct high-energy excitation rate is also to increase the detrimental effects associated with increasing the thermal electron temperature and density, until the inversion is eventually destroyed.

The $4d$–$5p$ inversion is caused solely by thermal electron capture and associated cascading due to both thermal electron-atom collisions and radiative transitions. The excitation from the ground state to the $4d$ level due to high-energy particles is negligible compared with the other means of populating this level. Solution of the rate equations with the direct excitation entirely neglected shows that the degree of inversion for the $4d$–$5p$ transition is slightly improved compared with that of the case where direct excitation is included. Thus, although direct excitation is required to produce an inversion in the $5s$–$4p$ transition, it is slightly detrimental to the formation of an inversion of the $4d$–$5p$ transition, principally because of cascading up from the $5s$ level to the $5p$ level of the upper inverted $4d$–$5p$ transition.

The important parameter in the design of a laser is not necessarily the inverted population ratio but is the ratio of the upper laser level to the threshold population for that level because this ratio has to be greater than 1 if oscillation is to be attained in a laser cavity. The threshold population for a single line (subscript L) is

$$n_{TL} = \frac{8\pi(1-R_m)}{L A_L \lambda_L^3} \sqrt{\frac{2\pi k T_a}{m_a}} \left(1 - \frac{n_{iL}}{n_{jL}} \frac{g_{jL}}{g_{iL}}\right)^{-1} \qquad (10)$$

where A_L is the radiative transition probability, λ_L is the wavelength, R_m is the power reflection coefficient of the cavity mirrors, n_j and n_i are the populations of the upper and lower laser levels, respectively, g_j and g_i are their corresponding degeneracies, and L is the cavity length. If the lines in a transition array are populated according to their degeneracies and the substitution

$$A_L \lambda_L^3 = \frac{64}{3} \frac{\pi^4}{h} \frac{S_L}{g_{jL}} \qquad (11)$$

is made in equation (10), the threshold population ratio is

$$\frac{n_{jL}}{n_{TL}} = \frac{8\pi^3 L_c n_{jA}}{3h(1-R_m) g_{jA}} \times \left(\frac{m_a}{2\pi k T_a}\right)^{1/2} \left(1 - \frac{n_{iA}}{n_{jA}} \frac{g_{jA}}{g_{iA}}\right) S_L \qquad (12)$$

The subscript A is for the total array, S_L is the line strength of an individual laser transition within the array, and L_c is the fission fragment stopping

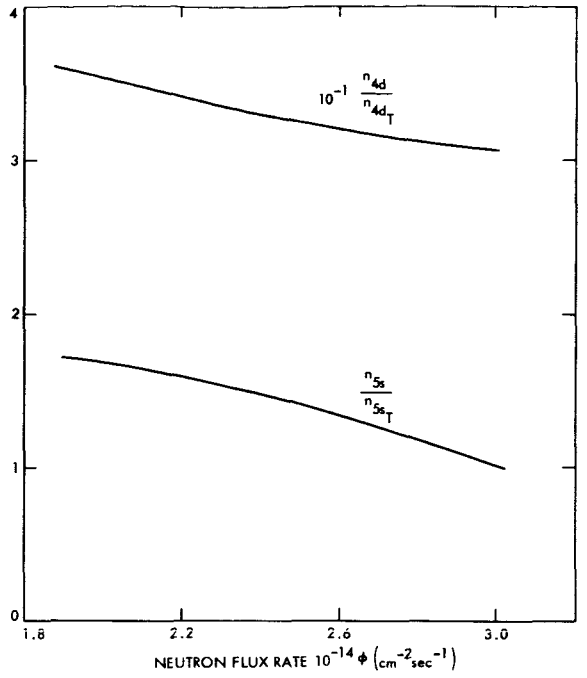

FIGURE 6.—*Threshold population ratios as a function of the neutron flux rate.* $n_a = 3 \times 10^{16}$; $T_a = 300°$ *K*; $R_{diff} = 10$ *cm*; *and* $R_m = 0.99$.

distance. Solution of the rate equations for the atomic excited states yields only the population ratios for the arrays. If S_L is set equal to the total line strength of an array, then n_{jL}/n_{TL} will be an upper bound for a given laser transition. In figure 6 the threshold population ratios are plotted for the 5*s*–4*p* and 4*d*–5*p* transitions as a function of the neutron flux rate where the power reflection coefficient R_m is equal to 0.99.

Note that the ratio for the 4*d*–5*p* transition is about an order of magnitude larger than that for the 5*s*–4*p* transition. Because the threshold ratio for the 5*s*–4*p* transition is not much larger than 1 and because it represents an upper bound for the array, it is very unlikely that oscillation can be achieved in a laser cavity utilizing this transition. The 4*d*–5*p* threshold ratio exceeds a value of 30 so that it is highly probable that oscillation can be attained with one or more lines from this transition array.

Threshold ratios for the 4*d*–5*p* and 5*s*–4*p* inversions were determined for a range of atom densities $2 \times 10^{16} < n_a < 7 \times 10^{16}$ cm^{-3} for a fixed value of the neutron flux rate. The results are shown in figure 7.

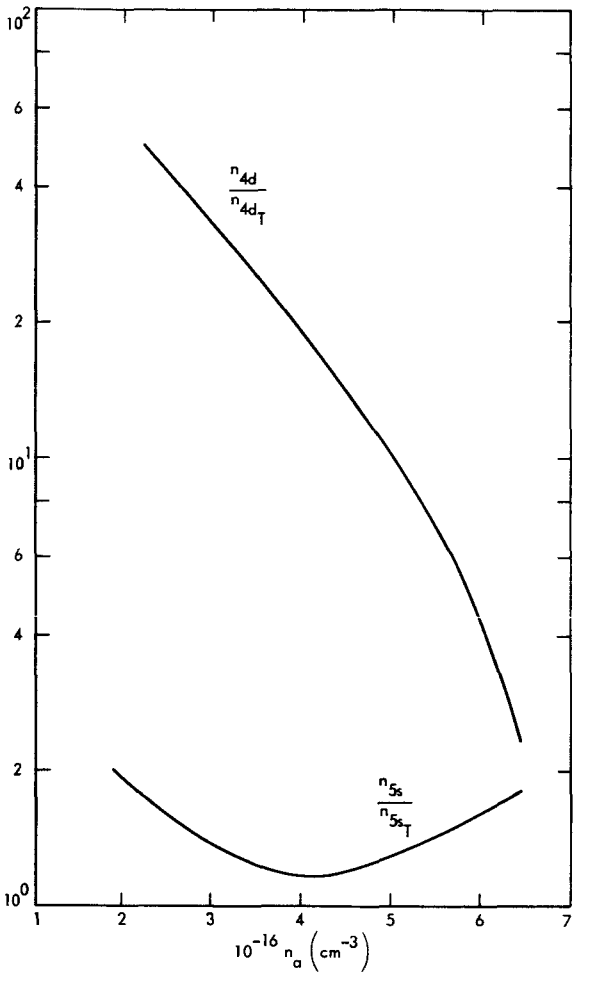

FIGURE 7.—*Threshold population ratios as a function of the atomic density for a neutron flux rate of* 2.54×10^{14} cm^{-2} sec^{-1}.

Values larger than 7×10^{16} cm^{-3} were not considered because the dissociative recombination rate at the larger atom densities starts to dominate the thermal electron loss rate and the theory is no longer valid. Values lower than 2×10^{16} cm^{-3} were not considered because the lower densities require excessively long laser cavities. Depending on the constraints imposed on the length of the laser cavity by the reactor geometry, the data plotted in figure 7 show that it is desirable to operate at as low a pressure as possible utilizing the 4*d*–5*p* population inversion. The range of cavity lengths required for a particular value of the threshold ratio is shown in figure 8. Note that the threshold ratios in excess of

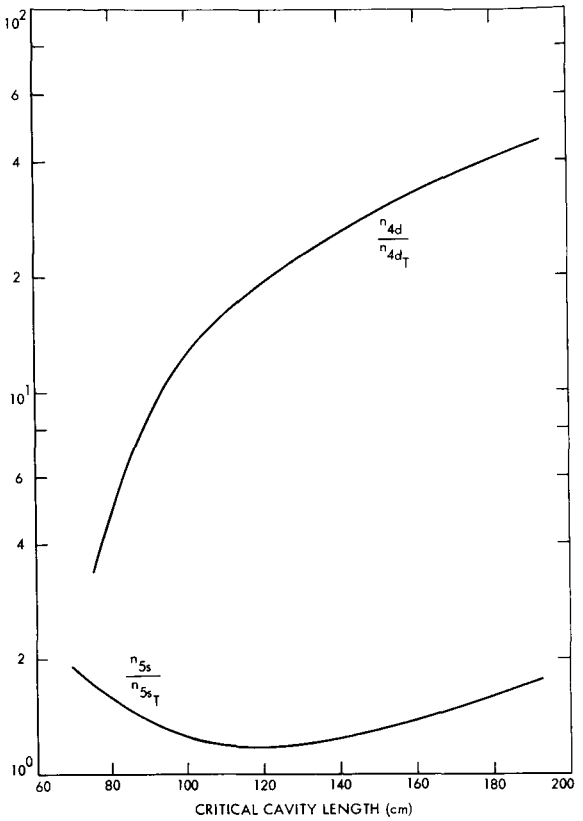

FIGURE 8.—*Threshold population ratios as a function of the critical cavity length for a neutron flux rate of* 2.54×10^{14} *cm*$^{-2}$ *sec*$^{-1}$.

10 can be attained for cavity lengths greater than about 100 cm.

It should be pointed out that in an experiment conducted with a fixed neutron pulse amplitude and a laser cavity of fixed dimensions one should expect a maximum in the laser output as the gas density is varied. If the gas density is too low, the fission fragments will not expend all their energy in the gas and so a reduction in the electron density and the population of the upper laser level will be caused which will cause a reduction in the laser output. If the gas density is too large the inverted population ratio will be decreased (see table I) again causing the laser power output to decrease. Depending on the detailed behavior of the line or lines that lase within the predicted transition array, this maximum could be quite sharp, and the power output quite sensitive to the operating pressure of the laser cavity.

TABLE I.—*Population Ratios of the* 5p–4d *Transition Array*

n_a, cm^{-3}	$\frac{n_{4d}g_{5p}}{n_{5d}g_{4d}}$	
	$\phi = 1.59 \times 10^{14}$ cm^{-2} sec^{-1}	$\phi = 2.54 \times 10^{14}$ cm^{-2} sec^{-1}
2×10^{16}	1.21	1.17
3	1.17	1.11
4	1.14	1.08
5	1.10	1.05
6	1.06	1.03
7	1.01	1.00

It is not known what the effect of a large increase in the atom density would be on the possible power output from the 5*s*–4*p* inversion. Figure 7 indicates that after it passes through a minimum at $n_a \cong 4 \times 10^{16}$ cm^{-3}, the threshold ratio continues to increase as the density is increased. However, further increases in the atom density will result in the production of excited states near the continuum, principally from the products of dissociation recombination, and an associated increase in the electron temperature. It is not known how this would affect the inversion at the 5*s* level.

CONCLUSIONS

It has been shown that both the effects of thermal recombining electrons and direct excitation from high-energy particles are important in the formation of population inversions in nuclear lasers. For the case of argon, one inversion (5*s*–4*p* transition) is formed principally by the process of direct excitation by high-energy particles, and another inversion (4*d*–5*p* transition) is formed indirectly by the recombination of thermal electrons. The gain of the (4*d*–5*p*) transition is an order of magnitude larger than that of the 5*s*–4*p* transition and is the most likely inversion to lase in a cavity of the order of 1 m in length. For the regime of plasma conditions treated in this analysis, where dissociative recombination is not a dominant electron loss mechanism, a limit in the atom density exists where the 4*d*–5*p* inversion is destroyed if the density is further increased. It is not known whether increases in the atom density beyond those considered in this analysis will continue to cause an increase in the

5*s*–4*p* inversion because of the dominance of dissociative recombination at large densities.

Large densities are desirable in nuclear lasers because of the large power potentially available in such devices. However, the theory of dissociative recombination dealing with the specification of the distribution of excited states formed in the reaction products has not yet progressed to the point where an analysis of nuclear lasers utilizing high-density noble gases can be undertaken.

REFERENCES

1. Herwig, L. O.: Res. Lab. Rept. No. C–110053–5, United Aircraft Corp., 1964.
2. DeShong, J. A., Jr.: ANL–7030, Argonne Natl. Lab., 1965.
3. Derr, V. E.; McNice, G. T.; and Rushworth, P. M.: Radioisotopes for Aerospace. Pt. 2. Plenum Press, 1966, p. 309.
4. Rush, J. R.; Cook, R. D.; Eerkins, J. W.; DeJuren, J. A.; and Davis, B. T.: Tech. Rept. AFAL–TR–68–256, 1968.
5. Leffert, C. B.; Rees, D. B.; and Jamerson, F. E.: J. Appl. Phys., vol. 37, no. 1, 1966, p. 133.
6. Smith, D.; and Cromey, P. R.: Proc. Phys. Soc., sec. 2, vol. 1, 1968, p. 638.
7. Oskam, H. J.; and Mittelstadt, V. R.: Phys. Rev., vol. 132, no. 4, 1963, p. 1435.
8. Oskam, H. J.; and Mittelstadt, V. R.: Phys. Rev., vol. 132, no. 4, 1963, p. 1445.
9. Platzman, R. L.: Appl. Radiation and Isotopes, vol. 10, 1961, p. 116.
10. Gryzinski, M.: Phys. Rev., vol. 138, no. 2A, Apr. 1965, p. 336.
11. Biberman, L. M.; Norman, G. E.; and Ulyonov, K. N.: Opt. and Spectros., vol. 10, 1961, p. 297.
12. Bates, D. R.; Kingston, A. E.; and McWhirter, R. W. P.: Proc. Roy. Soc., ser. A, vol. 270, 1962, p. 155.
13. Harstad, K. G.: J. Quant. Spectros. Radiation Transfer, vol. 9, 1969, p. 1273.
14. Bates, D. R.; and Damgaard, A.: Phil. Trans. Roy. Soc., vol. 242A, no. 14, 1949.
15. Rees, D. B.; Leffert, C. B.; and Rose, D. J.: J. Appl. Phys., vol. 40, no. 4, 1969, p. 1884.
16. Drawin, H. W.: Z. Phys., vol. 211, no. 404, 1968.
17. Russell, G. R.: J. Chem. Phys., vol. 50, 1969, p. 4597.

DISCUSSION

Monsler: What is the largest small signal gain that you calculated?

Russell: It is about 10 percent. The population inversions that I showed are the population inversions of the lump states. Each of the transition arrays is predicting a population inversion at a transition array with respect to the other one. It cannot be predicted which one of the lines in that array might be lasing with the line in the other array. The gain it shows is the gain of the population inversion of the two arrays and not the gain for the individual lines.

The population inversion ratios that I showed are those calculated assuming the line strength of an inverted transition to be equal to the total line strength of the transition array. Thus these ratios represent an upper boundary for a single transition within the array. The small signal gain calculated in this way is about 10 percent per meter.

Miley: If this swarm of thermalized electrons could be removed, would there be any flux level at which there would be a population inversion by direct excitation of fission fragments?

Russell: I think probably so, because the behavior of the cross sections at high energy would show an oscillatory nature. As a matter of fact, one of the inversions is caused by the high-energy particles. That inversion wouldn't be there at the same electron temperature and density if the high-speed particles were not there. The catch is that the amount of excitation due to the high-energy particles is smaller than or of the same order as the excitation due to the thermal electrons. There cannot be one without the other. I do not know how the thermal electrons could be removed.

Miley: But the thermal electrons do not interfere with the other process. Is that correct?

Russell: No. They do interfere because those excited states are being populated by thermal electron collisions and radiative transitions. The cross sections for the low energies, that is, the cross sections that are taken over a Maxwellian distribution at the thermal electron temperature, are different from the cross sections pertaining to the high-energy particles. It is a matter of chance. Sometimes the electrons might interfere and sometimes they might augment.

Miley: The temperatures seemed so low (approximately 2000° K) relative to normal discharges that their interference would be minimized.

Russell: That is right. But there is still enough energy in the tail of those distributions to have an appreciable effect.

Miley: I know there is a lot of discussion about Gryzinski cross sections. Could you comment on the validity of the basic cross sections for these calculations?

Russell: No; I really cannot. I do not think we have enough information to attempt to validate them. They are being used in chemical kinetics because there is nothing else available. They are shown to be much more accurate in the low-energy regime than are any of the other approximations.

Miley: One could, for example, use the Gryzinski approximations for the low-energy range and the Born approximation in the higher energy range.

Russell: But the Gryzinski cross sections have the same

asymptotic behavior, the same logarithmic dependence, in the high-energy range. And, even though the absolute value of the cross sections might differ, the ratios of the cross sections at various quantum numbers would probably not change very much between the Born approximation and the Gryzinski approximation.

Feichtner: Your paper is a very nice study and points out that in the laser systems there are more details to be looked at. But, I think that, from a practical point of view, what people really want are more efficient systems in terms of laser output versus energy input. Have you seen any glimmerings of hope that combinations of direct nuclear and electrical excitation would lead to more efficient laser systems in that sense?

Russell: No; there is nothing in this study which would lead to that. In fact, I think that the kind of laser that I described here is certainly not competitive with other lasers of similar power outputs and efficiencies. I solved this problem only to try to look into what really could be done by using just fission fragments without using any electrical excitation. Now, depending on the gas that you use, you could do an analysis like this with both the fission fragments and electrical excitation. I do not know what the result would be. Let me mention in this connection that the dominant mechanism here is three-body capture in upper excited-state levels which subsequently causes inversions in the lower levels. Thus a low electron temperature is needed for this case so the recombination rate will be very fast. There is only a very narrow regime in which you can achieve that because if you use a higher and higher neutron flux then the electron temperature of the plasma will be raised. A completely different problem would be to look at the case where population inversions occur at very high temperature, say in a pure uranium plasma. In that case it is really not clear what the result will be.

Rom: At the end of your paper you made some comments about a swarm of electron interactions in a plasma which lead me to ask the following question: Is there anything in your study that we should consider concerning the effect of electron interactions on the plasma in a gas-core reactor with respect to the spectral emission, the population distribution, etc.

Russell: I believe Dr. Thom mentioned this in his introductory comments. My own feeling is that those plasmas will be very nonequilibrium in nature and the fission fragment process; that is, the kinetics in the plasma will distort everything. It will distort the excited-state populations, which will distort the radiative spectrum. I think it is very unlikely that the plasma will be very near equilibrium, particularly at the edges.

Delmer: I do not think that the Gryzinski cross sections go to the right asymptotic limit for very high energy because they do not have the log E/E dependence which is a quantum mechanical effect. I have two questions which have to do with the geometry. First, I heard from Allen Burgess that the radiative recombination rate is dependent on low-energy radiation fields because of the importance of the high principle quantum number transition. This is a geometry effect depending on what field you have. Second, I would like to know how you calculate the escape probability of the lines.

Russell: The escape probability is calculated using a Holstein loss factor. I am not quite sure what your question is with regard to the radiation. The radiative recombination competes with the three-body recombination to determine the overall recombination.

Delmer: The stimulated emission is quite important for high principal quantum numbers, so that it dominates and can change the recombination rate and the populations of the high quantum number's states quite radically. Therefore, the optical thickness at low frequencies can significantly change the radiative recombination rate that you obtain.

Russell: In the plasmas that I have just described, the only trapping which is really effective is in the resonance lines. That trapping is roughly 10^{-4}. Gryzinski has published a number of papers; the first paper did not have the logarithmic dependency, but the last paper does.

Delmer: This is a quantum mechanical effect. I do not know if you can get that from straight calculations.

Russell: He gets it in a roundabout way, and it is really not clear what his motivation was for doing what he did. However, the cross sections in his last paper do have the logarithmic dependency. In the classical theory, Gryzinski rather arbitrarily chose a velocity distribution of the atomic electron which would yield the correct logarithmic dependency at high energy.

Theiss: Figure 8 shows a very large laser with a 100-cm diam. Let us go back to a practical laser of up to 10-cm diam and low gas pressure. Would your conclusions about the splitting between the direct impact by fission fragments and the high-energy deltas be valid there?

Russell: I did not particularly want to show this because it is rather speculative in details. The idea here is not that there is a 100-cm-diam cavity but that the cavity is about 100 cm long and about 10 cm in diam.

Theiss: I was asking whether one can use a w value in a low-pressure gas in which one cuts off the uranium range and uses only the first part of the trap. Calculations that I have made for direct impact show that the primary fission fragment contributes about 80 percent and the high-energy delta, about 20 percent. You have some numbers to compare with alpha particles, but I do not have the thermal numbers.

Russell: I set the cavity length equal to the stopping distance here so as to be consistent with the use of Platzman's results. If that is not done then the calculation must be done in detail.

Theiss: Yes, it is very complicated.

Page intentionally left blank

SESSION II

CONTAINMENT, FLOW, AND STABILITY

Chairman: **R. G. Ragsdale**

Experiments on the Containment of Simulated Fuel in Unheated and Heated Vortexes[1]

ARTHUR E. MENSING AND JEROME F. JAMINET
United Aircraft Research Laboratories

Experiments were conducted to investigate the simulated-fuel containment characteristics of vortex flows similar to those which would be employed in a nuclear light bulb engine. Isothermal tests using a 10-in.-diam vortex chamber showed that volume-averaged simulated-fuel partial pressures in excess of those required for the nuclear light bulb engine are feasible. Similar tests using a 1.26-in.-diam vortex chamber in which a temperature gradient of approximately 50 000° K/in. was impressed on the vortex flow showed that the temperature gradient resulted in a substantial reduction in the diffusion of the simulated fuel to the peripheral wall of the vortex chamber. This paper summarizes the results of experiments with both heated and unheated vortex flows. Additional descriptions of these investigations are given in reference 1.

The nuclear light bulb engine concept shown in figure 1 requires that the hot gaseous fuel be contained in a region within a transparent wall. The amount of gaseous fuel contained must be sufficient to satisfy criticality requirements and must be separated from the transparent walls by an inert transparent buffer gas (such as neon) to prevent condensation of the fuel on the transparent wall. In the reference engine described in the paper by Clark and McLafferty on page 23, a vortex flow is used to contain the nuclear fuel well away from the transparent-wall structure. The purpose of this investigation is to evaluate the containment characteristics of both heated and unheated vortex flows in terms of the fuel containment requirements of the nuclear light bulb engine.

[1] This research was supported by the joint AEC–NASA Space Nuclear Propulsion Office under contracts NASw–847 and SNPC–70.

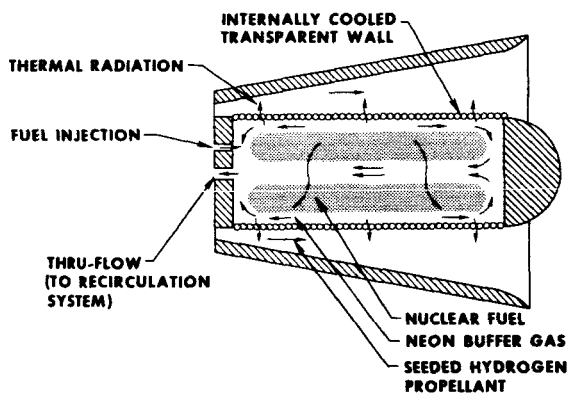

FIGURE 1.—*Sketch of nuclear light bulb engine concept.*

UNHEATED VORTEX TESTS

Unheated or isothermal tests were conducted in a 10-in.-diam vortex chamber 30 in. long, as shown in figure 2. Simulated buffer gas (air) was injected tangentially into the vortex chamber through two rows of wall jets 180° apart (see fig. 2). There were

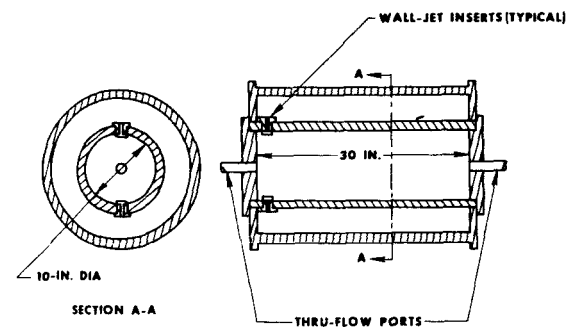

FIGURE 2.—*Sketch of chamber used in unheated vortex tests.*

28 jets in each row, and the total simulated-buffer-gas injection area was about 0.90 in.^{2}. Simulated fuel was injected radially inward through one or several ducts located on the peripheral wall of the vortex chamber. The simulated fuel consisted of a mixture of iodine vapor and one of several different carrier gases so that the molecular weight of the simulated fuel could be changed. Iodine vapor was used because its light absorption characteristics allow the use of optical methods for determining the simulated-fuel density. A description of this measurement technique is reported in references 2 and 3.

Results of containment tests are presented in figure 3, which shows the variation of the volume-averaged simulated-fuel partial pressure $\overline{P}_F$ (nondimensionalized by the vortex chamber static pressure P_1) with the ratio of simulated-fuel to simulated-buffer-gas volume flow rate Q_F/Q_B. The volume-averaged simulated-fuel partial pressure ratio $\overline{P}_F/P_1$ is also equal to the volume fraction of the simulated fuel within the vortex chamber. The data indicate that an increase in the ratio of simulated-fuel to simulated-buffer-gas volume flow rate results in an almost linear increase in the volume-averaged simulated-fuel partial pressure. The data also show that the simulated-fuel molecular weight had no significant effect on $\overline{P}_F/P_1$. The largest values of simulated-fuel partial pressure (the solid symbols in fig. 3) were obtained when a relatively large simulated-fuel injection area was employed (approximately 70 times the injection area for the data shown by open symbols in fig. 3). The reference nuclear light bulb engine requires a value of $\overline{P}_F/P_1$ of approximately 0.25 to satisfy criticality requirements. Values of $\overline{P}_F/P_1$ as high as 0.44 were obtained in these tests. Thus, values of average simulated-fuel partial pressure ratio in excess of those required for the nuclear light bulb engine have been obtained.

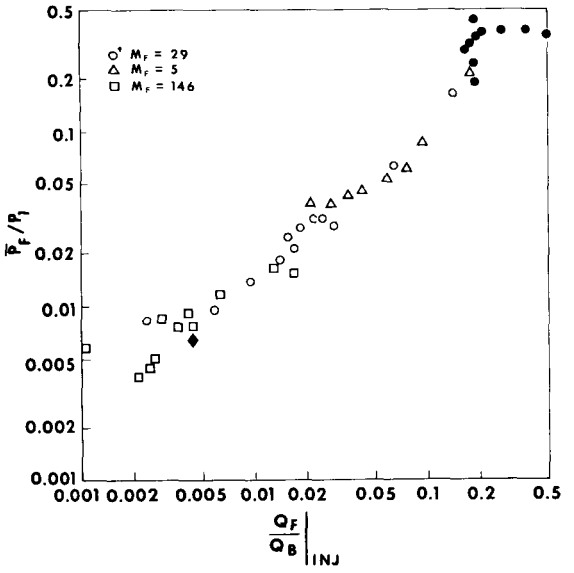

Figure 3.—Effect of ratio of simulated-fuel to simulated-buffer-gas injection volume flow rate on volume-averaged simulated-fuel partial pressure.

Figure 4 presents radial distributions of simulated-fuel partial pressure for configurations having both the large and small simulated-fuel injection areas. The larger injection area resulted in a much more desirable simulated-fuel distribution since the simulated-fuel partial pressure in the interior regions of the vortex was many times greater than that

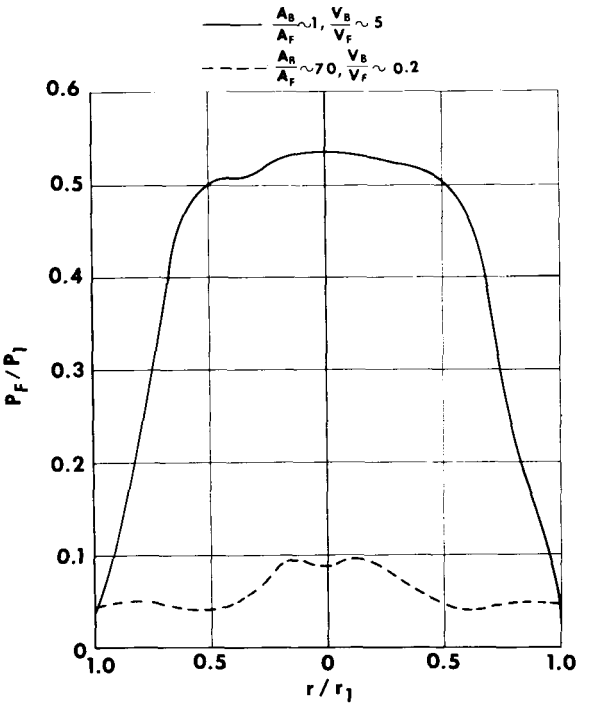

FIGURE 4.—*Radial distributions of simulated-fuel partial pressure.*

near the peripheral wall. Conversely, the small injection area with the resultant high injection velocity resulted in a simulated-fuel partial pressure that was essentially independent of radius. This is undesirable for the nuclear light bulb engine because the high fuel density near the peripheral wall would result in condensation of fuel on the transparent-wall surface.

Additional tests are planned to investigate other simulated-fuel injection configurations, both from the peripheral wall and from the end wall of the vortex chamber.

HEATED VORTEX TESTS

Tests were conducted in which a large temperature gradient was impressed on the vortex flow to determine if the presence of a temperature gradient would either decrease the loss rate of simulated fuel from the vortex or reduce the diffusion of simulated fuel to the peripheral wall of the vortex chamber. For these tests the vortex chamber had a diameter of 1.26 in. and a length of 3.0 in. The temperature gradient was established by rf induction heating the gas within the vortex chamber. A sketch of the vortex chamber is shown in figure 5. The peripheral

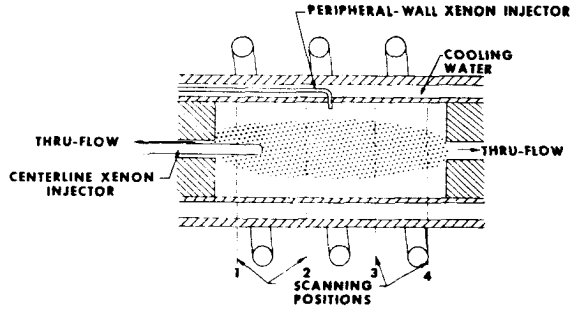

FIGURE 5.—*Sketch of chamber used in rf-heated vortex tests.*

wall consists of a 1.26-in.-i.d. water-cooled fused silica tube. The end walls are water-cooled copper. The simulated-buffer gas (argon) was injected tangentially at the peripheral wall of the vortex chamber. The argon was exhausted from the vortex chamber through through-flow ports located on the vortex centerline. The simulated fuel (xenon) was injected into the vortex at two different locations: (1) Radially inward through a duct on the peripheral wall or (2) axially along the vortex centerline through a water-cooled duct inserted in the through-flow port (see fig. 5). Xenon was not injected simultaneously through both simulated-fuel injection ports.

Approximately 10 kW of power was deposited into the plasma, and the pressure in the vortex chamber was 1.2 atm. The vortex flow confined the plasma away from the peripheral wall of the chamber.

Radiant energy emitted from the plasma was focused onto a monochromator. The monochromator was scanned vertically across the plasma image at the four axial positions shown in figure 5. The intensities of the ArI 4300-Å line and the XeI 4671-Å line and the continuum at 4320 Å were measured. The Abel inversion technique was used to convert the measured chordal intensity data to the variation of intensity with radius. The plasma was assumed to be optically thin and in local thermodynamic equilibrium. The degree of ionization and the percent of xenon present were small, so the measured vortex chamber pressure was assumed to be equal to the pressure of the argon neutral species.

The temperature of the plasma was determined from the measured intensity of the ArI 4300-Å line and the Boltzmann equation,

$$I_{4300} = C_1 \frac{P_{Ar}}{T} e^{-E_n/kT} \tag{1}$$

where

E_n upper energy level (equal to 14.50 eV for the ArI 4300-Å line)
k Boltzmann constant
C_1 proportionality constant

The partial pressure of the xenon within the plasma was also determined from the Boltzmann equation,

$$I_{4671} = C_2 \frac{P_{Xe^0}}{T} e^{-E_n/kT} \tag{2}$$

where

E_n upper energy level (equal to 10.97 eV for the XeI 4671-Å line)
P_{Xe^0} partial pressure of the neutral xenon species, atm
C_2 proportionality constant

Using the temperature determined from equation (1) and the measured intensity of the XeI 4671-Å

line, the partial pressure of the neutral xenon species was determined from equation (2). A species equilibrium calculation (ref. 4) was used to find the total xenon partial pressure (i.e., neutral plus ionized species).

Figure 6 shows typical radial distributions of temperature in argon vortexes with and without xenon injection. The upper curves are data with no xenon injection and show the radial temperature distribution at each of the four axial scanning locations shown in figure 5. Peak temperatures of 10 000° K were obtained near the central regions of the plasma and the temperature decreased near the end walls. The data indicate that temperature gradients as high as approximately 50 000° K/in. were present between the edge of the plasma and the peripheral wall of the vortex chamber. Injection of xenon (1.5 percent by weight) caused a reduction in temperature of about 800° K. The reduction in temperature may be attributed, in part, to a slight reduction in power deposited into the plasma when the xenon was injected.

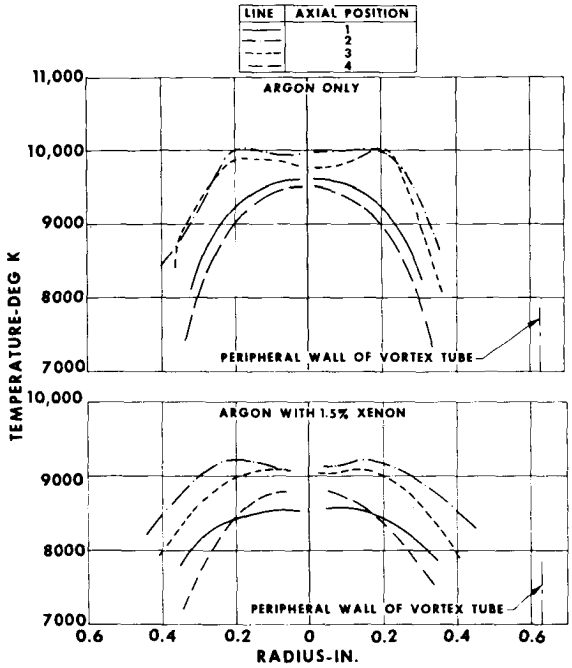

FIGURE 6.—*Radial temperature distributions in rf-heated vortex tests.*

Figure 7 presents the radial variation of the xenon partial pressure within the plasma (both neutral and singly ionized species are included in the xenon partial pressure). The highest xenon partial pressure occurred in the central regions of the plasma with the xenon partial pressure decreasing near the plasma boundaries. Also indicated in figure 7 is the value of xenon partial pressure $\overline{P}_F/P_1|_{mix}$ that would occur if the xenon had been uniformly distributed throughout the vortex chamber. The data presented in figure 7 show that the local xenon partial pressure near the vortex centerline was several times that of the fully mixed value, and near the edges of the plasma it was less than the fully mixed value.

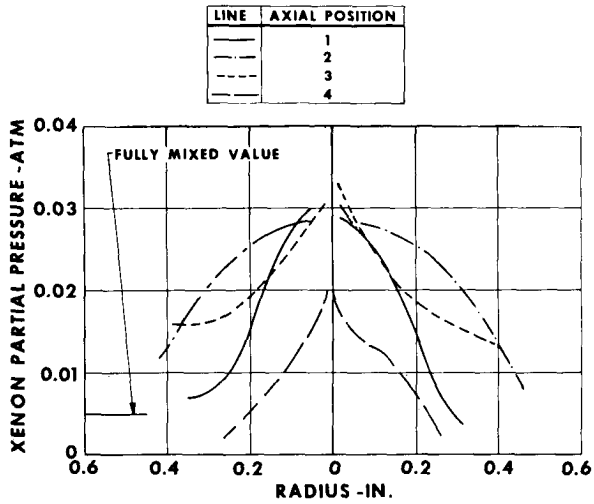

FIGURE 7.—*Radial distributions of xenon partial pressure in rf-heated vortex tests.*

To evaluate the effectiveness of a temperature gradient in reducing the diffusion rate of the xenon to the peripheral wall of the vortex chamber, gas samples were withdrawn at the peripheral wall and analyzed using a gas chromatograph. The results of these tests are presented in table I. Samples were withdrawn both with and without the temperature gradient present and also with xenon injected independently through the two different injection locations shown in figure 5. The measured xenon partial pressure at the peripheral wall $P_{Xe}|_{wall}$ was compared with the fully mixed value $P_{Xe}|_{mix}$. With xenon injection through the peripheral wall and with no temperature gradient present, the xenon partial pressure at the wall was equal to the fully mixed value. The presence of the temperature gradient reduced

TABLE I.—*Comparison of Xenon Partial Pressure at the Vortex Chamber Peripheral Wall for Unheated and Heated Tests*

Configuration	$P_{Xe\|mix}$, atm	$P_{Xe\|wall}$, atm
Peripheral-wall xenon injection:		
Unheated	60×10^{-4}	60×10^{-4}
Heated	60×10^{-4}	8×10^{-4}
Centerline-probe xenon injection:		
Unheated	70×10^{-4}	5×10^{-4}
Heated	60×10^{-4}	$< 1 \times 10^{-4}$

the wall xenon partial pressure by approximately an order of magnitude. When xenon was injected at the vortex centerline, the xenon partial pressure at the peripheral wall was substantially lower than the fully mixed value without a temperature gradient, and the presence of the temperature gradient further reduced the xenon at the peripheral wall by nearly an order of magnitude. These results show that the presence of a temperature gradient greatly inhibits the flow of the simulated fuel to the peripheral wall of the vortex chamber.

In the present experiments the amount of xenon injected into the vortex was relatively small and resulted in volume-averaged fuel partial pressure ratios much smaller than those desired. The solid diamond symbol shown in figure 3 represents data obtained in the heated vortex tests. The data shown in figure 3 indicate that larger values of simulated-fuel partial pressure can be obtained with larger volume flow rates of simulated fuel. Heated vortex tests employing larger xenon volume flow rates are planned.

REFERENCES

1. MENSING, A. E.; AND JAMINET, J. F.; Experimental Investigations of Heavy-Gas Containment in R-F Heated and Unheated Two-Component Vortexes. Rept. H-910091-20, United Aircraft Res. Lab., Sept. 1969.
2. MENSING, A. E.; AND KENDALL, J. S.: Experimental Investigation of Containment of a Heavy Gas in a Jet Driven Light-Gas Vortex. Rept. D-910091-4, United Aircraft Res. Lab., Mar. 1965.
3. KENDALL, J. S.; MENSING, A. E.; AND JOHNSON, B. V.: Containment Experiments in Vortex Tubes with Radial Outflow and Large Superimposed Axial Flows. (Rept. F-910091-12, United Aircraft Res. Lab., May 1967.) NASA CR-943, 1967.
4. MCMAHON, D. G.; AND ROBACK, R.: Machine Computation of Chemical Equilibrium in Reacting Systems. In Kinetics, Equilibria, and Performance of High Temperature Systems. Proc. First Conf. Western States Sec. Combustion Inst. (Los Angeles, Calif., Nov. 1959), G. S. Bahn and E. E. Zukoski, eds., Butterworths, Washington, 1960.

DISCUSSION

Ragsdale: How does the presence of a temperature gradient inhibit the fuel from moving out?

Mensing: I think several things happen. First of all, the temperature gradient has a stabilizing effect on the flow so that any turbulent mixing is going to be damped out drastically. We may go from turbulent to laminar flow, which would cut the fuel loss way down.

Schneider: How did you measure your partial pressures?

Mensing: We measured the intensity of the xenon 4671 line; we had also measured the intensity of the argon 4300 line. From the argon line we determined the temperature of the plasma. From the temperature and the intensity of the 4671 line the only unknown, the pressure, can be obtained.

Schneider: You observed temperature differences similar to those other people have found in a similar type of discharge. I would like your personal opinion as to the reason for the decrease in temperature in the center of the discharge.

Mensing: I do not think there is any question about a decrease in temperature; this has been observed too many times by too many people. It also can be shown that it exists theoretically, partially because of the skin effect. There is not enough energy deposited there and it is radiated away. I do not know whether this would happen in an optically thick plasma, but it does happen in an optically thin plasma; it is a radiation effect.

Schneider: What about the cases where you do not get a decrease?

Mensing: Some of this is just experimental error, I think. The dip in the center for plasmas which are at very low pressure is experimental error.

Kascak: Were your injection ports where you drove the vortex distributed axially or were they all on the side as your figure showed?

Mensing: They were distributed axially. We drew only one in order to show a typical case. There were 28 of them distributed uniformly down the line.

Page intentionally left blank

Exploratory Plasmadynamic Studies of Vortex and Coaxial Flow Geometries Employing Radiofrequency Induction Heating[1]

J. J. KEYES, JR., AND W. K. SARTORY

Oak Ridge National Laboratory

Experiments are described in which the effect of high energy-density volumetric heating on jet-driven vortex flow of argon and on coaxial flow of helium and argon have been determined. A radio-frequency power source capable of 50-kW output in the range from 0.4 to 4.0 mHz was used to heat argon and helium-argon plasmas inductively at atmospheric pressure to peak temperatures estimated to be between 10 000° and 15 000° K depending on plasma composition.

Experiments with 2-in.-diam by 6-in.-long water-cooled copper and quartz vortex tubes have revealed that significant increase in the ratio of tangential velocity to injection velocity above that measured at room temperature is effected when the argon gas is inductively heated to plasma conditions. Exit gas temperatures of up to 7000° K have been measured.

The Oak Ridge National Laboratory facility is unique in that it includes a 6-in.-i.d. superconducting magnet capable of generating reasonably uniform axial magnetic flux densities of up to 2.3 W/m² over the plasma region. This magnet is intended for use in evaluating the influence of strong magnetic fields on turbulent mixing in plasmas. Initial coaxial-flow studies using a 2-in.-diam quartz outer tube for helium and a 1¼-in.-diam graphite injection tube for argon have resulted in a positive correlation of magnetic flux density and coupling between the radiofrequency field and the plasma. This correlation can best be interpreted as suggesting that the magnetic field increases the effective argon concentration in the plasma, presumably because of decreased turbulent mixing.

Work at the Oak Ridge National Laboratory (ORNL) related to gas-core reactor feasibility has, since 1963, been focused on investigation of the effects of magnetic fields on flow stability, initially of jet-driven vortex flow and most recently of coaxial flows. This emphasis came about originally because of our interest in MHD power generation by use of a gas-core reactor heat source. Since we were in the rather unique position of having available very large magnets capable of very high fields in the ORNL Magnet Laboratory (Thermonuclear Division), we decided to take a look first at magnetic stabilization of vortex flow. Success in demonstrating the effect with an electrolytic conductor led us into some exploratory work with vortex flow of argon plasma and, most recently, some studies aimed at evaluation of the effect of a magnetic field on coaxial helium-argon plasma flow (the NASA-Lewis concept) by use of a superconducting magnet.

[1] Research sponsored by the U.S. Atomic Energy Commission under contract with the Union Carbide Corp.

VORTEX STUDIES

In 1965 we demonstrated experimentally what Prof. T. S. Chang and Dr. W. K. Sartory of ORNL had predicted, namely, that an axial magnetic field of sufficient strength can completely stabilize a jet-driven vortex flow of an incompressible electrically conducting fluid (aqueous NH_4Cl) having uniform properties throughout the flow field (refs. 1 and 2).

In figure 1, the observer is looking through Lucite end walls along the axis of a 4-in.-diam tube in which the vortex is generated by injection through four tangential slots. The flow spirals radially inward and is removed at the center of one end. The shadow of the exit tube is evident. The tangential Reynolds number is 10 000 and the radial Reynolds number is about 100. A neutrally buoyant dye is

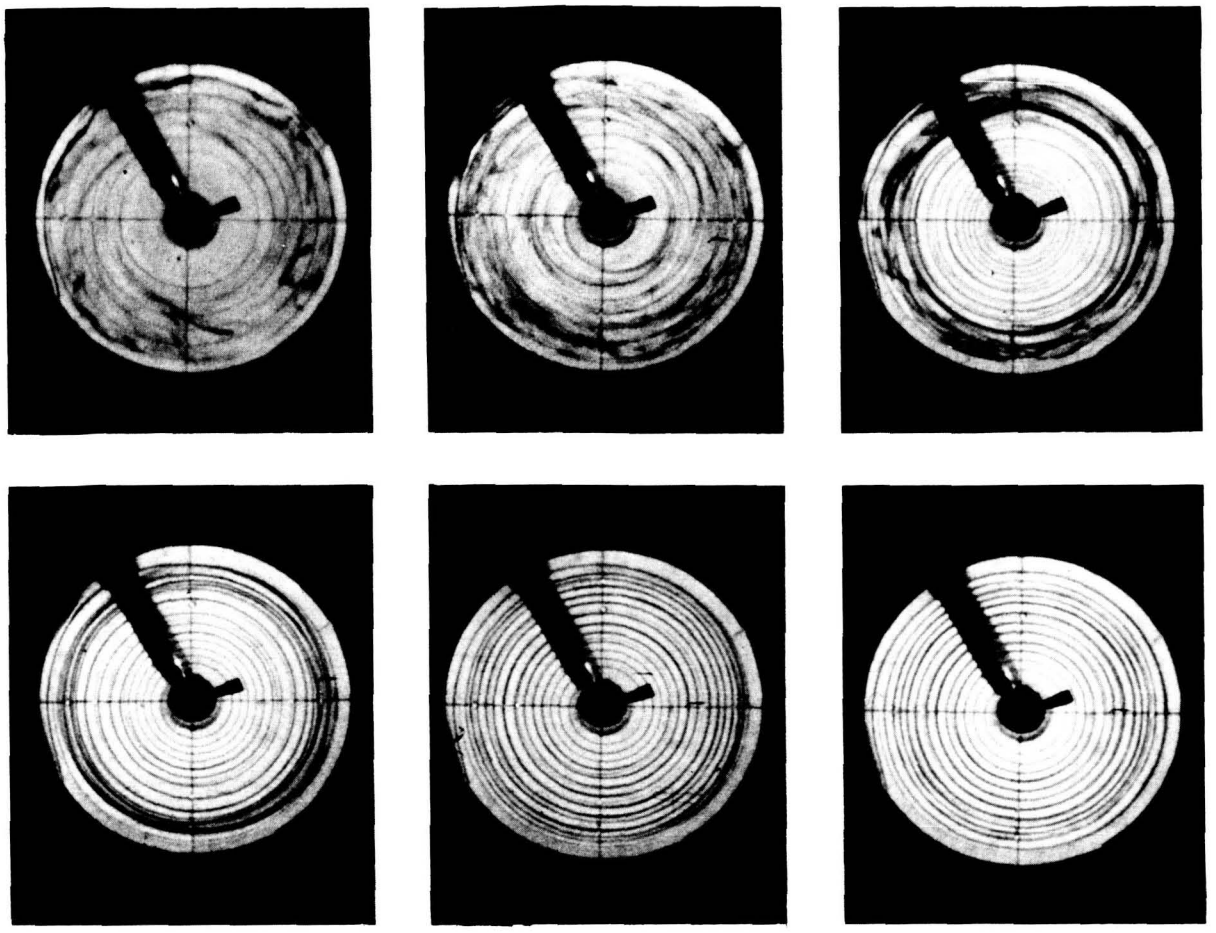

FIGURE 1.—*Stabilization of jet-driven vortex flow by an axial magnetic field. Upper left: no field; lower right: 75 kG.*

admitted through one of the slots, and at the upper left is seen the turbulent flow with no applied magnetic field characterized by large-scale mixing and absence of any well-defined spiral pattern. Now, as the magnetic field is increased in 15-kG increments to the maximum of 75 kG (lower right), progressive laminarization occurs as evidenced by reduction in eddy scale and appearance of spiral dye traces. In fact, in the last frame at 75 kG (Hartmann number of 172) the flow has been completely stabilized by the field.

We were encouraged by this demonstration that magnetic stabilization is, indeed, effective, but we recognized a significant difference between stabilization of an incompressible fluid having uniform properties and the case of practical interest for a gas-core reactor application with compressibility, heat transfer, large property variations, etc. to be reckoned with. Hence, in January 1967 we undertook an experimental study aimed at evaluation of magnetic field effects in vortex flow of plasma by use of radiofrequency (rf) induction heating of argon (simulating fuel) and helium (simulating coolant) to generate thermal gradients of the nature expected in a vortex reactor. We were not able to complete this work because of budget limitations. Significant accomplishments through June 1969 include:

(1) The principal variables affecting coupling of rf energy to the plasma were delineated, thereby making possible determination of optimum induction-coil geometry and frequency for energizing helium-argon plasmas in high-velocity, jet-driven vortex flow. Dr. Sartory, coauthor of this paper,

performed the analysis. The major conclusion is that maximum coupling to the plasma load, for a given plate voltage, load coil, length, and diameter is achieved when the inductance outside the load coil equals the load-coil inductance, which should be as low as possible, and the frequency should be low enough that the skin effect is negligible. This means that the load coil should have as few turns and be as small in diameter, relative to the plasma, as possible. When I^2R losses are considered, the frequency cannot be low enough to satisfy the criterion that the skin effect be negligible; hence, maximum coupling is not achievable in practice, and one has to design for optimum coupling which will transfer the maximum power to the plasma.

(2) Wall heat fluxes up to nearly 1.0×10^6 Btu/hr·ft^2 were sustained in a water-cooled quartz tube having a wall thickness of 0.030 in.

(3) Water-cooled copper and quartz jet-driven vortex tubes (2 in. in diam by 6 in. long) were successfully operated at plasma power inputs up to 20 kW and measured plasma exit temperatures (i.e., temperature of plasma removed from the center of one end of the vortex tubes) up to 7000° K. Pressure was atmospheric. The maximum temperature in the plasma was estimated to be between 10 000° and 15 000° K, depending on plasma composition.

Figure 2 is a cross section of the quartz tube (2-in. i.d.) with the water-cooled copper feed header inserted through a $\frac{5}{8}$-in.-wide slit in the quartz. The vortex is generated by injection of argon or argon-helium mixtures through twenty-six 0.055-in.-diam nozzles as indicated. Some flow is bled off. Figure 3 shows the quartz tube and feed header separated, and figure 4 is the assembled vortex tube. At the right is the water-cooled copper exit end plate and exhaust tube which is used as a calorimeter to determine the exit gas temperature; at the left is the water-cooled copper pressure tap end plate with 20 taps across the 1-in. radius for determining the radial pressure gradient from which the tangential velocity gradient is deduced. The vortex chamber is 2 in. in diameter by about 6 in. in length.

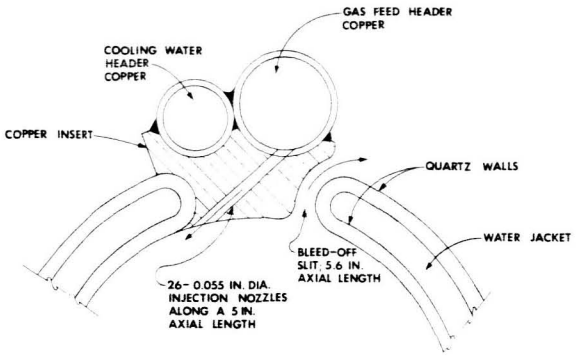

FIGURE 2.—*Cross section of vortex tube for plasma operation.*

Figure 5 is a photograph of the system in operation. The rf load coil is seen just left of the center of the figure.

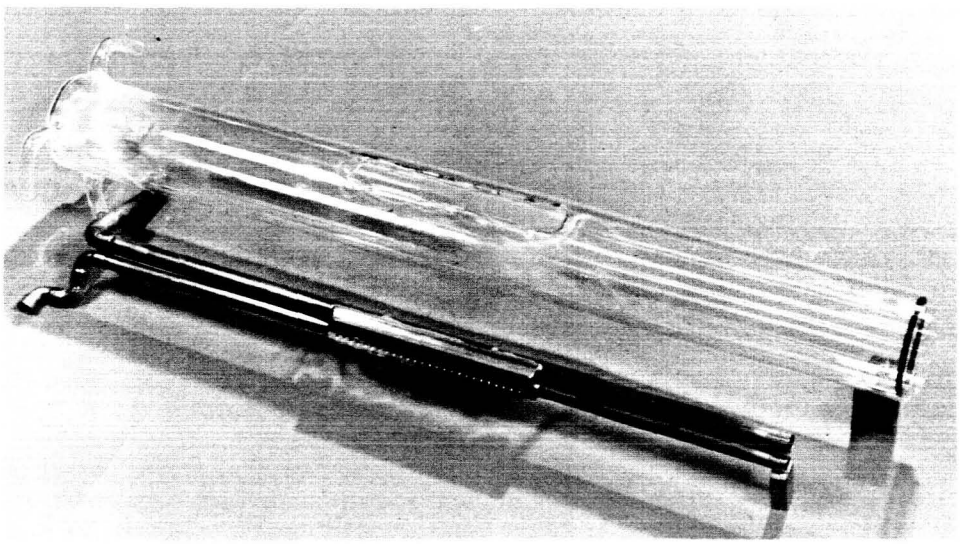

FIGURE 3.—*Quartz vortex plasma holder with copper injector.*

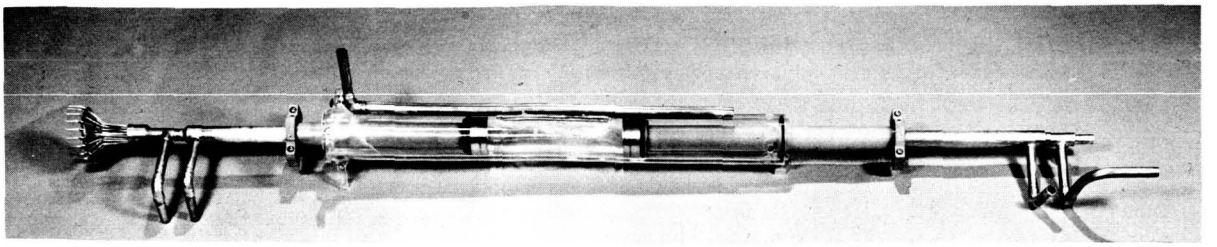

FIGURE 4.—*Vortex tube assembly including pressure tap end plate (left) and exhaust tube (right).*

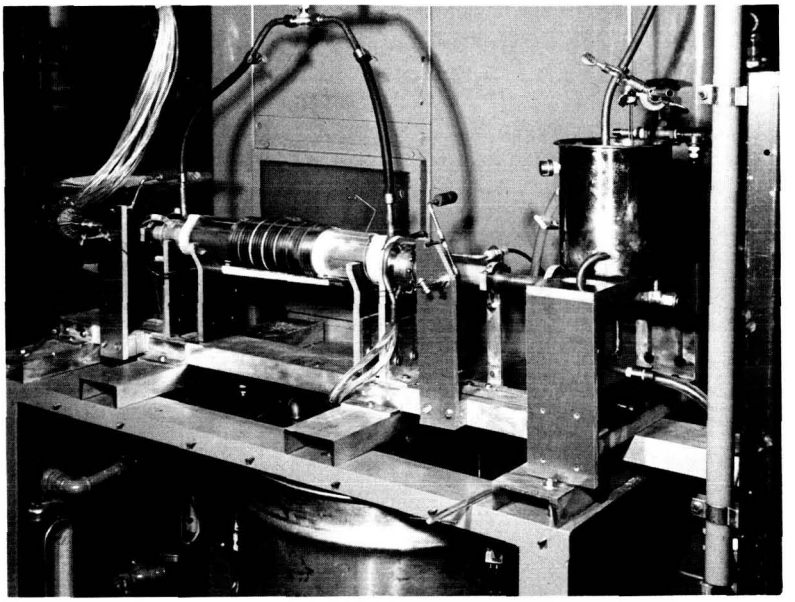

FIGURE 5.—*Vortex plasma system in operation.*

In order to start the system, a carbon arc energized by rf developed across one turn of the seven-turn load coil produces sufficient gaseous conductivity at atmospheric pressure to permit the rf to couple inductively. The discharge immediately grows about ¼ to 1½-in. in diam as the induced current generates the heat required for ionization. The carbon starting rod is then withdrawn and the cylinder of plasma continues to absorb rf energy. One great advantage of rf is, obviously, the elimination of electrodes and associated erosion and contamination problems.

We employed an 80-kW (maximum) input, about 50-kW-output, rf generator which could operate in the frequency range from 0.3 to 4.0 mHz. Most of the experiments were performed in the range from 2 to 3 mHz.

In figure 6 the observer is looking into the end of a water-cooled copper vortex tube open to the atmosphere. (This is at low tangential velocity to prevent air entrainment.) In all of the experiments the gas was discharged directly to the atmosphere; hence, the plasma pressure was very nearly atmospheric.

From the measured end-wall pressures and estimated plasma temperature we were able to make a rough comparison between tangential velocities for cold and hot operation. Typical results are depicted in figure 7. The ratio of local tangential velocity to injection velocity is plotted as a function of radius for an injection Mach number of 0.95, an exit radial Reynolds number of 105, and a ratio of mass flow bled off to exit mass flow of 12. The Reynolds number (based on the injection velocity, a temperature of 530° R, and a tube radius of 1 in.) is

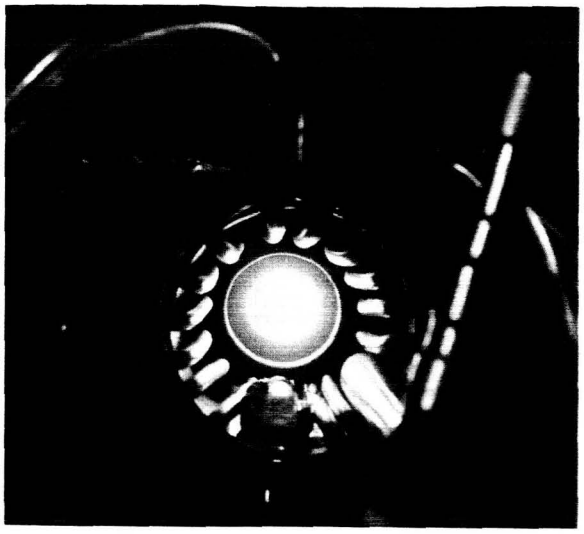

FIGURE 6.—*End view of low-velocity-vortex plasma in copper tube (slitted).*

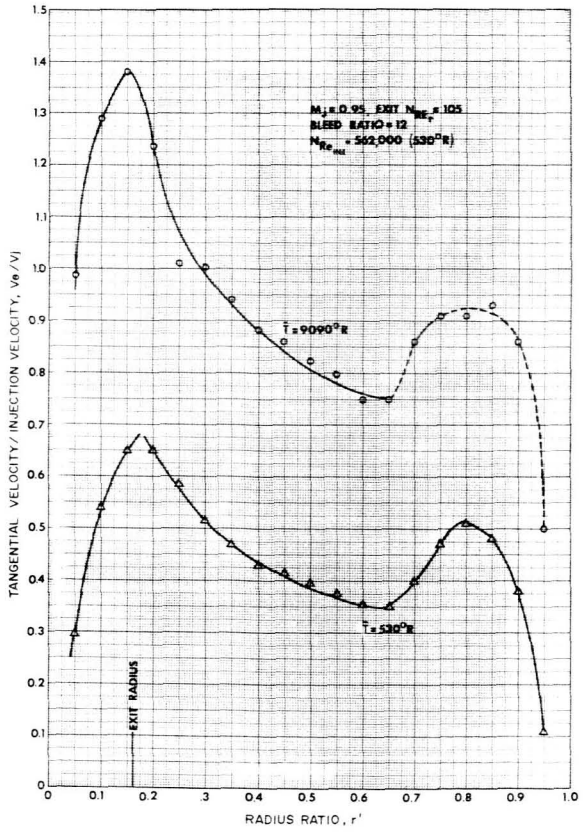

FIGURE 7.—*Effect of plasma heating on tangential velocity profile in a 2-in. quartz tube. Bleed ratio, 12;* $M_j = 0.95$; *exit* $N_{RE_r} = 105$; $N_{RE_{INJ}} = 562\,000$ *(530° R).*

562 000. The lower curve for operation at 530° R displays a peak at a radius ratio of 0.8; this corresponds to the effective radius of injection. The peak velocity ratio of about 0.7 occurs at $r' \cong 0.7$. By using a constant, average temperature of about 9100° R (5060° K), which is the measured exhaust gas temperature (well below the temperature in the plasma), the upper curve is obtained for hot operation in which the peak velocity ratio is about 1.4; this is double that for low-temperature operation. For $r' > 0.6$, the curve indicated is not accurate because this is the region of rapid decrease in temperature with increase in radius. Allowing for this decrease would smooth out the peak shown by a broken line on the graph. The calculation of velocity should have been based on a higher temperature at small values of r' (<0.3). This would have raised the peak and steepened the curve near the center. The conclusion, nevertheless, is that heating results in significant increase in tangential velocity for a fixed injection velocity and exit mass flow. Part of this increase may be attributable to decrease in wall shear because of the stabilizing effect of wall cooling. Furthermore, the stabilizing effect of outward increase in density is reinforced by the effect of an outward decrease in viscosity such that the Reynolds number near the center is about $\frac{1}{35}$ of that near the wall. Thus, a lower turbulence level would be expected throughout the flow field for plasma operation as compared with that for cold operation. Approximately the same comparison between hot and cold operation was found for a range of injection velocities and Reynolds numbers.

By June 30, 1969, a superconducting (Nb-Zr) magnet having a working volume with a 6-in. i.d. and 13-in. length had been tested to a maximum magnetic flux density of 24 kG. This magnet was designed by personnel of the Engineering Science Department, Thermonuclear Division, ORNL, to be used in the study of magnetic stabilization of plasma vortex flow. However, funding of the vortex research was terminated before magnet studies could be initiated. Thus the initial goal of investigating the magnetic stabilization of plasma vortex flow was not attained, and attention has been focused on an investigation of the effect of a magnetic field on coaxial plasma flow.

COAXIAL-FLOW EXPERIMENTS WITH MAGNET

Apparatus

In figure 8 the coaxial-flow plasma holder is seen to consist of a graphite injector tube for argon water-cooled copper gas-sampling probe could be admitted along the centerline of the coaxial geometry, with a thermal conductivity gas analyzer connected to the probe outlet. The mixture of helium and argon is discharged to the atmosphere through a

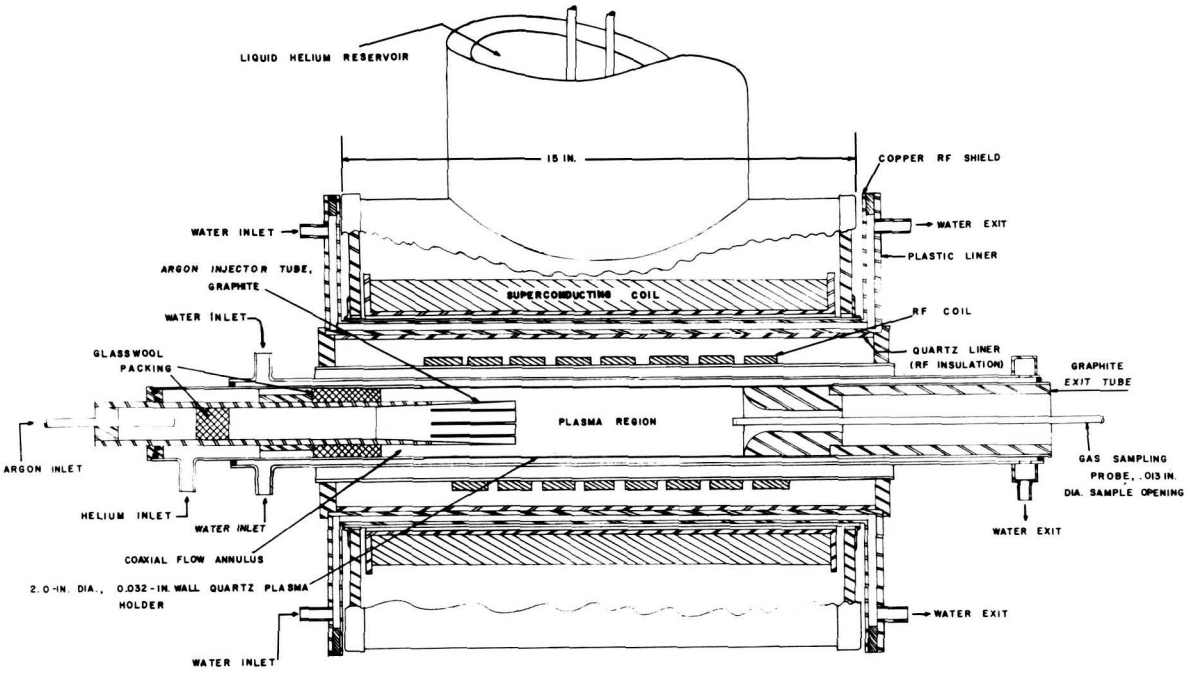

FIGURE 8.—*Coaxial-flow magnetoplasma dynamic experiment.*

(1.25-in. o.d.) coaxial with a 2.0-in.-i.d., thin-walled (0.030-in.), water-cooled quartz tube. Helium is admitted to the glasswool-packed annulus between the argon injector and the quartz tube and mixes with the center argon flow downstream from the injector outlet. No buffer-gas flow is employed. The wall thickness near the outlet tapers from $\frac{3}{16}$ in. to about $\frac{1}{32}$ in. over a 3-in. length. Axial slits cut back 2 in. from the end of the injector tube are filled with Al_2O_3 furnace cement to minimize premixing of helium and argon. These slits permit the rf field to penetrate into the end of the injector, thus assuring a nearly uniform field over the initial plasma region which is immediately downstream from the tip of the injector. Some distortion in the rf field does occur because of the graphite exit tube, the inlet of which was positioned 6 in. from the end of the injector for the runs discussed here. A $\frac{1}{4}$-in.-o.d., $\frac{5}{8}$-in.-diam nozzle, so that pressure in the plasma region is very close to atmospheric.

The rf coil ($3\frac{1}{2}$-in. i.d. by 10-in. length) forms a portion of the tank circuit of a self-excited oscillator capable of 50-kW output when loaded to about 80-kW (*maximum*) input. The operating frequency for these experiments was 2.0 mHz. The superconducting coil (6-in. i.d. by 13-in. length) provides a dc magnetic field of up to 24 kG having adequate uniformity over the 2- by 6-in. plasma region when supplied with a current of 58 A (425 G/A). The liquid-helium-cooled magnet coil is well isolated from rf pickup by a water-cooled copper shield and thermally isolated from the plasma by two water jackets and a liquid-nitrogen-cooled internal radiation shield (not shown). The closely spaced turns of the rf coil absorb much of the radiation from the plasma, and the remainder is absorbed

by the copper rf shield. Thus the plasma, operating at temperatures up to 15 000° K, does not detectably increase the boiloff rate of liquid helium at 4.2° K. Figure 9 is a photograph of the superconducting

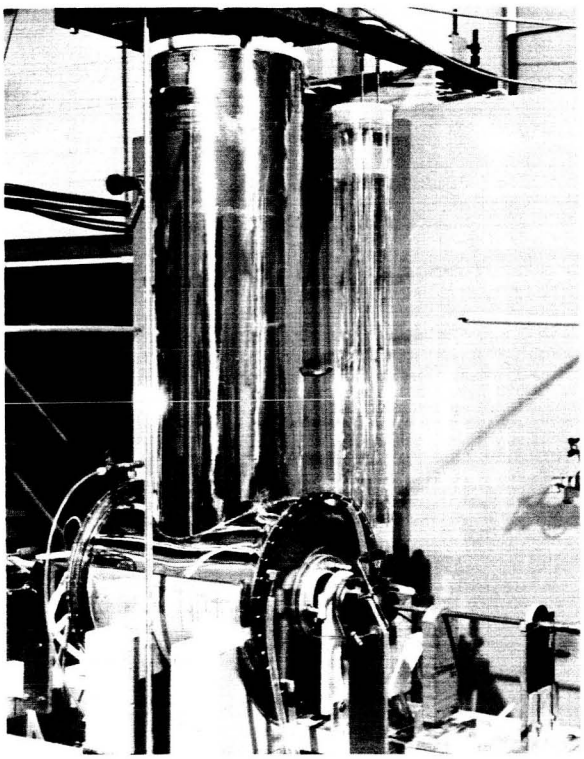

FIGURE 9.—*Superconducting magnet with coaxial-flow experiment installed.*

magnet with the coaxial-flow experiment installed, the view being toward the graphite discharge nozzle. The vertical tank contains liquid helium surrounded by liquid nitrogen.

Operational Techniques

The purpose of the preliminary experiments described herein was to ascertain, in as simple an experiment as possible, whether the application of a magnetic field in the direction of flow could increase the amount of argon held up in a given volume of plasma at any convenient value of the helium-to-argon flow ratio (not necessarily the maximum for the available power). Accordingly, a method for measuring or deducing an average or effective argon concentration in the plasma was required.

Plasma Concentration by Sampling

Much time was spent in attempting to obtain concentrations directly by sampling along the plasma centerline by use of the traversing probe. Results of these experiments were inconclusive. The main difficulty appeared to be a strong interaction between the probe and the plasma which resulted in decrease in coupling and, more significantly, in displacement of the plasma relative to the probe tip. Application of small magnetic fields (up to 1500 G) resulted in shifting of the plasma axially when the probe was in or near the plasma. Hence, in no case was it certain just where, relative to the plasma, the probe was actually sampling. The magnetic field did effect large changes in measured concentration at a fixed probe position, but these changes may have been due to axial shifting of the plasma.

To maintain the plasma with the probe inserted to a position 3 in. or less from the injector outlet, a mixture of argon and helium (about 23 percent helium) had to be fed to the annulus for the following reason. The probe caused a strong quenching effect which tended to decouple the plasma from the rf field, and this effect had to be compensated for by raising the argon concentration. The Reynolds number of the coaxial (annular) flow is estimated to be about 75 based on the tube radius of 1.0 in. and an assumed temperature of 5000° K, and the volumetric flow ratio of the 23-percent-helium-argon annular feed to the pure argon center feed was about 8. Under these conditions the probe results did suggest that mixing ahead of the plasma (i.e., between the injector and the hot plasma region) is less rapid than mixing either within the plasma or just downstream. Also, at any axial probe position, the argon concentration increased when the plasma was extinguished. The implication is that heating increases mixing. Contributing to this effect may be the high molecular diffusivity of helium in argon, which is about 150 times greater at 5000° K (an assumed mean temperature in the mixing region) than at room temperature. In order to reduce the molecular diffusivity, some runs were made with a nitrogen-argon mixture feeding the annulus. A small percentage of nitrogen was sufficient to extinguish the plasma at near maximum power input even with the sampling probe withdrawn, and it was concluded that the high energy of dissociation of the nitrogen and the resulting high effective thermal conductivity

resulted in a prohibitively strong cooling effect. No significant conclusions regarding the effect of diffusivity could be reached.

Effective Plasma Concentration From Grid Current Measurements

The dc grid current of a self-excited oscillator employing a fixed-grid bias resistor decreases with increase in load such as occurs when the coupling between the plasma and the rf field increases at constant plate voltage. The fact that the grid current changes over a relatively wide range for small changes in coupling is utilized to monitor changes in coupling due to changes in plasma characteristics (e.g., electrical conductivity and/or volume). The changes in grid current are interpreted, therefore, as resulting from changes in an effective argon concentration in the plasma. Figure 10, the calibration curve used to relate oscillator grid current to argon concentration, was obtained by measuring the grid current response to known (i.e., "true") compositions of argon-helium premixed and fed to the injector as well as to the annulus in the same flow ratios as those employed in the experiments with separate feed. Variation in the magnetic flux density from 0 to about 15 kG had a relatively small and random effect on grid current, as indicated by the scatter band. This is taken as evidence that the magnetic field does not significantly alter the electrical resistance in this collision-dominated plasma. The effective argon concentration for operation with separate feed of argon to the injector and helium to the annulus (coaxial flow) is defined as that concentration of premixed helium and argon which would give the same relative grid current as determined from figure 10. That is, the grid current measured with separate feed is assumed to depend only on the effective argon concentration, and this effective concentration is the same as the uniform, premixed (true) concentration which produces the same grid current. This indirect method has the advantage of eliminating disturbances to the plasma such as were produced by the probe; the disadvantage is uncertainty in interpretation of the effective argon concentration in terms of total argon holdup. A positive correlation between effective argon concentration and total argon in the plasma region must be assumed in order to interpret the results as indicating a beneficial effect of the magnetic field on argon holdup.

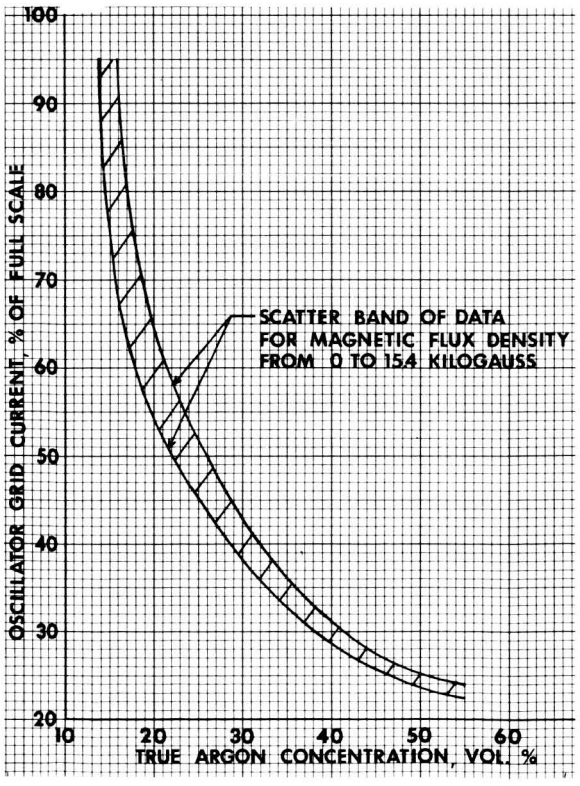

FIGURE *10.—Calibration curve for oscillator grid current and true argon concentration.*

Experimental Results

The most significant results are presented graphically in figures 11 through 14. In all cases, the argon volumetric flow rate was held constant at 0.22 standard ft^3/min, while the helium flow rate was varied from zero to the maximum for which the plasma could be sustained at a fixed oscillator plate voltage. All results pertain to a constant plate voltage of about 13 500 and dc power input of about 50 kW, of which more than 18 kW are generated in the plasma under conditions of maximum coupling.

Effective argon concentration (EAC), as determined from the change in grid current, is shown in figure 11 as a function of the ratio of helium volume flow rate to argon volume flow rate for constant values of the magnetic flux density B from 0 to 15.4 kG. These data were obtained by holding the field constant for all flow ratios. The EAC is greater, at any given flow ratio, with the field applied than without the field, but there are significant anomalies

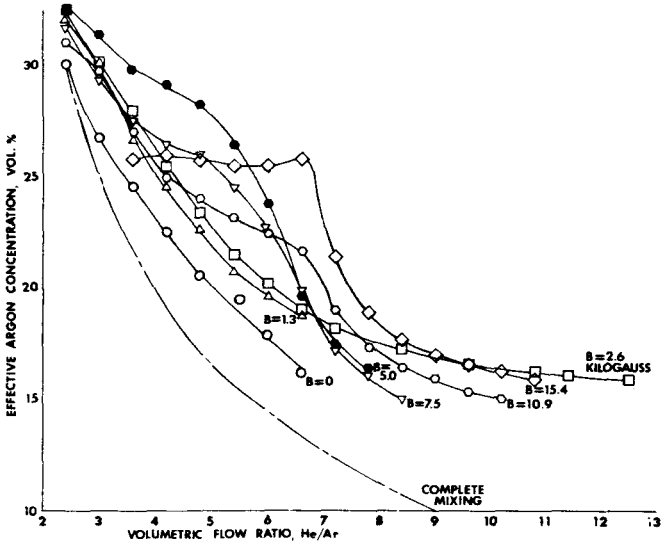

FIGURE 11.—*Effect of constant magnetic flux density* B *on effective argon concentration. Argon flow, 0.22 standard ft³/min.*

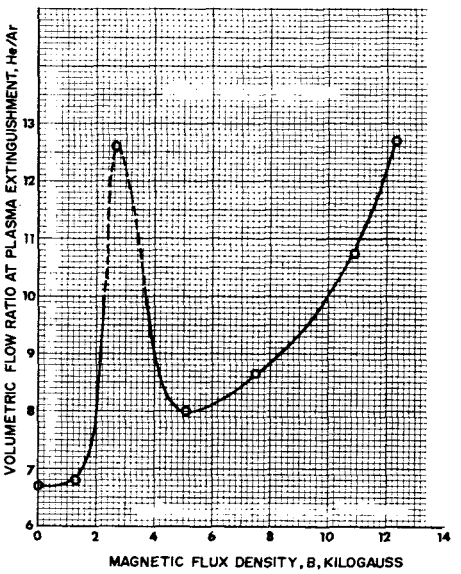

FIGURE 12.—*Effect of magnetic flux density on volumetric flow ratio at plasma extinguishment. Argon flow, 0.22 standard ft³/min.*

in the quantitative effect of the field, particularly at low and high flow rates. The largest and most consistent effect is observed at intermediate flow rates, the highest field (15.4 kG) producing the greatest increase in EAC at a flow ratio of 6.5. The lowest curve represents complete mixing between the inlet helium and argon streams and is seen to be closest to the curve for $B=0$; thus a possible interpretation of the results displayed in this figure is that the magnetic field decreases the mixing.

The terminal point at the right of each curve represents the maximum flow ratio at which the plasma could be sustained at each value of magnetic flux density. The influence of the field in increasing the volumetric flow ratio at which the plasma is extinguished due to insufficient heat generation relative to heat loss is illustrated in figure 12. The peak at about 2.7 kG is another example of the anomalous behavior referred to in connection with the preceding figure. Since the plasma is extinguished when the effective argon concentration is decreased to about 15 percent (fig. 11), figure 12 illustrates the effectiveness of the field in maintaining a nearly constant minimum of effective argon concentration over a 2-to-1 range in volumetric flow ratio.

In the course of this work it was found that, for each helium-argon volumetric flow ratio, there is an optimum value of magnetic flux density B^* which results in the maximum EAC. At fields above B^*, the plasma is observed to become unstable, as evidenced by large-amplitude fluctuations in grid current and flicker in light emission from the plasma. The mechanism of these instabilities is not known; they may be macroscopic (magnetohydrodynamic) in origin rather than microscopic (individual plasma species interacting with the field). Whatever their cause, the instabilities must be avoided if maximum EAC is to be achieved, and to accomplish this B must be continually adjusted for each flow ratio (i.e., B must be maintained approximately equal to B^* as the flow is increased).

In obtaining the results presented in figures 11 and 12, the magnetic field was held constant as the helium flow was increased; hence, these results are not optimum. In figure 13, however, the magnetic field was adjusted to be nearly optimum for each flow ratio. Under these conditions a near-optimum magnetic flux density of 8.5 kG increased the EAC by a factor of 2.1, as compared with the case for $B=0$. Note that the graph cannot be extended beyond a flow ratio of about 6.7 since this is the maximum at which a plasma is possible with no applied field.

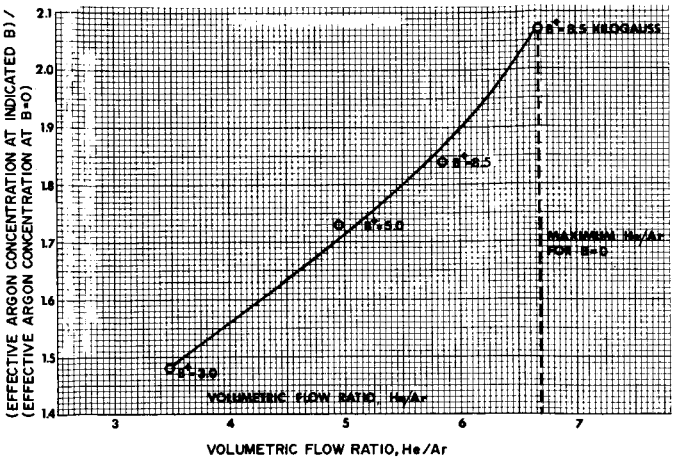

FIGURE 13.—*Effect of near-optimum magnetic flux density* B* *on effective argon concentration relative to results for* B = 0. *Argon flow, 0.22 standard ft³/min.*

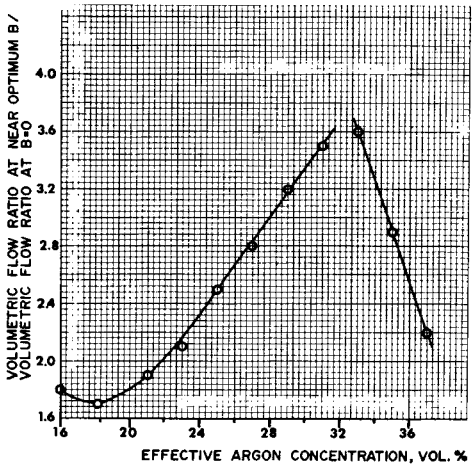

FIGURE 14.—*Effect of near-optimum magnetic flux density* B* *on volumetric flow ratio of helium to argon at near-optimum values of* B *relative to results for* B = 0. *Argon flow, 0.22 standard ft³/min;* $3.0 < B^* < 11.6$ *kG.*

In figure 14 the volumetric flow ratio at a near-optimum magnetic flux density of 11.6 kG is seen to increase the volumetric flow ratio by about 3.6 at an EAC of 32 percent.

DISCUSSION OF RESULTS

What is the significance of an increase in the effective argon concentration? If it is assumed that there is a positive correlation between EAC, defined as it is here in terms of coupling with the rf field, and the total amount of argon held up in the volume bounded by the quartz tube wall, the injector, and the exit tube, then increase in EAC means increase in argon holdup. That is, the results can be interpreted as suggesting a beneficial effect of the field.

The three major conclusions are therefore:

(1) Increase in argon holdup is effected, at constant volumetric flow ratio, by increase in magnetic flux density. Presumably, this increase in holdup results from decreased mixing due to the field.

(2) Increase in magnetic flux density increases the volumetric flow ratio of helium to argon (holding argon flow constant) at constant argon holdup.

(3) There is an optimum magnetic flux density for each flow ratio which results in the maximum argon holdup.

In summary, let it be emphasized that this is a status report of an exploratory experimental look at magnetic effects in coaxial plasma flow, and has, in a sense, raised more questions than it has answered. The assumption of a positive correlation between argon holdup and EAC is certainly tentative. More experimental and some analytical work is needed to define the relationship between coupling and holdup. An optical method for determining argon concentration throughout the plasma region could be developed for this application. Furthermore, preliminary experiments have covered a limited range of volumetric flow ratio, Reynolds number, Hartmann number (dimensionless magnetic flux density), geometry, and fluid properties. The injection geometry has not been optimized to permit operation at the maximum flow rates for the existing power capability. Improvement in the injection geometry (including the addition of a buffer-flow region between the inner and outer coaxial streams) and/or increase in power would make possible operation at more realistic flows and Reynolds numbers.

ANALYSIS OF MAGNETIC STABILIZATION

In the absence of turbulence, a coaxial flow reactor would exhibit a thin shear layer between the fuel and propellant streams. If the thickness of the shear layer were small compared with its radius, the cylindrical geometry might be approximated by the plane case of a flat shear layer between two semi-

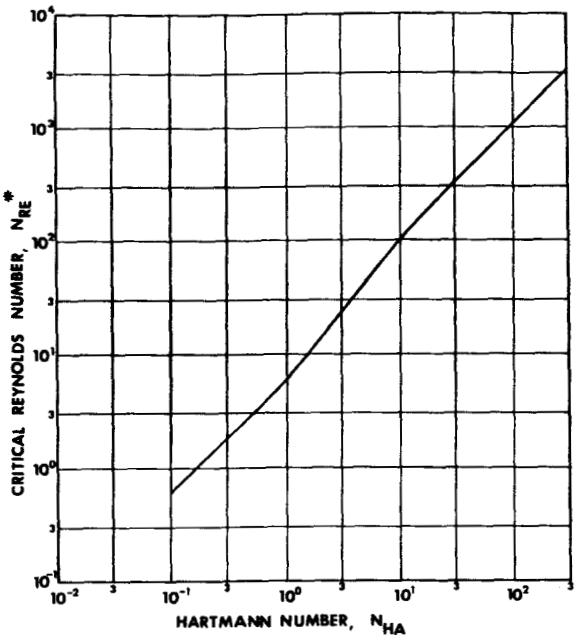

FIGURE 15.—*Critical Reynolds number versus Hartmann number.*

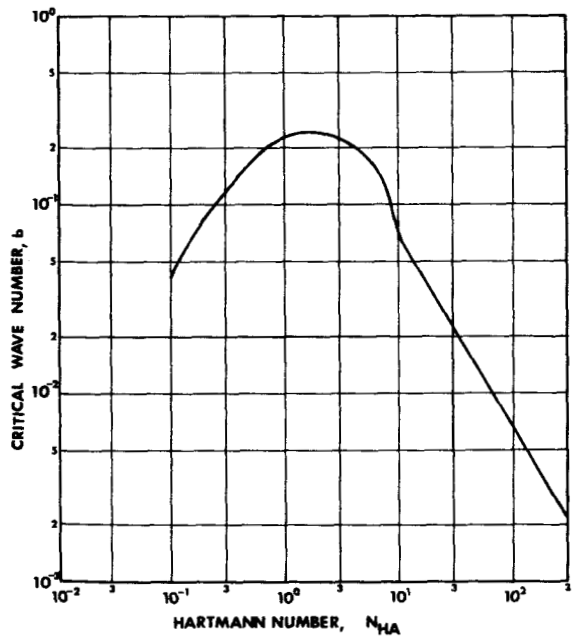

FIGURE 16.—*Critical wave number versus Hartmann number.*

infinite parallel streams. The hydromagnetic stabilization of such a shear layer by an applied colinear magnetic field has been investigated analytically by Bisshopp (ref. 3), in the limit of a small magnetic Prandtl number, for a single value of the Hartmann number of 0.1. The velocity profile in the shear layer was taken to be of hyperbolic tangent form. The stability equation was a hydromagnetic extension of the Orr-Sommerfeld equation.

Bisshopp's results have been extended to cover a range of Hartmann numbers from 0.1 to 300 by numerical integration of the stability equation by use of the method of Thomas (ref. 4). The calculated critical Reynolds number is shown as a function of Hartmann number N_{Ha} in figure 15. For $N_{Ha} \gtrsim 10$ and for $N_{Ha} \lesssim 1.0$ the log-log plot consists of nearly straight line segments of unit slope, which indicate proportionality between critical Reynolds number and Hartmann number. (All of the dimensionless parameters used are defined by Bisshopp (ref. 3) and are based on the half-width of the shear layer.) For intermediate Hartmann numbers, the slope is slightly greater than 1. The corresponding calculated critical wave number is shown in figure 16. The wave number approaches zero for both very large and very small values of the Hartmann number and reaches a maximum at intermediate values.

REFERENCES

1. KEYES, J. J., JR.: Hydromagnetic Stabilization Experiments With Jet-Driven Vortex Flow. Plasma Phys., vol. 10, 1968, pp. 1039–1049.
2. CHANG, T. S.; AND SARTORY, W. K.: Hydromagnetic Stability Analysis of Jet-Driven Vortex Flow. Plasma Phys., vol. 10, 1968, pp. 1029–1038.
3. BISSHOPP, F. E.: Theoretical Investigation of the Hydromagnetic Stability of a Free Boundary Layer. Rept. RTD-TDR-63-1099, United Aircraft Corp., 1963.
4. THOMAS, L. H.: Phys. Rev., vol. 91, 1953, p. 780.

DISCUSSION

Ragsdale: I know you said that you are not sure what that apparent anomaly you mentioned is; could it be that the low magnetic field has something to do with it?

Keyes: The first time it happened we thought it was just a fluke and so we went back and reproduced it two more times in other runs with almost the same magnitude. It appears to be some kind of resonance effect.

Kendall: Have you ever run this apparatus with loads

other than argon or other than gases—for example, with a solid load of some sort—to be sure (with and without the magnetic field) that this is not an effect of the magnetic field on the rf magnetic field?

Keyes: Yes; we have run it with a water-cooled copper load and found out that the direct current field can be turned on and off at will without affecting the coupling. It is not a direct effect on the rf field.

Mensing: Something bothered me in your using the grid current to determine the concentration. You cannot tell the difference between the temperature change and the concentration change. It could be either one. It could very easily be a change in the temperature of the plasma since the concentrations are the same all the way through.

Keyes: Except that in our calibrations we actually tried to include all the effects; that was the response to different concentrations under exactly the same operating conditions —same power, same ratios, same magnetic field, etc. Whatever is part of the coupling change when you run argon and gas mixtures is showing up.

Mensing: But it could be a temperature change. You are varying the concentration.

Keyes: I agree that the temperature changes. We know this because the power changes. But it is changing because the concentration changes.

Mensing: I realized that it was a qualitative result, namely, that there was an effect, but not that the effect was so great.

Keyes: The main thing is that I cannot say that this necessarily increases the total amount of argon. The assumption is that I am interpreting the data in terms of the total amount of argon. The concentration is increased as far as the plasma is concerned but that does not mean that the apparatus contains more argon; the distribution of argon could change and cause the same effect.

Keefer: I would like to suggest that perhaps this results from the change in the temperature profile that you get with a mixture; the temperature gradient would be decreased by the helium and this could cause an effective diameter change.

Keyes: I agree with that. I believe that the concentration has a lot of uncertainty associated with it, such as the diameter and the concentration distribution, and so the next step, if there is a next step, would have to be to establish the correlation between the total argon and the measurement of the coupling change. We would like to be able to make some optical measurements and I think that this is probably the only way we will be able to pin this down.

Experimental Study of the Effect of Inlet Conditions on the Flow and Containment Characteristics of Coaxial Flows[1]

BRUCE V. JOHNSON

United Aircraft Research Laboratories

This paper will describe some exploratory experiments for studying the effects of inlet flow conditions on the flow and containment characteristics of coaxial flows. These experiments were conducted as part of the feasibility study for the open-cycle gaseous-core nuclear rocket concept described in references 1 and 2. A sketch showing some of the fluid mechanics aspects of the reactor is shown in figure 1. The fluid mechanics requirements for this concept are, first, that a large fraction of the reactor chamber volume be filled with the gaseous nuclear fuel, and, second, that the ratio of the propellant flow rate to the nuclear fuel flow rate be as high as possible. In this study and in previous experimental coaxial-flow studies (refs. 3 through 8) the path of the simulated propellant has been approximately in the direction of the axis of symmetry and the flow cross-sectional area has been approximately constant for a significant distance from the inlet. These flow studies were an attempt to simulate a part of the

[1] This research was supported by the joint AEC–NASA Space Nuclear Propulsion Office under contract NASw–847.

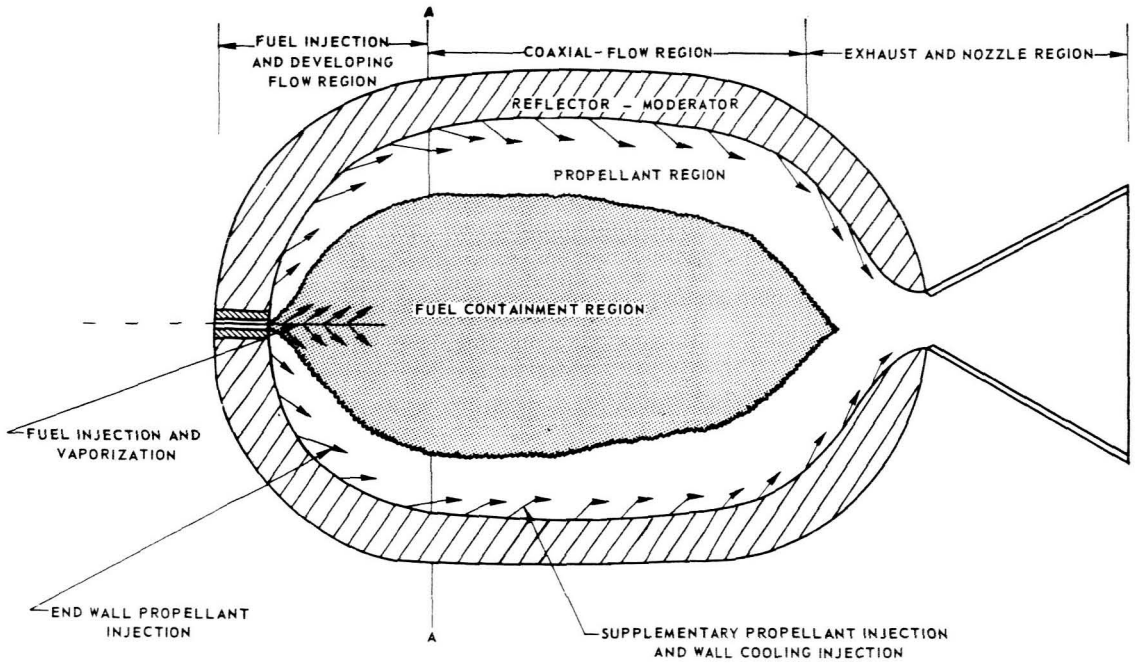

FIGURE 1.—*Sketch showing some fluid mechanics aspects of coaxial-flow gaseous nuclear rocket concept.*

coaxial-flow fluid mechanics (fig. 1) from plane A–A up to or through the nozzle and to determine the containment characteristics that can be obtained with given inlet flow conditions.

The general containment characteristics of the flows that were obtained in references 3 through 8 are shown in figure 2. The inlet flow conditions indicated for each flow regime were obtained from tests at United Aircraft Research Laboratories (UARL) with an inner-jet to outer-wall radius ratio of 0.5 and a buffer velocity region. These inlet flow conditions varied for each inlet geometry and chamber geometry; however, the general trends are the same. For ratios of outer-stream velocity to inner-jet velocity from 1 to 10 with air as the inner-jet gas, both the inner and outer streams are moving in the same direction (fig. 2(*c*)). For ratios of outer-stream velocity to inner-stream velocity above 10 with air as the inner-jet gas, the flow behind the inner jet recirculates like the flow behind a bluff body (fig. 2(*a*)). At intermediate ratios of outer-stream velocity to inner-jet velocity, the flow recirculated upstream of the exhaust nozzle (fig. 2(*b*)). The flows measured or observed (refs. 3 through 8) had undesirable turbulent mixing characteristics. The region between the streams was either well-developed turbulent flow or had axisymmetric eddies developing near the inlet which grew in size with increasing distance from the inlet and caused large fluctuations in the flow. The first part of the present study consisted of experimentally determining with flow visualization and hot-wire measurements some of the factors which influenced the formation and growth of the aforementioned large eddies. The second part consisted of additional flow visualization tests with inlets which showed the best characteristics during the first part of the study.

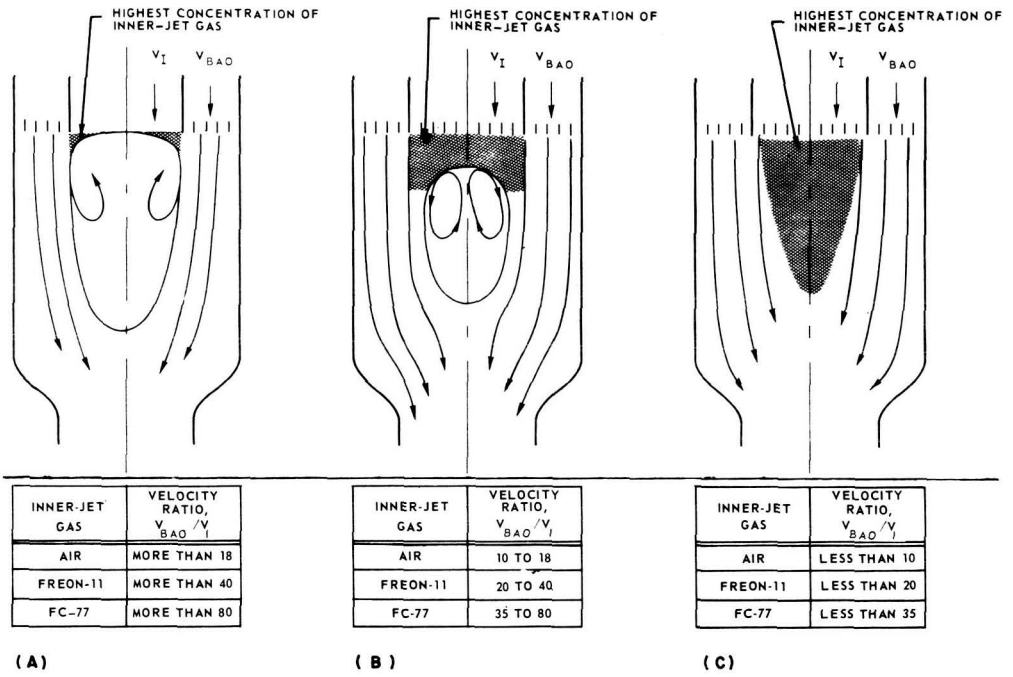

INNER-JET GAS	VELOCITY RATIO, V_{BAO}/V_I
AIR	MORE THAN 18
FREON-11	MORE THAN 40
FC-77	MORE THAN 80

(A)

INNER-JET GAS	VELOCITY RATIO, V_{BAO}/V_I
AIR	10 TO 18
FREON-11	20 TO 40
FC-77	35 TO 80

(B)

INNER-JET GAS	VELOCITY RATIO, V_{BAO}/V_I
AIR	LESS THAN 10
FREON-11	LESS THAN 20
FC-77	LESS THAN 35

(C)

FIGURE 2.—*Sketches of flow patterns for various inlet flow conditions. Velocity ratios indicated were obtained from reference 6 with buffer-layer flow and* $r_I/r_O = 0.5$. (a) *Recirculation zone directly behind inlet.* (b) *Recirculation zone forms downstream of inlet.* (c) *Turbulent mixing between streams without recirculation.*

The objectives of this paper are to show that the structure of the flow can be markedly changed from those of the currently obtained turbulent coaxial-jet

flows and that the apparent containment that resulted with one of the modified inlets is considerably greater than that which had been obtained previously.

A list of the symbols used in this paper is given at the end of the paper.

DESCRIPTION OF TEST APPARATUS

A schematic of the test apparatus and a photograph of the test facility are shown in figures 3 and

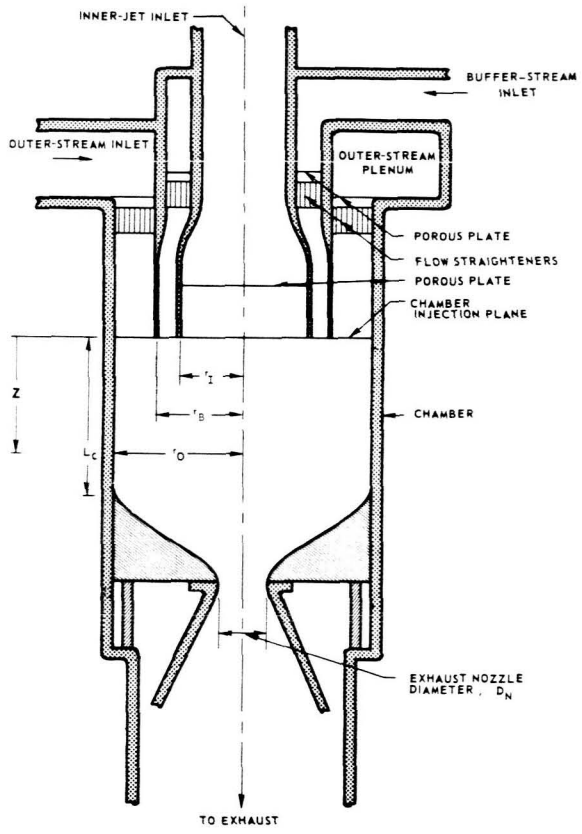

FIGURE 3.—*Schematic of test apparatus.*

4, respectively. Separate plenums supplied three streams to the chamber. These streams were denoted the inner jet, the buffer, and the outer stream. The gases flowed from plenums through a specific inlet configuration to a specific chamber configuration employed in a test. The flow was exhausted from the lower end of the chamber. Air was always used as

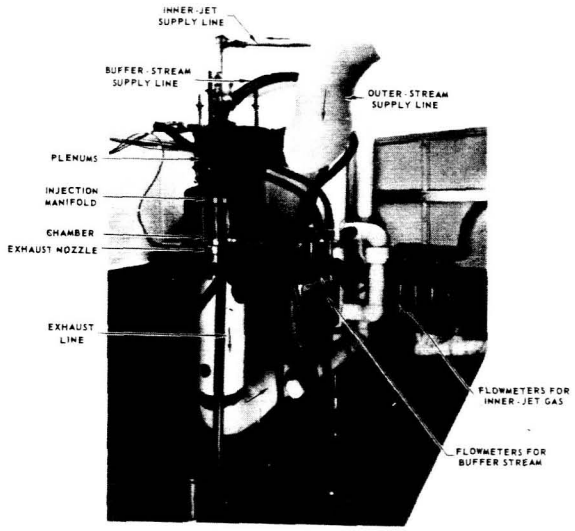

FIGURE 4.—*Photograph of test facility showing flow system.*

the buffer-stream and outer-stream gas; air or Freon-11 was used as the inner-jet gas for the tests reported herein. For the flow visualization tests the gases were heated to approximately 260° F and iodine vapor was added to the inner-jet gas as a trace gas. The chamber was constructed from a cast acrylic tube. The chamber diameter was 10 in. and the exhaust nozzle diameter was 6 in. for all tests. Sketches of the inlet configurations employed during the tests are shown in figure 5. The screen inlet (fig. 5(*a*)) was the same as that employed in reference 6. The foam inlet (fig. 5(*b*)) was constructed to obtain an inlet velocity profile with a moderate velocity gradient between the outer stream and the inner jet. The foam-and-perforated-plate inlet (fig. 5(*c*)) is a modification to the foam inlet and was developed late in the study to eliminate the radial inflow of the outer-stream gas past the inner-jet radius r_I. For most tests with both the foam inlet and the foam and perforated-plate inlet, no gas was injected from the buffer plenum; however, the outer-stream gas did flow radially inward within the foam from the porous plate to the chamber inlet plane for both inlets.

DISCUSSION OF RESULTS

Velocity Profiles

Axial velocity profiles were obtained during tests employing the screen inlet (fig. 5(*a*)) and the foam

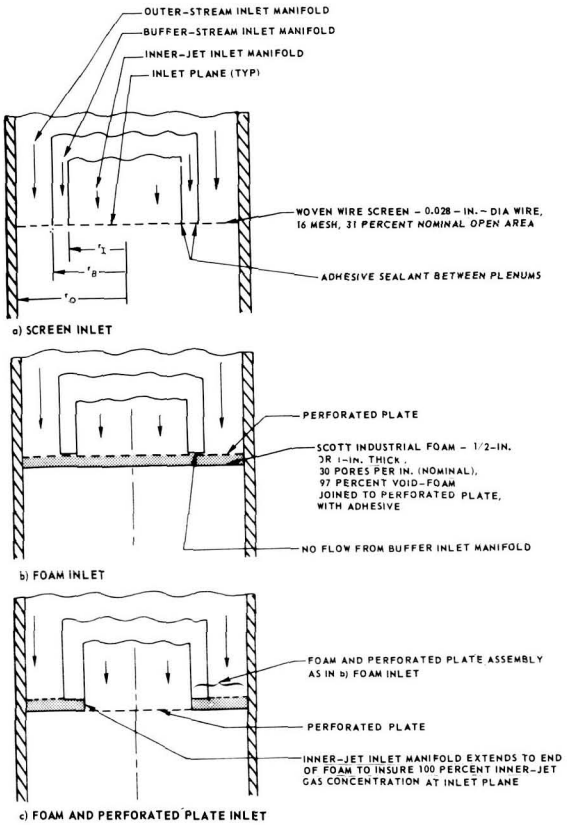

FIGURE 5.—*Sketches of inlet configurations.*

inlet (fig. 5(*b*)) with $r_I/r_O = 0.5$ and air as the inner-jet gas and are shown in figures 6 and 7, respectively. For tests with the screen inlet, total pressure profiles were obtained $2\frac{3}{8}$ in. from the inlet plane at eight azimuthal stations for buffer and outer-stream velocities of about 66 ft/sec and an inner-jet velocity of approximately 6 ft/sec. The local axial velocity was calculated by assuming that the local static pressure was equal to the wall static pressure at the axial location. The velocity profile was axisymmetric for the various values of θ and had a sharp velocity gradient between $r = 2.5$ and $r = 2.8$ in. For tests with the foam inlet, the profiles were obtained at 1 in. from the inlet plane with a hot-wire anemometer. The hot-wire was employed in order to measure the profiles in the low-velocity region accurately. Typical axial velocity profiles are shown in figure 7 for $V_{BAO} \approx 80$ ft/sec at several values of V_I. The axial velocities from $r = 0$ to $r = 2.0$ in. were approximately equal to V_I. From

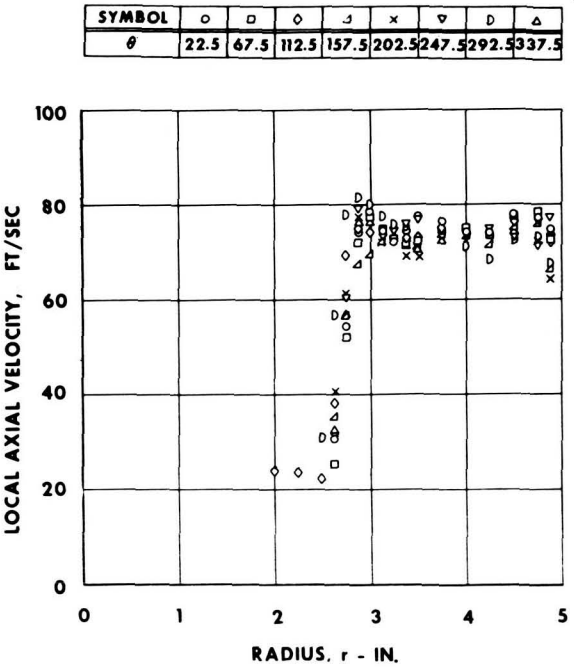

FIGURE 6.—*Inlet velocity profile obtained with screen inlet.* $V_O = V_B \approx 66$ *ft/sec and* $V_I \approx 6$ *ft/sec.*

SYMBOL	CASE	V_I, FT/SEC	V_B, FT/SEC	V_O, FT/SEC	V_{BAO}, FT/SEC	V_{BAO}/V_I	W_{BAO}/W_I
◇	55	0	0	94	72	∞	∞
△	66	1.8	0	107	83	46	137.2
□	75	2.9	0	105	80	27	81.026
○	67	8.8	0	107	83	9.3	27.98

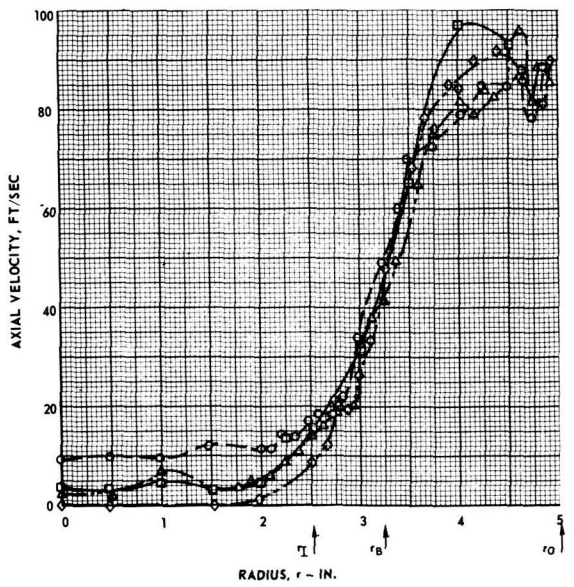

FIGURE 7.—*Inlet velocity profiles obtained with foam inlet.*

$r=2.0$ to 4.0 in. the velocity increased to a value greater than V_{BAO} but less than V_O. These results show that the desired low velocities downstream of the inner jet and high velocities near the outer wall were obtained with the desired gradual velocity profile between these two regions.

Axial velocity profiles were also obtained with the foam-inlet configuration at several axial locations for $V_{BAO}/V_I=27$ and $V_{BAO}=80$ ft/sec and are shown in figure 8. The local velocities at $z=1.0$ and

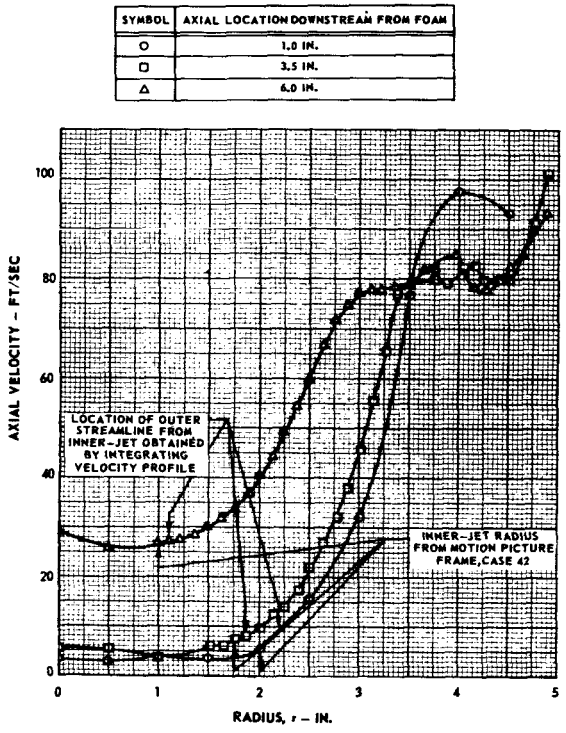

FIGURE 8.—*Velocity profiles at three axial stations for* $V_{BAO}/V_I=27$.

3.5 in. for $r<2.0$ in. are about equal to the inner-jet injection velocity V_I. At $z=6.0$ in. the effect of the converging exhaust nozzle was felt by the inner-jet gas as it was accelerated from the chamber. The velocity profiles were integrated from $r=0$ to the approximate location of the outermost streamline of the inner-jet gas as determined by the inner-jet volume flow rate. These locations, also shown in the figure, are in good agreement with the high-speed motion-picture flow visualization data which indicate the outer radius of the densely colored inner-jet gas. From this comparison, it was concluded that the motion pictures could be used to determine the approximate inner-jet gas containment.

Turbulence and Wave Disturbance Characteristics

The turbulence intensities downstream of the inlet plane were measured for several inlet flow conditions. Typical results for tests with the screen inlet and the foam inlet are shown in figure 9. For the screen inlet at $z=1$ in., the turbulent wakes from the plenum walls at $r=2.5$ and 3.25 in. provide the largest turbulence intensity levels. The turbulence intensities decay with increasing distance from the inlet plane. For this flow condition, the turbulence intensity remained greater than 0.1 for $r<3.5$ at all stations. For $r>4.0$ in., the fluctuations are probably from the flow through the screen. These turbulence intensities are lower than those in the shear region and the inner-jet region at this axial location, probably because the scale of turbulence is small because of screen grid size. The turbulence intensity distribution for tests with the foam inlet, presented in figure 9(*b*), shows that the turbulence intensity was greatly reduced in the central portion of the chamber compared with the results obtained from tests with the screen inlet shown in figure 9(*a*). The turbulence intensity downstream of the inlet is less than 0.08 for most locations and, for this flow condition, decays with increasing distance from the inlet. For other flow conditions with high velocity ratios, i.e., $V_{BAO}/V_I>5$, the turbulence intensity increased with increasing distance from the inlet plane, thereby indicating the production of turbulence energy downstream of the inlet from the mixing process.

The high-speed motion-picture sequences (fig. 10) obtained during tests with the screen inlet, the foam inlet, and the foam-and-perforated-plate inlet show the effect of inlet flow conditions on the wave disturbance characteristics for velocity ratios $V_{BAO}/V_I>15$. These flow rate ratios, with Freon-11 as the inner-jet gas, are of the same order of magnitude as that envisioned for the coaxial-flow region of the full-scale reactor. For cases 9013 and 9014 (ref. 6) the large-scale eddies, deemed undesirable, are present. For case 79, the large-scale eddies did not occur, but small-amplitude waves, not noticeable in these film sequences, did occur. Although the flow

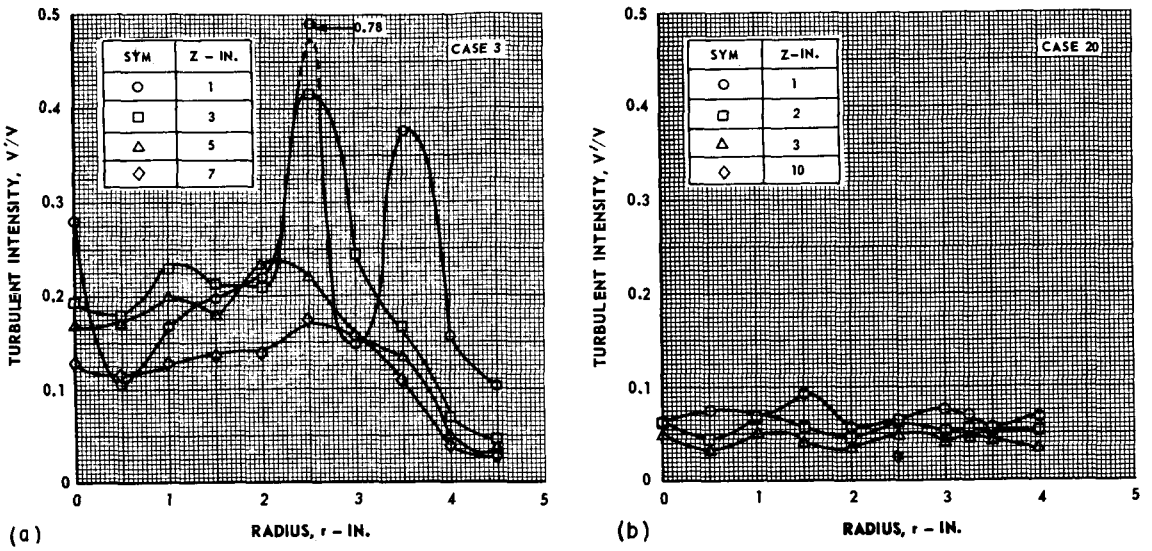

FIGURE 9.—*Comparison of turbulence intensities downstream of screen and foam inlets.* $V_B = V_O = 40$ *ft/sec,* $V_I = 20$ *ft/sec, and* $r_I = 2.5$ *in.* (a) *Short chamber and screen inlet.* (b) *Long chamber and 1-in. foam inlet.*

fluctuations for case 79 are essentially eliminated, the containment volume is low because radial flow within the foam layer caused the inner jet to contract. This contraction decreased the indicated velocity ratio, decreased the inner-jet inlet area to less than 15 percent of the chamber cross-sectional area, and limited the obtainable containment volume. In order to improve the containment characteristics, the foam inlet was modified by extending the inner-jet plenum to the inlet plane and removing the foam for $r < r_I$ (fig. 5(*c*)). For case 124 (fig. 10(*d*)), small eddies, similar to those previously observed in figures 10(*a*) and 10(*b*), appeared and grew with increasing distance from the inlet plane. However, the containment was improved, as will be shown in a later section.

Containment Characteristics

Individual frames from high-speed motion pictures were visually observed to determine the approximate amount of inner-jet gas contained in the chamber for tests employing the foam inlet (fig. 5(*b*)) and foam-and-porous-plate inlet (fig. 5(*c*)). Data were obtained with air and Freon-11 as the inner-jet gases and for inlet radius ratios r_I/r_O of 0.50, 0.60, and 0.7. A single frame was chosen to be representative of the flow and magnified with a projector to obtain the outline of the chamber and the dense inner-jet gas volume. The ratio of the apparent average partial pressure of the inner-jet gas to the total pressure was calculated for each case from the following equation:

$$\frac{\bar{P}_I}{P} = \frac{1}{L_C r_O^2} \int_0^{L_C} r^{*2}\, dz$$

where r^* is the outer radius of the dense inner-jet gas determined by visual observation.

For a given inlet configuration, decreasing the inner-jet gas flow rate decreased the outermost radius at which the inner-jet gas entered the chamber until a limiting radius, such as approximately 2 in. for the $r_I = 2.5$ in. configuration, was reached. Further decreases in the inner-jet flow rate did not reduce the inner-jet gas radius at the inlet but did result, at other axial locations, in a reduction of the inner-jet radius at which the gas became less dense. A comparison of the present data obtained employing the foam inlet and the previous data obtained employing the screen inlet with light absorption measurements (ref. 6) for $r_I/r_O = 0.5$ is presented in figure 11. This comparison shows that the average inner-jet gas containment was not changed for

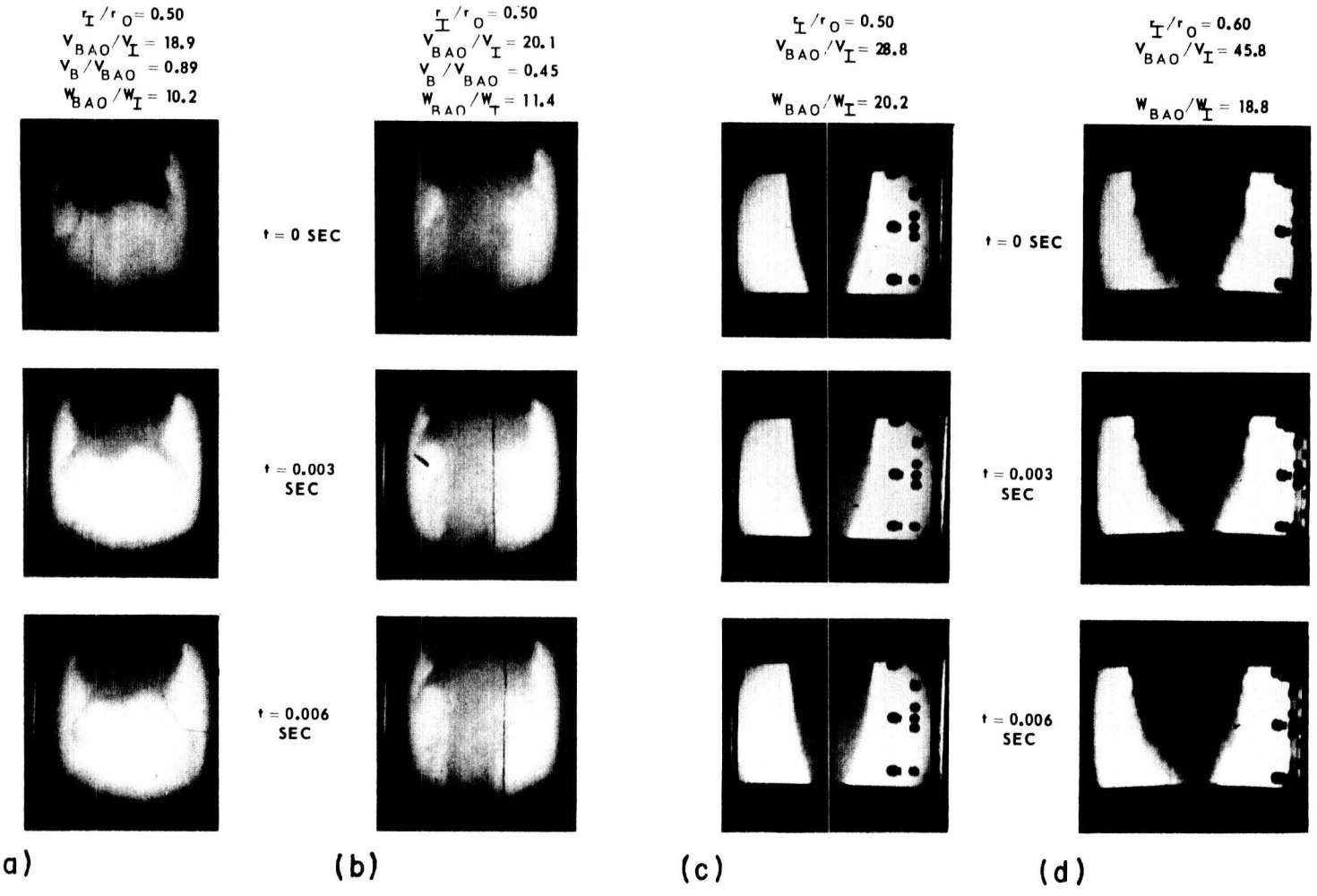

FIGURE 10.—*Effect of inlet flow condition on wave disturbance characteristics. Inner-jet gas is Freon-11;* $V_{BAO} \approx 80$ *ft/sec; data taken from reference 6.* (a) *Screen inlet; case 9013.* (b) *Screen inlet; case 9014.* (c) *Foam inlet; case 79.* (d) *Foam-and-perforated-plate inlet; case 124.*

SYMBOL	INLET CONFIGURATION	INNER-JET GAS	ρ_I/ρ_{BAO}	DATA OBTAINED
△—△	SCREEN	AIR	1.0	REF. 6
▲—▲	1/2-IN. FOAM	AIR	1.0	PHOTOGRAPHS
○—○	SCREEN	FREON-11	4.7	REF. 6
●—●	1/2-IN. FOAM	FREON-11	4.7	PHOTOGRAPHS

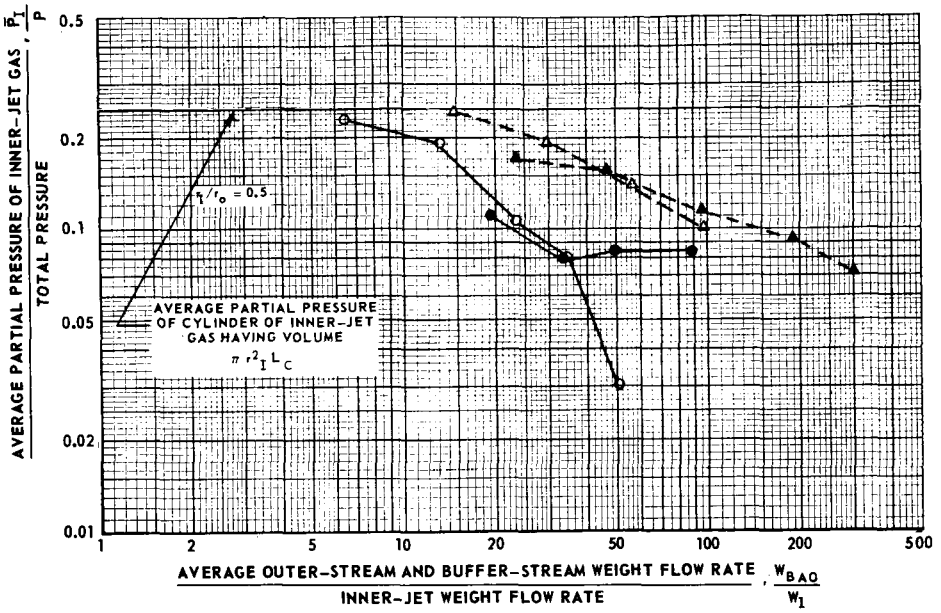

FIGURE 11.—*Comparison of apparent coaxial-jet containment with previous concentration measurements.* $r_I/r_O = 0.5$.

$\bar{P}_I/P > 0.1$. The results from these tests with the foam inlets have shown that, although the nature of the flow was markedly changed, the average inner-jet gas volume within the chamber did not increase in the region of interest.

Because of the above results with the foam inlet, the inlet was modified to insure that the inner-jet gas inlet radius would be maintained regardless of inner-jet gas flow rates. This was accomplished by extending the inner-jet gas plenum wall to the inlet plane and replacing the inner-jet foam with a porous plate, as shown in figure 5(*c*). The apparent inner-jet gas containment for this inlet is shown in figure 12 for Freon-11 as the inner-jet gas. The flagged symbols indicate flow conditions for which a small amount of recirculation occurred near the exhaust nozzle. As shown by the photographs in figure 10(*d*), mixing caused by turbulent shear in the wake behind the inner-jet gas plenum wall occurred for tests with this inlet. The maximum weight flow ratio for flow without recirculation can probably be increased by use of other inlet configurations. The apparent containment characteristics with Freon-11 as the inner-jet gas for tests with the foam inlet and the foam-and-porous-plate inlet are also compared in figure 12 with previous results (ref. 6) for tests with the screen inlet. The apparent containment volume with the foam-and-perforated-plate inlet for $W_{BAO}/W_I > 25$ is a factor of 2 higher than the data for tests with the other inlets.

Comparison of Results With Requirements

The fluid mechanics performance requirements for open-cycle gaseous nuclear rockets were outlined in reference 2. High-, intermediate-, and low-performance regions were defined for a mission which

would probably include an orbital nuclear-stage startup and are shown in figure 13. The nominal engine design point requires 20 percent of the engine volume to be filled with fuel for a ratio of propellant weight flow rate to fuel weight flow rate of 35. This volume fraction was selected in reference 2 from pressure level considerations, and the weight flow ratio was chosen from economic considerations, so that fuel costs would not be the major mission cost. Increasing either of these parameters at no expense to the other is desirable.

The best data from reference 6 for tests with air and Freon-11 as the inner-jet gases lie predominantly in the intermediate-performance region (fig. 12). The best data from the present tests are in the high-performance region and indicate that the containment characteristics for confined coaxial-flow jets have apparently been improved during this study. However, because of the difficulty of interpreting photographs, actual integration of concentration distributions will be required before firm conclusions can be made. Preparations are now being made to obtain these concentration distribution measurements.

The cavity flow in the full-scale reactor configuration shown in figure 1 was divided into three re-

SYMBOL	INLET CONFIGURATION	r_I/r_D	r_B/r_D	DATA OBTAINED
○——○	a) SCREEN	0.50	0.65	REF. 6
△- - -△	b) FOAM	0.50	0.65	PHOTOGRAPHS
▲- - -▲	b)FOAM	0.60	0.73	PHOTOGRAPHS
■——■	c) FOAM AND PERFORATED PLATE	0.60	0.73	PHOTOGRAPHS

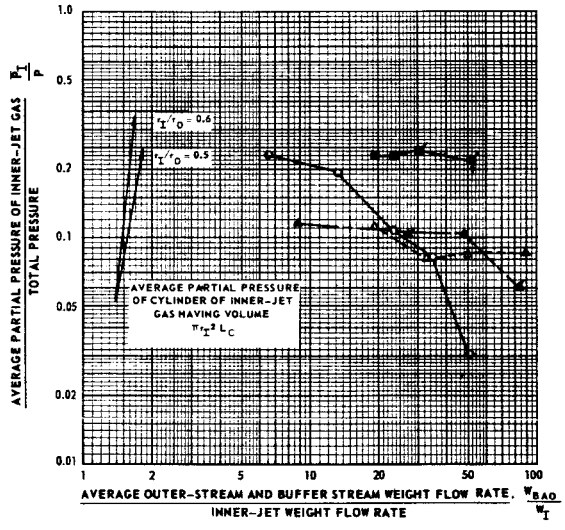

FIGURE 12.—*Comparison of apparent containment obtained for several inlet configurations with Freon-11 as the inner-jet gas.*

SYMBOL	INNER-JET GAS	ρ_I/ρ_{BAO}	MEASUREMENT TECHNIQUE	WORK
△	AIR	1.0	LIGHT ABSORPTION TECHNIQUE	REF. 6
▲	FREON-11	4.7		
□	AIR	1.0	ESTIMATED FROM PHOTOGRAPHS	PRESENT REPORT
■	FREON-11	4.7		

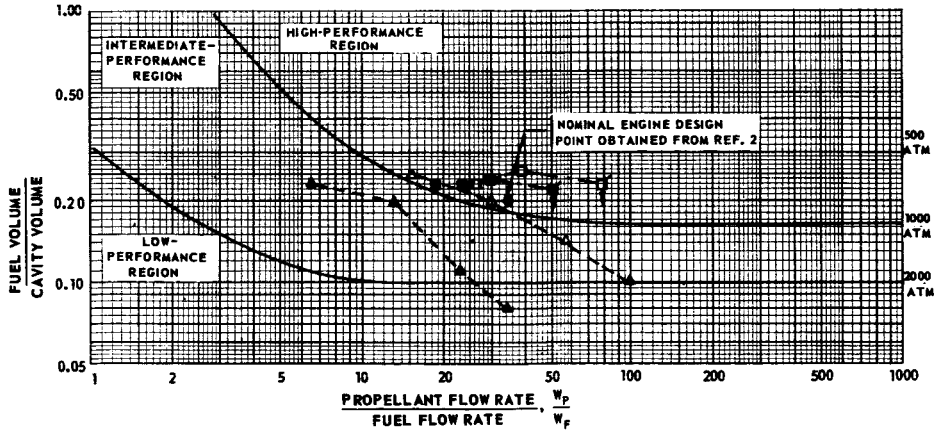

FIGURE 13.—*Comparison of present and previous coaxial-jet containment with open-cycle, gaseous-nuclear-rocket, fluid mechanics, performance requirements.*

gions. The studies described in this report are applicable to the central coaxial-flow region in figure 1 if the flow at the exit of the developing flow region can be made similar to that created by the inlets in the present tests. Therefore, the creation of a smoothed low-turbulence velocity profile at the exit of this developing flow region is shown to be of great importance by the results of the tests described herein.

CONCLUSIONS

The following conclusions were drawn from the tests described herein. First, the large-eddy disturbances which occurred in previous UARL coaxial-flow jet tests with discontinuous inlet-velocity profiles were essentially eliminated by the use of a porous material upstream of the inlet plane to smooth out the inlet-velocity profiles. (Use of these materials also decreased the rms axial velocity fluctuations from 40 percent to approximately 7 percent in the test chamber near the inlet plane.) Second, the apparent inner-jet gas containment obtained with the modified porous-material inlets was considerably improved over that obtained in previous tests. With Freon-11 as the inner-jet gas, the containment at a ratio of outer-stream flow rate to inner-jet flow rate of 25 was twice that for previous UARL tests.

SYMBOLS

L_C Length of chamber from inlet plane to beginning of nozzle, in. or ft

P Total pressure, lb/ft^2 or atm

P_I Average partial pressure of inner-jet gas, lb/ft^2

r Local radius from center of chamber, in. or ft

r_B Buffer-stream radius at inlet, in. or ft

r_I Inner-jet radius at inlet, in. or ft

r_O Peripheral-wall radius, in. or ft

r^* Outermost radius of dense inner-jet gas, in. or ft

v' Rms value of fluctuating component local velocity, ft/sec

V Local velocity, ft/sec

V_{BAO} Average inlet velocity of combined outer stream and buffer stream, $W_{BAO}/[\rho_{BAO}\,\pi(r_O^2-r_I^2)]$, ft/sec

V_I Inlet velocity of inner jet, ft/sec

V_O Inlet velocity of outer stream, ft/sec

W_{BAO} Combined weight flow rate of outer-stream and buffer-stream gases, lb/sec

W_F Weight flow rate of fuel or simulated fuel, lb/sec

W_I Weight flow rate of inner-jet gas, lb/sec

W_O Weight flow rate of outer-stream gas, lb/sec

W_P Weight flow rate of propellant or simulated propellant, lb/sec

z Axial distance downstream from inlet plane, in. or ft

θ Azimuthal location, deg

REFERENCES

1. Weinstein, H.; and Ragsdale, R. G.: A Coaxial-Flow Reactor—A Gaseous Nuclear Rocket Concept. Preprint 1518-60, Am. Rocket Soc., Inc., 1960.
2. Ragsdale, R. G.; and Rom, F. E.: Gas-Core Reactor Work at NASA/Lewis. NASA TM X-52309, 1967.
3. Ragsdale, R. G.; Weinstein, H.; and Lanzo, C. D.: Correlations of a Turbulent Air-Bromine Coaxial-Flow Experiment. NASA TN D-2121, 1964.
4. Zawacki, T. S.; and Weinstein, H.: Experimental Investigation of Turbulence in the Mixing Region Between Coaxial Streams. NASA CR-959, 1968.
5. Taylor, M. F.; and Masser, C. C.: Photographic Study of a Bromine Jet in a Coaxial Airstream. NASA TN D-4660, 1968.
6. Johnson, B. V.: Experimental Study of Multi-Component Coaxial-Flow Jets in Short Chambers. (Rept. G-910091-16, United Aircraft Res. Lab., Apr. 1968.) NASA Rept. CR-1190, 1968.
7. Kulik, R. A.; Leithem, J. H.; and Weinstein, H.: Effect of Free Stream Turbulence on Coaxial Mixing. NASA CR-1336, 1969.
8. Rozenman, T.: Experimental Investigation of Recirculation Patterns in the Initial Region of Coaxial Jets. Ph.D. thesis, Chem. Eng. Dept., Ill. Inst. Technol., Jan. 1969.

DISCUSSION

Moore: I am not sure I understand whether the large eddies (from the movie sequences and as shown in figures 10(a) and 10(b)) are the eddies on the margin or within the region that was in the middle of figure 2. (The movies are not included in this publication.) And was the zone with the big wake region in the middle of figure 2 composed of outer gas, buffer gas, or inner gas?

Johnson: The large eddies were in the margin or shear region between the inner stream and the outer stream. The recirculation region (shown in figs. 2(a) and 2(b)) occurred when there was a high velocity ratio between the outer stream and the inner stream. The previous study (ref. 6) showed a recirculation zone that came part way from the exhaust nozzle to the inlet plane (figs. 10(a) and 2(c)).

Moore: Is the fluid inside the closed recirculation region outer fluid or inner fluid?

Johnson: It is mixed fluid. The concentration in this region is relatively low, as was shown in the first movie sequence.

Keyes: In your movies, you showed the sequence with the foam (fig. 10c); the plume of the inner gas was necking down. Was that not due to change in the exit configuration? Did you change the exit configuration?

Johnson: Yes, some of the necking down of the fluid was attributed to the effects of the exhaust nozzle (and some of it was due to buoyancy effects because of the density differences between Freon-11 in the inner stream and air in the outer stream). I did not change the exit in any of those configurations. All had a 0.6 radius ratio. In the first sequence the chamber was a little bit longer than it was in the last two sequences, but I do not think that this affected the characteristics.

Page intentionally left blank

Self-Confined Rotating Flows for Containment[1]

F. K. Moore and S. Leibovich
Cornell University

Examples of fluid flows with regions of closed streamlines away from solid boundaries are described with gaseous nuclear fuel containment in mind. Confining mechanisms are rotation (either swirl or "smoke ring") or electromagnetic pinch. Experimental experience and a recent theory of vortex breakdown confirm the existence of such flows.

Further, it is shown that with suitable choices of parameters, theory predicts constant pressure (stagnation) in the confined regions, which is probably favorable in both stability and mixing-loss terms.

Effects of density difference and energy evolution and transfer are discussed, and problems for future study are delineated.

The possibility of vortex fuel containment for gas-core reactors has been studied extensively (refs. 1, 2, and 3). Usually, the vortex is to be produced by swirling entry of propellant gas at the chamber boundary. These schemes suffer from secondary flows which tend to pump the "contained" fuel back through the end-wall boundary layer to the chamber axis, thus defeating the purpose of containment. Such unwanted interaction of the vortex with chamber surfaces could perhaps be avoided by making the contained region more independent of surrounding surfaces. Evvard, in reference 4, proposed the use of a two-dimensional forced vortex such as might be found in the wake of a bluff body. Reshotko and Monnin, in reference 5, analyzed the stability of such a flow and found that it tended to be unstable.

In this paper, we consider the containment possibilities offered by flows that have enclosed regions of fluid relatively independent of chamber walls. A glycerine droplet falling in water furnishes an example of such a flow, where surface tension, rather than the presence of nearby walls, provides the necessary confining influence. For the gas-core reactor, one obviously needs a much more powerful confining influence than surface tension. One may think, for example, of the resistance to lateral deflection of magnetic field lines in a conducting fluid. Accordingly, we shall briefly mention the finite-amplitude Alfvén wave as a confinement mechanism.

Vortex lines, because of rotational inertia, also resist deflection, and we shall discuss the containment possibilities of the flows exemplified by vortex breakdown. Figure 1 shows the nearly spherical occlusion which may occur (on the scale of centimeters) along the axis of a swirling flow according to the experiments of Harvey (ref. 6). One may ask whether it is feasible to gather and keep fuel in such

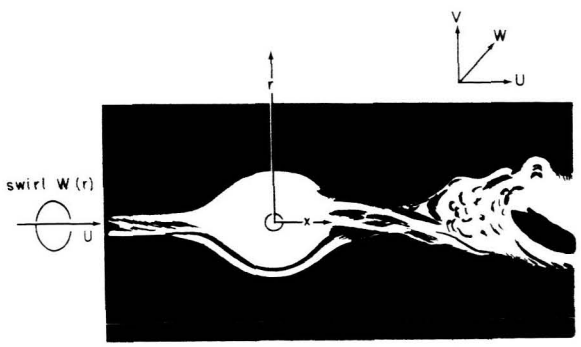

FIGURE 1.—*Sketch of Harvey's "spherical" breakdown. Width about equal to the core of uniform rotation in the oncoming flow. Maximum helix angle of swirling streamlines about 45°. Coordinate system superposed.*

[1] The work described herein was supported by NASA through grant NGR 33-010-042 and was technically monitored by Lewis Research Center.

an independent, spheroidal cloud held in place by the rotation of the surrounding propellant flow. Finally, we shall discuss a rotational flow in which the vortex filaments are transverse, in the manner of smoke rings, leading to a spherical occlusion bearing a superficial resemblance to the two-dimensional flow pattern described in reference 7.

When one discusses these self-confining flows, one must obviously pay attention to the problem of stability and to the related question of how the flow may be started. In this regard, certain special circumstances of the gas-core reactor should be noted:

(1) The fuel region is generating energy. This, in itself, is probably destabilizing because of the increase of criticality attending a constant-mass expansion (ref. 8).

(2) The fuel region is losing energy to the propellant, which is perhaps stabilizing because local hotspots would tend to lose their heat more quickly.

(3) The core gas is several times as dense as the confining propellant. The effect on stability of this density difference is not altogether clear. We believe, however, that Rayleigh-Taylor instability would be associated with velocity currents in the confined fuel. Therefore, in presenting theoretical models of these flows, we shall generally specify that the contained fluid is at rest, that is, at constant pressure and with no velocity currents. Perhaps surprisingly, a flow configuration is possible in each of the three flow categories mentioned (streamwise magnetic field lines and streamwise and transverse vortex lines), and we think it probable that they offer the best chances for practical containment.

Throughout this paper, we shall assume axial symmetry with or without swirl, and for simplicity we shall emphasize spherical fuel regions.

FINITE-AMPLITUDE ALFVÉN WAVE

For an incompressible inviscid fluid of infinite conductivity (e.g., a propellant gas, seeded if necessary) the steady Euler and Maxwell equations and Ohm's law are

$$\nabla(p+\tfrac{1}{2}\rho\mathbf{V}^2)=\mathbf{j}\times\mathbf{B}-\rho\boldsymbol{\omega}\times\mathbf{V} \qquad (1)$$

$$\nabla\cdot\mathbf{B}=\nabla\cdot\mathbf{V}=0 \qquad (2)$$

$$\left.\begin{aligned}\nabla\times\mathbf{B}/\mu&=\mathbf{j}\\ \nabla\times\mathbf{V}&=\boldsymbol{\omega}\\ \nabla\times\mathbf{E}&=0\end{aligned}\right\} \qquad (3)$$

$$\mathbf{E}+\mathbf{V}\times\mathbf{B}=0 \qquad (4)$$

where, **V, j, B, E,** and **ω** are the velocity, current, magnetic induction, electric field, and vorticity vectors. We assume a vanishing electric field and consider that a single stream function describes both velocity and magnetic fields (see ref. 9):

$$\frac{u}{U}=\frac{1}{r}\frac{\partial\psi}{\partial r}=\frac{B_x}{B_\infty} \qquad (5)$$

$$\frac{v}{U}=-\frac{1}{r}\frac{\partial\psi}{\partial x}=\frac{B_r}{B_\infty} \qquad (6)$$

We find the well-known equation for rotational flow (ref. 10)

$$\frac{\partial^2\psi}{\partial x^2}+\frac{\partial^2\psi}{\partial r^2}-\frac{1}{r}\frac{\partial\psi}{\partial r}=r^2H(\psi)-G(\psi) \qquad (7)$$

where G depends on the swirl velocity component w and H depends on G and the circumferential component of vorticity ω:

$$\frac{w}{U}=\frac{1}{r}g(\psi) \qquad G(\psi)\equiv gg' \qquad (8)$$

$$H(\psi)\equiv\frac{G}{r^2}-\frac{1}{r}\frac{\omega}{U} \qquad (9)$$

Now, if we assume that a sphere is immersed in a meridional flow ($w=0$) which is both irrotational and current-free both G and H vanish, and the stream function is that of classical potential flow, describing both velocity and magnetic fields.

Next, we ask if it is possible that the sphere consists of field-free fluid at rest. Figure 2 shows the

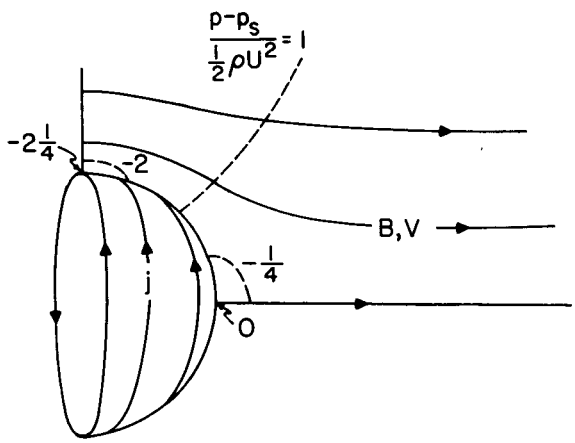

FIGURE 2.—*Streamlines (solid lines) and pressures (broken lines) in perfectly conducting fluid about field-free sphere at Alfvén speed* $U=(\rho\mu)^{-\frac{1}{2}}B_\infty$.

outer-flow pressure referred to the stagnation value. This pressure variation must be borne by a current sheet over the sphere. In particular, by integrating equation (1) across the sphere boundary, we see that pressure may be taken constant within the sphere, and the **B** and **V** fields vanish inside if $\mathbf{B}=\mathbf{V}$ outside; in turn, this is true if $U=B_\infty/\sqrt{\rho\mu}$. That is, the propellant must flow at the Alfvén speed over the fuel.

Quite apart from the difficulty of supplying the necessary magnetic field, we note that a shear layer of strength U and a current sheet of strength $U\sqrt{\rho/\mu}$ must be provided. Difficulties of maintaining such a sheet would seem to rule out this possibility. However, this simple MHD problem illustrates the principle of containment that we wish to explore. Further, we may remark that the purely fluid-mechanical flows to be emphasized in the rest of this paper could each be generalized to include suitable magnetic fields. The possible advantages of such procedures have not been considered.

CONTAINMENT BY SWIRLING ROTATION

We now consider the possibilities for containment using the rotational inertia of a general swirling motion, where the vortex filaments are in some ways analogous to the magnetic field lines of the previous case. Since they too resist deflection, they can assume traveling wave patterns, as we shall see.

Taylor's Solution for a Sphere in Uniform Rotation

Returning to equation (7), we record the solution found by Taylor in 1922 (ref. 10) for flow about a sphere of radius R, when the flow far away is given by a uniform stream U with solid-body swirl $W=\frac{U}{l}r$, where l is a length giving the intensity of swirl. We have in mind a theoretical representation of vortex breakdown (fig. 1), for example. Taylor's solution envisaged a solid sphere, whereas we are interested in a fluid sphere, and it seems that certain features of the solution which are interesting from the containment viewpoint have escaped notice. Noting that $g=(2/l)\psi$, we find that equation (7) becomes

$$\frac{\partial^2\psi}{\partial x^2}+\frac{\partial^2\psi}{\partial r^2}-\frac{1}{r}\frac{\partial\psi}{\partial r}+\frac{4}{l^2}\psi=\frac{2U}{l^2}r^2 \qquad (10)$$

which has a solution in terms of Bessel functions

$$\psi=\frac{1}{2}Ur^2\left(1+\kappa_1\frac{J_{3/2}(\xi)}{\xi^{3/2}}+\kappa_2\frac{N_{3/2}(\xi)}{\xi^{3/2}}\right) \qquad (11)$$

where $\xi\equiv\frac{2}{l}\sqrt{r^2+x^2}$

and $J_{3/2}(\xi)\equiv\sqrt{2/\pi\xi}\left(\frac{1}{\xi}\sin\xi-\cos\xi\right)$

and $N_{3/2}(\xi)\equiv\sqrt{2/\pi\xi}\left(\sin\xi+\frac{1}{\xi}\cos\xi\right)$ are Bessel functions of the first and second kind, respectively. The velocity components are

$$\frac{u}{U}=1+\kappa_1\left(\frac{J_{3/2}}{\xi^{3/2}}-2\frac{r^2}{l^2}\frac{J_{5/2}}{\xi^{5/2}}\right)+\cdots \qquad (12)$$

$$\frac{v}{U}=2\kappa_1\frac{xr}{l^2}\frac{J_{5/2}}{\xi^{5/2}}+\cdots \qquad (13)$$

$$\frac{w}{U}=\frac{r}{l}\left(1+\kappa_1\frac{J_{3/2}}{\xi^{3/2}}\right)+\cdots \qquad (14)$$

For convenience, the appropriate terms involving N are represented by dots.

Now, the solution just written down has the feature that both the J and N solutions vanish suitably at infinity, and after a boundary condition on the sphere is satisfied, a free constant remains. The difficulty has to do with the wave motions possible in a swirling flow. A recent study of this problem appears in reference 11.

The indeterminacy of Taylor's solution is troublesome if one is interested in an unbounded fluid. However, we are more concerned with the sphere, which we regard as fluid. Thus, the indeterminacy may be, for us, opportunity. First, we note that the J-solution by itself has no singularity inside the sphere, so we might hope to avoid boundary-layer problems by choosing that solution alone:

$$\psi=\frac{1}{2}Ur^2\left[1-\left(\frac{2R/l}{\xi}\right)^{3/2}\frac{J_{3/2}(\xi)}{J_{3/2}(2R/l)}\right] \qquad (15)$$

Special Case of a Stagnant Sphere

Probably the more useful possibility is obtained by noting that, if $J_{5/2}$ vanishes at the sphere, equations (11) to (14) say that all velocity components vanish on the sphere. Of course, w vanishes there by the circulation theorem, but differentiation shows that, if $J_{5/2}$ is zero, the circumferential shear vanishes also. Now, since the velocities vanish on the sphere, we may regard the sphere as a constant-

pressure free surface and the fluid inside as quiescent. The foregoing argument applies to the N-solution as well as to the J-solution, or to any combination of the two so long as circumferential shear is arranged to vanish. If J alone is chosen, $R/l=2.89$. (This represents very intense swirl, a free-stream helix angle of about 70° when $r=R$.) If N alone is chosen, $R/l=2.00$. Possible combinations presumably range between these values.

Figure 3 shows the streamline pattern and meridional velocity profile for the J-case,[2] when $R/l=2.89$ and, accordingly, $\kappa_1=43.7$. The wavelike character of the streamlines is remarkable. In fact, at about $r/l=5$, the stream surface closes into a ring. The thought naturally occurs that such a ring installed in a duct could serve to "key" the desired flow in position. Figure 4 shows the circumferential velocity profile, which has zero value and slope at the surface, and approaches $W=(U/l)r$ far from the sphere.

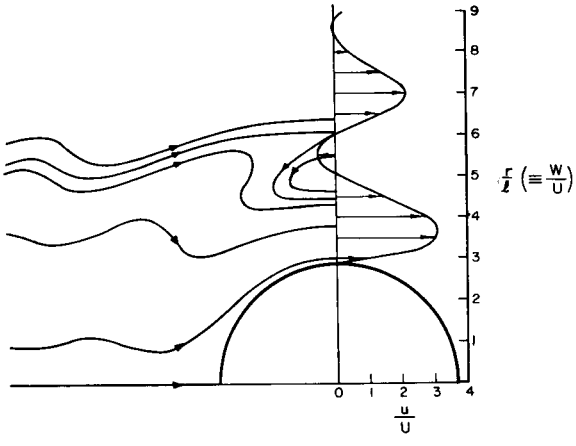

FIGURE 3.—*Streamlines and meridional velocity distribution for stagnant sphere of radius* R/l = 2.89.

Because the outer flow is brought to rest on the sphere, there is no velocity discontinuity requiring boundary-layer adjustment with the high drag, flow separation, and probable breakup of the fluid sphere which might ensue. However, there is a discontinuity of meridional (but not circumferential) shear which must in principle adjust in a weak boundary layer free of pressure gradient. The character of this boundary layer would depend crucially on the relative viscosities of the two gases.

[2] Many of the calculations to be described were performed by Lalere Ladeji of Cornell University.

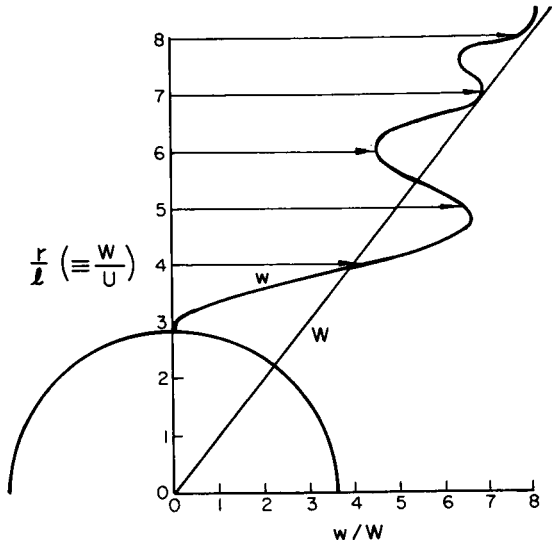

FIGURE 4.—*Swirl velocity for stagnant sphere of radius* R/l = 2.89.

Other Taylor Solutions

It might be mentioned that a wide variety of flows are represented by various choices of κ_1. Figure 5 suggests some of the possibilities in terms of meridional velocity. We have mentioned the case $\kappa_1=43.7$. If $\kappa=0$, there is no disturbance of a uniform stream. For a closed stream surface to occur, κ_1 must be at least 11.6. For values of κ_1 between 11.6 and 43.7, the ring occurs without any central sphere. If $\kappa_1=-3.76$, a stagnation point appears on the axis, and, for more negative values, spheres with no rings appear. Also in figure 5, we record the velocity profile for the N-case with sphere at rest. Apparently no ring is featured in that solution.

Long Waves

In the foregoing analyses, the confined flow regions have been spherical. However, in order to understand the spontaneous occurrence of vortex breakdown and to study the stability of such flows, it is simpler to consider slight displacements of the original vortex filaments. That is, the disturbance is long and slender and slowly varying in the x-direction. Under such an assumption, the enclosed eddy will probably never be strictly quiescent.

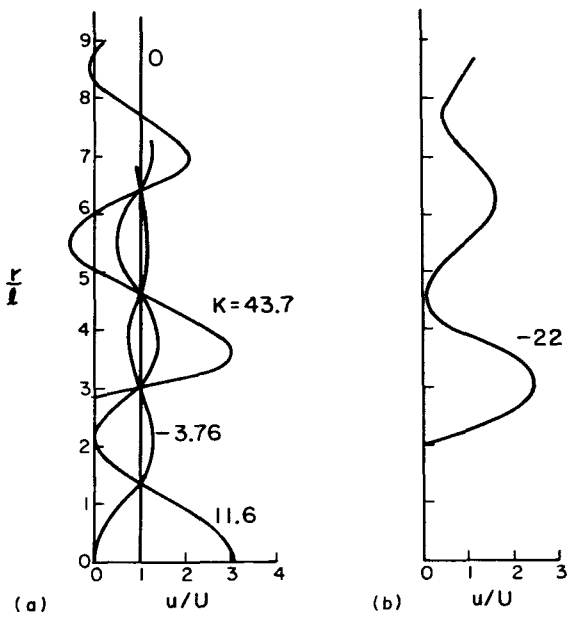

FIGURE 5.—*Meridional velocities.* (a) *Meridional velocity for various solutions of the first kind* J. (b) *Meridional velocity for stagnant sphere solution of the second kind* N.

The phenomenon of vortex breakdown (fig. 1) is thought to result from wave motion of this kind which may be sustained by a fluid in rotation. Benjamin, in reference 12, has put forward such an interpretation, and Leibovich, in references 13 and 14, has developed a rather complete theory of such waves. We will only outline the procedure and results here; details may be found in references 13 and 14.

It may be shown that the Euler equation can be satisfied by a stream function expansion of the form

$$\psi=\psi_o(r)+\epsilon A(x,t)\phi_o(r)+O(\epsilon^2,\epsilon k^2) \quad (16)$$

where ψ_o describes the given unperturbed axial flow. The amplitude of the perturbation is ϵ, and k is a slenderness parameter R/L, where R is a transverse dimension and L is an axial dimension (e.g., wavelength). Both ϵ and k are assumed to be small. The swirl velocity is, correspondingly,

$$w=W(r)+\epsilon A(x,t)w_o(r)+O(\epsilon^2,\epsilon k^2) \quad (17)$$

Again, $W(r)$ is a given swirl distribution, not solid body; therefore, w and ψ must be found separately. The amplitude function $A(x,t)$ itself depends on ϵ and k, and substitution of equations (16) and (17) into the Euler equations shows that A must satisfy

$$\frac{\partial A}{\partial t'}=C_o\frac{\partial A}{\partial x'}+\epsilon C_1 A\frac{\partial A}{\partial x'}+k^2C_2\frac{\partial^3 A}{\partial x'^3} \quad (18)$$

where $x'\equiv x/L$ and $t'\equiv W_o t/L$, with W_o being a representative swirl velocity, and C_0, C_1, and C_2 are constants.

From equation (18), in a weak, long wave, if $\epsilon\ll k^2$, a wave propagating at C_0 is dispersed and must finally die out. On the other hand, if $k^2\ll\epsilon$, nonlinear steepening must make the wave steepen and "break." To bring these effects into balance (one is looking for a permanent wave) one chooses $k^2=\epsilon$ and recognizes equation (18) as the Korteweg-deVries equation originally derived (in 1895) to deal with shallow-water waves. The permanent-wave solution has the form

$$A=\operatorname{sech}^2\left(\frac{1}{2}\sqrt{\frac{1}{3}\frac{C_1\epsilon}{C_2}}\frac{x}{R}\right) \quad (19)$$

where x is measured in the moving wave. The constant C_0 is the eigenvalue for ϕ_o, and C_1 and C_2 may be derived from the resulting solution for ϕ_o.

We take as an example the cases of decaying-vortex swirl in a uniform stream

$$\psi_o=\frac{1}{2}Ur^2;\ W=\frac{\beta}{r'}(1-e^{-\alpha r'^2})$$

where the constants α and β depend on the maximum value W_o and the place r' where it occurs. Figure 6 shows the assumed swirl distribution. To correspond with Harvey's experiment, in which $r'\approx 0.30$ where W is maximum, α may be taken as about 14. In that case, the wave speed (free-stream velocity in the steady case) is

$$U=0.97\,W_{\max}$$

which agrees quite well with Harvey's results. Also, in that case

$$\frac{1}{2}\sqrt{C_1/3C_2}=1.99$$

Figure 7 shows the calculated flow pattern for $\epsilon=0.8$. It is seen that a closed eddy is formed. Values of the stream function are indicated which show that motion within the eddy is weak near the eddy boundary, and even outside the eddy velocities are substantially less near the eddy boundary than in the free stream. Figure 6, which displays the

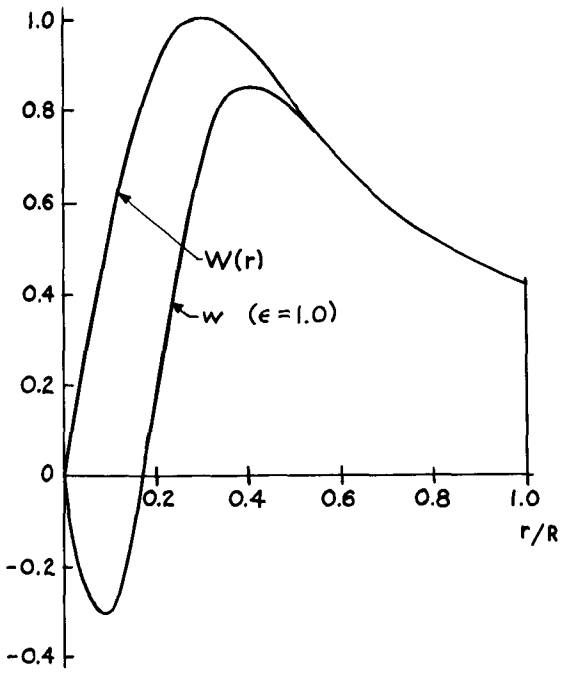

FIGURE 6.—*Swirl velocities in the decaying vortex for* $a = 14$ *(corresponding to Harvey's experiment) when undisturbed (upper curve) and when perturbed by a solitary wave (lower curve) with amplitude parameter* $\epsilon = 1$.

swirl velocity, confirms the suggestion that all velocities near the eddy boundary are quite small. This circumstance, as we have already argued, is probably favorable for containment of a heavy fuel.

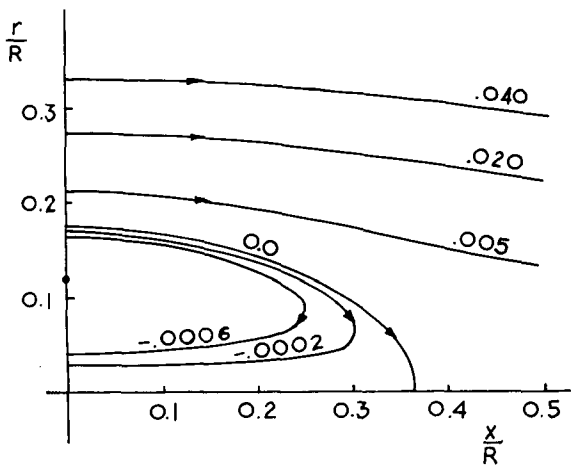

FIGURE 7.—*Streamlines in the region of the eddy formed by a solitary wave with* $\epsilon = 1$ *in a decaying vortex with* $a = 14$.

We should also observe that this permanent-wave theory yields a specific eddy size depending on amplitude; clearly, equation (19) gives a length scale of $R/\sqrt{\epsilon}$ for the disturbance.

Slender Eddy in a Wheel Flow

The foregoing theory cannot be applied to unbounded solid-body swirl. However, Leibovich (ref. 15) found a steady, small-disturbance solution in that case which has certain points of agreement with the solitary-wave calculation. The maximum possible eddy length was found to be $L_{max} = 2\pi UR/W$. The velocities in the eddy were found to be small, and it proved possible to set the swirl velocity equal to zero within the eddy itself.

Stability of a Swirling Flow

A configuration consisting of a heavy rotating fluid inside a lighter one intuitively appears unstable even to axially symmetric disturbances. However, this need not necessarily be true, as can be shown by considering a cylindrical flow as a model of a flow slowly varying in the axial direction. Examination of the dynamic stability of cylindrical flows with arbitrary swirl and axial velocity profiles (ref. 16) shows that stability depends on the relative changes of density and swirl velocity in the flow: if $\rho(r)$, $W(r)$, and $U(r)$ are the undisturbed distributions of density, swirl velocity, and axial velocity, respectively, then the flow is stable if

$$\frac{1}{r^3}\frac{d}{dr}(\rho r^2 W^2) \geqq \frac{1}{4}\rho\left(\frac{dU}{dr}\right)^2 \qquad (20)$$

In effect, axial shear tends to destabilize the motion, whereas rotation is stabilizing if the angular momentum increases outward. (By itself, this is Rayleigh's stability criterion.) Thus, it is possible to have a flow that is stable to axisymmetric disturbances even if ρ decreases outward, provided that the circulation increases outward sufficiently fast.

In regard to containment of heavy fuel, equation (20) suggests that wherever ρ must decrease outward, it would be helpful if velocities were small. For this reason, we feel that vortex containment schemes should have quiescent fuel regions if possible.

In the propellant region, the gas would be receiving copious quantities of heat by radiation and would be hottest and presumably least dense near

the fuel region. This would be stabilizing for the propellant, according to equation (20).

Finally, we suggest that if stability of coupled motions of fuel and propellant is studied it is probably correct to consider that the fuel, being dense, responds slowly to impressed pressure changes, and that the resulting coupled motions of interest are quasi-steady.

CONTAINMENT BY SMOKE-RING ROTATION

We now set aside the problem of containment by swirling rotation and consider purely meridional flows with rotation in the sense of a bundle of coaxial smoke rings in axial motion. We ask, can a quiescent region be confined by the resistance of smoke rings in the propellant to the stretching process involved in passing around the fuel?

One may think, in this regard, of Hill's spherical vortex (ref. 17) in which vorticity is continuously distributed in a sphere. However, there is no vorticity at all beyond the sphere, and, in fact, the flow is not statically stable without the interposition of, for example, surface tension at the sphere. Nevertheless, we now record the relevant solution of Euler's equations for further use.

Returning to equation (7), we see that $G=0$, and we assume that the vorticity is simply proportional to r, not just along each stream surface, but throughout the flow; $\omega=-ar$. Then the right-hand side of equation (7) becomes just ar^2, and a suitable solution for our purposes involves the sum of a particular solution, a free stream, and a potential doublet:

$$\psi=\frac{a}{10}r^2(x^2+r^2)+Mr^2+N\frac{r^2}{(x^2+r^2)^{3/2}} \qquad (21)$$

For Hill's vortex, one uses the first and second terms inside the sphere, and the second and third terms outside, with appropriate choices of M and N to make a sphere of radius R a streamline. A different set of choices was made by Lighthill (ref. 18), who was concerned with the rotational flow behind a curved bow shock washing over the forward part of a sphere. Thus, he determined M and N by applying a shock condition and a requirement that the sphere be a stream surface. His vorticity was, then, outside the sphere.

Somewhat similarly, we apply equation (21) outside the sphere, and choose M and N so that both components of velocity vanish at the sphere. Doing this, we find that $M=-\frac{1}{6}aR^2$, $N=\frac{1}{15}aR^5$, and the cylindrical velocity components are as follows (lengths are dimensionless by reference to R):

$$u=\frac{aR^2}{15}\left\{3[(x')^2+2(r')^2]-5+\frac{2(x')^2-(r')^2}{[(x')^2+(r')^2]^{5/2}}\right\} \qquad (22)$$

$$v=\frac{aR^2}{15}(3r'x')\left\{\frac{1}{[(x')^2+(r')^2]^{5/2}}-1\right\} \qquad (23)$$

Clearly, both expressions vanish when $(x')^2+(r')^2=1$.

One may now examine this solution to find stream surfaces and velocity and pressure distributions. Figure 8 assembles the essential features of this flow.

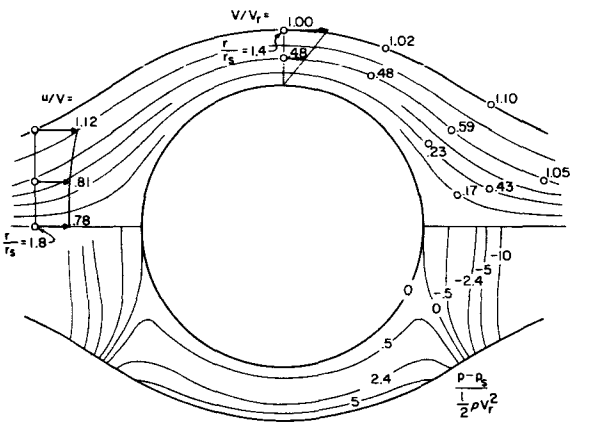

FIGURE 8.—*Streamlines, velocities, and pressure distribution in the smoke-ring solution. Streamlines are curves in the upper half of the figure. Velocities (referred to the speed at* $x=0$, $r/R_s=1.4$) *are indicated at various positions on the streamlines. The sphere* $r/R_s=1$ *is stagnant and at constant pressure* p_s. *Pressure distribution is given by curves in the lower half of the figure. The axial velocity at* $x/R_s=1.8$ *is indicated.*

Since velocities vanish on the sphere the fuel is at rest and at constant pressure p_s. The streamlines are sensibly shaped for flow over a sphere, but it should be noted that there is no free stream in this flow: Velocities approach infinity far upstream and far downstream. Thus, there is no characteristic velocity for this problem. In the figure, we denote the velocity at $r'=1.4$, $x=0$ as V_o, and indicate resultant velocities V in proportion to V_o.

It is remarkable how nearly constant V remains over the central part of each streamline path. This is reflected in the pressure contours as well; in the region 50° to either side of the vertical, where pressure is higher than p_s, pressure is nearly constant along streamlines. This circumstance should be helpful in maintaining an attached boundary layer along the duct walls.

It would seem a fairly simple matter to produce this flow. On the left in figure 8, we indicate an injection disk, with the required normal u velocity distribution. In addition, the correct transverse component must be supplied to establish the proper vorticity distribution. This might be arranged with a suitable set of deflection plates.

One may ask, is this flow unique? Given the initial assumption about outer vorticity, the sphere is perhaps the only shape within which the fuel is at rest. A different vorticity distribution might well yield another shape, provided the duct walls were also changed in the proper way. There seems to be no flow of this character in two dimensions, nor should it be expected; a straight vortex line can pass around a cylinder without stretching and hence without exerting a containing force. Therefore, the plane-flow experiment of reference 7 is probably only superficially comparable to the flow calculation just described. For example, strong eddy flows probably occur in the fuel region of that experimental device, and we feel that the axisymmetric geometry may be fundamental to the success of the approach.

Finally, the stability of the flow just described has not been determined. Obviously, the quiescent center is favorable, as is the positive outward pressure gradient. The weak streamwise pressure gradient is no doubt helpful for boundary-layer stability. Whether the position of the fuel cloud, viewed as a solid body, is stable is an important question which we cannot answer at this time.

CONCLUSIONS

Several examples of fluid flows with regions of closed streamlines have been discussed in terms of their containment possibilities for gas-core reactors. The confining mechanisms may be rotational inertia or electromagnetic pinch. Emphasis was placed on axisymmetric flows, with rotation external to the confined region, of either a swirling or a smoke-ring orientation.

Inviscid, incompressible, steady-state analysis showed that isolated, stagnant fuel regions of constant pressure may be produced by suitable choices of flow parameters. The existence of such flows is confirmed both by experiments on vortex breakdown and a recent wave theory of vortex breakdown, which predicts standing-wave patterns corresponding to confined flows of interest.

The effects of density difference and of energy evolution and transfer require much further study before practical containment applications can be claimed. However, stability theory suggests that it would indeed be desirable for a rotationally confined heavy fluid to be at rest. Also, if the fuel region is stagnant, viscous and turbulent momentum and mass losses should be minimized.

We feel that the flows discussed offer a new range of important possibilities for gaseous fuel confinement which should be explored experimentally without delay. Probably the smoke-ring case will be easiest to realize experimentally, but, as in all the cases discussed, control and stability of the flow will be the crucial consideration.

REFERENCES

1. Kerrebrock, J. L.; and Meghreblain, R. V.: Vortex Containment for the Gaseous-Fission Rocket. J. Aerospace Sci., vol. 28, no. 9, Sept. 1961, pp. 710–724.
2. Rosenzweig, M. L.; Lewellen, W. S.; and Ross, D. H.: Confined Vortex Flows with Boundary Layer Interaction. AIAA J., vol. 3, 1964, pp. 2127–2134.
3. McLafferty, G. H.: Survey of Advanced Concepts in Nuclear Propulsion. J. Spacecraft Rockets, vol. 5, no. 10, 1968, pp. 1121–1128.
4. Evvard, J. C.: Wheel-Flow Gaseous-Core Reactor Concept. NASA TN D-2951, 1965.
5. Reshotko, E.; and Monnin, C. F.: Stability of Two-Fluid Wheel Flows. NASA TN D-2696, 1965.
6. Harvey, J. K.: Some Observations of the Vortex Breakdown Phenomenon. J. Fluid Mech., vol. 14, 1962, pp. 585–592.
7. Ragsdale, R. G.; and Lanzo, C. D.: Summary of Recent Gaseous Reactor Fluid Mechanics Experiments. NASA TM X-1847, 1969.
8. Rom, F. E.: Comments on the Feasibility of Developing Gas Core Nuclear Reactors. NASA TM X-52644, 1969.

9. SHAFRANOV, V. D.: On Magnetohydrodynamical Equilibrium Configurations. Soviet Phys.—JETP, vol. 6, no. 9, pp. 545–554. Translated from Zhurnal Eksperimental' noi i Teoreticheskoi Fiziki, vol. 33, no. 3, 1957, pp. 710–722.
10. SQUIRE, H. B.: Rotating Fluids. Surveys in Mechanics, G. K. Batchelor and R. M. Davies, eds., Cambridge Univ. Press, 1956.
11. STEWARTSON, K.: On the Motion of a Sphere Along the Axis of a Rotating Fluid. Quart. J. Mech. Appl. Math., vol. 11, 1958, pp. 39–51. Also, Corrigenda, 1969, pp. 257–258.
12. BENJAMIN, T. B.: Some Recent Developments in the Theory of Vortex Breakdown. J. Fluid Mech., vol. 28, 1967, pp. 65–84.
13. LEIBOVICH, S.: Evolution of Nonlinear Waves in Rotating Fluids. Phys. Fluids, vol. 12, 1969, pp. 1124–1125.
14. LEIBOVICH, S.: Weakly Nonlinear Waves in Rotating Fluids. J. Fluid Mech., vol. 42, 1970, pp. 803–822.
15. LEIBOVICH, S.: Axially-Symmetric Eddies Embedded in a Rotational Stream. J. Fluid Mech., vol. 32, 1968, pp. 529–548.
16. LEIBOVICH, S.: Stability of Density Stratified Rotating Flows. AIAA J., vol. 7, 1969, pp. 177–178.
17. LAMB, H.: Hydrodynamics. Dover Pub. (New York, N.Y.), 1932, pp. 245–246.
18. LIGHTHILL, M. J.: Dynamics of a Dissociating Gas, Part I. Equilibrium Flow. J. Fluid Mech., vol. 2, 1957, pp. 1–32.

DISCUSSION

Johnson: Could you use a change of coordinates to go from a sphere to an ellipsoid—a long ellipsoid?

Moore: I am sure that different shapes would be possible. In each of the cases in which I was talking about a sphere, there was also a highly specific assumption about a swirl velocity. If there were some other shape from some other swirl distribution, something other than a sphere would be obtained. However, I would not be surprised if other ellipsoidal solutions would also permit particular solutions with zero velocity inside.

Page intentionally left blank

Stability of Two-Fluid Wheel Flows With an Imposed Uniform Axial Magnetic Field

CARL F. MONNIN AND JOHN J. REINMANN

NASA Lewis Research Center

The stability of an incompressible two-fluid wheel flow to infinitesimal helical disturbances is studied. The inner fluid is heavy and has infinite electrical conductivity, whereas the outer fluid is light and is nonconducting. An axial magnetic field is externally imposed on both fluids. This configuration may be viewed as a Rayleigh-Taylor problem in the frame of the rotating fluid and is dynamically unstable. Growth rates increase with increasing axial wavelength and azimuthal mode numbers but decrease with increasing axial magnetic field. By increasing the magnetic field sufficiently, the system can be made stable to short axial wavelength disturbances for any azimuthal mode.

Vortex containment of a heavy fissioning gas surrounded by a lighter coolant gas has been suggested for possible application to gaseous-core nuclear rockets (refs. 1 to 3). Another application of the vortex containment principle is found in the vortex magnetohydrodynamic (MHD) generator (ref. 4). The problem investigated in this report was originally conceived for studying the stability characteristics of the two-fluid wheel-flow reactor concept of Evvard (ref. 3). In this concept, a core of heavy fissioning gas in solid-body rotation is surrounded by a lighter coolant gas also in solid-body rotation at the same angular frequency. Since the centrifugal force is directed radially outward from the heavy inner fluid toward the lighter outer fluid, this flow configuration is dynamically unstable. When it is viewed from the rotating reference frame, the situation is analogous to the well-known Rayleigh-Taylor instability problem where a heavy fluid is supported against gravity by a lighter fluid. Reshotko and Monnin (ref. 5) investigated the nature of this two-fluid wheel-flow instability from hydrodynamic considerations only. They found the flow always unstable with growth rates that increase with increasing axial, as well as azimuthal, wave number.

Because the gaseous core is highly ionized and therefore electrically conducting, Evvard suggested that an externally imposed axial magnetic field might be used to stabilize the flow. Obviously, any realistic evaluation of the stability problems involved in this complex flow system would have to be determined by experiment, but the proposed concept does suggest an idealized flow configuration whose stability can be investigated mathematically by a straightforward perturbation analysis.

This idealized flow problem treated in the present report consists of two inviscid immiscible fluids of constant and uniform density separated by a cylindrical interface. The inner fluid is a perfect electrical conductor, whereas the outer fluid has the electrical properties of a vacuum. There is an externally imposed axial magnetic field which, at equilibrium, is uniform and has the same value in both fluids. This is a hydromagnetic flow in which the electromagnetic fields are coupled to the hydrodynamic flow fields. The hydromagnetic equations, with scalar pressure, were used to describe the flow.

Although the correspondence between the real flow problem and the idealized one is tenuous indeed, the idealized problem possesses the advantage that it can be readily solved and some of the results should be of use in the design of an experiment and in the interpretation of results. The idealized problem is also of interest in its own right since it has not been previously investigated. Furthermore,

in hydromagnetic fluids such as a liquid metal, the sharp boundary and the infinite electrical conductivity would correspond to a realistic physical situation.

Wilhelm (ref. 6) has investigated the stability of an idealized two-fluid wheel-flow configuration where the inner fluid was a perfect conductor and the outer fluid was a nonconducting gas. The equilibrium magnetic field was an azimuthal field produced by an axial sheet current at the interface between the inner and outer fluids. The basic equations used in the present report are identical to those of Wilhelm.

In the idealized model viscous effects were omitted, but, as Chandrasekhar (ref. 7) noted for rotating flows, viscosity severely diminishes the growth rate of short-wavelength disturbances. We should therefore expect the short-wavelength results of this report to be pessimistic in the predictions of stability. Finite resistivity effects have also been omitted in the analysis, but Kruskal and Schwarzschild (ref. 8) have found that for the kind of problem under consideration, namely, large electrical conductivity, the infinite conductivity assumption preserves the essential features of the real situation.

In this report, the hydromagnetic stability problem is solved by the normal-mode technique. We begin by writing the continuity, momentum, Ohm's law, and Maxwell equations for the inner and outer fluids. These equations are linearized by performing a perturbation analysis about an assumed equilibrium flow. Solutions to these equations are obtained for the inner and outer fluids, and the interfacial boundary conditions are derived. Simultaneous solution of the volume and boundary equations yields the dispersion relation. The dispersion relation is solved for complex frequencies and real wave numbers. The results suggest some methods that might be employed to stabilize this type of flow. Dimensional analysis is applied to determine the degree to which the idealized model is approximated by the wheel-flow reactor plasma and by the liquid metals sodium, potassium, and mercury. The relevance of the idealized model to situations where finite-amplitude disturbances and finite electrical conductivity exist is discussed in a qualitative way.

BASIC FLOW EQUATIONS

Inner-Fluid Equations

The hydromagnetic equations, in mks units, are used for the inner fluid:

$$\rho\left[\frac{\partial \mathbf{V}^*}{\partial t}+(\mathbf{V}^*\cdot\nabla)\mathbf{V}^*\right]=\mathbf{J}^*\times\mathbf{B}^*-\nabla P^* \tag{1}$$

$$\nabla\cdot\mathbf{V}^*=0 \tag{2}$$

$$\mathbf{E}^*+\mathbf{V}^*\times\mathbf{B}^*=0 \tag{3}$$

$$\nabla\times\mathbf{B}^*=\mu_o\mathbf{J}^* \tag{4}$$

$$\nabla\cdot\mathbf{B}^*=0 \tag{5}$$

$$\nabla\times\mathbf{E}^*=-\frac{\partial \mathbf{B}^*}{\partial t} \tag{6}$$

The asterisks indicate that the quantities are dimensional quantities. (All symbols are defined in app. A.) In these equations viscosity, electrical resistivity, space charge, and displacement current have all been set equal to zero.

The electric field vector $\mathbf{E}^*$ and current density vector $\mathbf{J}^*$ can be eliminated from equations (1) and (6) by use of equations (3) and (4) to yield (ref. 6)

$$\rho\left[\frac{\partial \mathbf{V}^*}{\partial t}+(\mathbf{V}^*\cdot\nabla)\mathbf{V}^*\right]=\frac{1}{\mu_o}(\mathbf{B}^*\cdot\nabla)\mathbf{B}^*-\nabla\left(P^*+\frac{B^{*2}}{2\mu_o}\right) \tag{7}$$

$$\nabla\cdot\mathbf{V}^*=0 \tag{8}$$

$$\nabla\cdot\mathbf{B}^*=0 \tag{9}$$

$$\nabla\times(\mathbf{V}^*\times\mathbf{B}^*)=\frac{\partial \mathbf{B}^*}{\partial t^*} \tag{10}$$

Outer-Fluid Equations

Since the outer fluid is an electrically nonconducting fluid, the electromagnetic equations are uncoupled from the hydrodynamic equations. Thus, for the outer fluid, the hydrodynamic equations are

$$\rho\left[\frac{\partial \mathbf{V}^*}{\partial t}+(\mathbf{V}^*\cdot\nabla)\mathbf{V}^*\right]=-\nabla P^* \tag{11}$$

$$\nabla\cdot\mathbf{V}^*=0 \tag{12}$$

The electromagnetic equations in the outer fluid are Maxwell's equations for a vacuum with the displacement current neglected. Only the magnetic field equations are required, and these are

$$\nabla\times\mathbf{B}^*=0 \tag{13}$$

$$\nabla\cdot\mathbf{B}^*=0 \tag{14}$$

BOUNDARY CONDITIONS

Next we describe the boundary conditions of the interface between the inner and outer fluids. In the real physical situation, there would be a continuous transition of fluid properties across a thin layer separating the two fluids. As is the usual case, we assume that the transition is discontinuous and then allow for a sheet current and a discontinuous jump in the field quantities. The appropriate equations may be integrated across the interface to obtain the following boundary conditions:

$$(P_2^* - P_1^*) + \left[\frac{(B_2^*)^2}{2\mu_o} - \frac{(B_1^*)^2}{2\mu_o}\right] = 0 \quad (15)$$

$$\hat{\mathbf{n}} \cdot (\mathbf{V}_2^* - \mathbf{V}_1^*) = 0 \quad (16)$$

$$\hat{\mathbf{n}} \cdot (\mathbf{B}_2^* - \mathbf{B}_1^*) = 0 \quad (17)$$

where $\hat{\mathbf{n}}$ is a unit vector normal to the interface. Equations (15) to (17) are to be evaluated at the displaced interface. A detailed derivation and discussion of the boundary conditions is given in appendix B.

It is also necessary to have a relation between the velocity field and the displacement of the fluid at the interface. Since all the equations in this report are given in the Eulerian form rather than the Lagrangian form, we cannot, in general, express the various field quantities in terms of a displacement vector. However, when the displacements are infinitesimal, the Lagrangian displacement can be related to the Eulerian velocity. Following reference 9, let the surface of the interface be defined by the function $F(r^*,\theta,z^*,t^*) = 0$. Since a particle lying in the surface must move tangentially to the surface, it follows that (ref. 9)

$$\frac{\partial F}{\partial t^*} + (\mathbf{V}^* \cdot \nabla) F = 0 \quad (18)$$

Let the interface be described by the function

$$F(r^*,\theta,z^*,t^*) = r^* - [\xi^*(\theta,z^*,t^*) + a] \quad (19)$$

where $\xi^*(\theta,z^*,t^*)$ is the radial displacement from the equilibrium position $r^* = a$.

We now obtain a relation between the interface position and the velocity by substituting equation (19) into equation (18). This yields

$$\left(-\frac{\partial \xi^*}{\partial t^*} + V_r^* - \frac{V_\theta^*}{r^*}\frac{\partial \xi^*}{\partial \theta} - V_z^*\frac{\partial \xi^*}{\partial z^*}\right)_{\text{At interface}} = 0 \quad (20)$$

Equation (20) will be used to determine the perturbation velocity in terms of the radial displacement of the interface.

Equilibrium Flow

The geometry of the two-fluid wheel flow is shown in figure 1. Cylindrical coordinates are used,

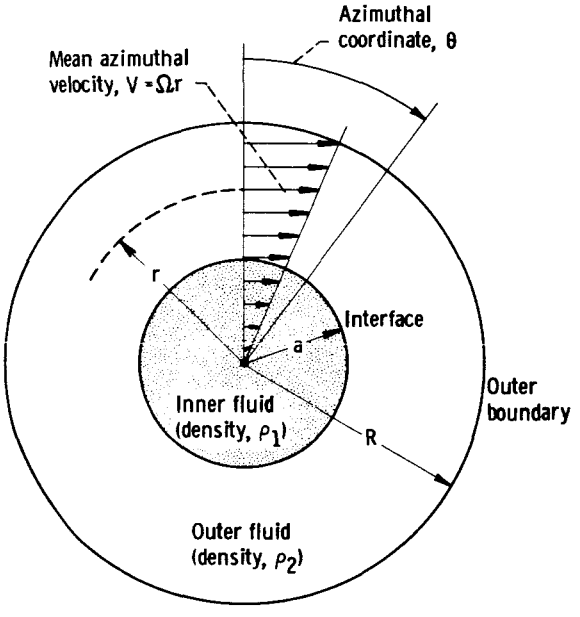

FIGURE 1.—*Geometry of two-fluid wheel flow.*

with the z-coordinate directed into the paper. The heavy inner fluid is given the subscript 1, and the outer fluid has the subscript 2. The interface between the two fluids is at radius a. The outer boundary of the outer fluid is at radius R, which is taken to be infinite in the following analysis. Clearly, the equilibrium flow is unaffected by a cylindrical boundary at a finite radius R as long as the boundary rotates with the angular velocity of the wheel flow. An infinite value of R was used so as to simplify the dispersion relation obtained from the perturbation analysis. Since the disturbance is generated at the interface and decays rapidly away from the interface, the outer boundary has little influence on the disturbance growth rates. Reshotko and Monnin (ref. 5) examined the effect of the outermost boundary at $r = R$ and concluded that "For values of ρ_1/ρ_2 and R of interest in wheel-

flow reactors, the stability characteristics are essentially those of the unbounded configuration."

The inner and outer fluids move in solid-body rotation at the same angular frequency Ω. Thus, the equilibrium flow velocity is azimuthal and depends only on the radial coordinate according to the relation

$$V_\theta^* = \Omega r^* \tag{21}$$

In equilibrium there are no zero-order electric currents; the externally imposed magnetic field is axial and uniform throughout space. Thus, in equilibrium the flow is purely hydrodynamic since the magnetic terms drop out of equation (7). It was shown in reference 5 that V_θ^*, given by equation (21), satisfies the pertinent hydrodynamic momentum and continuity equations (eqs. (7) and (8)). The equilibrium pressure distribution in the inner and outer fluids, consistent with boundary condition (15), was found to be

$$P_{0,1}^* = P_c^* + \rho_1 \frac{\Omega^2 r^{*2}}{2} \qquad 0 \leq r^* \leq a \tag{22a}$$

$$P_{0,2}^* = P_c^* + \rho_1 \frac{\Omega^2 a^2}{2} + \rho_2 \Omega^2 \left(\frac{r^{*2} - a^2}{2} \right) \qquad a \leq r^* \leq R \tag{22b}$$

FORMULATION OF STABILITY PROBLEM

Inner-Fluid Disturbance Equations

The equations governing the infinitesimal disturbances in the inner fluid are obtained from a linearization of equations (7), (8), and (10) about the assumed equilibrium flow. Let $\mathbf{B}^* = \hat{\mathbf{z}} B_0^* + \mathbf{b}^*$, $\mathbf{V}^* = \hat{\boldsymbol{\theta}} \mathbf{r}^* \Omega + \mathbf{v}^*$, and $P = P_0^* + p^*$. Then the linearized perturbation equations are

Momentum (eq. (7)):

$$\frac{\partial v_r^*}{\partial t^*} + \Omega \frac{\partial v_r^*}{\partial \theta} - 2\Omega v_\theta^* = \frac{B_0^*}{\mu_o \rho} \frac{\partial b_r^*}{\partial z^*} - \frac{1}{\rho} \frac{\partial}{\partial r^*} \left(p^* + \frac{B_0^* b_z^*}{\mu_o} \right) \tag{23}$$

$$\frac{\partial v_\theta^*}{\partial t^*} + \Omega \frac{\partial v_\theta^*}{\partial \theta} + 2\Omega v_r^* = \frac{B_0^*}{\mu_o \rho} \frac{\partial b_\theta^*}{\partial z^*} - \frac{1}{\rho r^*} \frac{\partial}{\partial \theta} \left(p^* + \frac{B_0^* b_z^*}{\mu_o} \right) \tag{24}$$

$$\frac{\partial v_z^*}{\partial t^*} + \Omega \frac{\partial v_z^*}{\partial \theta} = \frac{B_0^*}{\mu_o \rho} \frac{\partial b_z^*}{\partial z^*} - \frac{1}{\rho} \frac{\partial}{\partial z^*} \left(p^* + \frac{B_0^* b_z^*}{\mu_o} \right) \tag{25}$$

Faraday's law for a perfect conductor (eq. (10)):

$$\frac{\partial b_r^*}{\partial t^*} + \Omega \frac{\partial b_r^*}{\partial \theta} = B_0^* \frac{\partial v_r^*}{\partial z^*} \tag{26}$$

$$\frac{\partial b_\theta^*}{\partial t^*} + \Omega \frac{\partial b_\theta^*}{\partial \theta} = B_0^* \frac{\partial v_\theta^*}{\partial z^*} \tag{27}$$

$$\frac{\partial b_z^*}{\partial t^*} + \Omega \frac{\partial b_z^*}{\partial \theta} = B_0^* \frac{\partial v_z^*}{\partial z^*} \tag{28}$$

Continuity (eq. (8)):

$$\frac{\partial v_r^*}{\partial r^*} + \frac{v_r^*}{r^*} + \frac{1}{r^*} \frac{\partial v_\theta^*}{\partial \theta} + \frac{\partial v_z^*}{\partial z^*} = 0 \tag{29}$$

Equations (23) to (29) can be nondimensionalized by using the following definitions:

$$v^* = v v_{\text{ref}} \qquad t^* = t\Omega^{-1} \qquad p^* = p \frac{B_{\text{ref}}^2}{\mu_o}$$

$$B^* = B B_{\text{ref}} \qquad \omega^* = \omega \Omega \qquad v_{\text{ref}} = a\Omega$$

$$r^* = ar \qquad A_a^2 = \frac{B_{\text{ref}}^2}{\mu_o \rho_a v_{\text{ref}}^2} \qquad z^* = az$$

where subscript $a=1$ refers to the inner fluid and $a=2$ refers to the outer fluid. The nondimensional form of equations (23) to (29) becomes

$$\frac{\partial v_r}{\partial t} + \frac{\partial v_r}{\partial \theta} - 2v_\theta = A_1^2 B_0 \frac{\partial b_r}{\partial z} - A_1^2 \frac{\partial}{\partial r} (p + B_0 b_z) \tag{23a}$$

$$\frac{\partial v_\theta}{\partial t} + \frac{\partial v_\theta}{\partial \theta} + 2v_r = A_1^2 B_0 \frac{\partial b_\theta}{\partial z} - \frac{A_1^2}{r} \frac{\partial}{\partial \theta} (p + B_0 b_z) \tag{24a}$$

$$\frac{\partial v_z}{\partial t} + \frac{\partial v_z}{\partial \theta} = A_1^2 B_0 \frac{\partial b_z}{\partial z} - A_1^2 \frac{\partial}{\partial z} (p + B_0 b_z) \tag{25a}$$

$$\frac{\partial b_r}{\partial t} + \frac{\partial b_r}{\partial \theta} = B_0 \frac{\partial v_r}{\partial z} \tag{26a}$$

$$\frac{\partial b_\theta}{\partial t} + \frac{\partial b_\theta}{\partial \theta} = B_0 \frac{\partial v_\theta}{\partial z} \tag{27a}$$

$$\frac{\partial b_z}{\partial t} + \frac{\partial b_z}{\partial \theta} = B_0 \frac{\partial v_z}{\partial z} \tag{28a}$$

$$\frac{\partial v_r}{\partial r} + \frac{v_r}{r} + \frac{1}{r} \frac{\partial v_\theta}{\partial \theta} + \frac{\partial v_z}{\partial z} = 0 \tag{29a}$$

Since the coefficients of equations (23a) to (29a) are independent of t, θ, and z, the equations allow solutions of the form $q(r) \exp [i(m\theta + kz + \omega t)]$, where $q(r)$ is a complex disturbance amplitude, k and m are the nondimensional axial and azimuthal wave numbers, respectively, and ω is a nondimensional complex frequency. The wave numbers k

and m are real, and m is integral. The real part of ω is the nondimensional rotational frequency of the disturbance, and the imaginary part ω_i is the nondimensional growth rate of the disturbance. Disturbances grow, are neutral, or decay according to whether ω_i is negative, zero, or positive, respectively. For the assumed form of the disturbance, equations (23a) to (29a) become

$$icv_r - 2v_\theta = A_1^2 B_0 ikb_r - A_1^2\left(\frac{dp}{dr} + B_0\frac{db_z}{dr}\right) \qquad (23b)$$

$$icv_\theta + 2v_r = A_1^2 B_0 ikb_\theta - \frac{A_1^2}{r} im(p + B_0 b_z) \qquad (24b)$$

$$icv_z = -A_1^2 ikp \qquad (25b)$$

$$icb_r = B_0 ikv_r \qquad (26b)$$

$$icb_\theta = B_0 ikv_\theta \qquad (27b)$$

$$icb_z = B_0 ikv_z \qquad (28b)$$

$$\frac{dv_r}{dr} + \frac{v_r}{r} + \frac{imv_\theta}{r} + ikv_z = 0 \qquad (29b)$$

where $c = \omega + m$, and c is the wave frequency observed in the rotating frame. It is subsequently referred to as the relative frequency. Substitute equations (25b), (26b), and (28b) into equation (23b) and equation (27b) into equation (24b), and let

$$Q_1 = ic\left(1 - \frac{A_1^2 k^2 B_0^2}{c^2}\right) \qquad (31)$$

Then

$$Q_1 v_r - 2v_\theta = -\frac{A_1^2 Q_1}{ic}\frac{dp}{dr} \qquad (32)$$

$$Q_1 v_\theta + 2v_r = -A_1^2 \frac{m}{rc} Q_1 p \qquad (33)$$

Solve equations (32) and (33) for v_r and v_θ in terms of p to obtain

$$v_\theta = \frac{A_1^2}{\delta_1^2 ic}\left(\frac{2}{Q_1}\frac{dp}{dr} - \frac{im}{r}p\right) \qquad (34)$$

$$v_r = \frac{-A_1^2}{Q_1^2 \delta_1^2 ic}\left(Q_1^2\frac{dp}{dr} + \frac{2im}{r}Q_1 p\right) \qquad (35)$$

where

$$\delta_1^2 = 1 + \frac{4}{Q_1^2} \qquad (36)$$

Substitute equations (25b), (34), and (35) into equation (29b) to obtain

$$\frac{d^2p}{dr^2} + \frac{1}{r}\frac{dp}{dr} - \left(\frac{m^2}{r^2} + k^2\delta_1^2\right)p = 0 \qquad (37)$$

The general solution of equation (37) is a linear combination of Bessel functions of the first and second kinds. The form used here is

$$p = \mathcal{A}_1 J_m(ik\delta_1 r) + \mathcal{A}_2 H_m(ik\delta_1 r) \qquad (38)$$

The second term blows up at the origin, so $\mathcal{A}_2$ is set equal to zero. The solution in the inner fluid is

$$p_1 = \mathcal{A}_1 J_m(ik\delta_1 r) \qquad (39)^*$$

(The equations with an asterisk following the equation number will be used in the interface boundary condition equations to obtain the dispersion relation.) We obtain v_{1r} by substituting p_1 for p into equation (35):

$$v_{1r} = \frac{-\mathcal{A}_1 A_1^2}{Q_1\delta_1^2 ic}\left\{Q_1\frac{d}{dr}[J_m(ik\delta_1 r)] + \frac{2im}{r}J_m(ik\delta_1 r)\right\} \qquad (40)^*$$

The magnetic field component b_{1r} is obtained by substituting equation (40) into equation (26b):

$$b_{1r} = -\mathcal{A}_1\frac{B_0 k A_1^2}{Q_1\delta_1^2 ic^2}\left\{Q_1\frac{d}{dr}[J_m(ik\delta_1 r)] + \frac{2im}{r}J_m(ik\delta_1 r)\right\} \qquad (41)^*$$

Finally, b_{1z} is obtained by combining equations (25b), (28b), and (39):

$$b_{1z} = -\mathcal{A}_1\frac{B_0 k^2}{c^2}A_1^2 J_m(ik\delta_1 r) \qquad (42)^*$$

Outer-Fluid Disturbance Equations

Linearization of equations (11) to (14) about the equilibrium flow yields the disturbance equations for the outer fluid:

Momentum (eq. (11)):

$$\frac{\partial v_r^*}{\partial t^*} + \Omega\frac{\partial v_r^*}{\partial\theta} - 2\Omega v_\theta^* = -\frac{1}{\rho}\frac{\partial p^*}{\partial r^*} \qquad (43)$$

$$\frac{\partial v_\theta^*}{\partial t^*} + \Omega\frac{\partial v_\theta^*}{\partial\theta} + 2\Omega v_r^* = -\frac{1}{\rho r^*}\frac{\partial p^*}{\partial\theta} \qquad (44)$$

$$\frac{\partial v_z^*}{\partial t^*} + \Omega\frac{\partial v_z^*}{\partial\theta} = -\frac{1}{\rho}\frac{\partial p^*}{\partial z^*} \qquad (45)$$

Continuity (eq. (12)):

$$\frac{\partial v_r^*}{\partial r^*} + \frac{v_r^*}{r^*} + \frac{1}{r^*}\frac{\partial v_\theta^*}{\partial\theta} + \frac{\partial v_z^*}{\partial z^*} = 0 \qquad (46)$$

Div $\mathbf{B} = 0$ (eq. (13)):

$$\frac{\partial b_r^*}{\partial r^*} + \frac{b_r^*}{r^*} + \frac{1}{r^*}\frac{\partial b_\theta^*}{\partial\theta} + \frac{\partial b_z^*}{\partial z^*} = 0 \qquad (47)$$

Curl $\mathbf{B}=0$ (eq. (14)):

$$\frac{1}{r^*}\frac{\partial b_z^*}{\partial \theta}-\frac{\partial b_\theta^*}{\partial z^*}=0 \tag{48}$$

$$\frac{\partial b_z^*}{\partial r^*}-\frac{\partial b_r^*}{\partial z^*}=0 \tag{49}$$

$$\frac{\partial b_\theta^*}{\partial r^*}+\frac{b_\theta^*}{r^*}-\frac{1}{r^*}\frac{\partial b_r^*}{\partial \theta}=0 \tag{50}$$

The nondimensional forms of equations (43) to (50) are

$$\frac{\partial v_r}{\partial t}+\frac{\partial v_r}{\partial \theta}-2v_\theta=-A_2{}^2\frac{\partial p}{\partial r} \tag{51a}$$

$$\frac{\partial v_\theta}{\partial t}+\frac{\partial v_\theta}{\partial \theta}+2v_r=-\frac{A_2{}^2}{r}\frac{\partial p}{\partial \theta} \tag{52a}$$

$$\frac{\partial v_z}{\partial t}+\frac{\partial v_z}{\partial \theta}=-A_2{}^2\frac{\partial p}{\partial z} \tag{53a}$$

$$\frac{\partial v_r}{\partial r}+\frac{v_r}{r}+\frac{1}{r}\frac{\partial v_\theta}{\partial \theta}+\frac{\partial v_z}{\partial z}=0 \tag{54a}$$

$$\frac{\partial b_r}{\partial r}+\frac{b_r}{r}+\frac{1}{r}\frac{\partial b_\theta}{\partial \theta}+\frac{\partial b_z}{\partial z}=0 \tag{55a}$$

$$\frac{1}{r}\frac{\partial b_z}{\partial \theta}-\frac{\partial b_\theta}{\partial z}=0 \tag{56a}$$

$$\frac{\partial b_z}{\partial r}-\frac{\partial b_r}{\partial z}=0 \tag{57a}$$

$$\frac{\partial b_\theta}{\partial r}+\frac{b_\theta}{r}-\frac{1}{r}\frac{\partial b_r}{\partial \theta}=0 \tag{58a}$$

As before, the equations allow solutions of the form $q(r)\exp[i(m\theta+kz+\omega t)]$. Equations (51a), (52a), and (53a) become, respectively,

$$Q_2v_r-2v_\theta=-A_2{}^2\frac{dp}{dr} \tag{51b}$$

$$Q_2v_\theta+2v_r=-A_2{}^2\frac{imp}{r} \tag{52b}$$

$$Q_2v_z=-A_2{}^2ikp \tag{53b}$$

where $Q_2=ic$. And equation (54a) becomes

$$\frac{dv_r}{dr}+\frac{v_r}{r}+\frac{im}{r}v_\theta+ikv_z=0 \tag{54b}$$

Solve equations (51b) and (52b) for v_r and v_θ in terms of p to obtain

$$v_\theta=\frac{A_2{}^2}{ic\delta_2{}^2Q_2}\left(2\frac{dp}{dr}-\frac{Q_2imp}{r}\right) \tag{59}$$

$$v_r=-\frac{A_2{}^2}{ic\delta_2{}^2Q_2}\left(Q_2\frac{dp}{dr}+\frac{2imp}{r}\right) \tag{60}$$

where $\delta_2{}^2=1+(4/Q_2{}^2)$.

Substitute v_θ from equation (59), v_r from equation (60), and v_z from equation (53b) into equation (54b) to obtain the differential equation for the perturbation pressure in the outer fluid

$$\frac{d^2p}{dr^2}+\frac{1}{r}\frac{dp}{dr}-\left(\frac{m^2}{r^2}+k^2\delta_2{}^2\right)p=0 \tag{62}$$

This differential equation is of the same form as equation (37). The solutions to equation (62) are therefore

$$p=\mathcal{A}_1J_m(ik\delta_2r)+\mathcal{A}_2H_m(ik\delta_2r) \tag{63}$$

where H_m is the Hankel function of the first kind. It is usually denoted by $H_m{}^{(1)}$, but the superscript was removed to simplify notation in this report. As $r\to\infty$, the first term in equation (63) blows up, so $\mathcal{A}_1$ is set equal to zero. The solution for the perturbation pressure term in the outer fluid is therefore

$$p_2=\mathcal{A}_2H_m(ik\delta_2r) \tag{64}*$$

The perturbation velocity term v_r is obtained by substituting p_2 for p in equation (60); then

$$v_{2r}=-\frac{\mathcal{A}_2A_2{}^2}{ic\delta_2{}^2Q_2}\left\{Q_2\frac{d}{dr}[H_m(ik\delta_2r)]+\frac{2im}{r}H_m(ik\delta_2r)\right\} \tag{65}*$$

We obtain b_r and b_z from equations (55a), (56a), and (57a) which become, respectively, after assuming that all first-order quantities vary as $q(r)\exp[i(m\theta+kz+\omega t)]$,

$$\frac{db_r}{dr}+\frac{b_r}{r}+\frac{im}{r}b_\theta+ikb_z=0 \tag{55b}$$

$$\frac{im}{r}b_z-ikb_\theta=0 \tag{56b}$$

$$\frac{db_z}{dr}-ikb_r=0 \tag{57b}$$

Substituting b_θ from equation (56b) and b_r from equation (57b) into equation (55b) yields the differential equation for b_z in the outer region

$$\frac{d^2b_z}{dr^2}+\frac{1}{r}\frac{db_z}{dr}-\left(\frac{m^2}{r^2}+k^2\right)b_z=0 \tag{66}$$

Again, the general solution is a linear combination of Bessel functions of the first and second kinds

$$b_z=\mathcal{B}_1J_m(ikr)+\mathcal{B}_2H_m(ikr) \tag{67}$$

As $r\to\infty$ the perturbation field must remain finite, so $\mathcal{B}_1$ is set equal to zero. Then

$$b_{2z}=\mathcal{B}_2H_m(ikr) \tag{68}*$$

Substituting b_z from equation (68) into equation (57b) yields

$$b_{2r}=\mathcal{B}_2\frac{1}{ik}\frac{d}{dr}[H_m(ikr)] \qquad (69)^*$$

Application of Boundary Conditions at Interface

The boundary conditions requiring all perturbation fields to be finite at $r=0$ and $r=\infty$ have already been applied. The remaining conditions, applicable at the interface, are given by equations (15) to (17). The surface normal can be written as

$$\hat{\mathbf{n}}=\hat{\mathbf{r}}+\boldsymbol{n}$$

The zero-order surface normal is the unit vector in the radial direction $\mathbf{r}$. The quantity $\boldsymbol{n}$ is a first-order perturbation of the unit vector. The first-order boundary conditions on the normal components of velocity and magnetic field at the interface are obtained from equations (16) and (17) as

$$\hat{\mathbf{r}}\cdot(\mathbf{v}_2-\mathbf{v}_1)=v_{2r}-v_{1r}=0 \qquad \text{at } r=1 \qquad (70)$$

$$\hat{\mathbf{r}}\cdot(\mathbf{b}_2-\mathbf{b}_1)=b_{2r}-b_{1r}=0 \qquad \text{at } r=1 \qquad (71)$$

Strictly speaking, these two boundary conditions should be evaluated at the displaced interface. But, to within first order, equations (16) and (17) may be evaluated at the equilibrium interface position $r^*=a$ or, equivalently, $r=1$.

Substituting equations (35), (39), and (65) into equation (70) gives the condition of continuity of radial velocity at $r=1$,

$$\frac{A_1^2}{Q_1^2\delta_1^2}[Q_1^2J'_m(ik\delta_1)+2imQ_1J_m(ik\delta_1)]\mathcal{A}_1 =\frac{A_2^2}{Q_2^2\delta_2^2}[Q_2^2H'_m(ik\delta_2)+2imQ_2H_m(ik\delta_2)]\mathcal{A}_2 \qquad (72)$$

where the prime denotes differentiation with respect to r.

When equations (26b), (35), (39), and (69) are substituted in equation (71), the condition for continuity of radial magnetic field at $r=1$ becomes

$$\frac{ikB_0}{c^2Q_1^2\delta_1^2}\mathcal{A}_1[Q_1^2J'_m(ik\delta_1)+2imQ_1J_m(ik\delta_1)] =\frac{\mathcal{B}_2}{ik}H'_m(ik) \qquad (73)$$

The boundary condition in equation (15) states that the normal force is continuous across the displaced interface. Writing out equation (15) to all orders, in physical variables, results in

$$(P_{0,2}^*+p_2^*)-(P_{0,1}^*+p_1^*)+\left(\frac{\mathbf{B}_2^*\cdot\mathbf{B}_2^*}{2\mu_o}\right)-\left(\frac{\mathbf{B}_1^*\cdot\mathbf{B}_1^*}{2\mu_o}\right)=0 \qquad (74)$$

where all quantities in equation (74) are evaluated at $r^*=a+\xi^*$. Now

$$\mathbf{B}_\alpha^*\cdot\mathbf{B}_\alpha^*=(\mathbf{B}_0^*+\mathbf{b}_{\alpha z}^*)\cdot(\mathbf{B}_0+\mathbf{b}_{\alpha z}^*) =B_0^{*2}+2B_0^*\,b_{\alpha z}^*+\mathrm{b}_{\alpha z}^{*2}$$

We may now write out all terms in equation (74), which yields

$$\left[P_0^*+\rho_1\frac{\Omega^2a^2}{2}+\rho_2\Omega^2\frac{(a+\xi^*)^2-a^2}{2}+p_2^*(\xi^*)\right] -\left[P_0^*+\rho_1\Omega^2\frac{(a+\xi^*)^2}{2}+p_1^*(\xi^*)\right] +\left[\frac{B_0^{*2}}{2\mu_o}+\frac{B_0^*}{\mu_o}b_{2z}^*(\xi^*)+\frac{b_{2z}^{*2}(\xi^*)}{2\mu_o}\right] -\left[\frac{B_0^{*2}}{2\mu_o}+\frac{B_0^*}{\mu_o}b_{1z}^*(\xi^*)+\frac{b_{1z}^{*2}(\xi^*)}{2\mu_o}\right]=0 \qquad (75)$$

The radial displacement ξ^* is obtained from equation (20) where

$$V_r^*=v_r^*$$

$$V_\theta^*=r^*\Omega+v_\theta^*$$

$$V_z^*=v_z^*$$

Substituting these into equation (20) and treating ξ^* as first order yields *to first order*

$$\left(-\frac{\partial\xi^*}{\partial t^*}+v_r^*-\Omega\frac{\partial\xi^*}{\partial\theta}\right)_{r^*=a}=0$$

Assuming that ξ^* goes as $\exp[i(m\theta+\omega^*t^*+k^*z^*)]$, we get from the last equation

$$-i\omega^*\xi^*(a)+v_r^*(a)-im\Omega\xi^*=0$$

And, after rearranging,

$$\xi^*(a)=\frac{v_r^*(a)}{i(\omega^*+m\Omega)}$$

or

$$\frac{\xi^*(a)}{a}=\frac{v_r^*(a)}{i\Omega a\left(\frac{\omega^*}{\Omega}+m\right)}=-i\frac{v_r(1)}{c}$$

Thus, in dimensionless form the displacement is

$$\xi(1)=-\frac{iv_r(1)}{c} \qquad (76)$$

Retaining only first-order terms in equation (75) leaves

$$\rho_2\Omega^2 a\xi^* + p_2^*(\xi^*) - \rho_1\Omega^2 a\xi^* - p_1^*(\xi^*) + \frac{B_0^*}{\mu_o} b_{2z}^*(\xi^*) - \frac{B_0^*}{\mu_o} b_{1z}^*(\xi^*) = 0 \quad (77)$$

Nondimensionalizing equation (77) gives

$$\xi(1) + A_1^2 p_1(1) + A_1^2 B_0 b_{1z}(1) = \frac{\rho_2}{\rho_1}\xi(1) + \frac{\rho_2}{\rho_1} A_2^2 p_2(1) + \frac{\rho_2}{\rho_1} A_2^2 B_0 b_{2z}(1) \quad (78)$$

It follows from the definition of A_α^2 that $A_1^2 = (\rho_2/\rho_1)\, A_2^2$. If we choose V_{ref} so that $A_1^2 = 1$, equation (78) becomes

$$\xi(1) + p_1(1) + B_0 b_{1z}(1) = \frac{\rho_2}{\rho_1}\xi(1) + p_2(1) + B_0 b_{2z}(1) \quad (79)$$

Substituting into equation (79) the quantities $\xi(1)$ from equation (76), $p_1(1)$ from equation (39), $b_{1z}(1)$ from equation (42), $p_2(1)$ from equation (64), and $b_{2z}(1)$ from equation (68) results in the continuity of normal force boundary condition

$$\frac{\mathcal{A}_1}{c^2 Q_1^2 \delta_1^2}[Q_1^2 J'_m(ik\delta_1) + 2imQ_1 J_m(ik\delta_1)] + \mathcal{A}_1 J_m(ik\delta_1) - \frac{k^2 B_0^2}{c^2}\mathcal{A}_1 J_m(ik\delta_1) = \mathcal{B}_2 B_0 H'_m(ik) + \mathcal{A}_2 H_m(ik\delta_2) + \frac{\mathcal{A}_2}{c^2 Q_2^2 \delta_2^2}[Q_2^2 H_m(ik\delta_2) + 2imQ_2 H_m(ik\delta_2)] \quad (80)$$

DISPERSION RELATION

From equation (72) for continuity of radial velocity,

$$\mathcal{A}_1 = \left(\frac{\dfrac{\rho_1}{\rho_2 Q_2^2 \delta_2^2}\mathcal{H}_m}{\dfrac{1}{Q_1^2\delta_1^2}\mathcal{J}_m}\right)\mathcal{A}_2 \quad (81)$$

where

$$\mathcal{H}_m = Q_2^2 H'_m(ik\delta_2) + 2imQ_2 H_m(ik\delta_2) \quad (82)$$

$$\mathcal{J}_m = Q_1^2 J'_m(ik\delta_1) + 2imQ_1 J_m(ik\delta_1) \quad (83)$$

From equation (73) for continuity of radial magnetic field,

$$\mathcal{B}_2 = -\frac{\mathcal{A}_1 k^2 B_0}{c^2 Q_1^2 \delta_1^2}\frac{\mathcal{J}_m}{H'_m(ik)} \quad (84)$$

Substitute equations (81) and (84) into equation (80) to obtain

$$\frac{\left(\dfrac{\rho_1}{\rho_2 Q_2^2 \delta_2^2}\right)\mathcal{H}_m}{\left(\dfrac{1}{Q_1^2\delta_1^2}\right)\mathcal{J}_m}\left[\frac{\mathcal{J}_m}{c^2 Q_1^2\delta_1^2} + J_m(ik\delta_1) - \frac{k^2 B_0^2}{c^2} J_m(ik\delta_1) + \frac{k^2 B_0^2 \mathcal{J}_m H_m(ik)}{c^2 Q_1^2 \delta_1^2 H'_m(ik)}\right] = H_m(ik\delta_2) + \frac{1}{c^2 Q_2^2 \delta_2^2}\mathcal{H}_m \quad (85)$$

Using the definitions of Q_α, $\mathcal{J}_m$, and $\mathcal{H}_m$ and rearranging terms give

$$\left[\frac{\delta_1^2}{D} - \frac{\left(\dfrac{\rho_2}{\rho_1}\right)\delta_2^2}{F}\right]c^2 = \frac{\rho_2}{\rho_1} - 1 + k^2 B_0^2\left(\frac{\delta_1^2}{D} - \frac{1}{G}\right) \quad (86)$$

where, after setting $A_1 = 1$,

$$D \equiv \frac{J'_m(ik\delta_1)}{J_m(ik\delta_1)} + \frac{2im}{Q_1} \quad (87)$$

$$G \equiv \frac{H'_m(ik)}{H_m(ik)} \quad (88)$$

$$Q_2 \equiv ic \quad (89)$$

$$\delta_2^2 \equiv 1 - \frac{4}{c^2} \quad (90)$$

$$F \equiv \frac{H'_m(ik\delta_2)}{H_m(ik\delta_2)} + \frac{2im}{Q_2} \quad (91)$$

$$Q_1 \equiv ic\left(1 - \frac{k^2 B_0^2}{c^2}\right) \quad (92)$$

$$\delta_1^2 \equiv 1 - \frac{4}{c^2\left(1 - \dfrac{k^2 B_0^2}{c^2}\right)^2} \quad (93)$$

$$c \equiv \omega + m \quad (94)$$

The prime denotes differentiation with respect to r. Thus,

$$J'_m(ik\delta_1) = \left[\frac{d}{dr} J_m(ik\delta_1 r)\right]_{r=1}$$

and

$$H'_m(ik) = \left[\frac{d}{dr} H_m(ikr)\right]_{r=1}$$

Equation (86), with the definitions following it, is the dispersion relation. It is a complex equation since ω, and therefore c, is complex. In fact, the Bessel functions have complex arguments because of the δ_α factors. The dispersion relation was solved numerically by using an iterative technique on an IBM 7094 computer.

The dispersion relation has multiple roots some of which are nongrowing Alfvén waves. A technique was incorporated into the program to eliminate these uninteresting solutions.

APPROXIMATE SOLUTIONS TO DISPERSION RELATION

Long-Wavelength Limit

The long-wavelength solutions $k \to 0$ to the dispersion relation have been determined in appendix C. The results are

$$Re(c) = \frac{1}{\mathcal{R}} \tag{95}$$

or

$$Re(\omega) = -m + \frac{1}{\mathcal{R}} \qquad m > 0 \tag{96}$$

and

$$Im(c) = -\sqrt{\mathcal{R}m - 1} \qquad m > 0 \tag{97}$$

where

$$\mathcal{R} = \frac{\frac{\rho_1}{\rho_2} + 1}{\frac{\rho_1}{\rho_2} - 1} \tag{98}$$

These solutions were used as initial points in the iterative computer solutions.

Solutions Where Wave Frequency $c=0$

The values of k and B_0 for which c goes to zero are determined in appendix D. After a value of B_0 or k has been selected, the following relation gives the value of k or B_0 for which $c=0$:

$$\frac{k^2 B_0^2}{1 - \frac{\rho_2}{\rho_1}} = k^2 I_{m-1}(k) K_{m-1}(k) + m[I_{m-1}(k) K_m(k) - I_m(k) K_{m-1}(k)] - m^2 I_m(k) K_m(k) \tag{99}$$

Equation (99) is further reduced to the limiting cases of $k \to 0$ and $k \to \infty$ in appendix D. Equation (99) was used as a check of the computer solutions.

DISCUSSION

Although many stable modes of oscillation were found for the dispersion relation, only those solutions which indicate disturbances that grow with time are discussed. After the discussion of solutions to the dispersion equation, we explore some of the limitations of the normal mode approach to the stability problem and suggest some ways to interpret the results. Next, some physical implications about the magnetically stabilized plasma are considered. Potential methods are suggested to avoid the instabilities predicted by the present analysis.

Presented in figures 2 and 3 are curves of the imaginary and real parts, respectively, of the relative wave frequency c as a function of the axial wave number k. In these plots, the azimuthal wave number is a parameter, and results are presented for four different values of the externally imposed magnetic field. These curves are solutions to equation (86), the dispersion relation.

Typical fluid properties for the wheel-flow reactor (ref. 10) were used to establish the range of dimensionless magnetic fields found in figures 2 and 3. An angular velocity of 200 rad/sec was selected to provide a plasma Mach number of less than 0.1 at the interface. A density ratio ρ_1/ρ_2 of about 100, the largest envisioned, was chosen for the calculations because it is the most unstable configuration. The temperature chosen was 40 000° K, and the pressure was of the order of 100 atm. The reactor radius was 1 m and the density ρ_1 was 10.3 kg/m^3.

As shown in figure 2, in all but the weakest magnetic field case the growth rate c_i decreases to zero at a finite value of the axial wave number for a given value of m. For a given value of m and a given magnetic field, both the real (fig. 3) and imaginary (fig. 2) parts of c must go to zero at the same value of k. Because of the scales used in the figures, it appears on some plots that c_i and c_{re} go to zero at different values of k, but the computer results verify that both the real and imaginary parts go to zero at the same value of k. The value of k at which c goes to zero is referred to as the critical wave number k_{critical}. Beyond k_{critical} there are no solutions that correspond to a continuation of the curves presented in figures 2 and 3.

In the hydrodynamic case (ref. 5), the flow was found to be always unstable. However, figure 2 reveals that the effect of the magnetic field is to make the system stable to short-wavelength disturbances, $\lambda < 2\pi/k_{\text{critical}}$. The short wavelengths are stabilized

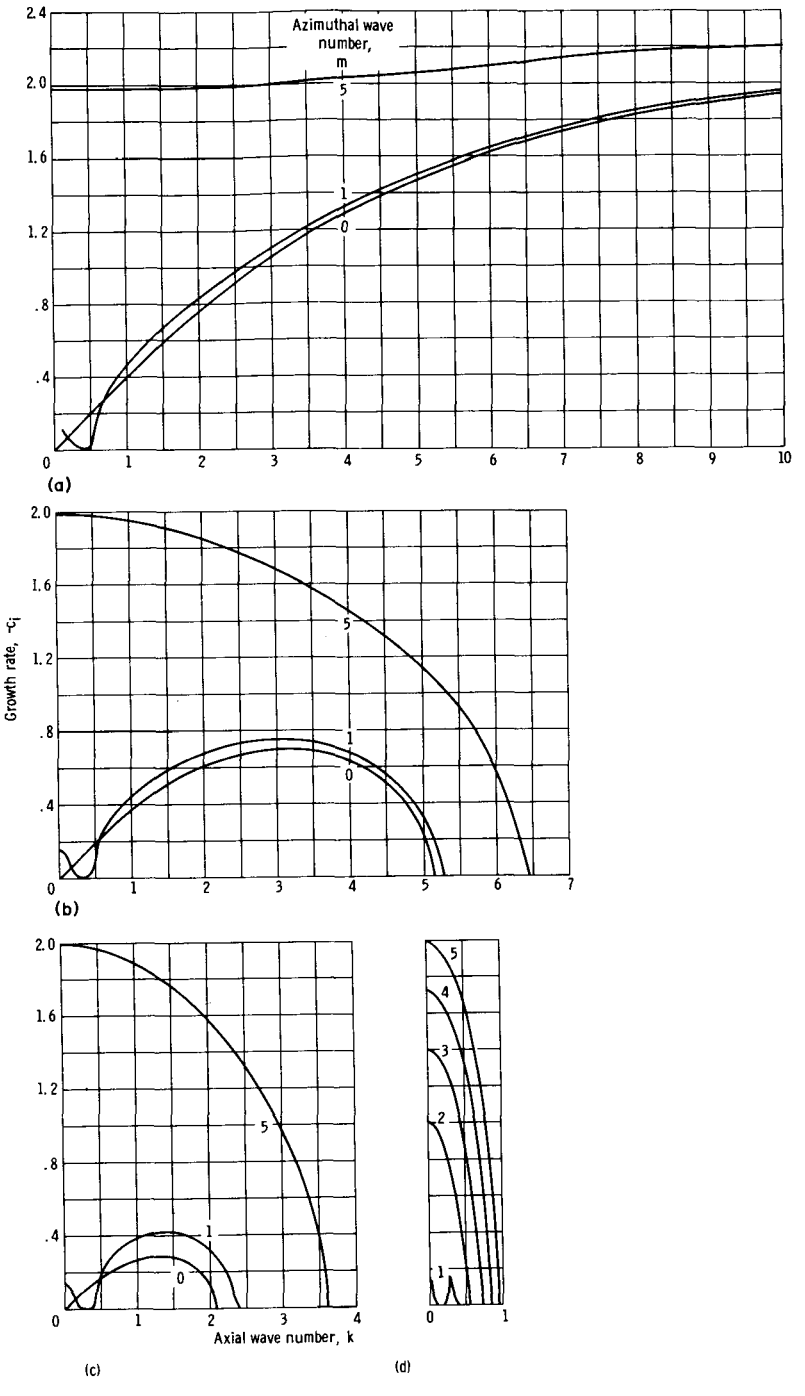

FIGURE 2.—*Disturbance growth rate as function of axial wave number with azimuthal wave number as parameter* (a) *Dimensionless magnetic field, 0.154.* (b) *Dimensionless magnetic field, 0.308.* (c) *Dimensionless magnetic field, 0.462.* (d) *Dimensionless magnetic field, 1.54.*

because the magnetic field lines, which are "frozen" into the fluid, undergo a distortion or "stretching" when the interface is perturbed. It requires energy to stretch the field lines. Thus, the energy that would normally be available to drive the instability is absorbed in the stretching process. In the hydro-

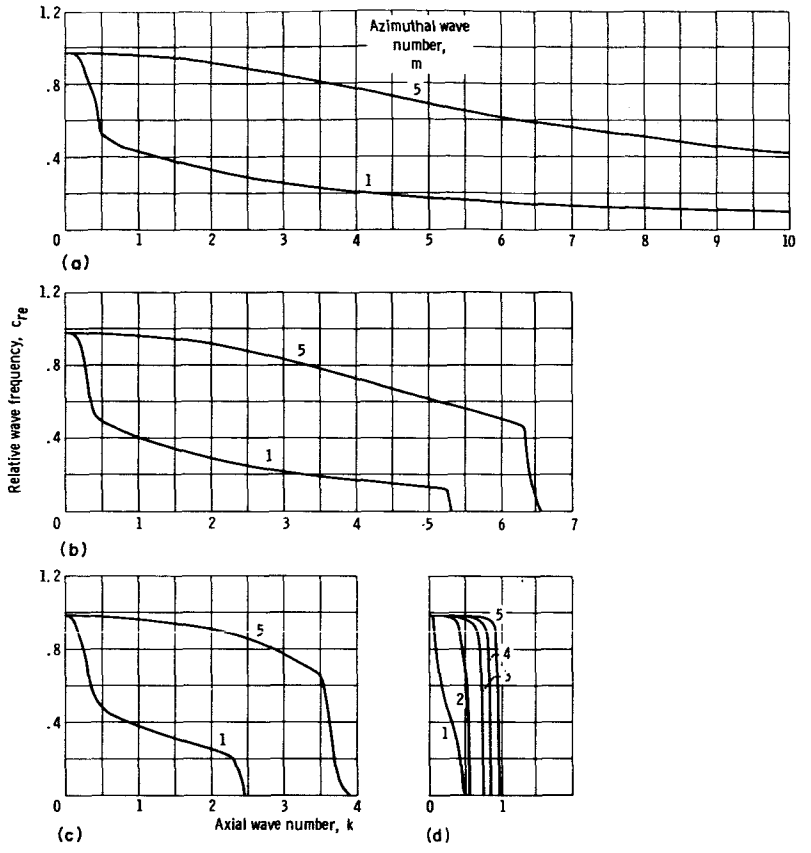

FIGURE 3.—*Disturbance relative wave frequency as function of axial wave number with azimuthal wave number as parameter.* (a) *Dimensionless magnetic field, 0.154.* (b) *Dimensionless magnetic field, 0.308.* (c) *Dimensionless magnetic field, 0.462.* (d) *Dimensionless magnetic field, 1.54.*

dynamic Rayleigh-Taylor problem, surface tension provides the "stretching" mechanism that stabilizes the short-wavelength disturbances.

Figure 2 reveals also that for a given value of k the growth rate increases as the azimuthal wave number increases. This suggests that smaller chunks of the heavy fluid have the most likelihood of tearing off at the interface. In figure 2, the $m=1$ curves have a dip in them near $k=0$. Although it is not obvious from the figure, the growth rate is finite at the minimum of the dip. This same peculiar dip occurred in reference 5, and we have no good physical explanation for its occurrence.

We note from figure 2 that the $k=0$ disturbances (infinitely long wavelength) are unstable for all azimuthal wave numbers except $m=0$. (When $m=0$ and $k=0$, there is no disturbance on the flow.) These unstable modes are the pure flute modes. They do not distort the magnetic field and, hence, are not stabilized by it. When $k=0$, the dispersion relation reduces to the simple form given in equations (95) to (98). From equation (95) and from figure 3, note that c_{re} reduces to $1/\mathcal{R}$ when $k=0$. Thus, to an observer moving with the rotating frame, all flute modes oscillate with the same frequency.

In figure 4, the value of magnetic field for which c goes to zero is presented as a function of k_{critical} with m as a parameter. These are plots of equation (99) in which the dispersion equation was solved subject to the requirement $c=0$. These curves have a simple interpretation: for those combinations of magnetic field and axial wave number that lie above the curve, the plasma is stable, whereas it is unstable if the combination falls below the curve. Information

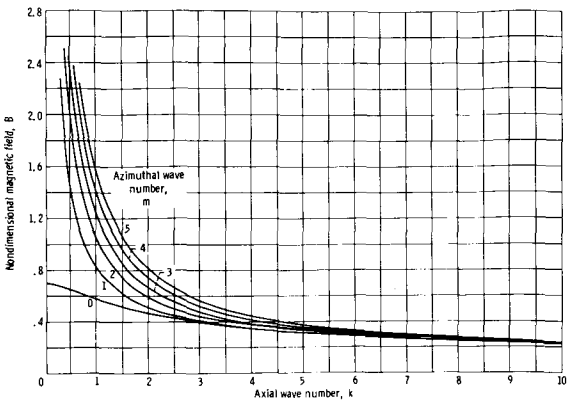

FIGURE 4.—*Neutral stability curve for various azimuthal wave numbers. (Flow is stable above curve and unstable below.)*

found from figures 2 to 4 and equation (C9) indicates that, no matter what value of magnetic field is chosen, a sufficiently high value of m will make the system unstable to long-wavelength disturbances. But when the value of m becomes so large that the azimuthal wavelength is comparable with the boundary-layer thickness, the analysis breaks down. The analysis implies that even the idealized concept of a two-fluid wheel-flow device is impractical unless some way is found to place restrictions on the axial wavelength and azimuthal wave numbers.

The dispersion relation was obtained from the linearized perturbation analysis about an assumed equilibrium flow. This suggests several interesting limitations to the analysis. We shall address ourselves to three of these problem areas.

First, it was assumed in the theoretical analysis that a particular equilibrium flow could be established. Experimentally this may not be possible. However, the stability analysis gives us some insight about the assumed equilibrium flow. If in establishing the equilibrium state the flow must pass through some of the perturbations that are predicted to be unstable, we can be certain of great difficulties in, if not the impossibility of, reaching the equilibrium situation. However, the analysis suggests that if the disturbances could be restricted to short axial wavelengths the equilibrium flow might be established. This might be accomplished by keeping the axial length of the machine short.

The second limitation is concerned with the assumption of small-amplitude disturbances and the attendant linearized analysis. Unstable solutions of the linearized problem represent only the first stage of growth, or of departure, of the system from the equilibrium state. As the disturbance amplitude becomes large, the flow should be described by nonlinear differential equations. It is possible for nonlinear effects to limit the disturbance amplitudes and produce nongrowing, finite-amplitude disturbances. We do not expect this in the present case. The state of minimum potential energy for the wheel-flow problem corresponds to the heavier fluid being at the outside with the lighter fluid at the center. The nonlinear effects may control the growth rate of the instabilities but should not terminate the growth. Even in the case of the short-wavelength disturbances, the predicted stability applies only to small amplitudes. For large-amplitude disturbances at these wavelengths the nonlinear effects could produce a positive growth rate.

The linearized perturbation analysis is useful in two respects. First, of course, it warns of regions where the system is unstable even to the infinitesimal perturbations. Second, it suggests which system parameters might be manipulated to maintain or improve the stability in regions where the infinitesimal perturbations do not grow. The linear analysis shows that improved stabilization is obtained by increasing the magnetic field and restricting the disturbances to short wavelengths. Stabilization against large-amplitude disturbances might be expected to improve with use of even larger magnetic fields and shorter wavelengths. The utility of this interpretation was demonstrated in reference 11, where the stability of a liquid-mercury–air interface was experimentally investigated. In these tests, mercury in glass tubes was subjected to vibrations of various frequencies and amplitudes, and the limits of interfacial stability were noted. As the amplitude and frequency of vibration were increased, a smaller tube diameter was needed to stabilize the interface. This was consistent with the Rayleigh-Taylor theory, with surface tension effects included, which predicts that the interface is stable against short-wavelength disturbances.

Finally, we want to know how the results of this report would be altered by the inclusion of finite electrical conductivity. Kruskal and Schwarzschild (ref. 8) obtained an approximate solution to a simple hydromagnetic problem with finite conduc-

tivity and small perturbations. They compared the results with those from the infinite conductivity case and concluded that the essential features of the large but finite conductivity problem were fairly represented if one assumed infinite conductivity while allowing for electric sheet currents and electric sheet charges at the plasma surface.

Intuitively, it seems that the result of finite, but large, conductivity would be somewhat larger growth rates and less stability at the shorter wavelengths than those predicted by the infinite conductivity case. The effect of finite conductivity is to allow the fluid to slip through the magnetic field without a proportional distortion of the field. The energy stored in the distorted field is less than it would be for infinite conductivity. Finite conductivity is accompanied by a dissipative effect because a fraction of the field energy created by the magnetic field distortions is converted into joule heat. By contrast, the energy-storage capacity of surface tension is independent of the growth rate because it is not accompanied by any dissipation of energy.

The importance of the finite conductivity can be deduced from dimensional analysis. When the fluid has finite conductivity, equation (10) is modified by the inclusion of another term, becoming

$$\frac{1}{\sigma\mu_o}\nabla^2\mathbf{B}^* + \nabla\times(\mathbf{V}^*\times\mathbf{B}^*) = \frac{\partial B^*}{\partial t^*} \quad (100)$$

When this equation is nondimensionalized, we get

$$\frac{1}{\Omega a^2\sigma\mu_o}\nabla^2\mathbf{B} + \nabla\times(\mathbf{V}\times\mathbf{B}) = \frac{\partial\mathbf{B}}{\partial t} \quad (101)$$

This equation can be reduced to equation (10) if $\Omega a^2\sigma\mu_o \gg 1$. The dimensionless quantity $\Omega a^2\sigma\mu_o$ is the magnetic Reynolds number. When the magnetic Reynolds number is large, the field restrains the fluid as it does in the infinite conductivity case, where fluid stays frozen to the field lines. The criterion of large magnetic Reynolds number can be rewritten as a requirement on the electrical conductivity, namely,

$$\sigma \gg \frac{1}{\Omega a^2\mu_o}$$

Choosing $\Omega = 200$ rad/sec, $a = 1$ m, and $\mu_o = 4\pi\times 10^{-7}$ H/m, we find that $\sigma \gg 4000$ mho/m is the requirement for the infinite conductivity assumption to apply.

For the proposed wheel-flow reactor, the plasma has a temperature of about 40 000° K and a pressure of a few hundred atmospheres. In order to estimate the electrical conductivity, we assume that the plasma is fully ionized and use the formula given by Spitzer (ref. 12, eqs. (5) to (37)) for electrical conductivity. In deriving the expression for conductivity, Spitzer neglected terms of the order $1/\ln\Lambda$, where $\ln\Lambda$ is the Coulomb logarithm. In the proposed wheel-flow reactor, $\ln\Lambda$ is of the order of 2.5 to 5. Thus, the conductivity can be estimated to an accuracy of 20 to 40 percent at best. The presence of multiply ionized ions would increase the calculated conductivity by slightly less than a factor of 2, whereas partial ionization would decrease the conductivity because of electron-neutral collisions and recombination. But the calculated conductivity should be valid to within an order of magnitude, which is sufficient for our purposes.

On the basis of Spitzer's formula, the conductivity is between 2500 and 5000 mho/m. Hence, finite conductivity effects will play an important role in the proposed wheel-flow reactor. The flow could, therefore, be substantially more unstable than that predicted by the infinite conductivity analysis.

In contrast to the wheel-flow reactor plasma, liquid metals have much higher conductivities. Typical conductivities for the liquid metals sodium, potassium, and mercury are, respectively, 10^7, 7×10^6, and 10^6 mho/m. These conductivities are well above 4000 mho/m, so the infinite conductivity approximation should apply to two-fluid wheel-flow configurations where the inner fluid is one of these liquid metals.

A second criterion for the infinite conductivity analysis to apply involves the characteristic time in which magnetic field perturbations are dissipated by joule heating. When the conductivity is so low that the diffusion term in equation (100) dominates over the flow term, we obtain the diffusion equation

$$\frac{1}{\sigma\mu_o}\nabla^2\mathbf{B}^* = \frac{\partial\mathbf{B}^*}{\partial t^*}$$

By dimensional arguments, the characteristic time for magnetic field inhomogeneities to decay or smooth out is shown to be

$$\tau^* = a^2\sigma\mu_o$$

For disturbances which occur in times short compared with τ^*, the fluid responds as though it had infinite conductivity. The growth times in this re-

port, and in reference 5, are proportional to $1/c_i\Omega$. For the infinite conductivity results of this report to apply, the growth times should be short compared with τ^*. Thus, the second criterion becomes

$$\tau^*\Omega c_i = \Omega a^2 \sigma \mu_o c_i \gg 1$$

Although the first criterion required only that the magnetic Reynolds number be large, the second criterion requires that the product of the magnetic Reynolds number and the growth rate must be large. From figure 2, the growth rates c_i are of the order of 3 or less for $m \leqq 5$. In applying the second criterion, the growth rate c_i will be given the value 3.0.

For the plasma and liquid-metal systems of interest, the following table gives typical values for magnetic Reynolds number, magnetic decay time, and the ratio of magnetic decay time to growth time.

System	Magnetic Reynolds number, $\Omega a^2 \sigma \mu_o$	Magnetic decay time, τ^*, sec	Ratio of magnetic decay time to growth time, $\tau^*\Omega c_i$
Plasma	0.6	3×10^{-3}	1.8
Sodium	2520	12.6	7560
Potassium	1680	8.4	5040
Mercury	260	1.3	780

For the wheel-flow reactor, both the magnetic Reynolds number and $\tau^*\Omega c_i$ are of order 1; this implies that the magnetic field will have very little influence and that the stability of such a system would be better represented by the hydrodynamic analysis of reference 5.

For the liquid metals, the opposite conclusion applies. The magnetic effects clearly dominate. Magnetic stabilization of a free surface may have application to those space power conversion systems that employ a liquid metal as the working fluid in a Rankine power cycle. A stable liquid-vapor interface must be maintained in the condenser to prevent vapor-locking of the condensate pump. Although there is a zero-gravity environment, there are local mechanical disturbances that tend to destabilize the interface. The results of this report, and those found in reference 13, indicate that strong magnetic fields and short wavelengths will provide a stabilizing influence. The disturbances can be restricted to short wavelengths by making the boundaries small. If the confining walls are made of metal, induced voltages in the fluid will be short circuited. And as in a short-circuited homopolar generator, the movement of the fluid would be severely restricted.

SUMMARY OF RESULTS

The stability of an incompressible two-fluid wheel flow to infinitesimal helical disturbances has been considered. The inner fluid is heavy and has infinite electrical conductivity, whereas the outer fluid is light and is nonconducting. Both fluids are inviscid. A constant and uniform axial magnetic field is impressed on both fluids. Important results are:

1. The growth rates of both propagating and nonpropagating waves are diminished by increasing the axial magnetic field.

2. For specific values of axial and azimuthal wave number, a value of magnetic field can be found which reduces the growth rates to zero.

3. Growth rates at a specific axial wave number increase for waves with increasing azimuthal wave number.

APPENDIX A

SYMBOLS

A	area
$\mathcal{A}$	constant in solution of differential equation
a	interface radius
B	magnetic field
$\mathcal{B}$	constant in solution of differential equation
b	disturbance magnetic field
C	contribution from cylindrical surface
c	wave frequency observed in rotating frame, $\omega + m$
c_i	growth rate
D	defined by eq. (87)
E	electric field
F	defined by eq. (91)
G	defined by eq. (88)
$H_m(x)$	Hankel function of first kind, argument x
$\mathcal{H}_m$	defined by eq. (82)
$I_m(x)$	modified Bessel function of first kind, argument x
Im	imaginary part of
J	current density
$J_m(x)$	Bessel function of first kind, argument x
$\mathcal{J}_m$	defined by eq. (83)
$K_m(x)$	modified Bessel function of second kind, argument x
k	axial wave number
L	length
m	azimuthal wave number
$\mathbf{n}$	vector normal to interface surface
$\boldsymbol{n}$	first-order perturbation of unit vector normal to surface
P	pressure
p	disturbance pressure
Q	defined by eq. (89) or (92) depending on subscript
$q(r)$	complex disturbance amplitude
$\hat{\mathbf{r}}$	unit vector in radial direction
R	outer radius
Re	real part of
$\mathcal{R}$	defined by eq. (98)
S	ratio of Alfvén speed to reference speed
s	surface variable
t	time
V	velocity
v	disturbance velocity
$W(a, b)$	Wronskian of a and b
r, θ, z	cylindrical coordinates
x, y, z	Cartesian coordinates
δ	defined by eq. (90) or (93) depending on subscript
ξ	radial displacement of interface from equilibrium
μ_o	permeability of free space
ρ	density
σ	electrical conductivity
Ω	angular wheel-flow velocity
ω	complex angular disturbance velocity

Subscripts:

c	equilibrium quantity at $r^* = 0$
critical	value of k for which c goes to zero
i	imaginary
m	order of the Bessel function or Hankel function
o	zero order, or equilibrium quantity
re	real
ref	reference quantity
a	dummy script
0	equilibrium quantity
1	inner fluid
2	outer fluid

Superscripts:

$( )'$	differentiation with respect to r
$( )^*$	dimensional quantity; following equation number indicates equation to be used in the interface boundary condition equations to obtain the dispersion relation
$\hat{( )}$	unit vector

APPENDIX B

DERIVATION OF BOUNDARY CONDITIONS

The boundary-condition equations (eqs. (15) to (17)) are found by integrating appropriate differential equations across the interface. In the real physical situation, there is a rapid but continuous transition of fluid properties across a thin layer separating the two fluids. Therefore, the differential equations that we use must be general enough to describe the flow on either side of, and through, the transition region. We therefore assume that both fluids satisfy the following conditions: The conductivity is finite; viscosity, space charge, and displacement current can be neglected; and the magnetic permeability is that of free space. Any idealized fluid properties that are different on opposite sides of the interface, such as finite conductivity on one side and zero conductivity on the other, must be introduced into the boundary conditions after the limits are taken.

Following the approach used in reference 14, we form a volume element fixed in space which instantaneously includes the interface (fig. 5). The volume will be a right cylinder such that at time t the lower face of the cylinder coincides with the interface. As time increases to $t+\delta t$, the interface moves up to the position shown in figure 5. The length of the cylinder Δ is considered to be very small. Thus, in the limit, the side walls make no contribution to those surface integrals with finite integrands. The surfaces at the top and bottom of the cylinder are small enough in area A to allow a surface integral to be approximated as the product of the integrand and the surface area.

The use of a fixed volume in space precludes the difficulties associated with moving reference frames. When one integrates across the interface while in a frame moving with the interface, the field quantities in the differential equations would have to be transformed into those fields that the moving observer would experience. The resulting boundary conditions for the moving frame then have to be rewritten in terms of the fields observed in the laboratory frame.

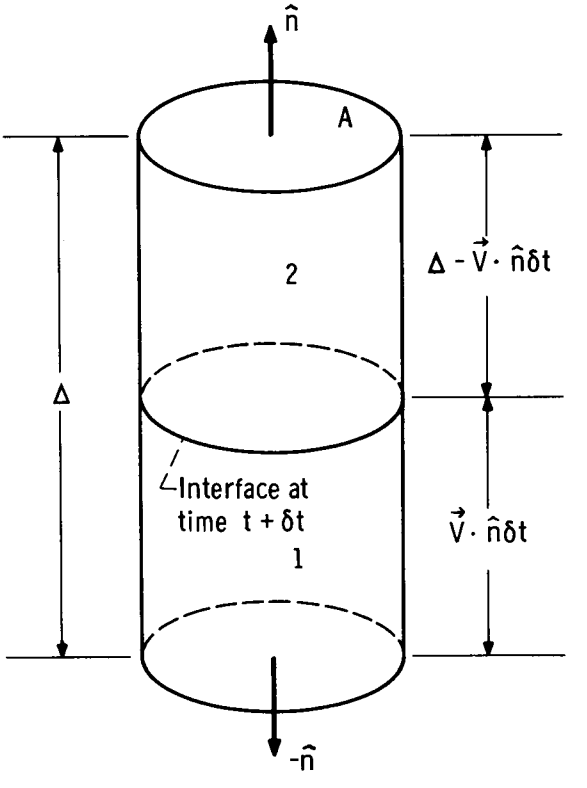

FIGURE 5.—*Volume element intersecting the interface between regions 1 and 2.*

Derivation of Equation (16)

Equation (16) is obtained by integrating the conservation-of-mass equation over the volume element of figure 5. The integral form of the conservation of mass over a fixed volume is

$$\frac{\partial}{\partial t}\int_v \rho\, dv+\int_v \nabla\cdot(\rho\mathbf{V})\,dv=0 \qquad \text{(B1)}$$

Using Gauss' theorem to transform the second integral of equation (B1) into a surface integral, we get

$$\frac{\partial}{\partial t}\int_v \rho\, dv+\int_s \rho \mathbf{V}\cdot\hat{\mathbf{n}}\, ds=0 \qquad \text{(B2)}$$

The first integral in equation (B2) is approximated as

$$\frac{\partial}{\partial t}\int_v \rho\, dv=\frac{1}{\delta t}\left[\int_v(\rho)_{t+\delta t}\, dv-\int_v(\rho)_t\, dv\right] \qquad \text{(B3)}$$

$$\frac{\partial}{\partial t}\int_v \rho\, dv=\frac{1}{\delta t}\left[(\rho_1)_{t+\delta t}\mathbf{V}\cdot\hat{\mathbf{n}}\delta t A + (\rho_2)_{t+\delta t}(\Delta-\mathbf{V}\cdot\hat{\mathbf{n}}\delta t)A-(\rho_2)_t\,\Delta A\right] \qquad \text{(B4)}$$

Using a Taylor expansion, we get

$$(\rho_1)_{t+\delta t}=(\rho_1)_t+\left(\frac{\partial\rho_1}{\partial t}\right)_t\delta t+\ldots \qquad \text{(B5)}$$

$$(\rho_2)_{t+\delta t}=(\rho_2)_t+\left(\frac{\partial\rho_2}{\partial t}\right)_t\delta t+\ldots \qquad \text{(B6)}$$

Substitute for $(\rho_1)_{t+\delta t}$ and $(\rho_2)_{t+\delta t}$ from equations (B5) and (B6), respectively, into equation (B4) to obtain

$$\frac{\partial}{\partial t}\int_v \rho\, dv=\frac{1}{\delta t}\left\{\left[(\rho_1)_t+\left(\frac{\partial\rho_1}{\partial t}\right)\delta t\right]\mathbf{V}\cdot\hat{\mathbf{n}}\delta t A+\left[(\rho_2)_t+\left(\frac{\partial\rho_2}{\partial t}\right)_t\delta t\right](\Delta-\mathbf{V}\cdot\hat{\mathbf{n}}\delta t)A-(\rho_2)_t\,\Delta A\right\} \qquad \text{(B7)}$$

$$\frac{\partial}{\partial t}\int_v \rho\, dv=\left\{\left[(\rho_1)_t+\left(\frac{\partial\rho_1}{\partial t}\right)_t\delta t\right]-\left[(\rho_2)_t+\left(\frac{\partial\rho_2}{\partial t}\right)_t\delta t\right]\right\}\mathbf{V}\cdot\hat{\mathbf{n}}A+\left(\frac{\partial\rho_2}{\partial t}\right)_t\Delta A \qquad \text{(B8)}$$

Now, passing to the limit, we obtain from equation (B8)

$$\lim_{\delta t,\,\Delta\to 0}\frac{\partial}{\partial t}\int_v \rho\, dv=(\rho_1-\rho_2)\mathbf{V}\cdot\hat{\mathbf{n}}A \qquad \text{(B9)}$$

The second integral in equation (B2) can be approximated as

$$\int_s \rho\mathbf{V}\cdot\hat{\mathbf{n}}\, ds=\rho_1\mathbf{V}_1\cdot(-\hat{\mathbf{n}})A+\rho_2\mathbf{V}_2\cdot\hat{\mathbf{n}}A+C(\Delta) \qquad \text{(B10)}$$

where $C(\Delta)$ is the contribution from the cylindrical surface. This term will vanish in the limit $\Delta\to 0$ because the integrand is finite over the cylindrical surface. Thus, the limit of equation (B10) becomes

$$\lim_{\Delta\to 0}\int_s \rho\mathbf{V}\cdot\hat{\mathbf{n}}\, ds=(\rho_2\mathbf{V}_2\cdot\hat{\mathbf{n}}-\rho_1\mathbf{V}_1\cdot\hat{\mathbf{n}})A \qquad \text{(B11)}$$

Substituting equations (B9) and (B11) into equation (B2) gives

$$(\rho_1-\rho_2)\mathbf{V}\cdot\hat{\mathbf{n}}+\rho_2\mathbf{V}_2\cdot\hat{\mathbf{n}}-\rho_1\mathbf{V}_1\cdot\hat{\mathbf{n}}=0$$

And, on rearrangement, we have

$$\rho_1(\mathbf{V}\cdot\hat{\mathbf{n}}-\mathbf{V}_1\cdot\hat{\mathbf{n}})-\rho_2(\mathbf{V}\cdot\hat{\mathbf{n}}-\mathbf{V}_2\cdot\hat{\mathbf{n}})=0 \qquad \text{(B12)}$$

Equation (B12) is satisfied if

$$\mathbf{V}\cdot\hat{\mathbf{n}}=\mathbf{V}_1\cdot\hat{\mathbf{n}}=\mathbf{V}_2\cdot\hat{\mathbf{n}} \qquad (16)^*$$

Equation (16) is the kinematic condition that the fluid velocity component normal to the boundary must equal the velocity of the boundary normal to itself. This applies to our situation, where the two fluids are immiscible. In this case no mass flows across the surface, and the fluids on opposite sides of the surface remain in contact with the surface.

When equation (B12) is satisfied but equation (16) is not, we have the boundary condition for a shock or detonation front where fluid can cross the interface.

Derivation of Equation (17)

Equation (17) is obtained by integrating the $\nabla\cdot\mathbf{B}=0$ equation (eqs. (9) and (14)) over the volume element of figure 5:

$$\int_v \nabla\cdot\mathbf{B}\, dv=0 \qquad \text{(B13)}$$

Using Gauss' theorem to convert to a surface integral, equation (B13) becomes

$$\int_s \mathbf{B}\cdot\hat{\mathbf{n}}\, ds=0 \qquad \text{(B14)}$$

The surface integral can be approximated by

$$\int_s \mathbf{B}\cdot\hat{\mathbf{n}}\, ds=\mathbf{B}_1\cdot(-\hat{\mathbf{n}})A+\mathbf{B}_2\cdot\hat{\mathbf{n}}A+C(\Delta)=0 \qquad \text{(B15)}$$

and passing to the limit gives

$$\lim_{\Delta\to 0}\int_s \mathbf{B}\cdot\hat{\mathbf{n}}\, ds=\hat{\mathbf{n}}\cdot(\mathbf{B}_2-\mathbf{B}_1)A=0 \qquad \text{(B16)}$$

or

$$\hat{\mathbf{n}}\cdot(\mathbf{B}_2-\mathbf{B}_1)=0 \qquad (17)^*$$

Derivation of Equation (15)

Equation (7) is applicable to both sides of the interface, subject to the conditions noted at the beginning of this appendix. Hence, we integrate

equation (7) over the volume element of figure 5:

$$\int_v \rho\left[\frac{\partial \mathbf{V}}{\partial t}+(\mathbf{V}\cdot\nabla)\mathbf{V}\right]dv=\frac{1}{\mu_o}\int_v(\mathbf{B}\cdot\nabla)\mathbf{V}\,dv-\int_v\nabla\left(P+\frac{B^2}{2\mu_o}\right)dv \tag{B17}$$

By making use of the continuity equation and the identities given below, we can replace the volume integral on the left side of equation (B17) with one that is more convenient to evaluate. Accordingly, we write the differential form of the continuity equation as

$$\frac{\partial \rho}{\partial t}=-\nabla\cdot(\rho\mathbf{V}) \tag{B18}$$

We also have the identity

$$\rho\frac{\partial \mathbf{V}}{\partial t}=\frac{\partial(\rho\mathbf{V})}{\partial t}-\mathbf{V}\frac{\partial \rho}{\partial t} \tag{B19}$$

If we substitute $\partial\rho/\partial t$ from equation (B18) into equation (B19), we get

$$\rho\frac{\partial \mathbf{V}}{\partial t}=\frac{\partial(\rho\mathbf{V})}{\partial t}+\mathbf{V}\cdot\nabla(\rho\mathbf{V}) \tag{B20}$$

By using equation (B20), the integrand of the volume integral on the left side of equation (B17) becomes

$$\rho\frac{\partial \mathbf{V}}{\partial t}+\rho(\mathbf{V}\cdot\nabla)\mathbf{V}=\frac{\partial}{\partial t}(\rho\mathbf{V})+\rho(\mathbf{V}\cdot\nabla)\mathbf{V}+\mathbf{V}\nabla\cdot(\rho\mathbf{V}) \tag{B21}$$

or

$$\rho\frac{\partial \mathbf{V}}{\partial t}+\rho(\mathbf{V}\cdot\nabla)\mathbf{V}=\frac{\partial}{\partial t}(\rho\mathbf{V})+\nabla\cdot(\rho\mathbf{V}\mathbf{V}) \tag{B22}$$

Substituting equation (B22) into equation (B17) gives

$$\int_v\frac{\partial}{\partial t}(\rho\mathbf{V})\,dv+\int_v\nabla\cdot(\rho\mathbf{V}\mathbf{V})\,dv=\frac{1}{\mu_o}\int_v(\mathbf{B}\cdot\nabla)\mathbf{B}\,dv-\int_v\nabla\left(P+\frac{B^2}{2\mu_o}\right)dv \tag{B23}$$

By application of the various forms of Gauss' theorem, the last three integrals in equation (B23) can be converted into surface integrals. Thus,

$$\int_v\nabla\cdot(\rho\mathbf{V}\mathbf{V})\,dv=\int_s\rho\mathbf{V}\mathbf{V}\cdot\hat{\mathbf{n}}\,ds \tag{B24}$$

$$\int_v(\mathbf{B}\cdot\nabla)\mathbf{B}\,dv=\int_s\mathbf{B}\mathbf{B}\cdot\hat{\mathbf{n}}\,ds \tag{B25}$$

$$\int_v\nabla\left(P+\frac{B^2}{2\mu_o}\right)dv=\int_s\left(P+\frac{B^2}{2\mu_o}\right)\hat{\mathbf{n}}\,ds \tag{B26}$$

Substituting equations (B24) to (B26) into equation (B23) gives

$$\frac{\partial}{\partial t}\int_v(\rho\mathbf{V})\,dv+\int_s\rho\mathbf{V}\mathbf{V}\cdot\hat{\mathbf{n}}\,ds=\frac{1}{\mu_o}\int_s\mathbf{B}\mathbf{B}\cdot\hat{\mathbf{n}}\,ds-\int_s\left(P+\frac{B^2}{2\mu_o}\right)\hat{\mathbf{n}}\,ds \tag{B27}$$

Each integral in equation (B27) will be separately evaluated for the volume element of figure 5.

The first integral in equation (B27) is evaluated in the same manner as was the first integral in equation (B2). Thus, we can write the result by replacing ρ in equation (B9) with $\rho\mathbf{V}$, and we get

$$\lim_{\delta t,\,\Delta\to 0}\frac{\partial}{\partial t}\int_v\rho\mathbf{V}\,dv=(\rho_1\mathbf{V}_1-\rho_2\mathbf{V}_2)\mathbf{V}\cdot\hat{\mathbf{n}}A \tag{B28}$$

The second integral in equation (B27) is approximated as

$$\int_s\rho\mathbf{V}\mathbf{V}\cdot\hat{\mathbf{n}}\,ds=\rho_2\mathbf{V}_1\mathbf{V}_1\cdot(-\hat{\mathbf{n}})A+\rho_2\mathbf{V}_2\mathbf{V}_2\cdot\hat{\mathbf{n}}A+C(\Delta) \tag{B29}$$

Passing to the limit gives

$$\lim_{\Delta\to 0}\int_s\rho\mathbf{V}\mathbf{V}\cdot\hat{\mathbf{n}}\,ds=(\rho_2\mathbf{V}_2\mathbf{V}_2\cdot\hat{\mathbf{n}}-\rho_1\mathbf{V}_1\mathbf{V}_1\cdot\hat{\mathbf{n}})A \tag{B30}$$

We may use equation (16) to reduce equation (B30) to

$$\lim_{\Delta\to 0}\int_s\rho\mathbf{V}\mathbf{V}\cdot\hat{\mathbf{n}}\,ds=(\rho_2\mathbf{V}_2-\rho_1\mathbf{V}_1)\mathbf{V}\cdot\hat{\mathbf{n}}A \tag{B31}$$

The third integral in equation (B27) is approximated as

$$\int_s\mathbf{B}\mathbf{B}\cdot\hat{\mathbf{n}}\,ds=\mathbf{B}_1\mathbf{B}_1\cdot(-\hat{\mathbf{n}})A+\mathbf{B}_2\mathbf{B}_2\cdot\hat{\mathbf{n}}A+C(\Delta) \tag{B32}$$

Passing to the limit gives

$$\lim_{\Delta\to 0}\int_s\mathbf{B}\mathbf{B}\cdot\hat{\mathbf{n}}\,ds=(\mathbf{B}_2\mathbf{B}_2\cdot\hat{\mathbf{n}}-\mathbf{B}_1\mathbf{B}_1\cdot\hat{\mathbf{n}})A \tag{B33}$$

By using equation (17), we can simplify equation (B33) to

$$\lim_{\Delta\to 0}\int_s\mathbf{B}\mathbf{B}\cdot\hat{\mathbf{n}}\,ds=(\mathbf{B}_2-\mathbf{B}_1)\mathbf{B}\cdot\hat{\mathbf{n}}A \tag{B34}$$

where

$$\mathbf{B}\cdot\hat{\mathbf{n}}=\mathbf{B}_1\cdot\hat{\mathbf{n}}=\mathbf{B}_2\cdot\hat{\mathbf{n}} \tag{B35}$$

Finally, the fourth integral in equation (B27) is approximated as

$$\int_s\left(P+\frac{B^2}{2\mu_o}\right)\hat{\mathbf{n}}\,ds=\left[\left(P_1+\frac{B_1^2}{2\mu_o}\right)(-\hat{\mathbf{n}})+\left(P_2+\frac{B_2^2}{2\mu_o}\right)\hat{\mathbf{n}}\right]A+C(\Delta) \tag{B36}$$

Passing to the limit gives

$$\lim_{\Delta\to 0}\int_s \left(P+\frac{B^2}{2\mu_o}\right)\hat{\mathbf{n}}\,ds=\hat{\mathbf{n}}\left[\left(P_2+\frac{B_2^2}{2\mu_o}\right)-\left(P_1+\frac{B_1^2}{2\mu_o}\right)\right]A \qquad \text{(B37)}$$

Now substitute equations (B28), B31), (B34), and (B37) into equation (B27) to obtain

$$(\rho_1\mathbf{V}_1-\rho_2\mathbf{V}_2)\,\mathbf{V}\cdot\hat{\mathbf{n}}+(\rho_2\mathbf{V}_2-\rho_1\mathbf{V}_1)\,\mathbf{V}\cdot\hat{\mathbf{n}}=(\mathbf{B}_2-\mathbf{B}_1)\,\mathbf{B}\cdot\hat{\mathbf{n}}-\hat{\mathbf{n}}\left[\left(P_2+\frac{B_2^2}{2\mu_o}\right)-\left(P_1+\frac{B_1^2}{2\mu_o}\right)\right] \qquad \text{(B38)}$$

The two terms on the left side of equation (B38) cancel each other, whereas the two terms on the right side are orthogonal to each other. The orthogonality condition follows from the fact that the vector $\mathbf{B}_2-\mathbf{B}_1$ lies in the surface of the interface. This is easily seen by noting that the magnetic field vectors $\mathbf{B}_1$ and $\mathbf{B}_2$ may be resolved into components normal and tangential to the interface, $\mathbf{B}_n$ and $\mathbf{B}_t$, respectively. Thus,

$$\mathbf{B}_2-\mathbf{B}_1=\mathbf{B}_{n2}+\mathbf{B}_{t2}-\mathbf{B}_{n1}-\mathbf{B}_{t1} \qquad \text{(B39)}$$

But from equation (17), the equation of continuity of the normal component of magnetic field at the interface, we have that

$$\mathbf{B}_{n2}=\mathbf{B}_{n1} \qquad \text{(B40)}$$

Thus,

$$\mathbf{B}_2-\mathbf{B}_1=\mathbf{B}_{t2}-\mathbf{B}_{t1} \qquad \text{(B41)}$$

Therefore each of the two terms on the right side of equation (B38) must independently be zero. This results in the following two boundary conditions:

$$\hat{\mathbf{n}}\left[\left(P_2+\frac{B_2^2}{2\mu_o}\right)-\left(P_1+\frac{B_1^2}{2\mu_o}\right)\right]=0 \qquad (15)^*$$

$$(\mathbf{B}_2-\mathbf{B}_1)\,(\mathbf{B}\cdot\hat{\mathbf{n}})=0 \qquad \text{(B42)}^*$$

Equation (B42) is not used in the text because it does not yield any zero-order or first-order information for the problem treated in this report. However, equation (B42) can be interpreted in general. It is interesting to note that if $\mathbf{B}_2-\mathbf{B}_1\neq 0$ (i.e., when there are surface currents, which in turn means that one of the fluids is a perfect conductor) equation (B42) requires that

$$\mathbf{B}\cdot\hat{\mathbf{n}}=\mathbf{B}_1\cdot\hat{\mathbf{n}}=\mathbf{B}_2\cdot\hat{\mathbf{n}}=0 \qquad \text{(B43)}$$

We infer from equation (B43) that the field on both sides of the interface is wholly tangential to the interface. This follows physically from the infinite conductivity assumption which causes the field lines and the fluid to be frozen together. We know from equation (18) that a particle once on the surface always remains on the surface. Since the magnetic field lines and particles are always frozen together, we should expect that the magnetic field lines once on the surface will remain always on the surface.

If $\mathbf{B}_{02}\neq\mathbf{B}_{01}$, equation (B42) yields first-order information about the boundary conditions. To demonstrate this we write out the zero- and first-order terms in equation (B42)

$$(\mathbf{B}_2-\mathbf{B}_1)\,(\mathbf{B}\cdot\hat{\mathbf{n}})=0 \qquad \text{(B44)}$$

$$(\mathbf{B}_{02}+\mathbf{b}_2-\mathbf{B}_{01}-\mathbf{b}_1)\,[(\mathbf{B}_{0a}+\mathbf{b}_a)\cdot(\hat{\mathbf{r}}+\boldsymbol{n})]=0 \qquad \text{(B45)}$$

where $a=1, 2$, or

$$(\mathbf{B}_{02}+\mathbf{b}_2-\mathbf{B}_{01}-\mathbf{b}_1)\,(\mathbf{B}_{0a}\cdot\hat{\mathbf{r}}+\mathbf{B}_{0a}\cdot\boldsymbol{n}+\mathbf{b}_a\cdot\hat{\mathbf{r}}+\mathbf{b}_a\cdot\boldsymbol{n})=0 \qquad \text{(B46)}$$

The zero-order terms of this equation are

$$(\mathbf{B}_{02}-\mathbf{B}_{01})\,(\mathbf{B}_{0a}\cdot\hat{\mathbf{r}})=0 \qquad \text{(B47)}$$

The first-order terms are

$$(\mathbf{B}_{02}-\mathbf{B}_{01})\,(\mathbf{B}_{0a}\cdot\boldsymbol{n}+\mathbf{b}_a\cdot\hat{\mathbf{r}})+(\mathbf{b}_2-\mathbf{b}_1)\,(\mathbf{B}_{0a}\cdot\hat{\mathbf{r}})=0 \qquad \text{(B48)}$$

If $\mathbf{B}_{02}\neq\mathbf{B}_{01}$, $\mathbf{B}_{0a}\cdot\hat{\mathbf{r}}=0$ from equation (B47) and equation (B48) reduces to

$$(\mathbf{B}_{02}-\mathbf{B}_{01})\,(\mathbf{B}_{0a}\cdot\boldsymbol{n}+\mathbf{b}_a\cdot\hat{\mathbf{r}})=0 \qquad \text{(B49)}$$

and, since $\mathbf{B}_{02}\neq\mathbf{B}_{01}$, equation (B49) requires that

$$\mathbf{B}_{0a}\cdot\boldsymbol{n}+\mathbf{b}_a\cdot\hat{\mathbf{r}}=0 \qquad a=1,2 \qquad \text{(B50)}$$

Equation (B50) is the first-order boundary condition that results when $\mathbf{B}_{02}\neq\mathbf{B}_{01}$. In the problem considered in this report $\mathbf{B}_{02}=\mathbf{B}_{01}$, and thus equation (B50) does not apply. Furthermore, in this report $\mathbf{B}_{0a}\cdot\hat{\mathbf{r}}=0$; hence, equation (B48) yields no first-order information.

Other Boundary Conditions

In reference 6, Wilhelm presents a boundary condition (eq. (1.7) of ref. 6) that was derived by integrating equation (10) of this report across the interface. Now equation (10) was obtained by substituting equation (3), which holds only for infinite conductivity, into equation (6). Since equation (10) does not hold on both sides of the interface, it can-

not be used to obtain boundary conditions. Fortunately, equation (4.6) of reference 6 can be obtained from equation (B38), so Wilhelm's results are valid.

In summary, the following table shows the differential equations and the corresponding boundary conditions obtained by integrating the equations across the interface.

Differential equation	Boundary condition
$\frac{\partial \rho}{\partial t} + \nabla \cdot (\rho \mathbf{V}) = 0$	$\hat{\mathbf{n}} \cdot (\mathbf{V}_2 - \mathbf{V}_1) = 0$
	$\hat{\mathbf{n}} \cdot (\mathbf{B}_2 - \mathbf{B}_1) = 0$
$\nabla \cdot \mathbf{B} = 0$	$\hat{\mathbf{n}} \left[\left(P_2 + \frac{B_2^2}{2\mu_o} \right) - \left(P_1 + \frac{B_1^2}{2\mu_o} \right) \right] = 0$
$\rho \left[\frac{\partial \mathbf{V}}{\partial t} + (\mathbf{V} \cdot \nabla) \mathbf{V} \right] = \frac{1}{\mu_o} (\mathbf{B} \cdot \nabla) \mathbf{B} - \nabla \left(P + \frac{B^2}{2\mu_o} \right)$	$(\mathbf{B}_2 - \mathbf{B}_1)(\mathbf{B} \cdot \hat{\mathbf{n}}) = 0$

APPENDIX C

LIMITING SOLUTION OF DISPERSION RELATION FOR SMALL AXIAL WAVE NUMBER

The dispersion relation equation (42) is to be solved in the limit of small axial wave number k. The Bessel functions become

$$\frac{\left[\frac{d}{dr}J_m(ik\delta_1 r)\right]_{r=1}}{J_m(ik\delta_1)} = m + \cdots \quad \text{(C1)}$$

$$\frac{\left[\frac{d}{dr}H_m(ik\delta_2 r)\right]_{r=1}}{H_m(ik\delta_2 r)} = -m + \cdots \quad \text{(C2)}$$

$$\frac{\left[\frac{d}{dr}H_m(ikr)\right]_{r=1}}{H_m(ik)} = -m + \cdots \quad \text{(C3)}$$

For $k \to 0$

$$\delta_1^2 \to \delta_2^2 = 1 - \frac{4}{c^2} \quad \text{(C4)}$$

$$Q_1 \to Q_2 = ic \quad \text{(C5)}$$

The dispersion relation can be rewritten

$$(c^2-4)(\mathcal{R}c^2 - 2c + m) = 0 \quad \text{(C6)}$$

where

$$\mathcal{R} = \frac{\frac{\rho_1}{\rho_2}+1}{\frac{\rho_1}{\rho_2}-1} \quad \text{(C7)}$$

The solutions to the dispersion relation are

$$c = \pm 2 \quad \text{(C8)}$$

$$c = \frac{1}{\mathcal{R}}(1 \pm i\sqrt{\mathcal{R}m-1}) \quad \text{(C9)}$$

For the solution given in equation (C8), $\delta_1^2 = \delta_2^2 \cong 0$. These solutions are rejected because the condition that the real part of $k\delta_2$ is greater than zero does not hold.

The solutions in equation (C9) are both valid solutions. The solution with the negative imaginary root grows while the solution with the positive imaginary root decays. Although both are possible, the growth solution is of more interest here since it persists.

APPENDIX D

DETERMINATION OF THE POINT WHERE WAVE FREQUENCY $c=0$

Let $c=0$. The dispersion relation (eq. (86)) becomes

$$0=\frac{\rho_2}{\rho_1}-1+k^2B_0^2\left[\frac{J_m(ik)}{J_m'(ik)}-\frac{H_m(ik)}{H_m'(ik)}\right] \quad \text{(D1)}$$

Differentiating the Bessel functions and rewriting them as modified Bessel functions gives

$$1-\frac{\rho_2}{\rho_1}=k^2B_0^2\left[\frac{I_m(k)}{kI_{m-1}(k)-mI_m(k)}+\frac{K_m(k)}{mK_m(k)-kK_{m-1}(k)}\right] \quad \text{(D2)}$$

$$1-\frac{\rho_2}{\rho_1}=k^2B_0^2\left\{\frac{kI_m(k)K_{m-1}(k)+kI_{m-1}(k)K_m(k)}{k^2I_{m-1}(k)K_{m-1}(k)+mk[I_{m-1}(k)K_m(k)-I_m(k)K_{m-1}(k)]-m^2I_m(k)K_m(k)}\right\} \quad \text{(D3)}$$

From the Wronskian of the modified Bessel functions

$$W[K_{m-1}(k), I_{m-1}(k)] = I_{m-1}(k)K_m(k)+I_m(k)K_{m-1}(k)=\frac{1}{k} \quad \text{(D4)}$$

Thus, the numerator of the factor containing the Bessel functions equals 1. Rearranging terms gives

$$\frac{k^2B_0^2}{1-\frac{\rho_2}{\rho_1}}=k^2I_{m-1}(k)K_{m-1}(k)+mk[I_{m-1}(k)K_m(k)-I_m(k)K_{m-1}(k)]-m^2I_m(k)K_m(k) \quad \text{(D5)}$$

Solving equation (D5) for B_z yields the value of k at which $c=0$. For several limiting cases, the equation can be further simplified. For all values of m as $k\to\infty$, equation (D5) reduces to

$$\frac{B_0^2}{1-\frac{\rho_2}{\rho_1}}=\frac{1}{2k} \quad \text{(D6)}$$

For $m=0$, $k\to 0$, equation (D5) becomes

$$\frac{B_0^2}{1-\frac{\rho_2}{\rho_1}}=\frac{1}{2} \quad \text{(D7)}$$

For $m=1$, $k\to 0$, equation (D5) becomes

$$\frac{B_0^2}{1-\frac{\rho_2}{\rho_1}}=\frac{1}{2k^2}-\frac{1}{2}\ln k \quad \text{(D8)}$$

For $m>1$, $k\to 0$, equation (D5) becomes

$$\frac{B_0^2}{1-\frac{\rho_2}{\rho_1}}=\frac{1}{4(m-1)}+\frac{m}{2k^2} \quad \text{(D9)}$$

REFERENCES

1. Kerrebrock, Jack L.; and Meghreblian, Robert V.: Vortex Containment for the Gaseous-Fission Rocket. J. Aerospace Sci., vol. 28, no. 9, Sept. 1961, pp. 710–724.
2. Rosenzweig, M. L.; Lewellen, W. S.; and Kerrebrock, J. L.: The Feasibility of Turbulent Vortex Containment in Gaseous Fission Rocket. ARS J., vol. 31, no. 7, July 1961, pp. 1873–1883.
3. Evvard, John C.: Wheel-Flow Gaseous-Core Reactor Concept. NASA TN D-2951, 1965.
4. Lewellen, W. S.; and Grabowsky, W. R.: Nuclear Space Power Systems Using Magnetohydrodynamic Vortices. ARS J., vol. 32, no. 5, May 1962, pp. 693–700.
5. Reshotko, Eli; and Monnin, Carl F.: Stability of Two-Fluid Wheel Flows. NASA TN D-2696, 1965.
6. Wilhelm, H. E.: Stability of a Rotating Plasma. Nucl. Fusion, vol. 2, Sept. 1962, pp. 6–11.
7. Chandrasekhar, S.: Hydrodynamic and Hydromagnetic Stability. Oxford Univ. Press, 1961.
8. Kruskal, M.; and Schwarzschild, M.: Some Instabilities of a Completely Ionized Plasma. Proc. Roy. Soc. (London), Ser. A, vol. 223, no. 1154, May 6, 1954, pp. 348–360.
9. Lamb, Horace: Hydrodynamics. Dover Publ. (New York, N.Y.), 1945.
10. Ragsdale, Robert G.; and Rom, Frank E.: Gas-Core Reactor Work at NASA/Lewis. Paper No. 67-499,

Third Propulsion Joint Specialist Conf., AIAA, July 1967.

11. KOESTEL, A.; AND REINMANN, J. J.: Mercury Condenser Research and Development. Government-Industry Conference on Mercury Condensing, Apr. 18, 1961, Pasadena, Calif. NASA TN D–1188, 1962, pp. 2–104.
12. SPITZER, LYMAN: Physics of Fully Ionized Gases. Second rev. ed., Interscience Publ., 1962.
13. HIDE, RAYMOND; AND ROBERTS, PAUL H.: Some Elementary Problems in Magnetohydrodynamics. Advances in Applied Mechanics. Vol. 7. H. L. Dryden and Th. von Kármán, eds., Academic Press, 1962, pp. 215–316.
14. MELCHER, JAMES R.: Field-Coupled Surface Waves. MIT Press, 1963.

Page intentionally left blank

Stability Considerations for a Transparent Wall in a Gaseous Nuclear Rocket[1]

C. K. W. TAM, D. B. GORACKE, AND W. S. LEWELLEN
Massachusetts Institute of Technology

The stability of infinitesimal disturbances on an inviscid, incompressible model of coaxial flow around a cylinder of stationary fluid of differing density separated by a thin, flexible wall is studied. The pinch mode of disturbance is found to be the most unstable. The wall strength required to insure that no disturbance will grow along the boundary is determined as a function of density ratio and the dynamic pressure of the flow. A numerical example indicates that adequate strength can be obtained within the thickness limit imposed by the heat absorption constraint existing in the nuclear light bulb concept of a gaseous nuclear rocket, but the margin is close enough to suggest that other possible additive effects merit further analysis.

Some gaseous nuclear rocket concepts (refs. 1 and 2) depend upon a transparent wall to separate the fissioning fuel from the propellant. In several schemes proposed this wall is used to confine the fission material to a core at reasonable pressure where there is relatively very little flow velocity. The transparent wall considered is extremely thin so as not to absorb too much of the large radiative energy fluxes passing through it. Outside the core the propellant flows predominantly in the axial direction and absorbs the radiative heat energy in the process. Because of the large heat flux involved the propellant is expected to have a substantial axial flow velocity. It is well known that a fluid interface (without the wall) of this configuration is unstable (Kelvin-Helmholtz instability) (refs. 3 and 4). In this paper our attention is focused on this interfacial instability with a thin flexible partition. Specifically, our aim is to determine the wall strength necessary to insure that no disturbance will grow along this boundary.

The flow field inside the core is usually quite complicated and cannot be expressed in simple mathematical form. For our present purpose we shall, however, make use of the fact that the flow velocity in this region is relatively small. As an approximation we shall adopt a model in which the fluid in the core is assumed to be stationary. Outside the core the propellant flow velocity is predominantly in the axial direction. To simplify matters we shall assume that the velocity is uniform throughout as shown in figure 1. Consistent with this assumption we shall regard the fluids as inviscid and to a first order incompressible. The transparent wall will be treated as a thin cylindrical shell of very small thickness. In the equilibrium configuration it is possible that the pressure inside the core may be slightly higher than that outside. In this case the transparent wall will be subject to tensile forces in the circumferential direction and probably also in the axial direction. In this paper we shall also investigate the effect of this prestressing of the wall on the stability characteristics.

FORMULATION

When it is assumed that the fluids are inviscid and incompressible in both the core and the annular regions (fig. 1), the linearized equations of motion are for region (1)

$$\nabla \cdot \mathbf{V}_1 = 0 \qquad (1)$$

[1] This research was partially supported by the NASA Space Nuclear Propulsion Office under contract NSR 22-009-288.

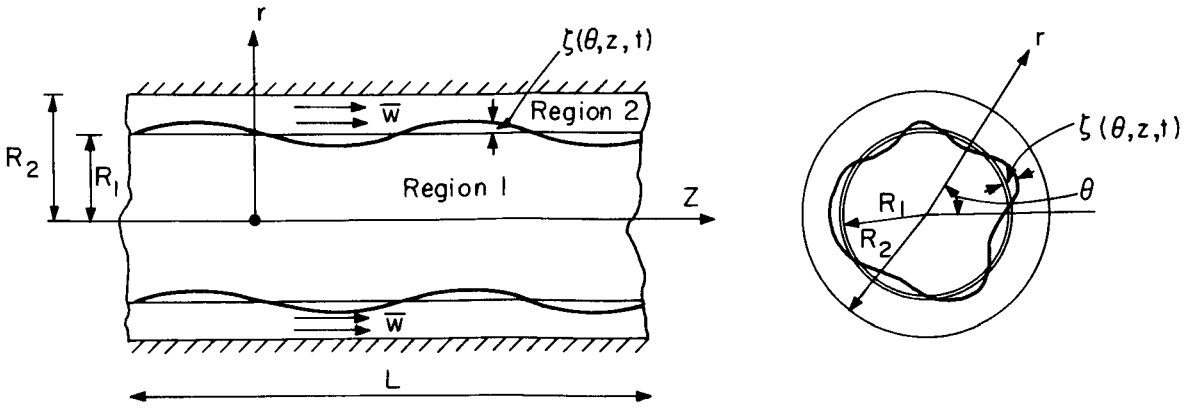

FIGURE 1.—*Transparent-wall configuration.*

$$\rho_1 \frac{\partial \mathbf{V}_1}{\partial t} = -\nabla p_1 \tag{2}$$

and for region (2)

$$\nabla \cdot \mathbf{V}_2 = 0 \tag{3}$$

$$\rho_2 \left(\frac{\partial \mathbf{V}_2}{\partial t} + \bar{w} \frac{\partial \mathbf{V}_2}{\partial Z} \right) = -\nabla p_2 \tag{4}$$

where ρ, $\mathbf{V}$, and p are the density, velocity, and pressure of the fluid, respectively, and $\bar{w}$ is the streaming velocity of the fluid in the annular region. The Z-axis is in the axial direction.

Let R_1 and R_2 denote the inner and outer radii of the annulus; then the appropriate boundary conditions at $r=R_2$ and $r=0$ are

$$u_2(r=R_2) = 0 \tag{5}$$

and

$$\mathbf{V}_1(r=0) \neq \infty \tag{6}$$

where u denotes the radial velocity component of the fluid.

If ζ, η, and ξ are the displacements of the transparent wall in the radial, circumferential, and axial directions, respectively, and ρ_w and h are its density and thickness, the boundary conditions at $r=R_1$ are, for kinematic conditions,

$$u_1 = \frac{\partial \zeta}{\partial t} \qquad u_2 = \frac{\partial \zeta}{\partial t} + \bar{w} \frac{\partial \zeta}{\partial Z} \tag{7}$$

and, for the dynamic condition,

$$p_1 - p_2 = q + \rho_w h \frac{\partial^2 \zeta}{\partial t^2} \tag{8}$$

The loading on the wall q in Equation (8) can be divided into two parts; i.e.,

$$q = q_b + q_\sigma \tag{9}$$

Here q_b denotes that part of the loading which is carried by the bending and stretching of the wall when it behaves as a thin cylindrical shell and q_σ is that part of the loading which is due to membrane stresses existing in the wall in its equilibrium configuration. If E and ν are the Young's modulus and Poisson's ratio of the wall material, then q_b is given by (ref. 5)

$$q_b = \frac{Eh}{R_1(1-\nu^2)} \left[\frac{h^2}{12} \left(R_1 \frac{\partial^4 \zeta}{\partial Z^4} + \frac{2}{R_1} \frac{\partial^4 \zeta}{\partial \theta^2 \partial Z^2} + \frac{1}{R^3} \frac{\partial^4 \zeta}{\partial \theta^4} \right) + \frac{\zeta}{R_1} - \frac{1}{R_1} \frac{\partial \eta}{\partial \theta} - \nu \frac{\partial \xi}{\partial Z} \right] \tag{10}$$

with

$$\frac{\partial^2 \xi}{\partial Z^2} + \frac{(1-\nu)}{2R_1^2} \frac{\partial^2 \xi}{\partial \theta^2} + \frac{(1+\nu)}{2R_1} \frac{\partial^2 \eta}{\partial Z \partial \theta} - \frac{\nu}{R_1} \frac{\partial \zeta}{\partial Z} = 0$$

$$\frac{1+\nu}{2} \frac{\partial^2 \xi}{\partial Z \partial \theta} + R_1 \frac{(1-\nu)}{2} \frac{\partial^2 \eta}{\partial Z^2} + \frac{1}{R_1} \frac{\partial^2 \eta}{\partial \theta^2} - \frac{1}{R_1} \frac{\partial \zeta}{\partial \theta} = 0$$

If in the equilibrium configuration the wall is subject to membrane tensile forces σ_Z and σ_θ per unit length in the axial and circumferential directions, then q_σ is given by

$$q_\sigma = -\sigma_Z \frac{\partial^2 \zeta}{\partial Z^2} - \frac{\sigma_\theta}{R_1^2} \left(\zeta + \frac{\partial^2 \zeta}{\partial \theta^2} \right) \tag{11}$$

In this paper we shall assume that the length of the rocket L (fig. 1) is much longer than the wavelength of any unstable wave; i.e., we shall con-

sider L as essentially infinite. With this approximation we shall neglect any possible end effects.

THE DISPERSION RELATION

Let us consider normal mode solutions which have a periodic dependence on the axial, angular, and temporal variables of the form exp $[i(kZ+n\theta-\omega t)]$; e.g.,

$$p=\hat{p}(r)\exp[i(kZ+n\theta-\omega t)]$$

where n is an integer. By straightforward elimination, equations (1) to (4) give the following equations for the pressures and radial velocities:

$$\frac{d^2\hat{p}_1}{dr^2}+\frac{1}{r}\frac{d\hat{p}_1}{dr}-\left(\frac{n^2}{r^2}+k^2\right)\hat{p}_1=0 \tag{12}$$

$$i\omega\hat{u}_1=\frac{1}{\rho_1}\frac{d\hat{p}_1}{dr} \tag{13}$$

$$\frac{d^2\hat{p}_2}{dr^2}+\frac{1}{r}\frac{d\hat{p}_2}{dr}-\left(\frac{n^2}{r^2}+k^2\right)\hat{p}_2=0 \tag{14}$$

$$i(\omega-\bar{w}k)\hat{u}_2=\frac{1}{\rho_2}\frac{d\hat{p}_2}{dr} \tag{15}$$

From equations (5) to (11) the boundary conditions on $\hat{p}_1$, $\hat{p}_2$, and ζ are found to be

$$\left.\begin{aligned}\frac{d\hat{p}_1(0)}{dr}&\neq\infty\\ \frac{d\hat{p}_2(R_2)}{dr}&=0\end{aligned}\right\} \tag{16}$$

and at $r=R_1$

$$\omega^2\hat{\zeta}=\frac{1}{\rho_1}\frac{dp_1}{dr}\qquad(\bar{w}k-\omega)^2\hat{\zeta}=\frac{1}{\rho_2}\frac{d\hat{p}_2}{dr} \tag{17}$$

$$\hat{p}_1-\hat{p}_2=\hat{q}_b+\hat{q}_\sigma-\rho_w h\omega^2\hat{\zeta} \tag{18}$$

where

$$\hat{q}_\sigma=\left[\sigma_Z k^2+\frac{\sigma_\theta}{R_1^2}(n^2-1)\right]\hat{\zeta}$$

$$\hat{q}_b=\frac{Eh}{R_1^2(1-\nu^2)}\left[\frac{h^2}{12R_1^2}(k^4R_1^4+2n^2k^2R_1^2+n^4)+1-\frac{\nu^2k^4R_1^4+2n^2k^2R_1^2+n^4}{(k^2R_1^2+n^2)^2}\right]\hat{\zeta}$$

Solutions of equations (12) and (14) which satisfy boundary conditions (16) can be written as

$$\left.\begin{aligned}\hat{p}_1(r)&=C_1I_n(kr)\\ \hat{p}_2(r)&=C_2I_n(kr)-\frac{I_n'(kR_2)}{K_n'(kR_2)}K_n(kr)\end{aligned}\right\} \tag{19}$$

where I_n and K_n are modified Bessel functions and the prime denotes differentiation with respect to the argument of the function. The constants C_1 and C_2 are undetermined; one constant is arbitrary and the other is to be determined by boundary conditions (17) and (18).

Let us introduce the following dimensionless parameters

$$\left.\begin{aligned}\rho^*&=\rho_1/\rho_2 & \rho^o&=\rho_w/\rho_2\\ \lambda&=kR_1 & R_2&=SR_1\\ \omega&=\bar{w}k\Omega & tR_1&=h\\ T&=\frac{Et}{\rho_2\bar{w}^2(1-\nu^2)}\end{aligned}\right\} \tag{20}$$

where T is the strength parameter. By substituting equations (19) into equations (17) and (18) and on imposing the condition of nontrivial solution the following dispersion relation in terms of the dimensionless parameters is obtained:

$$A_n(\lambda)\Omega^2+B_n(\lambda)(1-\Omega)^2=C_n(\lambda) \tag{21}$$

where

$$A_n(\lambda)=\rho^*[I_n(\lambda)/I_n'(\lambda)]+\rho^o\lambda t$$

$$B_n(\lambda)=\frac{I_n'(\lambda S)K_n(\lambda)-K_n'(\lambda S)I_n(\lambda)}{I_n'(\lambda)K_n'(\lambda S)-I_n'(\lambda S)K_n'(\lambda)}$$

$$C_n(\lambda)=\frac{\sigma_Z\lambda}{\rho_2\bar{w}^2R_1}+\frac{\sigma_\theta(n^2-1)}{\rho_2\bar{w}^2R_1\lambda}+\frac{T}{\lambda}\left[(\lambda^2+n^2)^2\frac{t^2}{12}+1-\frac{\nu^2\lambda^4+2n^2\lambda^2+n^4}{(\lambda^2+n^2)^2}\right]$$

Equation (21) is a quadratic equation for Ω. The criterion for stability, that Ω be real in this case, is easily found to be

$$[A_n(\lambda)+B_n(\lambda)]C_n(\lambda)\geqq A_n(\lambda)B_n(\lambda) \tag{22}$$

for all values of λ and integers n.

SIMPLIFIED STABILITY CRITERION

Equation (22) is the exact criterion for stability. However, as it is, tedious numerical calculation is required to establish the stability boundary in the parameter space. To avoid this complexity and to establish which are the important parameters that determine the stability criterion let us concentrate instead on the question of the minimum value of the strength parameter T which will insure stability. In order to simplify the problem we shall first consider the case in which $\sigma_Z=\sigma_\theta=0$. From equation

(22), for stability we must have

$$T \geqq \frac{A_n(\lambda)B_n(\lambda)\lambda}{A_n(\lambda)+B_n(\lambda)}\left[(\lambda^2+n^2)^2\frac{t^2}{12} + 1 - \frac{\nu^2\lambda^4+2n^2\lambda^2+n^4}{(\lambda^2+n^2)^2}\right]^{-1} \quad (23)$$

As will be shown below, if t is much smaller than unity (of the order 0.01 or smaller, which is the range of values currently under consideration in practice) the value of λ which maximizes the right-hand side of equation (23) (denoted by λ_m) is quite large, say, of the order of 10. For a large argument the asymptotic form of the modified Bessel functions can be used; i.e.,

$$I_n(\lambda) \approx \frac{e^\lambda}{(2\pi\lambda)^{1/2}} \qquad K_n(\lambda) \approx \left(\frac{\pi}{2\lambda}\right)^{1/2} e^{-\lambda} \qquad \lambda >> 1$$

On using these asymptotic values it is easy to show that

$$A_n(\lambda) \approx \rho^* + \rho^o\lambda t$$

$$B_n(\lambda) \approx \frac{e^{2\lambda(S-1)}+S}{e^{2\lambda(S-1)}-S} \approx 1$$

except for values of S very close to 1. On substituting these values into equation (23), for the first few modes (which are the most critical ones) we have

$$T \geqq \frac{\rho^*+\rho^o\lambda t}{\rho^*+\rho^o\lambda t+1}\,\frac{\lambda}{(\lambda^2+n^2)^2\frac{t^2}{12}+1-\nu^2} \quad (24)$$

When $\rho^* > 1$, as it is in our problem, the factor $(\rho^*+\rho^o\lambda t)/(\rho^*+\rho^o\lambda t+1)$ can vary at most from $\frac{1}{2}$ to 1. Hence in maximizing the right-hand side of equation (24) we may ignore this variation. By straightforward differentiation of equation (24) with respect to λ we find (for $t << 1$)

$$\lambda_m^2 \cong \frac{\left\{\left[\frac{n^4t^4}{9(1-\nu^2)^2}+\frac{t^2}{1-\nu^2}\right]^{1/2} - \frac{n^2t^2}{6(1-\nu^2)}\right\}}{\frac{t^2}{2(1-\nu^2)}} \quad (25)$$

Therefore,

$$\left.\begin{array}{ll} n=0 & \lambda_m^2 \cong 2(1-\nu^2)^{1/2}t^{-1} \quad \text{(pinch mode)} \\ n=1 & \lambda_m^2 \cong 2(1-\nu^2)^{1/2}t^{-1} - \frac{1}{3} \quad \text{(kink mode)} \\ n=2 & \lambda_m^2 \cong 2(1-\nu^2)^{1/2}t^{-1} - \frac{4}{3} \end{array}\right\} \quad (26)$$

It is clear from equations (26) and (24) that the pinch mode ($n=0$) requires the largest value of T for stability:

$$T_{\text{stable}} \geqq \frac{\rho^*+2\rho^o(1-\nu^2)^{1/4}t^{1/2}}{\rho^*+2\rho^o(1-\nu^2)^{1/4}t^{1/2}+1}\,\frac{1.06}{(1-\nu^2)^{3/4}t^{1/2}} \quad (27)$$

Or, since the term in parentheses in equation (27) is <1 and ν^2 is always $<<1$,

$$T_{\text{stable}} \gtrsim t^{-1/2} \quad (28)$$

If σ_Z is zero and σ_θ is finite, then an examination of the dispersion relation (22) shows that the pinch mode $n=0$ is still the most unstable mode. In fact, for this case σ_θ has a destabilizing effect. In order to insure stability the requirement on T is

$$T \geqq \left(\frac{\rho^*+\rho^o\lambda t}{\rho^*+\rho^o\lambda t+1}\lambda + \frac{\sigma_\theta}{\rho_2\bar{w}^2R_1}\right)\left(\frac{\lambda^4t^2}{12}+1-\nu^2\right)^{-1} \quad (29)$$

for all values of λ. The tensile force σ_Z has a stabilizing effect for all values of n.

DISCUSSION

We have shown that if there is no axial membrane tension on the transparent wall the pinch mode is the most unstable mode. If the wall is not prestressed, from equation (28) the minimum thickness required to stabilize the boundary is

$$\frac{h}{R_1} \gtrsim \left(\frac{\rho_2\bar{w}^2}{E}\right)^{2/3}$$

In order to see the meaning of this requirement for the nuclear light bulb concept (ref. 1) of a gaseous nuclear rocket, consider an example calculation. Assume that $\rho_1 \cong 1$ lb/ft^3, $\rho_2 \cong 0.3$ lb/ft^3, $\bar{w} \cong 100$ ft/sec, $R_1 \cong 1$ ft, and $E \cong 10^6$ psi. Then

$$h \gtrsim 0.9 \times 10^{-3} \text{ in.}$$

Thus, according to the present analysis, thicknesses of the order of a few mils will be required to stabilize the boundary against unstable disturbances. Since this is the order of thickness being considered for the nuclear light bulb (ref. 6), the analysis suggests that adequate strength can be obtained within the limits imposed by the heat absorption constraint, but the margin is close enough to suggest that other possible additive effects merit further analysis. Two possibly additive effects are the rotation of the inner fluid and the dependence of the cavity reactivity on the position of the interface. A vortex used inside the transparent wall to keep

the uranium density at the wall low should tend to destabilize the boundary. Also the increase in the reactivity of the cavity as the uranium gas spreads over a large fraction of the volume may cause the pressure inside the partition to increase and provide a destabilizing force to the pinch mode.

REFERENCES

1. McLafferty, G. H.: Survey of Advanced Concepts in Nuclear Propulsion. J. Spacecraft Rockets, vol. 5, no. 10, Oct. 1968, pp. 1121–1128.
2. Ragsdale, R. G.; and Rom, F. E.: Gas Core Reactor Work at NASA/Lewis. Paper No. 67-499, Third Propulsion Joint Specialist Conf., AIAA, July 1967.
3. Landau, L. D.; and Lifshitz, E. M.: Fluid Mechanics. Vol. 6. Course of Theoretical Physics. Addison-Wesley, 1959.
4. Chandrasekhar, S.: Hydrodynamic and Hydromagnetic Stability. Oxford Univ. Press. (London), 1961.
5. Timoshenko, S.; and Woinowsky-Krieger, S.: Theory of Plates and Shells. McGraw-Hill Book Co., Inc., 1959.
6. McLafferty, G. H.: Adsorption of Thermal Radiation in the Transparent Wall of a Nuclear Light Bulb Rocket Engine. J. Spacecraft Rockets, vol. 4, 1967, p. 758.

DISCUSSION

McLafferty: Using silicon of about 10-mil instead of 1-mil thickness helps us somewhat. In our reference engine the velocity is about 30 ft/sec instead of 100, which helps us by a factor of 10. I believe your analysis is for a thin flat plate rather than for a wall made up of tangent tubes. For cooling we have a double layer of silica which we make by a series of round tubes which increases the strength of the tube by a factor of 10 to 100. So, I suspect that we have two to four orders of magnitude more of a factor of safety than you indicated. I wish all of our problems were that easy.

Lewellen: I am not sure it is quite that easy. I think that the stability problem will probably come as near to killing the system as any. I think a velocity of 30 ft/sec is perhaps a little low when you consider that there are such large density differences in the propellant region which may set up convection cells in a g field. The forced flow should be large enough to dominate any free convection patterns.

McLafferty: I do not know how much the round tubes would improve the situation. There is a problem with the round wall tube in relation to the flow past it. It does not give the nice even flow on the outside that is preferable.

Page intentionally left blank

An Acoustic Instability Driven by Absorption of Radiation in Gases[1]

MICHAEL J. MONSLER
AVCO-Everett Research Laboratory

JACK L. KERREBROCK
Massachusetts Institute of Technology

Future engineering devices for propulsion and power generation may employ gases at extremely high temperatures of the order of 50 000° K. In such devices thermal radiation is likely to be the dominant energy transfer mechanism, the energy being radiated between different opaque regions of the gas rather than between walls containing a transparent gas. In order to transfer such large net heat fluxes, on the order of megawatts per square centimeter, very large temperature gradients will be involved, perhaps of the order of 10 000° K/cm. Such an extreme state of non-equilibrium may not be attainable because the state of the gas may be unstable with respect to small disturbances. That is, there may be conditions under which an infinitesimally small perturbation such as a sound wave may cause the state of the system to change spontaneously to some different stable state.

The cause of such an instability may be easily illustrated. Consider a wave in a radiating gas in which the opacity, or volumetric absorption coefficient, of the gas is an increasing function of temperature. If a large net flux of radiation is present, a local increase in temperature will lead to an increase in opacity, which will cause more absorption of the radiative flux. The resultant increase in the heating of the gas will cause the temperature to increase further and will lead to a runaway situation. This phenomenon has been observed in experiments involving the heating of a shock wave by a laser beam, but there is as yet no experimental evidence of an instability of a quiescent gas heated by radiation. This cannot happen in a uniform gas having no net heat flux, because then a region of temperature and opacity increase will be a net emitting instead of absorbing region; the energy excess will be radiated away and equilibrium will be regained.

There seem to be three factors which are necessary to this proposed mechanism for the amplification of waves. First, there must be a source of radiation present of higher temperature than the medium supporting the wave; second, the wave must be sufficiently opaque for the absorption of radiation to be a significant source of energy; and, third, the opacity of the gas must be an increasing function of temperature so that a runaway effect is possible. These considerations lead to the following very important questions which are answered by this research.

(1) Are there any conditions under which an *infinitesimally small disturbance*, i.e., an ordinary fluctuation of the gas, can grow into one of these radiation-driven shock waves?

(2) How is the criterion for wave growth dependent upon properties such as the flux of radiation or the rate of increase of opacity with temperature?

(3) If such waves can grow in a radiating gas, under what conditions will they cause a given radia-

[1] Submitted in partial fulfillment of the requirements for the degree of Doctor of Philosophy at the Massachusetts Institute of Technology Center for Space Research. Prepared under NASA contract no. NGR 22-009-019. Center for Space Research Report CSR T-69-4.

tion heat transfer problem to not have a stable steady-state solution?

A steady-state heat transfer problem is set up in which energy is transferred from a hot wall to a cooler wall by thermal radiation. The gas is assumed to be a perfect gas in local thermodynamic equilibrium. Molecular heat conduction and viscosity are ignored and a one-dimensional geometry is assumed. The radiation pressure and energy density are neglected. An opacity is assumed which is an average over photon frequencies but which depends on temperature and pressure. The stationary gas of arbitrary optical depth is contained between two black walls of constant temperature. We then ask what are the fluctuations, or natural oscillations, of this steady nonuniform radiating gas?

The equations of motion for the fluctuations of a radiating gas are derived through the usual linearized perturbation analysis of the equations of unsteady compressible gas dynamics. The result is a partial differential equation (having spacially varying coefficients) which is fourth order in space and third order in time and which governs the behavior of the oscillations.

The determination of the normal modes of oscillation of this gas requires the solution to an eigenvalue problem, the eigenvalues being the allowed complex frequencies selected by the boundary conditions. The wave equation with varying coefficients is solved by the WKB method. A computer program finds the roots of the determinant which results after application of boundary conditions. The complex roots, the parts of which are the frequency of oscillation and the damping or growth rates, are found in the form of a root locus as a function of increasing net heat flux. An example is given in figure 1.

It is found that a critical heat flux exists below which the gas is stable. For net heat fluxes larger than this critical value a mode of oscillation will grow exponentially with time, which indicates that the given radiative heat transfer problem does not have a stable solution.

In conclusion, the broad features of the proposed mechanism of an instability driven by absorption of radiation in a gas have been confirmed by the results of an eigenvalue problem, which may be summarized as follows:

(1) A previously unsuspected instability may arise in a nonuniform radiating gas, at least for the particular boundary conditions of black walls of constant temperature.

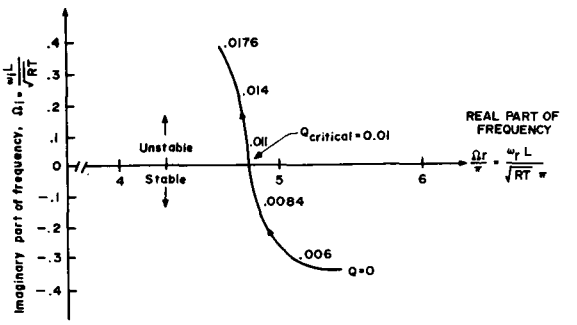

FIGURE 1.—*Typical root locus; net heat flux parameter* $Q = \frac{q_0}{2\sigma T^4}$

(2) The instability can occur only for moderately high temperatures. For low temperatures the radiative transfer is not strong enough to drive the instability, and for extremely high temperatures the radiative transfer is so efficient as to cause disturbances to be isothermal, which also is stabilizing.

(3) The instability can occur for opacities which vary more strongly than the fourth power of the temperature. That is, if $a \approx T^m$ the instability seems possible only for $m > 4$. A typical neutral stability curve is given in figure 2.

(4) The instability may arise only for a gas

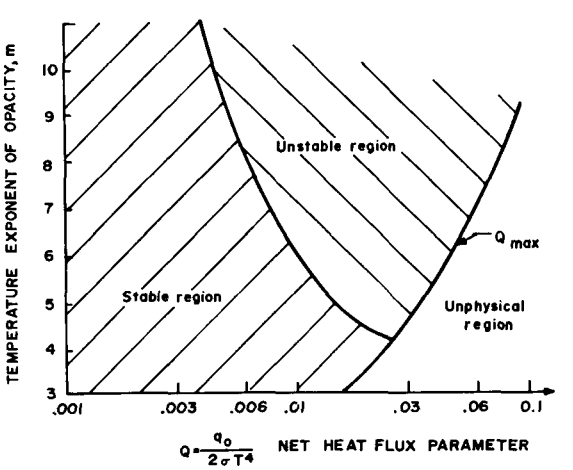

FIGURE 2.—*Neutral stability locus;* $a = T^m$.

which is optically thick. However, no unambiguous trend toward greater or lesser stability could be established on the basis of comparisons between average photon wavelength, disturbance wavelength, and distance between the walls.

(5) The lowest frequency normal modes will be most unstable or will become unstable first as the net radiative flux is increased.

(6) The criterion for the growth of traveling acoustic waves is not a reliable indicator of the onset of instability as predicted by the eigenvalue problem. This means that the boundary conditions do substantially influence the stability of the system, even for waves of short wavelength, and systems with different boundary conditions must therefore be treated on an individual basis.

In summary, previous work on fluctuations in a radiating gas has been extended to include an opacity which is a function of temperature and pressure and, most importantly, to include a net radiative heat flux and gradients in the thermodynamic variables. These extensions allow the investigation of an instability driven by the absorption of radiation by waves in the gas. The effect of this will be to limit the maximum possible net radiative heat flux in a problem to a value which can be substantially lower than that predicted by the usual steady-state heat transfer analysis.

DISCUSSION

McLafferty: The following problem has worried us for years. The criteria set up are not met in the nuclear light bulb because they occur primarily when the hydrogen is at about 15 000° or 20 000° R where the opacity goes up so rapidly. In the light bulb there are always conditions where the opacity increases with increasing temperature in both the propellant region and in the neon buffer region at the edge of the fuel. However, we spent much thought on this in the open-cycle engine. What happens is this: The hydrogen starts off at a low temperature where the opacity is entirely due to seeds. The temperature reaches a certain point where the hydrogen begins to get opaque, and then the opacity increases rapidly. The exponent n of the variation of opacity with temperature is on the order of 8, but it jumps up to the order of 10 at 80 000° R. A steady-state solution to the problem in which there is a temperature front advancing into the incoming fluid is obtained. In both the open-cycle vortex engine which we worked on a long time ago and in the more recent coaxial engine, the hydrogen comes in and jumps up in temperature. This temperature jump, at least in the calculations, occurred at one spot because there was a continuous flow of hydrogen across the spot which made up for radiant energy absorption. The NASA Lewis Research Center people have found the same kind of a temperature jump. The hydrogen is either below 15 000° R or about 60 000° or 70 000° R. The unanswered question was how stable that jump position is. This is the same problem that you are addressing yourself to, but I am not sure that your answer applies to our problem. Have you tried a temperature distribution in a moving fluid which fulfills the criteria that I am talking about and then tried to perturb it to see if the instability occurred?

Monsler: No. That is not the problem that we addressed at all but I agree that it is a very interesting problem. One finds that the addition of flow in the direction of the temperature gradient would be an extremely complicated situation and we address the simpler problem first. In reply to your first comment, indeed it would seem that the uranium has a decreasing opacity with temperature and would be quite safe. I am not quite sure about the hydrogen fuel region. In any regard, this analysis, which is the first that I know about, suggests that such an instability was not tied to a particular concept, of course, and I was thinking of radiative heat transfer devices in general.

Russell: In this high-temperature plasma the thermal conductivity due to the electrons ought to be very large and that is not mentioned here. I wonder if you have made any rough estimates as to what the effect would be. It is not clear that this conductivity would be either stabilizing or destabilizing and it ought to be coupled in with the radiation because both are functions of electron temperature.

Monsler: That's correct. We have not considered any two-fluid types of effects at all. They could very well be important and either stabilize or overwhelm this effect. I have done nothing more than treat it as a perfect gas of the appropriate average quantities to represent a particular situation. But I realize that the plasma could be far out of equilibrium.

Page intentionally left blank

Gas-Core Nuclear Rocket With Fuel Separation by MHD-Driven Rotation

CHUL PARK AND WENDELL L. LOVE
NASA Ames Research Center

A gas-core nuclear rocket is described in which fuel containment is achieved through the application of an MHD-centrifuge scheme. Solid-body rotation of the gas would be developed in a cylindrical cavity in order to obtain maximum separation of the fuel gas from the propellant gas. Heating of the propellant gas would be accomplished by radiative transfer from the fuel region near the wall as the propellant flows axially through the center region of the cavity. Encouraging results were obtained from a preliminary experiment to test the effectiveness of MHD-driven rotation for separating two gas species in a closed cylindrical chamber. The operating characteristics and projected performance of a gas-core nuclear rocket engine using this scheme for fuel containment were calculated and typical results are presented.

Several of the proposed schemes for fuel containment in gas-core nuclear rockets are based on rotating flows of one form or another (fig. 1). One of the first schemes considered (ref. 1) was based on a vortex flow field in which the rotation was produced by injecting gas tangentially at high velocity (fig. 1(*a*)). Originally, it was hoped that in this scheme the centrifugal force developed by the supersonic rotation would confine the heavy fuel to the outer region of the cavity while permitting the propellant to diffuse radially inward through the fuel region. Tests have shown, however, that the flow field developed in this configuration does not result in effective separation of the two gases (ref. 2).

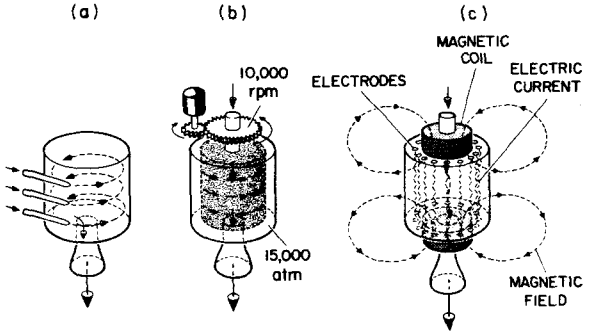

FIGURE 1.—*Centrifugal species separation schemes for gas-core nuclear rocket.* (a) *Fluid injection.* (b) *Mechanical notation.* (c) *MHD centrifuge.*

More recently, efforts were directed toward exploiting the high stability of the rotating flow instead of the centrifugal force in both the open-cycle (ref. 3) and closed-cycle (ref. 4) configurations. In these vortex-stabilization concepts, the local speed of rotation remains subsonic everywhere, and so centrifugal force would be negligibly small. The propellant is injected into the outer region of the cavity and, hopefully, remains there because of the inherent stability of the rotating flow while it bypasses the fuel gas region. Although considerable experimental effort has been expended on the open-cycle vortex-stabilized configuration, the results to date indicate that the fuel loss rate would be too great to permit economical engine operation (ref. 4). The closed-cycle operation (ref. 4) would result in little or no loss of fuel, but its practicability is yet to be proved experimentally. Thus, despite the fact that considerable effort has been expended on it in the last decade, the problem of containment of the gaseous nuclear fuel in the rocket chamber has not been solved to a satisfactory degree.

Tests involving these rotating flows show that the most effective centrifugal separation of the heavy fuel gas from the light propellant gas occurs in the

portion of the flow that resembles solid-body rotation. This suggests that perhaps a fuel containment scheme based on rotating gas flow would operate most successfully if the flow field possessed solid-body-like rotation. Since tangential gas injection develops into an inviscid vortex flow field which does not operate favorably as a centrifuge, it is necessary to employ a different means of driving the gas which will yield a solid-body-like rotation. Two possible schemes for achieving this are illustrated in figures 1(*b*) and 1(*c*). In figure 1(*b*), the cavity chamber would be rotated mechanically to induce a solid-body rotation in the gas. However, in order to achieve a desirable gas separation, the rotational speed of the chamber would lead to a centripetal acceleration in excess of 1 000 000 *g*. Such accelerations are beyond the structural limits of present materials, so it would be necessary to apply a gas pressure of at least 10 000 atm on the outside cavity chamber to reduce the hoop stresses in the rotating wall to a workable level. The friction loss at the outside surface of the rotating wall becomes prohibitively large in this case, so the scheme is rendered impractical. In the other scheme (fig. 1(*c*)), a rotating motion is developed by a unique axial-J, radial-B ($\mathbf{J}\times\mathbf{B}$) force which acts on the gas in the region near the cylindrical wall. It is proposed (ref. 5) that solid-body rotation of the gas can be established by this method. This scheme is free of the limitations just described and thus offers a possible means of obtaining effective gas separation which could be utilized for the purpose of fuel containment in a gas-core nuclear rocket.

In the schemes presented in figures 1(*b*) and 1(*c*), the fuel gas is in direct contact with or, in case transpiration cooling is incorporated (see the section of this paper entitled "Application"), in close proximity to the cavity wall. This closeness, coupled with the high velocities present, leads to a large heat transfer rate to the wall. The prevention of excessive wall heating was one of the initial motives for considering the propellant injection from the wall. With the anticipation of future progress in cooling technology, however, one is justified in re-examining the schemes shown in figures 1(*b*) and 1(*c*). The present paper describes the results of a preliminary experiment aimed at testing the effectiveness of the scheme of figure 1(*c*) (i.e., the MHD centrifuge scheme) and discusses the problems associated with it and the projected performance of a hypothetical gas-core rocket engine using this scheme to achieve fuel containment.

EXPERIMENTAL STUDY

A preliminary study of the feasibility of the MHD centrifuge scheme for separating two gases has been carried out at Ames Research Center (ref. 5). The apparatus used for the experimental tests was designed with the objective of attaining a rotation of the gas which approaches as nearly as possible that of a solid body. The geometrical arrangement employed is shown in figure 2. By using this arrangement of an axial electric current and a radial magnetic field in a cylindrical chamber, it was possible to use multiple electrodes located near the cylinder wall so that the current and hence the driving Lorentz force is likely to be evenly distributed and confined to the chamber perimeter. It was felt that these are the most probable conditions for developing a solid-body rotation.

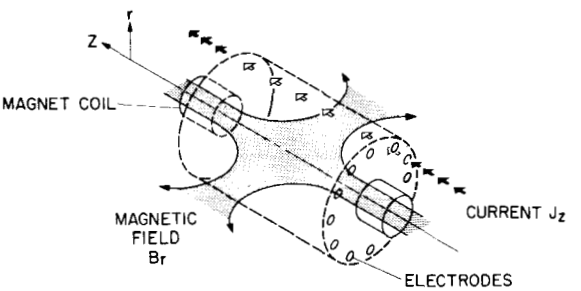

FIGURE 2.—*Arrangement of current and magnetic field in the experimental apparatus.*

A schematic of the test device is shown in figure 3. The cylindrical chamber encloses a volume of approximately 1 liter and operates at pressures less than atmospheric. A mixture of xenon and helium is used to simulate the uranium-hydrogen mixture of a gas-core reactor. There is no inflow or outflow of gas from the chamber during a test. Although such a closed configuration does not correctly simulate a gas-core rocket, it was felt suitable for this preliminary study. The chamber is of a heat-sink design with no cooling provided for the cylinder walls, magnet coils, or electrodes. Consequently, the tests are of short duration, typically less than 1 sec. During a test

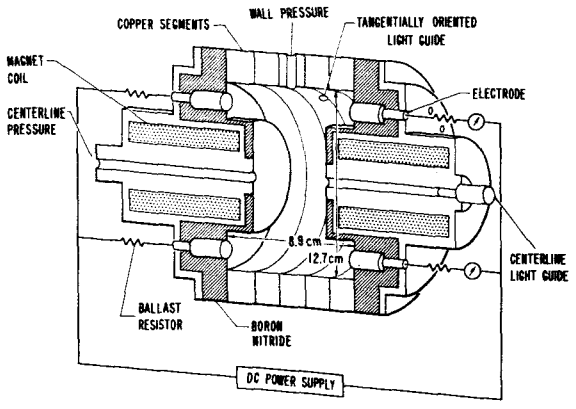

FIGURE 3.—*Sketch of the experimental apparatus for tests on MHD-driven rotation.*

measurements are made of the current and voltage for both the magnet and electrical discharge. Pressure is measured at the cylindrical wall of the chamber and at the axis of the chamber. Spectroscopic readings are obtained from the gas region near the centerline of the chamber and from a region near the wall. These measurements are used to determine the temperature of the gas in these two regions and to determine the resultant change in concentration of the two gas species at these locations brought about by the rotational motion.

The effectiveness of the Lorentz force in driving the gas and the likelihood that solid-body rotation will be produced are dependent on the mode of the electrical current discharge and on the current path. Extensive measurements of the current distribution among the 16 electrode pairs and the luminosity distribution within the chamber led to the conclusion that the electric current followed a path near the chamber perimeter and that a reasonably even current distribution around the outer circumference of the chamber was present. It was further concluded that, for the most part, a stable current discharge was established which was free of any strong arc-spoke mode. These conditions seemed to be reasonably close to the desired conditions for developing solid-body rotation of the gas.

The rotation of the gas was experimentally detected by measuring the pressure at the cylinder wall and at the centerline of the chamber. By combining the species conservation equation and an assumed temperature distribution with the radial momentum equation, an expression can be obtained (ref. 5) which relates the rotational velocity of the gas mixture to the ratio of wall-to-centerline pressure. Thus, an increase in the wall-to-centerline pressure ratio can be interpreted as an increase in the rotational velocity of the gas. The experimental results are shown in figure 4 with the wall-to-centerline pressure

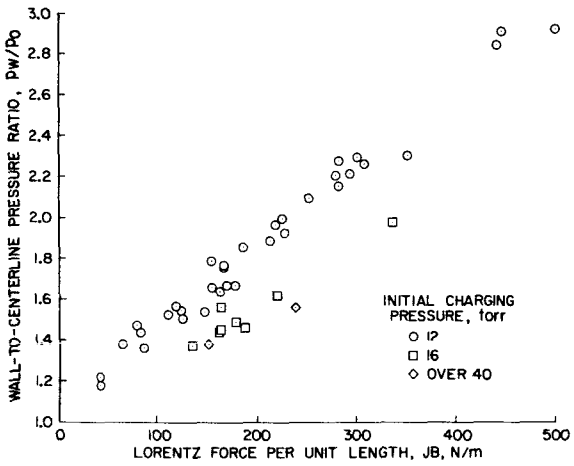

FIGURE 4.—*Wall-to-centerline pressure ratio as a function of Lorentz force.*

ratio plotted as a function of the Lorentz force. As seen from the figure, the pressure ratio seems to increase steadily with the Lorentz force, the maximum value attained being about 2.9.

The rotation of the gas, as evidenced by the difference in pressure between the centerline region and the wall surface, was accompanied by a measurable degree of separation between the xenon and the helium. The measure of separation was determined spectroscopically by recording the relative spectral intensities at various wavelengths taken at the centerline region and at the wall region of the chamber. The results are shown in figure 5 in which the degree of species separation, expressed as the concentration ratio $(N_{Xe}/N_{He})_{wall}/(N_{Xe}/N_{He})_{centerline}$, is plotted as a function of the wall-to-centerline pressure ratio. The measured concentration ratios are compared with theoretical values calculated from the relationship mentioned above. Both the theory and the predominance of the experimental data show a general trend of increasing separation as the rotation speed increases. Although there is a fair degree of scatter

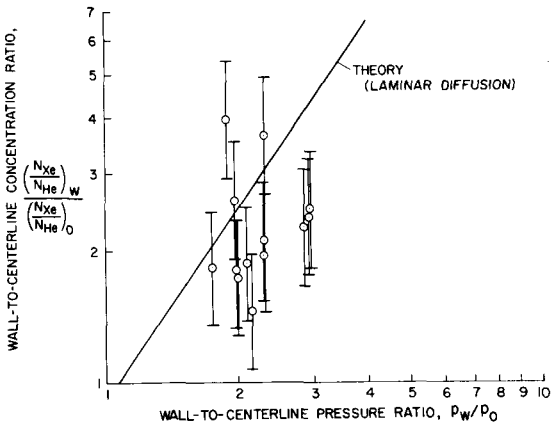

FIGURE 5.—*Measured concentration ratio as a function of wall-to-centerline pressure ratio.*

in the experimental data, the trend indicates that significant species separation is achieved. At the highest pressure ratios produced (i.e., near $p_w/p_o=2.9$), the degree of separation does not appear to be so great as at lower values of p_w/p_o. These runs correspond to a high electrical discharge current, and it may be that turbulence created by this relatively high current level acted to reduce the amount of species separation. The error bars on the data points correspond to uncertainty in the spectroscopic temperature measurements which, in turn, leads to uncertainty in evaluating the spectral line measurements for the purpose of establishing the concentration ratio.

The present experimental study, which was intended as a preliminary evaluation of the effectiveness of MHD-driven rotation for gas separation, does not correctly simulate a prototype gas-core rocket on the following two points. First, unlike in a real rocket, there was no flow through the system. The effect that through flow would have on the stability of the rotating motion and the degree of separation that could be maintained are unknown at present. A further experiment is planned to explore the effect of axial flow on the degree of species separation. Second, in a prototype the fuel gas will be highly ionized and thus will behave as a uniform conducting medium, whereas in the present test the ionized region is somewhat localized. Because of this difference, it is believed that the problems associated with the current discharge will be less in an actual gas-core rocket.

In a prototype rocket using the present scheme for fuel containment, the major portion of the light propellant gas would flow axially along the centerline of the cavity where it would be heated by radiation from the fuel region. The heated gas would then exit from the centerline region through the nozzle. Thus, barring the effects of axial flow on the species separation, the mixture ratio of the heavy to the light gas in the rocket exhaust would correspond to that at the centerline of the present experiment. It should be noted, however, that the results of the present test cannot be compared directly with the prototype condition since a mixture greatly enriched with the heavy gas was used in the present test instead of the light-gas-enriched mixture that is optimum for a prototype. Such a deviation from the exact simulation was made in the interest of maintaining a relatively high electrical conductivity (which would result from the fissioning process in the actual gaseous-core reactor).

Other factors that will influence the suitability of this approach for application in a gas-core rocket are the circulating flows through the end-wall boundary layer (ref. 6). Such flows provide a "leakage" path through which the fuel can leave the wall region and escape the cavity. It is possible, however, that this leakage can be substantially reduced by injecting propellant into the boundary layer through the cylindrical walls and the end walls. This injection will probably be required in any event to reduce the convective heat transfer rate to the wall, as will be discussed later.

APPLICATION

Under the assumption that the basic MHD centrifuge hypothesis is valid and also that the axial flow does not affect the performance, the feasibility of a prototype nuclear rocket is studied here. A schematic and the operating characteristics of a rocket operating on the MHD centrifuge principle are shown in figure 6 and in table I, respectively. The cavity is typically 7 to 8 m in diameter and in length. The radially oriented magnetic field, produced by a pair of cryogenically cooled magnet coils, has a strength of about 1.0 T near the cavity wall. The magnets draw a negligible amount of power and can be powered either from the same source that supplies the electrode currents or from a separate power supply. Total electrical current of about 20 000 A

TABLE I.—*Estimated Operating Characteristics and Weights*

Variable	Design of engine		
	High performance	Medium performance	Low performance
Dimension and performance:			
Cavity wall diameter, m	8	7	8
Cavity length, m	8	7	8
Weight of uranium contained, kg	8.16	8.4	8.33
Specific impulse, sec	1792	1770	1740
Thrust, tons (metric)	46.8	35.8	30.4
Thrust-to-weight ratio	1/121	1/112	1/135
Thermodynamic characteristics:			
Pressure at center, atm	50.1	39.8	15.9
Pressure at cavity wall, atm	53.9	43.6	18.3
Temperature of hydrogen at center, °K	6000	6000	6000
Peak temperature of uranium, °K	10 000	10 000	10 000
Concentration of uranium at center, mole fraction	0.00004	0.00015	0.0003
Concentration of uranium at wall, mole fraction	0.0046	0.0074	0.0121
Hydrogen-to-uranium mass flow ratio	106.4	28.4	14.2
Total mass flow rate, kg/sec	23.8	18.4	15.9
Peak tangential rotation velocity, m/sec	1720	1570	1530
Mach number of uranium at peak velocity	2.25	2.05	2.00
Mach number of mixture	1.62	1.64	1.72
MHD characteristics:			
Magnetic field strength at wall, T	1.0	1.0	1.0
Number of electrode pairs	240	240	180
Electrode current to individual electrodes, A	100	80	73
Total electrical current, A	24 100	19 200	13 100
Voltage gradient, V/cm	17.2	15.8	15.4
Anode-to-cathode overall voltage, V	13 800	11 070	12 300
Heat-transfer characteristics:			
Cavity surface temperature, °K	2500	2500	2500
Peak temperature in regenerative system, °K	1800	1800	1800
Peak temperature in liquid-metal cooling system, °K	1400	1400	1400
Radiator surface temperature, °K	1200	1200	1200
Wall heat transfer rate, W/cm^2	4700	4640	2960
Radiator area, m^2	1.39×10^5	1.06×10^5	8.83×10^5
Power:			
Power dissipated in wall friction, MW	333	211	161
MHD arc power, MW	336	214	164
Booster pump, MW	4.5	3.4	3.0
Magnet, MW	< 0.01	< 0.01	< 0.01
Power generated by turboelectric system, MW	341	217	167
Power transmitted to propellant, MW	2950	2230	1860
Power transmitted to wall, MW	11 810	8920	7440
Power radiated, MW	11 500	8710	7280
Total power generated by fission, MW	14 760	11 150	9300
Weight:			
Cavity structure, tons (metric)	124	69	42
Moderator-reflector system, tons (metric)	2150	1520	2150
Cryogenic magnet system, tons (metric)	128	98	128
Turboelectric generator system, tons (metric)	999	634	482
Radiator system, tons (metric)	2090	1580	1330
Miscellaneous equipment, tons (metric)	92	52	39
Total weight of engine, tons (metric)	5690	4010	4110

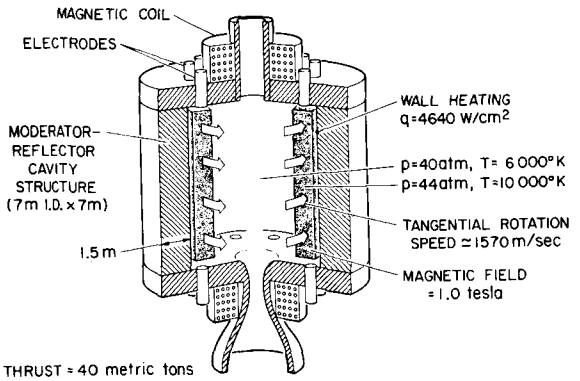

FIGURE 6.—*Sketch of gas-core nuclear rocket with species separation by MHD-driven rotation.*

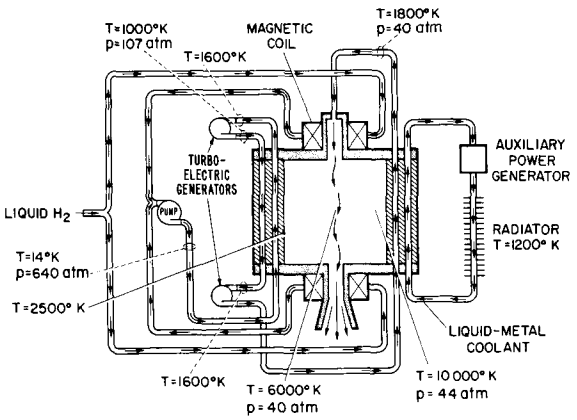

FIGURE 7.—*Sketch of power supply system for a prototype gas-core nuclear rocket with fuel separation by MHD-driven rotation.*

flows through 200 pairs of segmented electrodes. The chamber pressure is 20 to 60 atm, the centerline being at a pressure slightly lower than that at the wall. The maximum tangential rotation velocity is about 1.6 to 1.8 km/sec. The propellant gas is introduced along the centerline of the cavity and flows through the center of the cavity at a low velocity. The propellant gas absorbs heat from the fuel gas primarily through radiation and, to a lesser extent, by convection. The radiative transfer of energy to the hydrogen is enhanced by the radiative coupling between the uranium in the fuel region and the small amount of uranium (about 0.00015 mole fraction) which has diffused into the hydrogen at the centerline region of the cavity. The temperature varies from about 10 000° K at its peak near the cylindrical wall to about 6000° K at the centerline, which corresponds to a specific impulse of approximately 1770 sec. The thrust of the rocket is typically 40 metric tons.

The overall system is shown schematically in figure 7. The liquid hydrogen flows first through the superconducting magnet coils and maintains them at cryogenic temperatures. The liquid hydrogen is then pressurized by a booster pump to a pressure of typically 640 atm (for the medium-performance version, see table I) before it enters the heat exchanger comprising the moderator-reflector wall of the cavity. The hot gas emerging from the heat exchanger drives the first-stage turboelectric generator that supplies one-half the required MHD power. The pressure is about 107 atm at the exhaust of the first-stage turbine in the medium-performance design. The exhaust is fed again into the heat exchanger to drive the second-stage turbine. It is estimated that by employing a two-stage turboelectric generator system all required MHD power can be obtained. The power reclaimed by the turbogenerators represents only 3 percent of the energy transmitted to the wall. The remaining 97 percent of the heat energy entering the cavity structure is removed through a liquid-metal cooling system that rejects the unused energy through a radiator which has a surface temperature of 1200° K. A fraction of this power can be recovered by an auxiliary power generator system to supply power in the starting process and also to drive other equipment.

The performance and the operating characteristics of a typical rocket engine operating on the above-described principle are estimated from the following assumptions:

(1) The heat-transfer efficiency of the rocket chamber is 17 percent (i.e., 17 percent of the fission energy is transferred directly into the propellant gas in the cavity chamber). This is an *a priori* assumption with no rigorous reasoning. An additional 3 percent of the energy is added to the regenerative preheating, thus making the total thermal efficiency 20 percent.

(2) The wall friction is equivalent to twice that in a fully developed turbulent pipe flow evaluated in the hot region (i.e., the edge of the boundary layer which coincides with the electrical current path).

That is, the skin friction τ_w is calculated from

$$\tau_w = 2\left(\frac{f\rho_a v_a^2}{2}\right)$$

where f is the friction factor for a fully developed pipe flow, ρ_a and v_a are the density and tangential velocity of the uranium-hydrogen mixture, respectively, and the subscript a refers to the boundary-layer edge of the arc region. The friction factor f is calculated from the Reynolds number $Re = \rho_a v_a D/\mu_a$, (where D is the cavity diameter and μ is the viscosity) by using the relationship (ref. 7)

$$\frac{1}{\sqrt{f}} = 4.0 \log_{10}(Re\sqrt{f}) - 0.4$$

The viscosity μ is obtained from the work of Yos (ref. 8). The multiplicative factor of 2 for τ_w is an empirical correction factor obtained from the experimental results of reference 5; this accounts for the fact that the $\mathbf{J} \times \mathbf{B}$ force is applied in the vicinity of the wall and tends to increase the velocity gradient at the wall. In order to obtain the total friction, the resulting skin friction τ_w is multiplied by the effective total surface area which is taken as the sum of the cylinder surface area and the area of one end wall.

(3) The wall heat transfer rate is approximated by the formula for a fully developed turbulent pipe flow, which is (ref. 7)

$$q = \frac{0.023\, k\, Re^{0.8}\, Pr^{0.6}}{D}(T_{aw} - T_w)$$

The thermal conductivity k, the Reynolds number Re, and the Prandtl number Pr are estimated conservatively (i.e., large) and calculations are based on the frozen properties in the hot region (ref. 8). The wall temperature T_w is taken as 2500° K, and the adiabatic wall temperature T_{aw} is

$$T_{aw} = T_a\left[1 + Pr^{0.33}\left(\frac{\gamma - 1}{2}\right)M_a^2\right]$$

in which T_a is the temperature at the hot region and M_a is the Mach number of the mixture in the hot region. When applied to the experimental results of reference 5, the above formulas tend to overestimate the true heat transfer rate slightly. Therefore, the present method of calculating the heat transfer rate is considered to be conservative.

The radiation is neglected in the calculation of the heat transfer rate to the cylinder wall in comparison with the convective heat transfer rate. The works of Krascella (ref. 9) and Kesten and Krascella (ref. 10) indicate that the absorption coefficients for both hydrogen and uranium gas, under the condition considered here in the wavelength range of importance, are greater than 20 cm^{-1}. This means that the direct irradiation by the gas onto the wall surface would not be more than that of a blackbody radiating at the local temperature at a point 0.5 mm away from the wall. Since the local gas temperature at a point this close to the wall should not be substantially greater than the assumed wall-surface temperature of 2500° K, the direct irradiation would be comparatively very small, that is, on the order of 0.5 kW/cm^2 or $\frac{1}{10}$ of the convective heating rate. Radiation energy can also be transmitted indirectly via conversion into kinetic energy of the gas, and this leads to an increase in the convective heat transfer rate. Such a process resembles the laminar diffusion process, and the magnitude of the energy transfer rate by such a process is comparable to that of the convective heat transfer rate in a laminar boundary layer, which is much smaller than the turbulent convective heat transfer rate. Likewise, the heat released in the hydrogen molecule formation and uranium ion-electron recombination is neglected as being small compared with the turbulent convective heat transfer rate.

(4) The radiator surface temperature is assumed to be 1200° K and the emissivity, 0.7. The average radiator weight is taken as 15 kg/m^2 of the radiator area, which is an average of values predicted in the past (refs. 11 and 12).

(5) The moderator is assumed to be made by a composite of graphite and beryllium oxide with a volume V_m calculated from an empirical formula

$$V_m = 1.11D^3 + 2.78D^2 + 5.46D + 3.6 \text{ m}^3$$

which corresponds to a moderator thickness of 1 m for a 3-m-diam cavity and 1.7-m thickness for a 7-m-diam cavity. The formula used here matches the moderator requirements determined from critical mass calculations for cavity reactors (refs. 13 and 14).

(6) The weights of the remaining miscellaneous parts are estimated from the dimensions and materials required to withstand the expected stress load and heat-transfer characteristics. The details of such

calculations are omitted here because the contribution is only 15 percent of the total weight (see table I).

Assumptions (1) through (6) are believed to be conservative, except for assumption (3) for the heat transfer rate. Overestimating the heat transfer rate results in an increase in thrust because in the calculations the overall efficiency is assumed to be fixed. Thus, an overestimation of the heat-transfer rate does not necessarily lead to a conservative estimate of the overall performance. Furthermore, a possibility exists of a reduction in heat transfer rate by transpiration cooling.

Under the above assumptions, the operating characteristics of a prototype MHD gas-core nuclear rocket engine were calculated over a range of conditions by varying the chamber diameter, the hydrogen-to-uranium mass-flow rate ratio, the chamber pressure, and the peak rotation speed. The results of the calculation are shown in table I for three typical cases representing a high-, a medium-, and a low-performance design.

As seen in the table, the MHD power required to maintain the rotation is of the order of only 3 percent of the power rejected by the radiator. This power-requirement prediction is significantly lower than that predicted in references 15 and 16. A small MHD power is required in the present configuration because the $\mathbf{J} \times \mathbf{B}$ force must overcome only the skin friction; in the configurations of references 15 and 16, which require the diffusion of the propellant gas through the fuel in addition to the power used to overcome friction, MHD power was consumed in accelerating the injected propellant gas to a high rotating speed.

The calculation shows that, for a fixed quantity of uranium, there exists a set of optimum values of chamber radius, pressure, and rotation speed that minimizes the wall heat transfer rate; any deviation from the optimum condition increases the wall heat transfer. The minimum heat transfer rate under such an optimum design condition is a function mainly of the quantity of uranium contained. An increase in the moderator thickness therefore leads to a reduction in heat transfer rate; this is the reason why the weights of the moderator shown in table I are so large.

It is evident from table I that the proposed MHD gas-core nuclear rocket scheme has three major disadvantages, namely, (1) high wall heat transfer rate, (2) large radiator area required, and (3) large cavity structure; disadvantages (2) and (3) are the main causes for the low thrust-to-weight ratio, which is of the order of 1:100. These are the inherent difficulties of a gas-core nuclear rocket that allows the direct contact of high-velocity uranium gas with the wall. In particular, it would be quite difficult, although not inconceivable, to absorb the calculated heating rate of 5 kW/cm^2. Therefore either a considerable improvement in the wall-cooling technology has to be achieved or transpiration cooling must be incorporated.

Transpiration cooling at the wall is attractive not only because it is an effective method of reducing convective heat transfer rates but also because of other possible advantages. The injection of propellant gas would reduce the concentration of uranium in the boundary layer and hence should reduce the loss of uranium through the wall boundary-layer flow. The reduction in the heat transfer to the wall would increase the efficiency of the engine by increasing the rocket thrust and reducing the required radiator area, thereby leading to an improved thrust-to-weight ratio. Such a transpiration is known to be more effective in cooling than high-speed tangential gas injection for the same amount of injected mass, especially at high pressures (ref. 17). The acceleration of the injected gas in a rotating motion would be caused strictly by the MHD force and would result in the consumption of additional electrical power. Because the mass of propellant injected for transpiration cooling would be a relatively small fraction of the total flow, such an addition to the MHD powerload should not appreciably increase the total MHD power requirement, but its influence on the species separation is, as yet, unknown. The expected advantages of propellant transpiration should, therefore, be weighed against any negative effect it may have on the species separation. Likewise, a slight increase in the radiator temperature would reduce the radiator area greatly because of the T^4 proportionality of surface radiation. A further study on the attainable radiator surface temperature is desirable.

As is apparent from table I, an advantageous feature of the present concept is the capability of achieving critical masses in the chamber at lower pressures than those required for the pure fluid-

vortex concepts. The low operating-chamber pressure is afforded mainly because of the large concentration difference in uranium mole fraction between the centerline and the wall. Also, the bulk of the fuel gas is located near the cavity wall and therefore occupies a large fraction of the total cavity volume as compared with the fluid-vortex rocket concepts in which the fuel gas is in the centerline region.

In the present scheme the propellant gas moves slowly, with a resulting residence time of 10 to 100 msec within the chamber cavity (i.e., at least an order of magnitude longer than in the fluid-vortex scheme). This allows the temperature of the propellant gas to approach the fuel gas temperature more closely. The required peak temperature of the fuel gas is, therefore, lower than that in the fluid-vortex model, thus alleviating many problems associated with the high fuel temperature such as an appreciable increase in the pressure level and uncertainty in the thermodynamic properties of multiply ionized uranium.

The third important advantage of the present concept is that the uranium is located near the moderator-reflector wall. Since the peak thermal neutron flux will occur within the moderator, this arrangement locates the uranium fuel at the position of maximum neutron flux within the cavity proper. This should permit a more efficient use of the moderator than is possible with the configurations involving a central fuel region and thus lead to a reduction in the critical mass.

Finally, there exists a possibility that the present scheme could be used in combination with the other gas-core nuclear rocket schemes. For instance, one could utilize the MHD centrifuge merely to reclaim the fuel gas from the rocket exhaust. The exhaust from a vortex-stabilized rocket chamber would pass through the MHD chamber where the uranium gas is compressed near the wall and is then recirculated back to the main fission chamber through a small passage between the two chambers via a compressor. Because the MHD chamber would not contain a critical mass of uranium, the pressure and wall heating rate in the MHD chamber could be maintained at lower, more tolerable levels.

CONCLUSIONS

1. There is experimental evidence that, in the absence of a propellant gas flow, a solid-body rotation can be achieved by means of MHD-driven rotation in a unique axial-J, radial-B configuration that results in a significant degree of species separation.

2. By assuming that the propellant flow does not affect the separation characteristics, a direct application of the MHD centrifuge principle would result in a thrust-to-weight ratio on the order of 1:100 based on the engine weight alone.

3. The MHD nuclear rocket concept offers the advantages of low operating pressure, low uranium fuel temperature, and low critical-mass requirement.

4. The most significant disadvantages of the MHD rocket concept are the high wall heat transfer rates, the large radiator area, and the large chamber diameter. In particular, the high wall heat transfer rate is the primary obstacle. The use of transpiration cooling seems inevitable.

5. Additional experiments are needed to investigate the effects of axial flow and transpiration cooling on the species separation characteristics. A comprehensive study is required also to determine the radiative heat transfer characteristics.

REFERENCES

1. Rom, F. E.: Advanced Reactor Concepts for Nuclear Propulsion. Astronautics, vol. 4, no. 10, Oct. 1959, pp. 20–22.
2. Pivirotto, T. J.: Mass-Retention Measurements in a Binary Compressible Vortex Flow. TR 32-864, Jet Propulsion Lab., June 15, 1966.
3. McLafferty, G. H.: Survey of Advanced Concepts in Nuclear Propulsion. J. Spacecraft Rockets, vol. 5, no. 10, Oct. 1968, pp. 1121–1128.
4. Clark, J. W.; Johnson, B. V.; Kendall, J. S.; Mensing, A. E.; and Travers, A.: Open-Cycle and Light-Bulb Types of Vortex-Stabilized Gaseous Nuclear Rockets. J. Spacecraft Rockets, vol. 5, no. 8, Aug. 1968, pp. 941–947.
5. Love, W. L.; and Park, C.: An Experiment on the MHD-Driven Flow for a Gas Core Nuclear Rocket. Paper No. 69-727, AIAA, 1969.
6. Lewellen, W. S.; Ross, D. H.; and Rosenzweig, M. L.: Binary Diffusion in a Confined Vortex. AIAA J., vol. 4, no. 3, Mar. 1966, pp. 396–405.
7. McAdams, W. H.: Heat Transmission. Third ed., McGraw-Hill Book Co., Inc., 1954.

8. Yos, J. M.: Transport Properties of Nitrogen, Hydrogen, Oxygen and Air to 30,000° K. AVCO/RAD TM–63–7, Mar. 1963.
9. Krascella, N. L.: Tables of the Composition, Opacity, and Thermodynamic Properties of Hydrogen at High Temperatures. (Rept. B–910168–1, United Aircraft Res. Lab., Sept. 1963.) NASA SP–3005, 1963.
10. Kesten, A. S.; and Krascella, N. L.: Theoretical Investigation of Radiant Heat Transfer in the Fuel Region of Gaseous Nuclear Rocket Engine. NASA CR–695, 1967.
11. Parker, K. O.; and Stone, R. A.: Spur High-Temperature Space Radiator. In: Power Systems for Space Flight. Progress in Astronautics and Aeronautics, Vol. 11, M. A. Zipkin and R. N. Edwards, eds., 1963, pp. 505–533.
12. Krebs, R. P.; Winch, D. M.; and Lieblein, S.: Analysis of a Megawatt Fuel Direct Condenser-Radiator. In: Power Systems for Space Flight. Progress in Astronautics and Aeronautics, Vol. 11, M. A. Zipkin and R. N. Edwards, eds., 1963, pp. 475–504.
13. Hyland, R. E.; Ragsdale, R. G.; and Gunn, E. J.: Two-Dimensional Criticality Calculations of Gaseous-Core Cylindrical-Cavity Reactors. NASA TN D–1575, 1963.
14. Herwig, L. O.; and Latham, T. S.: Nuclear Characteristics of Large Reflector-Moderated Gaseous-Fueled Cavity Reactors Containing Hot Hydrogen. AIAA J., vol. 5, no. 5, May 1967, pp. 930–937.
15. Romero, J. B.; Fuel Containment in the Gaseous-Core Nuclear Rocket by MHD-Driven Vortices. AIAA J., vol. 2, no. 6, June 1964, pp. 1092–1099.
16. Johnson, K. P.: A Plasma-Core Nuclear Rocket Utilizing a Magnetohydrodynamically-Driven Vortex. AIAA J., vol. 4, no. 4, Apr. 1966, pp. 635–643.
17. Pappas, C. C.; and Okuno, A. F.: The Relation Between Skin Friction and Heat Transfer for the Compressible Turbulent Boundary Layer With Gas Injection. NASA TN D–2857, 1965.

DISCUSSION

Tang: Table I, which gives the estimated weights and characteristics, shows values different from those you gave in the preliminary abstract. There seems to be a 50-percent improvement in the thrust-to-weight ratio. Is this due to larger thrust or is it due to larger pressure?

Park: It is due to the larger thrust. The earlier version was calculated somewhat arbitrarily but the newer version is based on our experiment and so we have more faith in it.

Keyes: What variation in the radial magnetic field strength would you have along the axis? This is a cusp geometry. The radial field is at the midplane and the axial field is at the ends and this would lead to strong variations in the driving force and would tend to give secondary flows, I should think, and a very complicated flow pattern. What could this be expected to do to the separation and to the velocity of the profile?

Park: The arc is located as outlined in my presentation. We have some experimental data that show that.

Russell: Are you saying that the arc in the main field interacts so as to intersect the field lines going outward away from the center plane?

Park: We do not know what is happening in this region where the secondary electrical currents are flowing.

Page intentionally left blank

SESSION III

PROPERTIES OF URANIUM PLASMAS

Chairman: **T. D. Wilkerson**

A. *THEORETICAL DETERMINATIONS*

Current Status of the Analysis of the Optical Spectra of Uranium[1]

D. W. Steinhaus, L. J. Radziemski, Jr., and R. D. Cowan

Los Alamos Scientific Laboratory of the University of California

Uranium has one of the most complex optical spectra of any element. It is estimated that over 300 000 lines of U I and U II can be observed and measured with modern, high-resolution apparatus. New high-resolution spectroscopic systems and rapid precision data-reduction techniques are being used at the Los Alamos Scientific Laboratory to produce a new description of the uranium spectra. The present line list contains information on about 25 000 lines, of which 13 000 have a wave number accuracy better than 0.01 cm^{-1}. About 10 100 lines have been classified to 1050 levels of U I and U II, but only a few of the levels have been assigned to an electron configuration. Although the numbers of classified lines and levels appear large, much experimental work remains to be done before adequate descriptions of the uranium spectra exist. Some theoretical calculations have been made of the energy level structure of the low-lying configurations of U I through U VI. Agreement with known experimental levels of U I and U II is reasonably good for the lower levels. These calculations lead to ionization potentials for U I through U V which are, respectively, 6.22 ± 0.5, 10.6 ± 1, 18.9 ± 1, 32.1 ± 2, and 47.1 ± 2 V. Both theoretical and experimental work are continuing and will provide a greatly expanded analysis of the optical spectra of uranium.

From the description and analysis of optical spectra, one obtains the atomic properties of the elements in great detail and with very high accuracy. The atomic energy levels, electron configurations, and electron binding energies are determined along with the particular energy levels responsible for each spectral line. The physical and chemical properties of each element depend on these fundamental quantities. The thermodynamic properties of hot gases can be calculated well only when these quantities are known, and the design of spectroisotopic and spectrochemical procedures requires their use.

When one works with uranium plasmas the properties of all elements in the plasma are needed. We shall herein describe the present status of the description and analysis of the optical spectra of uranium by using material in the published literature (refs. 1 to 27)[2] and unpublished material from the Los Alamos Scientific Laboratory (LASL) and the Laboratoire Aimé Cotton, Orsay, France. We shall first outline what is known about this spectrum, and then we shall describe the work being done now which will result in a greatly expanded description and analysis of the optical spectra of uranium.

PRESENT STATUS OF KNOWN PROPERTIES OF THE URANIUM SPECTRUM

Experimental

Uranium has one of the most complex optical spectra of any element. Figure 1 shows a comparison of the uranium spectrum with that of iron. The spectrum of iron is commonly considered to be quite complex, but it can be seen that the uranium spectrum contains many more lines than does that of the iron. Table I shows a numerical comparison of the uranium, iron, and hydrogen spectra. The

[1] Work performed under the auspices of the U.S. Atomic Energy Commission.

[2] The authors also used information in a private communication received from J. R. McNally, Jr., in 1953 which listed published and unpublished values originally measured for refs. 1 and 4.

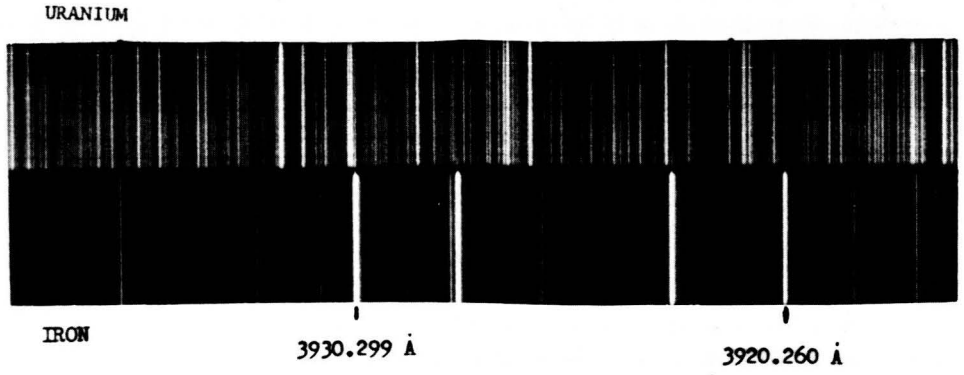

FIGURE 1.—*Uranium and iron spectra near 3930 Å.*

analysis of the hydrogen and iron spectra is almost complete. Note that the Massachusetts Institute of Technology (MIT) tables (ref. 1) list only a few more lines from uranium than from iron. Many uranium lines were missed when the MIT tables were compiled because modern high-resolution apparatus was not available. Over 25 000 uranium lines are known now and it is estimated that over 10 times this many can be observed and measured. The number of classified uranium lines is much smaller than the estimated number of lines. Note that the estimated number of lines is almost 3 times that contained in the MIT tables for all elements. In addition, they can be measured with a wave number accuracy 10 times better than that of most lines in the MIT tables.

Figure 2 shows the range of the known levels of U I and U II. The actual levels are not drawn because of their large number. Transitions, which give rise to spectral lines, take place only between odd and even levels. Only the wave number and J-value is known for most even levels. In addition to these values, the configuration and term of most low odd levels are known. The ionization potential of U I is known to be 6.11 eV (or about 49 000 cm^{-1}) from the electron impact experiments of J. B. Mann (ref. 28) and others (ref. 29). The ionization potential of U II is calculated to be about 10.6 eV or 87 000 cm^{-1}. The next four figures show the known levels in the low odd configurations. Figure 3 contains the known levels in the ground configuration of U I, $5f^3\ 6d\ 7s^2$. The dotted line connects the lower-state (LS) multiplets, as designated presently from experimental data. The known

TABLE I.—*Numerical Comparison of Hydrogen, Iron, and Uranium Spectra*

Element	Number of lines in MIT table (ref. 1)	Approximate number of lines known	Approximate number of lines classified	Approximate number of levels found	
H I	21	110	100	40	Analysis of spectra almost complete
Fe I	4 757	4 900	4 860	464	
Fe II		2 160	2 000	360	
U I	5 238	[a]25 380	7 800	800	Analysis of spectra far from complete
U II			2 300	250	
All elements	110 000				

[a] With modern high-resolution apparatus, it is estimated that 300 000 lines can be observed and measured.

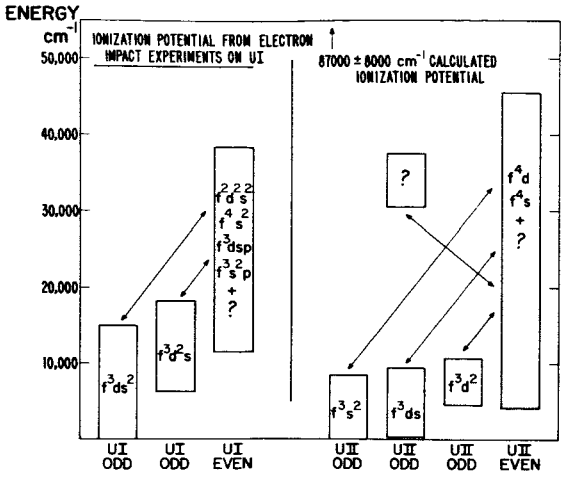

FIGURE 2.—*Range of known levels of uranium I and II.*

levels plus a few predicted levels for U I $5f^3\ 6d^2\ 7s$ are shown in figure 4. Several thousand more levels remain to be found in these two configurations. Figure 5 shows the levels known in the ground configuration $5f^3\ 7s^2$ of U II. The ground level of U II is the $^4I^0_{9/2}$ level. The known levels of the configuration $5f^3\ 6d^2$ of U II are also shown. Figure 6 shows the known levels plus a few predicted levels for the configuration $5f^3\ 6d\ 7s$ of U II. Again, several thousand more levels remain to be found in these odd configurations.

Figure 7 shows the range of measured isotope shifts for U I and U II levels. Plotted on the y-axis is the level value for ^{238}U minus the level value for ^{235}U. The isotope shift of a spectral line is the dif-

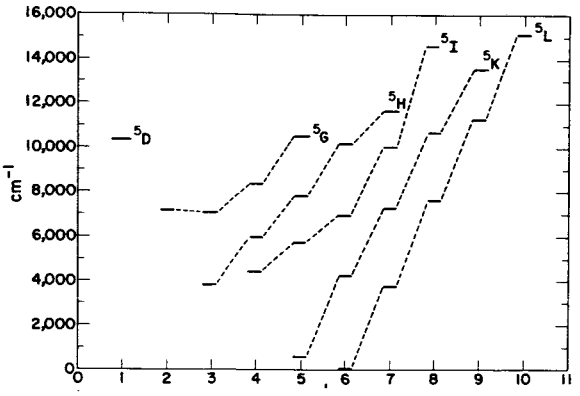

FIGURE 3.—*Low energy levels of U I* $5f^3\ 6d\ 7s^2$ *(odd).*

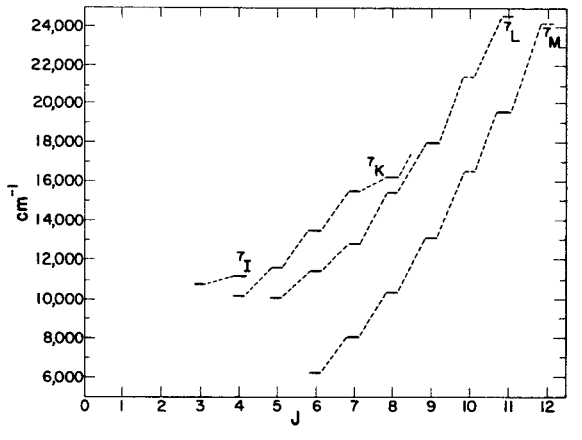

FIGURE 4.—*Low energy levels of U I* $5f^3\ 6d^2\ 7s$ *(odd).*

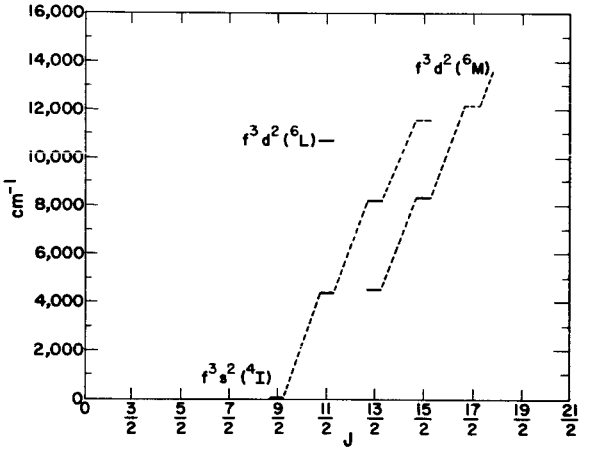

FIGURE 5.—*Low energy levels of U II* $5f^3\ 7s^2$ *(odd) and* $5f^3\ 6d^2$ *(odd).*

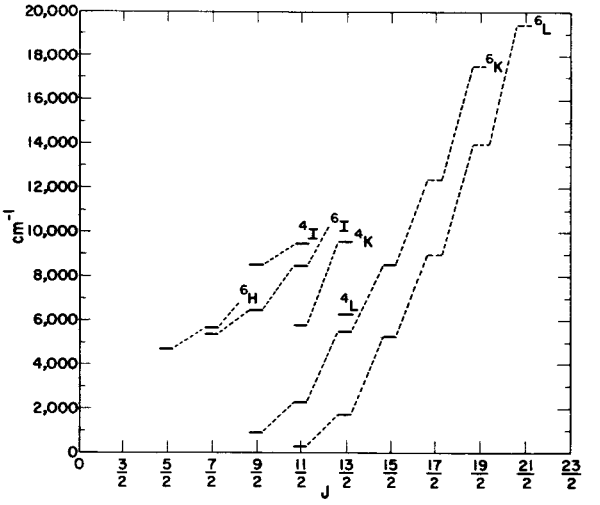

FIGURE 6.—*Low energy levels of U II* $5f^3\ 6d\ 7s$ *(odd).*

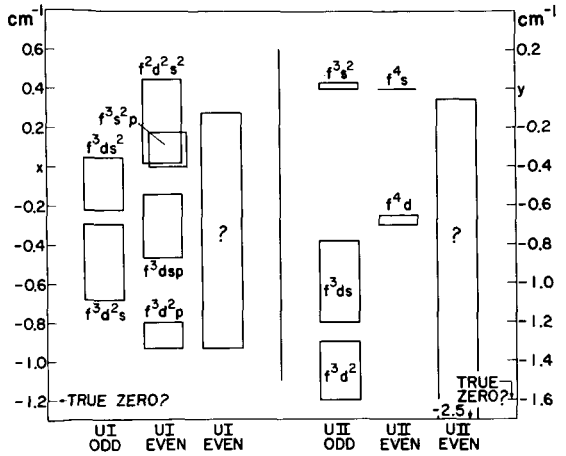

FIGURE 7.—*Range of isotope shifts for ^{238}U minus ^{235}U for U I and U II levels.*

ference between the shifts of the two levels giving rise to the spectral line. Thus it can be seen that shifts as large as 1.4 cm^{-1} are possible for U I lines and that the line shifts can go toward larger and smaller wave numbers. For U II the isotope shift can be as large as 2.5 cm^{-1}. The line most commonly used for isotope analysis of uranium (the line at 23553.96 cm^{-1} or 4244.37 Å) has a shift of 1.43 cm^{-1}.

The true isotope shift is defined with respect to the ionization limit, so the shift of the low levels will be greater than that of the high levels. It would be desirable to know exactly the absolute shift of the ground-state level so that the absolute shift of all the other levels could be obtained. This is very difficult to obtain precisely because of uncertainty in the limit, so the ground-state shift is arbitrarily set at zero as shown in the figure, and the shifts of the other levels are calculated accordingly. A guess at the "true zero" is marked for each spectrum; the value for the ground level of U I is labeled x and the value for the ground level of U II is labeled y. Approximate values for x and y are 1.2 cm^{-1} and 1.6 cm^{-1}. Uranium was the first spectrum in which the isotope shift values of many lines were used to extend and justify the analysis (ref. 14).

By using the known levels of uranium, a calculation of the ideal gas thermodynamic functions of uranium has been made and is available in a LASL report by Feber and Herrick (ref. 30). A revision of this report is in progress.

Theoretical Calculations

In order to provide additional evidence for checking the present empirical identification of energy levels and to help to extend the analysis in the future, some preliminary theoretical energy level calculations have been made. The calculations are based on the familiar Slater-Condon theory and involve two steps:

(1) One-electron radial wave functions are computed by solving an approximate form of the Hartree-Fock equations (ref. 31). These provide an absolute energy for the center of gravity of the electronic configuration involved (including a rough correction for relativistic effects) and also numerical values of the radial integrals which describe the electrostatic and spin-orbit interactions among the electrons.

(2) The center of gravity and radial integrals are used as input for a computer program which calculates the detailed energy level structure of the configuration together with the theoretically predicted composition of each level (refs. 32 and 33).

Figure 8 depicts schematically the calculation

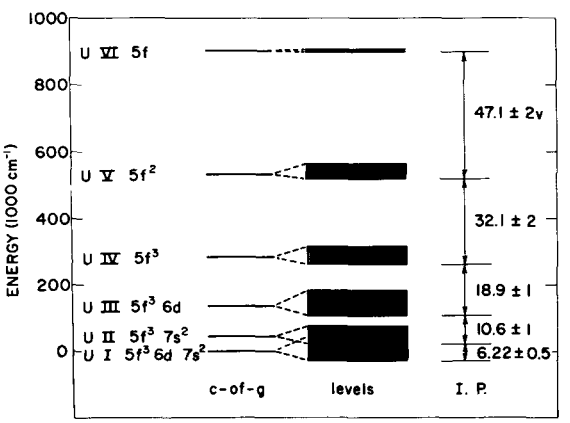

FIGURE 8.—*Energy-level range for ground-state configurations of U I through U VI and ionization potentials of U I through U V.*

procedure and the results for the ground-state configurations of U I through U VI. Byproducts of these calculations are values for the various ionization potentials shown in figure 8 (the uncertainties are primarily due to uncertainties in the relativistic corrections). The values are in good agreement with

U I experimental results (refs. 28 and 29) and with some theoretical calculations (ref. 34) but not with others (ref. 35).

An indication of the extreme complexity of the energy level structure of uranium is that levels, even of the ground configuration of U I, extended above the first ionization limit (i.e., above the ground level of U II) (see fig. 8). The computed and observed structure of the lowest levels of U I are compared in figure 9. The basic agreement is good, except

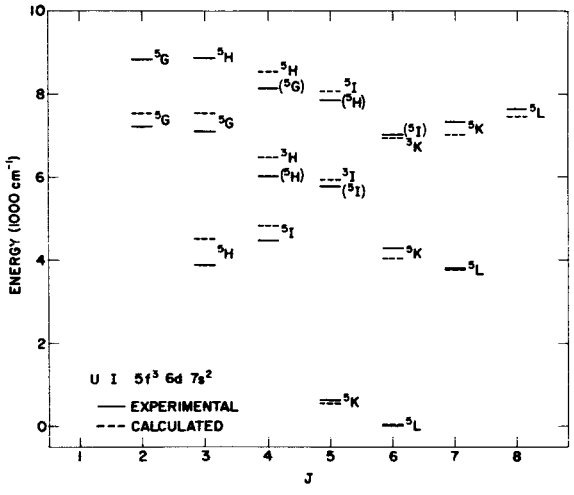

FIGURE 9.—*Observed and computed positions of low U I levels.*

that theory suggests that some of the empirically assigned level designations (shown in parentheses) should probably be changed.

Figure 10 shows a similar comparison for the low levels of the two lowest configurations of U II. (The energy scales have been adjusted to give agreement between theory and experiment for the lowest level of each configuration.) Figure 11 shows the lowest computed levels of U III, for which no experimental levels are yet known.

The difficulty in assigning meaningful designations to the levels of uranium is illustrated in table II which gives the computed compositions of the five lowest $J=6$ levels of U I $5f^3\ 6d\ 7s^2$ by using both an LS and a Jj basis representation. Although the lowest couple of levels can be given nonarbitrary LS names (for reasons discussed by Judd in ref. 36), successively higher levels quickly become hope-

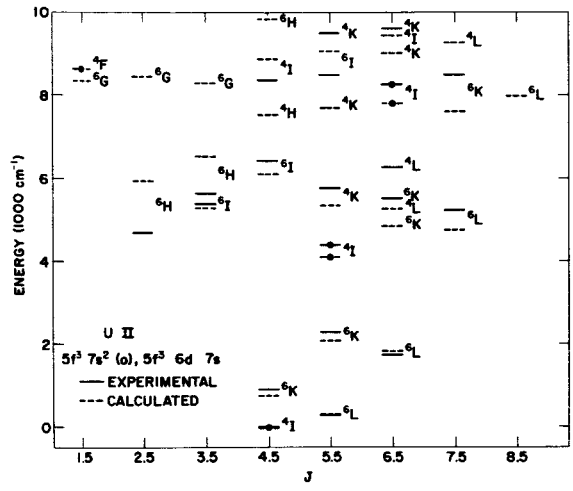

FIGURE 10.—*Observed and computed positions of low U II levels.*

lessly impure mixtures of the various LS basis states. Normally one expects Jj labels to be more appropriate than LS labels for heavy elements, and this is true to a slight extent for the five low levels in question (the average purity being 62 percent for Jj versus 52 percent for LS). Overall, however, the compositions are a jumbled mess, and the average purity of all levels is a low 30 percent for either representation.

It is doubtful that a great deal more can be done in the way of correlating additional experimental

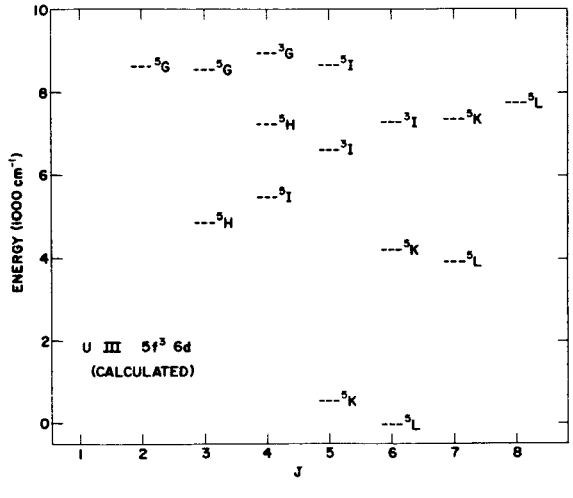

FIGURE 11.—*Calculated positions of low U III levels.*

TABLE II.—*Computed Compositions of the Five Lowest J=6 Levels in U I $5f^3$ 6d $7s^2$ (44 levels)*

E_{calc}, cm^{-1}	LS composition, %/100	*Jj* composition, %/100
0	$0.76(^4I)\,^5L + 0.13(^2H)\,^3K + 0.06(^4I)\,^3K$	$0.80(^4I_{7/2})\,d_{3/2} + 0.13(^2H_{9/2})\,d_{3/2}$
3978	$0.86(^4I)\,^5K + 0.06(^2H)\,^3I + 0.04(^4I)\,^3I$	$0.59(^4I_{11/2})\,d_{3/2} + 0.31(^4I_{9/2})\,d_{5/2}$
6903	$0.20(^4I)\,^3K + 0.17(^4I)\,^3I + 0.14(^4I)\,^5L$	$0.36(^4I_{9/2})\,d_{5/2} + 0.24(^4I_{11/2})\,d_{3/2}$
10462	$0.55(^4I)\,^5I + 0.11(^4I)\,^3I + 0.08(^2H)\,^3K$	$0.68(^4I_{11/2})\,d_{5/2} + 0.10(^2H_{9/2})\,d_{3/2}$
10973	$0.12(^4I)\,^5H + 0.23(^4I)\,^5I + 0.15(^4I)\,^3K$	$0.69(^4I_{13/2})\,d_{3/2} + 0.04(^4I_{11/2})\,d_{5/2}$
Av (low 5)	0.520	0.624
Av (44)	0.292	0.313
Av (all *J*)	0.293	0.290

levels with specific LS or *Jj* basis states or even with definite configurations. However, additional refined calculations are planned in the future to aid the experimental work as much as is feasible.

PRESENT STATUS OF MEASUREMENTS

One of the first goals of the present experimental program as LASL is a new description of the uranium spectra. Much improvement in measurement and analysis has been obtained, but much remains to be done. Table III shows the uranium lines now known to exist between two classified uranium lines. The present estimate is that a total of 300 000 lines can be observed and measured with modern high-resolution apparatus. This is about 12 times the

TABLE III.—*Typical Number of Unclassified Uranium Lines Being Found Between Two Classified Uranium Lines*

Measured on spectrogram		Measured on interferogram		Calculated from known terms of U I		
σ, cm^{-1}	I	Fraction	I	Fraction	Upper term	Lower term
24560.396	595	0.396	28	0.400	24 560	0
.586	401					
24561.061	448					
.607	501					
.947	463	.950	20			
24562.032	420					
.097	418					
.334	404					
.444	393					
.638	416					
.820	457					
.861	442					
24563.033	620	.032	33			
.214	437					
.427	394					
.632	426					
.726	351					
.862	396					
.985	390					
24564.115	365					
.443	408					
.595	509	.591	22			
.818	425					
.999	428					
24565.215	609	.212	31	.211	28 840	4275

known lines and 30 times the number of lines classified.

Table IV shows that many more lines are being measured on LASL spectrograms than were measured at MIT[3], NBS[3] (also ref. 17), or AERE (refs. 16, 18, and 20). Table V shows a test of the LASL and MIT[3] wave number precision. For this test the difference between the wave number values of two lines from the same upper level and ending on the two lowest levels of U I or U II are shown. This value should be a constant. The variation is a test of the wave number precision. The root-mean-square deviation of the LASL data is 12 (or 26) times less than the root-mean-square deviation of the MIT data. Figure 12 shows a different test of the wave number precision in the present uranium line list. The cluster of points between 20 000 and 27 000 cm^{-1} represents LASL data. Points outside this range (and a few points inside it) represent MIT[3], NBS[3] (also ref. 17), or AERE (refs. 16, 18, and 20) data. The superiority of the LASL data is clear. Figure 13 shows the same thing for isotope shift data in the present uranium line list. These data are from AERE (refs. 12, 15, 16, 18, and 20), France (refs. 14, 19, 21, and 22), and Russia (refs. 10 and 11). Again it is obvious that a considerable improvement in isotope shift values will be achieved with isotope shift measurements at LASL.

Because of the very large number of lines to be measured and the high accuracy desired, considerable effort has been expended to apply automation to the measurements. Figure 14 shows the LASL automatic comparator (ref. 37). This comparator uses a digital computer to do the complete job of finding and measuring each spectral line for position, wave number, intensity, and shape. Figure 15 shows a better view of a spectrum plate ready for

[3] Private communication received from J. B. McNally, Jr., in 1953 which listed published and unpublished values originally measured for refs. 1 and 4.

TABLE IV.—Wave Numbers of Some Uranium Spectral Lines

LASL spectrograms			LASL interferograms			MIT spectrograms			NBS spectrograms			AERE spectrograms		
σ, cm^{-1}	I_{Ac}	R	Fraction	I_e	R	Fraction	I_a	I_s	Fraction	I_a	I_s	Fraction	I_{va}	I_e
24705.400	458	0	-------	----	----	-------	----	----	-------	----	----	-------	----	----
.442	442	8	-------	----	----	-------	----	----	-------	----	----	-------	----	----
.509	461	8	-------	----	----	-------	----	----	-------	----	----	-------	----	----
.584	516	0	0.579	23	0	0.63	5	5	-------	----	----	0.67	35	75
.761	480	0	.763	22	0	-------	----	----	-------	----	----	-------	----	----
.835	435	8	-------	----	----	-------	----	----	-------	----	----	-------	----	----
24706.015	381	0	-------	----	----	-------	----	----	-------	----	----	-------	----	----
.276	529	0	.275	23	0	.25	3	5	-------	----	----	.41	35	----
.452	492	0	.460	21	0	-------	----	----	-------	----	----	-------	----	----
.561	411	8	-------	----	----	-------	----	----	-------	----	----	-------	----	----
.636	390	0	-------	----	----	-------	----	----	-------	----	----	-------	----	----
.773	434	0	.773	15	0	-------	----	----	-------	----	----	-------	----	----
24707.252	380	0	-------	----	----	-------	----	----	-------	----	----	-------	----	----
.385	379	8	-------	----	----	-------	----	----	-------	----	----	-------	----	----
.471	445	0	.462	20	0	-------	----	----	-------	----	----	-------	----	----
.673	411	0	-------	----	----	-------	----	----	-------	----	----	-------	----	----
.740	448	0	.737	17	3	-------	----	----	-------	----	----	.69	10	----
.856	382	8	-------	----	----	-------	----	----	-------	----	----	-------	----	----
24708.049	431	0	-------	----	----	-------	----	----	-------	----	----	-------	----	----
.094	417	0	-------	----	----	-------	----	----	-------	----	----	-------	----	----
.178	397	0	-------	----	----	-------	----	----	-------	----	----	-------	----	----
.236	387	8	-------	----	----	-------	----	----	-------	----	----	-------	----	----
.312	387	8	-------	----	----	-------	----	----	-------	----	----	-------	----	----
.374	405	8	-------	----	----	-------	----	----	-------	----	----	-------	----	----
.462	491	0	.468	21	0	-------	----	----	-------	----	----	-------	----	----
.555	534	0	.553	22	0	-------	----	----	0.54	1	–	.54	10	5

TABLE V.—*Difference in Energies of Two Lowest Energy Levels from Difference in Energies of Pairs of Spectral Lines from Common Upper Energy Levels*

U I		U II	
LASL, cm^{-1}	MIT, cm^{-1}	LASL, cm^{-1}	MIT, cm^{-1}
620.3204	620.35	289.0397	288.99
.3220	.33	.0399	289.04
.3214	.41	.0408	.03
.3223	.34	.0397	.05
.3206	.32	.0366	.06
.3227	.32	.0381	.00
.3186	.50	.0415	.01
.3228	.48	.0393	.09
.3291	.33	.0417	.08
.3222	.36	.0441	.05
Av = 620.3222	620.37	289.0401	289.05
Rms = 0.0023	0.06	0.0019	0.022
1 to 26		1 to 12	

measurement. To prepare the information on the spectrum plate for the computer, the transmission values at equal intervals along the spectrum are read and placed on an IBM compatible magnetic tape. The computer takes the data from this tape and measures each spectral line. One of the computer outputs is a microfilm plot as shown in figure 16. Plotted are 20 data readings per x-division, or a total of 600 readings. The reading interval was 5 μ, so this figure shows a 3-mm interval along the original spectrum plate. The y-axis is relative spectral intensity on a logarithmic scale. The wave number value and relative intensity of each line found by the computer are marked with a square, and the wave number value is printed below the line. Above

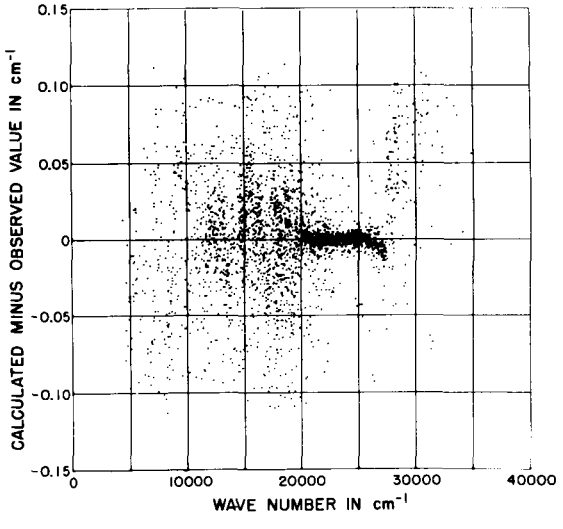

FIGURE 12.—*Calculated minus observed wave number values of uranium lines against wave number of each U I line in reference 25.*

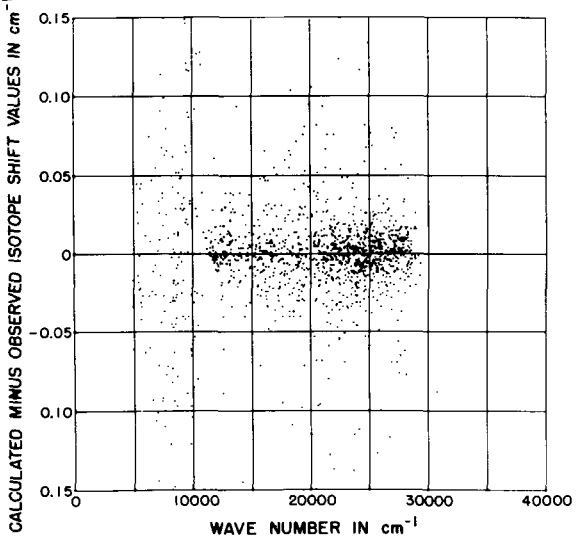

FIGURE 13.—*Calculated minus observed isotope shift values of uranium lines versus wave number of each U I line in reference 25.*

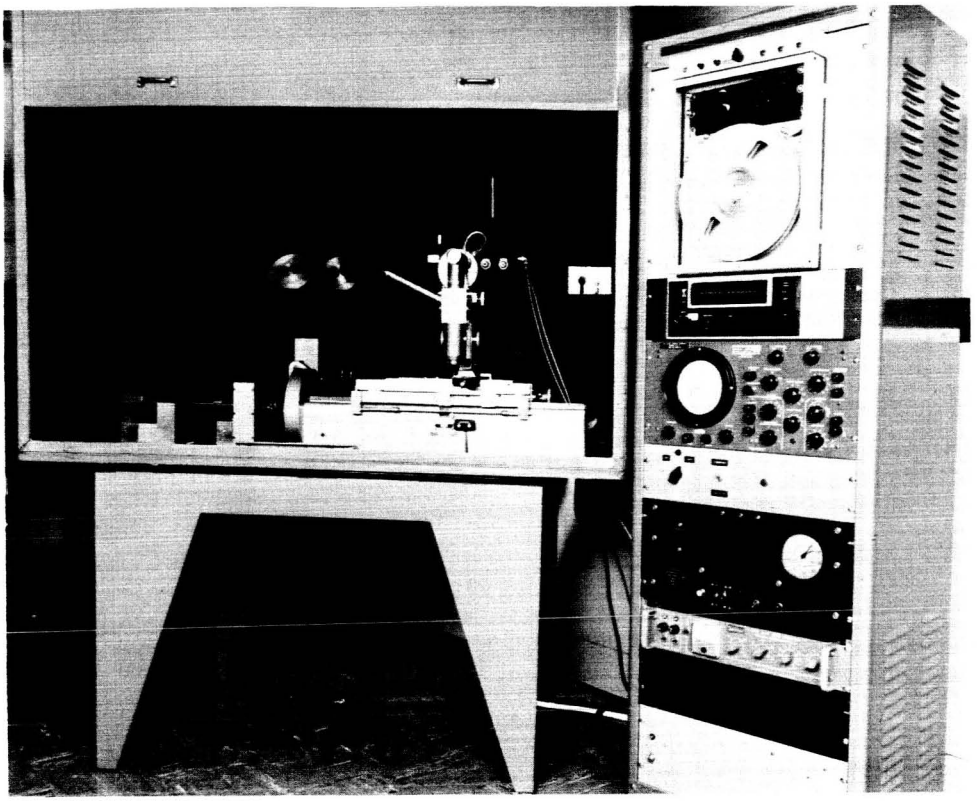

FIGURE 14.—*The LASL automatic comparator.*

the line is a remarks number. A zero indicates that it is a "good" line with a good measurement. A 9 indicates that the computer made an attempt to find a line at this place but failed for one of several reasons. An 8 means either that the line measured is on the side of another line or that the computer had some kind of trouble with the measurement. In any case, the measured values for "8" lines are considered to be poorer than those from other lines. Other remarks numbers (1, 2, or 4) indicate shaded lines (and the wave number direction of the shading) and wide lines. This figure is from a run on a uranium emission spectrogram. Figure 17 shows that the comparator works equally well on absorption spectrograms; also, the apparatus can be used directly on a scanning spectrometer, thus eliminating the need for a photographic record of the spectrum. This automatic comparator plus a number of other devices and computer programs are being used for precision wave number and intensity measurements.

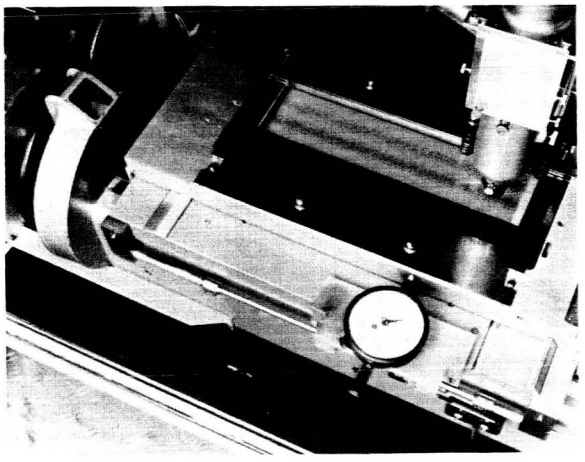

FIGURE 15.—*Spectrum plate on the LASL automatic comparator.*

FUTURE NEEDS AND PLANS

Although precision vacuum wave numbers are very important, they are not the only data needed

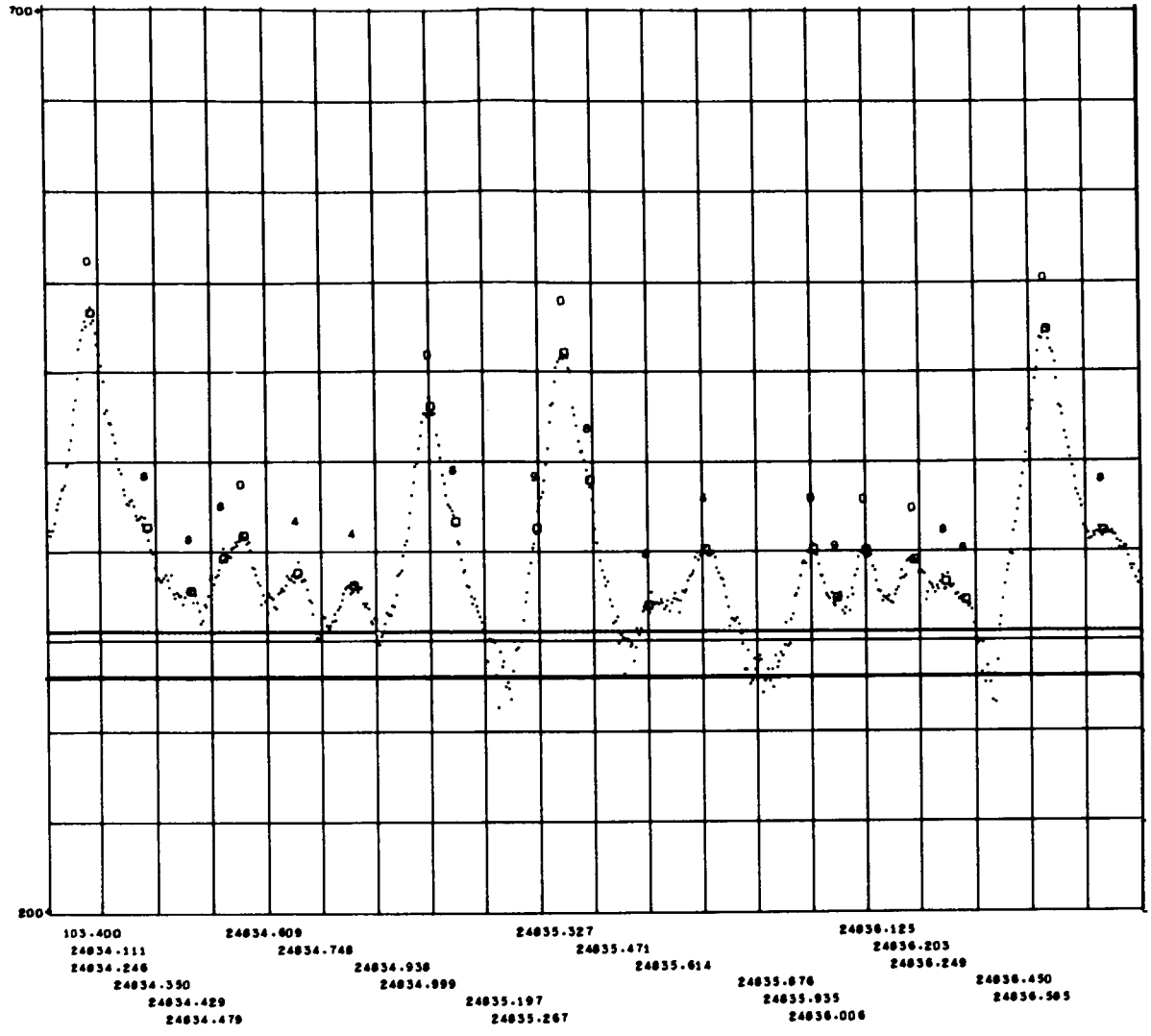

FIGURE *16.—Microfilm plot output from the LASL automatic comparator for emission spectra.*

for the analysis of spectra. All of the following useful measurements contribute to the analysis of spectra:

(1) Wave numbers:
- Precision vacuum wave numbers
- Zeeman effect
- Isotope shift
- Hyperfine structure

(2) Intensities:
- Precision relative intensities
- Changes in intensities with differing sources

Precision wave numbers are used to look for new levels and to calculate final level values. Additional information comes from putting the atom or ion in a magnetic field (Zeeman effect). The start toward the analyses of U I and U II came from the Zeeman effect on certain key uranium spectral lines. Additional Zeeman spectrograms are being studied now by Dr. Blaise. For complex spectra such as those of uranium, both the isotope shift and the hyperfine structure may turn out to be as powerful as the Zeeman effect for the completion of the analysis. Isotope shift had not been used for analysis

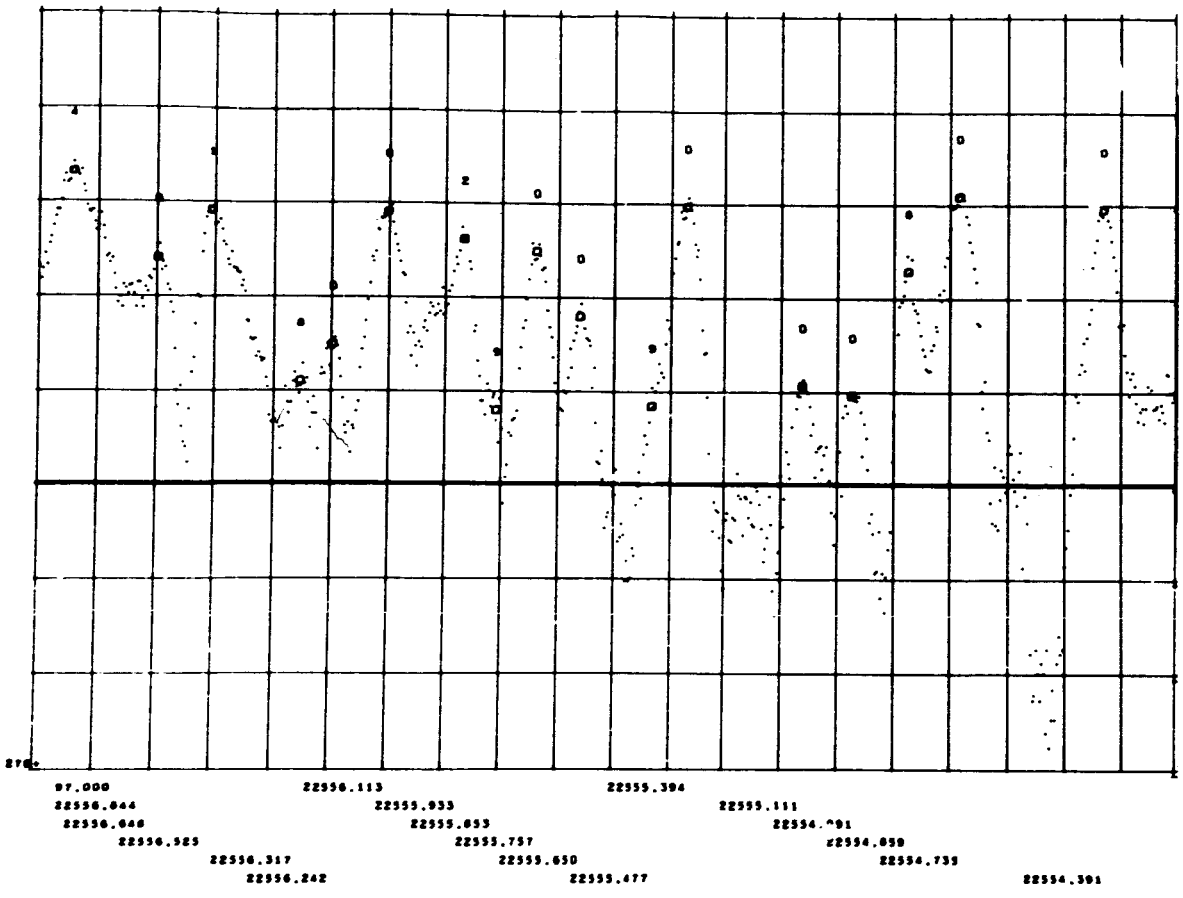

FIGURE *17.—Microfilm plot output from the LASL automatic comparator for absorption spectra.*

until recently when it was used to confirm some U I and U II levels, to reject others, and to help to find some new levels. Precision relative-spectral-line intensities have also been little used in the past. They will be of greater value when the theory is able to predict intensities better. Changes of intensities with different sources is a good way of separating spectra from different ionization stages. Such changes can also be used to identify lines involving low levels. Recent source developments indicate that this measurement may be of increasing importance in the near future.

The information contained in this paper and more will be contained in a forthcoming LASL report which is being prepared in collaboration with Dr. J. Blaise of the Laboratoire Aimé Cotton, Orsay, France. Material from a number of publications (refs. 1 to 27) and unpublished material from LASL and the Laboratoire Aimé Cotton will be used. The intent of this LASL report will be to show the present status of the analysis of the U I and U II spectra along with the wave number, Zeeman effect, and isotope shift evidence justifying the analysis.

No experimental analysis of the free ion U III or higher spectra has been made, but observations and measurements on these spectra have been and are being made at LASL and at the Lawrence Radiation Laboratory in collaboration with the Johns Hopkins University and the National Bureau of Standards.

CONCLUDING REMARKS

In conclusion, we have demonstrated that uranium has one of the most complex spectra of any element, that a good start has been made on the analysis,

and that a complete analysis of its spectra waits on further experimental measurements. Of the 300 000 lines that can be measured with present-day, high-resolution apparatus only 25 000 have been measured and only 10 100 of these have been classified. In addition to the increased knowledge of the uranium spectrum, its study has stimulated the development of new high-resolution spectroscopic apparatus, the spectroscopic use of high-speed digital computers, and an extension of the theory of complex spectra. All this is useful for many other spectroscopic tasks as well.

REFERENCES

1. HARRISON, G. R.; ET AL.: Massachusetts Institute of Technology Wavelength Tables. John Wiley & Sons, Inc., 1939.
2. SCHUURMANS, PH.: On the Analysis of Some Complex Spectra (Th and U). Thesis, Amsterdam, 1946. (AERE Lib. Trans. 513.)
3. SCHUURMANS, PH.: On the Spectra of Neodymium and Uranium. Physica, vol. 11, Feb. 1946, p. 419.
4. KIESS, C. C.; HUMPHREYS, C. J.; AND LAUN, D. D.: Preliminary Description and Analysis of the First Spectrum of Uranium. J. Res. Natl. Bur. Std., vol. 37, July 1946, p. 57.
5. SCHUURMANS, PH.; VAN DEN BOSCH, J. C.; AND DIJKWEL, N.: The Spectrum and Zeeman Effect of Uranium. Preliminary Analysis. Physica, vol. 13, 1947, p. 117.
6. VAN DEN BOSCH, J. C.; AND VAN DEN BERG, G. J.: The Zeeman Effect in the Arc and First Spark Spectrum of Uranium. Physica, vol. 15, 1949, p. 329.
7. VAN DEN BOSCH, J. C.: New Levels in the Uranium Spark Spectrum. Physica, vol. 15, 1949, p. 503.
8. MCNALLY, J. R., JR.; AND HARRISON, G. R.: Further Classification of the Spectrum of Singly-Ionized Uranium. Rept. No. Y340, U.S. At. Energy Comm., 1949.
9. KATZ, J. J.; AND RABINOWITCH, E.: The Chemistry of Uranium. McGraw-Hill Book Co., Inc., 1951.
10. STRIGANOV, A. R.; AND KOROSTYLEVA, L. A.: Investigations of the Isotope Effect in the Uranium Spectrum. Zh. Eksperim. i Teor. Fiz., vol. 29, 1955, p. 393; also, Soviet Phys.—JETP, vol. 2, 1956, p. 277.
11. KOROSTYLEVA, L. A.; AND STRIGANOVA, G. A.: Isotope Shift in the Uranium Spectrum. Opt. i Spektroscopiya, vol. 7, 1959, p. 137; also, Opt. and Spectry (USSR) (English transl.), vol. 7, 1959, p. 89.
12. RICHARDS, E. W. T.; AND CREW, M. D.: The Uranium Spectrum Between 3500 Å and 5500 Å with Associated Isotope Shifts. AERE–R 2941, 1959.
13. STEINHAUS, D. W.: Rapid Precision Wave Number Measurements From Fabry-Perot Interferograms. J. Opt. Soc. Am., vol. 50, 1960, p. 672.
14. DIRINGER, M.: Déplacements isotopiques dans le spectre de l'uranium. Compt. Rend., vol. 250, 1960, p. 828.
15. BEER, R.; AND BOVEY, L.: The Hyperfine Structure of Some Uranium and Americium Lines in the 1.6–2.1 Micron Region. Proc. Phys. Soc. (London), ser. A, vol. 76, 1960, p. 569.
16. ATHERTON, N.; AND BOVEY, L.: The Optical Spectra of Some Rare Earth and Actinide Elements in the 1–2.5 Micron Region. Part VI: The Spectrum of Uranium. AERE–R 3226, 1960.
17. MEGGERS, W. F.; CORLISS, C. H.; AND SCRIBNER, B. F.: Tables of Spectral-Line Intensities. Monogr. 32, Natl. Bur. Std., 1961.
18. BOVEY, L.; ATHERTON, N.; AND STEERS, E. B. M.: The Optical Spectrum of Uranium in the 1–2.5 μ Region. Spectrochim. Acta, vol. 17, 1961, p. 259.
19. RAO, P. R.: Isotope Shifts in the Uranium Spectrum. Proc. Indian Acad. Sci., vol. A 58, 1963, p. 353.
20. RICHARDS, E. W. T.; ATHERTON, N. J.; AND STEERS, E. B. M.: Further Observations of the Near Infra Red Emission Spectra of Uranium and Plutonium. AERE–R 3788, 1963.
21. GAGNÉ, J. M.; GERSTENKORN, S.; AND HELBERT, J. M.: Déplacements isotopiques relatifs dans le spectre de l'uranium. Compt. Rend., vol. 259, 1964, p. 3479.
22. DIRINGER, M.: Etude du déplacement isotopique de l'uranium (235–238). Contribution a la classification des spectres d'arc et d'étincelle de l'uranium. Thesis, Paris, 1963 (in French); also, Ann. Phys. (Paris), vol. 10, 1965, p. 89.
23. GUELACHVILI, G.: These de 3e Cycle (Paris), 1965.
24. STEINHAUS, D. W.; BLAISE, J.; AND DIRINGER, M.: Present Status of the Analysis of the Arc Spectrum of Uranium (UI). Rept. LA–3475, Los Alamos Sci. Lab., 1966.
25. LAUN, D. D.: Self-Reversal in the Spectral Lines of Uranium. J. Res. Natl. Bur. Std., vol. 70A, 1966, p. 323.
26. BEN OSMAN, Z.: Contribution à la classification des spectres d'arc et d'étincelle de l'uranium par l'étude des structures Zeeman entre 4700 et 3100 Å et du déplacement isotopique. These de 3e Cycle (Paris), 1966.
27. BLAISE, J.: Unification of the A and B Systems in Uranium Spark Spectrum. J. Phys. (France), vol. 30, suppl. no. 1, 1969, p. 1.
28. MANN, J. B.: Ionization of U, UO, and UO_2 by Electron Impact. J. Chem. Phys., vol. 40, 1964, p. 1632.
29. BAKULINA, I. N.; AND IONOV, N. I.: Determination of the Ionization Potential of Uranium by a Surface Ionization Method. Zh. Eksperim. i Teor. Fiz., vol. 36, 1959, p. 1001; also, Soviet Phys.—JETP, vol. 9, 1959, p. 709.
30. FEBER, R. C.; AND HERRICK, C. C.: Ideal Gas Thermodynamic Functions of Lanthanide and Actinide Elements. Rept. LA–3184, Los Alamos Sci. Lab., 1965.
31. COWAN, R. D.: Atomic Self-Consistent-Field Calcula-

tions Using Statistical Approximations for Exchange and Correlation. Phys. Rev., vol. 163, 1967, p. 54.

32. COWAN, R. D.: Theoretical Calculation of Atomic Spectra Using Digital Computers. J. Opt. Soc. Am., vol. 58, 1968, p. 808.
33. COWAN, R. D.: Theoretical Study of p^m–$p^{m-1}l$ Spectra. J. Opt. Soc. Am., vol. 58, 1968, p. 924.
34. SCHNEIDERMAN, S. B.: Theoretical Viscosities and Diffusivities in High Temperature Mixtures of Hydrogen and Uranium. (United Aircraft Res. Lab.) NASA CR-213, 1965.
35. WILLIAMSON, H. A.; MICHELS, H. H.; AND SCHNEIDERMAN, S. B.: Theoretical Investigation of the Lowest Five Ionization Potentials of Uranium. Rept. D-910099-2, United Aircraft Res. Lab., Sept. 1965.
36. JUDD, B. R.: Overlapping Atomic Multiplets. J. Opt. Soc. Am., vol. 58, 1968, p. 1311.
37. STEINHAUS, D. W.; ENGELMAN, R., JR.; AND FISHER, K. J.: Design and Operation of the Los Alamos Automatic Comparator for Measurement of Spectra. Rept. LA-4117, Los Alamos Sci. Lab., 1969.

DISCUSSION

Bauder: What kind of source did you use?

Radziemski: We used a hollow cathode lamp.

Bauder: You said that you were trying to change sources. What are you planning to use?

Radziemski: We are considering the ring discharge for separation. Right now I am doing experiments on foil separation. We have used the hollow cathode at different pressures and currents and tried to see if the intensity of the lines could be used to separate the lines into ionization stages in that type of source.

Delmer: I wonder if you considered configuration interaction when you did those level calculations?

Radziemski: The matrices are so large that one cannot really get a complete configuration into the computer. There were two procedures. If configuration interaction was put in the computer then we restricted ourselves to a single parent of the ion. This was not too satisfactory because it eliminated a lot of levels which would interact. On the other hand, when configuration interaction was not put in we could use many parents but then the effect is wide. It is difficult to estimate configuration interaction satisfactorily and it has not been done well yet.

Delmer: It seemed as though you obtained good agreement without it.

Radziemski: Yes; however, this is almost misleading because it happens only above the position where the levels become much denser and the configurations overlap much more seriously. There is not too much overlapping for the cases I showed.

Wilkerson: Do you intend to do high-resolution absorption spectroscopy on uranium vapor for looking at resonance absorption and autoionization effects which might really contribute to some of the plasmas being discussed?

Radziemski: In our absorption experiments we had not considered the type of absorption that you are talking about.

Wilkerson: I don't quite understand the overlap between U-I and U-II shown in one of your figures.

Radziemski: The splitting of the lowest configuration of U-I is so great that it has levels which are higher than those of the lowest ionization limit.

Wilkerson: Then all those other levels must also have series which converge with levels above.

Radziemski: Yes, but I was not showing a series. The reason that there are levels above the lowest ionization is that the parent for those levels is higher still.

Page intentionally left blank

Status of Opacity Calculations for Application to Uranium-Fueled Gas-Core Reactors

R. W. PATCH
NASA Lewis Research Center

The principal mode of heat transfer in gas-core nuclear reactors and rockets is thermal radiation. In order to assess the feasibility of such reactor and rocket concepts, the opacities of the substances in the reactor chamber must be known from calculations or experiments. The status and results of such calculations for hydrogen, seeds, and uranium are given and the status of experiments is discussed. It is concluded that present opacity calculations are probably accurate enough to assess the feasibility of a uranium-fueled gas-core reactor or rocket, but the confidence level is not yet satisfactory.

In the gas-core reactor concept, the working fluid, which is always a gas, is heated by thermal radiation from a hot, fissioning uranium plasma located in the center of the reactor chamber. If the reactor is part of a rocket engine, the optimum working fluid is hydrogen because its low molecular weight contributes to a high specific impulse when the hydrogen is expanded through an exhaust nozzle. Unfortunately, hydrogen is not sufficiently opaque at temperatures below 6000° K to prevent excessive thermal radiation from reaching the chamber walls and causing excessive wall heating. Hence the hydrogen should be seeded with some material to increase its opacity. To assess the feasibility of the gas-core reactor concept, the opacities of hydrogen, seeds, and uranium plasma must be calculated. This paper is a review of such work and a discussion of related experiments.

HYDROGEN

The problem of calculating the spectral absorption coefficient and opacities of hydrogen is an old one in astrophysics, but most of the calculations for temperatures of up to 50 000° K are for the low pressures that occur in the outer layers of stars and have small quantities of helium and metals added to the hydrogen. Since a gas-core nuclear reactor may be expected to operate at pressures of 100 to 1000 atm, the opacities calculated by astrophysicists are not applicable. For pure hydrogen, opacities or the closely related quantities called emissivities have been calculated by several investigators (refs. 1 through 10). Until recently, the opacities most frequently used in studying the gas-core reactor concept were those of Krascella (ref. 5) because he covered the appropriate temperature and pressure ranges.

More recent calculations of absorption coefficient and opacity (ref. 11) for appropriate temperatures and pressures took into account 15 absorption processes and used the latest and most realistic composition calculations (ref. 12), which include the ion H_3^+. These results, which differ significantly from those of reference 5, will now be summarized.

At low temperatures there are particularly large differences between the spectral absorption coefficients of references 5 and 11. Figure 1 shows this for a pressure of 1000 atm and a temperature of 2778° K. The spectral absorption coefficients from references 5 and 11 are given by broken and solid lines, respectively. In the infrared, pressure-induced molecular absorption was neglected in reference 5, so the absorption coefficient is low. For photon wave numbers less than 109 677 cm^{-1}, the absorption coefficient from reference 5 is due almost

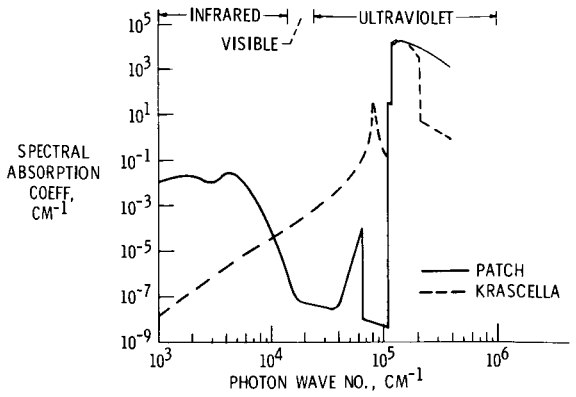

FIGURE 1.—*Theoretical spectral absorption coefficient of hydrogen. Temperature, 2778° K; pressure, 1000 atm.*

entirely to the Lyman α line. Unfortunately, the formula used in reference 5 for the absorption of Lyman α is believed valid only from about 81 300 to 83 300 cm^{-1}: for photon wave numbers much less than this, Olfe (ref. 4) indicates that the absorption coefficient is much less than that obtained in reference 5. In reference 11, for want of a valid treatment, the Lyman α line was neglected because this generally appeared to give more realistic absorption coefficients and opacities than those resulting from including Lyman α improperly. The peak in the solid curve in the near ultraviolet is due to quasimolecular absorption, which was neglected in reference 5.

Figure 2 is a graph of quantities the same as those shown in figure 1, but for a temperature of 38 889 °K. At such high temperatures the agreement between absorption coefficients in references 5 and 11 is much better.

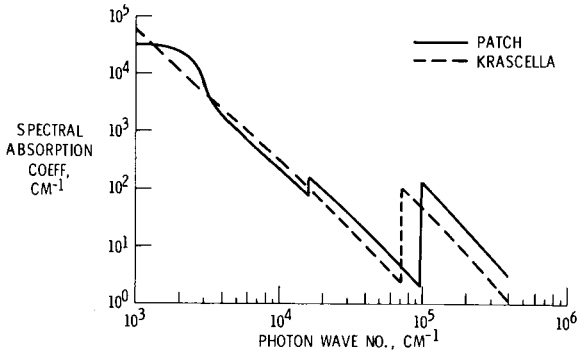

FIGURE 2.—*Theoretical spectral absorption coefficient of hydrogen. Temperature, 38 889° K; pressure, 1000 atm.*

To obtain the opacity, the spectral absorption coefficient must be averaged over the spectrum. Various kinds of averages give various kinds of opacity. For gas-core nuclear reactors, the gas is optically thick so we define opacity by

$$\mathbf{F}=\frac{-16\,\sigma T^3}{3a_R}\nabla T \tag{1}$$

where $\mathbf{F}$ is the heat flux due to thermal radiation, T is the temperature, σ is the Stefan-Boltzmann constant, and a_R is the Rosseland mean opacity. (Eq. (1) may not be a good approximation near the reactor cavity wall.) The Rosseland mean opacity of a nonscattering gas is consequently given by

$$a_R=\frac{\int_0^\infty \frac{\partial B_\nu}{\partial T}d\nu}{\int_0^\infty \frac{n^2}{a_\nu}\frac{\partial B_\nu}{\partial T}d\nu} \tag{2}$$

where ν is the photon wave number, B_ν is the Planck function, a_ν is the spectral absorption coefficient, and n is the real index of refraction.

Values of a_R for hydrogen are given in figure 3 for three pressures. The solid and broken curves

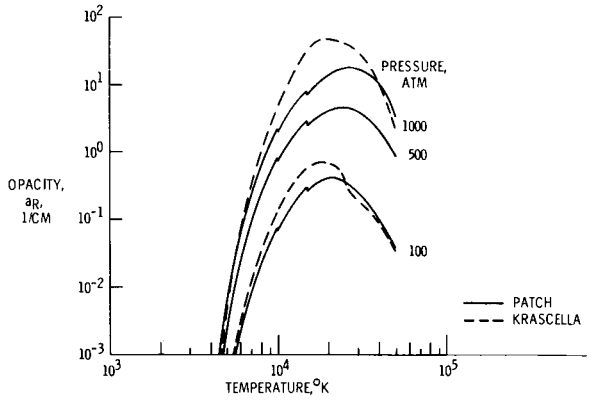

FIGURE 3.—*Theoretical opacity of hydrogen.*

are from references 11 and 5, respectively. The discontinuities in the solid curves at 10 000° and 15 000° K are due to lack of cross sections above these temperatures for quasimolecular and H_2^+ photodissociation transitions, respectively. Below about 6000° K, the opacity of pure hydrogen is

insufficient to prevent excessive radiant heat transfer to the chamber wall of a gas-core nuclear reactor.

Because of the omission or crude calculation of absorption coefficients for a number of radiative processes, the hydrogen results in reference 11 should be regarded as interim results. Atomic lines were neglected entirely because at high pressures the far wings are important, and there are no line shapes available that are valid in the far wings. Molecular ultraviolet bands have also been neglected because it appears that even at high pressures a line-by-line calculation of these may be necessary. Pressure-induced molecular infrared absorption was obtained from Linskey (ref. 13), who extrapolated a room-temperature theory which used an intermolecular potential that is unrealistic at high temperature (ref. 14). As a result of these and other approximations, the hydrogen opacities in reference 11 are probably accurate to within a factor of 4. With more work this can be reduced to a factor of 2.

There are a large number of measurements of the absorption coefficient of hydrogen, most of which tend to verify theories for the various radiative processes. However, there is no measurement at high temperature and high pressure which inspires much confidence.

The opacity of deuterium would not be greatly different from that of hydrogen. The principal differences would be due to a smaller degree of molecular dissociation and to shifts in the pressure-induced infrared absorption.

SEEDS

As mentioned before, the opacity of hydrogen is insufficient below about 6000° K to prevent excessive radiant heat transfer to the chamber wall. This necessitates the addition of some substance (called a seed) to the hydrogen to increase the opacity of the mixture for photon wave numbers from about 6000 cm^{-1} (infrared) to somewhere in the far ultraviolet where the H_2 absorption becomes large. Solid particles were proposed as seeds by Lanzo and Ragsdale (ref. 15). Solid particles are preferred over gases because of their high absorption coefficients and essentially gray spectra.

Solid particles both absorb and scatter light. The cross sections for these two processes are called absorption and scattering cross sections, respectively. Their sum is called the extinction cross section. All these quantities can be calculated from the Mie theory if index-of-refraction data are available. Such calculations have been made by Stull and Plass (ref. 16) for carbon particles; by Krascella (ref. 17) for tungsten, molybdenum, niobium, thallium, cadmium, nickel, palladium, silicon, aluminum, carbon, hafnium, iridium, iron, platinum, cobalt, titanium, vanadium, and zirconium; by Williams, Clement, Shenoy, Partain and Jacobs (ref. 18) for carbon, silicon, and tungsten; and by Grevesse-Guillaume and Wickramasinghe (ref. 19) for graphite. The Rosseland mean opacity was calculated by Krascella (ref. 17) for tungsten particles. The Rosseland and Planck mean opacities were calculated by Kellman and Gaustad (ref. 20) for graphite particles. In both these calculations scattering was neglected in calculating the Rosseland mean opacity although it should not have been (refs. 21 and 22). Also, bremsstrahlung was neglected, although at high temperatures it may be important (ref. 23) because the particles thermionically emit electrons.

The Rosseland mean opacities of the particles (refs. 17 and 20) are shown near the left side of figure 4. The curves are terminated at the temperatures at which one-half the mass of particles would evaporate for an initial seed-to-hydrogen mass ratio of 0.01 and a total pressure of 500 atm. In actuality, particles of graphite would react chemically with hydrogen at lower temperatures and hence disappear.

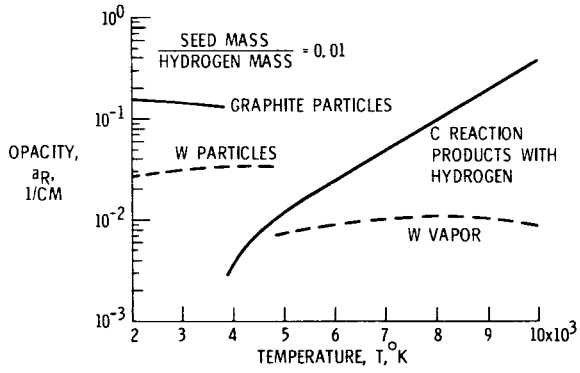

FIGURE 4.—*Theoretical seed opacities. Total pressure, 500 atm; seed radius, 0.05 μ.*

When particles react with hydrogen or vaporize, the resulting gas may have an opacity quite different from that of the particles. The Rosseland mean opacity of tungsten vapor was calculated by Krascella (ref. 17) by use of a semiempirical model and is shown in figure 4. The Rosseland mean opacity of carbon-hydrogen reaction products was calculated by Main (ref. 24), who used all available data. The increase in the Rosseland mean opacity of hydrogen due to contributions from carbon-hydrogen reaction products was calculated from references 11 and 24, and is shown in figure 4.

The accuracy of calculated opacities for vapor and reaction products is probably not great. The opacity of tungsten vapor (fig. 4) is probably accurate to within a factor of 10. Main states that his opacities for carbon-hydrogen reaction products may be inaccurate by several orders of magnitude at 3000° K but are probably correct to within a factor of 2 or 3 at 8000° to 10 000° K.

Measurement of the absorption or extinction coefficients of solid particles is difficult because the particles tend to agglomerate. Lanzo and Ragsdale (ref. 25) measured the extinction coefficient of carbon particles in air. Marteney (ref. 26) measured the extinction and scattering coefficients of carbon and tungsten particles in helium and nitrogen. Keng and Orr (ref. 27) measured the extinction coefficient of carbon and alumina particles and the heat transfer to ferrous sulfide, cupric oxide, zinc, tungsten, carbon, and alumina particles in a carrier gas. Burkig (ref. 28) measured light transmission of tantalum carbide, iron, tungsten carbide, tungsten, and graphite particles in helium at temperatures of up to 3300° K. Cory and Bennett (ref. 23) measured the transmittance and energy absorptivity of tantalum carbide particles in helium and hydrogen at temperatures of up to 6600° K. Williams, Clement, Shenoy, Partain, and Jacobs (ref. 18) measured the extinction coefficient of carbon, tungsten, and silicon particles in hydrogen and of carbon particles in nitrogen at temperatures of up to 3450° F. It appears that they compared measured extinction coefficients with theoretical absorption coefficients. Consequently, it is not clear whether differences between theory and experiment are real or are due to neglect of scattering in the theory. This applies also to many of the other experiments. Two other difficulties in comparing theory and experiment are that particles in experiments usually are not round and are various sizes.

URANIUM

Calculation of the opacity of uranium from first principles is exceedingly complex, and there are no experimental data available for many of the energy levels and radiative processes that are important. Consequently, Kesten and Krascella (ref. 29) used a semiempirical model for uranium.

The more recent calculation of Parks, Lane, Stewart, and Peyton (ref. 30) is less empirical. They employed a relativistic description of the atom with a scaled Thomas-Fermi potential. The scaling parameters were determined from measured X-ray levels and self-consistent field calculations. Their Rosseland mean opacity is shown in figure 5 and

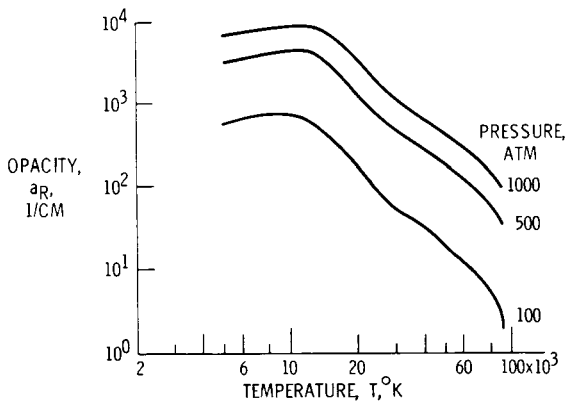

FIGURE 5.—*Theoretical opacity of uranium.*

is believed to be accurate to within a factor of 10. Their opacity should be more accurate at high temperature than at low temperature because the different Boltzmann factors of the states of each electronic configuration were assumed to be equal. The opacities in figure 5 are much higher than optimum for a gas-core nuclear reactor and so cause an excessive temperature in the center of the uranium plasma. This temperature decreases the uranium density, so the chamber pressure must be increased to compensate. Unfortunately, the opacity of plutonium plasma is probably roughly the same as that of uranium plasma.

Quantitative measurements of the absorption co-

efficient of a uranium plasma are few. Meggers, Corliss, Bozman, and Schribner (refs. 31 and 32) measured line intensities in a steady 5100° K arc in air at 1 atm by using copper-uranium electrodes. Their data may be used to derive the average absorption coefficient of the lines in a pure uranium plasma at 5100° K and 3.58×10^{-4}-atm pressure. The scaled Thomas-Fermi theory is compared with the arc results in figure 6. The arc results, which

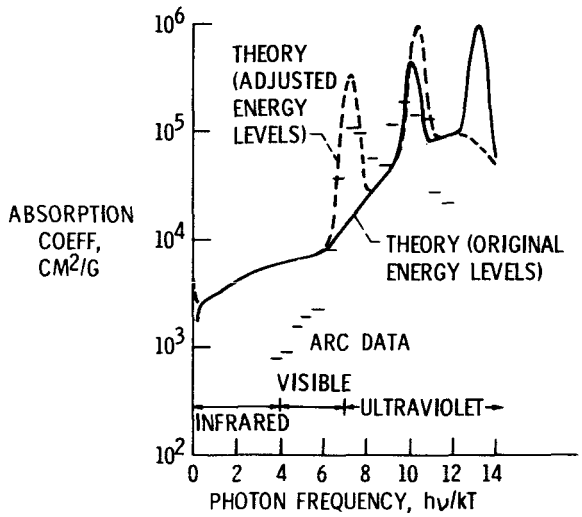

FIGURE 6.—*Theory and arc data for the uranium absorption coefficient. Temperature, 5100° K; pressure, 3.58×10^{-4} atm.*

do not include continuum, are shown as short horizontal lines. Originally, the two peaks in the theoretical absorption coefficient were at higher photon frequencies than were the arc peaks. However, by adjusting two energy levels in the theory, better agreement was obtained (see broken lines in fig. 6). This change has not been made in the calculations of opacity (fig. 5).

Additional experimental work on the opacity of a uranium plasma is being performed by Miller and Wilkerson at the University of Maryland with the use of a shock tube. Absorption coefficients from preliminary data are shown in figure 7 together with theoretical values from reference 30 without the adjusted energy levels. On the left-hand side, the theory is going up to the first of its two peaks. The second peak is at a still shorter wavelength which is off the scale of the graph. The need to adjust an

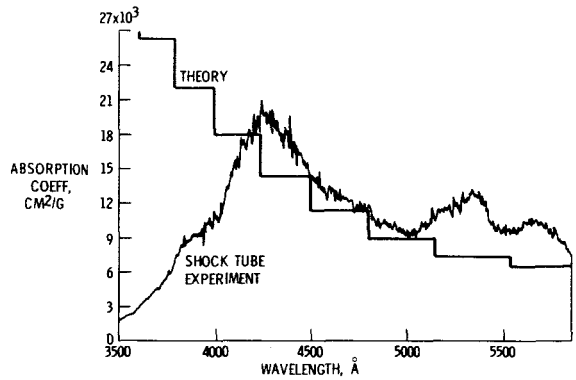

FIGURE 7.—*Optical absorption coefficient of uranium plasma. Temperature, 10 000° K; uranium pressure, 0.104 atm.*

energy level in the theory to move the first peak to longer wavelengths so that it will agree with that of the experiment is evident here, just as it was in figure 6.

TYPICAL CASE

A typical case for a gas-core nuclear reactor was taken from figures 2(b) and 5(b) of reference 33. The opacity at a station 1.05 m from the front of the reactor chamber is shown in figure 8 based on opacities from figures 3 to 5 of this paper.

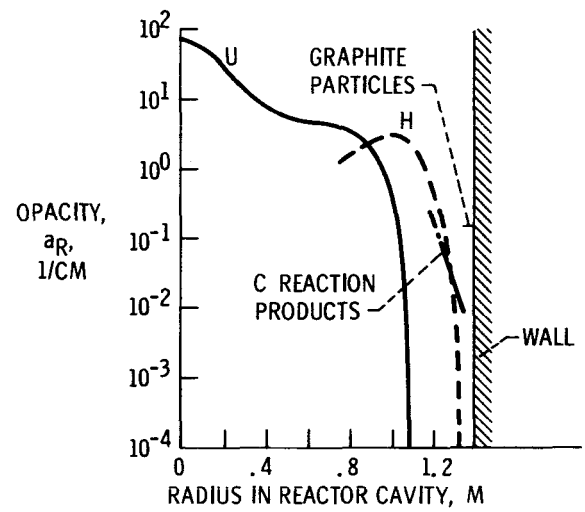

FIGURE 8.—*Uranium, hydrogen, and carbon opacities. Pressure, 500 atm; distance from front, 1.05 m; particle radius, 0.05μ;* $\frac{\text{Seed mass}}{\text{Hydrogen mass}} = 0.01$.

Graphite seeds were assumed. From the centerline to about 0.6 of the wall radius the uranium opacity predominates. Farther out the hydrogen opacity is largest. Still farther out the opacity of carbon reaction products exceeds those of the others. Near the wall the graphite particles have the highest opacity. In the region where both uranium and hydrogen are present, the opacities were calculated from the partial pressures of uranium and hydrogen. This is an approximation because the degrees of ionization of these two plasma components are actually coupled to each other because of the free electrons. In the region where both hydrogen and carbon are present, all coupling in the gas phase was taken into account by Main (ref. 24).

CONCLUSIONS

The opacity of hydrogen has been calculated to within a factor of about 4 and can be calculated to within a factor of about 2 without recourse to further experiments.

There are many calculations and measurements of the absorption and scattering of seed particles, but calculations and measurements where scattering is treated as a function of angle are needed and should not present great problems. Also, calculations should include the effect of bremsstrahlung due to thermionic emission from hot particles.

The absorption coefficient of the vapor or reaction products generated by seed particles has not been measured, and calculations are believed to be accurate to within a factor of only 10.

The absorption coefficient of uranium has been calculated to within a factor of about 10 by using a complex theory. Comparison with experimental results indicates that changes in the theory are needed. Further experiments are needed to provide the information required to make these changes with confidence.

The opacity calculations described in this paper are probably accurate enough for meaningful preliminary assessments of the feasibility of a uranium-fueled gas-core reactor or rocket. However, the confidence level of such estimates is not so satisfactory as one would like. Improvements in both theory and experiment are desirable.

REFERENCES

1. Menzel, Donald H.; and Pekeris, Chaim L.: Absorption Coefficients and Hydrogen Line Intensities. Mon. Notic. Roy. Astron. Soc., vol. 96, no. 1, Nov. 1935, pp. 77–111. (See also Selected Papers on Physical Processes in Ionized Plasmas, Donald H. Menzel, ed., Dover Publ. (New York, N.Y.), 1962, pp. 3–37.
2. Tsao, H. T. Hsieh: Opacity of a Highly Compressed Hydrogen Gas. Astrophys. J., vol. 119, no. 1, Jan. 1954, pp. 70–80.
3. Aroeste, Henry; and Benton, William C.: Emissivity of Hydrogen Atoms at High Temperatures. J. Appl. Phys., vol. 27, no. 2, Feb. 1956, pp. 117–121.
4. Olfe, D. B.: Equilibrium Emissivity Calculations for a Hydrogen Plasma at Temperatures up to 10,000° K. J. Quant. Spectros. Radiat. Transfer, vol. 1, no. 2, Mar. 1961, pp. 104–134.
5. Krascella, N. L.: Tables of the Composition, Opacity, and Thermodynamic Properties of Hydrogen at High Temperatures. NASA SP-3005, 1963.
6. Lasher, L. E.; Wilson, K. H.; and Greif, R.: Radiation from an Isothermal Hydrogen Plasma at Temperatures up to 40,000° K. J. Quant. Spectros. Radiat. Transfer, vol. 7, no. 2, Mar.-Apr. 1967, pp. 305–322.
7. Yakobi, Yu. A.; Komin, A. V.; and Ivaniya, S. P.: Spectral and Total Radiation of Hydrogen Plasma. J. Quant. Spectros. Radiat. Transfer, vol. 8, no. 2, Feb. 1968, pp. 805–821.
8. Yakobi, Yu. A.; Ivaniya, S. P.; and Komin, A. V.: Radiative Escape of Energy From a Dense Hydrogen Plasma. Optics Spectros., vol. 24, no. 1, Jan. 1968, pp. 13–15.
9. Moskvin, Yu. V.: Emissivity of Some Gases at High Temperatures of 6000–(2000)–12,000° K. High Temp., vol. 6, no. 1, Jan.-Feb. 1968, pp. 1–7.
10. Mandell, D. A.; and Cess, R. D.: Radiative Transport Quantities for a Hydrogen Plasma. J. Quant. Spectros. Radiat. Transfer, vol. 9, no. 7, July 1969, pp. 981–994.
11. Patch, R. W.: Interim Absorption Coefficients and Opacities for Hydrogen Plasma at High Pressure. NASA TM X-1902, 1969.
12. Patch, R. W.: Components of a Hydrogen Plasma Including Minor Species. NASA TN D-4993, 1969.
13. Linskey, Jeffrey, L.: On the Pressure-Induced Opacity of Molecular Hydrogen in Late-Type Stars. Astrophys. J., vol. 156, no. 3, June 1969, pp. 989–1006.
14. Patch, R. W.: Calculated Interaction Energy and Dipole Moment in Collisions of Two Hydrogen Molecules. NASA TN D-5486, 1969.
15. Lanzo, Chester D.; and Ragsdale, Robert G.: Experimental Determination of Spectral and Total Transmissivities of Clouds of Small Particles. NASA TN D-1405, 1962.
16. Stull, V. Robert; and Plass, Gilbert N.: Emissivity of Dispersed Carbon Particles. J. Opt. Soc. Am., vol. 50, no. 2, Feb. 1960, pp. 121–129.
17. Krascella, N. L.: Theoretical Investigation of the

Absorptive Properties of Small Particles and Heavy-Atom Gases. NASA CR–693, 1967.

18. WILLIAMS, J. R.; CLEMENT, J. D.; SHENOY, A. S.; PARTAIN, W. L.; AND JACOBS, W. R.: The Attenuation of Radiant Energy in Hot Seeded Hydrogen—An Experimental Study Related to the Gaseous Core Nuclear Rocket. Quart. Status Rept. No. 3, Project No. A–1045, Ga. Inst. Tech., May 1969.
19. GREVESSE-GUILLAUME, C.; AND WICKRAMASINGHE, N. C.: On the Optics of Small Graphite Spheres. III. Mon. Notic. Roy Astron. Soc., vol. 132, no. 4, May 1966, pp. 471–473.
20. KELLMAN, S. A.; AND GAUSTAD, J. E.: Rosseland and Planck Mean Absorption Coefficients for Particles of Ice, Graphite, and Silicon Dioxide. Astrophys. J., vol. 157, no. 3, pt. 1, Sept. 1969, pp. 1465–1467.
21. MAYER, HARRIS: Methods of Opacity Calculations. Rept. LA–647, Los Alamos Sci. Lab., Mar. 1948.
22. STEWART, JOHN C.; AND PYATT, KEDAR D., JR.: Theoretical Study of Optical Properties. Rep. GA–2528, vol. 1, (AFSWC–TR–61–71, vol. 1), Gen. Atomic Div., Gen. Dynamics Corp. Sept. 1961.
23. CORY, J. S.; AND BENNETT, A.: Thermal Absorption in Seeded Gases. (Rept. DAC–60779, McDonnell-Douglas Astronautics Co.) NASA CR–100700, 1969.
24. MAIN, ROGER P.: Optical Constants of Carbon-Hydrogen Mixtures. NASA CR–72570, 1969.
25. LANZO, CHESTER D.; AND RAGSDALE, ROBERT G.: Heat Transfer to a Seeded Flowing Gas From an Arc Enclosed by a Quartz Tube. 1964 Heat Transfer and Fluid Mech. Inst., Warren H. Giedt and Solomon Levy, eds., Stanford Univ. Press (Stanford, Calif.) 1964, pp. 226–244.
26. MARTENEY, P. J.: Experimental Investigation of the Opacity of Small Particles. NASA CR–211, 1965.
27. KENG, EDWARD Y. H.; AND ORR, CLYDE, JR.: Heat Transfer to a Gas Containing a Cloud of Particles. NASA CR–73880, Jan. 1969.
28. BURKIG, VALERIE C.: Thermal Absorption in Seeded Gases. (Rept. DAC–59208, Douglas Aircraft Co.) NASA CR–78152, 1966.
29. KESTEN, A. S.; AND KRASCELLA, N. L.: Theoretical Investigation of Radiant Heat Transfer in the Fuel Region of a Gaseous Nuclear Rocket Engine. NASA CR–695, 1967.
30. PARKS, D. E.; LANE, G.; STEWART, J. C.; AND PEYTON, S.: Optical Constants of Uranium Plasma. (Rept. GA–8244, Gulf General Atomic, Inc.) NASA CR–72348, 1968.
31. MEGGERS, W F.; CORLISS, C. H.; AND SCRIBNER, B. F.: Tables of Spectral-Line Intensities. Monogr. 32, Natl. Bur. Std., Pt. I, Dec. 29, 1961, and Pt. II, Oct. 2, 1961.
32. CORLISS, C. H.; AND BOZMAN, W. R.: Experimental Transition Probabilities for Spectral Lines of Seventy Elements. Derived from the NBS Tables of Spectral-Line Intensities. Monogr. 53, Natl. Bur. Std., July 20, 1962.
33. KASCAK, ALBERT F.; AND EASLEY, ANNIE J.: Effect of Turbulent Mixing on Average Fuel Temperatures in a Gas-Core Nuclear Rocket Engine. NASA TN D–4882, 1968.

DISCUSSION

Franklin: Have you made an estimate of the temperature reduction which you would get on the carbon seeding material before it disappeared because of reaction with the hydrogen propellant?

Patch: Reduction in temperature of the seeding material itself?

Franklin: Yes; the temperature at which the seeds would really disappear because they would be reacting with the propellant.

Patch: No; one has to rely on experiments for that. Richard Williams at the Georgia Institute of Technology has done some experiments on the subject and so I suggest that you talk with him.

Page intentionally left blank

Conditions for Local Thermodynamic Equilibrium in Uranium

T. N. DELMER AND W. G. VULLIET
Gulf General Atomic, Inc.

Possible effects on uranium opacities due to populations of bound states not in local thermodynamic equilibrium (LTE) are investigated. The simple model used to calculate the pertinent atomic parameters is described. Although the model is capable of giving only qualitative results, it gives estimates of situations in which a uranium plasma will show deviations from thermodynamic equilibrium. Temperatures and densities at which these deviations become significant are given. Some cases in which non-LTE effects are important are discussed in detail, and the LTE values of the opacity and source function are compared with the correct values.

A system which can be described at any point by classical thermodynamics is said to be in local thermodynamic equilibrium (LTE). Such a system can be completely described by just a few parameters, such as, for instance, temperature, pressure, and composition. It is clear that this is a simplified view of the real system and cannot be true for systems where transport of energy, material, etc. are important. However, the assumption that LTE holds gives a very adequate description of most physical problems and allows a large reduction in the number of parameters required to describe the real situation.

The opposite assumption requires at least six parameters to describe each particle. Indeed, to investigate a system in this detail would be hopeless. The intermediate possibility exists that a reasonably finite number of parameters may be adequate for the description. Typical extensions of the LTE analysis are the addition of different temperatures to describe the Maxwellian distributions of the electrons and ions, the detailed description of the velocity distribution of the ions (as is required to describe fission fragments), and the detailed description of the populations of the excited states of ions which are responsible for producing the emission and absorption of radiation. The last problem is the one considered here.

The non-LTE effects on excited-state populations are important when radiative rates dominate collisional rates. In this case the deviations from LTE are important when the radiation field is not equal to the local source function, as when the incident radiation is from a source at a higher temperature or the local radiation escapes. These last two examples are cases in which the radiation temperature changes considerably over unit optical depth. The excited-state populations usually show the first signs of going out of equilibrium as the plasma density is decreased, with the kinetic distributions remaining Maxwellian (see work of Bohm and Aller (ref. 1) for a discussion of this in gaseous nebulae).

The problem is set at finding the non-LTE excited-state populations of uranium ions. Because of the complexity of these ions, it is necessary to formulate a simple model to obtain any results whatsoever. This is done in the next section where the model is described and the sources of the necessary atomic parameters are mentioned. After this, the model is applied to calculating some LTE opacities which are compared with other results. The model is then applied to some arbitrary situations along with one experimental density and temperature, all of which show nonequilibrium effects.

MODEL FOR URANIUM

To find the populations of the excited electronic states (hereinafter referred to as states) of an ion, the rate equations for each of the states must be set up. Thus, one must know not only the energy levels and optical transition probabilities (or, alternatively, the oscillator strengths) but also the collision rates to and from a level. The oscillator strengths must be known for the equilibrium calculation of opacities; the collisional rates are an additional requirement of the nonequilibrium calculations. These rates are known with some degree of confidence for hydrogenic ions (cf. ref. 2) and have been incorporated into various rate equations by Mihalas (ref. 3) and Delmer (ref. 4). Since setting up and solving the rate equations is straightforward once the radiative and collisional rates are given, no further mention will be made of this. Rather, the rates used in the calculation will be defined.

The complexity of the uranium ions is so great that the most complete opacity calculations to date (those of Parks, Lane, Stewart, and Peyton (ref. 5)) have relied heavily on approximate and statistical methods. Since the concern here is with demonstrating non-LTE effects rather than with tabulating opacities, a much greater simplification was required. It was decided to consider only two stages of ionization at a time, the upper stage being considered only in the ground state and the lower stage having only a few (of the order of 10) excited states. As can be seen from this, the approximation is in the vein of making uranium ions look like hydrogenic ions.

Atomic Parameters

To proceed further in this direction, the energy levels were taken as hydrogenic with ground state at principal quantum number 5 but scaled so as to give the correct ionization energy. The ionization energies χ were taken from reference 5. This report contained data for a sufficient number of ions for the densities and temperatures used here. The degeneracies of the levels were taken as hydrogenic except for the upper stage of ionization which was considered to have a ground-state degeneracy of 50. Thus, the energy levels E_i and degeneracies g_i were taken as

$$E_i=\chi\left[1-\left(\frac{5}{i+4}\right)^2\right]$$
$$g_i=2(i+4)^2$$

It will be noted that the analogy up to now is with a hydrogenic ion with its first four shells unavailable for the single electron considered here. The analogy does not hold, however, for oscillator strengths f_{ij}. Since the model has only one active electron, the Thomas-Kuhn sum rule must be satisfied; i.e.,

$$\sum_i f_{ij}=1$$

where appropriate summation or integration must be carried out over the discrete states or continuum. If one were to identify the oscillator strengths with hydrogenic oscillator strengths f^{H} as

$$f_{ij}=f_{i+4\ j+4}{}^{\mathrm{H}} \qquad \text{(Incorrect)}$$

one would find the sum rule exceeded for $j=1$ and $i=2$ since

$$f_{65}{}^{\mathrm{H}}=1.231$$

(cf. ref. 6). It appears reasonable to set

$$f_{ij}=f_{ij}{}^{\mathrm{H}}$$

for transitions between bound states, but this requires a modification from the hydrogenic bound-free oscillator strengths to fit the sum rules. The photoionization cross section is assumed to fall off as the inverse cube of the photon energy. The photoionization cross section is then (cf. ref. 7)

$$\sigma_i=\frac{\pi e^2}{mc}\frac{df_i}{d\nu}=\left(\frac{\nu_{oi}}{\nu}\right)^3 a_i$$

where a_i is determined by

$$\int_{\nu_{oi}}^{\infty} d\nu\frac{df_i}{d\nu}=\frac{8}{3\sqrt{3}\,\pi i}$$

where the right side is the required value for the hydrogenic sum rule and ν_{oi} is the threshold photon frequency

$$h\nu_{oi}=\chi-E_i=\left(\frac{5}{i+4}\right)^2\chi$$

and the other symbols have their usual meaning. These requirements give the threshold cross section as

$$a_i=\frac{16he^2}{3\sqrt{3}\,mci}\frac{1}{(\chi-E_i)}$$

If $a_i{}^{\mathrm{H}}$ is the hydrogenic cross section for this level, then

$$\frac{a_i}{a_i{}^{\mathrm{H}}}=\frac{Z^2Ry}{\chi}\frac{(i+4)^2}{25i^2}$$

where Z is the ion charge plus 1. The result is that the photoionization cross sections are substantially increased over the hydrogenic values for low levels.

Line Radiation

If the previously discussed model were taken literally, the transitions between excited states would give rise to discrete lines in absorption and emission. It was preferred to consider the discrete levels as being centers of distributions of energy levels insofar as lines are concerned. This follows rather closely the procedure in reference 5 where a specific distribution of levels was taken around the calculated levels. In the present case, the line radiation and absorption were calculated as if they were in discrete lines and then convolved in photon energy with a Gaussian of full-width kT. This approximates line formation from levels which are evenly distributed about the calculated levels and are populated as a Gaussian of full-width kT.

LTE OPACITIES

To obtain results comparable with the opacities calculated in reference 5, it was decided to calculate mean opacities at densities and temperatures corresponding to the 100-atm values given in that report. Since only one active ion can be treated at a time, the stage of ionization was varied until the most populous stage was found. The LTE population of this stage of ionization was calculated along with that of the next higher stage. This put a substantial portion of the population in the high stage of ionization which in the present approximation has no active electrons.

Initially, it was hoped to get a realistic value for both the Rosseland and Planck mean opacities. Indeed, the whole idea of broadening the line transitions was to make it possible to calculate a reasonable Rosseland mean. It was found, however, that, whereas the most populated stage of ionization contributed most to the Planck mean, the next lower stage of ionization contributed most to the Rosseland mean. Since only one active ion could be treated, values of only the Planck mean opacity were calculated.

The first calculations were made at a temperature of 5100° K and a density of 1.24×10^{-7} g/cm^3 so as to compare the results with the experimental opacity deduced from measurements. Figure 1 shows figure 5 of reference 5 with the present results inserted as broken lines. The bars are the experimental values as translated by those authors from measurements; the solid curve gives the results of the detailed calculations. Notwithstanding the apparent discrepancy, the Planck mean is only 25 percent below the value in reference 5. Clearly, if two stages of ionization could have been simultaneously handled there would have been fewer gaps and the mean would have been higher.

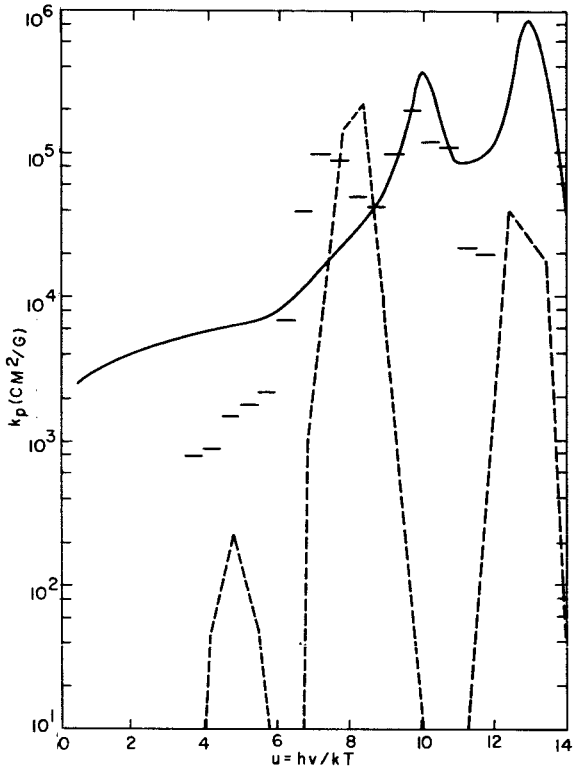

FIGURE 1.—*Experimental and theoretical opacities for* $\rho = 1.24\times10^{-7}$ *g/cm*^{3} *and* T = 0.439 *eV.*

With the initial try so successful it was decided to calculate a series of opacities for densities and temperatures corresponding to the 100-atm data available. Figure 2 shows these values plotted as a broken line along with the values from reference 5 plotted as a solid line. The 5000° K value is too large because two lines appear to be at much lower photon energies than those from reference 5. This puts them in a position where they contribute substantially to the Planck mean, whereas they would not if they were positioned at higher energies. The values for higher temperatures are factors of 2 to 4

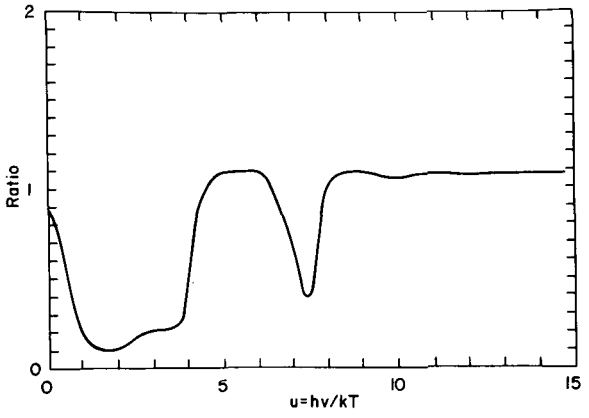

FIGURE 2.—*Planck mean opacities.*

too low as expected in a single-ion, single-electron model.

NON-LTE OPACITIES

In order to determine when non-LTE effects are important, a set of densities and temperatures was determined for which the radiative downward rate from the first excited level was four times the collisional downward rate from that level, these rates being calculated for the most populous ion for LTE at the given density and temperature. The results of these calculations are shown in figure 3. For densities an order of magnitude above this the plasma will be strictly LTE.

Finally, for a few points on this curve the ratio of the non-LTE to LTE opacities and source functions were calculated. It was assumed that there was no incident radiation field and that all radiation escaped. In these circumstances there are a few predictions one would make about the results. The expected effects are an increase in opacity which is generated by transitions from excited states and a general decrease in the source function. All of these effects are due to a decrease in the populations of higher states and an increase in the ground-state populations.

However, since the densities are low, some of the above effects are not apparent and an unexpected result arises. The increase in the ground-state population is very slight because the ions are almost completely in the ground state at LTE (this is a low-density effect). Thus, the expected increase in the

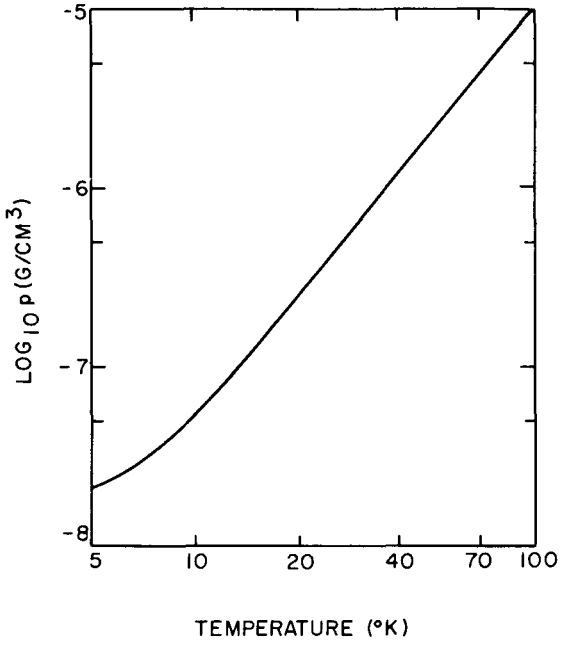

FIGURE 3.—*Density against temperature for non-LTE plasmas.*

opacity due to transitions from the ground state does not occur. Further, since the ground state is almost completely populated, there is little probability of radiative recombination and the continuum source function associated with this recombination is substantially reduced. There is even the possibility (not considered here) that the dominant stage of ionization may be shifted downward. Figures 4

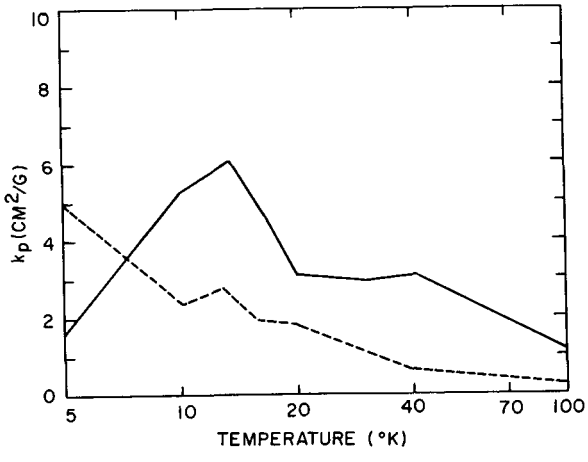

FIGURE 4.—*Opacity curve for* $\rho = 2.63 \times 10^{-7}$ *g/cm*^{3}, T = *1.72 eV and* Z = *4.*

and 5 show these effects. Figures 6 and 7 show the same temperature as do the previous two figures but twice the density. It is seen that the deviation

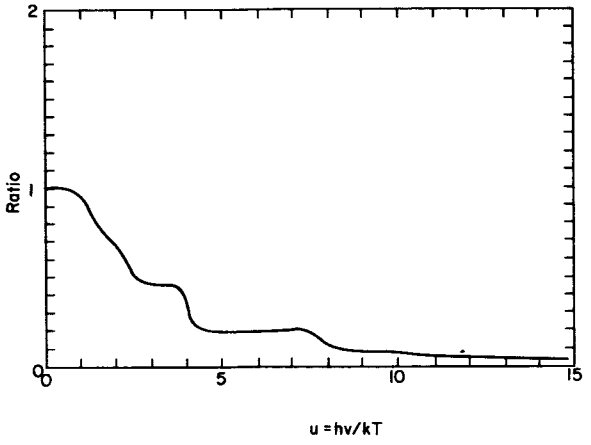

FIGURE 5.—*Source function curve for* $\rho = 2.63 \times 10^{-7}$ *g/cm*^{3}, T = *1.72 eV, and* Z = *4.*

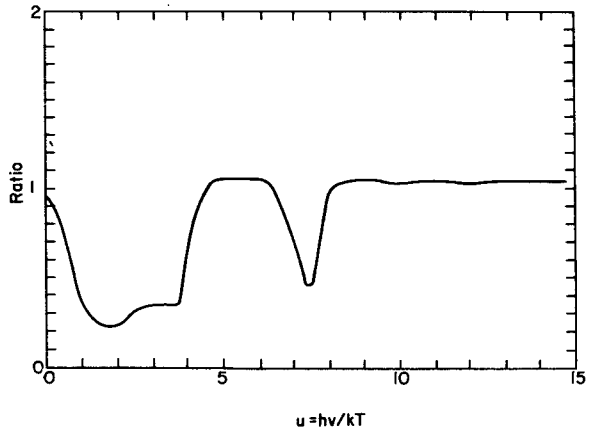

FIGURE 6.—*Opacity curve for* $\rho = 5.27 \times 10^{-7}$ *g/cm*^{3}, T = *1.72 eV, and* Z = *4.*

from LTE is inversely proportional to density, and the previously mentioned order-of-magnitude increase in density would be required to eliminate non-LTE effects.

Figures 8 and 9 show a non-LTE calculation for uranium at a density giving the same electron density as that reported in reference 8. It is seen that there are substantial deviations from LTE although the deviations are within the experimental errors.

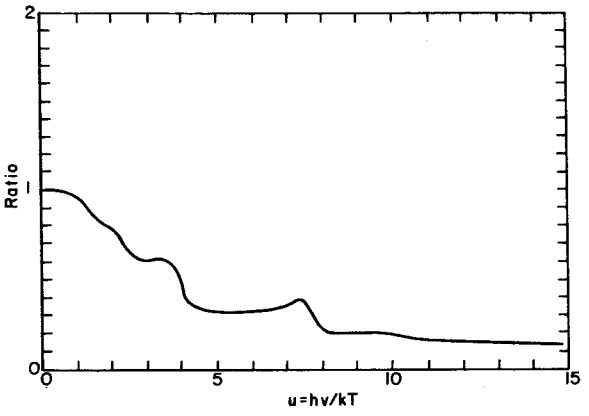

FIGURE 7.—*Source function curve for* $\rho = 5.27 \times 10^{-7}$ *g/cm*^{3}, T = *1.72 eV, and* Z = *4.*

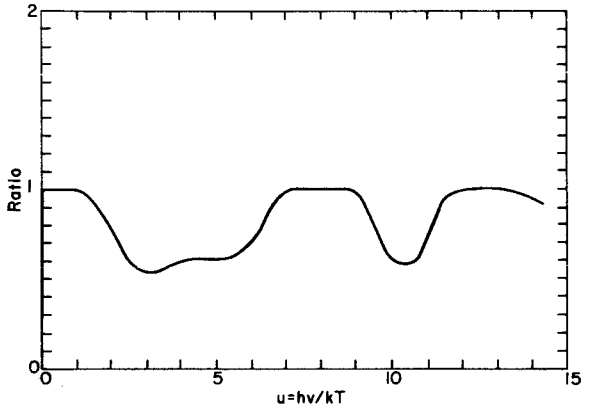

FIGURE 8.—*Non-LTE opacity curve for* $\rho = 1.24 \times 10^{-7}$ *g/cm*^{3}, T = *0439 eV, and* Z = *2.*

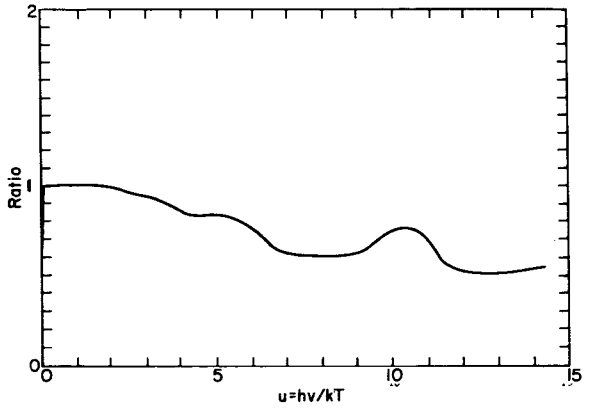

FIGURE 9.—*Non-LTE source function curve for* $\rho = 1.24 \times 10^{-7}$ *g/cm*^{3}, T = *1.72 eV, and* Z = *2.*

SUMMARY OF RESULTS

A simple model of uranium has been developed which allows the calculation of LTE and non-LTE properties. The model assumes only one stage of ionization to be important and that there is only one active electron. This electron is supposed to undergo transitions which are describable by atomic constants valid for hydrogenic ions.

The model was tested by calculating LTE mean opacities and comparing the results with more detailed calculations. The agreement was better than an order of magnitude although the results of the detailed calculations may be incorrect by an order of magnitude.

Densities as a function of temperature were determined where non-LTE effects were important and non-LTE source functions and opacities were compared with LTE values for some cases. Further, it was pointed out that some experimental measurements were made at a density too low for LTE to give a correct description of the plasma.

REFERENCES

1. Bohm, D.; and Aller, L. H.: Ap. J., vol. 105, 1947, p. 1. Reprinted in: Selected Papers on Physical Processes in Ionized Plasmas, D. H. Menzel, ed., Dover Publ. (New York, N.Y.), 1962.
2. Percival, I. C.: Nucl. Fusion, vol. 6, 1966, p. 182.
3. Mihalas, D.: Ap. J., vol. 149, 1967, p. 169.
4. Delmer, T. N.: Rept. GA-8633, Gulf Gen. Atomic Corp., 1968.
5. Parks, D. E.; Lane, G.; Stewart, J. C.; and Peyton, S.: Optical Constants of Uranium Plasma. NASA CR-72348, 1968.
6. Condon, E. U.; and Shortley, G. H.: Theory of Atomic Spectra. Cambridge Univ. Press (Cambridge), 1964.
7. Menzel, D. H.; and Pekeris, C. L.: M.N.R.A.S., vol. 96, 1935, p. 77. Reprinted in: Selected Papers on Physical Processes in Ionized Plasmas, D. H. Menzel, ed., Dover Publ. (New York, N.Y.), 1935.
8. Corliss, D. H.; and Bozmann, W. R.: Experimental Transition Probabilities for Spectral Lines of Seventy Elements Derived From the NBS Tables of Spectral-Cine Intensities. Monogr. 53, Natl. Bur. Std., 1962.

DISCUSSION

Wilkerson: I want to make an observation about the comparison involving the old arc results which has now appeared a couple of times. I believe they were derived from Megger's data. I think those are, in fact, synthetic experimental data where the uranium lines were extracted from a number of others and then put down and recombined into a spectrum of their own numerically.

Delmer: That's right and it is a very good point.

Page intentionally left blank

SESSION III

PROPERTIES OF URANIUM PLASMAS

Chairman: T. D. Wilkerson

B. *EXPERIMENTAL DETERMINATIONS*

Boiling Point of Uranium

A. G. RANDOL III
Nuclear Fuel Services, Inc.

R. T. SCHNEIDER AND C. D. KYLSTRA
University of Florida

Current techniques for boiling-point determinations rely on extrapolation of low-temperature vapor pressure data (usually collected below 2500° K) through the Clausius-Clapeyron equation. Since the temperature limitation is, in most cases, difficult to overcome, it is necessary to rely heavily on indirect methods for the evaluation of boiling points. Under special environment conditions there is evidence that an interpretation of uranium plasma electrical characteristics can lead to reasonable estimates of the boiling point.

The device used to generate the uranium plasma, the University of Florida high-pressure uranium arc, is described. Details of the electrical power, cooling, high-pressure, gas, and data-acquisition systems are given.

A modification of the Nottingham equation for electric arc potential versus current is presented. The application of this arc electrical characteristics model is discussed in terms of the determination of the boiling point of the uranium anode. The evaluated boiling points of uranium between 1 and 7 atm are compared with the extrapolations of other authors.

The experimental uranium plasma program at the University of Florida was initiated in 1966. The successful operation of the first plasma experiment (ref. 1) pointed to the potential of further work. A dc arc struck between fixed tungsten and uranium electrodes in a subatmospheric helium environment generated the plasma. Experimental test times were typically of the order of 1 to 3 min and were limited by heat dissipation, graphite crucible sublimation, and uranium electrode losses.

The growing interest in the thermal characteristics of uranium in the plasma state prompted a continuation of the program. The extension of the experiment into the regime of gaseous-core feasibility resulted in the development (ref. 2) of the device shown in figure 1. As in the prototype, the uranium plasma was generated in a dc arc. The system improvements included internal electrode cooling, high-pressure capability, a method for arc stabilizing, and an adjustable electrode configuration.

The arc is struck between a tipped tungsten cathode pin and a ^{238}U anode pellet. The anode pellet sits in a tungsten crucible brazed into the copper anode pedestal. Both electrodes are internally cooled with a single-pass water flow. The pressure cell is designed for 200 atm at a wall temperature of 500° F. Cell wall temperatures are held below 150° F with the water-cooled, thermal shield.

The chamber pressure environment is derived from a bottled, high-pressure gas cylinder. The gas is injected into the chamber in a concentric sheath about the plasma column periphery. The axial downflow of the gas stabilizes the column during high-pressure, high-power operation.

Arc ignition is obtained with a pneumatic electrode drive. A manual control initiates the downward motion of the cathode and at the onset of current a sensing device triggers the extraction of the electrode. Electric power is derived from a 40-kW dc generator with a maximum current rating of 160 A.

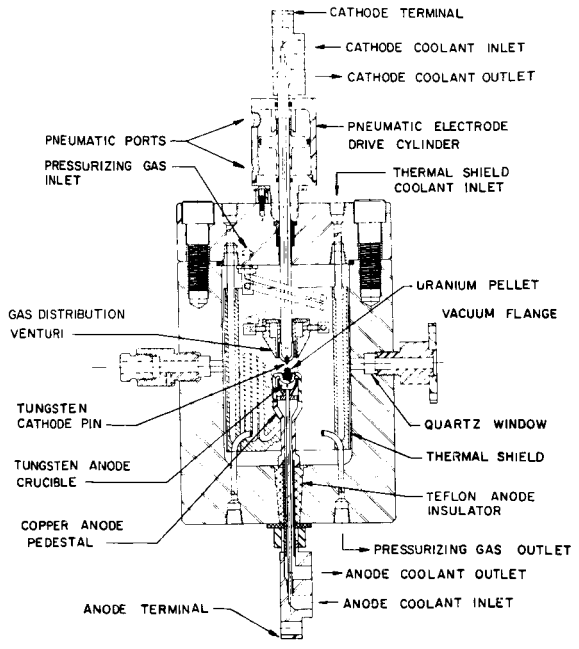

FIGURE 1.—*High-pressure uranium plasma device.*

In addition to a complete program of plasma temperature and number density diagnostics, the relation between the plasma electrical characteristics and the ambient pressure and temperature was of interest. With an appropriate model it is possible to predict gaseous-core engine startup characteristics by assuming that the initial uranium core volume is to be supplied through a consumable electrode system.

Arc electrical characteristics were analyzed with the model described in equation (1):

$$V_{arc}=V_{anode}+V_{cathode}+\frac{Cdp^m}{I^n} \qquad (1)$$

The voltage drops across the sheath regions of each electrode are accounted for in V_{anode} and $V_{cathode}$. The term describing the positive column of the arc includes functional dependences on the electrode separation d, ambient chamber pressure p, and the arc current I. The model subjected to computer analysis was

$$V_{obs}=IR_{system}+V_{sheath}+\frac{Cdp^m}{I^n} \qquad (2)$$

where an additional term IR_{system} accounts for voltage drop in the electrodes. The independent laboratory variables were d, p, and I.

A least-squares curve fitting routine was used to determine R_{system}, V_{sheath}, the constant C, the exponent m, and the exponent n.

Samples of the arc current-voltage characteristics analyzed are shown in figure 2. The most important

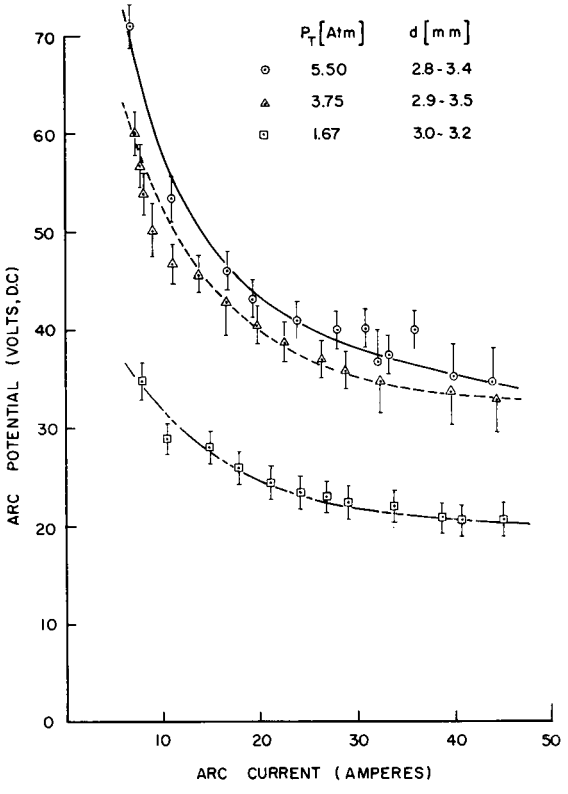

FIGURE 2.—*High-pressure uranium arc voltage-current characteristics.*

characteristic of these curves is the hyperbolic characteristic from which the exponent n of the current I can be evaluated.

The boiling-point parameter n is related to the boiling point of the anode material through the following expression:

$$n=2.62\times10^{-3}\,T_{anode} \qquad (3)$$

This relationship was the result of work performed and compiled in 1924 by Nottingham (ref. 3). The experiment performed in 1924 was similar to the experiment under discussion. A subsequent attempt to repeat one of Nottingham's measurements was made by Suits (ref. 4). His failure challenged the

value of the arc technique for boiling-point determination and has resulted in the use of more direct techniques.

However, under special conditions there is evidence that the Nottingham relationship is reliable. In particular, table I attests to the fact that a uranium arc in an inert helium atmosphere is well described by the empirical relationship. Table I lists the complement of pressures and electrode separations for which the uranium arc current-voltage model was analyzed. The gradual increase of the sheath voltage with increasing pressure is an expected trend and the magnitude indicates that the arc is supported by the uranium species rather than by the helium. The computed values of the Nottingham boiling-point parameter are listed together with the corresponding evaluation of the anode boiling point. The excellent agreement between the results of this experiment and accepted values for the vapor pressure of uranium is illustrated in figure 3. The broken curves are two state-of-the-art extrapolations of vapor pressure measurements made at temperatures below 2100° K (refs. 5 and 6). These measurements were made under vapor pressure conditions three orders of magnitude lower than the pressures of interest.

It is important to note that the ordinate is total system pressure P_A, the sum of the uranium and helium partial pressures as measured external to the plasma chamber. The necessary correlation is that the vapor pressure measured in an equilibrium experiment, that is, effusion experiment, is equivalent to the ambient pressure in the quasi-equilibrium arc method.

Etherington (ref. 7) reports an atmospheric boiling point of 4090° K, which is within 6 percent of the value deduced from this experiment.

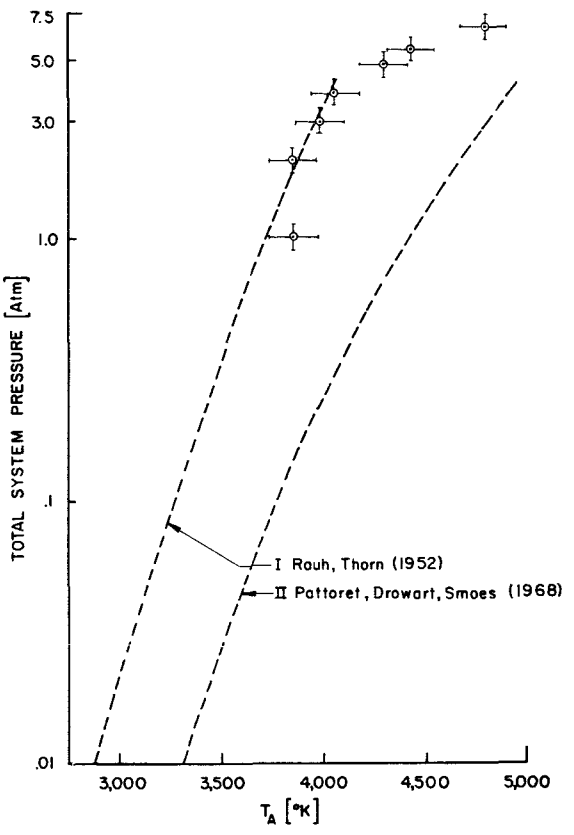

FIGURE 3.—*Total system pressure versus apparent anode boiling temperature. Broken curves are extrapolated from empirical data.*

The early criticism of Nottingham's method was its lack of any theoretical basis. Unfortunately, electric arc phenomena are not well understood.

TABLE I.—*Uranium Arc Voltage—Current Model*

Experimental parameter		Computer results		
Total pressure, p, atm	Electrode gap, d, mm	Sheath voltage V, V	Nottingham parameter, n	Anode boiling point temperature, T, °K
1.0	4.07	14.28	1.008	3847
2.0	3.0 to 3.2	16.3	1.0056	3838
2.86	4.75	16.5	1.050	4007
3.72	2.9 to 3.5	17.9	1.068	4076
4.82	6.01	17.3	1.128	4305
5.6	2.8 to 3.4	23.06	1.170	4465
6.8	6.01	26.8	1.270	4847

However, there is a means available to evaluate the tacit assumption of arc quasi-equilibrium. For the physical picture of anode material evaporating in the plasma column and diffusing radially to the walls of the plasma chamber, it is possible to determine the uranium number density in the arc.

A balance equation for the uranium population in the plasma column can be written as

$$\frac{dN}{dt}=\dot{n}-\beta N \tag{4}$$

where N is the uranium number density in the active plasma volume, $\dot{n}$ is the rate of uranium atom supply, and β is the probability that a particle will remain in the active volume. The value of β is derived from a diffusion concept and is the inverse of the persistence time τ, which is related to the diffusion coefficient through the relationship

$$D=\frac{r_o^2}{\tau(2.405)^2} \tag{5}$$

where r_o is the radius of the active plasma volume and τ for this calculation was deduced from the empirical results shown in figure 4. The work by

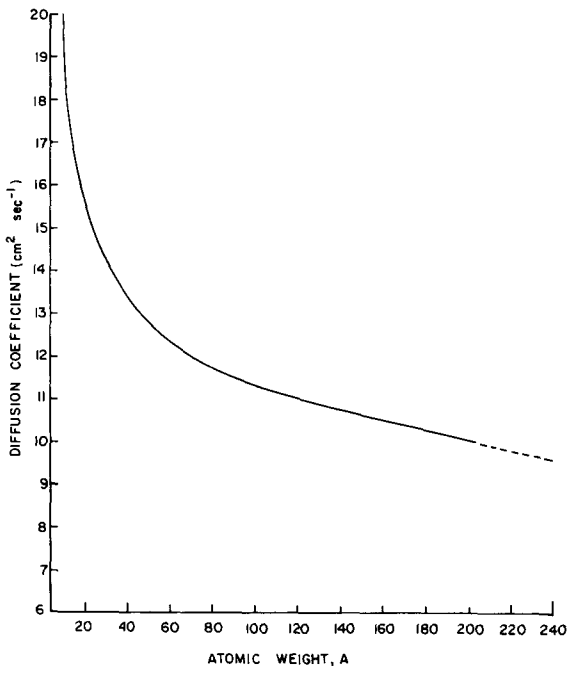

FIGURE 4.—*Experimental diffusion coefficients versus atomic weight.* p = *1 atm*; I = *10 amp dc*; r_o = *3.5 mm*; *electrode separation, 5.0 mm. Measurements made by Raikhbaum and Malykh (ref. 6).*

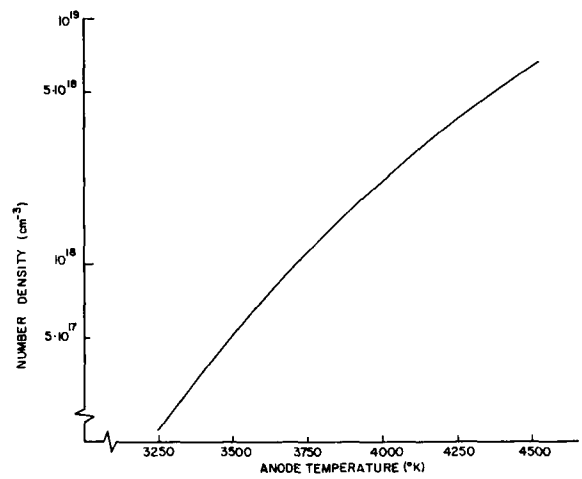

FIGURE 5.—*Uranium number densities versus anode temperature for vaporization with diffusion.*

Raikhbaum and Malykh (ref. 8) derived diffusion coefficients from an arc similar to the arc of this experiment. An extrapolation to a uranium equivalent diffusion coefficient was made.

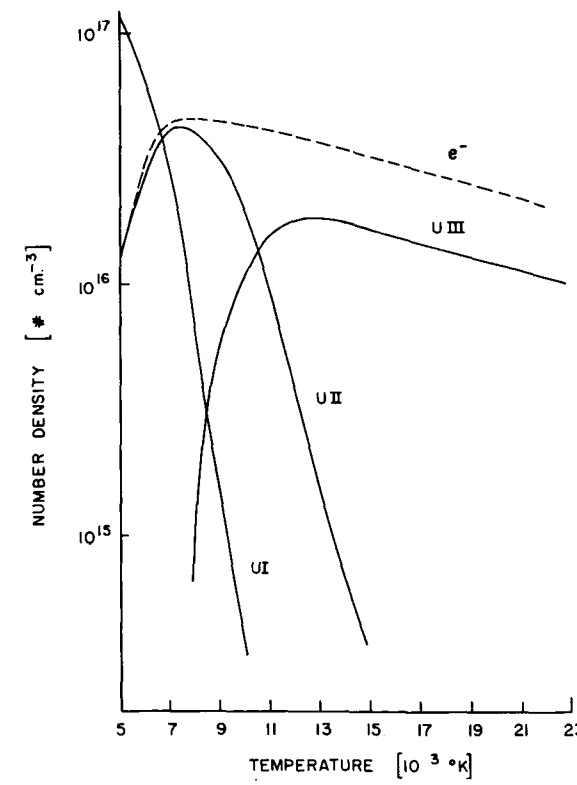

FIGURE 6.—*Uranium plasma composition versus temperature at 0.1 atm.*

The uranium number density can then be calculated from

$$N=J\cdot\frac{\mathcal{A}}{A}\cdot\tau \tag{6}$$

Under the assumption of quasi-equilibrium

$$\frac{dN}{dt}=0 \tag{7}$$

Here J is the mass flux determined by the temperature of the anode, $\mathcal{A}$ is Avogadro's number, and A is the uranium atomic mass. The results of this analysis of vaporization with diffusion are depicted in figure 5. In order to relate this calculation to conditions in the plasma column, the effects of ionization must be considered. The number densities calculated are atom densities and in the 8000° K plasma environment the majority of the atoms have been singly ionized.

Figure 6 shows the results of a solution of the Saha equation at 0.1-atm uranium partial pressure. These results, together with the number density measurements made on the arc (ref. 2), indicate that the preceding analysis is close to reality. The vaporization model suggests a number density 20 percent higher than that measured. However, the accuracy of the uranium partition functions used in the spectroscopic number density measurements is questionable so it is impractical to quote an error limit.

In summary, the authors of the present paper feel that the arc boiling-point technique can be useful in some circumstances. The substantiation of uranium boiling points beyond the temperature limits of current metallurgy has made a contribution to the uranium technology needed for meaningful gaseous-core analysis.

REFERENCES

1. Deese, S. M. F.: Development of a Plasma Chamber and Determination of the Radial Temperature Distribution of Uranium Plasma Sources by Comparative Spectroscopic Analysis. Ph.D. thesis, Univ. of Fla., Dec. 1967.
2. Randol, A. G., III: A Determination of High Pressure, High Temperature Uranium Plasma Properties. Ph.D. thesis, Univ. of Fla., Aug. 1969.
3. Nottingham, W. B.: Phys. Rev., vol. 28, 1926.
4. Suits, C. G.: Phys. Rev., vol. 55, 1939.
5. Rauh, E. G.; and Thorn, R. J.: Vapor Pressure of Uranium. J. Chem. Phys., vol. 22, 1954, p. 1515.
6. Drowart, J.; Pattoret, A.; and Smoes, S. J.: Nucl. Mat., vol. 12, 1964, p. 312.
7. Etherington, H.: Nuclear Engineering Handbook. McGraw-Hill Book Co., Inc., 1958.
8. Raikhbaum, Y. D.; and Malykh, V. D.: A Spectroscopic Method for Studying the Diffusion of Atoms on an Electric Arc. Opt. and Spectros., vol. IX, no. 4, Oct. 1960.

DISCUSSION

Patch: Did you consider thermal diffusion at all in getting the difference in atomic weights and, also, what kind of accuracy do you attribute to the number densities you derived?

Randol: Thermal diffusion was not accounted for, primarily because we assumed a significant tendency of migration of uranium from one electrode to the other. Your second question was, what reliability did we assess to the Saha equation solution?

Patch: Your derived number densities from the experimental data.

Randol: A significance of, say, ±50 percent. Is this the type of answer that you are looking for? What we attempted to do was to establish whether we were "in the ballpark," and that we were within an order of magnitude indicated to us that, at least, the technique was reasonable with the type of data that we had available to us. We had no real measurements of diffusion losses for a column of the geometry and conditions that we operated under.

Williams: You mentioned that you had some problems in running hydrogen. What kinds of problems did you have?

Randol: We just envisioned too many problems to make it even worth our while to try.

Williams: Did these have to do with maintaining the arc or just the fact that you had high-pressure hydrogen?

Randol: The fact that we had high-pressure hydrogen.

Miller: What sort of radial temperature gradients did you measure?

Randol: Hugh Campbell is about to present exactly those results, so I'll let him answer that question.

Wilkerson: I was interested to see that uranium is really such a refractory material. It is difficult to boil and it suggests that in a certain configuration an anode might be useful as a higher temperature radiation standard than, let's say, the carbon arc which is limited to about 4000° K. It appears that, by pressure control, with that kind of source one could go up to perhaps 5000° K.

Page intentionally left blank

Spectroscopic Study of a Uranium Arc Plasma[1]

H. D. CAMPBELL, R. T. SCHNEIDER, AND C. D. KYLSTRA
University of Florida

A. G. RANDOL III
Nuclear Fuel Services, Inc.

Measurements of temperatures, particle densities, emission, and absorption coefficients of a uranium arc are reported. The motivation for this research was to acquire fundamental knowledge of the physical properties of uranium plasmas which will, in turn, eventually lead to the design of a self-sustaining fissioning plasma.

The arc is generated in a high-pressure cell capable of withstanding pressures of up to 100 atm. The current passes between a tungsten pin cathode and a uranium pellet anode. A cover gas of helium is used and substantial vaporization of uranium takes place as the pellet temperature rises and the arc stabilizes. The atomic characteristics of the helium and uranium are such that the emitted line radiation originates primarily from singly ionized uranium.

Spectroscopic diagnostics were used throughout the investigation. Several methods of temperature determination were employed, including Boltzmann plots, relative line intensities, and brightness emissivity methods. Although there are difficulties associated with each method, all temperature measurements were found to lie in the range of 7500° to 12 000° K.

The measurements of emission and absorption coefficients of the plasma were taken over the pressure range of 3 to 15 atm and current range of approximately 15 to 50 A. The corresponding partial pressure of uranium over this range was estimated to be 0.1 to 0.5 atm.

Interest in uranium plasmas has arisen from the possibility of using a self-sustaining uranium plasma as a plasma source for the gaseous-core reactor. Because of the very high temperatures associated with such a device, it will be necessary to remove the energy generated in the reactor by radiative coupling to some working fluid. Hence, it is necessary to study the optical and kinetic properties of high-pressure uranium plasmas.

Of particular interest for future design considerations would be knowledge of emissive power as a function of operating pressures, temperatures, wavelengths, and system geometry. All calculations concerning criticality, radiative heat transfer to the working fluid, and system startup and control require the above information. At present these calculations must rest upon theoretical predictions. Unfortunately, however, the basic constants and properties of uranium which are required for such predictions are poorly known.

The need for experimental work on uranium plasmas to measure radiation emission characteristics is clearly indicated. This paper describes some of the initial spectroscopic measurements on a uranium arc plasma and the diagnostic methods employed to analyze the data. The plasma device has been described in the paper by Randol, Schneider, and Kylstra on page 181.

MEASUREMENTS OF TEMPERATURE AND PARTIAL PRESSURES

Spectroscopic diagnostics, both photographic and photoelectric, were used throughout the investigation. The basic requirement for evaluation of spectroscopic measurements discussed in this section is

[1] Work supported by NASA contract NRG-10-005-089.

the achievement of local thermal equilibrium (LTE) within the plasma. The different criteria for establishing the existence of LTE (ref. 1) were examined, and it was shown that the LTE assumption was valid for the plasma conditions under which data were taken.

Uranium Spectrum

The first experimental investigation of uranium spectra was undertaken in 1946 (ref. 2) and until recently there has been no serious effort to catalog any data beyond the first ionization stage. The results reported by Corliss and Bozmann (ref. 3) were generated by an electric arc operating at approximately 5000° K. At this temperature no significant radiation from the doubly or higher ionized species is expected.

In the present experiment the task of evaluating the emitted uranium spectra was not so difficult as in the one mentioned above (ref. 3). Both the arc temperature and the uranium particle density were relatively high. Consequently, the majority of observed emission lines were those characteristic of singly ionized uranium (U II). In addition, only the strongest U I (atomic uranium) and a trace of helium lines were observed (ref. 4). From this spectrum evaluation it was possible to estimate the maximum arc temperature to be within the range 8000° to 15 000° K. Preliminary temperature measurements (ref. 5) verified this to be so.

The uranium atom naturally possesses a complicated electronic structure as well as a highly complex emission spectrum. So far, no fewer than 1159 U I lines and 315 U II lines have been cataloged (ref. 6) between 2000 and 9000 Å. This high density of spectral lines complicates standard diagnostic techniques, and suitable modifications of standard methods is required before reliable measurements can be performed.

The Boltzmann Plot

The Boltzmann plot method is a relative line method which is independent of number densities and partition functions.

The emission coefficient ϵ for line radiation between two excited states (i.e., power radiated per unit volume per unit solid angle) is given by

$$\epsilon=\frac{h\nu}{4\pi}An\frac{g}{Z}\exp\left(-E/kT\right) \tag{1}$$

where $h\nu$ is the photon energy of the transition, A is the transition probability, n is the total population density of the species, g is the statistical weight of the upper level of the transition, Z is the partition function of the species, E is the energy of the upper state, k is Boltzmann's constant, and T is the temperature. This relation is valid if LTE is established within the plasma. The intensity I of emitted radiation for an optically thin plasma is

$$I=\int\epsilon dL=\bar{\epsilon}L \tag{2}$$

where L is the plasma thickness along the line of sight and $\bar{\epsilon}$ is the average value of the emission coefficient. Using the preceding two equations plus the relation between wavelength and frequency ($\lambda=c/\nu$) and taking the logarithm of both sides of the equation, we obtain

$$\log\frac{I\lambda}{gA}=C-\frac{5040E}{T} \tag{3}$$

where E and T are expressed in eV and °K, respectively. Now T is some average temperature along the line of sight; normally, it is within 10 percent of the maximum temperature. The equation is that of a straight line where the slope can be related to the temperature.

When such a temperature graph (Boltzmann plot) is constructed for different values of log ($I\lambda/gA$) measured from an arc, the points may not fall on a straight line for several reasons. Self-absorption and inhomogeneity along the line of sight as well as experimental errors will result in nonlinearity. These phenomena are common since the light emitted from the high-temperature region of the arc center must traverse the low-temperature region at the edge of the arc, where the lower levels are relatively much more populated with atoms capable of absorbing. The plotted points usually have an upper envelope which consists, to a good approximation, of a straight line of negative slope; this straight line is the locus of those points which pertain to spectrum lines emitted under conditions of optical thinness (ref. 7).

If it is possible to determine by some independent means, such as through an absorption experiment, that the plasma is indeed optically thin for a majority of the spectral lines selected for the Boltzmann plot, the slope may be determined by a least-squares fit.

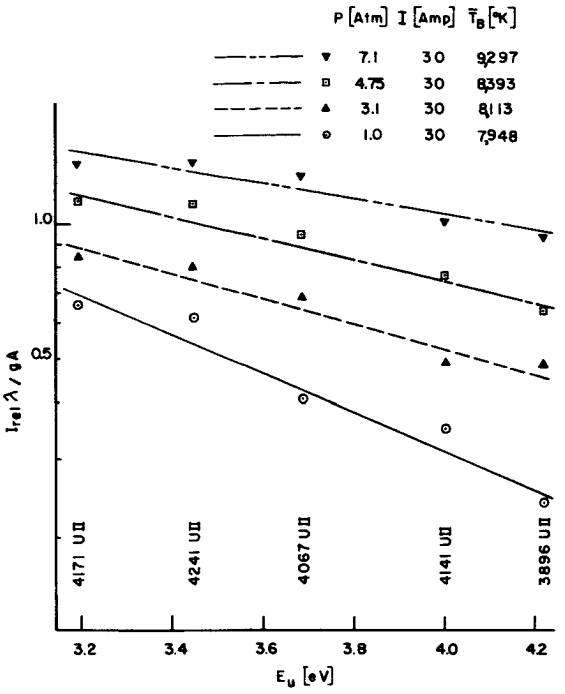

FIGURE 1.—*Ionic Boltzmann plot using chordal intensities of U II lines.*

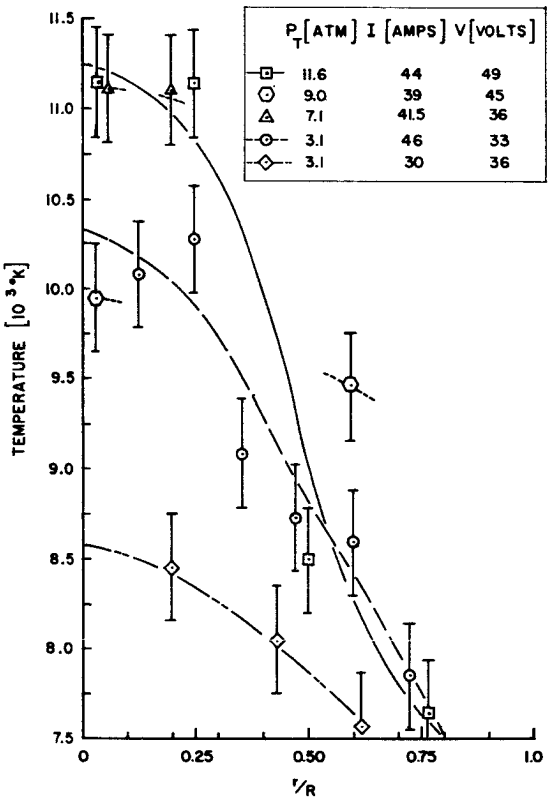

FIGURE 2.—*Uranium plasma temperature profiles from Boltzmann plot determinations.* $P_T = P_U + P_{He}$

Figure 1 shows a Boltzmann plot of arc centerline intensities used to characterize the plasma temperature as a function of pressure. The curves shown are the linear least-squares fit to the data points. The temperature is then determined from the slope of these curves. The increase in temperature for increasing pressure is expected, since at constant current the power input increases.

Figure 2 shows a family of plasma temperature profiles which were derived from Boltzmann plot temperatures at the chordal positions x/X corresponding to the radial positions r/R.

The Fowler-Milne Method

The Fowler-Milne method relies on the fact that the emission coefficient for any given spectral line passes through a maximum at a unique temperature. It is possible to determine this "norm-temperature" (ref. 8) by solving

$$\frac{d\epsilon}{dT} = 0 \tag{4}$$

for the unique temperature T_n. The solution of this equation is coupled to the pressure through the ground-state number density evaluated with Saha's equation (see eq. (7)).

For the experiment reported here, the radial emission coefficient profile exhibits an off-axis maximum for each line studied. The method of analysis thus requires that a value be assigned to the norm-temperature T_n, which is a function of the uranium partial pressure. One can then proceed to solve the relative line relationship

$$\frac{I(r)}{I(r_n)} = \frac{Z(T_n)}{Z(T_r)} \frac{n(r)}{n(r_n)} \exp \frac{Eu}{k}\left(\frac{1}{T_r} - \frac{1}{T_n}\right) \tag{5}$$

for the temperature profile $T(r)$ corresponding to the observed intensity $I(r)$.

Calculation of Emission Coefficients

By referring to equations (1) and (2) it can be seen that the intensity of an emission line is temperature dependent in a manner dictated by the temperature dependence of the three quantities

$n(T)$, $Z(T)$, and exp $(-E/kT)$. Although the last quantity is easily handled the first two are not. The techniques and approximations required for determining the form of $n(T)$ and $Z(T)$ will now be discussed.

If the plasma is assumed to be in LTE, then the following form of the ideal gas law is a good equation of state:

$$P=n_t kT=kT\sum_i n_i \tag{6}$$

where P is the total pressure, n_t is the total particle density, and n_i is the particle density of the ith species (i.e., electrons, neutrals, ions, etc.).

For a given temperature Saha's equation can be used to relate the densities of particles in different stages of ionization:

$$\frac{n_{i+1}n_e}{n_i}=\frac{2Z_{i+1}(T)}{Z_i(T)}\left(\frac{2\pi m_e kT}{h^2}\right)^{3/2}\exp-\left(\frac{IP-\Delta E}{kT}\right) \tag{7}$$

where n_i is the particle density of the ith ionized species, IP is the ionization potential of the ith species, and ΔE is the lowering of the IP due to electric microfields in the plasma (ref. 9).

The one additional relation required in order to determine the particle densities uniquely is the assumption of charge neutrality. Charge balance is expressed by

$$n_e=\Sigma Z_i n_i \tag{8}$$

where Z_i is the positive ion charge.

The above equations can now be solved to give the plasma composition as a function of temperature and total pressure.

Writing Saha's equation in the form

$$\frac{n_{i+1}n_e}{n_i}=S_{i+1}(T) \tag{9}$$

and using equations (6), (7), and (8) we obtain the following cubic equation in n_e:

$$n_e{}^3+(2S_2)n_e{}^2+[3S_1S_2-(PS_1/kT)]n_e - (2PS_1S_2/kT)=0 \tag{10}$$

This expression assumes that only singly and doubly ionized uranium ions are present (as indicated previously). The single positive root of the above equation is the desired solution for n_e. This solution then leads to a complete description of the plasma composition. Number densities for a pressure of 0.1 atm are shown in figure 3. Since the third ion stage is not included in these calculations, the U III and electron number densities shown are only approximate for temperatures less than 15 000° K. The predominant species at typical uranium arc temperatures is the first ion; hence the lowering of the ionization potential, which is proportional to $Z_i{}^2$, can be neglected in the Saha equation solution.

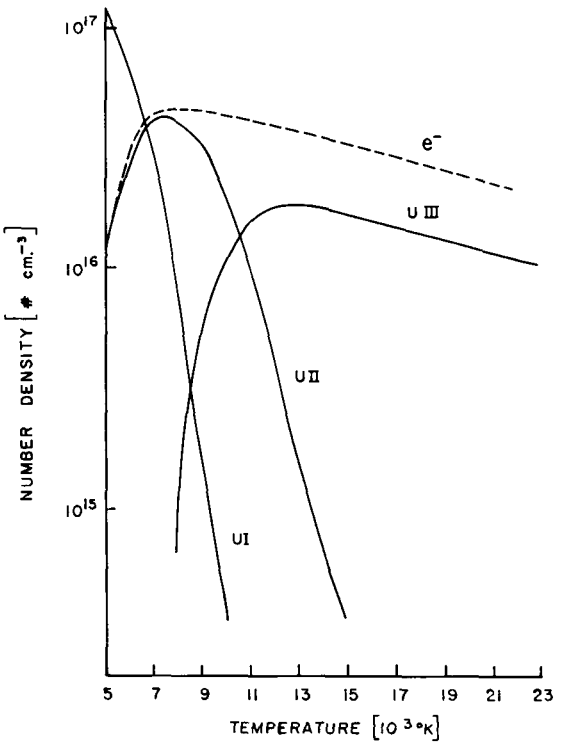

FIGURE 3.—*Uranium plasma composition versus temperature at 0.1 atm.*

In the plasma column the total pressure is determined by the sum of the helium partial pressure, the electron pressure, and the sum of the uranium species partial pressures. Because of the presence of helium, it would appear necessary to include the helium ionization equation in the above calculations. However, the high ionization potential of helium inhibits any significant ionization below 15 000° K.

It has been tacitly assumed so far that the partition functions are known. Unfortunately, this is not so. There appears to be disagreement between reported theoretical values for these functions (refs. 10, 11) and those forwarded to the authors by J. T. Waber of the Los Alamos Scientific Laboratory in

May 1966. In order to proceed it was necessary to evaluate the available information and to construct a consistent set of partition functions.

By definition, the partition function of the ith species is a sum over all available energy levels

$$Z_i(T) = \sum_u g_{iu} \exp(-E_{iu}/kT) \qquad (11)$$

where g_{iu} and E_{iu} are the statistical weights and energies of the uth excited energy level of the ith species. At low temperatures one can approximate the partition function by the statistical weight of the ground state. For U I the ground-state value is 85, and for U II this value is 52.

Figure 4 shows available values for the partition

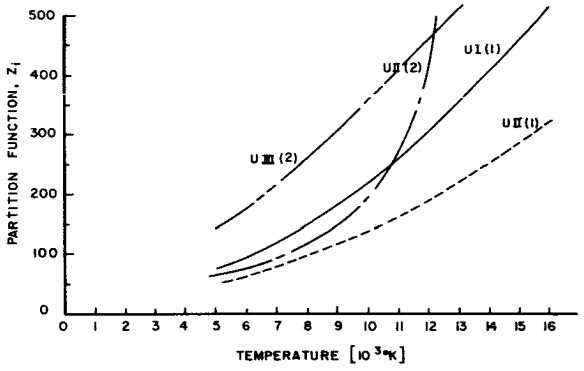

FIGURE 4.—*Temperature dependence of uranium I, uranium II, and uranium III partition functions. (1) data from reference 10; (2) data from reference 11.*

functions of U I, U II, and U III. The curves of reference 10 were anchored to the values of 52 for U I and 82 for U II for the ground states. Figure 4 shows a modification of these curves obtained by use of the correct ground-state degeneracies. The values computed by Waber for U II were in good agreement up to approximately 10 000° K. Data from reference 11 are also shown.

A two-term exponential function was used to approximate these values (least-squares fit) to provide simple temperature-dependent expressions. The results of the fit were

$$\left.\begin{aligned} Z_{\text{U-I}} &= 46.25 \exp(0.159T) + 755.2 \exp(-1.69T) \\ Z_{\text{U-II}} &= 9.201 \exp(0.21T) + 35.603 \exp(0.05T) \end{aligned}\right\} \qquad (12)$$

for temperature T, in units of 10^{-3} °K. These fitted functions were accurate to within 5 percent of the reported values from 5000° to 15 000° K.

In referring back to equation (1), it is evident that it is now possible to determine the temperature dependence of the emission coefficient. Figure 5

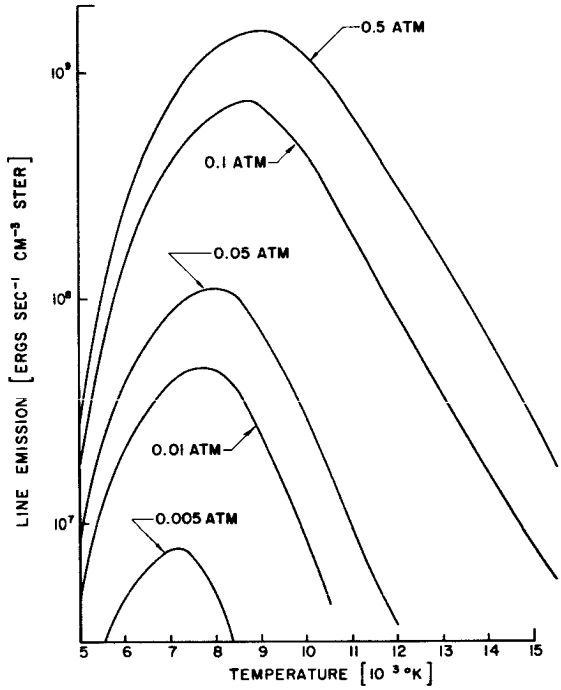

FIGURE 5.—*Line emission or the 4171 U II transition versus temperature for different pressures.*

shows the results of these calculations for several pressures.

Temperature Profiles From Arc Intensity Profiles

The radial analysis of a spectral line, with use of a density gradient corresponding to a radial plasma intensity gradient, yields an arc intensity profile. Two of these profiles are shown in figure 6. One profile represents the intensity distribution before Voigt analysis (ref. 12) and the other represents the distribution after Voigt analysis. The pronounced difference between these profiles is observed in zones near the arc centerline where the pressure is highest and pressure broadening is dominant. The data points extend to only zone 10 because photographic analysis of the spectral line beyond that

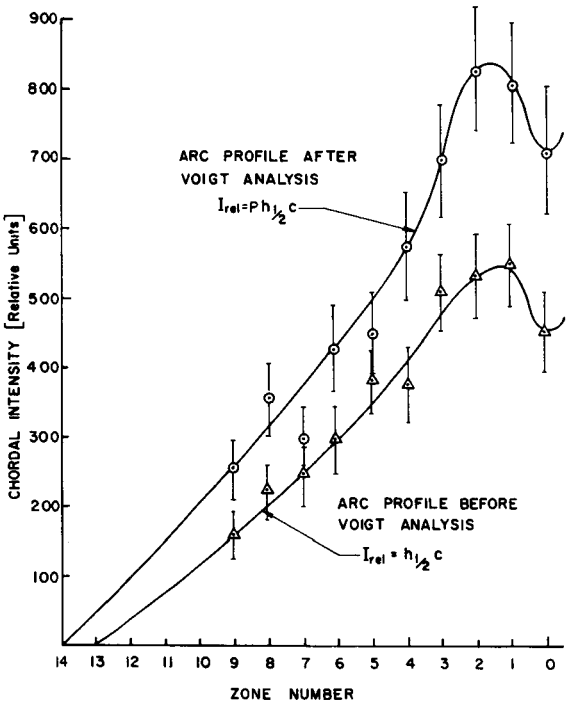

FIGURE 6.—*Arc intensity profiles with and without Voigt analysis.* $P_T = 3.1$ *atm*; $I = 30.5$ *Å.*

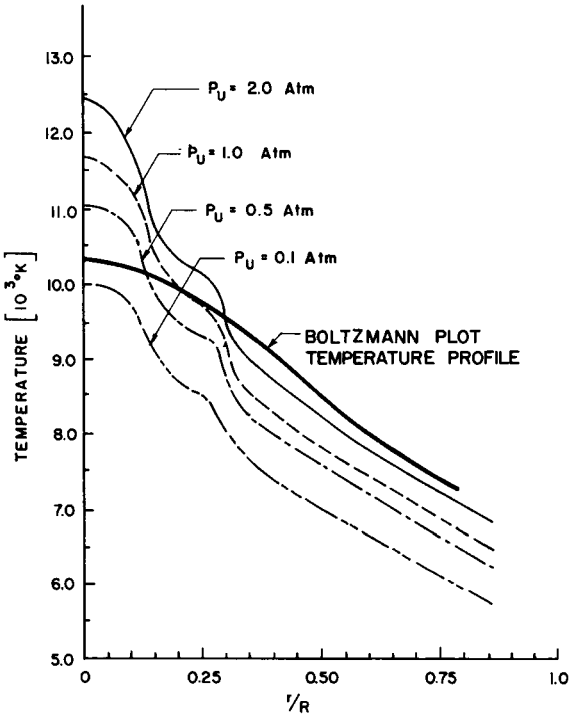

FIGURE 7.—*Uranium plasma temperature profiles from relative intensity analysis.*

point is impractical because of low radiation intensity. The temperature profile of the arc can be obtained from the intensity profile (fig. 6) by using the results of the line intensity calculations (fig. 5). However, knowledge of the number densities of uranium is required.

Partial Pressure of Uranium

The number densities of uranium can be obtained in the following manner. A set of uranium pressures varying between 0.1 and 3.0 atm is assumed and an intensity profile as shown in figure 6 is evaluated by using the assumed pressures. This results in a family of temperature profiles for one single measured intensity profile, the assumed pressure being the parameter as indicated in figure 7. Since these intensity profiles must agree with the temperature profile obtained by the Boltzmann plot method, it is now possible to select the appropriate uranium pressure for each location in the arc. Wherever the Boltzmann plot profile in figure 6 intersects one of the relative intensity profiles the pressure parameter attached to the intersected curves is the correct uranium pressure.

The final result is given in figure 8 for two different operating conditions of the arc. Large uncertainties are introduced into this measurement because of the errors propagated through the Abel inversion of the intensity profiles. No realistic error can be assigned, since part of the error is due to the assumption that one temperature is sufficient to describe the emission from a given zone. Another difficulty encountered is the high sensitivity of the pressure determination to errors in the temperature.

It can be assumed that the partial pressure given in figure 8 for the center of the arc is of reasonable accuracy. Because of the fact explained above the accuracy decreases toward the outer zones of the arc. The "pressure walls" indicated in figure 8 are certainly real; however, their absolute height may be exaggerated for reasons discussed in the next section.

MEASUREMENT OF ABSORPTION AND EMISSION COEFFICIENTS

The "brightness emissivity method" (or line reversal method) of measurement is generally applied

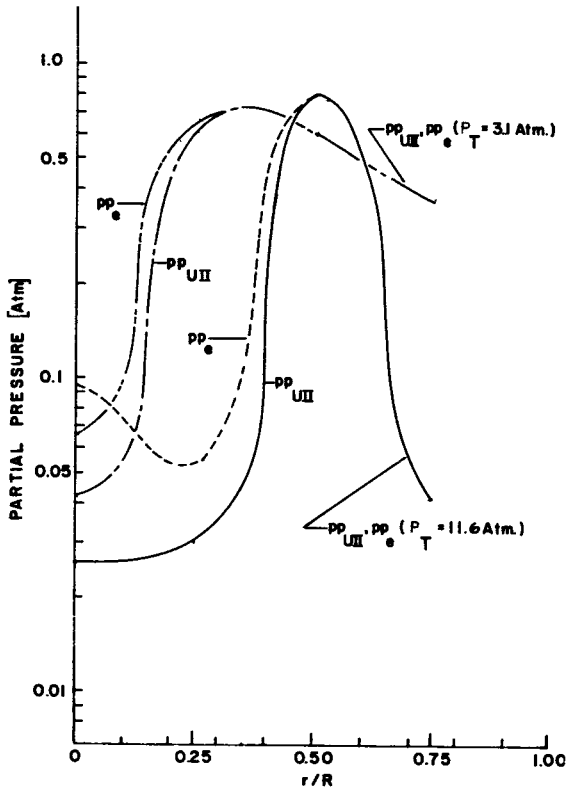

FIGURE 8.—*Uranium II and electron partial pressure profiles.* $P_T = 3.1$ *atm*; $I = 46.0$ *Å.*

to homogeneous transient plasmas such as those produced in shock tubes (ref. 13). In fact, the plasma should be in thermal equilibrium and uniform in order that the method be applicable. Although the uranium plasma exhibits LTE it is definitely not uniform. Consequently, only spatially averaged quantities can be measured.

The underlying theory and practical applications of the method are clearly described in the literature (refs. 8 and 13), and so only the important features are presented here.

Essentially one proceeds by measuring the intensity of radiation emitted by a plasma both with and without a background standard source. The absorption of the background source radiation by the plasma can be used to determine both the temperature and optical thickness of the plasma. Measurements must be taken at a location in the spectrum where the plasma is radiating a strong emission line in order that significant absorption takes place.

The equation of radiative transfer

$$\frac{dI}{dx} = \epsilon - \kappa I \tag{13}$$

where κ is the absorption coefficient, has been solved for simple geometries. In particular, if the intensity of the plasma and background source alone are I_P and I_F, respectively, and if the intensity of the plasma and background source together is I_T, then

$$I_T = I_P + I_F e^{-\tau} \tag{14}$$

where τ is the optical thickness of the plasma at that wavelength. If the thickness of the emitting plasma is L, then the average absorption coefficient $\bar{\kappa}$ is given by

$$\bar{\kappa} = \frac{\tau}{L} = \frac{1}{L}\log\left(\frac{I_F}{I_T - I_P}\right) \tag{15}$$

If Wien's function is used to approximate the blackbody Planck function, then the relation

$$\frac{1}{T_P} = \frac{1}{T_F} + \frac{\lambda}{C_2}\log\left(\frac{I_F + I_P - I_T}{I_P}\right) \tag{16}$$

can be derived where T_P, and T_F are the temperatures of the plasma and background source, respectively, λ is the wavelength at which the measurement is being taken, and C_2 is a constant. The background source (a high-intensity flash lamp) was calibrated with both a tungsten filament lamp and a carbon arc.

Figure 9 displays the measurements of the absorption coefficient for the U II 4090 Å emission line as a function of pressure. The average temperature of the plasma for these measurements was only 7500° K, a value slightly lower than that mentioned previously.

These results indicate that the line optical thickness is much higher than that which might have been expected from interpreting the temperature measurements from the Boltzmann plot (see fig. 1). The effect of this high optical thickness would be an overestimate of the Boltzmann plot temperature, which would in turn result in an overestimate of the uranium partial pressures (see fig. 8) and, in particular, an overestimate of the pressure walls.

The average line emission coefficient can be determined from the previous measurements by using Kirchhoff's law. Of more practical value, however, is information of the radiation emitted over the entire spectrum.

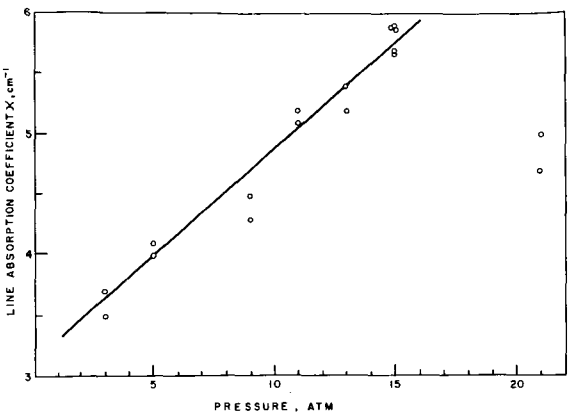

FIGURE 9.—*Average absorption coefficient for U II 4090-Å emission line. Plasma temperature, 7500° K.*

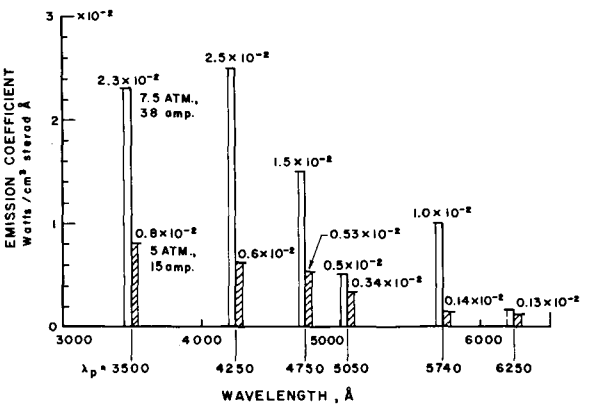

FIGURE 10.—*Average emission coefficients of uranium.*

A thermopile and a series of optical filters were used to measure the emission coefficient over the visible spectrum (approximately 3300 to 7000 Å). Various combinations of filters were used to obtain data in approximately 700-Å step intervals. The measurements represent averages along the line of sight taken at the center of the arc. Typical results for two sets of operating conditions are shown in figure 10.

CONCLUSIONS

The results of our research program to date have been primarily directed toward development of diagnostic techniques for measuring properties of a uranium plasma. A range of different approaches has been taken, all with varying degrees of success, but, on the other hand, all yielding reasonably similar results.

The objective of the work was to obtain measurements of emission and absorption coefficients of a uranium plasma as a function of pressure and temperature. This goal has been partially achieved in that a number of measurements directed to this end have been obtained. The results reported here are typical of a uranium plasma of 0.1- to 0.5-atm pressure at a temperature of 7500° to 10 000° K.

In conclusion, it should be noted that the measurements are of a preliminary nature. In order to cover a sufficient pressure and temperature range—which is essential for plasma core reactor design—further research is required.

REFERENCES

1. GRIEM, H. R.: Plasma Spectroscopy. McGraw-Hill Book Co., Inc., 1964.
2. KEISS, C. C.; HUMPHREYS, C. J.; AND LAUN, D. D.: Preliminary Description and Analysis of the First Spectrum of Uranium. J. Res. Natl. Bur. Std., vol. 37, 1946.
3. CORLISS, D. H.; AND BOZMANN, W. R.: Experimental Transition Probabilities for Spectral Lines of Seventy Elements. Natl. Bur. Std. Monogr., July 20, 1962.
4. SHIPMAN, G. R.: Uranium Arc Spectra. Paper presented at 8th Ann. ANS Student Conf., Apr. 1969.
5. SCHNEIDER, R. T.; SHIPMAN, A. R.; AND RANDOL, A. G., III: Spectroscopic Measurements on a High-Pressure Uranium Arc. 20th Ann. Mid-America Symp. on Spectros., May 1969.
6. MEAGERS, W. F.; CORLISS, C. H.; AND SCRIBNER, B. F.: Tables of Spectral-Line Intensities. Monogr. 32, Natl. Bur. Std., pt. I, Dec. 29, 1961.
7. HEFFERLIN, R.; AND GEARHART, J.: Laboratory High-Excitation Relative *f*-Values for Manganese I. J. Quant. Spectros. and Radiative Transfer, vol. 4, 1964.
8. LOCHTE-HOLTGREYEN, W.: Plasma Diagnostics. North-Holland-Amsterdam (Amsterdam), 1968.
9. DRAWIN, F.; AND FELENBOK, P.: Data for Plasmas in Local Thermodynamic Equilibrium. Gauthier-Villars (Paris), 1965.
10. KRASCELLA, N. C.; AND BURNWELL, W. G.: Theoretical Investigation of the Composition and Line Emission Characteristics of Argon-Tungsten and Argon-Uranium Plasmas. Rept. No. G-910092-10, United Aircraft Res. Lab., Sept. 1968.

11. PARKS, D. E.; LANE, G.; STEWART, J. C.; AND PEYTON, S.: Optical Constants of Uranium Plasma. NASA CR-72348, 1968.
12. VAN DE HULST, H. C.; AND REESINCK, J. J. M.: Line Breadths and Voigt Profiles. Astrophys. J., vol. 106, 1947.
13. REEVES, E. M.; AND PARKINSON, W. H.: Temperature Measurements for Shock Heated Powdered Salts. Sci. Rept. No. 1, Harvard College Observatory.

DISCUSSION

Bostick: Have you tried to scan the radial profile with your absorption technique to see whether you get the humps in the partial pressure in the uranium at positions off the axis?

Campbell: No; we have not done that yet, but that would be a reasonable thing to do.

Wilkerson: On that score, it seems to me that plasma streaming has been discussed several years back by Megger and others in the general arc field.

McLafferty: You evidently used a version of the Abel integral technique to go from chordal distributions to radial distributions when you were doing the intensity measurements. Did you also, when you were using the Boltzmann plot, do that with each of the wavelengths or each of the energy levels before you made those plots for each radius?

Campbell: Each of the energy levels or each of the emission lines?

McLafferty: Each of the lines.

Campbell: Yes; this was done.

Wilkerson: I wonder if you have any comments as to the relative smaller or larger sensitivity of the various methods.

Campbell: No, I would not say that any of the methods are highly sensitive at all.

Page intentionally left blank

Uranium Plasma Opacity Measurements[1]

M. H. MILLER, T. D. WILKERSON, AND D. W. KOOPMAN

Institute for Fluid Dynamics and Applied Mathematics
University of Maryland

Absolute opacities of uranium plasma (2800 to 8800 Å) are measured by using a gas-driven shock tube. Temperatures (7500° to 12 000° K) and partial pressures (1/50 to 1/5 atm) approach those anticipated at the hydrogen-uranium interface of proposed gaseous-core nuclear reactors. At these conditions uranium (U I, U II, and U III) is essentially the only spectroscopically active constituent of shock tube test gases composed of 0.2 to 2.0 percent UF_6 in neon. Absolute opacities at 5000 Å are measured photoelectrically both in emission and in absorption. Time-resolved photographic recording was used to determine the variation of opacity with wavelength. Visible opacities are two to five times smaller than those of theoretical predictions, the variance depending on plasma state. The relative contribution to the opacity from the continuum appears to be tenfold greater than that predicted. The variation of opacity with wavelength was found to fit theory well between 4000 to 8800 Å, but observed opacities decreased rapidly in the uv range, whereas theory predicts that they should increase strongly.

By obtaining the best radiative coupling between the fissioning core and the working fluid of a gas-core reactor, it should be possible to maximize the efficiency and to minimize materials problems of such reactors. To this end, the amount of light emitted by hot gaseous uranium and its spectral distribution must be known as functions of the thermal state of the gas.

We at the University of Maryland are using a conventional, gas-driven shock tube to study the absolute emissivity of uranium plasmas over wavelengths of 2000 to 8000 Å. Our experiment covers uranium pressures of 0.02 to 0.2 atm and temperatures of 7500° to 12 000° K. Our data are intended primarily to test theoretical treatments, which should apply just as well to shock tube plasmas as to hotter and denser fissioning gases (ref. 1). To some extent, however, the present data should prove useful in their own right, since the pressure-temperature domain approximates the conditions of uranium at the hydrogen interface (ref. 2) of proposed reaction engines and open-cycle MHD generators.

Our shock tube has for several years been used to study the strengths and shapes of spectral lines of the lighter elements and of metals in the iron group (refs. 3 to 5). Therefore, at the start of the present work, questions concerning plasma homogeneity, boundary layers, and the existence of local thermal equilibrium (LTE) had already been examined quite thoroughly. Such problems as the reliability of absolute photometric (refs. 6 and 7) and pressure calibrations had also been worked out well enough that we could routinely expect accuracies of 20 percent for the absolute strengths of prominent spectral features.

Any hopes we may have entertained that uranium could be treated as a straightforward extension of our previous work were, however, soon put to rest by two factors. The first is that the uranium lines, particularly the prominent U II lines from low-lying states, had widths which were small when compared with instrument widths. Profiles of strong lines could not be accurately cor-

[1] Research supported by NASA grant NGR-21-002-167 and by the University of Maryland through the Regents, the Minta Martin Fund, the Department of Electrical Engineering, and the Institute for Fluid Dynamics and Applied Mathematics.

rected for possible self-absorption in the plasma (refs. 7 and 8). Moreover, because there are so many lines, as well as a strong continuum, optical radiation plays more than a trivial role in the energy balance of the shock tube. This is detrimental because it prevents us from covering the pressure-temperature range that would normally be accessible. The influence of radiative cooling is shown in figure 1. We have plotted, as a function of

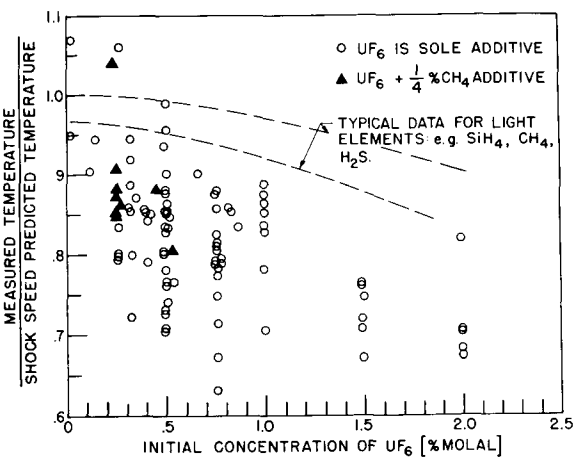

FIGURE 1.—*Ratio of measured temperature to predicted (Rankine-Hugoniot theory) temperatures against initial molal concentration of* UF_6.

the molal concentration of uranium, the ratio of the directly measured plasma temperature to that computed by using the theory of shock tube operation (ref. 9) and the measured, local incident shock speed. The theory, which does not include energy loss by radiation, overestimates temperatures by as much as 30 to 40 percent. For comparison, we have indicated that the gases containing comparable amounts of light elements, e.g., carbon and silicon, are affected to a far lesser extent (ref. 10).

A second major experimental problem is posed by the properties of uranium hexafluoride, the only uranium compound with enough vapor pressure for use in the shock tube: a typical test gas is composed of a 99.5-percent neon carrier plus 0.5 percent UF_6. The questionable stability of UF_6 opens the possibility of interaction with the apparatus, while its formidable molecular weight impedes uniform mixing with lighter gases. Preliminary tests gave no indication that UF_6 interacted with, or was absorbed by, the apparatus. It will be seen shortly, however, that we underestimated the difficulty in preparing uniform mixtures of UF_6 and neon.

EXPERIMENTAL DATA

Present instrumentation is shown in figure 2. The shock tube has a 3- by 4-in. cross section and is

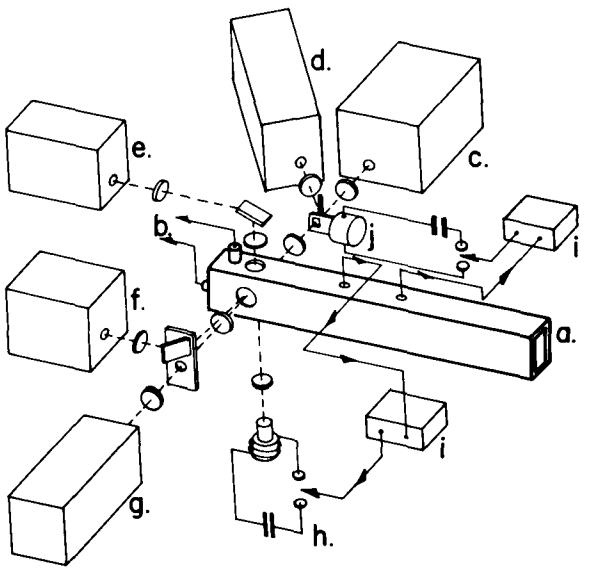

FIGURE 2.—*Current instrumentation.* a, *test section of shock tube;* b, *pressure transducers;* c, *photographic spectrograph, covers 6000 Å with 2½-Å resolution;* d, *photographic spectrograph covers 1800 Å with ¼ Å resolution;* e, *2-channel polychromator;* f, *12-channel polychromator;* g, *5-channel polychromator;* h, *high-intensity flashlamp;* i, *time-delay generators;* j, *exploding wire fast shutter.*

chromium plated to retard corrosion. Test gases are mixed in a Monel flask and are admitted to the shock tube a few moments before firing. Typically, 1000 psi of cold hydrogen is used to drive shocks into 5 to 40 torr of test gas. Under these conditions the slug of hot gas behind the reflected shock attains a volume of the order 1 liter and persists in steady state at the spectroscopic line of sight for 50 to 200 μsec. The only optically active constituents in the plasmas are uranium in various states of ionization and a few well-known red neon lines (ref. 11). From Roger Bengtson's work with fluorine (ref. 5) that used this same apparatus, we know

that temperatures in excess of 12 000° K are needed before the most prominent fluorine lines attain even a marginal brightness.

Several spectrographs view the plasma in a common plane a few millimeters upstream from the end wall. Spectrographs *g*, *f*, and *e* are employed as polychromators, each housing 2 to 10 absolutely calibrated photomultipliers. Spectrographs *c* and *d* employ photographic recording. These can be time-resolved by an exploding-wire shutter *j* or by a revolving drum camera. In order to measure pressure, one quartz transducer *b* is located in the side wall and a second, facing upstream, is in the end wall. Located underneath the shock tube is a short-duration flash lamp *h*, the continuum emission of which is made to pass vertically through the shock tube to be recorded by the two-channel polychromator *e*.

Interaction between the flashlamp radiation and the shock tube plasma is used to find the plasma's temperature and to obtain its emissivity in a very direct manner (ref. 6). The situation as seen by a single photomultiplier with a 4-Å bandpass (situated at 5000 Å) is presented in figure 3. From the time t_a, when the reflected shock passes the line of sight, until the time t_b, when the flashlamp discharge is initiated, the intensity I_{em} is due solely to the steady-state emission of the shock tube plasma. After time t_b, the signal consists of I_{em} plus the transient radiation of the flashlamp. Because the maximum brightness of the flashlamp corresponds to a radiation temperature that is greater than the shock tube temperature, the intensity of the lamp fired by itself in the absence of any attenuating shock tube plasma (broken curve) will at two points cross the previously recorded trace. These two points C and D (the so-called "reversal points") occur at the blackbody intensity of the shock tube plasma. Since the photomultiplier is absolutely calibrated, the Planck function can be solved for the plasma's temperature. The intensity ratio

$$I_{em}/I_{C,D}=\int I_\lambda/B_\lambda d\lambda=\int(1-e^{-\tau})\,d\lambda$$

is the slit-averaged emissivity of the plasma. It will be noted that any errors in absolute calibration will not affect emissivity measured in this way.

Figure 4 compares the reversal temperatures measured simultaneously by two channels, located at 5000 and 5020 Å, respectively. The two sets of

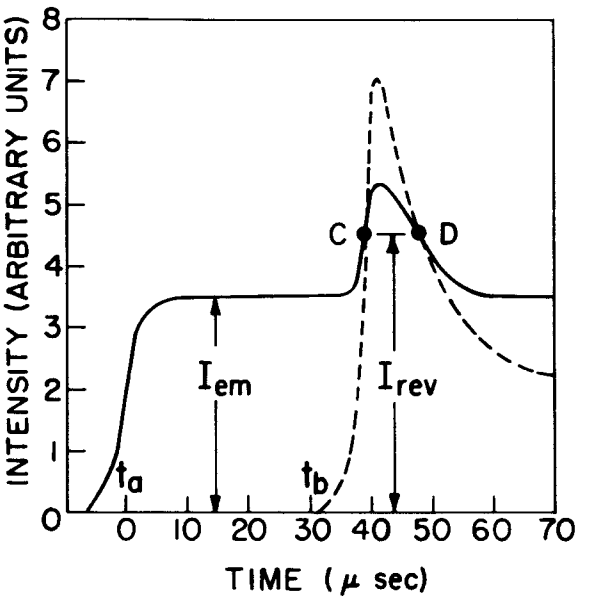

FIGURE 3.—*Schematic CRO display of intensity reversal measurement. Solid curve is emission intensity of shock tube* I_{em} *augmented after* t_b *by the plasma-attenuated flashlamp signal. Broken curve is unattenuated flashlamp signal, subsequently recorded. Points* C *and* D *are reversal points marking blackbody intensity level for shock tube plasma.*

determinations agree within estimated precisions. Emissivities obtained from the two channels, however, are not equal, as seen in figure 5. These data do fit quite well to the resulting curve if the mean

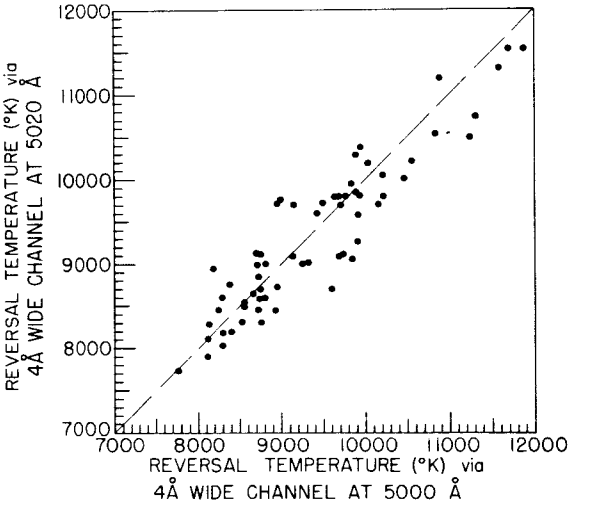

FIGURE 4.—*Comparison of reversal temperatures measured simultaneously by two photoelectric channels.*

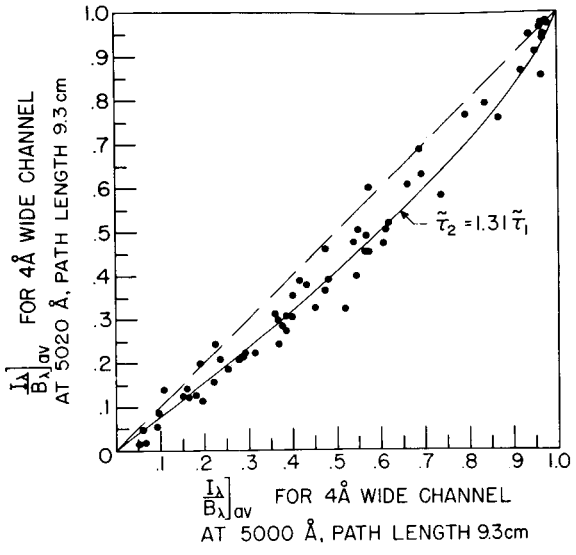

FIGURE 5.—*Comparison of slit-averaged emissivities* $\int_{-2Å}^{-2Å} I_\lambda/B_\lambda d\lambda$ *measured simultaneously by two photoelectric channels.*

optical depth $\tilde{\tau}$ at 5000 Å defined by

$$4Å(1-e^{-\tilde{\tau}}) \cong \int_{-2Å}^{2Å} (1-e^{-\tau})\, d\lambda$$

were 30 percent greater than that at 5020 Å.

A more conventional technique utilizing absolute emission data was also employed to measure emissivities in the neighborhood of 5000 Å. Nine absolutely calibrated photomultipliers, viewing the shock tube horizontally, sample 1-Å-wide bands of the spectrum spread over a 25-Å interval. Figure 6 compares the signals from these nine channels (units of carbon arc intensity) against their average for a given experiment. One channel (channel 3) reads consistently higher than the others. We regard this discrepancy as being instrumental because the pattern persists at levels closely approaching the blackbody limit. With this exception, it will be noted that the relative scatter between channels decreases with increasing intensity, thus indicating a less "gappy" character of the spectrum as emissivities approach unity.

Emissivities deduced from these data are compared (fig. 7) with those obtained via the reversal technique. Once the difference in the lengths of the horizontal and vertical light paths is taken into

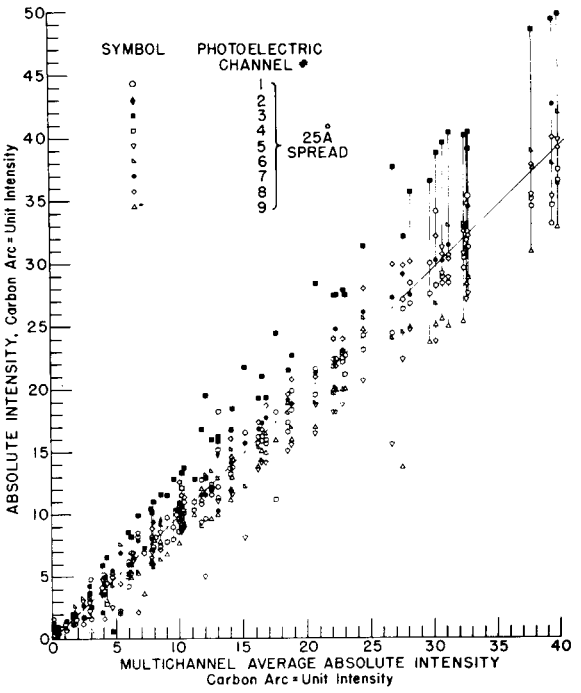

FIGURE 6.—*Absolute intensities recorded simultaneously by nine photoelectric channels versus their average intensity for a given run. Bypass of each channel is 1 Å.*

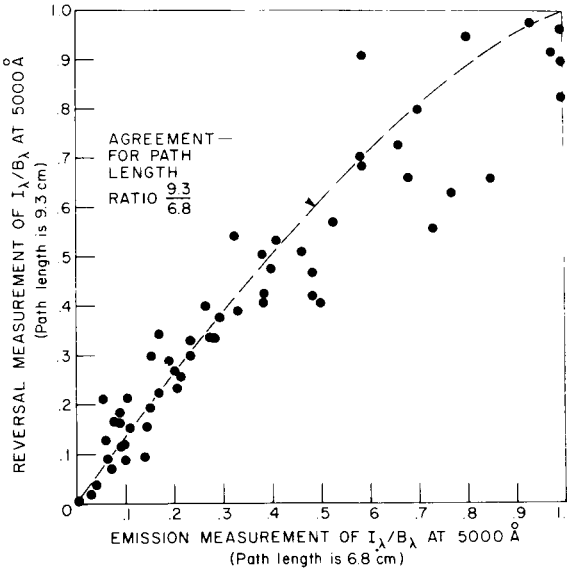

FIGURE 7.—*Comparison of slit-averaged emissivities obtained by reversal technique (fig. 5) and those obtained by absolute emission technique (fig. 6).*

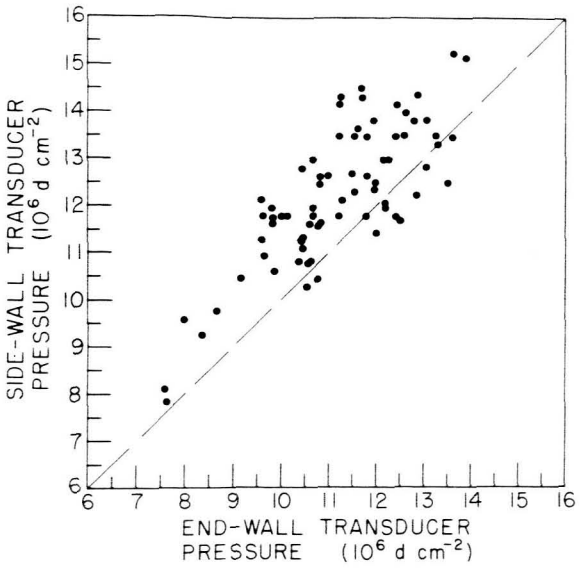

FIGURE 8.—*Comparison of pressures measured by sidewall and end-wall quartz transducers.*

account results from the two complementary methods are seen to agree satisfactorily.

Figure 8 compares the pressures simultaneously measured by transducers looking side-on and end-on. Precision of these measurements is to some extent hampered by ringing in the gages. The two sets of data agree on the average to 8 percent, which is within our estimate of experimental tolerance.

The 70-mm-wide drum camera spectrogram reproduced in figure 9 covers the region from 4800 to 5900 Å. Resolution in wavelength is 1.3 to 1.5 Å and in time (running upwards) is 10 μsec. The steady-state duration behind the reflected shock wave is approximately 110 μsec. The appearance of this spectrum is representative of experiments using lean (e.g., ¼ percent) test gas mixtures, which lead to plasma temperatures in the range of 10 000 to 11 000° K and uranium partial pressures of 0.05 to 0.08 atm. Somewhat greater detail but no basic differences emerge when the fast shutter is used to obtain spectroscopic plates with five times the resolution (0.24 Å) shown here.

The same wavelength region (4800 to 5900 Å) is covered by the spectrogram shown in figure 10, which is representative of data obtained with richer mixtures (e.g., ¾ percent) that give uranium plasma pressures of 0.15 to 0.2 atm and temperatures of 8000° to 9000° K. The complicated line structure of figure 9 is seen to persist at higher uranium concentrations, but the apparent con-

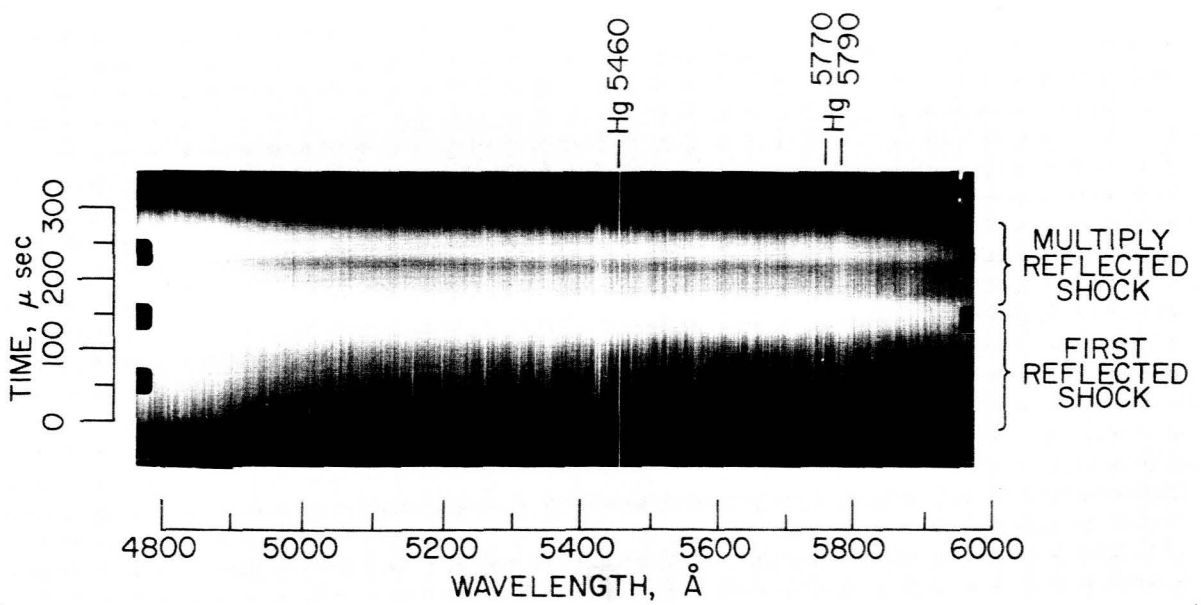

FIGURE 9.—*Time-resolved drum camera spectrogram for uranium plasma from 4800 to 5900 Å. Increasing time runs upwards and wavelength decreases to the left. (Test gas: 0.25 percent UF_6 in neon.)*

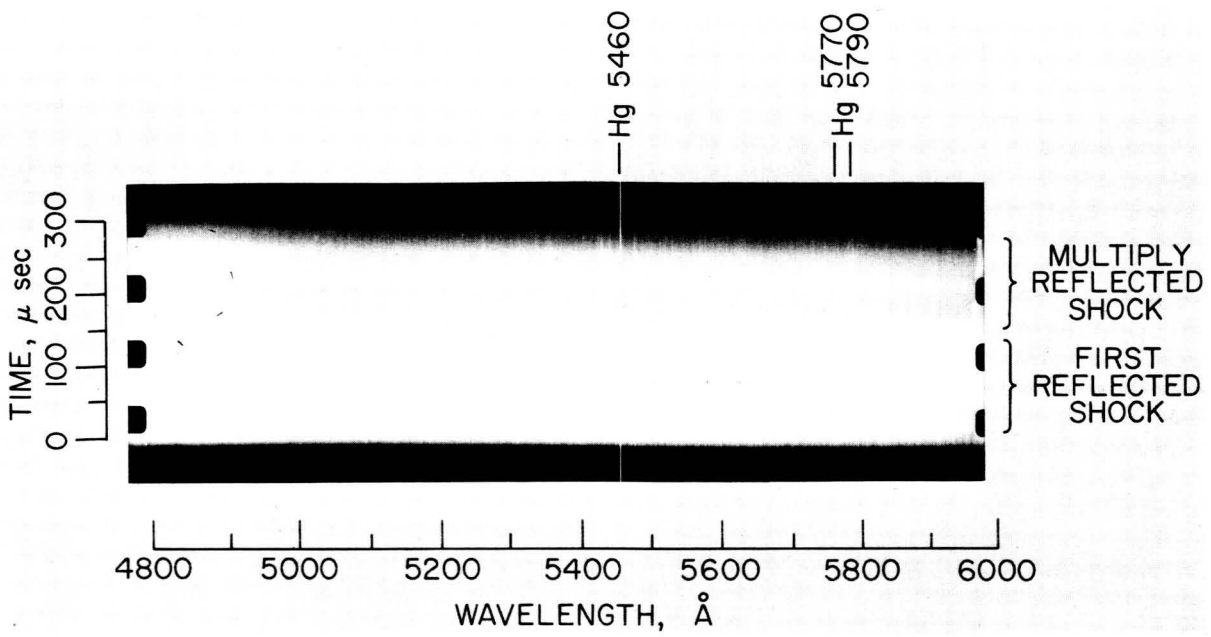

FIGURE *10.—Time-resolved drum camera spectrogram for uranium plasma from 4600 to 5700 Å. Same spectrograph settings as in figure 9 but for a plasma of higher uranium concentration (0.75 percent UF_6 in neon).*

tinuum radiation has gained in strength relative to the line spectrum. Radiative cooling causes a monotonic decrease of light levels as time progresses (upward). Resonance lines of U I are seen sometimes in absorption and sometimes in emission, the state depending upon the thickness of the boundary layer at any instant. These are the only lines affected by these thin, cooler layers, and, fortunately, there are too few of these lines to affect measured emissivities appreciably.

A digitized microdensitometer and associated computer codes are used to reduce spectra such as these to charts of relative intensity against wavelength. The absolute sensitivity of each film is determined on a shot-to-shot basis by fitting the relative intensity profiles to the intensities recorded simultaneously by the several absolutely calibrated photomultipliers.

RESULTS AND DISCUSSION

Figure 11 depicts typical results obtained from the photographic data. For a stated set of plasma conditions, the variation of mass absorption with wavelength is plotted for our data and for the theoretical predictions of Parks et al. (ref. 1). The experimental curve is normalized to theory at 5000 Å by a scaling factor to be considered shortly. The object here is to show that from 4000 to 8000 Å the shapes of the two curves agree very well indeed,

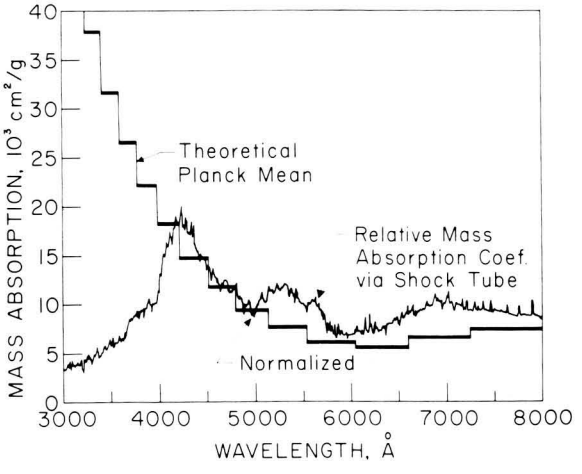

FIGURE *11.—Variation of uranium mass absorption coefficient with wavelength. Experiment normalized to theory at 5000 Å; T = 10 000° K; PP_U = 0.6 atm.*

considering their complexity. Around 4000 Å, however, a striking change sets in: in contrast to the predicted ultraviolet surge, the observed absorption diminishes rapidly with decreasing wavelength. By 3000 Å, this amounts to a tenfold discrepancy with theory.

Absolute emissivity data for uranium at 5000 Å are shown in figure 12. In lieu of a three-dimensional representation, we show emissivity as a function of uranium number density, and we use different plotting points to distinguish between data collected within four 1000° K temperature intervals. The scatter, which is three to four times worse than we experienced with any previous element, is not quite so serious as a first impression would suggest. That is, there are indeed significant differences in the behavior of data from different temperature regimes. By considering the various types of plotting points one at a time, we find the scatter to be approximately 50 percent. This is still annoying enough to consider the problem further. At the start of our investigation, the scatter was, in fact, much worse. At that time, the Monel mixing and storage tank was connected through small orifices to a pair of pressure gages that had internal volumes comparable in size to the tank itself. On the assumption that the gas in the gages could be richer or leaner in UF_6 than the gas in the tank, the variation depending upon unspecified details in the way neon was admitted to the apparatus, we replaced the gages with much smaller ones and added rudimentary provisions for mechanically stirring the mixtures. These measures brought about reduction in scatter by a factor of 2½. The apparatus is being refined further; for data shown here, considering photometric precisions, and the lumping of data onto a rather coarse temperature grid, we estimate that random inhomogeneities of 20 percent in local UF_6 concentrations would fully account for the observed scatter.

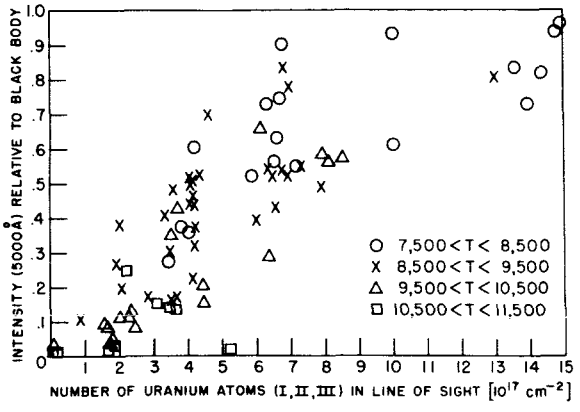

FIGURE 12.—*Absolute emissivity of uranium at 5000 Å versus number density (U I, U II, U III) with temperature as a parameter.*

These same emissivity data have been converted into "mean" optical depths for figure 13. Under the least favorable circumstances, self-absorption could cause us to underestimate the average optical depth in a 2-Å bandpass by 20 percent. The object of this full-logarithmic display is to show that our data fall intermediate between a linear and a square dependence on the density of uranium; that is, between results one would obtain from a spectrum composed exclusively of optically thin lines (linear case) and those one would expect from a purely continuous spectrum (square dependence). By considering the probability of self-absorption as well as the predicted slight continuum contribution, the behavior expected from Park's calculations is essentially linear. The functional dependence of the

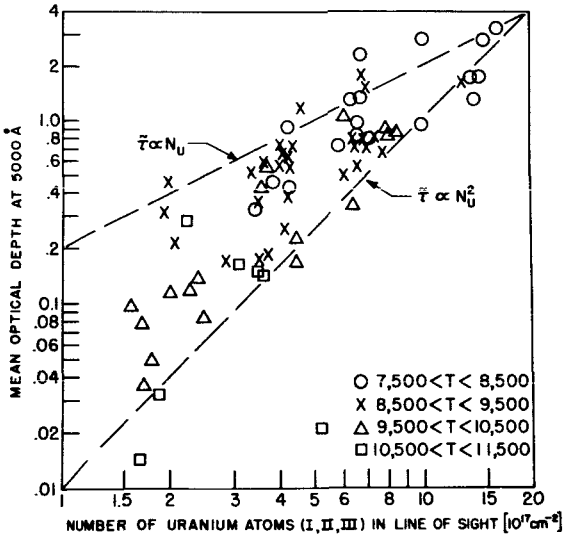

FIGURE 13.—*Slit-averaged (mean) optical depth of uranium at 5000 Å against number of uranium (U I, U II, U III) atoms with temperature as a parameter.*

photoelectric data, therefore, reinforces the indications from the photographic profiles that the continuum contributes a significant fraction of uranium's opacity.

The measured absolute mass absorption coefficient at 5000 Å is given as a function of uranium pressure and temperature in figure 14. Predicted contours of constant absorption are shown for comparison. Over the accessible band in pressure-temperature space our results differ from the predictions of Parks et al. by factors of 2 to 5. Our data show a somewhat stronger (50 to 100 percent) dependence on temperature than one expects theoretically (but in the same direction). Our data also exhibit a pronounced dependence on pressure, which is fully an order of magnitude greater than that called for theoretically. If this enhanced pressure dependence is borne out by further work and is found to persist as one approaches the 1000 times greater pressures of a fissioning core, current models of radiative transfer in gaseous fission reactors will require some drastic revisions.

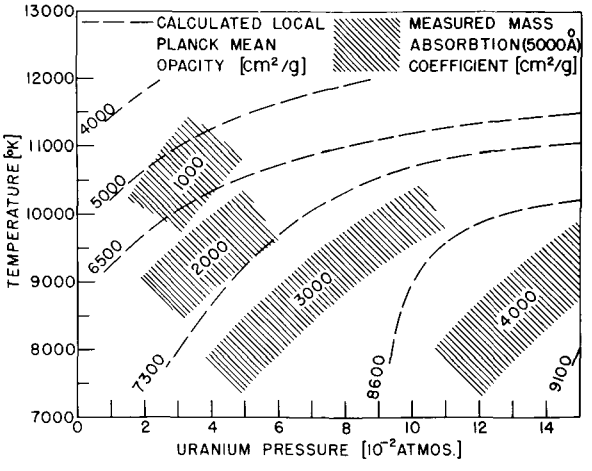

FIGURE *14.—Measured and predicted mass absorption of uranium at 5000 Å as a function of temperature and uranium partial pressure.*

REFERENCES

1. PARKS, D. E.; LANE, G.; STEWART, J. C.; AND PEYTON, S.: Optical Constants of Uranium Plasma. (Rept. GA–8244, Gulf Gen. Atomic, Inc.) NASA CR–72348, 1968.
2. ROM, FRANK E.: Comments on the Feasibility of Developing Gas Core Nuclear Reactors. NASA TM X–52644, 1969.
3. WILKERSON, T. D.; KOOPMAN, D. W.; MILLER, M.; BENGTSON, R.; AND CHARATIS, G.: Phys. Fluids, Suppl. I, vol. 22, 1969.
4. MILLER, M. H.: Tech. Note BN 550, Univ. of Md., 1968.
5. BENGTSON, R. D.: Tech. Note BN 559, Univ. of Md., 1968.
6. MILLER, M. H.; AND BENGTSON, R. D.: J. Quant. Spectros. Radiative Transfer, vol. 9, 1970, p. 272.
7. ROBINSON, D.; AND LENN, P.: Appl. Opt., vol. 6, 1967, p. 893.
8. GRIEM, H. R.: Plasma Spectroscopy. McGraw-Hill Book Co., Inc., 1964.
9. BRADLEY, J. N.: Shock Tubes in Chemistry and Physics. Methuen (London), 1962.
10. BENGTSON, R. D.; MILLER, M. H.; KOOPMAN, D. W.; AND WILKERSON, T. D.: Phys. Fluids, vol. 13, 1969, p. 372.
11. BRIDGES, J. M.; AND WIESE, W. L.: Phys. Rev., vol. 2-A, 1970, p. 285.

DISCUSSION

Randol: What attempt did you make to determine the equilibrium condition in the arc or in the shock tube? What models did you use?

Miller: A homogeneous LTE plasma. We measured the temperature in a number of different ways that depended on the assumption of LTE in entirely different ways, some of them quite critically, some of them not at all so, and we never found anything that departed from this assumption. Also, we measured transition probabilities in plasmas which varied by as much as a factor of 8 in electron density. Electrons are rather crucial in establishing LTE and if, by hypothesis, you were off LTE, then there should be some correlation between electron density and the populations you observe in the upper state emission. This correlation was never found. To top it all off, our electron densities are at least 10^{16} and typically more like 10^{17}, which is well within what the theory calls for.

Generation of a Fissioning Plasma

C. D. KYLSTRA AND R. T. SCHNEIDER
University of Florida

Measurements of the radiation emission properties of a uranium plasma, such as those made at the Los Alamos Scientific Laboratory and reported in the paper by Steinhaus, Radziemski, and Cowan on page 151, by the United Aircraft Corp. (ref. 1), and at the University of Florida (ref. 2), have been made on thermally excited plasmas. That is, an electrical discharge, either rf or dc, is used to supply energy to the plasma by electron-atom, electron-ion collisions. These plasmas are essentially high-pressure, collision-dominated, local thermal equilibrium (LTE) plasmas.

However, in a plasma-core reactor, the fission process is the source of energy. The energy appears in the form of kinetic energy of the two fission fragments or products. The heavy fission fragment has a kinetic energy of approximately 65 MeV, and the light fission fragment has approximately 100 MeV of energy. This is considerably above the thermal energy of the uranium atoms and ions, which is characterized by ½ to possibly 3 eV. The process of slowing down and thermalizing these fission fragments will cause extensive nonequilibrium ionization and excitation. Many additional stages of ionization and excitation of the uranium will occur. It is possible that the resultant radiation spectrum may be considerably different from the thermal equilibrium spectrum with no fissions occurring. Even more important, we would like to know what fraction of the fission energy is emitted from the plasma as nonequilibrium radiation compared with the amount of fission energy deposited by "heating up" the plasma and what is the spectrum of the nonequilibrium radiation.

Thus, the decision to conduct a fissioning uranium plasma experiment coincided with the realization that we needed the ability to generate a "pure" uranium plasma. That is, no cover gas or impurities were to be present. The previously mentioned electrically excited plasmas use an inert cover gas. Since we cannot, from a practical standpoint, compute the radition spectrum from a fission fragment excited plasma, we did not want any emission lines from material other than uranium to show up in the spectrum since we have no way to separate them. Also, with only uranium present, it is possible that we can deduce better values for the emission constants (statistical weights times transition probabilities) while operating without fissions.

To aid this process and so that we can start out with the simplest system, the phase I experiments will not use a uranium arc but will heat the uranium in an enclosed tungsten oven. Thus the uranium plasma temperatures will be accurately determined by measuring the tungsten oven temperature.

There are, to put it mildly, several problems involved with generating a pure uranium plasma. The uranium vapor will condense on cold surfaces; therefore, there cannot be any cold surfaces. The vapor pressure of uranium is low even at the highest solid temperatures, and thus the uranium number density is low, thereby causing the fission rate to be very low relative to that possible in metallic uranium. Later, we will use a dc arc to increase the plasma temperature, but there will be a corresponding decrease in the uranium number density. The ^{235}U is expensive, approximately \$20/gm for 93 percent enriched; thus we want to minimize loss of the uranium. There are safety problems involved when one works with ^{235}U, since it is a radioactive alpha emitter. There are also radiation hazards associated with the experimental

device, since it will be activated by neutron absorption.

EXPERIMENTAL DEVICE

Figure 1 is a schematic of the fissioning uranium plasma device for the phase I experiments. It is a

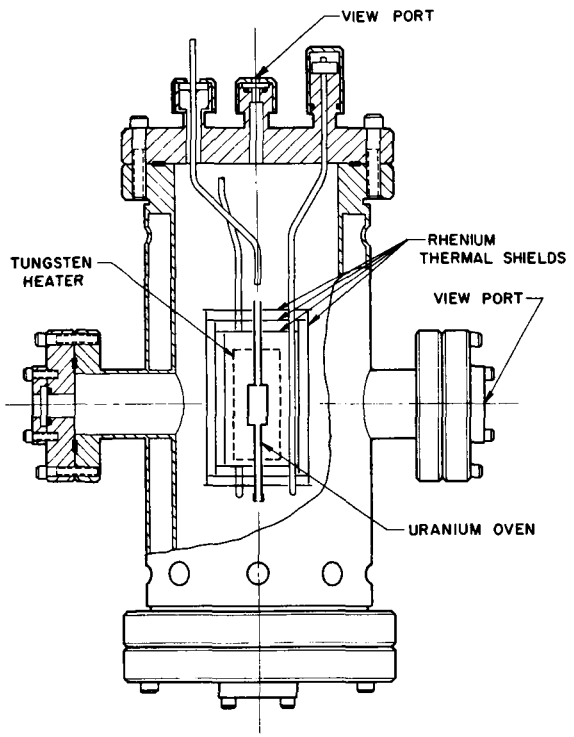

FIGURE 1.—*Schematic drawing of device for fissioning uranium plasma.*

stainless-steel vacuum chamber with two side windows, a vacuum system connection, and windows in the top and bottom flanges. The top flange contains the support rods for the internal components, electrical leads for a tungsten heater, a window, and a deflector system to help keep the uranium which escapes from the oven off the window. The heart of the internal components is the uranium oven. This is a tungsten can which contains the uranium plasma. Two slots allow radiation (and unfortunately the uranium plasma) to escape from the oven for spectroscopic measurements; otherwise, it is essentially a blackbody cavity. A tungsten wire heater surrounds the oven and three rhenium thermal shields surround the heater. This arrangement will permit oven temperatures of 3000° K with an input power to the heater of approximately 5 kW.

The thermal shields have two sets of sight holes that permit the wall of the oven to be viewed through the side windows for temperature measurements. A thermal pile and optical system will be mounted on one window so that the oven temperature can be measured when the device is in a neutron field. For some experiments, a Langmuir probe will be inserted into the oven through the bottom sight tube.

The device will operate in the water shield tank of the University of Florida training reactor (UFTR). The natural convection of the water will cool the chamber.

CALCULATIONS

Let us now look at some quantities that are calculatable for a uranium plasma. Figure 2 shows

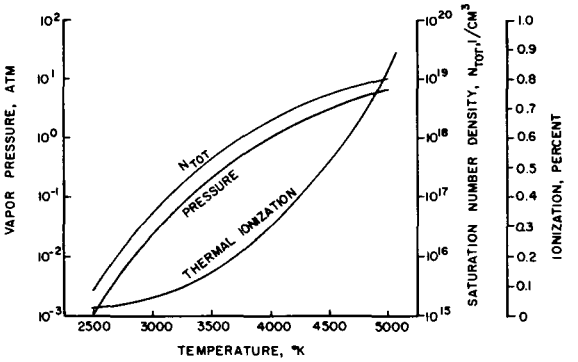

FIGURE 2.—*Vapor pressure of uranium.*

the vapor pressure curve for uranium, as discussed in the paper by Randol on page 181. The total particle number density N_{TOT} and the percentage ionization are also shown. These quantities were calculated assuming thermal equilibrium and a saturated uranium vapor or gas. Note that, at 3000° K, the reference temperature for the phase I experiments, the uranium pressure is approaching 0.1 atm, the number density is approximately 0.5×10^{17} particles/cm^3, and the degree of ionization is approximately 0.07 percent. Thus, we have essentially a neutral uranium gas at 3000° K.

To obtain an indication of the intensity of the radiation emitted by this thermal equilibrium 3000° K gas, the intensity of the 3839.6-Å line was computed as shown in figure 3. This is one of the prominent atom lines. At 3000° K, it has an intensity of approximately 10^{-2}W/cm³ sr. This is quite adequate for spectroscopic measurements.

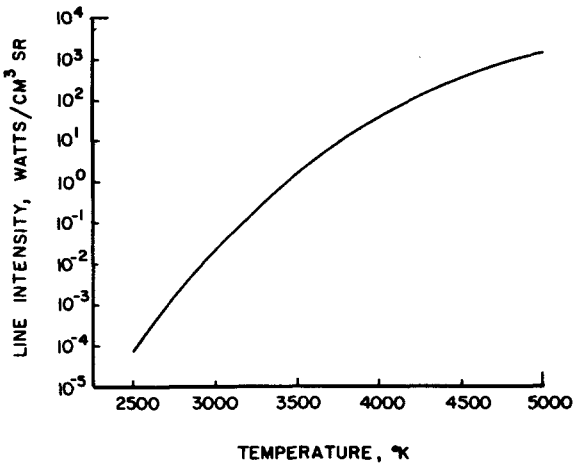

FIGURE 3.—*Emission coefficient of the U-I 3839.6 Å line for saturation conditions.*

If we now turn on the neutrons, figure 4 shows the fission rate for saturation conditions. The scale on the right-hand side is for a neutron flux Φ of 10^{11}N/cm² sec. This is the approximate flux level available in the water shield tank of the UFTR reactor. For 3000° K, this results in a fission rate of approximately 3×10^6 fissions/cm³ sec. In a high-power reactor or in a plasma-core reactor, the flux level will probably be as high as 10^{15}N/cm² sec, which leads to a 10^4 increase in the fission rate and thus the fission power.

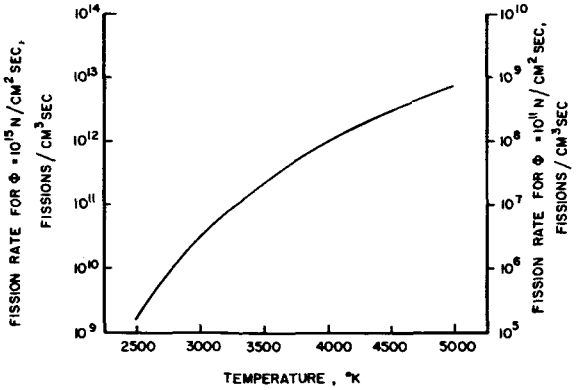

FIGURE 4.—*Fission rate for ^{235}U for saturation conditions with thermal neutrons at 20° C.*

It is interesting to compare the magnitude of the fission power rate in the uranium plasma with the internal energy of the plasma as an indication of the increased radiation emission from the plasma caused by fissions. Figure 5 shows an approximate ratio of P_f, the fission power in eV/cm³ sec, to U, the plasma internal energy in eV/cm³.

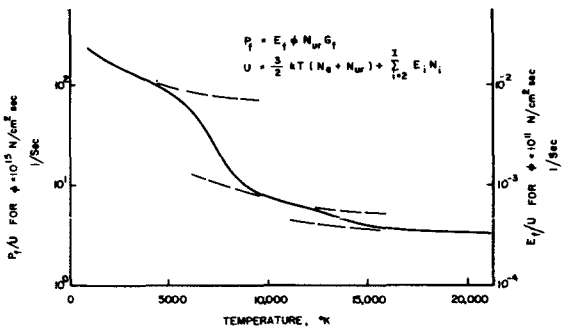

FIGURE 5.—*Approximate ratio of fission power to plasma energy content with thermal neutrons at 20° C.*

For a neutron flux of 10^{11}N/cm² sec at 3000° K, the fission events add approximately 1 percent of the internal energy to the plasma every second. Thus, in 100 sec the energy of the plasma would be doubled if no energy escaped as radiation. This "enhancement" of the thermal equilibrium radiation by the fission events should be readily detected, particularly since it should appear as nonequilibrium radiation. For higher flux levels, the fission energy released every second can easily exceed the internal energy content of the plasma, even at high temperatures.

The planned measurements with the fissioning uranium plasma device are as follows:

(1) Without neutrons:
- Identification of all lines (impurities)
- Intensity of certain lines (known temperature)
- Deduce basic constants
- Langmuir probe
- Total radiation

(2) With neutrons:

Identify spectrum change
Intensity change of certain lines
Langmuir probe
Neutron flux
Total radiation

With no neutrons, but with a hot (3000° K) uranium gas, we will identify (assign wavelengths to) all of the emitted lines, including any impurities that may be present. The computerized spectrum analysis system that we have developed and reported in the literature (ref. 3) will enable us to do this quickly. Certain prominent lines will be selected and their intensities determined for later reference. With the temperature known accurately, by measuring the uranium oven temperature, the transition probability times the statistical weight for the line can be calculated and checked against the published values.

A Langmuir probe will be inserted into the uranium oven in some experiments to compare the electron temperature with the oven temperature. The integrated radiation intensity will be measured as an indication of the energy content of the plasma.

Now, we may have some problems interpreting the data obtained with no neutrons; that is, the thermal equilibrium data. The plasma is in a blackbody cavity, but with a line of sight through the cavity. Thus we may see no lines, but just a 3000° K blackbody spectrum. However, the fact that the line of sight goes completely through the cavity probably means that we won't see a continuous blackbody spectrum but rather a spectrum of lines whose wavelengths correspond to the uranium lines and whose intensity corresponds to the intensity of the blackbody spectrum at 3000° K. Regardless of the outcome, a reference spectrum with no neutrons will be available for comparison with the spectrum obtained with fissions occurring.

The device will be placed in the neutron field and the measurements repeated. Any new lines in the spectrum will be found by processing the data through the computerized spectrum analysis system. Any shift in the distribution will be checked to see if the various lines are enhanced or maybe even depressed. From this, we hope to be able to determine the degree of nonequilibrium present in the plasma and the trend for extrapolating to other operating conditions. A Langmuir probe will also be used in some experiments, particularly as a function of time. Neutron flux calibration measurements will be made so that the fission rate can be determined. The integrated radiation intensity will be measured, although not much change in total radiation is expected for our operating conditions, as indicated earlier in figure 5.

FINAL REMARKS

Now that we have discussed our purpose in pursuing a fissioning uranium plasma research program as well as the experimental device and the planned measurements, it is only appropriate to give a status report. We have accomplished the original planning, design, and construction of the experimental device. Some support equipment is still being assembled. We are starting preliminary checkout and calibration tests. Experiments with no fissions using ^{238}U should start in the near future, barring the appearance of major problems. We will start experiments with a fissioning uranium plasma later this year. We look forward to some illuminating results.

REFERENCES

1. Marteney, P. J.; Mensing, A. E.; and Krascella, N. L.: Experimental Investigation of the Spectral Emission Characteristics of Argon-Tungsten and Argon-Uranium Induction Heated Plasmas. Rept. G–910092–11, United Aircraft Res. Lab., Sept. 1968.
2. Campbell, H. D.; Schneider, R. T.; and Kylstra, C. D.: Properties of a Uranium Plasma. Paper 70–43, AIAA 8th Aerospace Sci. Meeting (New York, N.Y.), Jan. 1970.
3. Kylstra, C. D.; and Schneider, R. T.: Computerized Spectrum Analysis. J. Appl. Spectros., Jan.-Feb. 1970.

DISCUSSION

Delmer: I would like to make a comment to see what you think about it. You were comparing the energy obtained from the fission with the internal energy of the plasma. It seems that a large fraction of this fission energy would go into electrons or some other very high energy product so that it is really not relevant to compare it with the internal energy because the electrons will be capable of excitations much beyond the thermal energy of the plasma.

Whether there is 1 or even 0.001 percent you should still see new lines.

Kylstra: I would expect so. I am not comparing it and trying to discern whether I shall see new lines or not; it is just a pure energy consideration. The fission energy should go into very high energy electrons and create highly ionized uranium. The whole problem will probably depend on the abundance of these ions and atoms. Energy considerations are just an indication as to whether they may be energetic enough to be measured.

Park: Your hope of getting a multi-ionized line by this method may not be too fruitful because to do so you need transition of more than one electron and that is highly unlikely. The only possible meaningful result from this would be a one-electron transition from the inner core and that would be in the X-ray range, and I suspect that the X-ray lines would be the most prominent discoveries that you would make. The presence of such high-energy particles, either photons or electrons, does not really change the spectra of the basic species, which are neutral species. The computer calculations done at Stanford University last year by James Shaw indicate that even if you had very energtic electrons the spectral of neutral species is not very ordered. An ordered species occurs only in the ultraviolet.

Kylstra: I am not trying to predict what we are going to measure. That determination is one of the purposes of the experiment.

Schneider: The idea is that the fission products should ionize the uranium atom. Therefore, you might end up with Uranium II, III, IV, or V. There is an ion and the ion can get excited but you do not need a double transition of electrons. The transition of excited ions will generate a set of lines which is completely different from that of the previous U II or U I. The resonance lines, which are the stronger lines of this transition, are expected to be in the vacuum uv. And, therefore, there is some hope of detecting the more prominent lines of U II and U III. I don't know what you meant by needing two electrons to make a transition.

Park: If a multiply ionized uranium is to be produced, several electrons must be stripped off at a time. Of course, this has to be done by one impact. Now if you are trying to watch the manner in which it relaxes, then, of course, you can do it. However, I am afraid you would see only singly ionized species because I do not think you can actually count on two electron transitions or multielectron transitions by one impact. However, suppose that one impact excites an inner-core electron configuration. Then it will relax and it will emit all kinds of lines. But again this will be in the vacuum ultraviolet. I suspect there will be levels of autoionization, which is typical. Under such conditions autoionization occurs very prominently.

Wilkerson: I would like to digress slightly and mention something about furnace technology. There is a very strange peculiar feature of recent furnace work we probably ought to keep an eye on. The old King furnace measurements for atomic oscillator strengths have now been apparently slightly degraded in some people's eyes by work with shock tubes and an arc. About 10 years ago at Michigan we found that the astronomers' suspicion that the chromium work by Hill and King had a furnace temperature error in it was really true. In fact, Hill and King had underestimated their furnace temperature by at least 10 percent, and there is recent work which indicates that the fundamental King furnace work on iron apparently had serious temperature error in it, something like a 400° to 2000° K error. Apparently the furnace temperature was underestimated; it is most surprising when one finds a 10, 20, or higher percentage of error in furnace temperatures. We should all be more careful, particularly in the regime where vapor pressures and other things are sensitively dependent on these temperatures. It appears that looking into a cavity puts little holes in it to begin with, and the effect of these little holes will be much greater than we suspected. It's a peculiar business.

Keng: Could you tell me roughly the mean free path of the fission fragments for this kind of density condition?

Kylstra: The high-energy fission fragment will probably have a mean free path of about 2 or maybe 3 cm; at lower energies, it will be less than that.

Keng: And the furnace dimensions?

Kylstra: About 1-cm diam so that a lot of the fission fragment energy will end up in the wall.

Ho: That's what I suspected. The furnace is too small to provide meaningful results.

Kylstra: First of all we will have uranium on the walls, of course, in equilibrium with the 3000° K wall. From this wall fission fragments will be emitted into the plasma. Those fission fragments may or may not reach the other side. The fission occurring in the plasma itself will, of course, go toward the wall, but the high-energy range of the slowing down of the fragments will occur in the plasma. Is this what you mean by the distortion of the results? I don't know how we take that into account at the present time.

Page intentionally left blank

Investigation of Arc Plasma at Extremely High Pressures

UWE H. BAUDER AND ERICH E. SOEHNGEN

Aerospace Research Laboratories
Wright-Patterson Air Force Base

Some aspects of the high-pressure plasma research program of the Aerospace Research Laboratories are described. This program is concerned with studies of electric arc discharges in selected gases at pressure levels up to 1000 atm.

Under the initial phase transport properties of argon at pressures up to 150 atm are being determined. The method involves measurements of the integral arc parameters and of the radial temperature distribution from which the electrical and thermal conductivities as well as the radiation source strength of the plasma may be determined as a function of temperature and pressure. The test facility and the measurement technique are described and first results obtained with argon are presented. Extension of the method to measurements in gas mixtures containing uranium vapor appears feasible and may be planned.

The basic objective of the high-pressure plasma research program is to extend the current knowledge of energy exchange processes in high-temperature plasma systems to pressure levels up to 1000 atm. Initiation of such a program was motivated by the dearth of information on the physics of high-pressure plasmas and their transport properties, which must be known for the analysis and utilization of high-pressure plasma phenomena. The relevance of research efforts in this virgin field is quite obvious in view of the promising technical utilization of high-pressure plasmas in nuclear gas-core reactors, closed-cycle-reactor MHD power systems, and high-intensity radiation sources and in view of their presence on reentering space vehicles and in reentry simulation devices. Since no facilities for steady-state investigations of high-pressure plasma seem to exist, a high-pressure research facility in a hazard-free underground laboratory space has been established and a systematic research program has been planned. This program will be concerned with the nature of high-temperature, high-pressure plasma under static conditions, that is, its thermophysical and transport properties, and with its behavior under dynamic conditions as affected by interactions with magnetic and gas flow fields. This program includes studies of arc stability, electrode phenomena, and magnetically induced plasma streaming as well as investigations of high-pressure plasma flow through channels and nozzles. Related studies will be concerned with electromagnetic properties of high-pressure plasma; that is, the absorption, transmission, and reflection of electromagnetic waves.

For the experiments, a medium-pressure facility for pressure levels up to 200 atm is presently being operated; a larger facility for pressures up to 1000 atm is in its completion stage. Both facilities feature pressure chambers of 20-liter volume. They are equipped with optical windows for side-on and head-on spectroscopic measurements and ports for gas and water systems and diagnostic probes. High-pressure gas is supplied through a compressor and storage bottle system. It is connected with a closed-loop water system through an "accumulator" which maintains a low pressure difference between gas and water. In essence, the accumulator consists of a cylinder with a floating piston forming a partition between gas and water systems. In this way the water is pressurized by the gas and the pressure difference between the gas and water may be maintained within 10 atm at a 1000-atm pressure level

(ref. 1). With this facility, it can be shown (ref. 2) that electrical arc discharges can be continuously operated under well-defined boundary conditions at pressures up to 100 atm. Present efforts are concerned with extension of these pressures up to 150 atm.

MEASUREMENT OF TRANSPORT PROPERTIES

Because the accuracy of the evaluation and interpretation of measurements in plasma systems depends on the knowledge of plasma properties, the first phase of the high-pressure plasma program is concerned with the determination of basic transport properties.

A wall-stabilized cylindrical arc column is used as a plasma source. The arc column is confined within a water-cooled cylindrical tube of about 5-mm diam (fig. 1). By using the "cascade" arc technique

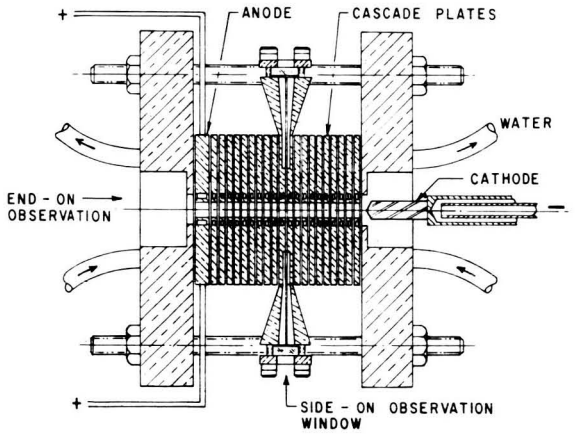

FIGURE 1.—*Schematic of cascade arc.*

first described by Maecker (ref. 3), extremely high power densities and plasma temperatures may be obtained. The confining tube or cascade is assembled from a stack of copper disks of about 2-mm thickness having a central bore of 5-mm diam. Each disk is individually water cooled and, within the stack, electrically insulated from one another.

Through the carefully chosen geometry of the internal water channels within the thin wafers extremely high heat flux values up to 20 kW/cm^2 may be obtained (ref. 4); this allows steady-state operation of arcs with centerline temperatures exceeding 20 000° K (ref. 5). The arc electrodes are located at both ends of the cascade constrictor tube. The cathode consists of a water-cooled tungsten pin and the anode is a modified cascade disk of 5-mm thickness.

End-on observation of the arc column is possible through the hollow anode, while side-on observation may be afforded through a small slit between two wafers. The wafers also serve as plasma probes for measuring the field strength of the arc column.

The cascade arc assembly is installed in the high-pressure chamber as shown in figure 2, which de-

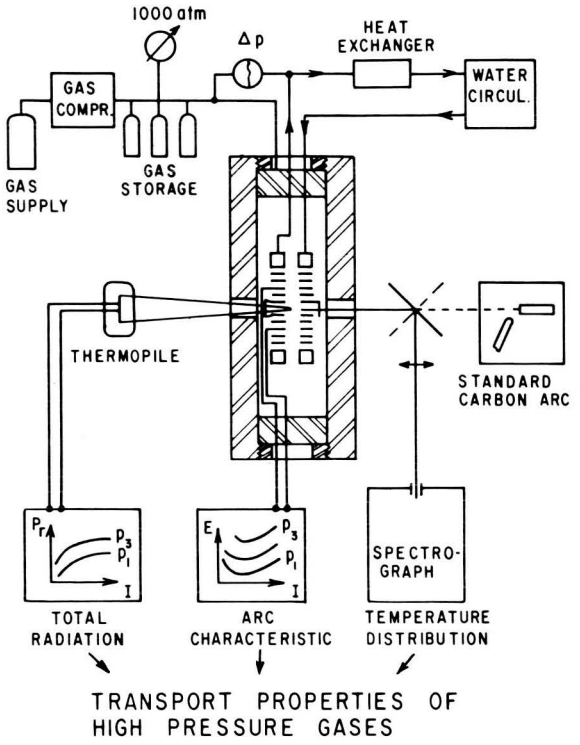

FIGURE 2.—*High-pressure facility.*

picts schematically the experimental arrangement.

From measurements in such a cascade arc the plasma properties may be derived by means of the energy balance equation under the assumption that the plasma is optically thin, that self-magnetic effects are negligible, and that the plasma column is developed, that is, the temperature profile is constant along the axis of the arc. Under such conditions the energy input into a volume element of plasma by ohmic heating is dissipated to the walls only by

thermal conduction and radiation. In cylindrical coordinates, the energy equation assumes the following form

$$\sigma E^2 - u + \frac{1}{r}\frac{d}{dr}\left(rk\frac{dT}{dr}\right) = 0 \qquad (1)$$

with the boundary conditions

$$\left(\frac{dT}{dr}\right)_{r=0} = 0$$

and

$$T_{\text{wall}} = \text{Constant and known}$$

where

σ electrical conductivity
E field strength of the column
u total radiation source strength
k total thermal conductivity, including energy transport by thermal diffusion of ionization and excitation energy
T temperature

It has been shown (refs. 6 and 7) that through this equation the transport properties $\sigma(T,p)$, $k(T,p)$, and $u(T,p)$ may be derived from measurements of the radial temperature distribution, the electric field strength, the total current

$$I = 2\pi E \int_0^R \sigma r\, dr \qquad (2)$$

and the total radiation per unit arc length

$$P_r = 2\pi \int_0^R ur\, dr \qquad (3)$$

The solution of equation (1) may be simplified by the introduction of the heat flux potential

$$\Phi = \int_{T_w}^{T} k\, dt \qquad (4)$$

which yields the following form of the energy balance equation:

$$\sigma E^2 - u + \frac{d^2\Phi}{dr^2} + \frac{1}{r}\frac{d\Phi}{dr} = 0 \qquad (5)$$

RESULTS

The electrical arc characteristic, represented by its voltage-current behavior, was recorded by a high-impedance X–Y recorder by using two cascade plates as voltage probes. Figure 3 shows a resulting family of curves of field strength against current with the pressure as parameter. In addition, the voltage distribution along the arc axis has been recorded (fig. 4); it may be used for obtaining information on the dependence of the electrode falls on the pressure. In first approximation the field strength in the column rises as $E \sim p^{1/2}$ at constant arc current. This correlation agrees with predictions based on the theory of the electrical conductivity at low degrees of ionization.

The total radiation emitted from the arc column is measured side on with a calibrated thermopile. Figure 5 shows an example of the results. The strong increase in total radiation with higher pressures is due to the increasing number densities of the radiating particle species within the plasma at constant temperature.

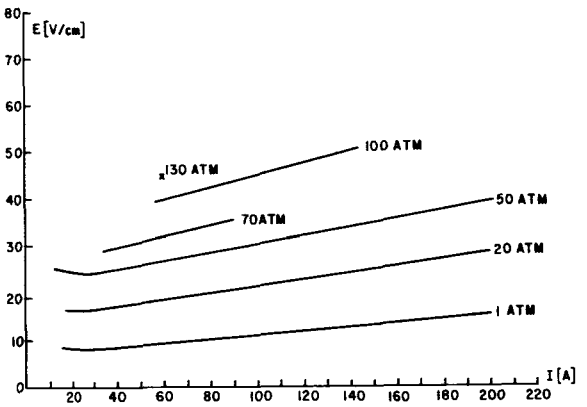

FIGURE 3.—*Electrical characteristics of a 5-mm argon arc.*

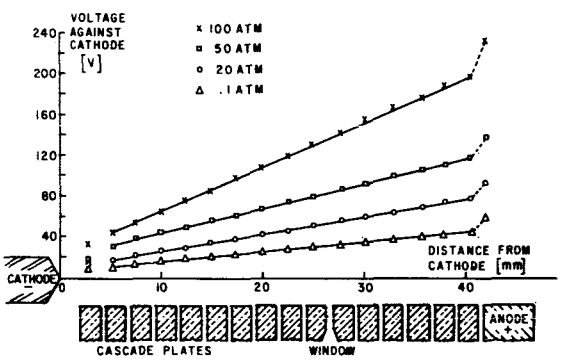

FIGURE 4.—*Voltage distribution along cascade channel* $I = 70\ A$.

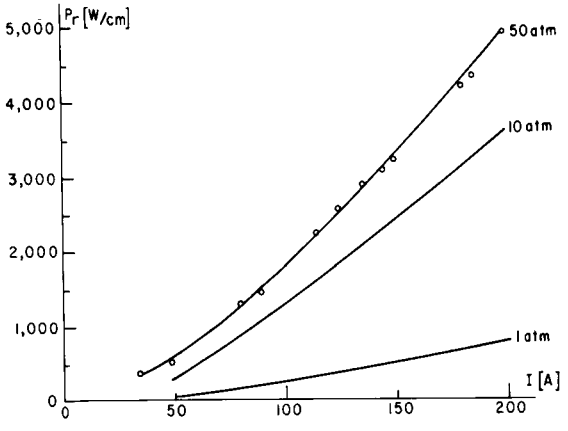

FIGURE 5.—*Total radiation of a 5-mm argon arc.*

The temperature distribution of the column is measured spectroscopically. A magnified image of the side-on view of the arc is projected onto the entrance slit of a stigmatic grating spectrograph ($f=0.75$ m). The photographically recorded intensity distributions are transformed into lateral profiles of the emission coefficient by the Abel inversion technique. Under the operating conditions of the arc discharge the argon is in local thermodynamic equilibrium; thus, the Saha equation may be used to relate number densities and temperatures. In the temperature range up to 50 atm the temperature distributions are determined from the measurement of the absolute continuum and A-I line intensities in the range between 3800 and 4700 Å. At pressures exceeding 50 atm the pressure broadening of the lines makes it difficult to integrate the line intensities; therefore, only the continuum radiation in wavelength regions relatively free of lines is used for the measurements.

Figure 6 shows some of the temperature profiles which were obtained at a pressure of 50 atm for various currents, that is, arc diameters. As may be clearly seen, with increasing current the temperature distribution becomes more uniform; the arc undergoes a transition from a conduction-dominated to a radiation-dominated discharge. The same trend prevails for constant current arcs with increasing pressure as long as the assumptions of equation (1) are applicable.

The absorption coefficient of the plasma is determined by a self-consistency check comparing the blackbody radiation for the experimentally determined temperature with the measured emission coefficient at one wavelength. As a result of this check it was found that the optical depth of the arc column was smaller than $\tau=0.02$ at the wavelengths used for the spectroscopic measurements.

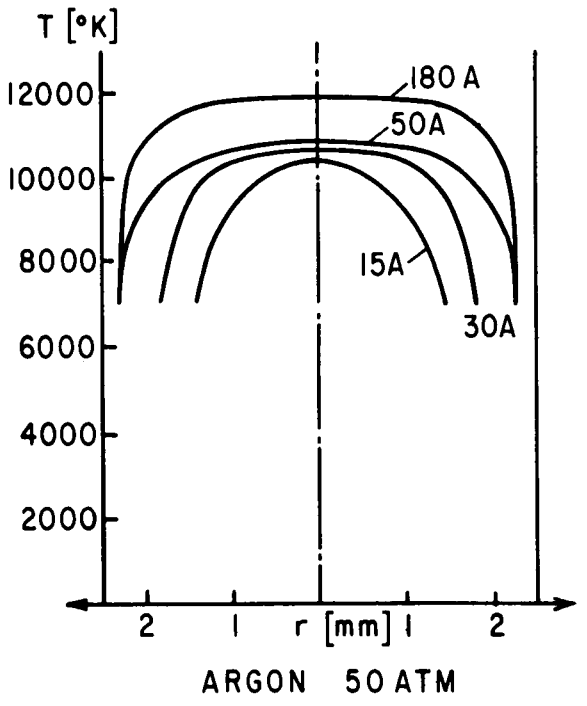

FIGURE 6.—*Temperature profiles obtained at 50-atm pressure for various currents.*

Figure 7 shows, as a first result, experimentally obtained data of the electrical conductivity of argon at 50-atm pressure in comparison with a curve theoretically derived by S. Devoto that was reported in a private communication.

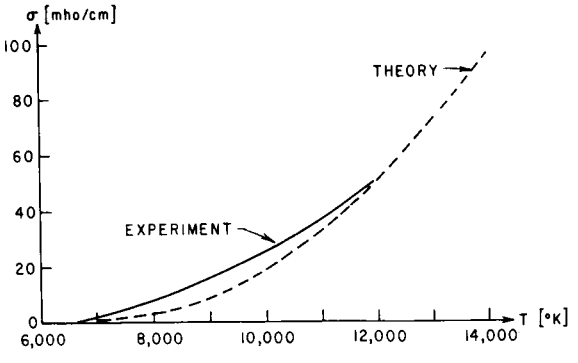

FIGURE 7.—*Electrical conductivity of argon at 50-atm pressure.*

CONCLUDING REMARKS

It has been shown that plasma properties may be experimentally determined under steady-state conditions with the available medium-pressure facility for pressures up to 150 atm by using a modified cascade arc technique. Extension to higher pressures up to 1000 atm will become feasible in the near future.

It appears quite possible to apply these methods also to the determination of properties of uranium plasma at pressure levels of interest to the operation of gas-core nuclear reactors. In this case free-burning or wall-stabilized arc discharges in a mixture of uranium vapor and a propellant gas may be studied. Some difficulties may arise because of condensation of uranium vapor at the cascade walls, the unknown effect of thermodiffusion in the gas mixture which has to be accounted for by analytical means, and self-absorption effects on the radiative transport term of the energy equation.

REFERENCES

1. BAUDER, U.; AND DYE, D.: Instr. and Control Syst., vol. 41, 1968, p. 89.
2. BAUDER, U.: Proc. IX Conf. on Phen. of Ion. Gases (Bucharest), 1969.
3. MAECKER, H. Z.: Naturforsch., vol. 119, 1956, p. 457.
4. MAECKER, H.; AND STEINBERGER, S.: Z. angew. Phys., vol. 23, 1967, p. 456.
5. BAUDER, U.: Z. Phys., vol. 205, 1967, p. 303.
6. MONTERDE-GARCIA, A.: Z. Phys., vol. 181, 1964, p. 317.
7. UHLENBUSCH, U.: Z. Phys., vol. 179, 1964, p. 347.

DISCUSSION

Randol: I am assuming that you use the laser to establish some sort of an absorption coefficient with an optically thick model. What type of laser was it, what was its wavelength, and does it correspond to a convenient line?

Bauder: It was a helium/neon laser.

Randol: Didn't you indicate that you did use line radiation at some point?

Bauder: That was for the temperature measurements. We were using line intensities where it was safe to do so. At 50 atm we used the absolute continuum intensity.

Wilkerson: Was that argon line radiation or something else?

Bauder: It was argon line radiation.

Park: Do you foresee any difficulty in mixing uranium in the cascade arc?

Bauder: Yes, we shall of course get condensation on the wall and mass separation will certainly become an important factor. We planned to run the uranium in a free-burning arc instead of in a cascade arc. Cascade arcs are especially helpful if one wants to work on transport properties, but the free-burning arc is a much simpler device.

Page intentionally left blank

SESSION IV

NUCLEONICS AND RADIATION

Chairman: **M. J. Ohanian**

Page intentionally left blank

Neutron Kinetics of Cavity Reactors[1]

WALTER N. PODNEY
Institute for Defense Analyses

HAROLD P. SMITH, JR.
University of California, Davis

A. K. OPPENHEIM
University of California, Berkeley

A theory is presented that describes power-level variations in a cavity reactor produced by density changes in a gaseous nuclear fuel within the cavity. Effects of a density change are accounted for in terms of a cavity grayness, which is the ratio of the net thermal neutron current to thermal neutron flux at the cavity wall. The percent change in power level per neutron generation is shown to be proportional to reactivity plus a term proportional to rate of change of grayness. The rate-dependent term is unique to cavity reactors and is expected to have a pronounced effect on reactor stability.

Implications for stability of cavity reactors to motion of fuel within the cavity are considered. For a large cavity radius, defined in terms of a minimum critical radius, power level is sensitive to motion of fuel toward or away from the cavity wall. Expansion of a central fuel region within the cavity increases reactivity, and, conversely, contraction decreases reactivity. Power excursions with periods of the order of 10^{-2} sec can result if natural damping forces provided by pressure and temperature gradients within the cavity are not strong enough or quick enough to arrest an initial expansion or contraction.

Work on gaseous-core cavity-reactor development has been largely concerned with two fundamental problems: (1) Determining conditions that would realize a critical system (ref. 1), and (2) establishing stable flow fields required to realize acceptable fuel containment (ref. 2). Recent design estimates indicate that the two problems are compatible (see papers by Ragsdale and Lanzo on pp. 13). Not surprisingly, unprecedented operating conditions would be required. Interactions between the neutron field and the flow field, however, have not been investigated to the extent required for a full understanding of reactor stability.

[1] Part of this work was supported by the U.S. Air Force through the Air Force Office of Scientific Research under grant AFOSR 129-67 and by the National Aeronautics and Space Administration under grant NsG-702105-003-050.

McNeill and Becker (ref. 3) have indicated that acoustic instabilities analogous to those exhibited by chemical rocket engines could develop because power density depends on the density of the fuel. Latham and associates have reported results of investigations of the dynamic characteristics of a nuclear light bulb engine in a paper on page 285. In effect, they assume that pressure disturbances generated by the neutron field are instantly communicated throughout the flow field and so consider reactor behavior in the time domain alone. (The assumption is more appropriate for a small "unit cavity," as in the nuclear light bulb concept, than for a large cavity, as in the coaxial-flow concept.)

Measurements made in zero-power cavity reactors (ref. 1), however, have shown that neutron lifetimes are of the order of 2 to 3 msec, which is

somewhat less than a transit time for acoustic waves. Furthermore, the fission rate is sensitive to position of fuel within the cavity, and appreciable reactivity increases have been measured as fuel is moved toward the cavity wall. Consequently, significant interaction in both space and time between the neutron field and flow field is to be expected. The interaction may have a pronounced effect on reactor stability.

For example, in both the coaxial-flow and nuclear light bulb concepts, fuel is confined to a central region within the cavity, and coolant flows between the fuel and cavity wall. Expansion of the central fuel region would accelerate the fission rate and consequently generate an energy pulse in the fuel. If the concomitant pressure pulse acts only to drive a continuing expansion, then, of course, the reactor is inherently unstable. It may also act, however, to decrease the amount of fuel in the cavity either by restricting the incoming flow or by increasing the loss rate and so may decelerate the fission rate and quench the expansion. Expansion may also be arrested by enhanced energy transfer to the coolant because of the larger radiating surface area and higher temperature of the fuel region.

Relative strengths and reaction times of the driving energy pulse and damping effected by pressure gradients and energy transfer determine the inherent stability of the reactor. They can be properly assessed only for a given design. (In the nuclear light bulb concept, for example, the transparent wall enclosing the fuel region interrupts pressure communication between fuel and coolant but does not interrupt energy transfer.) Unqualified statements about inherent stability or instability of a gaseous-core reactor concept cannot be made without detailed study of the interaction of the neutron and flow fields. Nevertheless, existence of an appreciable energy source to drive potentially unstable motions of the fuel region gives cause for concern.

The purpose of the present paper is to estimate the strength and reaction time of the driving force and, in so doing, to formulate the problem so that the effect of natural damping mechanisms can be conveniently included in the formalism. We defer the problem of establishing stability criteria when damping effects are included. Our aim then is to describe the kinetics of the neutron field in a cavity reactor and its dependence on fuel configuration within the cavity.

We base the analysis on a model used by Safanov (ref. 4) to calculate critical states of cavity reactors. Because material within the cavity is tenuous, the mean free path for neutron scattering is large, and no significant energy moderation takes place in the cavity. Thus we consider the cavity region to be transparent to fast neutrons and purely absorbing for thermal neutrons. Fast neutrons produced by fissions in the fuel enter the reflector, are moderated almost instantly to thermal energy, and diffuse monoenergetically thereafter until they either are absorbed in the fuel, coolant, or reflector material or are lost.

In the tenuous cavity region, neutrons effectively travel in straight lines until they are absorbed or pass through to be either returned by the reflector or lost. In the dense reflector material surrounding the cavity, neutrons undergo many collisions and thus diffuse throughout the reflector. Neutron travel in the cavity region must necessarily be described by transport theory. Diffusion theory is an adequate approximation in the reflector. Neutron moderation in the reflector can be described either in terms of energy groups or in terms of a continuous slowing-down model. In either case, we assume the net current of nonthermal neutrons to be zero at the cavity wall, in accordance with the assumed transparency of the cavity region to fast neutrons.

Because of the disparity of neutron transport in the two adjacent regions, we conceptually separate the regions and, following Safanov, introduce a coupling coefficient called cavity grayness, which is the ratio of the net thermal neutron current at the cavity wall to the thermal neutron flux at the wall. The conceptual separation is both useful and convenient. The kinetics of the neutron field can be determined in terms of variations in cavity grayness alone, and changes in grayness can be related to effects of the flow field on the fuel region. Cavity grayness, then, is a fundamental quantity used in describing interaction of the fields.

The concept of grayness is somewhat limited, however. A precise definition requires the net thermal neutron current to be normal to the cavity wall, which in turn requires that material in the cavity be distributed symmetrically although not necessarily uniformly. Nevertheless, asymmetric distri-

butions can be accounted for provided the resulting variation in thermal neutron flux over the cavity wall is small over a distance of a neutron mean free path in the reflector (ref. 5). This restriction should not be a severe limitation for initial stability investigations, since only quantities of perturbation magnitude would be considered.

Besides choosing to adopt the concept of cavity grayness in describing kinetic behavior, we use a mathematical technique based on Green's functions to express the kinetic behavior in terms of parameters closely allied with experimental techniques. Thus, we appeal to pulsed-neutron measurements and define pertinent parameters in terms of the response of the reactor to a burst of neutrons emitted in the cavity or elsewhere in the reactor. The advantage of this method, combined with the concept of cavity grayness, is that experimental verification can be obtained without using a fissionable gas in the cavity. Boron-10 trifluoride can be used instead of a uranium plasma. Thus, essential features of the kinetic behavior of the neutron field can be determined in the laboratory without resorting to precautions required in an isolated critical facility.

In a previous paper (ref. 6), we presented and established the range of validity of a kinetic equation for the neutron field in a cavity reactor. Our considerations were then restricted to prompt neutrons and spherical geometry with an infinite reflector to simplify exposition of the method. In this paper, we consider both spherical and cylindrical geometry with finite reflectors and include the effect of delayed neutrons.

THEORY

The kinetic behavior may be interpreted as follows: A distributed source of thermal neutrons arises in the reflector from the slowing down of fast neutrons leaving the cavity. Spatial distribution of the source is constant in time, and its strength varies in proportion to the net thermal neutron current at the cavity wall. The source drives the thermal neutron population in the reflector, which in turn feeds the source by producing fissions in the cavity. Cavity grayness determines the extent of coupling between the source and the thermal neutron flux.

Neutron Conservation

We base the analysis on a diffusion theory approximation to express neutron conservation in the reflector region and consider spherical and cylindrical cavities of such symmetry that the thermal neutron flux $\phi(r,t)$ depends only on a radial coordinate r and time t. Neutron conservation is then expressed in terms of $\phi(r,t)$ by

$$\frac{-D}{r^n}\frac{\partial}{\partial r}\left(r^n\frac{\partial\phi}{\partial r}\right)+\Sigma_a\phi+\frac{1}{v}\frac{\partial\phi}{\partial t}=S(t)\,q(r) \quad (1)$$

where D is the diffusion coefficient of the reflector material, Σ_a is the absorption coefficient, v is the thermal neutron speed, and $n=1$ for a cylinder and $n=2$ for a sphere. The function $q(r)$ gives the spatial distribution of the slowing-down source, and $S(t)$, its time dependence. The slowing-down source is separable in space and time to a good approximation, because the time required for fast neutrons to reach thermal energy is small compared with the lifetime of thermal neutrons.

The thermal neutron flux vanishes at the outer boundary r_b of the reflector and satisfies the boundary condition

$$\mathbf{n}_i\cdot\mathbf{J}(r_\omega,t)=\Gamma(t)\,\phi(r_\omega,t) \quad (2)$$

at the cavity wall r_ω, where $\mathbf{n}_i$ is a unit vector normal to the cavity wall and is directed inward. The net thermal neutron current at the wall $\mathbf{J}(r_\omega,t)$ is related to the thermal neutron flux, according to Fick's law, by

$$\mathbf{J}(r_\omega,t)=D\left.\frac{\partial\phi}{\partial r}\right|_{r=r_\omega}\mathbf{n}_i \quad (3)$$

Equation (2) defines the cavity grayness $\Gamma(t)$. The calculation of grayness by transport theory methods is discussed in the section entitled "Cavity Grayness."

The number of fast neutrons crossing the cavity wall per unit time $S(t)$ can be written as

$$S(t)=\eta(1-\beta)\pi(2r_\omega)^n\,\Gamma(t)\,\phi(r_\omega,t)+\sum_i\lambda_iC_i(t) \quad (4)$$

where η is the number of fast fission neutrons produced per neutron absorbed in the fuel, $\beta=\sum_i\beta_i$, β_i is the fraction of delayed neutrons in the ith group, and λ_i, the decay constant for the ith group. The number of delayed neutron precursors $C_i(t)$ is determined by the rate equation

$$\frac{dC_i(t)}{dt}=\eta\beta_i\pi(2r_\omega)^n\,\Gamma(t)\,\phi(r_\omega,t)-(\lambda_i+\lambda_r)C_i(t) \quad (5)$$

where $\lambda_r = 1/\tau_r$ and τ_r is an effective residence time of precursors in the cavity, so that

$$\lambda_i C_i(t) = \eta\pi(2r_\omega)^n \lambda_i\beta_i \int_0^t \Gamma(t-\tau)\,\phi(r_\omega,t-\tau)\,e^{-(\lambda_i+\lambda_r)\tau}d\tau \qquad (6)$$

after the contribution of the initial concentration has lapsed.

If fuel residence time in the cavity is small compared with the shortest delay time ($\sim$0.1 sec), then delayed neutrons are lost. The net effect then would be to reduce η by the factor $(1-\beta)$. In writing equation (4), we have neglected parasitic neutron absorption in the coolant or structural components within the cavity. It can be easily included, however, by introducing appropriate multiplicative factors in the first term of equation (4).

Kinetic Equation

The time-dependent boundary condition associated with cavity grayness (eq. (2)) poses the principal mathematical difficulty in obtaining a simple expression for the thermal neutron flux. A more explicit formulation that exhibits the nature of the problem is obtained by introducing a response function and expressing neutron conservation in terms of an integral equation. We choose the response function to correspond to the thermal neutron flux produced in a reference reactor, initially at zero power, by a unit pulse of thermal neutrons located at a distance r_o in the reflector. The reference reactor has all the characteristics of the actual reactor except that the gas in the cavity is nonmultiplying and cavity grayness is constant. Its value is that of the actual grayness at the time the pulse is emitted.

The thermal neutron flux generated by a unit pulse of thermal neutrons emitted at position r_o and time τ in the reference reactor is given by the response function $G(r,t;\ r_o,\tau)$ that vanishes at the outer boundary of the reflector and satisfies

$$\frac{-D}{r^n}\frac{\partial}{\partial r}\left(r^n\frac{\partial G}{\partial r}\right)+\Sigma_a G+\frac{1}{v}\frac{\partial G}{\partial t}=\frac{\delta(r-r_o)}{\pi(2r_o)^n}\delta(t-\tau) \qquad (7)$$

and

$$D\left.\frac{\partial G}{\partial r}\right|_{r=r_\omega}=\Gamma(\tau)\,G(r_\omega,t;\ r_o,\tau) \qquad (8)$$

and the causality condition $G(r,t;\ r_o,\tau)=0$ for $t<\tau$. Here $\delta(x)$ denotes the Dirac delta function. Since grayness now depends only on the parameter τ, an expression for the Laplace transform $\tilde{G}(r,s;\ r_o,\tau)$ of the response function can be readily determined from equations (7) and (8). Transformation back to the time domain is more difficult; however, it is not necessary for our purposes, as we show subsequently.[2]

Our immediate concern is the time dependence of the reactor power level, which is proportional to the net thermal neutron current at the cavity wall. Consequently, we require only time dependence of the thermal neutron flux at the wall. By using a common mathematical technique (ref. 7), we express the thermal neutron flux at the wall in terms of the integral equation

$$\phi(r_\omega,t)=\int_0^t S(\tau)\,G_f(r_\omega,-\tau;\ -t)\,d\tau-\pi(2r_\omega)^n \int_0^t[\Gamma(\tau)-\Gamma(t)]\,\phi(r_\omega,\tau)\,G(r_\omega,-\tau;\ r_\omega,-t)\,d\tau \qquad (9)$$

where

$$G_f(r_\omega,t;\ \tau)=\int_{r_\omega}^{r_b} q(r_o)\,G(r_\omega,t;\ r_o,\tau)\,\pi(2r_o)^n\,dr_o \qquad (10)$$

and we have neglected the contribution of the initial flux. The function $G_f(r_\omega,t;\ \tau)$ is the thermal neutron flux at the wall, at time $t>\tau$, produced by a unit pulse of fast neutrons emitted symmetrically in the cavity at time τ.

Slowly Varying Approximation

As we have shown before (ref. 6), the range of the kernels in the integrals is of the order of a neutron lifetime. If cavity grayness changes little during a neutron lifetime, then we can make the reasonable approximation

$$\Gamma(\tau)\,\phi(r_\omega,\tau)\cong\Gamma(t)\,\phi(r_\omega,t)+(\tau-t)\,[\Gamma(t)\,\phi(r_\omega,t)]' \qquad (11)$$

where the prime denotes a time derivative, and carry out the integrations in equation (9). The result is the differential equation

$$\frac{l(t)}{P(t)}\frac{dP(t)}{dt}=\rho(t)-\bar{\beta}+\frac{B(t)}{\Gamma(t)}\frac{d\Gamma(t)}{dt} \qquad (12)$$

[2] We could alternatively choose to define the response function for an empty cavity $\Gamma(\tau)=0$. The number of neutrons returning to the cavity, however, depends strongly on grayness, so that the response function for an empty cavity is of little value for defining the multiplication constant and neutron lifetime.

which describes the variation in reactor power level $P(t)$. The prompt reactivity $\rho(t)$ is given in terms of the effective multiplication factor $K_e(t)$ by $\rho(t)=1-1/K_e(t)$, where

$$K_e(t)=\pi(2r_\omega)^n\,\eta\Gamma(t)\int_t^\infty G_f(r_\omega,\tau;\,t)\,d\tau \quad (13)$$

Neutron lifetime $l\,(t)$ is given by

$$l(t)=(1-\bar{\beta})\,l_p(t)+l_d \quad (14)$$

where

$$\bar{\beta}=\lambda_r\sum_i\frac{\beta_i}{\lambda_i+\lambda_r}$$

and

$$l_d=\sum_i\frac{\lambda_i\beta_i}{(\lambda_i+\lambda_r)^2}$$

is the average delay time produced by delayed neutron precursors. The prompt neutron lifetime $l_p(t)$ is defined by the relation

$$l_p(t)=\frac{\int_t^\infty(\tau-t)\,G_f(r_\omega,\tau;\,t)\,d\tau}{\int_t^\infty G_f(r_\omega,\tau;\,t)\,d\tau} \quad (15)$$

and is the average time elapsed between the birth of a fast neutron in the cavity and its capture in the fuel as a thermal neutron. The coefficient $B(t)$ measures the sensitivity of power-level variations to rate of change of grayness. It is defined by

$$B(t)=\frac{\int_t^\infty(\tau-t)\,G(r_\omega,\tau;\,r_\omega,t)\,d\tau}{\eta\int_t^\infty G_f(r_\omega,\tau;\,t)\,d\tau} \quad (16)$$

and represents an average time to capture in the fuel for a thermal neutron emitted at the cavity wall. Since thermal neutrons that are eventually captured in the fuel spend most of their lifetime racing back and forth across the cavity, the coefficient B is of the same order of magnitude as the prompt neutron lifetime l_p.

The integrals in equations (13), (15), and (16) can be easily evaluated by taking the Laplace transform of the integrands with respect to $(\tau-t)$ and evaluating limits of the transformed functions as the transform variable approaches zero. Consequently, explicit time dependence of the response function is not required for determining power-level variations in the slowly varying approximation. As shown in the appendix, only an explicit expression for its Laplace transform is required to determine $K_e(t)$, $l_p(t)$, and $B(t)$. Expressions for $K_e(t)$, $l_p(t)$, and $B(t)$ in spherically and cylindrically symmetric geometries, based on a two-group theory, are given in the appendix.

We remark that each of the quantities $K_e(t)$, $l_p(t)$, and $B(t)$ can, in principle, be easily measured using pulsed neutron techniques and boron-10 trifluoride to simulate the gaseous fuel. Admittedly, it may prove to be difficult experimentally to attain the high degree of symmetry assumed in the analysis. The symmetry, however, is not fundamental to their definition. We would expect equation (12) to represent power-level variations adequately provided asymmetric effects do not severely distort the thermal neutron flux at the wall.

Dynamic Inhour Equation

For sudden changes in cavity grayness to a new constant value, as may result from a sudden disturbance of the flow field, the power level varies exponentially with a time constant $\Lambda_a=v\Sigma_a\,(a^2-1)$ after four or five neutron lifetimes have elapsed. As we have shown, the value of a is obtained from equation (9) by using a Laplace transform technique to evaluate the integral (ref. 6). When delayed neutron precursors are included in the source, the result is the relation

$$K_e(\Gamma,a)\left[1-\sum_i\beta_i\left(1+\frac{\lambda_i}{\lambda_r+\Lambda_a}\right)^{-1}\right]=1 \quad (17)$$

that determines the value of a in terms of the new value of grayness Γ. The quantity $K_e(\Gamma,a)$ is given by

$$K_e(\Gamma,a)=\pi(2r_\omega)^n\,\eta\Gamma\int_0^\infty e^{-y\Lambda_a}G_f(r_\omega,y;\,0)\,dy \quad (18)$$

It is the effective multiplication factor for prompt neutrons corresponding to grayness Γ and a reflector absorption cross section $a^2\,\Sigma_a$. At the critical state with $\Gamma=\Gamma_c$, the power level is stationary, so that $a=1$ and $K_e(\Gamma_c,1)\,(1-\bar{\beta})=1$. For short residence times $\lambda_r\gg\lambda_i$, the prompt multiplication factor is reduced approximately by the factor $1-\beta$.

The prompt reactivity associated with a sudden change in grayness to the value Γ is determined by the relation $\rho(\Gamma)=1-1/K_e(\Gamma,1)$, which can be used together with equation (17) to relate the prompt reactivity insertion to reactor period. It is

more convenient, however, to work directly in terms of grayness. Equation (17), then, is the dynamic inhour equation (ref. 8) for a cavity reactor and relates reactor period to a sudden change in cavity grayness.

CAVITY GRAYNESS

To determine cavity grayness, we use a P_1 approximation for the angular flux $\Psi(r_\omega,\mathbf{\Omega})$ at the cavity wall and calculate the number of neutrons entering the cavity per unit area that are absorbed in unit time by a purely absorbing medium within the cavity. The absorption rate N_a is proportional to grayness since by definition

$$N_a=\mathbf{J}(r_\omega)\cdot\mathbf{n}=\Gamma\phi(r_\omega) \tag{19}$$

We assume that the absorber is distributed symmetrically within the cavity, so that $\mathbf{J}(r_\omega)$ is normal to the wall and $\phi(r_\omega)$ is uniform over the surface.

From transport theory, the number of neutrons entering the cavity per unit area in unit time traveling in the direction $\mathbf{\Omega}$ is given by $\Psi(r_\omega,\mathbf{\Omega})(\mathbf{\Omega}\cdot\mathbf{n}_i)$, and in P_1 approximation

$$\Psi(r_\omega,\mathbf{\Omega})=\frac{1}{4\pi}[\phi(r_\omega)+3\mathbf{\Omega}\cdot\mathbf{J}(r_\omega)] \tag{20}$$

The rate of neutrons reentering the cavity per unit area N_i is then given approximately by the expression

$$N_i=\int_{2\pi}\Psi(r_\omega,\mathbf{\Omega})(\mathbf{\Omega}\cdot\mathbf{n}_i)\,d\mathbf{\Omega}=\frac{\phi(r_\omega)}{4}(1+2\Gamma) \tag{21}$$

The probability of absorption for a neutron traversing the cavity in the direction $\mathbf{\Omega}$ is $1-\exp[a(\mathbf{r}_\omega,\mathbf{r})]$. The optical thickness $a(\mathbf{r}_\omega,\mathbf{r})$ in the direction $\mathbf{\Omega}$ is given by

$$a(\mathbf{r}_\omega,\mathbf{r})=\int_o^R\Sigma_a(\mathbf{r}-s\mathbf{\Omega})\,ds \tag{22}$$

where $\mathbf{r}=\mathbf{r}_\omega+R\mathbf{\Omega}$, $R=|\mathbf{r}-\mathbf{r}_\omega|$ is the chord length, and $\Sigma_a(\mathbf{r})$, the absorption cross section. The fraction f_Γ of neutrons entering the cavity per unit area in unit time that is absorbed can be expressed as

$$f_\Gamma=\int[1-e^{-a(\mathbf{r}_\omega,\mathbf{r})}]\,Y_\Gamma(R)\,dR \tag{23}$$

where $Y_\Gamma(R)\,dR$ is the number of chords having a length R within dR. Consequently, $Na=N_if_\Gamma$, and, from equations (19), (21), and (23), then, we obtain the relation

$$\Gamma=\frac{1}{2}\left(\frac{f_\Gamma}{2-f_\Gamma}\right) \tag{24}$$

The chord distribution function, Y_Γ, isolates the geometrical factors influencing cavity grayness. Following Dirac (ref. 9) we define the number of chords of length R drawn from a point on the cavity wall to be proportional to $[1+3\Gamma(\mathbf{\Omega}\cdot\mathbf{n}_i)](\mathbf{\Omega}\cdot\mathbf{n}_i)$ for $\mathbf{\Omega}\cdot\mathbf{n}_i>0$, corresponding to the angular distribution of the incoming flux, and zero for $\mathbf{\Omega}\cdot\mathbf{n}_i<0$. The probability that a chord has length R within dR is then given by

$$Y_\Gamma(R)\,dR=\frac{\int\int_R[1+3\Gamma(\mathbf{\Omega}\cdot\mathbf{n}_i)](\mathbf{\Omega}\cdot\mathbf{n}_i)\,d\mathbf{\Omega}\,dA}{\int\int[1+3\Gamma(\mathbf{\Omega}\cdot\mathbf{n}_i)](\mathbf{\Omega}\cdot\mathbf{n}_i)\,d\mathbf{\Omega}\,dA} \tag{25}$$

where the subscript R in the numerator indicates that the integral over $\mathbf{\Omega}$ includes only those values of $\mathbf{\Omega}\cdot\mathbf{n}_i$ that give chords of length R at each point of the surface. The denominator is the total number of chords, so that $\int Y_\Gamma(R)\,dR=1$.

The quantity f_Γ is not sensitive to angular distribution of the incoming flux and so does not depend strongly on Γ. For our purposes,[3] it can be replaced by the quantity f_o corresponding to $\Gamma=0$, so that, to a good approximation

$$\Gamma=\frac{1}{2}\left(\frac{f_o}{2-f_o}\right)$$

We mention that an explicit expression for grayness can be deduced in terms of escape probabilities without introducing a chord distribution function and refer the reader to the work of Kear and Rudermann (ref. 10) for a concise and clear derivation. The derivation based on a chord distribution function, however, has greater intuitive value and allows a quick comprehension of factors influencing grayness when fuel is not uniformly distributed throughout the cavity.

IMPLICATION FOR REACTOR STABILITY

In order to obtain a first estimate of the sensitivity of reactor power to fuel distribution within the cavity, we consider the effect of fuel radius on reactivity. We suppose the fuel to be uniformly distributed within a region of radius $r_f\leqq r_\omega$ and take the mass of fuel to be constant, so that the mean free

[3] The fraction f_o is related to the self-shielding factor f by $f_o=\overline{R}\,\overline{\Sigma}\,f$ where $\overline{V}=\int\Sigma(\mathbf{r})\,d\mathbf{r}$ and $\overline{R}=\int R\,Y_o(R)\,dR$ is the average chord length.

path in the fuel λ changes with fuel radius according to $\lambda=\lambda_o(r_f/r_\omega)^{2n-1}$, where λ_o is the mean free path when fuel is uniformly distributed throughout the cavity.

We first consider the effect on grayness. The fraction f_Γ of neutrons entering the cavity that are absorbed can be expressed as the product $f_\Gamma=h_\Gamma f_\Gamma'$, where the factor h_Γ is the fraction of neutrons (chords) entering the cavity that strikes the fuel region, and f_Γ' is the fraction of neutrons striking the fuel region that are absorbed. The factor h_Γ is given in terms of the chord distribution function by

$$h_\Gamma=\int_* Y_\Gamma(R)\,dR \tag{26}$$

where the limit * denotes that the integral extends only over chords intersecting the fuel region. The factor f_Γ' is given by

$$f_\Gamma'=\int[1-e^{-\alpha'(\mathbf{r}_f,\mathbf{r})}]Y_\Gamma'(R)\,dR \tag{27}$$

where $\alpha'(\mathbf{r}_f,\mathbf{r})$ is the optical thickness through the fuel region and Y_Γ', the chord distribution for the fuel region.

For example, the chord distribution function Y_o for an isotropic angular distribution (ref. 9) is given by $Y_o(R)=R/2a^2$, for a sphere of radius a. Since only chords having a length greater than $R_o=2r_\omega\sqrt{1-(r_f/r_\omega)^2}$ intersect the fuel region,

$$h_o=\int_{R_o}^{2r_\omega}\frac{R}{2r_\omega{}^2}dR=(r_f/r_\omega)^2 \tag{28}$$

For a uniform distribution of fuel, optical thickness is proportional to chord length, so that $\alpha'=R/\lambda$ and f_o' is given by

$$f_o'=\int_0^{2r_f}(1-e^{-R/\lambda})\frac{R}{2r_f{}^2}dR \tag{29}$$

Consequently,

$$f_o=h_of_o'=(r_f/r_\omega)^2\left\{1-\frac{2}{\beta^2}[1-(1+\beta)e^{-\beta}]\right\} \tag{30}$$

where $\beta=2r_f/\lambda$ or $\beta=\beta_o(r_\omega/r_f)^2$ with $\beta_o=2r_\omega/\lambda_o$, since $\lambda=\lambda_o(r_f/r_\omega)^3$ for a sphere.

The function f_o (r_f/r_ω) increases monotonically from zero to $f_o(1)$ as r_f/r_ω ranges from zero to unity. Grayness then also increases monotonically and so, too, then does reactivity. To a good approximation grayness changes according to the prescription

$$\Gamma=1/2\left(\frac{f_o}{2-f_o}\right)$$

and reactivity, approximately linearly with grayness.

In order to estimate the effect of fuel expansion on reactivity, we consider a spherical cavity 1 m in radius that is surrounded with a 1-m-thick deuterium reflector. (Material constants and an outline of the calculations are given in the appendix.) Enough ^{235}U fuel is confined in a central sphere of radius 1/2 m to achieve a critical state, which corresponds to a grayness of 0.0344, so that $f_o=0.129$. If the fuel region expands uniformly to fill the cavity, then f_o increases to 0.16 and Γ, to 0.0435. The reactivity available from a complete expansion is then 0.074, which is quite large. To compensate for the reactivity increase due to expansion, about 22 percent of the fuel mass or 740 g of ^{235}U would have to be removed from the cavity.

The corresponding prompt neutron lifetime decreases from the value 4.47 msec at the critical state to 4.06 msec. Consequently, the reactor period is approximately 55 msec after expansion. We have neglected the effect of delayed neutron precursors, since residence times of the fuel are likely to be too short to allow delayed neutrons to appreciably influence neutron lifetime.

Although we have chosen a complete expansion as an example, it indicates that reactor power level can double within times of the order of 10^{-2} sec because of fuel expansion. To be stable, then, a gaseous-core reactor must have strong and quick natural damping forces other than delayed neutrons, which cannot be effective unless fuel residence times exceed about 10 sec.

More generally, the reactivity available as grayness increases is a strong function of cavity radius, as shown in a general way in figure 1. As cavity radius increases beyond the minimum critical radius a_m, below which a self-sustaining reaction cannot be maintained, the available reactivity increases rapidly. More important, the rate of change of reactivity with grayness near the critical state ($\rho=0$) increases sharply. Consequently, large cavities are very sensitive to relatively small changes in grayness, so that even small expansions can lead to appreciable power excursions.

Furthermore, neutron lifetime decreases as grayness increases. The effect is not so pronounced, however. As is indicated by figure 2, neutron lifetime

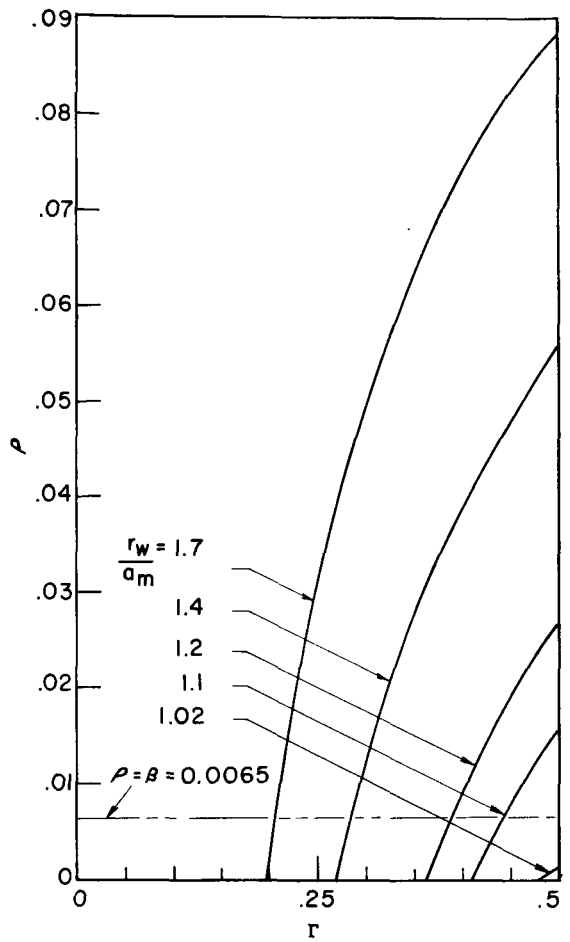

FIGURE 1.—*General dependence of reactivity ρ on cavity grayness Γ and cavity radius r_ω/a_m in units of the minimum critical radius a_m.*

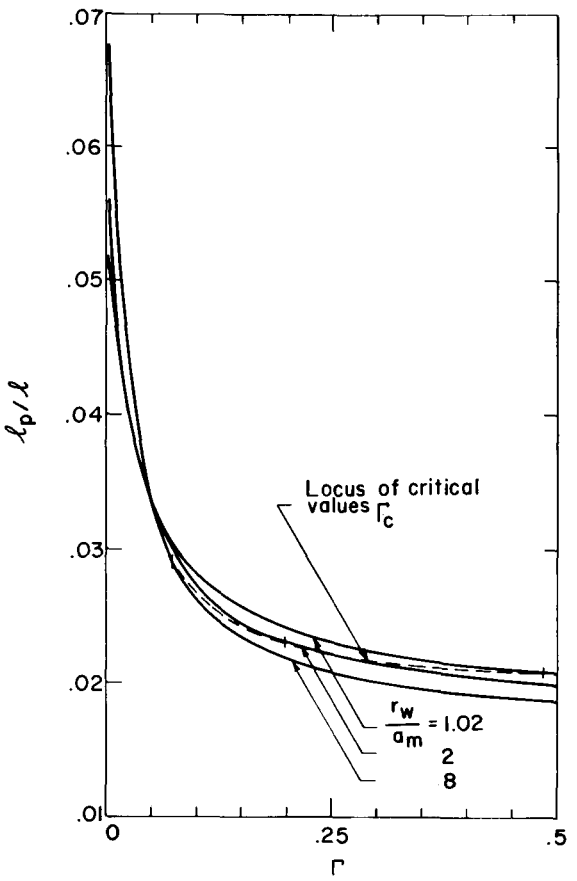

FIGURE 2.—*General dependence of prompt neutron lifetime l_p/l in units of the average time to absorption in the reflector material l on cavity grayness Γ and cavity radius* r_ω/a_m in units of the minimum critical radius a_m. *Deuterium reflector; Z = 75 msec.*

decreases rather slowly as grayness increases beyond the value at the critical state Γ_c. Nevertheless, for large cavity radii the rate of decrease becomes steeper.

Because part of the cavity volume must be taken up by coolant and because hydrodynamic stability limits the attainable fuel loading, cavity radii must necessarily be large. We thus expect that reactor power level will be sensitive to small perturbations in the fuel configuration. The energy released would act as a strong driving force for potentially unstable motions of the fuel.

Although we have here considered spherical geometry with the approximation $f_\Gamma \cong f_0$ for simplicity, the results are characteristic of cylindrical geometry as well and do not change appreciably if the isotropic approximation for f_Γ is not made. The essential feature is the interplay between the increasing surface area and decreasing optical thickness of the fuel region during expansion. The increase in surface area dominates throughout, so that grayness and, hence, reactivity increase monotonically for an expansion of the fuel region. Conversely, reactivity decreases monotonically for a contraction of the fuel region.

CONCLUSION

Although it was realized as early as 1956 that expansion of a central fuel region in a cavity reactor

would increase reactivity (noted in a private communication from Dr. G. Safonov), its importance to reactor stability has not been sufficiently appreciated. This is not surprising since fuel confinement itself has been the major concern. Nevertheless, our initial estimate indicates that the effect can provide a strong energy source to drive potentially unstable motions. It is a cause for concern but not a cause for condemnation.

The reactivity increase, in principle, can be eliminated altogether by confining the fuel in an annular region within the cavity to bring the interplay between surface area and optical thickness into balance. Confinement of the fuel, however, would then be more difficult. Alternatively, it can be mitigated by, in effect, proliferating "unit cavities" as in the nuclear light bulb concept, which has more of the nuclear characteristics of an inhomogeneous reactor than of a cavity reactor. Albeit, the fuel rods would be few and unique. Nevertheless, for the conceptually simple coaxial-flow engine, which might be analogously called a "nuclear candle," sensitivity of power level to fuel fluctuation warrants serious consideration.

In that regard, the theory presented here and the concept of grayness would provide a useful tool for sorting out more important feedback effects. A stability analysis in the spirit of that reported by Welton (ref. 11) for a homogeneous reactor is required and should be based on the kinetic equation derived here. The substance would be quite different, however, because power level in a cavity reactor is influenced not only by changes in grayness but also by its rate of change. Thus, characteristic time constants of the neutron and flow fields become even more significant.

Before reasonably accurate estimates of stability criteria can be made, however, the theory must be generalized to include asymmetric effects of the fuel distribution. This seems to be attainable by using an expansion of the flux in terms of spherical harmonics. It would then be profitable to introduce flow-field variations through a generalized concept of cavity grayness, at first using an acoustic approximation.

Finally, we must emphasize that the kinetic theory presented here is structured in such a way that its present and future development can be verified by experiment in a convenient way.*

* *Note added in proof:* Measurements of the neutron flux excited in a large spherical cavity by a pulsed neutron source have recently been reported by Nelson et al. (ref. 12).

APPENDIX

MATERIAL CONSTANTS AND CALCULATIONS

Evaluation

Explicit expressions for the effective multiplication factor K_e, prompt neutron lifetime l_p, and coefficient B in terms of cavity grayness Γ are presented here for spherical and cylindrical cavities. In each case, the radius of the cavity is denoted by r_ω, and the outer radius of the reflector, by r_b.

Fast neutrons entering the reflector are assumed to diffuse monoenergetically until they enter the thermal neutron group, so that the spatial distribution of the thermal neutron source $q(r)$ is determined by the equation

$$\frac{-1}{r^n}\frac{\partial}{\partial r}\left(r^n\frac{\partial q}{\partial r}\right)+\kappa_f^2 q=0 \qquad \text{(A1)}$$

and the boundary conditions

$$\left.\frac{\partial q}{\partial r}\right|_{r=r_\omega}=\frac{-\kappa_f^2}{\pi(2r_\omega)^n} \qquad \text{and} \qquad q(r_b)=0$$

The quantity $\kappa_f=1/L_f$, where L_f is the diffusion length for fast neutrons.

Because we take cavity grayness to be constant in defining the response function, its Laplace transform $\tilde{G}(r,\sigma;\ r_o)$ is determined by the equation

$$\frac{-1}{r^n}\frac{\partial}{\partial r}\left(r^n\frac{\partial \tilde{G}}{\partial r}\right)+\sigma^2\tilde{G}=\frac{\delta(r-r_o)}{D\pi(2r_o)^n} \qquad \text{(A2)}$$

and the boundary conditions

$$\left.\frac{\partial \tilde{G}}{\partial r}\right|_{r=r_\omega}=\left(\frac{\Gamma}{D}\right)\tilde{G}(r_\omega,\sigma;\ r_o) \qquad \text{and}$$

$$\tilde{G}(r_b,\sigma;\ r_o)=0$$

where $\sigma^2=\kappa^2+\frac{s}{vD}$, $\kappa=1/L$, L is the diffusion length for thermal neutrons, and s is the transform variable.

The effective multiplication factor K_e can be evaluated in the transform space directly and is determined by the relation

$$K_e=\pi(2r_\omega)^n\,\eta\Gamma\lim_{s\to 0}\tilde{G}_f(r_\omega,\sigma) \qquad \text{(A3)}$$

where

$$\tilde{G}_f(r_\omega,\sigma)=\int_{r_\omega}^{r_b} q(r_o)\tilde{G}(r_\omega,\sigma;\ r_o)\pi(2r_o)^n dr_o \qquad \text{(A4)}$$

Similarly, the prompt neutron lifetime and the coefficient B are determined by the relations

$$l_p=\frac{l}{2}\lim_{s\to 0}\left\{\frac{-\sigma}{\tilde{G}_f(r_\omega,\sigma)}\frac{d\tilde{G}_f(r_\omega,\sigma)}{d\sigma}\right\} \qquad \text{(A5)}$$

and

$$B=\frac{l}{2\eta}\lim_{s\to 0}\left\{\frac{-\sigma}{\tilde{G}_f(r_\omega,\sigma)}\frac{d\tilde{G}(r_\omega,\sigma;\ r_\omega)}{d\sigma}\right\} \qquad \text{(A6)}$$

where $l=1/v\Sigma_a$ is an average time to absorption in the reflector material.

By evaluating equations (A3), (A5), and (A6), we obtain the general results, encompassing both spherical and cylindrical geometry,

$$K_e=\frac{\eta\mu(\mathcal{L}_f-\omega\mathcal{L})}{(\mu+\mathcal{L})(1-\omega^2)\mathcal{L}_f} \qquad \text{(A7)}$$

$$l_p=\frac{l}{2}\left\{\frac{(\kappa\mathcal{L})'(\mu\omega+\mathcal{L}_f)}{(\mu+\mathcal{L})(\mathcal{L}_f-\omega\mathcal{L})}-\frac{2\omega^2}{(1-\omega^2)}\right\} \qquad \text{(A8)}$$

and

$$B=\frac{l}{2\eta}\left\{\frac{(\kappa\mathcal{L})'(1-\omega^2)\mathcal{L}_f}{(\mu+\mathcal{L})(\mathcal{L}_f-\omega\mathcal{L})}\right\} \qquad \text{(A9)}$$

where $\mu=\Gamma/\kappa D$, $\omega=\kappa/\kappa_f$, $\mathcal{L}=\mathcal{L}(\kappa r_\omega,\kappa r_b)$, $\mathcal{L}_f=\mathcal{L}(\kappa_f r_\omega,\kappa_f r_b)$, and $(\kappa\mathcal{L})'=\mathcal{L}+\kappa\frac{d\mathcal{L}}{d\kappa}$.

For a spherical cavity,

$$\mathcal{L}(\kappa r_\omega,\kappa r_b)=\frac{1}{\kappa r_\omega}+\coth\kappa(r_b-r_\omega) \qquad \text{(A10)}$$

For a cylindrical cavity,

$$\mathcal{L}(\kappa r_\omega,\kappa r_b)=\frac{I_o(\kappa r_b)K_1(\kappa r_\omega)+K_o(\kappa r_b)I_1(\kappa r_\omega)}{I_o(\kappa r_b)K_o(\kappa r_\omega)-K_o(\kappa r_b)I_o(\kappa r_\omega)} \qquad \text{(A11)}$$

where I_o, I_1 and K_o, K_1 are modified Bessel functions of the first and second kind, respectively.

Calculation Outline for a Spherical Cavity

The data for a spherical cavity are:

Cavity radius . . . . . $r_\omega = 1$ m
Fuel radius . . . . . $r_f = \frac{1}{2}$ m
Reflector thickness . . . $d = 1$ m
Fuel, ^{235}U . . . . . $\eta = 2.08$
Reflector, D_2O . . . . . $L = 116$ cm, $D = 0.817$ cm
$L_f = 14$ cm, $l = 75$ msec

The value of the diffusion length for fast neutrons L_f is chosen such that the minimum critical radius within an infinitely thick reflector is the same as that derived from age-diffusion theory. It is approximately equal to the square root of the neutron age at thermal energy.

The calculations are based on equations (30), (A7), (A8), and (A10). From the data and equation (A10) we obtain the values $\omega = 0.121$, $\mathcal{L} = 2.59$, and $\mathcal{L}_f = 1.14$, so that

$$K_e = \frac{1.53\mu}{\mu + 2.59}$$

from equation (A7) and

$$\Gamma = (7.05 \times 10^{-3})\mu$$

At the critical state $K_e = 1$, so that $\mu_c = 4.89$, $\Gamma_c = 0.0344$, and

$$f_o = \frac{4\Gamma_c}{1 + 2\Gamma_c} = 0.129$$

From equation (30) we obtain $\beta = 1.15$. Therefore, $\beta_o = (r_f/r_\omega)^2 \beta = 0.288$ and $f_o(1) = 0.16$, so that

$$\Gamma = \frac{1}{2}\left[\frac{f_o(1)}{2 - f_o(1)}\right] = 0.0435$$

and $\mu = 6.16$ after expansion. Consequently, $K_e = 1.079$ and $\rho = 1 - 1/K_e = 0.074$. From the data and equation (A8) we obtain the relation

$$l_p = \frac{24.1(1.14 + 0.121\mu)}{\mu + 2.59} - 1.1 \quad \text{msec}$$

so that $l_p = 4.47$ msec at $\mu = \mu_c = 4.89$ and $l_p = 4.06$ msec at $\mu = 6.16$.

REFERENCES

1. Pincock, G. D.; and Kunze, J. F.: Cavity Reactor Critical Experiment. NASA CR-72234, 1967.
2. Ragsdale, R. G.; and Lanzo, C. D.: Summary of Recent Gaseous Reactor Fluid Mechanics Experiments. NASA TM-X-1847, 1969.
3. McNeill, H.; and Becker, M.: Trans. Am. Nucl. Soc., vol. 11, 1968, p. 31, and vol. 12, 1969, p. 1.
4. Safonov, G.: Externally Moderated Reactors. A/CONF. Proc. Int. Conf. Peaceful Uses At. Energy (Geneva), 1958, p. 625.
5. Davison, B.: Neutron Transport Theory. Oxford Univ. Press, 1958, pp. 102–105.
6. Podney, W. N.; and Smith, Harold P., Jr.: Prompt Neutron Kinetics of a Spherical-Cavity Reactor. Nucl. Sci. and Eng., vol. 29, 1967, p. 373.
7. Morse, P. M.; and Feshback, H.: Methods of Theoretical Physics. Pt. I. McGraw-Hill Book Co., Inc., 1953, p. 857.
8. Gozani, Von T.: The Concept of Reactivity and Its Application to Kinetic Measurements. Nukleonik, vol. 5, 1962, pp. 55–62.
9. Case, K. M.; De Hoffman, F.; and Placzek, G.: Introduction to the Theory of Neutron Diffusion. Los Alamos Sci. Lab., 1953, p. 21.
10. Kear, G. H.; and Rudermann, M. H.: An Analysis of Methods in Control Rod Theory and Comparisons With Experiment. GEAP-3937, Gen. Elect. Co., May 1962.
11. Welton, T. A.: System Kinetics. Proc. Symp. Appl. Math., vol. XI, Nuclear Reactor Theory, Am. Math. Soc., 1961, p. 309.
12. Nelson, G. W.; Forehand, H. M.; and Al-Saji, A. W.: Time and Space Dependence of Neutron Flux in Large Single Cavities. Trans. Am. Nucl. Soc., vol. 13, no. 1, June 1970.

DISCUSSION

Latham: You assumed the stored fluid mass of nuclear fuel was constant?

Podney: That's right. The mass in the cavity in all cases was constant.

Latham: In the next session Richard Rodgers will give a paper on our nuclear light bulb concept in which the stored mass of fuel is allowed to vary with changes in chamber pressure. This tends to accelerate fuel out through the throughflow port and also to retard any fuel injection. We find then that the reactivity associated with stored fuel is a far greater effect than the reactivity associated with radius changes.

Podney: I think that in either case you could incorporate this effect into the grayness if you adopt the concept of cavity grayness. The gain would depend on what goes on in the cavity, which is certainly a function of the amount of fuel in the cavity and is also a function of where it is and how fast it moves. I don't know which is the strongest ef-

fect, but I think that one has to be careful because it is sensitive.

Bettenhausen: Does this analysis take into account temperature dependence of cross sections?

Podney: No. That would relate to absorption properties of the core, the concept of grayness. There is, however, a temperature distribution in the reflector. This determines the energy of the thermal neutron, or at least in first approximation. The temperature of the fuel changes absorption properties.

Bettenhausen: Does this model describe time dependencies?

Podney: Yes. If one correlates the unknowns with the opaqueness, and if one can calculate that, the model provides a close approximation to the time behavior of the reactor, provided it doesn't go too fast.

Alemnas: Are these one-dimensional calculations?

Podney: Yes; because of symmetry.

Ohanian: In regard to the pulsed neutron measurements that you mentioned were possible, what kind of experimental geometry do you suggest? Do you put the source in the center of the cavity?

Podney: At first it would be best to have a symmetrical arrangement in the center of the cavity. In this way you can define the concept of grayness, and you can extend that definition by putting the source at another position in the cavity and seeing how that changes the neutron distribution returning to the cavity.

Ohanian: The reason I raised that question is because I see some practical difficulties in trying to place the pulse source in the center of the cavity. It is not a very easy thing to do.

Podney: Why do you say that?

Ohanian: One needs a very long tube to get the neutron source into the center of the cavity and this could disturb the neutron field. Have you thought about that?

Podney: This would be the case for any place that we put it.

Ohanian: In usual pulsed neutron measurements we always put the pulse source at some kind of a boundary.

Podney: If you put it at the boundary of the cavity you would have to distribute it evenly around the boundary and that would be even more difficult.

Ohanian: That's right. Well, thank you very much.

Coupled Fluid and Neutronic Oscillations in High-Temperature Gaseous Uranium

HARRY MCNEILL AND MARTIN BECKER

Rensselaer Polytechnic Institute

The similarity of the core of the gaseous-core nuclear rocket to the combustion chamber of a chemical rocket suggests that acoustic instabilities which have been troublesome in chemical rocket systems may also occur in the gaseous-core nuclear rocket system. The analysis of a simplified and idealized physical model with the radiant heat transfer characteristics of a high-temperature uranium plasma shows that two distinct wave phenomena can occur. One wave, called a heat wave, is stable, but the other wave, which is an acoustic wave, can become unstable. Neutronic damping due to gas dynamic field and neutron field interaction results in a significant influence toward stability of the acoustic oscillation. The results of investigations show that, even with the stabilizing effect of radiant heat transfer and neutronic damping, instabilities can occur within the size envelope of current gas-core rocket conceptual designs.

Desire for increased nuclear rocket propulsion capability has led to interest in gaseous-core nuclear rockets. Concepts advanced to date generally have required large volumes of gaseous uranium (or possibly plutonium). The existence of a large volume of gas leads to concern about the possibility of fluid oscillations in the gas. In addition, the gaseous uranium would have an intrinsic density-dependent heat source (from nuclear fission). It is well known, however, that unstable fluid oscillations of an acoustic character can exist in a compressible fluid with a density-dependent heat source (ref. 1). This type of instability is a recognized problem in the design of chemical rockets and jet-engine afterburners. In this paper we shall discuss acoustic oscillations in a uranium gas with a fission heat source. We shall also discuss the feedback to the oscillation caused by external (reflector) moderation and diffusion of neutrons.

Because this study is an introductory investigation, the models used are simplified and idealized and will lead to only qualitative conclusions. In addition, this paper will be brief because a more detailed account of a constant flux model (no neutronic feedback) is given in references 1 and 2 and a more detailed account of the neutronic feedback model is given in reference 3.

SYMBOLS

A_i	coefficients in dispersion equation
a	reciprocal diffusion length
C_p	specific heat at constant pressure
D	diffusion coefficient
d	effective reciprocal diffusion length in transform space
E_n	nth-order exponential integral
e	base of natural logarithm
erf	error function
G	slowing down and diffusion term in transfer function
$H(k,s)$	power-density transfer function
K	effective thermal conductivity for radiant heat transfer
k,s	transform variables for space, time
l	cavity thickness
M	linear differential operator
n	number of state variables
p	pressure
Q	nuclear heat source
Re	real part

t	time
T	temperature
u	velocity of cavity fluid
v	speed of thermal neutrons
W	neutron feedback term in dispersion equation
x,y	spatial variables
Γ	blackness term in transfer function
Σ_a	absorption cross section in cavity
γ	cavity transmission function
γ_c	ratio of specific heats
η	number of fast neutrons produced per thermal neutron absorbed in cavity
λ	wave length
ρ	density
τ	Fermi age
Φ	state variable

Subscripts

i,j	indices for state variables
l	index for roots of dispersion equation
o	unperturbed quantity

Superscripts

i	power index in polynomial part of dispersion equation
$(\ )'$	perturbed part of a quantity

THEORY

Previous papers (refs. 1 and 2) have demonstrated that the conservation laws of the gas dynamic field, radiation field, and neutron field can be expressed in a linearized form in which M_{ij} is a linear operator and Φ_j is a state variable:

$$\sum_{j=1}^{n} M_{ij}\,\Phi_j = 0 \qquad (1)$$

This set of equations can be Fourier transformed in space and Laplace transformed in time to obtain a linear set of algebraic equations in terms of transformed field variables. The determinant of this set of equations can be defined as a dispersion function while zeros of this function correspond to roots of a dispersion equation. The roots correspond to the complex frequencies of time-dependent exponential functions and in general depend on both the equilibrium state variables and the wave number k (which can be related to the size of the system). The system will be stable when the real parts of the Laplace transform variable are negative, marginally stable when they are zero, and unstable when they are positive. A stability criterion can be expressed as:

$$Re(s_l) < 0 \qquad l = 1, 2, \cdots \qquad (2)$$

The wave number can be related to the size of the system in the following way. Assume that the critical core length (above which the system is unstable) corresponds to one-half the critical wave length (distance between nodes). This corresponds to hard-wall end conditions and has been used in previous work (ref. 1). Different end conditions (depending on the specific features of the injection systems, nozzles, etc.) would imply somewhat different relations between wave number and system size.

Mathematical Model of Gaseous-Core Reactor

The cavity reactor system is shown in figure 1. The cavity is of finite width, bounded by an infinite

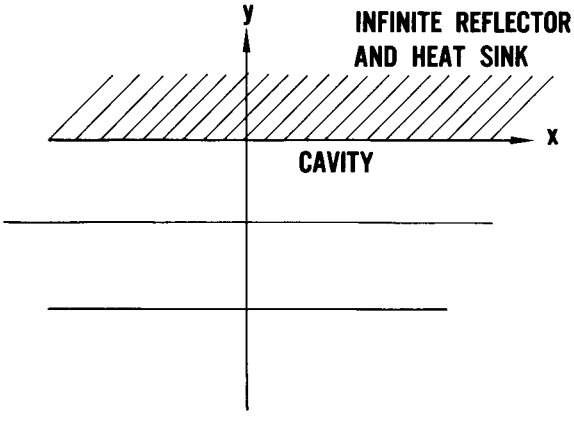

FIGURE 1.—*Geometry of cavity reactor system.*

transverse reflector, and of infinite length in the longitudinal direction. The reactor is critical at power level Q_o with the cavity gas assumed stationary and initially uniform. No temperature gradient exists except for transverse gradients consistent with heat removal requirements at steady state. The specialized case of plane wave propagation in the longitudinal direction is investigated by assuming that transverse dependence can be sepa-

rated from longitudinal dependence so as to yield perturbation equations involving only time and the x-direction. The linearized conservation laws of continuity, momentum, energy, neutronics, and state can be expressed as:

$$\frac{\partial p'}{\partial t}+\rho_o\frac{\partial u'}{\partial x}=0 \tag{3}$$

$$\rho_o\frac{\partial u'}{\partial t}+\frac{\partial p'}{\partial x}=0 \tag{4}$$

$$\rho_o C_p\frac{\partial T'}{\partial t}-\frac{\partial p'}{\partial t}=Q'+K_o\frac{\partial^2 T'}{\partial x^2}+\frac{Q_o T'}{T_o} \tag{5}$$

$$\frac{Q'}{Q_o}=H\frac{\rho'}{\rho_o} \tag{6}$$

$$\frac{p'}{p_o}=\frac{\rho'}{\rho_o}+\frac{T'}{T_o} \tag{7}$$

The prime superscript and the o subscript indicate perturbed and steady-state quantities, respectively.

Dispersion Equation

The dispersion equation is obtained by the transformation previously described. The expression

$$\sum_{i=1}^{4}A_i(k)\,s^{i-1}=W(k,s) \tag{8}$$

results where

$$A_4=1 \tag{9}$$

$$A_3=\frac{K_oT_o(\gamma_{c-1})k^2}{\rho_o}+\frac{Q_o(\gamma_{c-1})}{\rho_o} \tag{10}$$

$$A_2=\frac{\gamma_c p_o k^2}{\rho_o} \tag{11}$$

$$A_1=\frac{K_oT_o(\gamma_{c-1})k^4}{\rho_o}+\frac{Q_o(\gamma_{c-1})k^2}{\rho_o} \tag{12}$$

and

$$W(k,s)=\frac{-Q_o(\gamma_{c-1})H(k,s)}{\rho_o} \tag{13}$$

Constant Flux Model

Transformation of equation (6), the neutron equation, identifies the function $H(k,s)$ as the power-density transfer function. The value $H=0$ corresponds to zero power perturbation and, therefore, there is no source of instability. When $H=1$ the corresponding physical model is that of no neutron field perturbation or constant flux. In this case

$$\sum_{i=1}^{4}A_i(k)\,s^{i-1}=-Q_o\frac{(\gamma_{c-1})}{\rho_o} \tag{14}$$

The dispersion equation is a real polynomial. The existence of roots in the positive half-plane can be determined by using Routh's criterion to obtain a stability criterion in terms of wavelength as (ref. 1)

$$\lambda^2\leqq\frac{4\pi^2K_oT_o(\gamma_{c-1})}{Q_o(2-\gamma_c)} \tag{15}$$

Greater insight can be obtained by transforming from complex frequency to complex wave number in the dispersion equation. A closed-form solution (refs. 2 and 3) can be obtained for equation (14) by making the assumption that radiant heat transfer and fission heat generation are first-order effects and, therefore, higher order terms can be neglected. Two sets of roots are obtained. The first pair of roots has an associated wave which we term a heat wave. It is strongly dependent on radiant heat transfer through the heat transfer coefficient K_o. When heat transfer increases the roots vanish and the waves become undamped nonpropagating exponential waves. As heat transfer decreases the roots become large and increased damping and eventual disappearance of the wave results. This wave does not contribute to instabilities. The second pair of roots corresponds to a sound wave since it has a phase velocity equal to the equilibrium speed of sound. Attenuation of the wave results from radiant heat transfer while amplification results from the nuclear heat source. At low frequencies, the heat source predominates and the system is unstable, but as the frequency increases the attenuation grows and drives the system stable.

Field Interaction Model

When the gas-dynamic field and the neutron field interact, the power-density transfer function is no longer constant but is related in a complex way to the nuclear parameters of the cavity system (ref 3). We first consider an idealized neutron cycle.

A fission occurs in the gaseous core producing fast neutrons. Since the core consists of ^{235}U gas it can be considered transparent to fast neutrons; therefore, the neutrons pass with no interaction into the reflector moderator. Age theory can be used to describe the slowing down of these neutrons to thermal energy. Diffusion theory is used to describe

the thermal neutrons in the reflector. At the core-reflector interface, blackness theory is applied, assuming that ^{235}U is a pure absorber, with the result that the net current of thermal neutrons into the core and, therefore, the rate of absorption and fission in the core is obtained. The fissions then lead to a source of fast neutrons and the cycle is complete.

The equilibrium or steady-state values of the appropriate nuclear parameters are obtained by imposing a criticality condition consistent with the fuel concentration and temperature level of the core. The power feedback is obtained by expanding and linearizing expressions for cavity neutron power generation in terms of the fractional variation of flux and the fractional variation in cavity neutron transmission. As a result the power-density transfer function can be expressed as (ref. 3):

$$H(k,s) = \Gamma_o/[1+\gamma_o G(k,s)] \tag{16}$$

In the expression we define:

$$\Gamma_o = \frac{\Sigma_{a,0} l}{2\gamma_o}\left[\frac{2E_{2,0}(1+3E_{4,0})+3E_{3,0}(1-2E_{3,0})}{(1+3E_{4,0})^2}\right] \tag{17}$$

$$G(k,s) = 1-\frac{\eta e^{-k^2\tau+d^2\tau}[1-erf(d\sqrt{\tau})]}{\gamma D} \tag{18}$$

$$d^2 = k^2+\frac{s}{Dv}+\frac{\Sigma a}{D} \tag{19}$$

DISCUSSION OF RESULTS

The models described have been applied to the study of a reference design (refs. 1 to 4) with core characteristics based on those used by Krascella (ref. 5). Table I shows the reference values for key parameters for a graphite moderated system. Equivalent parameters have been obtained for beryllium and water moderation.

TABLE I.—*Parameters for Reference Case (Carbon)*

Name	Value
Rosseland opacity coefficient, erg/°K cm sec	0.380×10^{7}
Pressure, dyn/cm²	0.505×10^{8}
Density, gm/cm³	0.400×10^{-2}
Temperature, °K	0.1357×10^{5}
Ratio of specific heats	0.167×10^{1}
Fission power, erg/sec cm³	0.440×10^{9}
Diffusion coefficient, cm	0.915
Neutron velocity, cm/sec	0.22×10^{6}
Absorption cross section, cm⁻¹	0.35×10^{-3}
Fermi age, cm²	0.364×10^{3}
Perturbation coefficient	0.959
Transmission function	0.406×10^{-1}

The results of the numerical analysis are tabulated in table II. A plot of wave number versus the real part of the complex frequency is shown in figure 2. The crossover point $Re(s) = 0$ corresponds to the critical wave number for each system. We note that the constant-flux model with no neutronic feedback is the least stable while, on the other hand, the water reflector is the most stable. Plots have been made of the power-density transfer function which explain this behavior (ref. 3). In brief, results indicate that the reflector with the largest migration area permits a smearing out or spatial equilization of neutrons in the reflector. Such a smearing tends to dissipate neutron feedback because of the weak correlation between the location of cause and location of effect.

TABLE II.—*Results of Numerical Analysis*

[Reference core length from ref. 5 is 300 cm]

Moderator	Critical wavelength, cm	Critical size, cm
No neutronic feedback	100	50
C	150	75
Be	232	116
H_2O	3500	1750

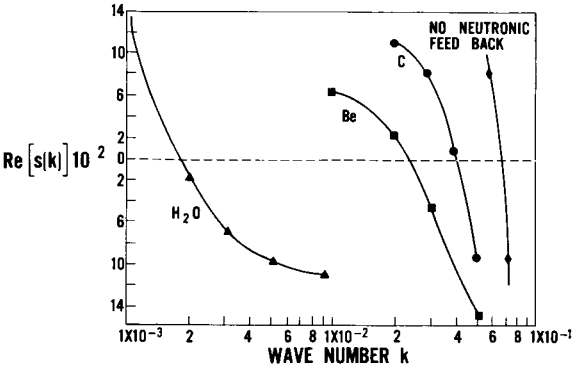

FIGURE 2.—*Wave number against real part of complex frequency. Critical wave number corresponds to* Re(s) = 0.

At the likely temperatures of gaseous reactor

operation, the uranium gas will be ionized. Some preliminary consideration has been given to plasma effects (ref. 4) which did not lead to any fundamental changes in our conclusions. However, more detailed study will be required before definitive assessments about plasma effects can be made.

CONCLUDING REMARKS

Because of the simplified and idealized models used and because there is some uncertainty as to what the ultimate configuration of a gaseous-core reactor will be it would seem prudent to draw conclusions on a qualitative, instead of a quantitative, basis. We conclude, first, that acoustic instability is a potential problem for gaseous-core reactors. Second, we conclude that, although neutronic feedback has a significant stabilizing influence, that influence is not sufficiently large to eliminate acoustic instability as a source of concern in gaseous-core reactor development.

REFERENCES

1. McNeill, H.; and Becker, M.: Trans. Am. Nucl. Soc., vol. 11, 1968, p. 31.
2. McNeill, H.; and Becker, M.: AIAA J., vol. 8, 1970, p. 354.
3. McNeill, H.; and Becker, M.: Nucl. Sci. Engr., vol. 42, 1970, p. 220.
4. McNeill, H.: Ph.D. thesis, Rensselaer Polytechnic Inst., 1968.
5. Krascella, N.: Rept. E–910092–9, United Aircraft Res. Lab., 1966.

Page intentionally left blank

The Radiant Heat Flux Limit of Bypass Flow in a Uranium Plasma Rocket

ALBERT F. KASCAK
NASA Lewis Research Center

A two-dimensional radiative-convective analysis showed that about 80 percent of the hydrogen flow could be bypassed in a gas-core reactor. The actual mass of hydrogen in the cavity is reduced in two ways. First, the reduced amount of hydrogen that is passed through the cavity must pick up the original reactor power. Therefore, in the bypass situation the hydrogen temperatures inside the reactor cavity are higher, and the hydrogen density is lower. The decreased density reduces the mass of hydrogen in the reactor. The combined effects of a decrease in both the hydrogen flow rate and the hydrogen density is to reduce the mass and momentum flux of the hydrogen in the reactor cavity (as long as the hydrogen flow area is not changed). This flux reduction would probably reduce the mixing rate between the uranium and the hydrogen, which is a desirable effect. One might therefore choose to reduce the cavity size so as to reduce further the amount of hydrogen between the fuel and the moderator. Bypassing 80 percent of the total hydrogen flow reduces the actual mass of hydrogen between the moderator and the uranium plasma to the range of about 1/25 to 1/5 of that in the nonbypass case. The exact fraction within this range was not calculated in the present analysis because to do so would require taking into account effects of bypass flow on the mixing process of the hydrogen and the uranium.

A two-dimensional radiative-convective analysis was used to calculate the temperature distribution in the annular propellant region. A diffusion approximation was used in this part of the analysis. A transport analysis was then used to calculate the wall heat flux from the propellant temperature distribution. The maximum wall heat flux increased from near zero to about 0.5 kW/in.^{2} when 80 percent of the total hydrogen flow was bypassed.

In the wall heat flux calculation, the hydrogen in the cavity was assumed to contain 0.7 weight percent solid seed material with an absorption cross section of 50 000 cm^2/g (5000 m^2/kg). These are values that have been experimentally achieved. The 0.7 weight percent of seed material in the cavity would amount to about 1 percent of the total hydrogen flow. This amount of seed would have a negligible effect on specific impulse.

The overall conclusion of this study is that a large fraction of the hydrogen propellant can bypass the engine cavity without causing an excessive radiant heat flux on the cavity wall.

The uranium plasma nuclear rocket is a proposed propulsion system which features a high specific impulse (1500 to 2500 sec) and a relatively high thrust (10^5 to 10^6 lb). One type of configuration (fig. 1(*a*)) is known as the coaxial-flow concept. This flow system employs a cylindrical geometry with a low-velocity fissioning uranium plasma flowing axially down the centerline of the reactor cavity. High-velocity hydrogen propellant flows coaxially around the fuel. Heat generated on the uranium plasma is transferred by thermal radiation to the propellant, thus increasing the enthalpy of the propellant. The propellant is then expanded through the nozzle, giving the desired thrust and specific impulse.

The system is externally moderated; therefore, neutrons which are thermalized in the moderator must travel through the hydrogen propellant before they can cause fissions in the uranium plasma. A recent study (ref. 1) shows that the hydrogen propellant acts as a poison in the reactor, thus causing the critical mass to be very large. If the ma-

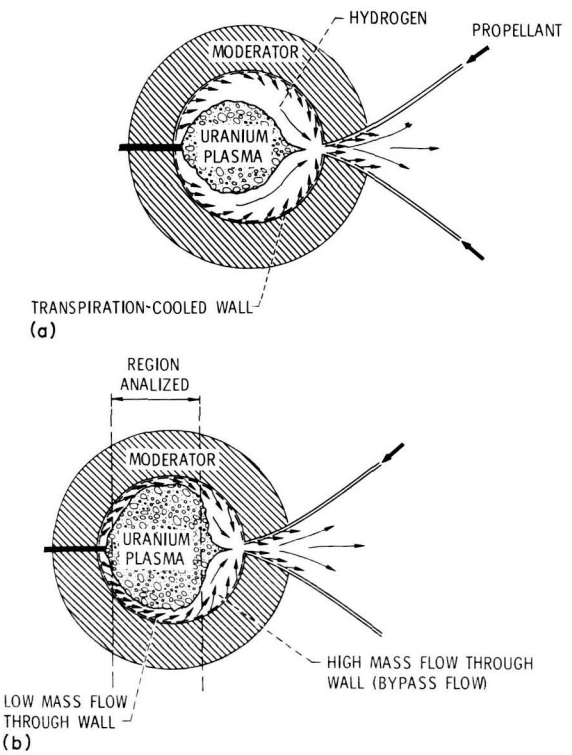

FIGURE 1.—*Uranium plasma rocket engine.* (a) *Without bypassed flow.* (b) *With bypassed flow.*

jority of the hydrogen could be removed from the cavity, the critical mass could be reduced by a factor of 1/2 to 1/3.

The objective of this study is to determine if it is possible to reduce the amount of hydrogen between the moderator and uranium plasma without exceeding wall heat flux limits. The reduction could be accomplished in an engine by using the bypass-flow concept shown in figure 1(*b*). (The idea of bypassed flow was suggested several years ago for the vortex-flow rocket concept by the authors of ref. 2.) In the bypass idea, a small fraction of the total hydrogen flow is injected relatively uniformly through most of the curved, porous wall of the cavity. The rest of the total hydrogen flow is added just upstream of the nozzle, as illustrated in figure 1(*b*).

The bypass-flow concept has two advantages. First, the flow area may be reduced; this decreases the volume (and therefore the mass of hydrogen) between the moderator and the uranium plasma. Second, since a constant amount of energy is generated in the uranium plasma and a small fraction of the propellant is used to convect this energy out of the cavity, the average temperature of the propellant in the cavity is increased. The resulting density decrease further decreases the mass of hydrogen between the moderator and the uranium plasma.

The bypass-flow concept has two potential disadvantages because of the higher temperature of the hydrogen in the cavity: First, higher fuel temperature, and second, higher wall heat flux. Reference 3 has shown that the increase in average fuel temperature is small for any increase in the hydrogen temperature as long as the hydrogen temperature does not approach the average fuel temperature.

The specific objective of this study is to reduce the amount of hydrogen flowing through the cavity until the wall heat flux approaches a transpiration-limited value, and then to determine the resultant reduction in the amount of hydrogen between the uranium plasma and the moderator.

SYMBOLS

a	absorption coefficient, 1/m
C_p	specific heat, J/(kg) (°K)
q	heat flux, W/m^2
R	distance between source and sink of radiation, m
r	radial position in cavity, m
S	dummy variable of integration
T	temperature, °K
u	axial velocity, m/sec
z	axial position in cavity, m
ρ	density, kg/m^3
σ	Stefan-Boltzmann constant, 5.67×10^{-8} W/m^2 (°K)^4
τ	optical depth
Ω	spherical angle

Subscripts

f	fuel-propellant interface
i	inlet to cavity
P	Planck mean
R	Rosseland mean
w	transpiration-cooled cavity wall

ANALYSIS

The analysis was carried out using a simplified, cylindrical geometry to represent the central portion

of the flow, as shown in figure 1(*b*). The model does not include the more complex flow patterns that would exist near the front and rear of the engine cavity. Figure 2 shows the model of the annular propellant region. In the model, bypass of some of the hydrogen is accomplished by simply reducing the hydrogen flow rate through the annular region that is between the fuel and the cavity wall. In an engine, bypass flow could be achieved by injecting most of the hydrogen flow through a small part of the cavity wall at the exit end of the cavity just upstream of the nozzle throat region.

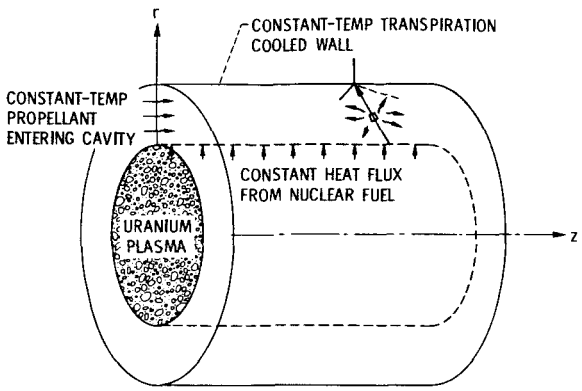

FIGURE 2.—*Model of annular propellant region.*

The diffusion approximation was used to describe the radiative heat transfer and resulted in the following equation:

$$0=-\rho u C_p\frac{\partial T}{\partial z}+\frac{1}{r}\frac{\partial}{\partial r}\left(\frac{16\sigma T^3}{3a_R}r\frac{\partial T}{\partial r}\right) \quad (1)$$

The heat flux on the inner cylindrical surface and the temperature of the outer cylindrical surface were prescribed constants and were used as the radial boundary conditions:

$$q(r_f,z)=q_f \quad (2a)$$

$$T(r_w,z)=T_w \quad (2b)$$

The propellant entered the cavity at a prescribed constant temperature and was used as the axial boundary condition

$$T(r,0)=T_i \quad (3)$$

Equation (1) was numerically solved subject to the boundary conditions (2) and the initial condition (3). This solution predicted temperatures through the propellant region. Using these temperatures, a transport analysis was used to predict the wall heat flux:

$$q_w=\frac{1}{\pi}\int_\Omega\left(\int_0^{\tau_f}\sigma T^4e^{-\tau}d\tau+\sigma T_f^4e^{-\tau_f}\right)d\Omega \quad (4)$$

$$\tau=\int_0^R a_p dS \quad (5)$$

The propellant was assumed to be hydrogen seeded with small solid particles. These particles were assumed to remain solid up to the temperature at which hydrogen began to absorb radiation. The seed densities were assumed small enough so that pure hydrogen properties could be used. The hydrogen that flows through the reactor cavity was assumed to contain 0.7 percent by weight of solid particles. The absorption cross section of these particles was taken to be 50 000 cm^2/g (5000 m^2/kg) in the present calculations. These values of weight percent and cross section have been experimentally achieved (refs. 4 and 5).

DISCUSSION

The two-dimensional radiative-convective analysis was applied to the annular propellant region using the pure hydrogen properties of references 6 and 7. The propellant was seeded with small solid particles which were assumed to remain solid up to the temperature at which hydrogen began to absorb radiation. The hydrogen in the cavity was assumed to contain 0.7 weight percent of solid seed material with an absorption cross section of 50 000 cm^2/g (5000 m^2/kg). These are reasonable values that have been achieved in experiments (refs. 4 and 5). The inlet propellant temperature as well as the cavity wall temperature were assumed to be 3000° R (1633° K). The heat flux at the edge of the fueled region was 2880 MW/m^2. This heat flux corresponded to that of a rocket engine having a thrust of 1 000 000 lb (4.45 MN) and a specific impulse of 1500 sec.

Using the preceding values as input, several cases were solved. In each of these cases, the amount of flow bypassed was increased until the maximum wall heat flux was about 0.5 MW/m^2. This final case is shown in figure 3.

Figure 3 shows the propellant region with the radial dimension enlarged. The cavity is 2 m in axial length. The fueled region is the cylinder whose

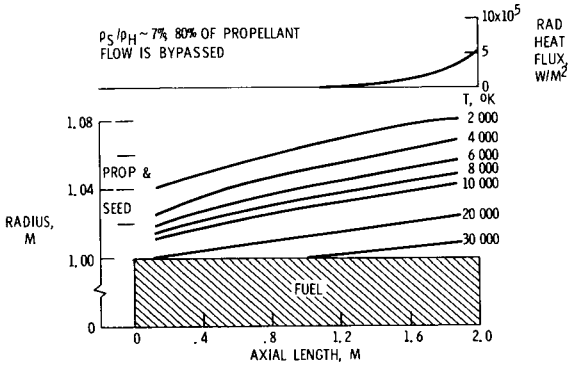

FIGURE 3.—*Isotherms in propellant region.*

radius is 1 m. The cavity wall is located at 1.1 m. The hydrogen propellant region is the annular region with a radius from 1.0 to 1.1 m.

Isotherms are shown in the annular propellant region. These vary from 2000° to 30 000° K. Also shown is the cavity-wall heat flux. For the case shown in figure 3, 80 percent of the flow was bypassed, and 20 percent of the flow went through the cavity. The inlet flow area was reduced to 20 percent of the nonbypassed case (the original case); thus the volume of the propellant region was reduced to 20 percent of its original volume. The combined effect of flow area reduction and density decrease resulted in the amount of hydrogen in the propellant region being reduced to about 1/25 of the original amount of hydrogen.

The mass flux of the outer stream is the same as that in the nonbypassed case. However, the momentum flux of the hydrogen in the cavity is five times greater than that in the nonbypassed case. This momentum flux increase might increase the mixing of the fuel and propellant. Therefore, the effect of hydrogen flow area changes on the mixing process between the hydrogen and uranium streams would have to be considered in order really to determine how much the hydrogen flow area would be reduced. The present analysis did not include any mixing effects. Therefore, it was not possible to determine precisely how much the hydrogen flow area would be reduced. However, the actual value would probably be somewhere between the two extremes of (1) no area reduction, or (2) an 80-percent area reduction. Thus, the amount of hydrogen present in the cavity, with 80 percent of the hydrogen bypassing the cavity, should be between 1/25 and 1/5 of the amount present with no bypass flow.

The preceding conclusion is, of course, only an estimate of the effect. The relatively large amount of hydrogen that can be bypassed indicates that further study is worthwhile (because of the large potential savings of critical mass). Even with the simplifying assumptions used in this analysis the conclusion that a large fraction of the flow can bypass the cavity without causing an excessive radiant heat flux on the cavity walls should be substantially correct. This study did not examine the rather complicated effects associated with remixing the bypassed flow with the cavity through flow.

REFERENCES

1. KUNZE, J. F.; PINCOCK, G. D.; AND HYLAND, R. E.: Cavity Reactor Critical Experiments. Nucl. Appl., vol. 6, no. 2, Feb. 1969, pp. 104–115.
2. ANON.: Investigation of Gaseous Nuclear Rocket Technology—Unclassified Programs. Quart. Progr. Rept. 3–U, Rept. C–910093–5, United Aircraft Corp., June 26, 1964.
3. KASCAK, ALBERT F.: Estimates of Local and Average Fuel Temperatures in a Gaseous Nuclear Rocket Engine. NASA TN D–4164, 1967.
4. LANZO, CHESTER D.: Measurement of the Transmissivity of a Carbon-Particle-Seeded Nitrogen Jet. NASA TN D–4722, 1968.
5. WILLIAMS, J. R.; CLEMENT, J. D.; SHENOY, A. S.; AND PARTAIN, W. L.: The Attenuation of Radiant Energy in Hot Seeded Hydrogen. Quart. Status Rept. 2, Project A–1045, Eng. Exp. Sta., Ga. Inst. Tech., 1969.
6. KRASCELLA, N. L.: Tables of the Composition, Opacity, and Thermodynamic Properties of Hydrogen at High Temperatures. (Rept. B–910168–1, United Aircraft Res. Lab., Sept. 1963.) NASA SP–3005, 1963.
7. PATCH, R. W.: Interim Absorption Coefficients and Opacities for Hydrogen Plasma at High Pressure. NASA TM X–1902, 1969.

DISCUSSION

Franklin: I have two questions: First, what is the limiting factor on the heat flux to the wall? Is it the material temperature or is it a thermal stress problem?

Kascak: The walls are presumably transpiration cooled. An assumed limit of heat transfer at 0.5 kW/in.^{2} does not seem very large to me. I think, eventually, one may go a factor of 10 above this.

Franklin: The other question is: As you bypass the

propellant you reduce the radiating area to this bypassed propellant and therefore you're cutting down your available volumetric heat flux. Are you making it up with the propellant that flows through the cavity?

Kascak: Yes. What happens is that the propellant that flows through the cavity gets heated approximately five times more than does the bypassed propellant. Downstream both become mixed. I have not yet looked at this problem of mixing.

Franklin: Can you establish some sort of performance limit simply on the basis of enthalpy addition?

Kascak: There should be such a performance limit because the propellant as it expands through the nozzle is not at a constant temperature. But, again, I have not looked at this so I cannot answer that question.

Park: How does radiative heat transfer compare with the heat transfer due to turbulence?

Kascak: In a previous study I found that turbulent heat transfer is small compared with the radiant heat transfer. I cannot say this in our particular case. When I looked at it previously, I considered the transfer from the hot core through the hydrogen that was solely due to jet mixing. In this case one should add turbulence brought about from the flow through very small pores in the wall. I feel that the resulting increase of heat transfer will be small but it could be of the same order as radiation. It would not be much larger; I can say that definitely.

Swander: From your interesting observations one may conclude it best not to bypass too much hydrogen simply because it results in a negative reactivity effect in the vicinity of the plasma, depending on expansion rates of the uranium plasma and of hydrogen. Did you look into this?

Kascak: Hydrogen acts as a poison there. When the uranium plasma expands the fuel comes closer to the moderator and, secondly, the poison is removed. There are then two combined effects that increase reactivity.

Swander: On the other hand, if the hydrogen heats up and becomes more of a poison faster than the uranium expands it would have a negative effect.

Kascak: But the amount of hydrogen is reduced in this area so that there is very little interaction between the neutrons coming across from the moderator to the uranium. If there is an interaction, the hydrogen absorbs the neutrons, or absorbs a large fraction. The upscatter is worse in this case, but I don't think upscatter will be the biggest part of the problem. It is the fact that hydrogen is poison.

Page intentionally left blank

A Study of Thermal Radiation Absorption Processes in Gas-Core Reactors[1]

W. L. PARTAIN, J. R. WILLIAMS, AND J. D. CLEMENT

Georgia Institute of Technology

Recent data on the thermal emission spectrum from uranium plasma indicate that the radiant energy entering the propellant region of a gas-core reactor would lie in the wavelength range between 1200 and 7000 Å. Since hydrogen at temperatures below about 8000° K is transparent to this radiation, it must be seeded to make it absorb this radiant energy and become heated. Submicron-sized refractory metal particles appear to be the best seed material for this application because they are highly absorbing throughout this wavelength range and can withstand high temperatures without vaporizing. Calculations using the Mie theory show that submicron-sized particles of carbon, tungsten, and silicon are highly absorbing, whereas submicron-sized particles of nonconducting materials, such as aluminum oxide, are almost purely scattering and would therefore not be useful as a seed material. The extinction parameters of submicron-sized particles of carbon, tungsten, and silicon in hydrogen gas were measured over a broad wavelength range at 1-atm pressure and found to be about 40 000 cm^2/g for carbon, about 15 000 cm^2/g for tungsten, and about 65 000 cm^2/g for silicon. These values agree well with those from the Mie theory. The carbon-hydrogen aerosol exhibited a slight increase in extinction parameter as the temperature was raised to 2170° K. The carbon particles react with hydrogen to produce methane at temperatures above 1000° K; however, small concentrations of methane (less than 1 mole percent) greatly retard the reaction rate. Similar measurements of the extinction parameter of tungsten-hydrogen aerosols at 12.5-atm pressure showed a significant increase in the extinction parameter with temperature from about 18 000 cm^2/g at 730° K to about 50 000 cm^2/g at 1770° K. The extinction parameter of tungsten carbide in hydrogen at 11.9 atm and 1650° K is about 50 000 cm^2/g. Measurements of the scattering of a 6328-Å laser beam from submicron-sized carbon, tungsten, silicon, tungsten carbide, and silicon carbide particles dispersed in nitrogen gas demonstrate the highly forward nature of the scattering. Most of the light is scattered at angles of less than 30°. Electron micrographs illustrate the sizes and shapes of the particles used for these investigations.

The gas-core nuclear rocket is the concept receiving the most attention as the next step beyond the solid-core nuclear rocket engine which has already been developed. The gas-core concept envisions hydrogen propellant flowing past a core of hot, fissioning uranium or plutonium gas with little or no coupling between the two flows. The temperature of the core would probably be in the range of from 15 000° to 50 000° K and that of the hydrogen propellant, of the order of 8000° K. Essentially all of the energy from the core would be delivered to the propellant as radiant energy. Recent investigations (refs. 1 and 2) of the emission spectrum of hot gaseous uranium indicate that the radiant energy will consist of wavelengths below 7000 Å (fig. 1). The hydrogen propellant, transparent to this thermal radiation, may be seeded with submicron-sized particles of a suitable material in order to make it absorb this radiant energy.

The absorption of thermal radiation by a gas is usually greatly enhanced by the dispersion of small particles in the gas. The particles become heated by absorbing radiant energy and the gas is heated by conduction from the particles. If the particles are small enough, they remain essentially in thermal

[1] This research was supported by NASA grant NGR–11–002–068.

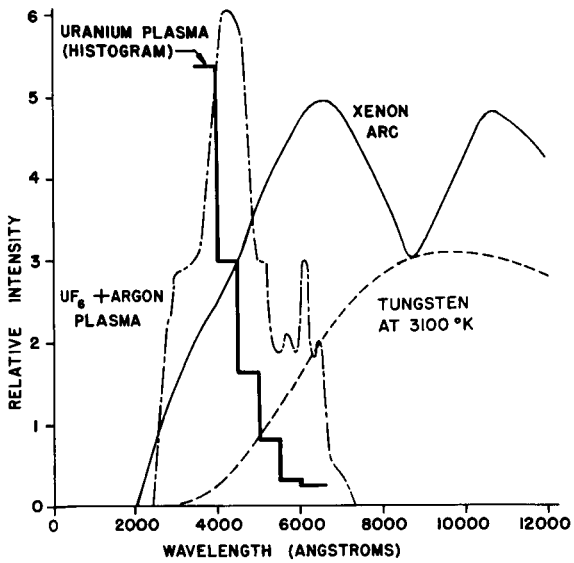

FIGURE 1.—*Thermal emission spectra of uranium plasma and other intense sources. (Uranium data taken from refs. 1 and 2.)*

and dynamic equilibrium with the gas as the particles and gas are heated.

When thermal radiation or light interacts with a cloud of particles, some of the radiant energy may be absorbed and some scattered. Only the energy that is absorbed serves to heat the particles. Particles of materials which have low electrical conductivities scatter much more energy than they absorb. Such scattering particle clouds have been found useful for optical screening when the objective is to limit visibility. Absorbing particle clouds composed of metallic particles have been found more useful for thermal radiation shielding and to enhance heat transfer to gases.

There are three significant mechanisms by which radiant energy interacts with a gas containing particles: (1) Absorption by the gas, (2) absorption by the particles suspended in the gas, and (3) scattering by the particles. The importance of each of these three mechanisms depends on the composition, temperature, and pressure of the gas, the composition, sizes, and shapes of the particles, the particle number density, and the spectrum of the radiant energy.

The attenuation of a beam of monochromatic radiant energy by a gas containing particles is governed by the expression

$$I(\lambda,x) = I(\lambda,o)\, e^{-k_T(\lambda)x} \tag{1}$$

where $k_T(\lambda)$ is the total linear attenuation coefficient for radiant energy of wavelength λ and x is the distance the beam traverses through the seeded gas. The total linear attenuation coefficient for all three interaction processes is equal to the sum of the linear attenuation coefficients for each process separately; that is,

$$k_T(\lambda) = k_a^g(\lambda) + k_a^p(\lambda) + k_s^p(\lambda) \tag{2}$$

where $k_a^g(\lambda)$ is the linear attenuation coefficient due to absorption by the gas alone, $k_a^p(\lambda)$ is the linear attenuation coefficient due to absorption by the particles, and $k_s^p(\lambda)$ is the linear attenuation coefficient due to scattering by the particles. Coefficients $k_a^p(\lambda)$ and $k_s^p(\lambda)$ are proportional to the number density of the particles so long as the particles are randomly oriented and the average distance between the particles is much greater than their effective radius, so it is convenient to define the absorption parameter $\mu_a(\lambda)$ and the scattering parameter $\mu_s(\lambda)$ by

$$\left.\begin{aligned} \mu_a(\lambda) &= \frac{k_a^p(\lambda)}{\rho} \\ \mu_s(\lambda) &= \frac{k_s^p(\lambda)}{\rho} \end{aligned}\right\} \tag{3}$$

where ρ is the particle density in grams of particles per cubic centimeter of aerosol. Parameter $\mu_a(\lambda)$ is also called the mass absorption coefficient. The totality of processes by which energy is removed from a beam by a particle cloud is called extinction, so the extinction parameter is given by

$$\mu_e(\lambda) = \mu_a(\lambda) + \mu_s(\lambda) \tag{4}$$

The absorption, scattering, and extinction parameters are independent of the concentration of particles.

One may now consider the absorption of radiant energy by particle-seeded gases to be the sum of two independent processes, absorption by the gas itself and absorption due to the particles in the gas. The absorption coefficient of the gas $k_a^g(\lambda)$ depends only on the composition, temperature, and pressure of the gas, whereas the absorption and scattering parameters of the particles $\mu_a(\lambda)$ and $\mu_s(\lambda)$ depend on the composition, sizes, and shapes of the particles. Thus, $k_a^g(\lambda)$ may usually be determined for the pure gas and $\mu_a(\lambda)$ and $\mu_s(\lambda)$, for the particles

in any transparent medium, and then $k_T(\lambda)$ is calculated for the particle-seeded gas using equations (2) and (3). However, this procedure becomes difficult, if not impossible, when the composition of the gas and the sizes and shapes of the particles are changed by chemical reactions between the particles and the gas.

The basic mechanisms of radiant energy absorption by particle clouds and by gases are quite different. Since atoms and molecules of a gas absorb radiant energy in discrete quanta, the absorption coefficient of a gas may change many orders of magnitude over a wavelength interval of a few angstroms. The familiar absorption spectra of various gases attest to the wide variations of $k_a{}^{\varrho}(\lambda)$ as λ is changed. The energy level diagram and spectra of the hydrogen atom are presented in figure 2. At low temperatures, the hydrogen atoms are essentially all in the ground state, and radiant energy of 1216-Å wavelength or shorter is required to excite or ionize the atom. This means that hydrogen atoms in the ground state are incapable of absorbing radiant energy of wavelengths greater than 1216 Å. Since the wavelength region of interest for the propellant region of the gaseous-core nuclear rocket is above this, hydrogen alone at low temperature is seen to be transparent to the thermal radiation from the core. At higher temperatures, however, a significant number of hydrogen atoms are thermally excited to the first excited state ($n=2$). As is seen from figure 2, radiant energy of wavelengths as long as 6563 Å will cause ionization. At slightly higher temperatures, the third excited state becomes sufficiently populated to permit significant absorption of radiant energy of wavelengths as long as 18 760 Å. Krascella (ref. 3) and Patch (ref. 4) have calculated the composition, opacity, and thermodynamic properties of hydrogen at high temperatures and pressures. The data for figures 3 and 4 were taken from reference 3 to illustrate the increase in the

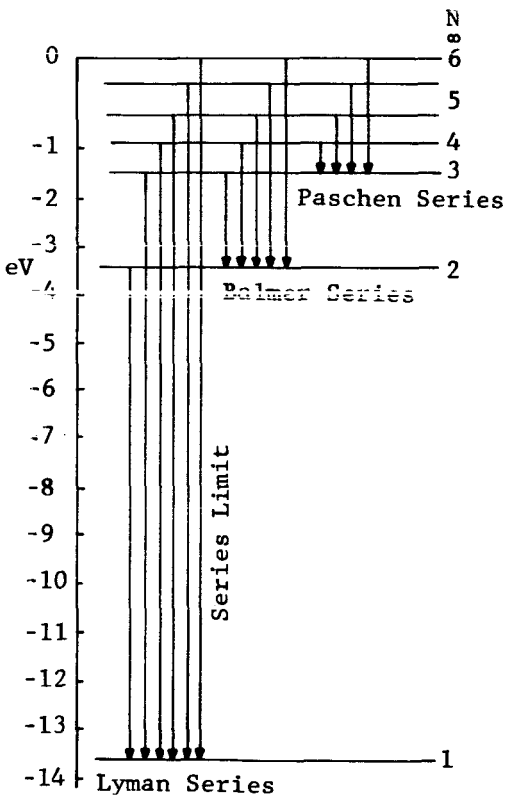

Name of series	Energy levels involved, N		Wavelength, Å
	Upper level	Lower level	
Lyman	2	1	1 216
	3	1	1 026
	4	1	970
	5	1	949
	6	1	940
	∞	1	912
Balmer	3	2	6 563
	4	2	4 861
	5	2	4 341
	6	2	4 102
	7	2	3 970
	∞	2	3 650
Paschen	4	3	18 760
	5	3	12 820
	6	3	10 940
	7	3	10 050
	8	3	9 500
	∞	3	8 220

FIGURE 2.—*Energy-level diagram and spectra of the hydrogen atom.*

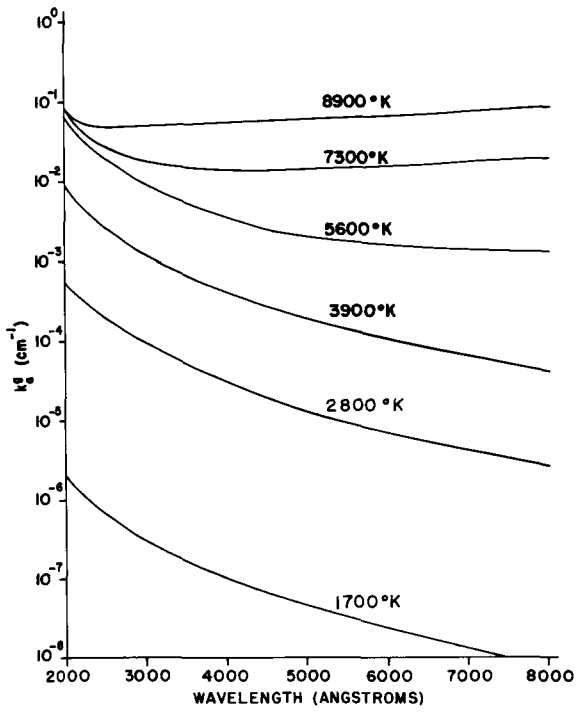

FIGURE 3.—*Absorption coefficient of hydrogen at 100-atm pressure.*

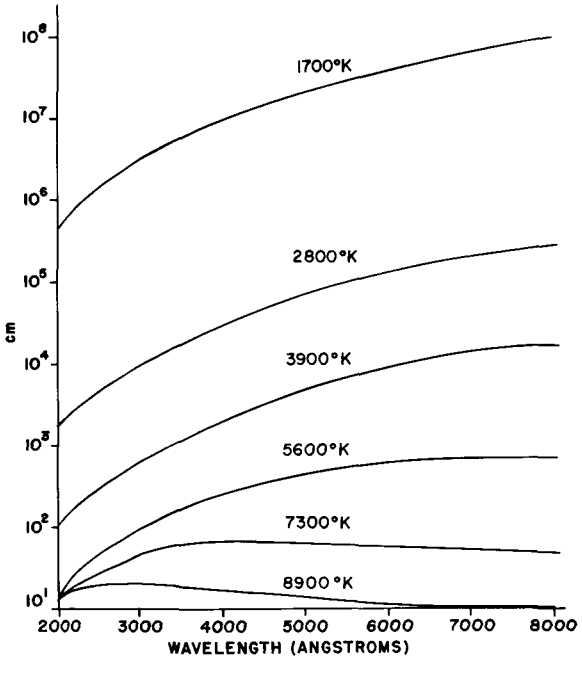

FIGURE 4.—*Distance over which radiant energy attenuated by* e *in hydrogen at 100-atm pressure.*

absorptivity of hydrogen in the wavelength range from 2000 to 8000 Å.

The absorption coefficient $k_a{}^g(\lambda)$ of hydrogen at 100-atm pressure from 2000 to 8000 Å is presented in figure 3 to illustrate the effect of temperature. This effect can be more readily understood by examining figure 4 which presents the reciprocal of the absorption coefficient, which is equal to the distance over which the radiant energy is attenuated by a factor of e in hydrogen at 100-atm pressure. It is seen that, at temperatures above about 7000° K, most of the energy would be absorbed in 1 m of hydrogen over the whole wavelength range of interest. Since the hydrogen opacity is roughly proportional to pressure, most of the energy would be absorbed over a 1-m distance at 5500° K and 500-atm pressure.

Whereas gases tend to absorb in lines and bands, the absorption and scattering characteristics of particle clouds vary only gradually with the wavelength of the incident radiant energy. Thus, $\mu_a(\lambda)$ and $\mu_s(\lambda)$ are smoothly varying functions of wavelength. Scattering enhances energy absorption in particle clouds by increasing the average path length traversed by the radiant energy. However, in any given unit volume of aerosol, the particle-gas mixture is heated only by absorption, not by scattering. For this reason it is convenient to define the absorption coefficient of the aerosol $k_a(\lambda)$ by

$$k_a(\lambda) = k_a{}^g(\lambda) + k_a{}^p(\lambda) = k_a{}^g(\lambda) + \rho\mu_a(\lambda) \tag{5}$$

Then the scattering coefficient for the aerosol is equal to the scattering coefficient of the particles alone, since scattering by the gas is negligible:

$$k_s(\lambda) = k_s{}^p(\lambda) = \rho\mu_s(\lambda) \tag{6}$$

The effect of scattering depends not only on the value of $\mu_s(\lambda)$ but also on the angular dependence of the scattered energy. Scattering from small particles is usually highly anisotropic.

A rigorous solution to Maxwell's equations for the absorption and scattering of radiant energy by homogeneous spherical particles of any composition suspended in a homogeneous nonmagnetic transparent medium was published in 1908 by Gustav Mie (ref. 5) and is now commonly known as the Mie theory. Krascella (ref. 6) applied a transformation procedure developed by Aden (ref. 7) to the Mie equations to calculate the effect of particle size,

wavelength, and particle temperature on particle opacity in those regions of the ultraviolet, visible, and infrared spectra for which complex index-of-refraction data were available. Shenoy (ref. 8) used Krascella's program to extend these calculations to other types of particles and to a broader wavelength range.

Svatos (ref. 9) has recently published a solution to Maxwell's equations for extinction by flattened ellipsoids; however, at present there is no theory to predict accurately the absorption and scattering characteristics of irregularly shaped particles. The Mie theory predicts that $\mu_a(\lambda)$ is a maximum when the particle radius is of the order of the wavelength λ divided by 2π. Thus, for a given particle seed density ρ, the absorption of thermal radiation in the near infrared, visible, and ultraviolet regions of the spectrum is greatest for submicron-sized particles of refractory materials. Such particles are generally highly irregular in shape, so the Mie theory can be used only as an approximation to their absorption and scattering characteristics.

The equation for steady-state thermal radiation transport through a transparent gas seeded with particles may be written

$$\frac{1}{\rho}\frac{dI(\lambda,\Omega)}{ds} = -\mu_e(\lambda)I(\lambda,\Omega) + j(\lambda) + \mu_s(\lambda)\int_0^{4\pi} I(\lambda,\Omega')\,p(\lambda,\cos\theta)\frac{d\Omega'}{4\pi} \tag{7}$$

where

I	intensity of radiant energy in a unit wavelength interval at λ traveling in direction Ω
s	distance
Ω	solid angle
j	emission coefficient
p	scattering amplitude function
θ	angle of scattering

It is seen from this equation that the four important parameters one must know in order to evaluate radiant heat transfer through particle-seeded gases are:

$\mu_e(\lambda)$	extinction parameter
$\mu_s(\lambda)$	scattering parameter
$p(\lambda, \cos\theta)$	scattering amplitude function
$j(\lambda)$	emission coefficient

These parameters must be known over the applicable temperature and wavelength range. In addition, $p(\lambda, \cos\theta)$ must be known for scattering angles of from 0° to 180°.

It is very difficult if not impossible to formulate an exact analytical solution to this integro-differential radiant heat transfer equation. One approach to seeking an approximate solution involves expanding the scattering amplitude function in spherical harmonics (Legendre polynomials). The number of terms required in the expansion depends on the accuracy desired. Another, perhaps more basic, approach is the Monte Carlo technique. This method consists of following photons along probable paths through the cloud until they are either absorbed or leave the cloud. This technique introduces none of the necessary simplifying assumptions or approximations that are required to make an analytical solution possible. As the photon travels through the cloud, it will interact with the particles. At each interaction, the photon will be either absorbed or scattered into a new direction. The basis of the Monte Carlo approach is to assign probabilities to each of these occurrences and then, using a digital computer, to follow photons through the cloud until they either are absorbed or pass out of the cloud. The interactions at each decision point are determined by an appropriate probability distribution function based upon the absorption parameter, the scattering parameter, and the scattering amplitude function.

Photons are emitted from appropriately chosen points in random directions if they are emitted from a volume element, since this type of emission is isotropic. The maximum distance that the photon could travel in this direction is calculated from geometric considerations. The probable path length before interaction is calculated according to the interaction probabilities. If the maximum path length is less than the probable path length, the photon is said to have left the cloud. If the photon is scattered within the cloud, a new direction is calculated according to the scattering amplitude function and the calculations proceed as before until the photon leaves the cloud. When a photon leaves the cloud or is absorbed, a new photon history is initiated. Many such histories are needed in order for good statistical data to be obtained.

It is obvious that the results obtained are highly dependent on how accurately the physical param-

eters, such as the absorption and scattering parameters and the scattering amplitude function, are known. Several approximations of the scattering amplitude function p (λ, cos θ) have been used in heat transfer calculations. The simplest is the assumption of isotropic scattering. However, most data taken to date show that scattering is highly anisotropic.

MIE THEORY RESULTS

The Mie theory is the best known and most useful theory which describes the absorption and scattering of electromagnetic radiant energy by particles. It applies to homogeneous spherical particles of any diameter situated in a homogeneous transparent nonmagnetic medium. Mie solved Maxwell's equation with the appropriate boundary conditions and evaluated the total scattered energy as well as the total energy removed from an incident beam and so arrived at the scattering and extinction cross sections σ_s and σ_e. The absorption cross section of the spherical particle is then $\sigma_a = \sigma_e - \sigma_s$, and the extinction, absorption, and scattering parameters are given by

$$\left.\begin{aligned} \mu_e &= \frac{\sigma_e}{\rho_P V} \\ \mu_a &= \frac{\sigma_a}{\rho_P V} \\ \mu_s &= \frac{\sigma_s}{\rho_P V} \end{aligned}\right\} \qquad (8)$$

where ρ_P is the mass density of the material of which the particle is composed and V is the volume of the spherical particle. Excellent discussions of the derivation of the Mie equations are found in the literature (refs. 10 to 14).

Mie's solution, though derived for a single sphere, also applies to absorption and scattering by any number of spheres, provided that they are all of the same diameter and composition and provided also that they are randomly distributed and separated from each other by distances that are large compared with the particle radius. Under these circumstances there are no coherent phase relationships between the light that is scattered by the different spheres, and the total scattered energy is equal to the energy scattered by one sphere multiplied by their total number. Similarly, for a distribution of sizes, the energy scattered by the spheres of each particular size may be summed to obtain the total scattered energy.

Calculations using the Mie theory require a knowledge of the particle radius, the wavelength of the radiant energy, and the complex index of refraction of the spherical particles. Methods for the direct or indirect determination of N are discussed in the literature (refs. 14 to 18). The real part of the refractive index is believed to vary slowly with temperature, although experimental data at temperatures other than room temperature are quite limited (refs. 17 and 18).

Highly absorbing particles, such as carbon, have been shown to have a scattering parameter about equal to the absorption parameter when the particle diameter is large compared with the wavelength, and one much smaller than the absorption parameter when the particles are small compared with the wavelength. Thus, carbon particles of very small sizes can be considered to be purely absorbing (fig. 5). Other metallic particles generally

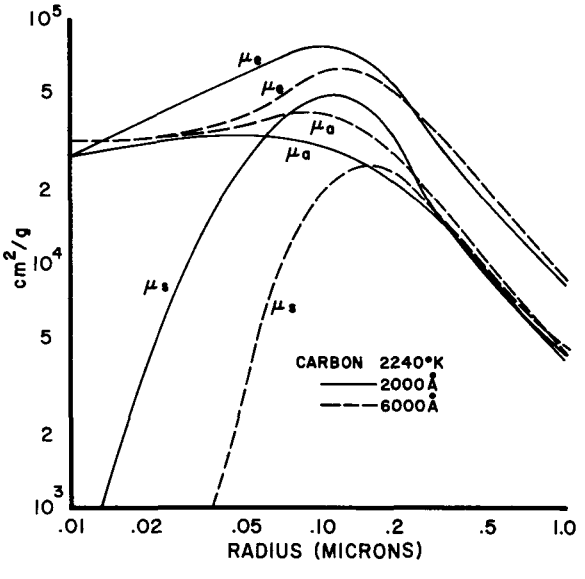

FIGURE 5.—*Extinction, absorption, and scattering parameters of submicron carbon particles calculated using the Mie theory.*

have scattering parameters several times higher than their absorption parameters but are purely absorbing for very small particle sizes (fig. 6). Nonconducting particles, such as magnesium oxide,

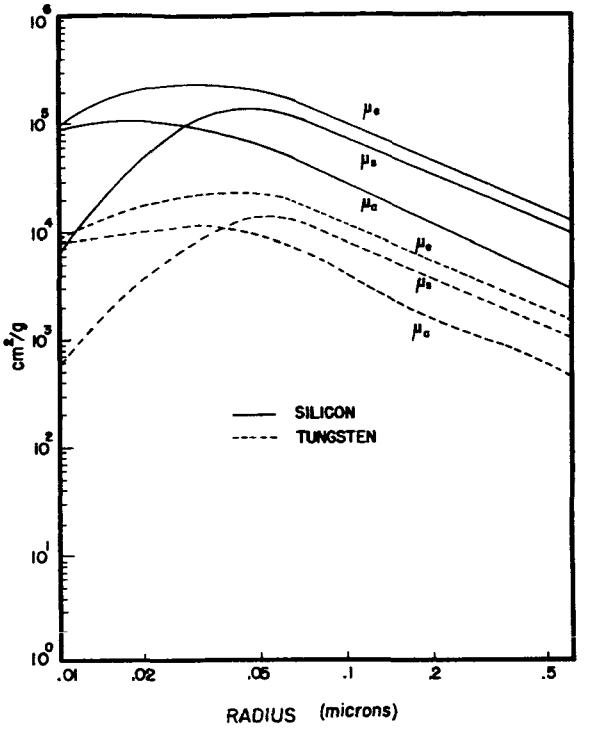

FIGURE 6.—*Extinction, absorption, and scattering parameters of submicron silicon and tungsten particles calculated using the Mie theory. Wavelength, 2400 Å.*

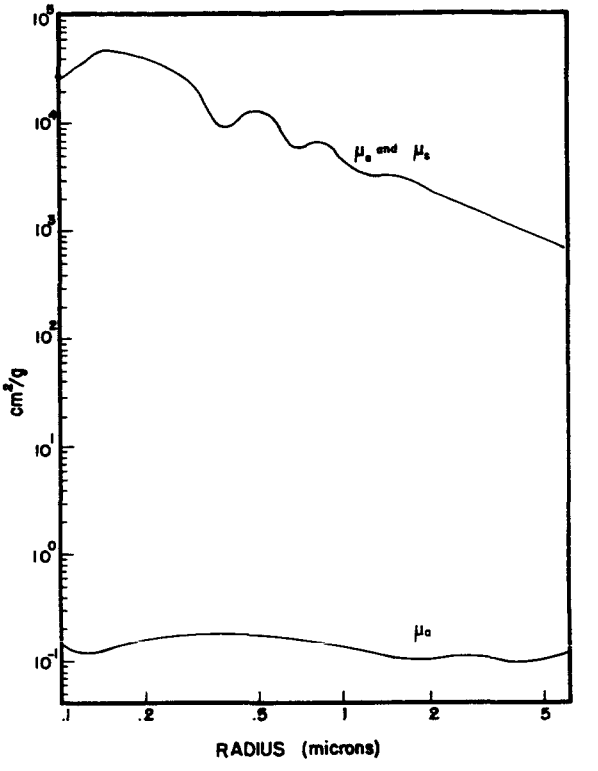

FIGURE 7.—*Extinction, absorption, and scattering parameters of aluminum oxide particles calculated using the Mie theory (data taken from ref. 18). Wavelength, 5000 Å.*

aluminum oxide, or silica, have scattering parameters several orders of magnitude higher than their absorption parameters, so they scatter much more thermal radiation than they absorb (fig. 7). The same is true of liquid droplets such as water droplets in rain clouds. For any type of particle, the extinction parameter is a maximum for particles with diameters of the order of the wavelength divided by π.

Particles which have diameters which are very small compared with the wavelength backscatter as much light as they scatter forward, and such scattering is symmetric about a scattering angle of 90°. This type of scattering is called Rayleigh scattering. As the diameter is increased the scattering becomes more forward. The tendency of larger particles toward more highly forward scattering, when the particle diameters are of the same order of magnitude as the wavelength, is called the Mie effect. Particles which are large compared with the wavelength generally scatter in a very highly forward direction.

The angular scattering characteristics of particle clouds have an important effect on radiant heat transfer through the cloud. Forward-scattering particles are less effective in diffusing radiant energy than are particles which tend to scatter energy at larger angles.

PREVIOUS EXPERIMENTAL RESULTS

Of particular interest for gas-core reactors are submicron-sized particles of refractory metals. Such particles not only are highly absorbing for thermal radiation in the ultraviolet, visible, and near-infrared regions of the spectrum but can also withstand the high temperatures that are often encountered without vaporizing.

Various groups have experimentally investigated the absorption and scattering parameters of gases seeded with refractory particles. Lanzo and Ragsdale (refs. 19 and 20) measured the absorption of thermal radiation by suspended particles as a func-

tion of material, size, and concentration. This experiment involved radiating energy from an electric arc to air that contained submicron-sized refractory particles. Seeded air was introduced into an annular heat exchanger. The arc was initiated and the unseeded air temperature in the annulus reached 556° K. When carbon particles were added to the airstream, they absorbed radiant energy which caused the outlet temperature to increase to 667° K, thus showing that particle-seeded air will absorb radiant energy from the electric arc. McAlister and Orr (refs. 21 and 22) reported theoretical and experimental studies of radiant heat transfer from a heated tungsten cylindrical enclosure to a particle cloud within it. A transparent gas, helium, was passed through the tube and the tube dimensions and helium flow rate were selected to give a low thermal efficiency for forced convection heating. The addition of tungsten or carbon particles to render the gas opaque caused a significant increase in heat absorption.

Marteney (ref. 23) studied techniques of producing dispersions of submicron-sized solid particles in a carrier gas and investigated the optical parameters of these particles for several wavelengths. Tests were conducted with carbon and tungsten particles having nominal radii of 0.0045 and 0.01 μ dispersed in helium and nitrogen. These studies showed that the application of aerodynamic shear forces to a carbon aerosol resulted in an increase by a factor of 5 in the absorption parameter. This increase is believed to be caused by a reduction in the size of particle agglomerates, since theoretically a decrease in the average agglomerate size should result in an increase in the value of the extinction parameter.

The first experimental work involving particle-seeded gases at high temperatures was reported by Burkig (ref. 24). In this experiment, a cloud of particles in a gas was injected into a transparent quartz tube and exposed to a flash of a xenon flash tube. The temperature rise of the gas was inferred from the pressure rise measured with a fast-response pressure transducer. The bulk of the work was with micron-sized particles of carbon, iron, and tantalum carbide. In general, initial pressures of 2 and 5 atm were investigated for both helium and hydrogen. During the flash, as indicated by the pressure transducer, the temperature of the carbon aerosol rose to about 2500° K or more for about 1 msec. Williams and Shenoy (ref. 25) measured the extinction parameters of submicron-sized particles of carbon, tungsten, and silicon at various temperatures up to 2200° K for a wavelength range of 1600 to 6000 Å (figs. 8 to 11). Their experimental values showed

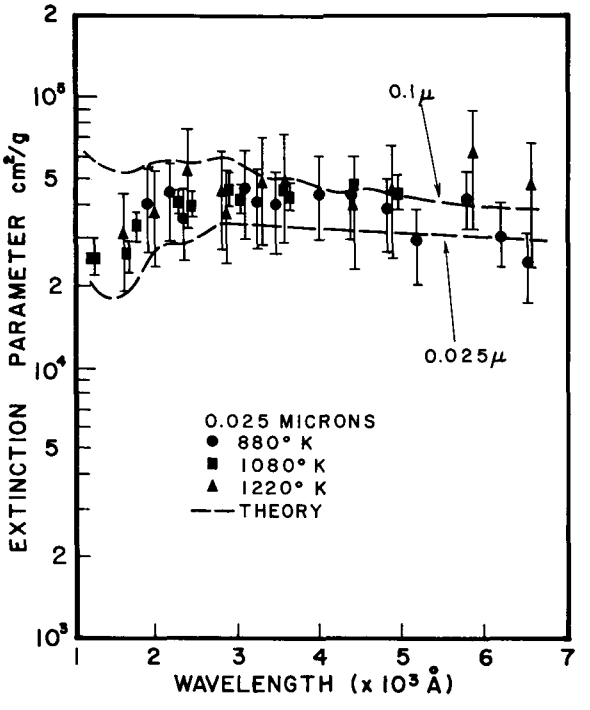

FIGURE 8.—*Extinction parameter of submicron carbon (spheron 6) particles at 1-atm pressure.*

good agreement with the Mie theory at those temperatures and wavelengths for which the availability of complex refractive index data made Mie calculations possible.

The extinction parameter is one of the essential parameters for heat transfer design studies of the gas-core nuclear rocket. Measurements of the extinction parameters of different seed materials in hydrogen and knowledge of the scattering parameter μ_s permit μ_a, the absorption parameter, to be calculated. The extinction parameter for a particular seed material is a function of temperature, wavelength, and particle size distribution. It is sometimes necessary to include pressure as a parameter in order to observe the effect of chemical reactions and of pressure on the breakup and recoagulation of particle agglomerates.

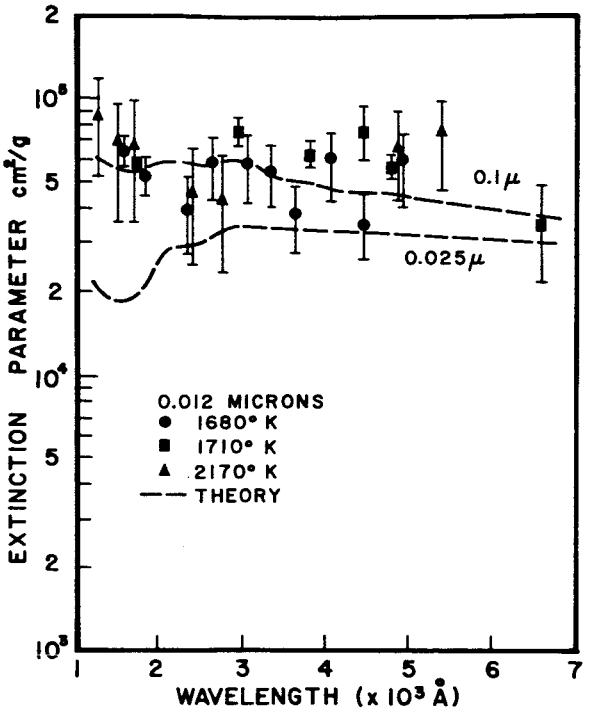

FIGURE 9.—*Extinction parameter of submicron carbon (carbolac 2) particles at 1-atm pressure.*

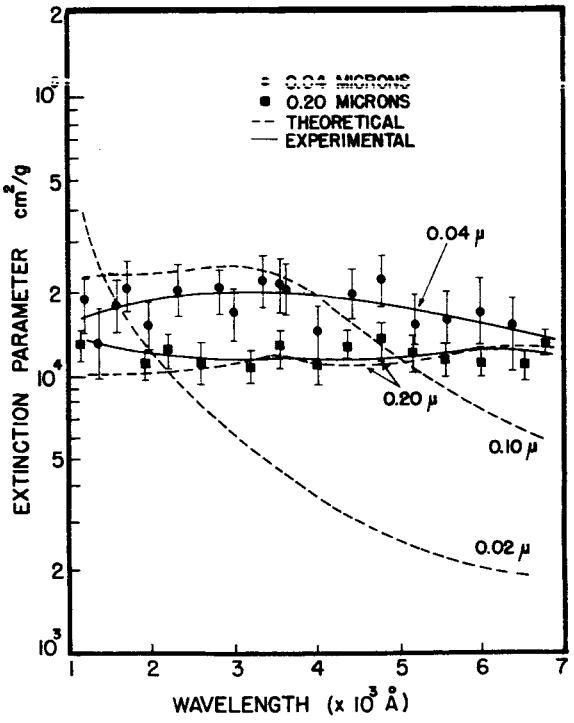

FIGURE 10.—*Extinction parameter of submicron tungsten particles at 1-atm pressure and 300° K.*

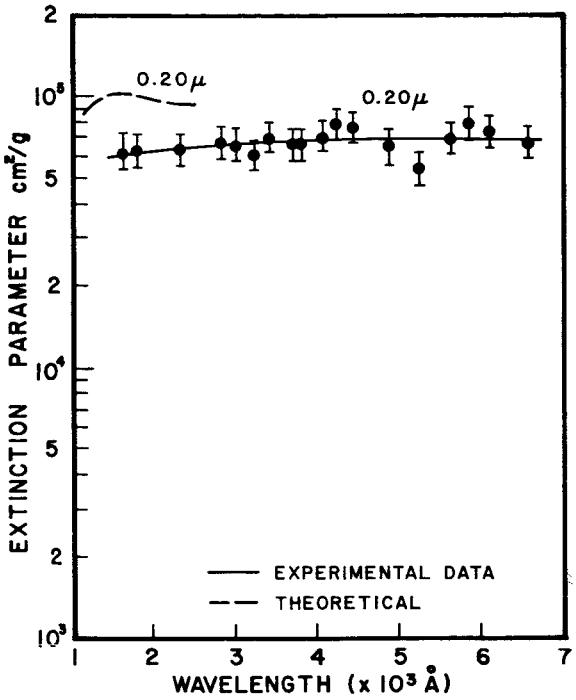

FIGURE 11.—*Extinction parameter of 0.20 μ silicon particles at 1-atm pressure and 300° K.*

The seed materials which have been investigated at the Georgia Institute of Technology are carbon, silicon, tungsten, silicon carbide, and tungsten carbide. It is desirable that potential seed materials have a high absorption parameter, high vaporization point, low reaction rate with hydrogen, and a low neutron absorption cross section.

One significant aspect of the previous work by Williams et al. (ref. 25) was the observation of chemical reactions and their effect on the extinction parameter being measured. Figure 12 shows the percentage reduction in carbon aerosol density as a function of furnace temperature corrected for the thermal expansion of the hydrogen. This was the first indication of chemical reactions in the carbon-hydrogen aerosol. The significance of this observation is the low temperature (900° K) at which the reaction became important, since reaction rate data from large chunks of carbon indicated hydrogen-carbon reaction would not become important until a temperature of the order of 2000° K is reached. The gas-core nuclear rocket will have a propellant temperature on the order of 1000° K at the entrance point and one on the order of 8000° K at the exit

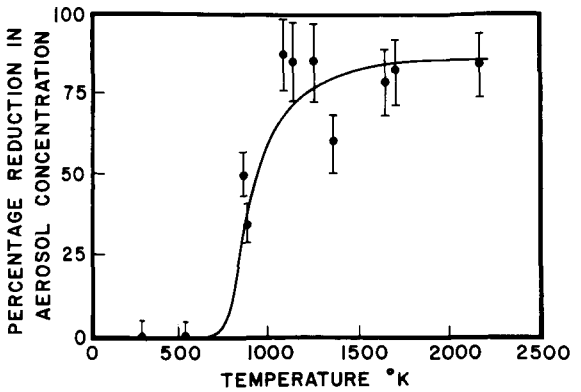

FIGURE 12.—*Percentage reduction in aerosol concentration due to heating.*

at a pressure of 100 to 1000 atm. Thus, since seed-hydrogen chemical reactions are highly pressure dependent, measurements of the extinction parameter as a function of pressure as well as of temperature and wavelength are needed for designing the rocket engine.

PROCEDURE FOR HIGH-PRESSURE MEASUREMENTS

If $I(\Omega)$ is the intensity of the radiant heat flux in direction Ω at a given point in a particle cloud dispersed in a transparent gas, then the energy absorbed and scattered in a unit volume of aerosol at that point is $k_T I(\Omega)$. The extinction parameter is then given by

$$\mu_e = \frac{k_T}{\rho}$$

Thus, if μ_e is known for a particular particle seed material dispersed in a transparent gas, then k_T may be found for any particle seed density ρ. The attenuation coefficient may be measured directly by passing a beam of radiant energy of a particular wavelength through a cloud of particles and measuring the intensity transmitted. If I_o is the intensity of the beam entering the cloud and I is the intensity of the beam transmitted through a distance x of the cloud, then the decrease in the beam intensity is given by

$$I/I_o = e^{-k_T x}$$

so

$$k_T = \frac{1}{x} \ln \frac{I_o}{I}$$

If the particle density ρ is measured simultaneously with k_T, then μ_e is given by

$$\mu_e = \frac{k_T}{\rho}$$

A beam of broad spectrum radiant energy was passed through high-pressure, high-temperature hydrogen and into a spectrometer which utilized a photomultiplier tube to measure the intensity of the diffracted light from a motor-driven diffraction grating. A second photomultiplier tube was used to measure the intensity of the total transmitted beam in order to monitor variations in the aerosol density or light-source intensity. A tungsten-rhenium thermocouple was placed in the hydrogen flow channel at the point where the radiant energy beam penetrates for temperature measurements. A sample of the aerosol was drawn before it entered the furnace and another sample of the heated aerosol was simultaneously drawn. From these two samples a comparison of the particle seed density before and after heating was made. The seed density of the sample drawn from the heated aerosol was used to calculate the extinction parameter from the attenuation coefficient.

Figure 13 shows the light source, the furnace, and the spectrometer assembly. Photomultiplier 1 recorded the diffracted light while photomultiplier 2 monitored the total beam intensity. The diffraction grating was driven by a synchronous motor which allowed a correlation of chart speed and wavelength on the oscillograph. This oscillograph recorded the amplified signals from the photomultipliers.

Figure 14 is a rendering of the high-pressure furnace which was designed to heat a flow of hydrogen to about 2800° K at 100-atm pressure. At the bottom of the furnace, one of the water-cooled copper bus bars is shown. The power to the furnace is provided by a 0- to 20-kW dc power supply. The hydrogen aerosol enters at the bottom of the furnace and passes into the boron nitride heating chamber which has a $\frac{5}{8}$-in. i.d. and is 16 in. long. The boron nitride heating chamber contains a strip of tungsten bent over a $\frac{1}{8}$-in. strip of boron nitride. The tungsten strip is nominally 28 in. long, $\frac{1}{2}$ in. wide, and 35 mils thick. Just above the top of the tungsten filament is located a tungsten-tungsten rhenium thermocouple. A tungsten sampling tube at the top of the heating chamber allows

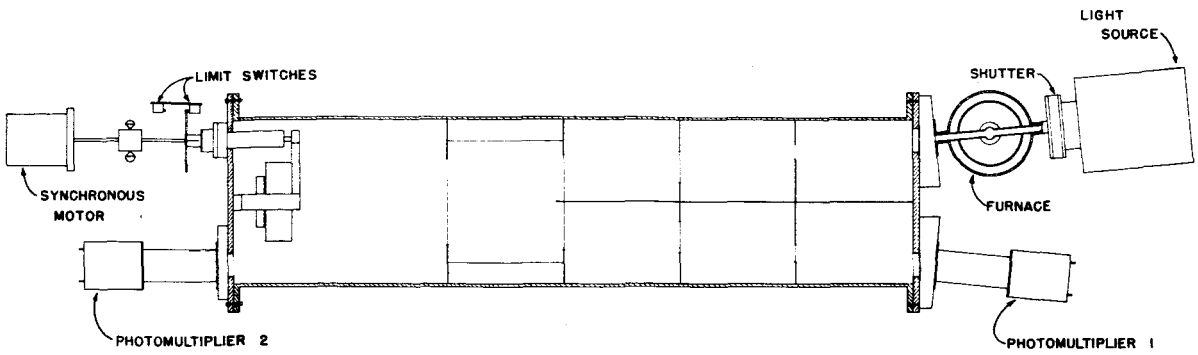

FIGURE 13.—*Arrangement of light source, furnace, and spectrometer.*

representative samples of the aerosol and aerosol reaction products to be withdrawn. Hydrogen is flowed through the sight ports to prevent seed material from entering them. This purge flow is a small percentage of the total flow. The boron nitride heating chamber is insulated with carbon felt. There are three cooling systems, one for the water flow through the two bus bars, the second for the main cooling coil which is adjacent to the inner pressure chamber wall, and the third for the extension to the upper end plate of the furnace which cools the aerosol as it passes out of the furnace. After the gas leaves the furnace it passes through a seed filter where the seed material is removed. A back-pressure regulator maintains a set pressure in the furnace independent of the flow rate through the furnace. The effluent is then exhausted to the atmosphere.

Well-dispersed aerosols are difficult to obtain with low hydrodgen flow rates (approximately 1 ft^3/min at standard temperature and pressure). A high-speed food blender has been adapted for use in a pressure chamber and produces satisfactory aerosols of carbon, silicon carbide, and silicon. A vibrating chamber with a dispersion nozzle was used to generate a tungsten aerosol.

An electrostatic aerosol sampling apparatus (fig. 15) was used to collect representative samples of particles on electron-microscope grids. The effect of temperature on the particle size distribution was studied using the resulting electron micrographs and no observable effect was seen. Thus, in the case of carbon, it is believed that some of the particles (perhaps those closer to the heating element) reacted with hydrogen whereas other slightly cooler particles remained. Apparently the resulting methane sufficiently retarded the reaction rate so that some carbon particles remained in the aerosol at temperatures as high as 1920° K.

RESULTS OF MEASUREMENTS AT 12 ATM

Measurements of the extinction parameter for 0.2-μ tungsten particles are presented in figures 16 to 18. A nominal value at room temperature and 12.5 atm is about 20 000 cm^2/g. The theoretical values of the extinction parameter for 0.2-, 0.1-, and 0.02-μ diam spherical particles are plotted for comparison. The magnitude of the extinction parameter increases with temperature and increases most rapidly at the shorter wavelengths. This may be the effect of thermal agitation on the aerosol. As agglomerates are broken up into smaller particles the Mie theory would predict a larger extinction parameter at the shorter wavelengths. The tungsten seed material was obtained as 0.2-μ-diam particles, but electron microscopy showed this to be an upper limit on the size of the particle with the average diameter much less. Values of the extinction parameter larger than those predicted by theory are not unreasonable since the theory assumes spherical particles, and electron micrographs show the particles to be quite irregular in shape and to have a corresponding larger surface area.

Figure 19 presents measured values of the extinction parameter for tungsten carbide at 11.9 atm and at 1650° K. The nominal value is 50 000 cm^2/g. Electron micrographs indicate that the average particle size is slightly less than 1 μ.

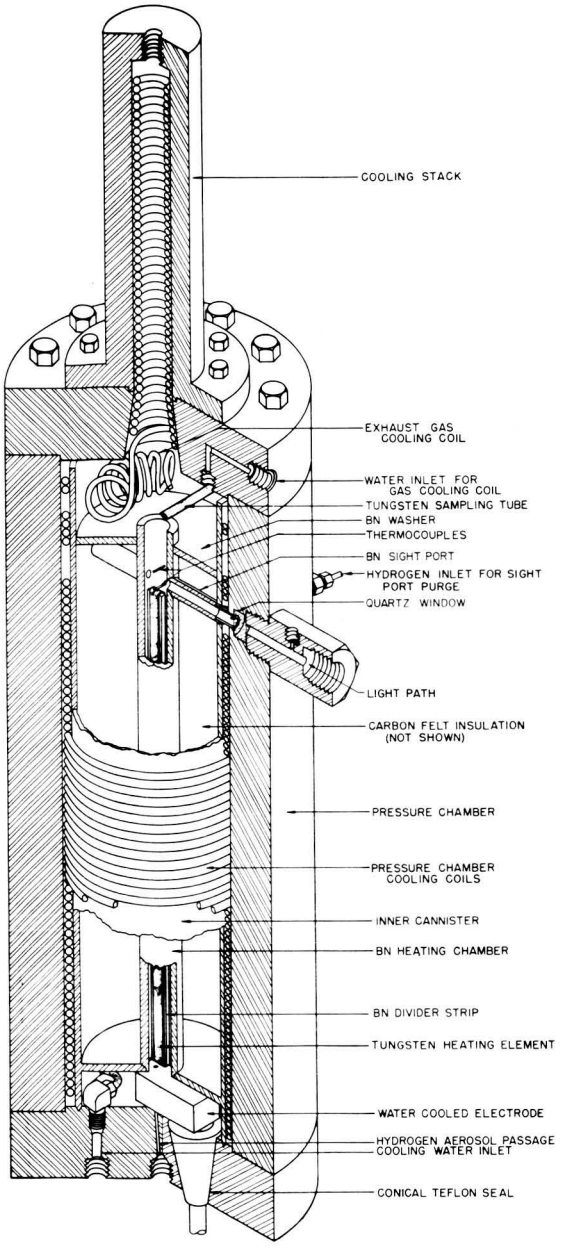

FIGURE 14.—*High-pressure furnace.*

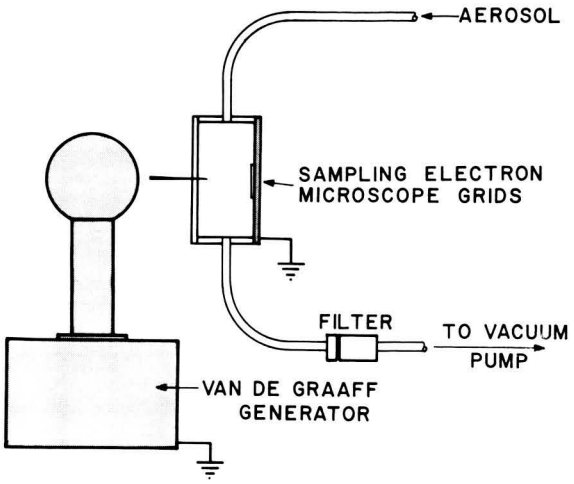

FIGURE 15.—*Electrostatic aerosol sampling apparatus.*

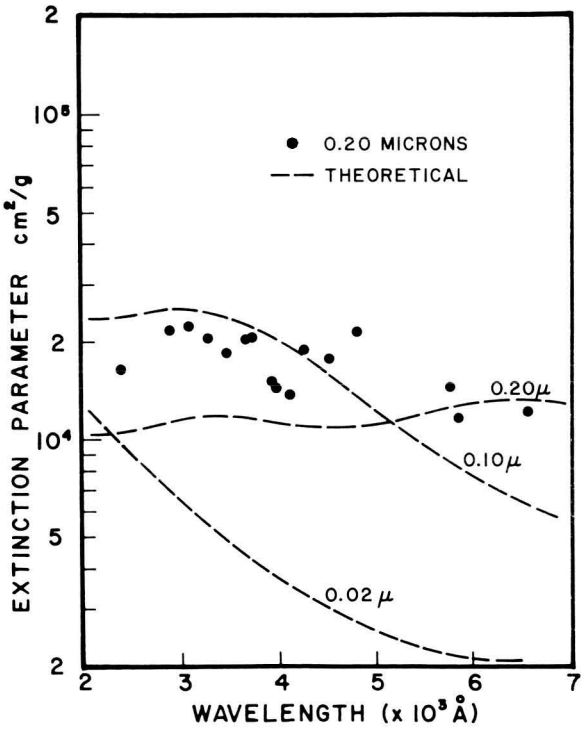

FIGURE 16.—*Extinction parameter of tungsten particles in hydrogen at 730° K and 12.5 atm.*

Attempts to measure the extinction parameter of silicon were unsuccessful at higher temperatures and pressures. The nominal value for the extinction parameter of silicon at room temperature is 65 000 cm^2/g.

Further measurements of the extinction parameter for carbon, silicon, silicon carbide, tungsten, and tungsten carbide are being made at higher temperatures and higher pressures to provide a range of data that will be useful in design studies of the gas-core nuclear rocket concept.

The scattering amplitude function and extinction parameter of μ-sized aluminum oxide particles was reported by T. J. Love (ref. 26) for wavelengths

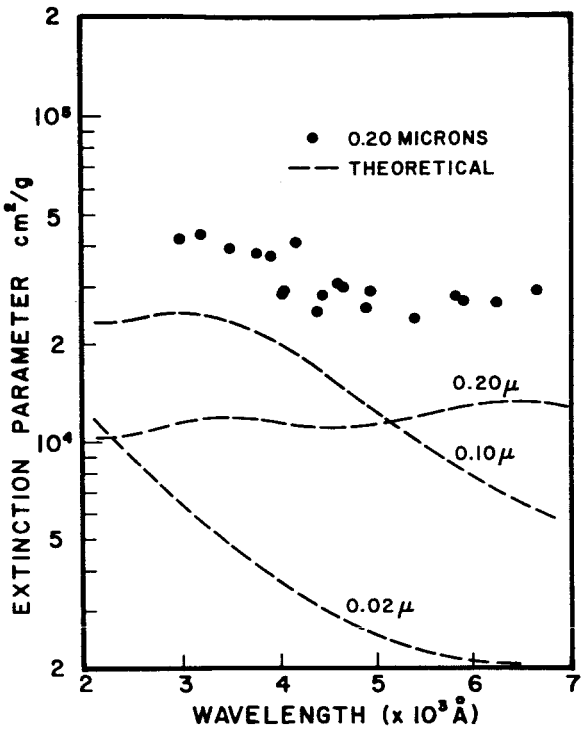

FIGURE 17.—*Extinction parameter of tungsten particles in hydrogen at 1240° K and 12.5 atm.*

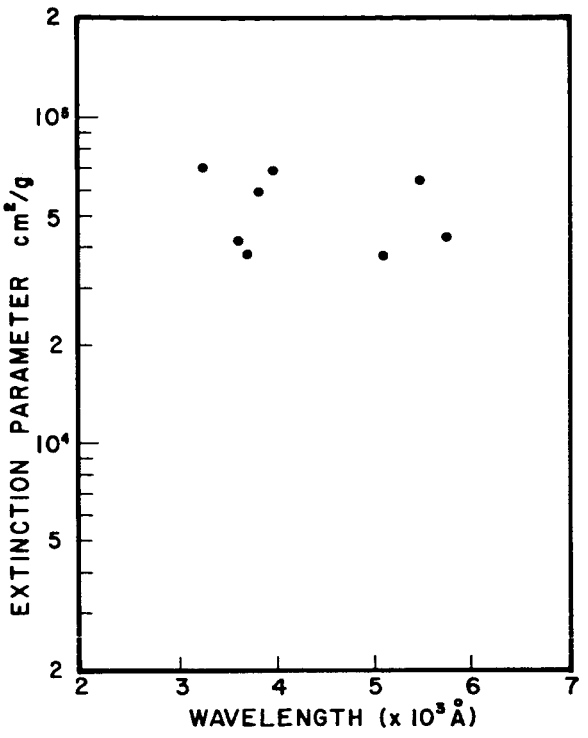

FIGURE 19.—*Extinction parameter of 1-μ tungsten carbide particles in hydrogen at 1650° K and 11.9 atm.*

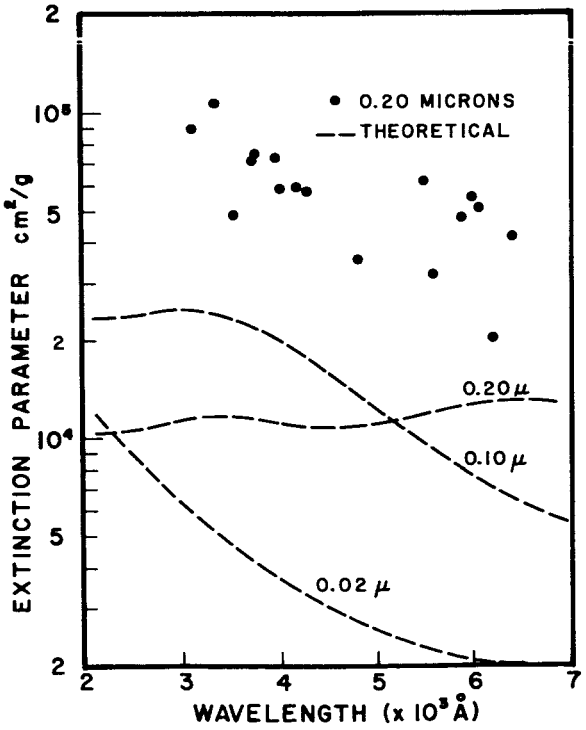

FIGURE 18.—*Extinction parameter of tungsten particles in hydrogen at 1770° K and 12.5 atm.*

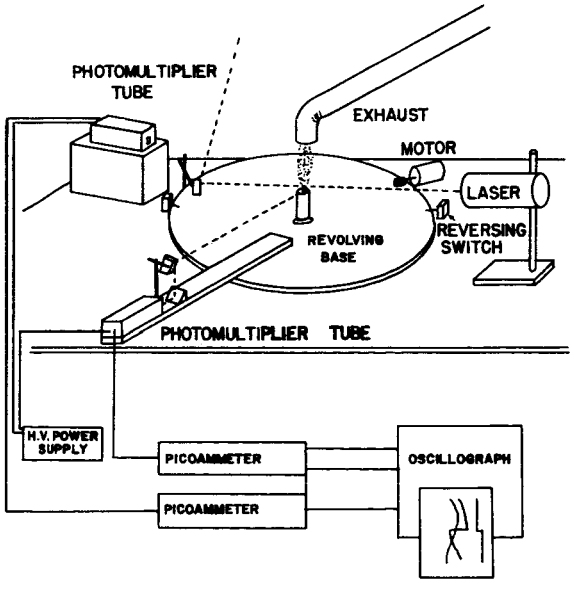

FIGURE 20.—*Appartus for measuring scattering amplitude function.*

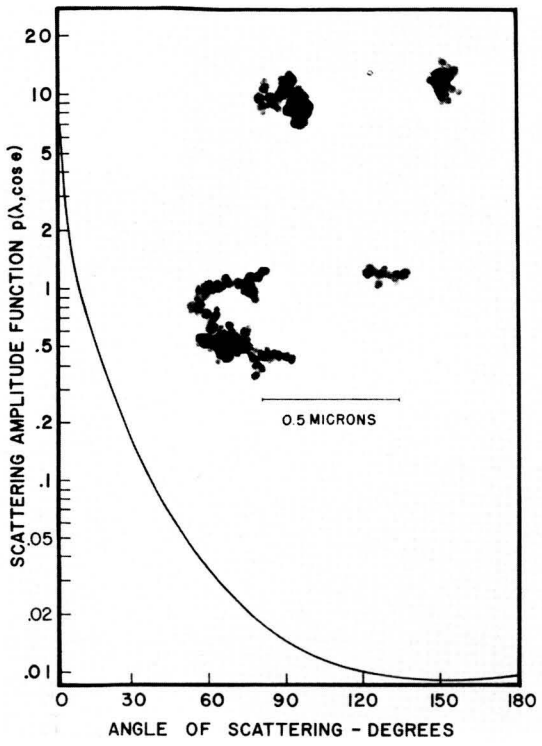

FIGURE 21.—*Scattering amplitude function of submicron-sized carbon particles. Wavelength, 6328 Å.*

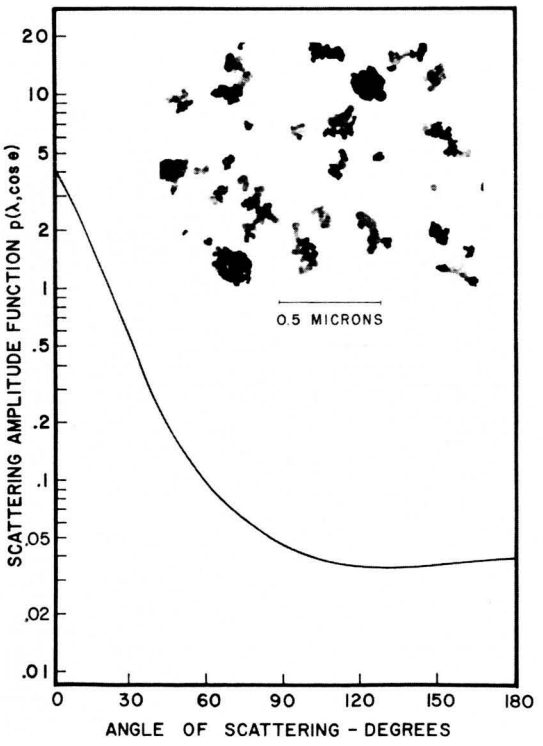

FIGURE 22.—*Scattering amplitude function of submicron-sized tungsten particles. Wavelength, 6328 Å.*

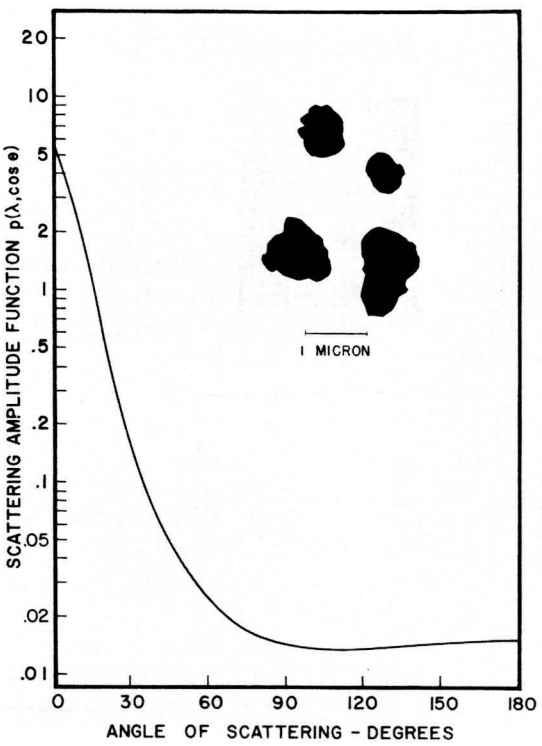

FIGURE 23.—*Scattering amplitude function of submicron-sized tungsten carbide particles. Wavelength, 6328 Å.*

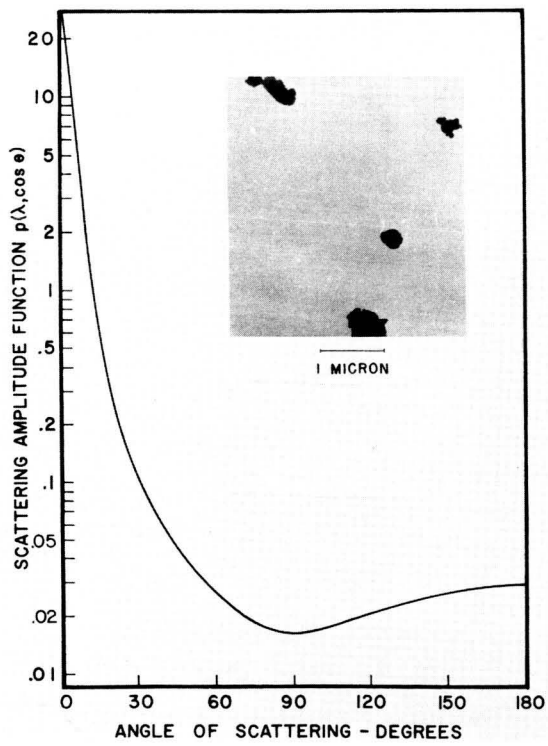

FIGURE 24.—*Scattering amplitude function of submicron-sized silicon particles. Wavelength, 6328 Å.*

in the infrared region between 4 and 16 μ. Marteney (ref. 23) showed that light scattering from submicron-sized carbon and tungsten particles is highly forward. Williams (ref. 27) measured the intensity of He-Ne laser light scattered from submicron-sized particles of tungsten, carbon, silicon, tungsten carbide, and silicon carbide over a 30° angle and demonstrated the forward nature of the scattering.

Measurements of the scattering amplitude function of these particle materials for scattering angles from 1° to 179° were made using the equipment illustrated by figure 20. A helium-neon laser beam was passed through the aerosol as it issued from a ½-in-diam tube. The intensity of the scattered light was recorded as a function of angle using a photomultiplier detector mounted on the circular base. A second photomultiplier tube monitored changes in the aerosol concentration by observing the intensity of light scattered by the optically thin aerosol at a fixed angle. These data were used to correct for fluctuations in the total scattered intensity as the scattering amplitude function was being measured. The results of these measurements are presented in figures 21 to 25. The same seed materials which had been used for extinction measurements were used for these scattering investigations.

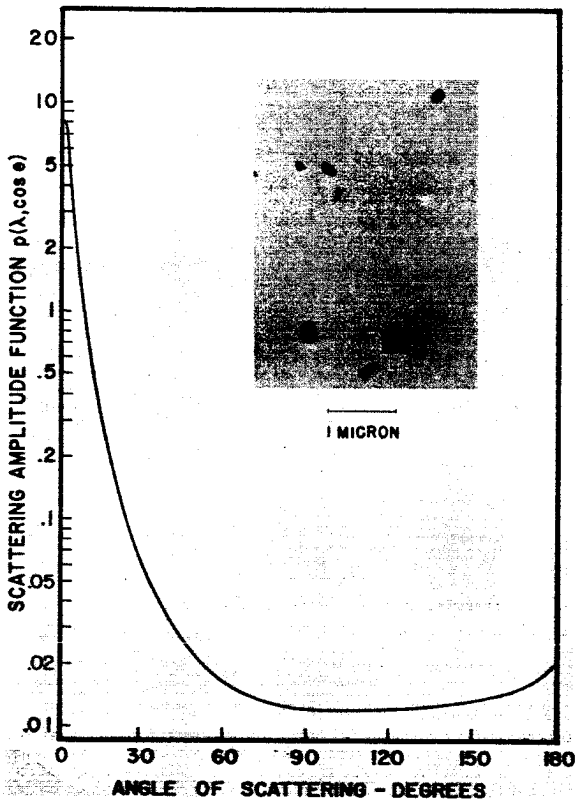

FIGURE 25.—*Scattering amplitude function of submicron-sized silicon carbide particles. Wavelength, 6328 Å.*

REFERENCES

1. RANDOL, A. G., III: Determination of High Pressure, High Temperature Uranium Plasma Properties. Ph.D. thesis, Univ. of Fla., Aug. 1969.
2. MARTENEY, P. J.; MENSING, A. E.; AND KRASCELLA, N. L.: Experimental Investigation of the Spectral Emission Characteristics of Argon-Tungsten and Argon Uranium Induction Heated Plasmas. Rept. G-910092-11, United Aircraft Res. Lab., Sept. 1968.
3. KRASCELLA, N. L.: Tables of the Composition, Opacity, and Thermodynamic Properties of Hydrogen at High Temperatures. NASA SP-3005, 1963.
4. PATCH, R. W.: Components of a Hydrogen Plasma Including Minor Species. NASA TN D-4993, 1969.
5. MIE, G. A.: Beitrage zur Optik truber Medien, Speziell Kolloidaler Metallosungen. Ann. Physik, vol. 25, 1908, p. 377.
6. KRASCELLA, N. L.: Theoretical Investigations of the Absorption and Scattering Characteristics of Small Particles. Rept. C-910092-1, United Aircraft Res. Lab., Sept. 1964.
7. ADEN, A. L.: Electromagnetic Scattering From Spheres With Sizes Comparable to the Wavelength. J. Appl. Phys., vol. 22, no. 5, 1951, pp. 601–605.
8. SHENOY, A. S.: The Attenuation of Radiant Energy in Hot Seeded Hydrogen. Ph.D. thesis, Ga. Inst. Tech., June 1969.
9. SVATOS, J.: Light Scattering by Flattened Ellipsoids. Astron. Inst. of Czech. Bull., vol. 18, no. 2, 1967, pp. 114–119.
10. VAN DE HULST, H. C.: Light Scattering by Small Particles. John Wiley & Sons, Inc., 1957.
11. STRATTON, J. A.: Electromagnetic Theory. McGraw-Hill Book Co., Inc., 1941.
12. PLASS, G. N.: Mie Scattering and Absorption Cross Sections for Absorbing Particles. Appl. Opt., vol. 5, no. 2, Feb. 1966, p. 279.
13. KATTANAR, G. W.; AND PLASS, G. N.: Electromagnetic Scattering from Absorbing Spheres. Appl. Opt., vol. 6, no. 8, Aug. 1967, p. 1377.
14. BORN, M.; AND WOLF, E.: Principles of Optics. Second ed., Macmillan Co. (New York, N.Y.), 1964.
15. ROBERTS, S.: Optical Properties of Nickel and Tungsten and Their Interpretation According to Drudis Formula. Phys. Rev., vol. 114, no. 1, 1959, pp. 104–115.
16. STULL, V. R.; AND PLASS, G. N.: Emissivity of Dispersed Carbon Particles. J. Opt. Soc. Am., vol. 50, no. 2, 1960.
17. PLASS, G. N.: Mie Scattering and Absorption Cross

Sections for Aluminum Oxide and Magnesium Oxide. Appl. Opt., vol. 3, no. 7, 1964, p. 867.

18. PLASS, G. N.: Temperature Dependence of the Mie Scattering and Absorption Cross Sections for Aluminum Oxide. Appl. Opt., vol. 4, no. 10, Dec. 1965, p. 1616.
19. LANZO, C. D.; AND RAGSDALE, R. G.: Experimental Determination of Spectral and Total Transmissivities of Clouds of Small Particles. NASA TN D–1405, 1962.
20. LANZO, C. D.; AND RAGSDALE, R. G.: Proceedings of the 1964 Heat Transfer Fluid Mechanics Institute. Stanford Univ. Press, 1964.
21. MCALISTER, J. A.; KOCSIS, D.; AND ORR, C.: Heat Transfer to a Gas Containing a Cloud of Particles. Semiann. Status Rept. no. 8, Proj. A–635–002, Elect. Eng. School, Ga. Inst. Tech., June 1966.
22. KENG, E.; AND ORR, C.: Investigation of Radiant Heat Transfer to Particle-Seeded Gases for Application to Nuclear Rocket Engine Design. NASA CR–953, 1967.
23. MARTENEY, P. J.: Experimental Investigation of the Opacity of Small Particles. Rept. C–910092–2, United Aircraft Res. Lab., Sept. 1964.
24. BURKIG, V. C.: Theoretical Absorption in Seeded Gases. Rept. DAC–59985, Douglas Aircraft Co., Jan. 1967.
25. WILLIAMS, J. R.; CLEMENT, J. D.; SHENOY, A. S.; PARTAIN, W. L.; AND JACOBS, W. R.: The Attenuation of Radiant Energy in Hot Seeded Hydrogen—An Experimental Study Related to the Gaseous Core Nuclear Rocket. Status Rept. No. 3, Proj. A–1045, Ga. Inst. Tech., May 1969.
26. LOVE, T. J.: An Experimental Investigation of Infra-Red Scattering by Clouds of Particles. Rept. ARL–64–109, Aerospace Res. Lab., June 1964.
27. WILLIAMS, J. R.: Thermal Radiation Transport in Particle-Seeded Gases. ANS Trans., Dec. 1969, p. 12.

Radiation Transport in a Uranium Plasma Reactor With Reflecting Walls

S. KELM AND W. PESCHKA

Deutsche Forschungs- und Versuchsanstalt für Luft- und Raumfahrt e.V.
Stuttgart, Germany

Two applications of the uranium plasma reactor or the gas-core reactor are possible. First, the plasma reactor can serve as a propulsion system. In this case, a hydrogen plasma beam of more than 10 000° K leaves the plasma reactor through a nozzle with a high velocity (refs. 1 and 2). Second, the plasma reactor can be used for magnetoplasmadynamic (MPD) energy converters (refs. 3 and 4). Thus, a plasma beam of the same high temperature leaves the plasma reactor through the nozzle and flows through the channel of an inductive electrodeless MPD converter in which the kinetic energy of the plasma beam is converted into electric energy. A high electrical conductivity of the flowing plasma of the order of 5000 mho/m is required for this type of MPD converter. This requirement is fulfilled here, since the plasma leaving the reactor has a high enough temperature so that the electrical conductivity is of this order. For MHD applications it is not so important that the exiting plasma beam has the lowest possible percentage of uranium because a closed cycle can be built and the uranium regained.

In the present paper the temperature distribution and the radiation flux is determined for the plasma region of a plasma reactor which is appropriate for MPD energy conversion. The pressure of the uranium plasma will be of the order of 50 atm. Therefore, the diameter of the fuel plasma zone should attain 1 m because the reactor must become critical.

The plasma reactor investigated here uses liquid lithium flowing along the inner walls of the reactor in the axial or azimuthal direction. The flowing liquid lithium acts as a mirror so that the total radiation flux near the plasma boundary is reduced considerably. Liquid lithium reflects more than 90 percent of the optical radiation from about 2500 Å to the far-infrared region of the spectrum. Therefore, the optical radiation of the plasma does not damage the inner solid walls of the reactor.

The liquid lithium absorbs 10 percent of the optical radiation and therefore a part of it can be vaporized. Before it leaves the reactor by the nozzle it is ionized, so that a highly ionized, lithium plasma of high electrical conductivity flows through the MHD channel. Only pure lithium of at. wt 7 can be used in the reactor since the common lithium has a certain percentage of lithium of at. wt 6, which would absorb too many neutrons.

The calculation of the radiation flux at the boundary of the plasma is difficult because the radiation field becomes maximally anisotropic there, whereas the anisotropy of the radiation field is not so high in the inner core of the plasma. If the exact solution of the radiation flux is used for the determination of the plasma temperature distribution, then the numerical calculation by means of the computer takes too long a time. The exact solution could be used only for simpler cases and for simple expressions of the spectral absorption coefficient (ref. 3). An approximation of the radiation flux in the case of an optically thick plasma was developed which can also be applied near the plasma boundary, since it includes the effect of extreme anisotropy there. As a result, the temperature distribution near the walls can be calculated. An approximation of the radiation flux for the determination of the temperature distribution was also used in the case of reflecting walls at the plasma boundary. In this approxi-

mation the anisotropy near the boundary is also considered, although this effect is not so large in the case of reflecting walls.

ABSORPTION COEFFICIENT OF URANIUM

For the calculation of the radiation flux it is necessary to know the absorption coefficient of the uranium plasma for all transitions. Assumptions are made for the absorption coefficients and for the oscillator strength per unit energy, as was done similarly by Krascella (ref. 5). The effect of the lowering of the ionization energy was also included in the evaluation of the absorption coefficient because this effect is very high with a high-pressure plasma.

Since only a very small number of measurements concerning the continuous absorption coefficient of uranium exist, one can use only theoretical values for hydrogenlike atoms and ions as an approximation. The absorption coefficient for a transition from a bound discrete level to a continuous free state is given by Unsöld (ref. 6):

$$\kappa_{\nu n}=n_n\frac{\pi e^2 h}{m_e c}\frac{df}{dE}e^{\Delta E_F/kT} \tag{1}$$

Here n_n denotes the particle density in the discrete state n; n is the effective quantum number defined here by $n^2=E_i/E_n$, where E_i is the ionization energy of the uranium atom and E_n is the energy of the state n calculated from the ionization limit. The effective quantum number is usually defined by $n_{\mathrm{eff}}{}^2=E_{i\mathrm{H}}/E_n$, where $E_{i\mathrm{H}}$ is the ionization energy of the hydrogen atom, but here the other definition is used because the evaluation of the absorption coefficient becomes clearer in this case. The value given by Ecker and Kröll (ref. 7) was applied for ΔE_F, which denotes the lowering of the ionization energy which occurs in the Saha equation. Also, df/dE denotes the oscillator strength per unit energy and is proportional to the transition probability between the discrete state n and the continuous state having the width $\Delta E=1$. For the absorption coefficient of spectral lines this equation of the absorption coefficient is also valid, because the uranium atom has a large number of discrete states which can be treated as a continuous state in a first approximation.

The evaluation of the absorption coefficient is shown here only for the uranium atom. The calculation of the absorption coefficient of the single or double ionized uranium can be performed by the same procedure as that given here.

The particle density of the state n is given by the equation

$$n_n=\frac{g_n}{2Z^{(1)}}\frac{n_i n_e\, e^{-\Delta E_F/kT}}{2.414\times10^{15}\,T^{3/2}}e^{E_n/kT} \tag{2}$$

where g_n is the statistical weight of the state n, $Z^{(1)}$ is the sum over the states of the uranium ion, n_i is the density of the uranium ions, n_e is the electron density, and $E_n=E_i/n^2$. When equation (2) is introduced into equation (1) the lowering ΔE_F of the ionization energy in the exponents is canceled. Only the particle densities n_i and n_e depend on the lowering ΔE_F, because the particle densities $n_i=n_e$ can be replaced by a function which depends on the total plasma pressure and on the Saha equation. The Saha equation depends on the real ionization potential which corresponds to the theoretical value of 6eV less the lowering ΔE_F.

A mean statistical weight g for each energy level of the uranium ion and, also, a mean distance between two consecutive levels $\Delta E_s=0.05$ eV were assumed so that the summation over the states could be performed by using the formula of the geometric series. For $\Delta E_s/kT\ll1$ the sum $Z^{(1)}$ can be represented by the equation

$$Z^{(1)}\approx\bar{g}+\frac{\bar{g}}{\Delta E_s}kT\approx\bar{g}\frac{kT}{\Delta E_s} \tag{3}$$

If one assumes that the mean statistical weight of the uranium atom and that of the ion are equal in a first approximation, the ratio $g_n/Z^{(1)}$ in equation (2) can be substituted by:

$$g_n/Z^{(1)}=\Delta E_s/kT \tag{4}$$

For the continuous distribution of the oscillator strengths df/dE a hydrogenlike proportionality was chosen for transitions between states having a greater energy difference ($E\geqq E_{dn}$) (fig. 1)

$$\frac{df}{dE}\sim\frac{1}{n^5E^3} \tag{5}$$

where n is the effective quantum number of the state from which the transition begins and $E=h\nu$ is the energy of the absorbed photon. For transitions between lower levels ($E\leqq E_{dn}$) the oscillator strength per unit energy was assumed to be constant as an approximation (see fig. 1(*a*)), because, first, only

few transition probabilities between lower states are known and, second, the following integral, which is the oscillator strength sum rule of Kuhn, Thomas, and Reiche, must remain finite:

$$\int_{-\infty}^{+\infty} \frac{df}{dE} dE = 2 \qquad (6)$$

The value of this integral corresponds to the number of the two outer electrons of the uranium atom and this equation must be fulfilled.

The absolute constant for positive values of df/dE in equation (5) is chosen such that if df/dE is inserted into equation (1) the bound-free absorption coefficient of Kramers and Unsöld is obtained. However, df/dE is negative for transitions from higher to lower levels. For this case, the proportionality in equation (5) was assumed if the energy difference between the two levels is not small.

If the energy difference is small, df/dE was set equal to a negative constant. The absolute constants of negative values of df/dE and $E_{dn}^{(-)}$ (fig. 1) were found by inserting the positive and negative df/dE values into equation (6), which must be fulfilled.

Krascella (ref. 5) made similar assumptions for df/dE. He assumed a proportionality $df/dE \sim 1/n^4E^3$ but he did not include negative df/dE values.

The distribution of the oscillator strengths for absorption transitions (positive df/dE values) can be represented by the following equations which include also transitions between discrete levels:

$$\frac{df}{dE} = \frac{1}{n^5}\frac{E_i^2}{E^3} \quad \begin{cases} \text{case } E_n \geqq E_{C1} & \text{for } E \geqq E_{dn} \\ \text{case } E_n \leqq E_{C1} & \text{for } E \geqq \Delta E_s \end{cases} \qquad (7)$$

$$\frac{df}{dE} = \frac{1}{n^5}\frac{E_i^2}{E_{dn}^3} \qquad \begin{matrix} \text{only for case } E_n > E_{C1} \\ \text{for } \Delta E_s \leqq E \leqq E_{dn} \end{matrix} \qquad (8)$$

The distribution function of the oscillator strength for emission transitions (negative df/dE values) is given by the following equations in which the energy E of the absorbed photon is negative:

$$\frac{df}{dE} = \frac{1}{n^5}\frac{E_i^2}{E_{dn}^{(-)3}} \qquad \text{case } E_n > E_{C1}$$
$$\text{for } E_{dn}^{(-)} \leqq E \leqq -\Delta E_s \qquad (10)$$

Here δE_s is chosen so small that equation (6) is fulfilled. The absorption coefficient of a single continuum would be proportional to about $1/n^3E^3$ if the statistical weight $g_n = 2n^2$ is hydrogenlike. This was assumed only for levels with $n \geqq 6$.

But here a mean value $g_n = \bar{g}$ was assumed for the uranium atom for $n \leqq 6$ so that the absorption coefficient of a single continuum becomes proportional to about $1/n^5E^3$. A nonhydrogenlike property was introduced into the absorption coefficient of the uranium atom so that the absorption coefficient is not completely hydrogenlike.

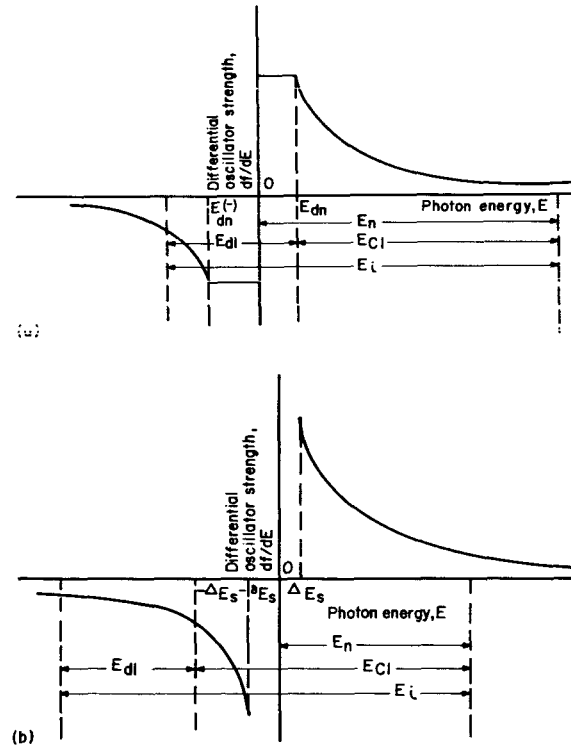

FIGURE 1.—*Schematic distribution of the oscillator strength depending on the absorbed photon energy.* $E_{d1} = 0.355\ E_1$. (a) *Case* $E_n > E_{c1}$. (b) *Case* $E_n < E_{c1}$.

$$\frac{df}{dE} = \frac{1}{n^5}\frac{E_i^2}{E^3} \begin{cases} \text{case } E_n \geqq E_{C1} & \text{for } E \leqq E_{dn}^{(-)} = -E_i \sqrt{\dfrac{1-0.645n^2}{n^2 - \frac{4}{3}n^5(1-0.645n^2)}} \\ \text{case } E_n \leqq E_{C1} & \text{for } E \leqq -\Delta E_s - \delta E_s \end{cases} \qquad (9)$$

The total spectral absorption coefficient for $\nu \geqq \Delta E_s/h$ can be determined now if the summation of all absorption coefficients of each level to those of all the other levels is accomplished: $\kappa_\nu = \sum_n \kappa_{\nu n}$ since the uranium atom has a very large number of energy levels, a mean distance between two consecutive levels was assumed to be of the order of 0.05 eV. Thus, the summation of all absorption coefficients could be performed easily, and, furthermore, the summation was approximated by an integration. It is of interest that the total absorption coefficient depends only weakly on the mean distance of the levels.

For frequencies $\nu \leqq \Delta E_s/h$ the total spectral absorption coefficient was evaluated by starting with the summation of the absorption coefficients above the limit where the energy levels begin to overlap themselves by the line broadening effect caused by the very high electron density so that the upper bound levels go into the free continuous state. This spectroscopic effect appears as a lowering of the ionization energy. But this lowering ΔE_g of the ionization energy differs from that ΔE_F given by Ecker and Kröll (ref. 7) which can be set only into the Saha equation. Brunner (ref. 8) has described a method to calculate ΔE_g, but at the moment it is very difficult and extensive to calculate ΔE_g for the uranium atom and so the ΔE_F of Ecker and Kröll (ref. 7) was used as an approximation. The difference between ΔE_g and ΔE_F is not so great, so the used approximation is justified.

For $\nu \leqq \Delta E_s/h$ and for $\nu \geqq \Delta E_s/h$ the absorption coefficient of the free-free continuum (bremsstrahlung) must be added to the absorption coefficients mentioned above.

The value ΔE_g influences the magnitude of the total spectral absorption coefficient for low frequencies $\nu \leqq \Delta E_s/h$. The magnitude of the last one considerably affects the magnitude of the Rosseland mean opacity (defined by eq. (11)) for lower plasma temperatures. The value of ΔE_g determines also at which temperature the Rosseland mean opacity begins to increase very fast.

The total spectral absorption coefficient was also calculated for the case in which for $n \leqq 6$ the distance of the energy levels becomes smaller with a function which is inversely proportional to the effective quantum number

$$\Delta E_s \sim \frac{1}{n}$$

This assumption seems to be more probable for the uranium atom. But it could be shown that the result does not deviate very much from that for the case in which the distance between consecutive levels is constant.

The Rosseland mean opacity can be evaluated now from the total spectral absorption coefficient κ_ν by the well-known equation

$$\frac{1}{\bar{\kappa}_R} = \int_0^\infty \frac{1}{\kappa_\nu} \frac{dB_\nu}{dT} d\nu \Big/ \int_0^\infty \frac{dB_\nu}{dT} d\nu \qquad (11)$$

The dependence of $\bar{\kappa}_R$ on the temperature for a total plasma pressure of 50 atm is shown in figure 2. Here $\bar{\kappa}_R$ increases very fast above 3500° K. But since the boiling point of uranium for 50 atm is approximately 5200° K (ref. 9), the curve of $\bar{\kappa}_R$ is valid only above this temperature. Plutonium has a very much lower boiling point and for this case $\bar{\kappa}_R$ in figure 2 is also valid for lower temperatures.

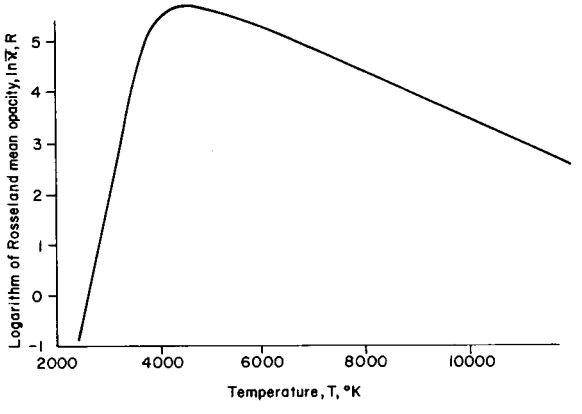

FIGURE 2.—*Rosseland mean opacity as a function of temperature.*

RADIATION FLUX AND TEMPERATURE DISTRIBUTION

An approximation for the radiation flux can be applied for the determination of the temperature distribution in a plasma reactor of a cylindric geometry. This approximation includes also the effect that the radiation field is extremely anisotropic near the plasma boundary, because the approximation was

derived from the exact expression for the radiation flux (see ref. 10).

$$E_o(\tau) = \frac{4}{3}\sigma_s \frac{d(T^4)}{d\tau} + \sigma_s T^4 e^{-1.41\tau} - \frac{2}{3}\sigma_s \cdot \frac{d(T^4)}{d\tau} e^{-1.37\tau} \quad (12)$$

where τ is the optical depth

$$\tau = \int_r^{r_o} \bar{\kappa}_R \, dr \qquad d\tau = -\bar{\kappa}_R \, dr$$

and σ_s denotes the Stefan-Boltzmann constant.

This equation for the radiation flux is valid if the plasma is optically thick or the temperature gradients are not too high. It is right to use the Rosseland mean value in the first term, but in the two other terms the Rosseland mean opacity is used as an approximation.

If τ is greater than 3 in equation (12), the radiation flux is considered at a certain distance from the plasma boundary and the two last terms with the exponential functions vanish in the equation. Then the radiation flux inside the plasma assumes the well-known form:

$$E_o'(\tau) = \frac{4}{3}\sigma_s \frac{d(T^4)}{d\tau} \quad (13)$$

But near the boundary, where τ is zero, the radiation flux becomes

$$E_o(0) = \sigma_s T_{(0)}^4 + \frac{2}{3}\sigma_s \frac{d(T^4)}{d\tau}\bigg|_{\tau=0} \quad (14)$$

When we consider the case of a cylindrical plasma with reflecting walls and also include anisotropy, the radiation flux $E_o(\tau)$ is lowered by subtracting two terms

$$E_s(\tau) = E_o(\tau) - x\left[\sigma_s T_{(0)}^4 e^{-1.41\tau} + \frac{2}{3}\sigma_s \cdot \frac{d(T^4)}{d\tau}\bigg|_{\tau=0} \cdot e^{-1.37\tau}\right] \quad (15)$$

The first term on the right-hand side of the equation corresponds to the radiation flux without reflecting walls and x denotes the reflection coefficient of the mirror at the plasma boundary.

If we set $\tau = 0$, then we obtain at the boundary

$$E_s(0) = (1-x)\left[\sigma_s T_{(0)}^4 + \frac{2}{3}\sigma_s \frac{d(T^4)}{d\tau}\bigg|_{\tau=0}\right] \quad (16)$$

In the case of a liquid mirror, which has a reflection coefficient of 90 percent, the total radiation flux is reduced down to 10 percent in comparison with the case where there are no reflecting walls.

Now the temperature distribution can be determined in the plasma region of the reactor by using the energy equation in which the total radiation flux $2\pi r h E_s(\tau)$, the influence of the ionization of the lithium A, and energy sources are considered (h = 1.0 m):

$$2\pi r h E_s(\tau) + A = \int_0^r P(r') 2\pi r' h dr' \quad (17)$$

The transport of heat by thermal conductivity was neglected in equation (17) because it is smaller than the radiation transport term. The spatial energy sources correspond to the production P of energy per unit volume by nuclear fissions

$$P = n_u \phi = 3.14 \times 10^{-17} n_u \text{ W cm}^{-3} \quad (18)$$

where n_u is the total uranium particle density and ϕ is the neutron flux.

In equation (18) the distribution of the flux of the neutrons is set constant as an approximation. In that temperature region of the plasma where the uranium is fully ionized, the uranium particle density n_u can be replaced by $p/2kT$ so that equation (18) becomes

$$P = \frac{6 \times 10^6}{T(r)} \text{ W cm}^{-3} \quad (19)$$

For a temperature of 20 000° K, e.g., the production term P corresponds to an energy of 300 W cm^{-3}. The term A represents the heating and ionization of the lithium

$$A(r) = [H(T_o) - H(T_{(r)})] \frac{\dot{m}}{m_{\text{Li}}} \quad (20)$$

$\dot{m}$ mass flow rate of the lithium flowing in the radial direction from the walls to the center of the plasma

m_{Li} mass of the lithium atom

$H(T_o)$ enthalpy of the lithium plasma in the center of the plasma

$H(T)$ enthalpy at an arbitrary distance from the plasma center

The enthalpy $H(T)$ of the lithium plasma is given by the equation

$$H(T) = \frac{5}{2}kT + c(T) \cdot (E_{\text{Li}} + \frac{5}{2}kT) \quad (21)$$

where E_{Li} is the ionization of the lithium atom and $c(T)$ is the ionization degree of the lithium.

The assumption is made here that the lithium flowing into the reactor is ionized in only the parts of the plasma from about 5000° to 8000° K by the fission fragments. Therefore, the energy equation has the form of equation (17).

The calculation of the temperature distribution is also possible with two energy equations, if the lithium vapor is ionized by the optical radiative energy only when the lithium flows in the radial direction or, in another concept, when it flows mainly in the axial direction. In the last case one must use an energy equation for the uranium plasma zone and another energy equation for the lithium plasma zone in which the absorbed radiative energy of the uranium plasma zone occurs.

Energy equation (17) can be now differentiated with respect to r and multiplied by the factor $-1\bar{\kappa}_R$ so that only derivatives by τ occur in the differentiated equation (17):

$$\frac{1}{r}\cdot\frac{d[rE_s(\tau)]}{d\tau}+\frac{1}{2\pi rh}\cdot\frac{dA}{d\tau}=-\frac{1}{\bar{\kappa}_R}\cdot P(\tau) \quad (22)$$

Two terms in the equation have the factor $1/r$. The radius r can be replaced by the relation ($r_o=50$ cm):

$$r=r_o-\int_0^\tau \frac{d\tau'}{\bar{\kappa}_R[T(\tau')]} \quad (23)$$

Thus energy equation (17) was brought into the form of differential equation (22) which can be solved with corresponding boundary values.

The following values at the boundary of the plasma were used:

$$T_{(0)}=7\times10^3\ ^\circ\text{K}, \qquad \frac{dT}{d\tau}=250^\circ\ \text{K}$$

The results show that the temperature can rise up to 21 000° K in the middle of the reactor (fig. 3). Though the temperature gradient is very steep near the boundary of the plasma, the radiation flux there is only 15 MW per m^2, which is not too high. The total radiation flux through the surface of the cylinder ($h=1.0$ m) attains 47 MW, but this radiative energy is necessary to vaporize the liquid lithium which is flowing into the reactor if the mass flow rate of the lithium is just 2000 g/sec.

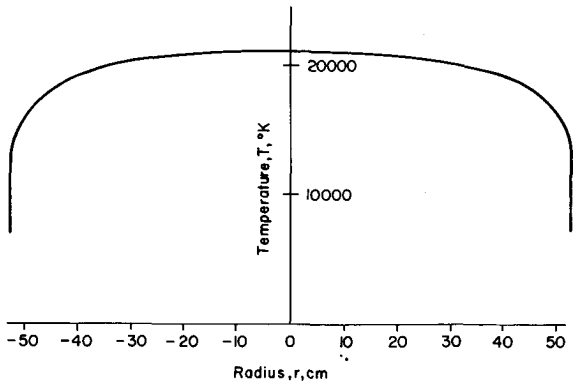

FIGURE 3.—*Temperature distribution in the plasma reactor.*

If the blackbody radiation temperature is not 7000° K but is 5200° K, which is more probable because the absorption coefficient is still very high at this temperature (this temperature will not be lower than 5200° K because of the boiling point of uranium), then the total radiation flux is only 14.4 MW and a mass flow rate of 610 g sec^{-1} is necessary.

CONCLUSIONS

The results of the calculations for a uranium plasma reactor have shown, first, that the total radiation flux near the walls is reduced considerably despite the very high temperatures at the middle of the reactor, because the temperature of the blackbody radiation near the plasma boundary is lower than 7000° K. Second, the radiation flux is reduced by the reflecting walls. Therefore, the optical radiation of the plasma is not too high to damage the inner solid walls of the reactor.

The lithium plasma leaving the plasma reactor by a nozzle has a high temperature (about 10 000° K) and is fully ionized because the temperature in the center of the reactor is 21 000° K. Therefore the electrical conductivity of the lithium plasma is in the order of 5000 mho/m or higher. This conductivity is sufficient so that the flowing lithium plasma can be used most effectively for an inductive MPD generator.

REFERENCES

1. McLAFFERTY, G. H.: Survey of Advanced Concepts in Nuclear Propulsion. J. Spacecraft Rockets, vol. 5, no. 10, Oct. 1968, pp. 1121–1128.

2. RAGSDALE, R. G.; AND ROM, F. E.: Gas Core Reactor Work at NASA/LEWIS. Paper No. 67–499, Third Propulsion Joint Specialist Conf., AIAA, July 1967.

3. PESCHKA, W.; AND KELM, S.: High Temperature Energy Systems With Plasma Reactors and Inductive Magnetoplasmadynamic Converters. Electricity from MHD, vol. 2. Int. Symp. Magnetohydrodynamic Elec. Power Generation (Warsaw, Poland, 1968), 1968, pp. 1133–1150.
4. PESCHKA, W.: Hochtemperatur-Energiesysteme unter Verwendung von Plasmareaktoren und induktiven magnetoplasmadynamischen Wandlern. DLR FB 67–59, Deut. Luft- und Raumfahrt, 1967.
5. KRASCELLA, N. L.: Theoretical Investigation of the Opacity of Heavy-Atom Gases. Rept. D–910092–4, United Aircraft Res. Lab., Sept. 1965.
6. UNSÖLD, A.: Physik der Sternatmosphären. Springer-Verlag (Berlin), 1955.
7. ECKER, G.; AND KRÖLL, W.: Lowering of the Ionization Energy for a Plasma in Thermodynamic Equilibrium. Phys. Fluids, vol. 6, 1963, pp. 62–69.
8. BRUNNER, J.: Die "effektive" Ionisierungsenergie der Atome eines Plasmas und der Beitrag der höchsten Atomkerne zur kontinuierlichen Emission. Z. Physik, Bd. 159, 1960, pp. 288–310.
9. LANDOLT-BÖRNSTEIN: Zahlenwerte und Funktionen. Bd. 2, T. 2, Bdteil. a, Springer-Verlag (Berlin-Göttingen-Heidelberg), 1960.
10. KELM, S.: Radiative Energy Transport in a Plasma Reactor. DLR FB 70–18, Deut. Luft-und Raumfahrt, 1970.

DISCUSSION

Keyes: What was the maximum temperature of the lithium in your calculations, and what did you do with the lithium? Just recycle and cool it? It did not go into the MHD generator, I assume.

Kelm: There are several possibilities. The lithium is vaporized. It can diffuse into the center of the reactor and then to the nozzle. After passing the nozzle the lithium plasma flows through the channel of the inductive MPD generator with a temperature of about 10 000° K. But there are also other possibilities of closed cycle concepts where the lithium plasma does not flow through the channel of the MPD generator.

Page intentionally left blank

Radiation Hazard From Backflow of Fission Fragments From the Plume of a Gas-Core Nuclear Rocket

CHARLES C. MASSER
NASA Lewis Research Center

Analytical calculations are performed to determine the particle flux that leaves a rocket plume in a vacuum and strikes the rocket forward of the nozzle. The rocket plume is generated by the products of a gas-core nuclear reactor and consists of hydrogen, uranium, and fission fragments. The backflow flux is determined by the number of particles that leave the continuum of the plume and strike the rocket without experiencing any particle collisions. A percentage of these particles that strike the rocket are fission fragments and the radiation dose to the crew is calculated.

A total of 1.68 lb of fission fragments is formed from a gas-core rocket that produces 10^6 lb of thrust at a specific impulse of 1500 sec for a propellant consumption of 10^6 lb. Of the 1.68 lb of fission fragments only 0.42×10^{-5} lb flow back from the plume and only 0.66×10^{-10} lb strike the rocket. This weight of fission fragments causes a total integrated dose of less than 1.3×10^{-4} rad to the crew, which is well below acceptable levels.

In the open-cycle gas-core nuclear rocket concept (fig. 1) the heat source is fissioning uranium gas. This released heat is radiated to and absorbed by the hydrogen propellant. The heated propellant is exhausted through a nozzle, producing thrust. In an open-cycle gas-core rocket the fission fragments that are formed and the unfissioned uranium fuel are also exhausted into the vacuum of space. As the exhaust plume is formed, a small percentage of the plume products have a sufficient velocity and the proper direction to leave the plume and flow back toward the rocket. It is the purpose of this paper to evaluate the radiation hazard to the crew associated with a backflow of fission fragments that strike the rocket. It is assumed that the fission fragments striking the rocket stick to it.

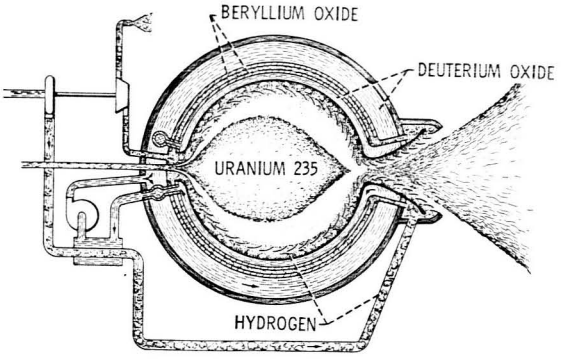

FIGURE 1.—*Gas-core nuclear rocket concept.*

There are other radiation sources associated with the gas-core reactor such as radiation from the reactor core and radiation from inside the plume itself. These radiation sources, along with solar radiation, must be ultimately considered. This study, however, is concerned only with that part of the total radiation problem that arises from fission fragments leaving the plume and striking the rocket.

ROCKET ENGINE CHARACTERISTICS

Certain exit nozzle conditions are selected in order to make a specific calculation of the backflow of fission fragments from the plume. Roback (ref. 1) calculated performance parameters for hydrogen at various stagnation pressures and temperatures. The selection was made to pick performance param-

eters which produced a high flow of fission fragments and so maximized the radiation problems. A 10^6 lb propellant storage capacity was picked, which is typical of a manned Mars mission. The following parameters were picked:

Thrust, lb	10^6
Specific impulse, sec	1500
Chamber pressure, atm	1000
Chamber temperature, °R	10 000
Reactor power, MW	41 900

From table 168 of Roback (ref. 1) for a

$$\frac{\text{Pressure nozzle exit}}{\text{Pressure nozzle throat}}=10^{-3}$$

Exit temperature, °R	3460
Exit density, lb/ft^3	7.978×10^{-4}
Exit velocity, ft/sec	48 507
Exit Mach number	4.587
Exit molecular weight	2.015
Molecular diameter, cm	2.75×10^{-8}

For the given thrust of 10^6 lb and a specific impulse of 1500 sec, the propellant flow rate is 667 lb/sec. Therefore, if the propellant storage for the mission is 10^6 lb the total firing time is 1500 sec.

CALCULATION OF PLUME DENSITY

It has been shown that in nozzle plume flows the mass flux ρV varies inversely as the square of the distance from the source point. (Symbols used in the paper are defined in the appendix.) Hill and Draper (ref. 2) have shown that the density in the plume can be closely approximated by

$$\rho=\frac{4\rho_e M_e B}{\left(1+\frac{\gamma-1}{2}M_e^2\right)^{1/2}\left(\frac{2}{\gamma+1}\right)^{(\gamma+1)/2(\gamma-1)}}\left(\frac{r_e}{r}\right)^2 e^{-\lambda^2(1-\cos\theta)^2} \tag{1}$$

where the coordinates r and θ are shown in figure 2, ρ is density at any point in the plume, ρ_e is exit density, M_e is exit Mach number, γ is the ratio of specific heats, and B and λ are constants.

Also from Hill and Draper (ref. 2) we have

$$B=\frac{\lambda}{4\sqrt{\pi}}\left(\frac{\gamma-1}{\gamma+1}\right)^{1/2}\left(\frac{2}{\gamma+1}\right)^{1/(\gamma-1)} \tag{2}$$

$$\lambda=\frac{1}{\sqrt{\pi}\left(1-\frac{C_F}{C_{F_{\max}}}\right)} \tag{3}$$

where C_F and $C_{F_{\max}}$ are thrust coefficients and are evaluated using equations (4.33) and (4.34) of Shapiro (ref. 3).

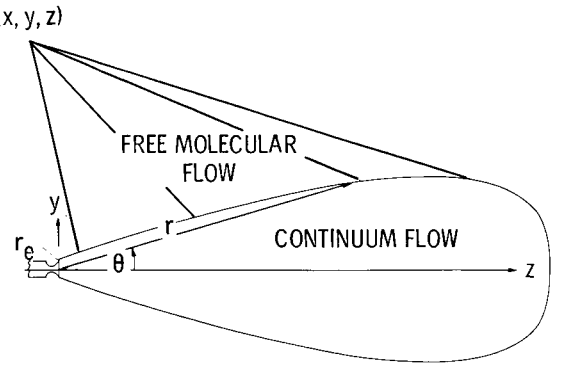

FIGURE 2.—*Model used for calculations.*

DEFINITION OF PLUME BOUNDARY

The gas inside the plume is considered to be a continuum. As the plume expands, the density decreases to a point where free molecular flow can be assumed. At this point we can define our plume boundary. From Grier (ref. 4), the plume boundary is defined by a surface on which the Knudsen number is constant. The Knudsen number K is defined as

$$K\equiv\frac{l}{r} \tag{4}$$

where r is the distance from the plume source point to the plume boundary, and l is the mean free path of the particle and is given by Santeler et al. (ref. 5) as

$$l=3.736\times10^{-25}\frac{m}{\rho\delta^2} \tag{5}$$

where m is molecular weight and δ is molecular diameter.

Solving equation (5) for density and substituting in equation (4) we have

$$\rho=3.736\times10^{-25}\frac{m}{K\delta^2 r} \tag{6}$$

Combining equation (6) and equation (1) we have the equation of a constant Knudsen surface, which defines the boundary of the plume:

$$\frac{r}{r_e}=\frac{1.07\times10^{25}\,\rho_e M_e B K\delta^2 r_e}{m\left(1+\frac{\gamma-1}{2}M_e^2\right)^{1/2}\left(\frac{2}{\gamma+1}\right)^{(\gamma+1)/2(\gamma-1)}}e^{-\lambda^2(1-\cos\theta)^2} \tag{7}$$

In this equation the maximum value of θ was taken to be the maximum Prandtl-Meyer expansion angle for a Mach number of 4.87. The backflow of flux is determined by the number of particles that leave this defined boundary and strike a particular point $P(x,y,z)$. A model of this is shown in figures 2 and 3.

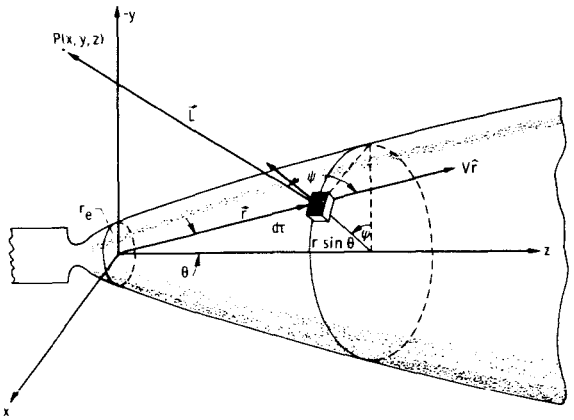

FIGURE 3.—*Coordinate system used in calculations. (Note that* **n** *is normal to surface at* d *and* $\mathrm{r} = \mathbf{r}/\mathrm{r}$.)

CALCULATION OF BACKFLOW FLUX

Nöller (ref. 6) has calculated the density at a point $P(x,y,z)$ due to the molecules leaving an elemental volume $d\tau$ adjacent to a constant Knudsen surface. Nöller's result was

$$\frac{dn_p}{n_\tau} = \pi^{-3/2} e^{-U^2}\left\{\frac{1}{2}U\cos\psi + \left(\frac{1}{2}+U^2\cos^2\psi\right) \times e^{U^2\cos^2\psi}\left(\frac{\sqrt{\pi}}{2}\right)[1+\mathrm{erf}(U\cos\psi)]\right\} d\Omega \quad (8)$$

where n_τ is the number density of molecules in $d\tau$, ψ is the angle between the direction of **V** and the direction of flight of the molecules contributing to the density at $P(x,y,z)$, $U = \mathbf{V}/(2RT/m)$, R is the gas constant, T is the temperature, and $d\Omega$ is the differential solid angle of $d\tau$ as seen from $P(x,y,z)$. Figure 3 shows the coordinate system used.

Equation (8) was recalculated in this study to express mass flux F instead of density. The following equation resulted:

$$\frac{dF}{n_\tau} = \frac{\pi^{-2/3}}{2} e^{-U^2}\left\{(1+U^2\cos^2\psi) + \sqrt{\pi}\,U\cos\psi \times\left(\frac{3}{2}+U^2\cos^2\psi\right) [1+erf\,(1+\cos\psi)]e^{U^2\cos^2\psi}\right\} d\Omega \quad (9)$$

From Grier (ref. 4) $d\Omega$ is given by

$$d\Omega = \left[\frac{y}{r_e}\sin\theta\cos\varphi\,(1+2\lambda^2\cos\theta - 2\lambda^2\cos^2\theta)\right] - \frac{r}{r_e} + \frac{z}{r_e}(\cos\theta - 2\lambda^2\sin^2\theta + 2\lambda^2\sin^2\theta\cos\theta) \left(\frac{r}{r_e}\right)^2\left(\frac{r_e}{L}\right)^3 \sin\theta\,d\theta\,d\varphi \quad (10)$$

where **L** is the vector from $d\tau$ to the point $P(x,y,z)$. Also, from Grier (ref. 4) $|\mathbf{L}|$ is given by

$$\frac{|\mathbf{L}|}{r_e} = \hat{\mathbf{r}}\left(\frac{y}{r_e}\sin\theta\cos\varphi - \frac{r}{r_e} + \frac{z}{r_e}\cos\theta\right) + \hat{\boldsymbol{\theta}}\left(\frac{y}{r_e}\cos\theta\cos\varphi - \frac{z}{r_e}\sin\theta\right) - \hat{\boldsymbol{\varphi}}\frac{y}{r_e}\sin\varphi \quad (11)$$

The particle mass flux at any point upstream of the nozzle face is

$$F = \frac{\pi^{-3/2}}{2} e^{-U^2}\int_{\theta=0}^{\theta=\theta_{max}}\int_{\varphi=-(\pi/2)}^{\varphi=(\pi/2)} n_\tau\left\{(1+U^2\cos^2\psi) + \sqrt{\pi}\,U\cos\psi\times\left(\frac{3}{2}+U^2\cos^2\psi\right) [1+erf(U\cos\psi)]e^{U^2\cos^2\theta}\right\} d\Omega \quad (12)$$

CALCULATION OF FISSION FRAGMENT FORMATION

The total engine running time is calculated by dividing the total mass of propellant carried by the mass flow of propellant. This results in a total engine running time of 1500 sec. The number of fission fragments formed is calculated using equation (2.49) of Glasstone and Sesonske (ref. 7)

$$\text{Reactor power}_{(\text{watts})} = \frac{\text{Fissions per second}}{3.1\times10^{10}} \quad (13)$$

Since reactor power and engine running time are known, the number of fission fragments is known. It is also assumed that the average molecular weight of the fission fragments is 117.5. Therefore we have the values shown in the following table:

Item	Number of particles	Weight of particles, lb
Fission fragments	3.896×10^{24}	1.68
Hydrogen propellant	1.36×10^{32}	10^6
Unfissioned uranium	1.163×10^{28}	10^4

It is assumed that the fission fragments are uniformly distributed throughout the plume which is composed chiefly of hydrogen and that the number of fission fragments flowing from the plume is of the same relative concentration as is the plume. This assumption should give an overestimate of the number of fission fragments leaving the plume because of the higher mobility of the hydrogen molecules.

MASS FLUX TO ROCKET

In order to calculate the number of fission fragments that strike and stick to the rocket, a particular shape was picked. The configuration picked was a cylinder 33 ft in diam and 400 ft long. This size is sufficient for a tankage volume needed to store 10^6 lb of hydrogen which is typical of a manned Mars mission. The crew is assumed to be located at the front of the rocket 400 ft from the nozzle.

The distribution of fission fragments over the rocket is computed so that the distance from the fission fragments to the crew is known. In figure 4

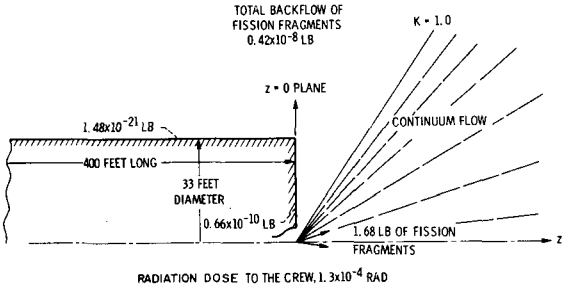

FIGURE 4.—*Distribution of fission fragments for plume Knudsen number* $K \equiv l/r = 1.0$. *Total backflow of fission fragments,* 0.42×10^{-8} *lb.*

we have an enlarged view of the rocket nozzle area. The plume boundary is for the case of a Knudsen number equal to 1. For this case the total weight of fission fragments formed is 1.68 lb. Of this amount only 0.42×10^{-8} lb flow back across the plane $z=0$. Of this 0.42×10^{-8} lb, 0.66×10^{-10} lb deposits on the end surface of the rocket. It can easily be seen that only a small percentage of the total backflow ever strikes the rocket.

RADIATION DOSE TO THE CREW

The radiation dose to the crew is calculated in two parts: The radiation from the fission fragments that strike the end surface and the radiation from the fission fragments that strike the side of the rocket. In all cases studied the radiation dose level to the crew from the fission fragments striking the side of the rocket is at least six orders of magnitude less than the dose from the fission fragments striking the end of the rocket. Therefore only the radiation from the fission fragments striking the end of the rocket will be discussed.

In calculating the radiation dose several assumptions are used in order to determine the highest dose that one could expect from the backflow. First, the gamma radiation from the fission fragments is released after they flow back and strike the rocket. Second, the fission fragments of the uranium atom release their total 6 MeV of energy (Glasstone and Sesonske, ref. 7) in decay in 1 sec. Third, an unshielded point-kernel calculation was used to calculate the dose to the crew.

The total radiation dose to the crew for these extremely conservative assumptions in the case where the Knudsen number $K=1$ is 1.3×10^{-4} rad. For a Knudsen number of 1.0 the mean free path of the particles is equal to the distance from the nozzle. This is shown in figure 4. This level of radiation is small so no hazard to the crew is expected. Since the amount of fission fragments that strike the rocket may depend on the definition of the plume boundary, a variation of this definition is shown in figure 5. The plume boundaries represent the cases where the Knudsen number K is equal

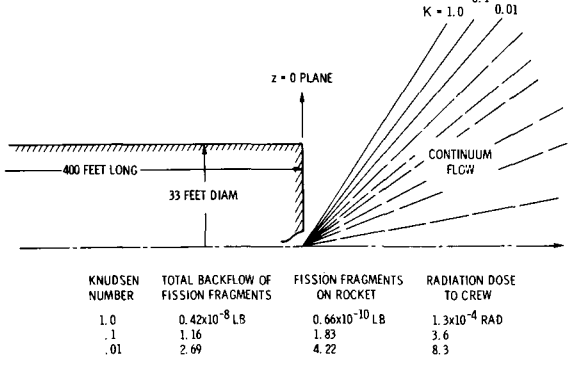

FIGURE 5.—*Distribution of fission fragments for plume Knudsen number* $K \equiv l/r = 1.0, 0.1,$ *and* 0.01.

to 0.01, 0.1, and 1.0. The total radiation doses for these three cases are 8.3×10^{-4}, 3.6×10^{-4}, and 1.3×10^{-4} rad, respectively. However, even for the case where $K=0.01$ the radiation level to the crew is small. Therefore, from the cases studied the radiation dose to the crew from fission fragments that flow back from the plume is considered not to be hazardous.

APPENDIX

SYMBOLS

B	defined by equation (2)
C_F	thrust coefficient
$C_{F_{max}}$	maximum thrust coefficient
erf	error function
F	mass flux
K	Knudsen number
$\mathbf{L}$	vector distance from d_τ on constant Knudsen surface to point $P(x,y,z)$
l	mean free path of gas molecules
M	Mach number
m	molecular weight
n_p	particle density at point $P(x,y,z)$
n_τ	particle density in volume element
R	gas constant
r,θ,φ	spherical coordinates
T	temperature
U	dimensionless velocity $\lvert\mathbf{V}\rvert/(2RT/m)^{1/2}$
$\mathbf{V}$	mean velocity of particles in plume
x,y,z	Cartesian coordinates
γ	ratio of specific heats
δ	molecular diameter of molecules
λ	defined by eq. (3)
ρ	mass density
ψ	angle between direction of $\mathbf{V}$ and direction of $\mathbf{L}$

Subscript:

e	nozzle exit

Superscript:

$(\hat{\ })$	unit vector

REFERENCES

1. ROBACK, R.: Theoretical Performance of Rocket Engines Using Gaseous Hydrogen in the Ideal State at Stagnation Temperatures up to 200 000 R. NASA CR-696, 1967.
2. HILL, JACQUES A. F.; AND DRAPER, JAMES STARK: Analytical Approximation for the Flow From a Nozzle Into a Vacuum. J. Spacecraft Rockets, vol. 3, no. 10, Oct. 1966, pp. 1552–1554.
3. SHAPIRO, ASCHER H.: The Dynamics and Thermodynamics of Compressible Fluid Flow. Vol. 1. Ronald Press Co., 1953.
4. GRIER, NORMAN T.: Back Flow From Jet Plumes in Vacuum. NASA TN D-4978, 1969.
5. SANTELER, DONALD J.; HOLKEBOER, DAVID H.; JONES, DONALD W.; AND PAGANO, FRANK: Vacuum Technology and Space Simulation. NASA SP-105, 1966.
6. NÖLLER, H. G.: Approximate Calculations of Expansion of Gas From Nozzles into High Vacuum. J. Vacuum Sci. Tech., vol. 3, no. 4, July/Aug. 1966, pp. 202–207.
7. GLASSTONE, SAMUEL; AND SESONSKE, ALEXANDER: Nuclear Reactor Engineering. Third ed., D. Van Nostrand Co., Inc., 1967.

Page intentionally left blank

Application of Zoning Techniques in Practical Radiative Energy Transport Problems[1]

EDWARD Y. H. KENG
Georgia Institute of Technology

Zoning techniques were first introduced by Hottel and coworkers to solve various radiative energy transport problems (refs. 1 and 2). The system was divided into wall and gas zones and each zone was assumed to have uniform properties. Similar approaches have been used to attack many other radiative energy transfer problems (refs. 3 and 4). This study introduces methods which use zoning techniques to extend the existing results of a simple model and thereby permits solutions to be obtained for many complex systems. A cylindrical geometry is chosen here as a demonstration of these methods.

The general treatment of radiative energy transfer from an emitting wall to a gas containing particles involves, separately, the energies absorbed by the carrier gas and by the suspended particles. The combination of these two factors is termed here the radiative energy transfer to the aerosol. Therefore, the extinction coefficient k for these circumstances represents the total extinction coefficient of the aerosol. In the case of an absorbing gas free of particles, k is the extinction coefficient of the absorbing gas alone. In the case of a nonabsorbing gas containing absorbing particles, k is the extinction coefficient of the particles. The view factor F is the fraction of energy emitted from a black surface and received by the aerosol. For gray surfaces, f is employed as the view factor. Because infinite reflections occur in a gray-surface system, f is always larger than F for systems of the same geometry. It should be noted that the view factors represent only the fraction of the emitted energy incident on a surface or absorbed by the aerosol. They are dimensionless and do not show by any means the magnitude of the actual heat transfer.

[1] Research supported by NASA research grant NsG-273-62.

VIEW FACTORS FOR BLACKBODY SYSTEMS

In general, the rate of radiative energy transfer from an isothermal black surface of area A_w to an aerosol nearby or flowing over the surface can be expressed as

$$q_{w\to a} = A_w F_{wa} \sigma T_w^4 \tag{1}$$

where the subscript w denotes the wall surface and a, the aerosol.

If the extinction coefficient of the aerosol k is assumed to be constant, the view factor from the wall to the aerosol F_{wa} for a system can be written as

$$F_{wa} = \frac{1}{\pi A_w} \int_{V_a} \int_{A_w} \frac{k e^{-kS} \cos \beta_w}{S^2} \, dA_w dV_a \tag{2}$$

where S is the distance between an emitting surface element and a receiving differential volume of aerosol. The angle between the direction of the radiation and the direction normal to the surfaces of the wall is β_w. Equation (2) can be expressed for a cylindrical system by the coordinates shown in figure 1 as:

$$F_{wa} = \frac{k}{2\pi^2 L_w} \int_0^{2\pi} \int_0^R \int_0^{2\pi} \int_0^{L_a} \int_0^{L_w} \frac{r(R - r\cos\Psi)}{[(x_w - x_a)^2 + R^2 + r^2 - 2Rr\cos\Psi]^{3/2}} \times \exp\{-k[(x_w - x_a)^2 + R^2 + r^2 - 2Rr\cos\Psi]^{1/2}\} dx_w dx_a d\Psi \, dr \, d\theta \tag{3}$$

If the absorbing aerosol is completely within the

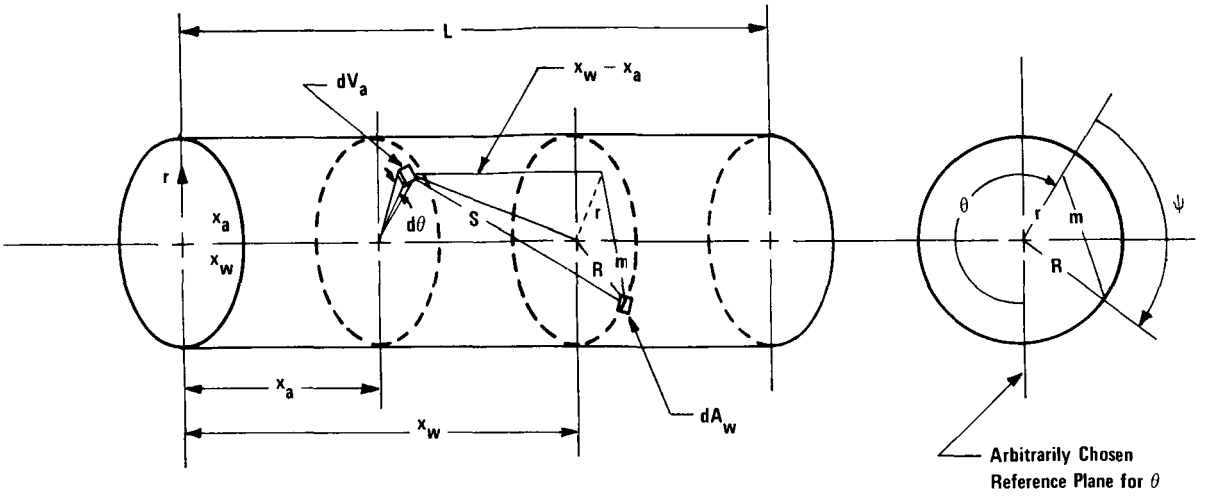

FIGURE 1.—*Definitions of geometric variables for the wall-to-aerosol view-factor formulations.*

cylinder, then $L_a=L_w=L$. Thus equation (3) becomes

$$F_{wa}=\frac{k}{\pi L}\int_0^R\int_0^{2\pi}\int_0^L\int_0^L \frac{r(R-r\cos\Psi)}{[(x_w-x_a)^2+R^2+r^2-2Rr\cos\Psi]^{3/2}} \times\exp\{-k[(x_w-x_a)^2+R^2+r^2 -2Rr\cos\Psi]^{1/2}\}dx_w dx_a d\Psi\, dr \qquad (4)$$

where L and R are the length and radius of the cylindrical system, respectively.

The integrations against x_w and x_a were performed analytically by means of a series expansion of the exponential term. The subsequent integrations for Ψ and r were performed numerically by use of closed-form, Newton-Cotes, quadrature formulas. The results for aerosols of various extinction parameters kR are presented in figure 2 as a function of the length-to-radius ratio L/R. The rate of radiative energy transfer can be easily evaluated by inserting the value read from figure 2 into equation (1) (ref. 5).

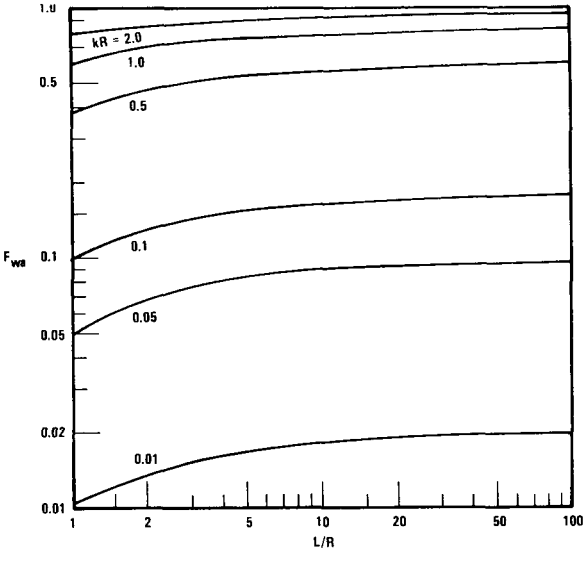

FIGURE 2.—*Wall-to-aerosol view factors for black-wall cylinders containing aerosols.*

VIEW FACTORS FOR GRAYBODY SYSTEMS

Classical radiative energy transfer problems assume blackbody behavior. In general, systems existing in practice are very seldom black. Analysis of a nonblackbody system is complex, but an approximate result can be obtained relatively easily provided assumptions are made. If a system can be assumed to have surfaces that are perfectly diffuse emitters and reflectors, the analysis can be much simplified. A surface usually can be assumed to be diffuse if it is relatively rough compared with the wavelength of the incident radiation. This means that all surfaces will behave more diffusely when the incident radiation comes from a higher temperature source with the same emitting property.

In a black-surface, cylindrical system, that portion of the radiation passing through the aerosol and reaching the wall of the cylinder is absorbed completely by the wall. But in a gray-wall system, the portion reaching the wall is partially absorbed and partially reflected. The reflected energy is available for further absorption by the aerosol. This infinitely continuing process adds to the absorption as more reflection occurs. If f_{wa} is assumed to be the view factor for the gray-surface system which includes the initial view factor and the view factors of the continuing process of reflection, then the radiative energy transfer from the wall to the aerosol can be expressed as

$$q_{w\to a} = A_w f_{wa} \epsilon \sigma T_w^4 \tag{5}$$

where ϵ is the total emissivity of the wall surface. The view factor f_{wa} can be expressed by an infinite series as

$$f_{wa} = F_{1a} + \rho_w F_{1w} F_{2a} + \rho_w^2 F_{1w} F_{2w} F_{3a} + \rho_w^3 F_{1w} F_{2w} F_{3w} F_{4a} + \ldots \tag{6}$$

where ρ_w is the reflectivity of the wall surface. The view factors F_{1a}, F_{2a}, F_{3a}, . . . represent, respectively, the fractions of the radiative energy leaving the wall that are intercepted by the aerosol in the first pass, second pass, third pass, etc. The view factors F_{1w}, F_{2w}, F_{3w}, . . . represent the fractions of radiative energy leaving the wall that pass through the aerosol and are incident again on the wall during the first pass, second pass, third pass, etc.

A gray surface is assumed to be a perfectly diffuse emitter and reflector. Thus it may be assumed that

$$F_{1a} = F_{2a} = F_{3a} = \ldots = F_{wa} \tag{7}$$

and

$$F_{1w} = F_{2w} = F_{3w} = \ldots = F_{ww} \tag{8}$$

Equation (6) now can be reduced to

$$f_{wa} = F_{wa}(1 + \rho_w F_{ww} + \rho_w^2 F_{ww}^2 + \ldots) \tag{9}$$

The value of $\rho_w F_{ww}$ is always less than unity. Thus the expression for f_{wa} can be further simplified to

$$f_{wa} = \frac{F_{wa}}{1 - \rho_w F_{ww}} \tag{10}$$

Substituting f_{wa} into equation (5) gives

$$q_{w\to a} = A_w \left(\frac{\epsilon F_{wa}}{1 - \rho_w F_{ww}} \right) \sigma T_w^4 \tag{11}$$

The values of F_{wa} are shown in figure 2 for various systems. In order to evaluate F_{ww}, the expression

$$F_{w1w2} = \frac{1}{\pi A_w} \int_{A_{w2}} \int_{A_{w1}} (e^{-kS}) \left(\frac{\cos \beta_{w1} \cos \beta_{w2}}{S^2} \right) dA_{w1}\, dA_{w2} \tag{12}$$

may be employed. Equation (12) can be expressed in terms of the coordinates as

$$F_{ww} = \frac{R^3}{2\pi^2 L} \int_0^{2\pi} \int_0^{2\pi} \int_0^L \int_0^L \frac{(1 - \cos \Psi)^2}{[(x_{w1} - x_{w2})^2 + 2R^2 - 2R^2 \cos \Psi]^2} \times \exp\{-k[(x_{w1} - x_{w2})^2 + 2R^2 - 2R^2 \cos \Psi]^{1/2}\} dx_{w1}\, dx_{w2}\, d\Psi\, d\theta \tag{13}$$

or

$$F_{ww} = \frac{R^3}{\pi L} \int_0^{2\pi} \int_0^L \int_0^L \frac{(1 - \cos \Psi)^2}{[(x_{w1} - x_{w2})^2 + 2R^2 - 2R^2 \cos \Psi]^2} \times \exp\{-k[x_{w1} - x_{w2})^2 + 2R^2 - 2R^2 \cos \Psi]^{1/2}\} dx_{w1}\, dx_{w2}\, d\Psi \tag{14}$$

The value of F_{ww} can be obtained similarly to that of F_{wa} except one less integral term is involved than for F_{wa} because of the constant radius R. Hoffman and Gauvin (ref. 3) obtained solutions for cylinders of length equal to one, two, and three times the diameter. Their results are modified and are presented in figure 3 with interpolation and extrapolation added.

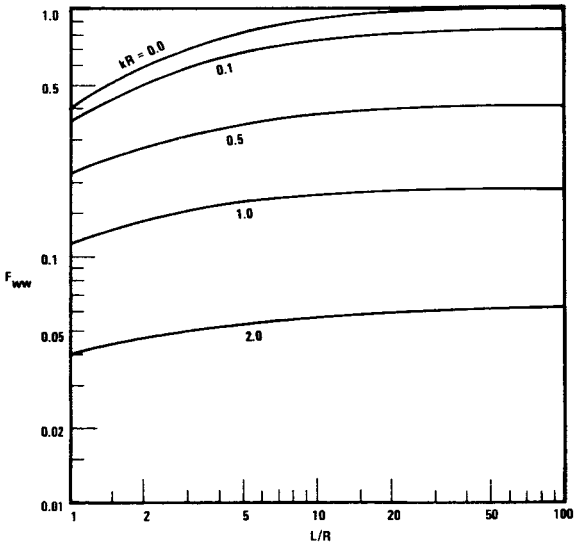

FIGURE 3.—*Wall-to-wall view factors for black-wall cylinders containing aerosols.*

The view factors calculated by equation (10) are nearly exact for relatively dense aerosols. For systems of dilute aerosols, small errors are to be expected for short (length less than radius) or long (length greater than five time radius) cylinders. This results from the nearly uniform irradiation within short cylinders and the negligible end effects for long cylinders. For intermediate-length cylinders, the center portion receives more radiative energy per unit area than does each of the end portions. For example, the center portion of a cylinder having a length equal to three times the radius receives about 3 percent more of the emitted radiative energy than each of the end portions receives if the extinction parameter kR is assumed to be 0.1. An error analysis with consideration of this uneven irradiation for a surface of reflectivity of 0.5 was performed, and the final result showed no significant difference from that obtained by equation (10) in which the assumption of uniform irradiation was made. Apparently, the increase in absorption due to uneven irradiation is very small.

VIEW FACTORS AMONG ZONES

If a cylinder with a black wall is arbitrarily divided into two zones, as shown in figure 4, the view

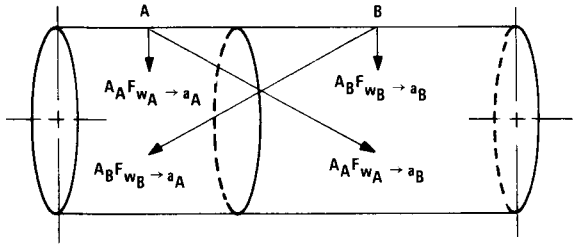

FIGURE 4.—*Radiative energy transfer in two adjacent zones.*

factors for each of the zones to the aerosol in its zone can be obtained from figure 2. The view factor from the wall w_A of zone A to the aerosol a_B in zone B can be evaluated by the equation

$$F_{w_A \to a_B} = \frac{k}{\pi L_A} \int_0^R \int_0^{2\pi} \int_0^{L_A} \int_{L_A}^{(L_A+L_B)} \frac{r(R - r\cos\Psi)}{[(x_B - x_A)^2 + R^2 + r^2 - 2Rr\cos\Psi]^{3/2}} \times \exp\{-k[(x_B - x_A)^2 + R^2 + r^2 - 2Rr\cos\Psi]^{1/2}\}\, dx_B\, dx_A\, d\Psi\, dr \quad (15)$$

where L_A and L_B are the lengths of zones A and B, respectively. Both of the coordinate variables x_A and x_B are along the axis of the cylinder.

Similarly, the view factor from the wall w_B, of zone B to the aerosol a_A in zone A can be expressed by

$$F_{w_B \to a_A} = \frac{k}{\pi L_B} \int_0^R \int_0^{2\pi} \int_{L_A}^{(L_A+L_B)} \int_0^{L_A} \frac{r(R - r\cos\Psi)}{[(x_B - x_A)^2 + R^2 + r^2 - 2Rr\cos\Psi]^{3/2}} \times \exp\{-k[(x_B - x_A)^2 + R^2 + r^2 - 2Rr\cos\Psi]^{1/2}\}\, dx_A\, dx_B\, d\Psi\, dr \quad (16)$$

If two zones are separated by a third zone, an equation with some modification is needed. In figure 5, for example, zones A and C are separated by

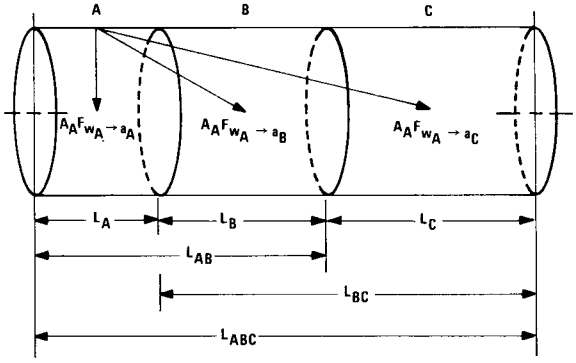

FIGURE 5.—*Radiative energy transfer to a zone separated by another zone.*

zone B. The view factors from the wall of zone A to the aerosol in zone C and from the wall of zone C to the aerosol in zone A can be expressed by

$$F_{w_A \to a_C} = \frac{k}{\pi L_A} \int_0^R \int_0^{2\pi} \int_0^{L_A} \int_{(L_A+L_B)}^{(L_A+L_B+L_C)} \frac{r(R - r\cos\Psi)}{[(x_C - x_A)^2 + R^2 + r^2 - 2Rr\cos\Psi]^{3/2}} \times \exp\{-k[(x_C - x_A)^2 + R^2 + r^2 - 2Rr\cos\Psi]^{1/2}\}\, dx_C\, dx_A\, d\Psi\, dr \quad (17)$$

and

$$F_{w_C \to a_A} = \frac{k}{\pi L_C} \int_0^R \int_0^{2\pi} \int_{(L_A+L_B)}^{(L_A+L_B+L_C)} \int_0^{L_A} \frac{r(R - r\cos\Psi)}{[(x_C - x_A)^2 + R^2 + r^2 - 2Rr\cos\Psi]^{3/2}} \times \exp\{-k[x_C - x_A)^2 + R^2 + r^2 - 2Rr\cos\Psi]^{1/2}\}\, dx_A\, dx_C\, d\Psi\, dr \quad (18)$$

respectively.

By examining equations (15) to (18), the following relationships are obtained:

$$A_B F_{w_B \to a_A} = A_A F_{w_A \to a_B} \tag{19}$$

$$A_C F_{w_C \to a_A} = A_A F_{w_A \to a_C} \tag{20}$$

For two adjacent cylinders, let $L_{AB} = L_A + L_B$. Then the relationship between the view factors can be expressed as

$$(AF_{wa})_{L_{AB}} = (AF_{wa})_{L_A} + (AF_{wa})_{L_B} + A_A F_{w_A \to a_B} + A_B F_{w_B \to a_A} \tag{21}$$

From equations (19) and (21) there is obtained

$$A_A F_{w_A \to a_B} = A_B F_{w_B \to a_A} = \tfrac{1}{2}[(AF_{wa})_{L_{AB}} - (AF_{wa})_{L_A} - (AF_{wa})_{L_B}] \tag{22}$$

or

$$L_A L_{w_A \to a_B} = L_B F_{w_B \to a_A} = \tfrac{1}{2}[L_{AB}(F_{wa})_{L_{AB}} - L_A(F_{wa})_{L_A} - L_B(F_{wa})_{L_B}] \tag{23}$$

The view factors F_{wa} for various length-to-radius ratios are available in figure 2.

If two zones of interest, such as zones A and C in figure 5, are not adjacent, the relationship between the view factors can be expressed by

$$L_A F_{w_A \to a_C} = L_A F_{w_A \to a_{BC}} - L_A F_{w_A \to a_B} \tag{24}$$

where a_{BC} represents the aerosol in adjacent zones B and C and can be considered to be a single zone of length L_{BC}. Equation (24) may be reduced to

$$F_{w_A \to a_C} = F_{w_A \to a_{BC}} - F_{w_A \to a_B} \tag{25}$$

The values of $F_{w_A \to a_{BC}}$ and $F_{w_A \to a_B}$ can be evaluated by equation (22). Similarly, there is obtained

$$F_{w_C \to a_A} = F_{w_C \to a_{AB}} - F_{w_C \to a_B} \tag{26}$$

For gray-wall systems, the view factors for gray walls are used in the above equations. The values of view factors can be obtained from

$$L_A f_{w_A \to a_B} = L_B f_{w_B \to a_A} = \tfrac{1}{2}[L_{AB}(f_{wa})_{L_{AB}} - L_A(f_{wa})_{L_A} - L_B(f_{wa})_{L_B}] \tag{27}$$

If equation (27) is written in energy terms, it becomes

$$q_{w_A \to a_B} = 2\pi R L_A f_{w_A \to a_B} \epsilon \sigma T_w^4 \tag{28}$$

The quantity $q_{w_A \to a_B}$ includes the radiation emitted and reflected from the wall of section A and absorbed directly by the aerosol in section B plus that portion absorbed from the reflected energy by the wall of section B but originally emitted and reflected from the wall of section A. In other words, the quantity $q_{w_A \to a_B}$ represents the additional portion of absorption due to the presence of section A.

NONISOTHERMAL EMISSION CONDITIONS

The view factors for a system having a black wall and a uniform absorbing medium have been discussed in a previous section. If the wall is not isothermal, the rate of radiant heat transfer cannot be evaluated by a simple expression such as that given by equation (1). The temperature term is not a constant, thus it cannot be removed from the integral function for the view factor. The equation for a nonisothermal wall system when the absorbing medium is still assumed to be constant may be written as

$$q_{w \to a} = \frac{\sigma k R}{\pi} \int_0^{2\pi} \int_0^R \int_0^{2\pi} \int_0^{L_a} \int_0^{L_w} \frac{\epsilon_w T_w^4 r(R - r\cos\Psi)}{[(x_w - x_a)^2 + R^2 + r^2 - 2Rr\cos\Psi]^{3/2}} \times \exp\{-k[(x_w - x_a)^2 + R^2 + r^2 - 2Rr\cos\Psi]^{1/2}\} dx_w\, dx_a\, d\Psi\, dr\, d\theta \tag{29}$$

where the wall temperature T_w is a function of x_w, Ψ, and θ, and ϵ_w is usually a function of T_w.

An analytical solution of equation (29) has to be obtained for each individual temperature condition. The integration procedure is very laborious even when T_w is only a simple function of x_w. Fortunately, the solution can be approximated by the results and analysis presented in the previous sections. The procedure of evaluating the rate of radiative heat transfer from a nonisothermal cylindrical system to an absorbing medium of constant extinction coefficient is demonstrated below. This procedure can be used for any conduit of uniform cross-sectional area provided that the view factors for isothermal conditions are available.

The temperature of a high-temperature conduit generally varies only longitudinally at steady state. The conduit may be so divided that each zone can be assumed to be isothermal. Of course, the number of zones is dependent on the temperature distribu-

tion. The length of each zone does not have to be identical. Uneven wall temperatures are generally attributed to three causes. One is that the wall is not evenly heated by the energy source; one is that the absorbing medium flows into the conduit with a greater temperature difference at the inlet than thereafter, and thus the heat transfer rates by convection and conduction are different from section to section; and the other is that the radiant energy received by the conduit wall itself is greater at the middle than at the ends where a large part of the radiation is lost. The temperature of an isothermal zone is uniform by definition but not exactly so for some actual conditions. A mean temperature could be used for each zone in these cases. The mean temperature of a cylindrical zone can be evaluated by

$$T_m^4 = \frac{\int_0^{L_z}\int_0^{2\pi} T^4 R\, d\theta\, dL}{\int_0^{L_z}\int_0^{2\pi} R\, d\theta\, dL} = \frac{1}{2\pi L_z}\int_0^{L_z}\int_0^{2\pi} T^4\, d\theta\, dL \qquad (30)$$

where L_z is the length of the zone.

The view factors among zones discussed in the last section apply to the conditions here because they do not depend on the wall temperature of the receiving zones except when the optical properties vary from zone to zone. Optical properties such as emissivity and reflectivity are functions of temperature and surface conditions. The value of emissivity of each zone is directly related to the output rate of radiant energy from that zone, so it should be used in the calculation for that zone. The reflectivity is assumed to be the same throughout the conduit so that view factors among zones for gray-wall systems can be used. Errors arising from this assumption are not significant because the total contribution of the reflective energy from other zones is small compared with that of direct radiation. Therefore, an average value of reflectivity may be used in all the graybody view-factor calculations. The emissivity of each zone is employed to calculate the energy emitted from its wall.

If a conduit is divided into n isothermal zones, the radiant energy transferred from the entire conduit wall to an arbitrarily chosen zone j can be expressed by the sum of the portion from each zone as

$$q_{w\to a_j} = q_{w_1\to a_j} + q_{w_2\to a_j} + \cdots + q_{w_j\to a_j} + \cdots + q_{w_n\to a_j} \qquad (31)$$

where $q_{w\to a_j}$ is the rate of radiant heat transfer from the conduit (which consists of all the isothermal zones) to the aerosol in zone j and $q_{w_i\to a_j}$ is the rate from the wall of zone i to the aerosol in zone j.

For black-wall systems, the quantities in equation (31) can be expressed by

$$q_{w_i\to a_j} = A_{w_i} F_{w_i\to a_j} \sigma T_{w_i}^4 \qquad (32)$$

where $q_{w_i\to a_j}$ and $F_{w_i\to a_j}$ are, respectively, the rate of radiative energy transfer and the view factor from the wall of zone i to the aerosol in zone j, and A_{w_i} and T_{w_i} are, respectively, the area and temperature of the wall of zone i.

For gray-wall systems, it may be written that

$$q_{w_i\to a_j} = A_{w_i} f_{w_i\to a_j} \epsilon_{w_i} \sigma T_{w_i}^4 \qquad (33)$$

where ϵ_{w_i} is the wall emissivity of zone i. The view factors can be obtained from figure 2 or equations (23) and (25). Thus the total rate of radiative energy transfer from the wall of all zones to the aerosol of all zones is

$$q_{w\to a} = \sum_{j=1}^{n} q_{w\to a_j} = \sum_{j=1}^{n}\left(\sum_{i=1}^{n} q_{w_i\to a_j}\right) \qquad (34)$$

APPROXIMATION FOR SYSTEMS OF VARIABLE EXTINCTION COEFFICIENT

When an absorbing medium flows through a heated conduit, its temperature rises as it moves forward. The extinction coefficient of the gaseous medium, if absorbant, will change according to the gas temperature. Particle concentration will be reduced as the carrier gas expands. In this case, an assumption of constant extinction coefficient is not applicable except when the conduit is short and a proper average value can be calculated.

Zoning techniques can be employed again. The absorbing medium is divided into several zones, each of which is assumed to be uniform in wall temperature and aerosol extinction coefficient. The radiative energy absorbed by a zone comes mainly from its own wall and the walls of neighboring zones. A practical example is given here in support of this contention. The length of each zone is chosen as the radius of the cylinder, and the wall is assumed to be black and isothermal. The aerosol in a zone at the center of a long conduit absorbs about ½ of the total absorption of that zone from its own wall and about ⅙ from each of the adjacent

zones when the average value of kR is 0.01. In this case, only about $1/12$ of the total absorption is from each side of this zone outside zones immediately adjacent.

In those cases where the extinction coefficient k is not the same in zone A and zone B, but is, say, k_A and k_B, respectively, the equations discussed previously cannot be applied without modification. The rate of radiative energy transfer mainly depends on two factors: The rate of radiative energy penetrating the boundary of the two zones and the absorption efficiency of the receiving zone with respect to the penetrated radiation. The former is independent of the characteristics of the receiving zone; i.e., the rate of radiative energy penetrating the boundary will be the same regardless of whether the receiving zone has the same extinction coefficient. The latter factor is a function of $k\bar{S}$ (ref. 6), where $\bar{S}$ is the mean beam length of the radiation penetrating the receiving zone.

Some view factors are defined as:

$F_{w_A \to a_B}(k_A, k_A)$ view factor from the wall of zone A to the aerosol in zone B when both zones have extinction coefficients of k_A

$F_{w_A \to a_B}(k_A, k_B)$ view factor from the wall of zone A to the aerosol in zone B when their extinction coefficients are k_A and k_B, respectively

$F_{wa}(k_A)_{L_A}$ view factor from the wall of zone A to the aerosol in zone A when the extinction coefficient is k_A

$F_{wa}(k_A)_{L_B}$ view factor from the wall of zone B to the aerosol of zone B when the extinction coefficient is k_A

$F_{wa}(k_A)_{L_{AB}}$ view factor from the walls of zone A and zone B to the aerosol in zone A and zone B when the extinction coefficient is k_A

$F_{wa}(k_B)_{L_B}$ view factor from the wall of zone B to the aerosol of zone B when the extinction coefficient is k_B

$F_{ww}(k_A)_{L_A}$ view factor from the wall of zone A to the wall of zone A when the extinction coefficient is k_A

The rate of radiative energy transfer from the wall of zone A to the aerosol of zone B, if the wall is black and the extinction coefficient is k_A in both zones, can be expressed by

$$q_{w_A \to a_B} = 2\pi R L_A F_{w_A \to a_B}(k_A, k_A)\, \sigma T_{w_A}^4 \qquad (35)$$

where

$$F_{w_A \to a_B}(k_A, k_A) = \frac{1}{2L_A}\left[L_{AB} F_{wa}(k_A)_{L_{AB}} - L_A F_{wa}(k_A)_{L_A} - L_B F_{wa}(k_A)_{L_B}\right] \qquad (36)$$

The rate of radiative energy transfer from the wall of zone B to the aerosol of zone A can, similarly, be expressed by

$$q_{w_B \to a_A} = 2\pi R L_B F_{w_B \to a_A}(k_A, k_A)\, \sigma T_{w_B}^4 \qquad (37)$$

where

$$F_{w_B \to a_A}(k_A, k_A) = \frac{1}{2L_B}\left[L_{AB} F_{wa}(k_A) L_{AB} - L_A F_{wa}(k_A)_{L_A} - L_B F_{wa}(k_A)_{L_B}\right] \qquad (38)$$

The rate of radiative energy transfer from the wall of zone A to the aerosol of zone B, if the extinction coefficients are k_A and k_B, respectively, can be expressed by

$$q_{w_A \to a_B} = 2\pi R L_A F_{w_A \to a_B}(k_A, k_B)\, \sigma T_{w_A}^4 \qquad (39)$$

where

$$F_{w_A \to a_B}(k_A, k_B) = \frac{1 - \exp(-k_B \bar{S}_{AB})}{1 - \exp(-k_A \bar{S}_{AB})} F_{w_A \to a_B}(k_A, k_A) \qquad (40)$$

The term $\bar{S}_{AB}$ is the mean beam length of the radiation in zone B which is emitted from the wall of zone A and penetrates into zone B. Its value is assumed to be the same for k_A and k_B since they usually do not differ greatly from one another (ref. 6). When the values of $k_A \bar{S}_{AB}$ are small, equation (40) can be simplified to

$$F_{w_A \to a_B}(k_A, k_B) = \frac{k_B}{k_A} F_{w_A \to a_B}(k_A, k_A) \qquad (41)$$

If the system consists only of zone A and zone B,

the total rate of radiative energy transfer is the sum of the rates to the aerosol in zone A and zone B. Letting T_{w_A}, k_A and T_{w_B}, k_B be the wall temperatures and extinction coefficients of zone A and zone B, respectively, the total rate of radiative energy transfer to the aerosol in the system can be expressed by

$$q_{w\to a} = (q_{w_A\to a_A} + q_{w_B\to a_A}) + (q_{w_A\to a_B} + q_{w_B\to a_B}) \tag{42}$$

where

$$q_{w_A\to a_A} = 2\pi R L_A F_{wa}(k_A)_{L_A}\sigma T_{w_A}^4 \tag{43}$$

$$q_{w_B\to a_A} = 2\pi R L_B \frac{1-\exp(-k_A\bar{S}_{BA})}{1-\exp(-k_B\bar{S}_{BA})} F_{w_B\to a_A}(k_B,k_B)\sigma T_{w_B}^4 \tag{44}$$

$$q_{w_A\to a_B} = 2\pi R L_A \frac{1-\exp(-k_B\bar{S}_{AB})}{1-\exp(-k_A\bar{S}_{AB})} F_{w_A\to a_B}(k_A,k_A)\sigma T_{w_A}^4 \tag{45}$$

$$q_{w_B\to a_B} = 2\pi R L_B F_{wa}(k_B) L_B \sigma T_{w_B}^4 \tag{46}$$

The values of the mean beam lengths $\bar{S}_{AB}$ and $\bar{S}_{BA}$ depend on the values of k_A, k_B, L_A, L_B, and R. If the quantity of $F_{A\to AB}(k_A)$, which is the portion of radiative energy emitted from the wall of zone A and received at the boundary of zone A and zone B, is known, then the value of $\bar{S}_{AB}$ can be estimated by

$$\bar{S}_{AB} = -\frac{1}{k_A}\ln\left[1-\frac{F_{w_A\to a_B}(k_A,k_A)}{F_{A\to AB}(k_A)}\right] \tag{47}$$

Similarly,

$$\bar{S}_{BA} = -\frac{1}{k_B}\ln\left[1-\frac{F_{w_B\to a_A}(k_B,k_B)}{F_{B\to AB}(k_B)}\right] \tag{48}$$

where $F_{B\to AB}(k_B)$ is the view factor from the wall of zone B to the boundary of zone A and zone B.

The view factors from the wall of a zone to the boundary adjacent to another zone can be evaluated by

$$F_{A\to AB}(k_A) = \tfrac{1}{2}[1-F_{wa}(k_A)_{L_A} - F_{ww}(k_A)_{L_A}] \tag{49}$$

and

$$F_{B\to AB}(k_B) = \tfrac{1}{2}[1-F_{wa}(k_B)_{L_B} - F_{ww}(k_B)_{L_B}] \tag{50}$$

The rates of radiative energy transfer between two zones of different wall temperatures and extinction coefficients can be calculated by the equations given above. The information obtained will be useful in evaluating total heat transfer at a local area if the local heat transfer coefficient is known.

Usually the extinction coefficient changes very little in a short distance. In this case, the assumption that neighboring zones have an extinction coefficient the same as the one being calculated is considered acceptable. Calculations then can be performed by employing the method of the preceding section. The curve parameter kR from the corresponding value of k in figure 2 will be used for each zone. For example, if k_j is the extinction coefficient of the medium in the jth zone, then the k_jR curves will be used to evaluate all the q values in equation (31). If the extinction coefficient decreases in the direction of the flow because of the thermal expansion of the carrier gas, then the actual radiative energy transferred to the jth zone from upstream zones is slightly lower than the calculated value and that from downstream zones is slightly higher. The errors, apparently both very small, are opposite and very nearly equal. The calculated results for unit zones determined by this approach are nearly exact for systems of constant wall temperature. For systems of violently changing extinction coefficient, however, errors are incurred, but other opposing factors change also and reduce the overall error. The results are believed to be sufficiently accurate for most practical calculations.

CONCLUDING REMARKS

The methods suggested in this study are of potential value in design applications because of their simplicity and versatility. The results presented in figures 2 and 3 for coaxial cylinders, square conduits, etc. are needed to apply this technique to geometries other than cylinders. View-factor values used in the equations should be determined by machine or other methods if high accuracy is desired.

REFERENCES

1. Hottel, H. C.; and Cohen, E. S.: Radiant Heat Exchange in a Gas-filled Enclosure: Allowance for Nonuniformity of Gas Temperature. Am. Inst. Chem. Eng. J., vol. 4, 1958, pp. 3–14.

2. ERKKU, H.: Radiant Heat Exchange in Gas-filled Slabs and Cylinders. Ph.D. thesis, Mass. Inst. Tech., 1959.
3. HOFFMAN, T. W.; AND GAUVIN, W. H.: An Analysis of Spray Evaporation in a High Temperature Environment. Can. J. Chem. Eng., vol. 39, 1961, pp. 179–188.
4. EINSTEIN, T. H.: Radiant Heat Transfer to Absorbing Gases Enclosed in a Circular Pipe with Conduction, Gas Flow, and Internal Heat Generation. NASA TR R–156, 1963.
5. KENG, E. Y. H.; AND ORR, C., JR.: Investigation of Radiant Heat Transfer to Particle-Seeded Gases for Application to Nuclear Rocket Engine Design. NASA CR–953, 1967.
6. KENG, E. Y. H.; AND ORR, C., JR.: Particle Size and the Rate of Radiant Heat Transfer to Gas-Suspended Particles. Power Technol., vol. 1, 1968, pp. 323–327.

Page intentionally left blank

SESSION V

NUCLEAR LIGHT BULB ENGINE

Chairman: **C. E. Franklin**

Page intentionally left blank

Investigation of Nuclear Light Bulb Startup and Engine Dynamics[1]

THOMAS S. LATHAM, HAROLD E. BAUER, AND RICHARD J. RODGERS
United Aircraft Research Laboratories

Analytical studies were conducted to determine the operating conditions of a nuclear light bulb engine during startup and the transient response of the engine to various perturbations at the nominal full-power operating level. The objectives of these studies were (1) to define the transient operating conditions during reactor startup with particular emphasis on temperature and critical mass characteristics, (2) to develop a digital simulation program for studying the dynamic response of the nuclear light bulb engine to perturbations occurring at full power, and (3) to use the simulation program to investigate the response of the engine to various perturbations and to identify parameters through which the engine could be controlled.

The purpose of this paper is to describe the dynamic characteristics of the uncontrolled nuclear light bulb engine at full-power operating conditions. The variations of critical mass and fuel and moderator average temperatures during engine startup are also discussed.

Additional details of these studies are presented in reference 1.

ENGINE CONCEPT

A sketch of the nuclear light bulb unit cavity is shown in figure 1. Neon buffer gas is injected tangentially from the transparent wall to drive a vortex. The neon spirals axially toward the end walls and is removed along with entrained fuel and fission products through a port at the center of one or both end walls.

An internally cooled fused-silica transparent wall isolates the neon buffer gas from the seeded hydrogen propellant. Fission energy deposited in the gaseous fuel cloud is transferred by thermal radiation through the transparent wall to the seeded hydrogen propellant. The seeded propellant passes through the annulus between the moderator and the transparent wall and is exhausted through a nozzle.

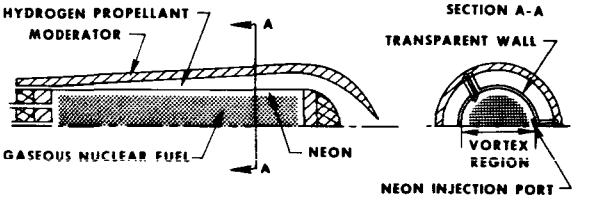

FIGURE 1.—*Nuclear light bulb unit cavity.*

REFERENCE ENGINE CONFIGURATION

Sketches depicting a reference engine configuration are shown in figure 2. Seven cavities are

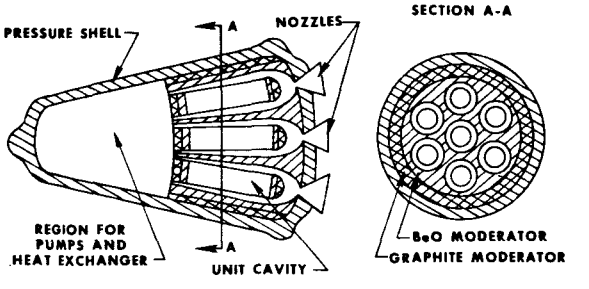

FIGURE 2.—*Nuclear light bulb engine.*

[1] This research was supported by the joint AEC–NASA Space Nuclear Propulsion Office under contracts NASw-847 and SNPC-70.

located in a beryllium oxide moderator, which is surrounded by an annular graphite reflector-moderator. The end-wall moderator region and a region which houses necessary pumps and heat exchangers are also shown in figure 2. An outer pressure vessel contains the entire configuration. The reference engine has the following performance characteristics: Cavity pressure, 500 atm; specific impulse, 1870 sec; thrust, 92 000 lb; engine power, 4600 MW; and engine weight, 70 000 lb.

A block diagram of the nuclear light bulb engine flow circuits is shown in figure 3. Fuel and neon

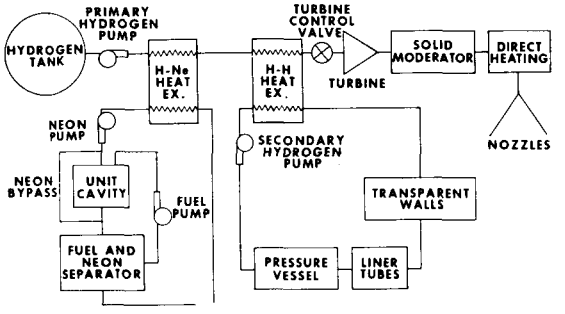

FIGURE 3.—*Nuclear light bulb flow diagram.*

buffer gas are separately pumped into the unit cavity. Neon bypass flow is added to the mixture of entrained fuel and fission products at the exit of the unit cavity. Condensed fuel is separated from the neon and is pumped back into the cavity. The neon is further cooled by transferring heat to the primary hydrogen circuit through the hydrogen-neon heat exchanger. The pressure vessel, cavity liner tubes, and transparent walls are cooled by a secondary hydrogen circuit which rejects heat to the hydrogen-hydrogen heat exchanger. The primary hydrogen is then expanded through a turbine which drives the fuel and coolant flow pumps. Heat from the beryllium oxide and graphite moderators is transferred to the primary hydrogen propellant before it enters the unit cavity.

ENGINE DYNAMICS MODEL

The principal assumptions made in the engine dynamics simulation are as follows:

Total power and radiating temperature:

$$P \approx n\sigma_f M_F$$

$$T^* \approx \sqrt[4]{P/S_F}$$

Reactivity feedbacks:

$$(\delta k/k)/(\delta M_F/M_F) = 0.348$$

$$(\delta k/k)/(\delta T_M/T_M) = 0.045$$

Stored nuclear fuel:

$$M_F \approx \rho_{B6} \frac{p_C}{T^*} \left(\frac{W_F}{W_B}\right)^{1.2}$$

Nuclear fuel injection rate:

$$W_F \approx A_F (p_F - p_C)^{0.5}$$

Primary propellant, choked flow:

$$\frac{W_P \sqrt{T_P}}{p_C} = \text{Constant}$$

A complete description of the simulation model is presented in reference 1. The engine power P is a time-dependent function of the neutron flux level n, the average fission cross section σ_F, and the contained fuel mass M_F. The surface radiating temperature T^* of the fuel cloud is proportional to $\sqrt[4]{P/S_F}$, where S_F is the radiating fuel surface.

The principal reactivity coefficients considered are associated with changes in the contained fuel mass M_F and the moderator temperature T_M. These coefficients were obtained from two-dimensional diffusion-theory perturbation calculations and from one-dimensional transport-theory calculations reported in reference 2. The positive temperature reactivity coefficient results from a non-$1/v$ variation of the ^{233}U fission cross section due to fission resonances in the 1.0- to 5.0-eV range.

It is estimated by using results of constant-temperature gas vortex tests that the average residence time of fuel in the cavity would be approximately 20 sec. Delayed neutron precursors which emit delayed neutrons at times greater than 20 sec after fission would, on the average, contribute no neutrons to the active volume of the core. This is similar to the circulating-fuel reactor, the important difference being that compressible gases are used in the nuclear light bulb engine, whereas incompressible liquid solutions are conventional for the circulating-fuel reactor. Because of this element of

compressibility, it is possible to have variations in the total fuel loading and fuel residence time which result from pressure, temperature, and fluid dynamic variations. Thus, the fraction of delayed neutrons which are lost from the active core and the total mass of the nuclear fuel within the active core are functions of time. This fact has a strong influence on the overall dynamic behavior of the engine.

The amount of stored fuel is assumed to be proportional to the product of the buffer gas density at the edge of the fuel region ρ_{BG} and the fuel to buffer-gas flow rate ratio to the 1.2 power $(W_F/W_B)^{1.2}$. This empirical relationship was obtained by fairing curves through experimental results from isothermal, two-component gas vortex tests reported in reference 3. Results of recent tests reported in reference 4 indicate that the exponent may be as low as 0.9. However, for small perturbations, this difference is not believed to be important. The buffer-gas density is related to the edge-of-fuel temperature and the chamber pressure according to the ideal gas law.

The nuclear-fuel injection rate W_F is proportional to the fuel injection valve flow area A_F and the square root of the difference between the fuel pump outlet pressure and the cavity pressure $(p_F - p_C)^{1/2}$.

It was assumed that the primary propellant flow is choked. Thus, the product of the propellant flow rate W_P and the square root of the propellant exit temperature divided by the chamber pressure $\sqrt{T_p}/p_C$ is equal to a constant for a constant-area nozzle. This condition was used to calculate the propellant flow rate.

DYNAMIC RESPONSES OF ENGINE

Figure 4 shows the calculated dynamic response of the nuclear light bulb engine to a $\delta k = \$1$ step reactivity perturbation. The fuel residence time t_F for this case was 20 sec. Power-level excursions with time for neutron lifetimes l^* equal to 0.5, 2.5, and 5.0 msec are shown in figure 4 (a). The power-level excursions were rapidly damped and the greatest power-level changes correspond to the condition having the shortest neutron lifetime. The slope of the initial power-level excursion is steepest for the case having the shortest lifetime. The magnitude of

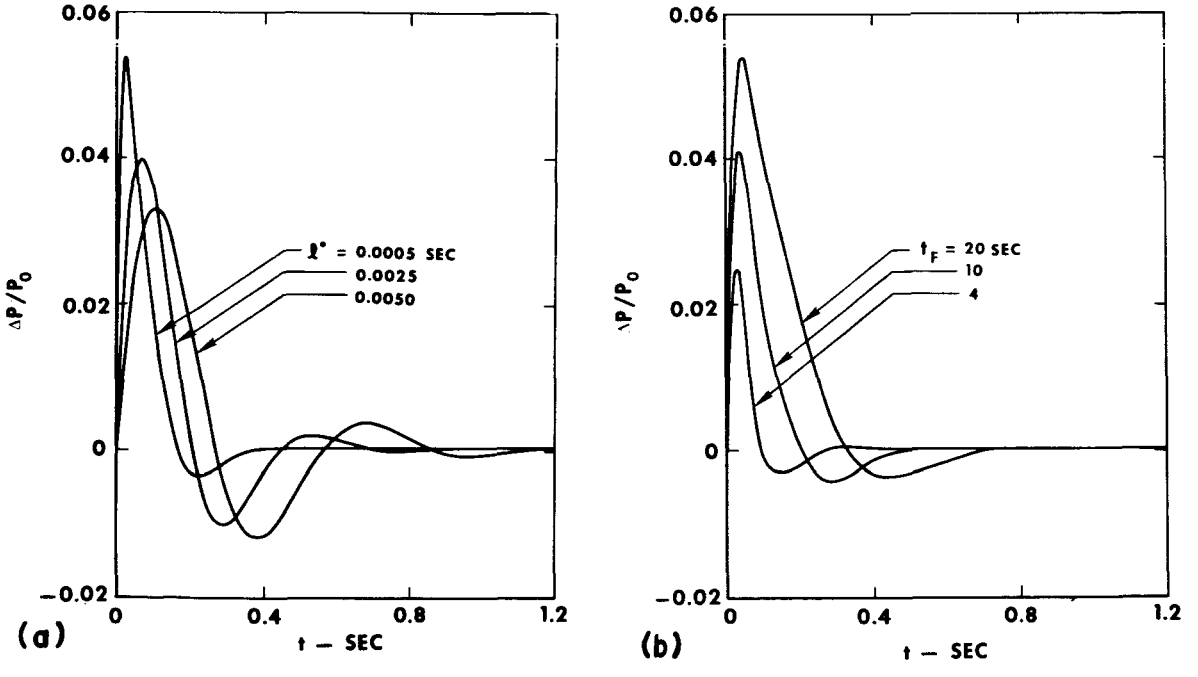

FIGURE 4.—*Power-level response of nuclear light bulb engine to step change in imposed reactivity.* (a) $\delta k = +\$1.00$; $t_F = 20$ *sec.* (b) $k = +\$1.00$; $l^* = 0.0005$ *sec.*

the power-level excursion is limited primarily because the increased chamber pressure associated with the power-level change causes a reduction of the injection rate of nuclear fuel into the cavity.

Calculated power-level responses are shown in figure 4(b) for a constant neutron lifetime of $l^* = 0.5$ msec, which is approximately the neutron lifetime expected in the reference engine. Results are shown for fuel residence times of $t_F = 4$, 10, and 20 sec for a $\delta k = \$1$ step change in imposed reactivity. The excursions in all cases are rapidly damped. The greatest power-level excursion occurs for the longest fuel residence time because the fuel is contained in the cavity for a longer time, and the time required for the amount of stored fuel in the cavity to decrease when the fuel injection rate decreases is greatest for the longest fuel residence time.

The results shown in figure 5 depict the nuclear pressure difference. For the results shown in figure 5, the initial pressure difference was assumed equal to 20 atm. After the step area change, the fuel injection rate adjusts to a new equilibrium value. Results are shown in figure 5(a) for a fuel residence time of 20 sec and for neutron lifetimes of 0.5, 2.5, and 5.0 msec. The shortest neutron lifetime resulted in the steepest power-level rise. However, this excursion is rapidly damped and resulted in the lowest maximum power-level change. The steady-state value of the power-level ratio $\Delta P/P_o$ approached 1.018 and the equilibrium chamber pressure increased from 500 to 503.45 atm.

Similar results for a neutron lifetime of 0.5 msec are shown in figure 5(b) for fuel residence times of 4, 10, and 20 sec. These engine responses are rapidly damped and approach different equilibrium values of the power-level ratio. The steepest

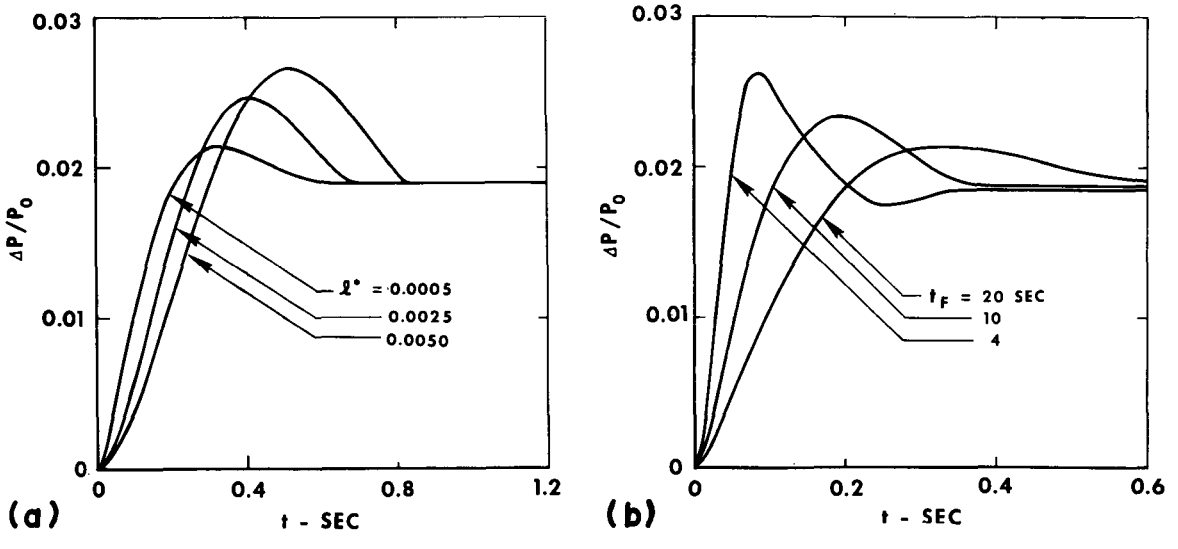

FIGURE 5.—*Power-level response of nuclear light bulb engine to step change in fuel-injection valve area.* (a) $A_F = 1.10\, A_{F_o}$; $W_F = K_F A_F (p_F - p_C)/20^{0.5}$; $t_F = 20$ *sec.* (b) $A_F = 1.10\, A_{F_{o_{0.5}}}$; $W_F = K_F A_F (p_F - p_C)/20$; $l^* = 0.0005$ *sec.*

light bulb engine responses to a step increase of 10 percent in fuel injection valve area A_F. The fuel injection rate is proportional to the product of the valve area and the square root of the ratio of the pressure difference between the fuel pump outlet and the chamber pressure at time t to the initial

rise occurs for the 4-sec fuel residence time (as expected) since more fuel is injected per unit time for the shorter residence time and the initial increase in contained mass in the cavity is greater following the step change in the fuel injection valve area.

ENGINE STARTUP

A study of engine startup characteristics was conducted using a simplified analytic model of the reference engine. The startup sequence used in the model is as follows: (1) Fill hydrogen ducts and neon system from storage to a pressure equal to approximately 20 atm; (2) turn on neon recirculation pump; (3) inject fuel until critical mass is reached; (4) increase power level and adjust flow rates and cavity pressure to maintain criticality and limit component temperatures to tolerable levels; (5) inject propellant seeds when 10 percent of full power is reached; and (6) increase power to desired operating level. The sequence of events during a startup power ramp was taken to be independent of the length of startup time, and in this analysis $t=0$ corresponds to a condition at which the reactor is critical but at zero power. It is assumed that the startup can be controlled so that power increases on a linear power ramp from zero to full power in a given time t. Initially, two linear power ramps were considered (60 and 600 sec long). It was also assumed that the fission energy was uniformly released throughout the volume of the gaseous fuel cloud. At low reactor power energy transfer is chiefly by convection, whereas at higher reactor power the energy released is transferred by thermal radiation. Since convective heat transfer processes are relatively inefficient at the low flow rates used during the early stages of the startup process, the fission energy is trapped in the fuel region and the fuel-cloud temperature rises rapidly.

The transient behaviors of the average fuel and average BeO moderator temperatures are shown in figure 6 for two linear startup power ramps. Note the rapid fuel temperature rise for both power ramps within the first few seconds when heat transfer by convection is dominant. Within 5 sec, the average fuel temperature is $\approx 12\,000°$ R. This temperature level is such that rapid fuel vaporization is assured. When heat transfer by thermal radiation becomes the dominant mode for energy removal, the fuel temperature rises as the fourth root of time or power, since power is proportional to time. The bends in the fuel temperature curves, which occur at a temperature of approximately 15 000° R, are indicative of the transition point to the radiation-dominated regime. The average

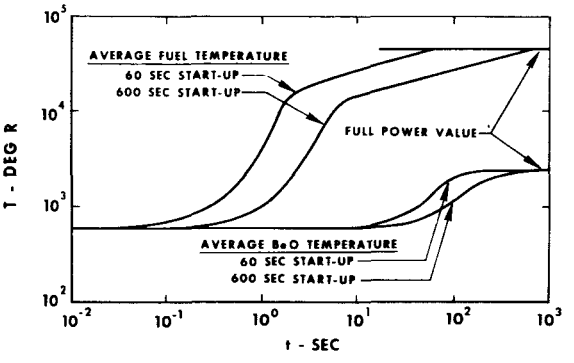

FIGURE 6.—*Average fuel and BeO temperature during startup power ramps.*

fuel temperature rises to approximately 45 000° R at full-power operation.

The lower curves in figure 6 illustrate the behavior of the BeO moderator temperature for both power ramps. The large moderator mass has a large heat capacity which causes the moderator temperature to rise more slowly than does the fuel temperature. The average moderator heat deposition rate is 10^5 Btu/sec during a linear power ramp, and 3×10^7 Btu are required to raise the temperature of the BeO and graphite moderators from 600° R to nominal operating values of 2400° and 3200° R, respectively. Thus, the solid moderator regions require approximately 300 sec to reach full-power operating conditions.

For the 60-sec startup ramp, the BeO moderator temperature greatly lags behind the fuel temperature, attaining its steady-state full-power value in approximately 300 sec. In the case of the 600-sec ramp, the BeO moderator temperature lags behind the fuel temperature in the initial stages of the startup; however, the BeO reaches its steady-state temperature after 600 sec because the startup time is long relative to the 300-sec moderator heating time.

For the 60- and 600-sec-long startup ramps, 2.7 and 27 percent, respectively, of the hydrogen propellant required for a nominal 20 min of full-power operation is consumed during startup; hence, the shortest possible startup time is desired. Since 85 percent of the energy transferred to the propellant is by direct radiation from the fuel cloud, the moderator-temperature lag associated with short startup times does not seriously affect the

propellant outlet temperature once full power is reached. Current calculations indicate that startup times on the order of 6 sec may be feasible.

Critical mass requirements for ^{233}U fuel are shown in figure 7 for 60- and 600-sec-long linear power ramps. A one-dimensional spherical model of the full-scale engine was used for this calculation. The calculated critical mass of ^{233}U varied from 18.6 lb at zero power to 30.9 lb at full power. For the 60-sec power ramp, the critical mass rises to 28.2 lb at full power and then further to 30.9 lb after 300 sec. This difference is caused by the time required for the bulk moderator temperature to rise to its steady-state value. For the 600-sec ramp, the critical mass reaches 30.9 lb when full power is reached. In this case the startup time is long compared with the moderator heating time, and the result is that full-power fuel loading and system temperatures and pressures are reached simultaneously after 600 sec.

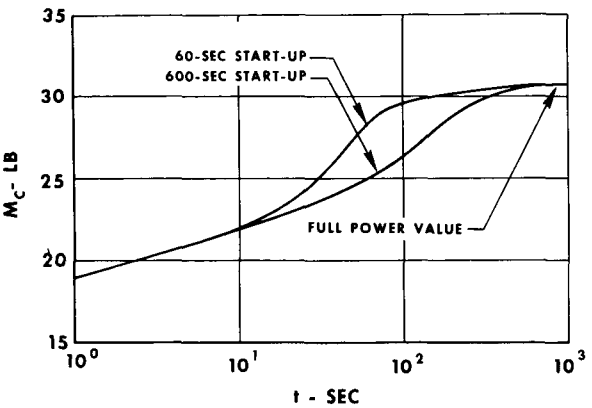

FIGURE 7.—*Variation of ^{233}U critical mass during startup power ramps.*

REFERENCES

1. LATHAM, T. S.; BAUER, H. E.; AND RODGERS, R. J.: Studies of Nuclear Light Bulb Start-Up Conditions and Engine Dynamics. Rept. H–910375–4, United Aircraft Res. Lab., Sept. 1969.
2. LATHAM, T. S.: Nuclear Studies of the Nuclear Light Bulb Rocket Engine. (Rept. G–910375–3, United Aircraft Res. Lab., Sept. 1968.) NASA CR–1315, 1968.
3. MENSING, A. E.; AND KENDALL, J. S.: Experimental Investigation of Containment of a Heavy Gas in a Jet-Driven Light-Gas Vortex. Rept. D–910091–4, United Aircraft Res. Lab., Mar. 1965.
4. MENSING, A. E.; AND JAMINET, J. F.: Experimental Investigations of Heavy-Gas Containment in R-F Heated and Unheated Two-Component Vortexes. Rept. H–910091–20, United Aircraft Res. Lab., Sept. 1969.

DISCUSSION

Podney: How does the pressure communicate between the inner light bulb region and the propellant region; do they equalize instantly?

Rodgers: Eventually we are going to have a control system with a short response time to balance the pressure on both sides.

Podney: In an uncontrolled system, what pressure does the wall experience during the initial power excursion?

Rodgers: Pressure pulses probably were of the order of 2 or 3 atm for our case.

Podney: Is that not enough to break the wall?

Rodgers: We have a short response time; the pressure between the propellant and the fuel region can be balanced.

Latham: With regards to the pressure pulse, what Richard Rodgers was referring to is that this is the total pressure rise in response to the power excursion. We have assumed in this model that we have a pressure balance system with a short response time relative to the power rise such that we shall limit pressure rises to about ⅔ atm across the transparent wall. We would like to have the transparent wall under a bursting load of about ¼ to ½ atm at all times.

Schultz: Am I correct in my understanding of your figures? You inserted a \$1 step change in reactivity and under the very worst possibility obtained only a 6-percent change in power. This seems somewhat incredible. Introducing some rough figures, say $\beta = 0.007$ within one lifetime (I think you used 5×10^{-4} sec), we should have power rising somethink like e^{15t}; this comes to much more than 6 percent in ½ sec. Have I missed something?

Rodgers: You must remember that this system does have control on it and, as I indicated before, the dominant mechanism for seizing this perturbation is the retardation of the fuel injection. This takes hold very quickly and contains it.

Schultz: That quickly?

Rodgers: Yes.

Calculations of the Spectral Emission From the Fuel Region of a Nuclear Light Bulb Reactor[1]

NICHOLAS L. KRASCELLA
United Aircraft Research Laboratories

Prior to the present study, most calculations of the flux of thermal radiation emitted from the uranium fuel region of a gaseous-core nuclear reactor have assumed that the emitted radiation originates from a gray gas at the assumed edge-of-fuel temperature (refs. 1 and 2). Subsequent calculations indicated that the spectral distribution of thermal radiation differed appreciably from that of a blackbody. However, the effects of changes in the heavy-atom model parameters (used to describe the composition and spectral properties of the nuclear fuel) on the emitted spectral flux were not assessed; similarly, the effects of the addition of seed gases on the emitted flux were not studied.

An additional problem arises in considering radiation emitted from the fuel region in an axial direction. Axially directed radiation would impinge upon highly reflecting end walls in the full-scale engine. It was anticipated that a large fraction of the incident flux would be reflected. Obviously, a large flux of reflected radiation would significantly alter the edge-of-fuel temperature and the temperature distribution in the outer layer of fuel facing the reflecting wall. No estimates of the effect of highly reflecting end walls on the spectral distribution of radiant flux emitted from the fuel region had been made before the current investigation.

Accordingly, a program was formulated to determine the effect on the spectral radiation emitted from the fuel region of a nuclear light bulb engine of, (*a*) changes in the heavy-atom model parameters, (*b*) addition of a seed gas, and (*c*) inclusion of reflective end walls. The program is described in detail in reference 3.

[1] This research was supported by the joint AEC–NASA Space Nuclear Propulsion Office under contracts NASw–847 and SNPC–70.

ANALYTICAL METHOD

Because of the high fuel opacity, the radiation spectrum emitted from the fuel region of a nuclear light bulb engine is controlled by conditions existing in the outermost layer of the region. At the temperatures and pressure anticipated in the full-scale engine, the dominating region is typically a few cm in depth. Thus, the region controlling spectral radiation emission may be considered as a plane-parallel gas layer containing a relatively low concentration of nuclear fuel. Since low nuclear-fuel density in the edge-of-fuel region precludes extensive energy release by nuclear fission in this region, the outermost layer of fuel is characterized by a constant total energy flux at all points within the region.

The spectral distribution of emitted flux may be estimated by use of a transport analysis of the radiative transfer process. The radiation flux profile is a function of the temperature distribution in the outer fuel layer as well as of the composition and spectral absorption coefficients of the nuclear fuel. These fuel properties are functions of both pressure and temperature.

Iterative Procedure

The temperature and corresponding radiative flux profiles were determined for a specified fuel concentration profile utilizing existing one-dimensional UARL simplified gray-gas and spectral transport computer codes. A distribution of Rosseland mean opacity as a function of temperature was

assumed for a specified fuel partial pressure variation with position in the fuel region. These mean opacity data, a specified total heat flux Q^* (constant throughout the medium), and an edge-of-fuel temperature were used as input for the simplified gray-gas computer code to calculate a temperature profile using the optically thick approximation. The estimated temperature profile and a specified fuel partial pressure distribution were used as input for the spectral transport computer code to calculate the corresponding fuel absorption coefficients and the spectral flux distribution at each position within the outer layer of the fuel. Finally, the spectral fluxes at each position were integrated to ascertain the total integrated flux Q_i. If the integrated flux Q_i and the total flux Q^* did not agree to within 5 percent the assumed mean opacity distribution was modified and the procedure repeated. Approximately 10 iterations were required to achieve convergence.

The edge-of-fuel temperatures required to initiate the calculations were determined by application of the "temperature jump approximation" described in reference 4.

Unit Cavity Configuration and Conditions

A fuel-containment region 0.681 ft (20.75 cm) in radius at a total pressure of 500 atm was selected for the radiation emission analysis of the nuclear light bulb engine unit cavity schematically depicted in figure 1. It was assumed that nuclear

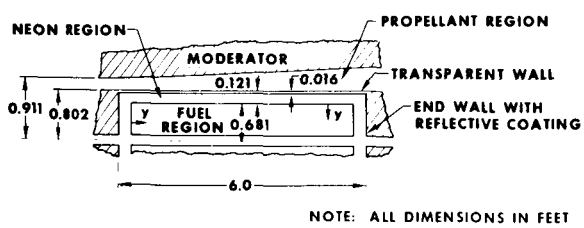

FIGURE 1.—*Unit cavity of a nuclear light bulb engine.*

fuel existed at a constant pressure of 200 atm from the centerline or core of the containment region out to a radius of 0.3405 ft (10.38 cm). At radial positions beyond 0.3405 ft, the fuel partial pressure decreased linearly to a pressure of 0.01 atm at the edge-of-fuel position. The fuel partial pressure profile is graphically illustrated in figure 2. Note

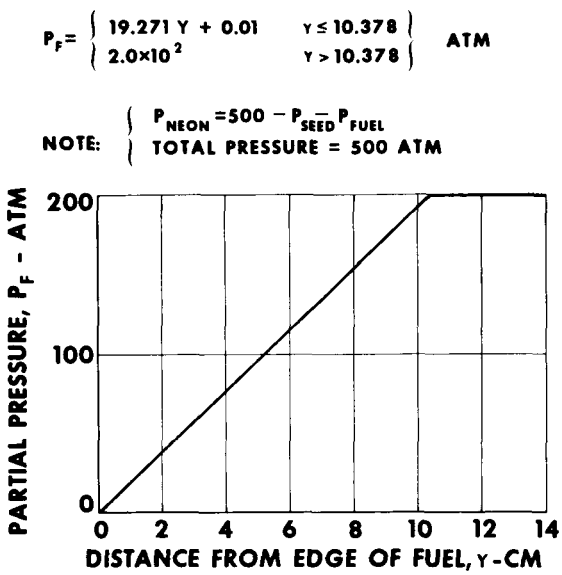

FIGURE 2.—*Assumed nuclear fuel partial-pressure distribution.*

that the distance y in the fuel region is measured from the edge-of-fuel position ($y=0$) inward to the centerline ($y=20.75$ cm) for analysis of the spectrum emitted radially outward. For analysis of the spectrum emitted in an axial direction, y is measured in the axial direction. The difference between the total pressure of 500 atm and the fuel partial pressure at any position was attributed to neon (the absorption of the neon was neglected) and any seed present in the system.

All calculations were made for an assumed effective radiating temperature T^* of 15 000° R (8333° K) which corresponds to an effective total radiative blackbody flux Q^* of 24 300 Btu/ft² sec (2.757×10^{11} erg/cm² sec).

Note that the calculated fluxes represent radiation leaving the fuel region and do not account for possible absorption of radiation in the buffer-gas region. In effect, the calculations represent an upper limit to the radiative flux incident upon the transparent containment wall or the reflective end walls.

Description of Cases

The analytical method, cavity configuration, and conditions described in preceding paragraphs were employed in all subsequent calculations of the spectral distributions of radiative energy emanating

from the fuel region of a nuclear light bulb engine.

The heavy-atom model (refs. 5 and 6) was required in order to calculate the requisite composition and spectral absorption characteristics of the nuclear fuel as a function of temperature and pressure for use as input in the spectral transport machine code. Six cases are discussed herein. In cases 1 and 2, the continuum-type oscillator distribution function was employed to define transition probabilities in the line region of the fuel spectrum. With the continuum approximation, distinct line structure in heavy-atom spectra is ignored and the absorption coefficients are slowly varying functions of wave number (see refs. 5 and 6 for details). Cases 1 and 2 differ in the fuel species ionization potentials employed. The uranium ionization potentials for case 1 are termed the low set and were of the following magnitude: 6.1, 11.46, 17.94 and 31.14 eV (private communication from J. T. Waber, D. Liberman, and D. T. Cromer of the Los Alamos Scientific Laboratory dated June 1966); similar ionization potentials for case 2 are termed the high set and were of the following magnitude: 6.1, 17.1, 38.8, and 65.6 eV (ref. 7).

In case 3, the low ionization potentials of case 1 were retained; however, a band-type oscillator strength distribution function was used in the heavy-atom model. In the band-type oscillator strength distribution function, transition probabilities in the line region are approximated by summing known oscillator strengths for various uranium lines over wavelength intervals of 200 Å. The method is described in reference 8 and is an approximation designed to account for line structure in the fuel spectrum.

The effect of hydrogen seed gas on the emitted flux was examined in case 4.

Cases 5 and 6 consider end-wall effects in which a fraction of the energy emitted from the fuel region in an axial direction could be reflected back into the fuel. In both cases, the heavy-atom-model parameters of case 1 were incorporated. In case 5, a uniform end-wall reflectivity of 0.50 was assumed at all wavelengths. In case 6, the end walls were considered to be aluminum and the spectral reflectivity of aluminum (refs. 9 through 12) was used in the system.

SPECTRAL EMISSION FROM THE NUCLEAR FUEL REGION

Calculated Temperature Distributions Near Edge of Fuel

Final temperature distributions as a function of distance from the edge of fuel for all cases examined are shown in figure 3. Cases 1, 2, and 3 demonstrate the effect of changes in the heavy-atom model parameters on the temperature distribution. Comparison of curves for cases 3 and 4 in figure 3 shows the effect on the temperature distribution of the addition of 10 atm of hydrogen to the fuel region as a seed gas. The same heavy-atom model parameters were used for both cases. The curves in figure 3 for cases 5 and 6 exhibit the anticipated increase in edge-of-fuel temperature as a result of reflection of radiation from the end walls.

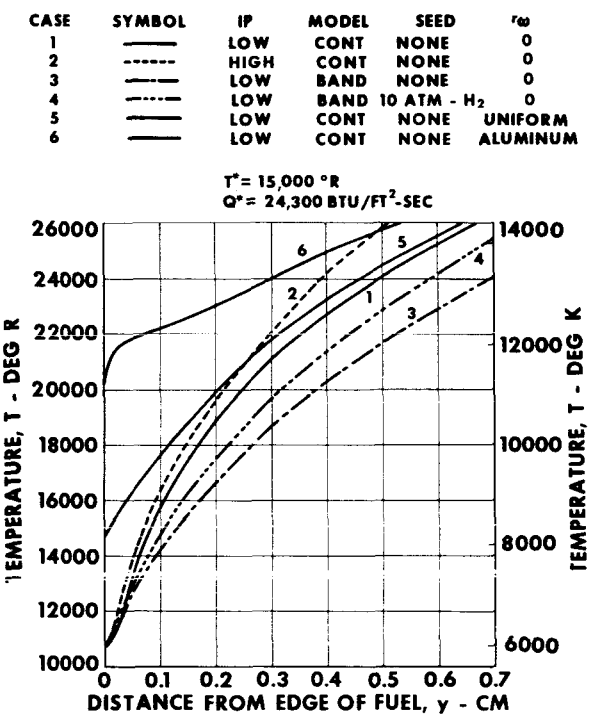

FIGURE 3.—*Final temperature distributions in outer layer of fuel region for various cases.*

Effects of Changes in Heavy-Atom Model Parameters on Calculated Fuel Spectrum

Typical spectral absorption coefficients for edge-of-fuel conditions are shown in figure 4 for cases

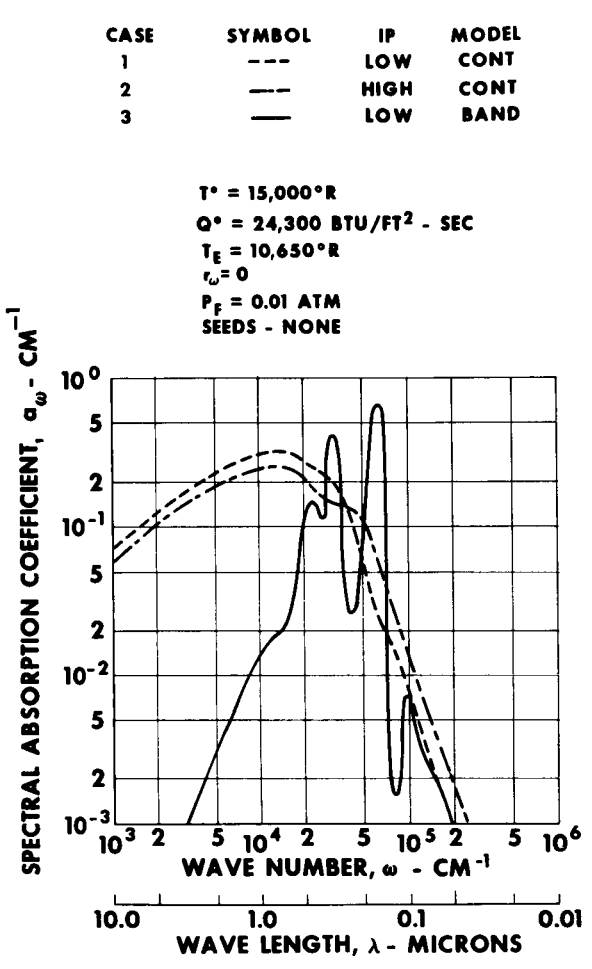

FIGURE 4.—*Typical fuel spectral absorption coefficients at edge-of-fuel conditions.*

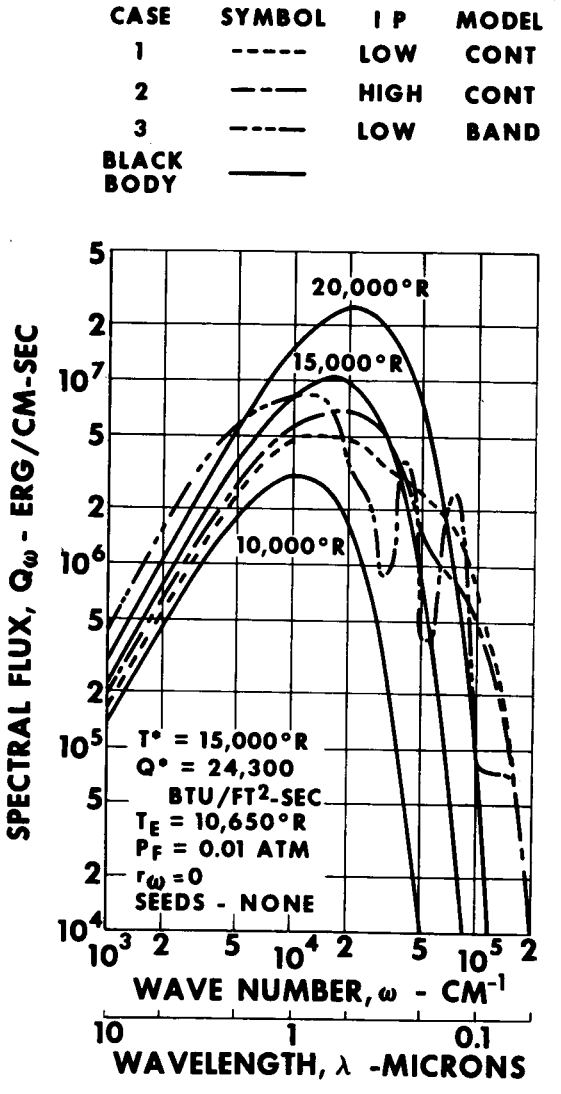

FIGURE 5.—*Typical spectral-flux distributions emitted from nucelar fuel region.*

1, 2, and 3. These absorption coefficients and absorption coefficients for conditions at various positions within the fuel were required as input to the spectral transport code. Similar spectral absorption coefficient results were obtained for cases 4 through 6.

In figure 5, the effect of variations in the heavy-atom model parameters on the spectral flux emitted from the fuel region are illustrated. In cases 1 and 2, by using the continuum oscillator strength distribution function in the heavy-atom model and different ionization potentials only moderate differences in the spectral energy distribution curves are noted as shown in figure 5. In case 3, the low ionization potentials and a band-type oscillator strength distribution function were used in the heavy-atom model. More pronounced changes appear in the spectral flux distribution than those noted between cases 1 and 2. The spectral flux for case 3 exceeded that of a blackbody at a temperature of 15 000° R for wave numbers between 1.0×10^3 and 1.0×10^4 cm^{-1} (wavelengths between 10.0 and 1.0 μ). The smoothly varying spectral flux distribution observed for cases 1 and 2 was also

noted for case 3 up to a wave number of 1.0×10^4 cm^{-1} (wavelength 1.0 μ). However, the spectral structure noted for the case 3 spectral absorption coefficient distribution (e.g., fig. 4) influences the spectral flux distribution in figure 5 at wave numbers between 1.0×10^4 and 1.0×10^5 cm^{-1} (wavelengths between 1.0 and 0.1 μ). Two "windows" are observed in figure 5 at wave numbers of approximately 3.0×10^4 and 5.5×10^4 cm^{-1} (wavelengths at 0.33 and 0.182 μ). Similarly, two peaks in the spectral flux distributions are observed at wave numbers of 4.0×10^4 and 7.5×10^4 cm^{-1} (wavelengths at 0.25 and 0.133 μ). In general, the spectral flux for case 3 was less than that for a 15 000° R blackbody between wave numbers of approximately 1.0×10^4 and 7.0×10^4 cm^{-1} (wavelengths at 1.0 and 1.14 μ). The peak at a wave number of 4.0×10^4 cm^{-1} (wavelength at 0.25 μ) was about equal to the 15 000° R blackbody flux. For wave numbers greater than 5.5×10^4 cm^{-1} (wavelengths less than 0.33 μ), the emitted spectral flux exceeds that of a 15 000° R blackbody.

The spectral flux results in figure 5 for cases 1, 2, and 3, and the spectral flux results for a blackbody at the indicated temperatures (10 000°, 15 000°, and 20 000° R), were used to estimate relative fractional-flux distributions. These results (relative fractional fluxes) are plotted as a function of wave number in figure 6. The curves indicate the fraction of the radiation emitted in any wave number interval relative to the total flux radiated over all wave numbers. The results illustrated in figure 6 show that considerably more energy is radiated in the ultraviolet spectral region by the nuclear fuel than by a blackbody at a temperature of 15 000° R (8333° K). For example, the fraction of total energy radiated by a 15 000° R (8333° K) blackbody in the wave-number interval between 50 000 and infinity (wavelengths between 0.2 and 0 μ) is 2.5×10^{-2}, which is equivalent to a flux of 6.08×10^2 Btu/ft^2 sec. The relative fraction of emitted energy from the nuclear fuel is 2.5×10^{-1} (6.08×10^3 Btu/ft^2 sec) for case 3.

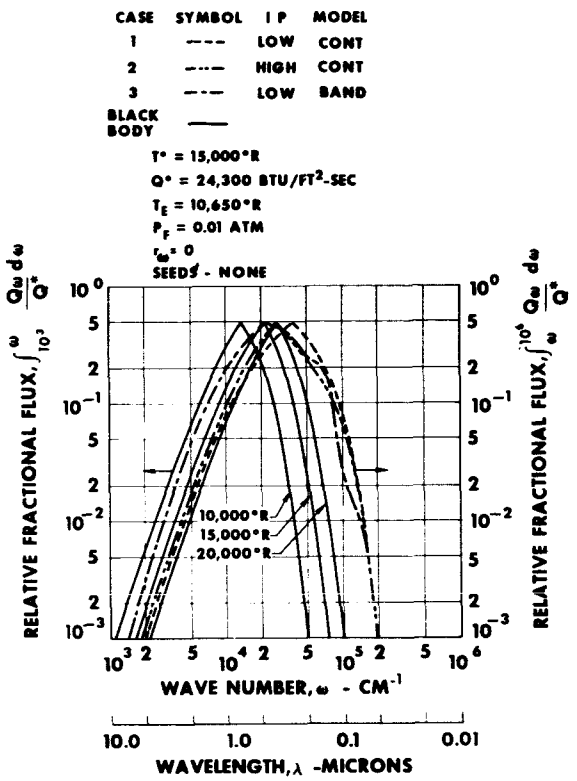

FIGURE 6.—*Relative fractional-flux distributions at edge of fuel for cases 1, 2, and 3.*

Effects of Seed Gases on Fuel Spectrum

The preceding results indicate that a substantial fraction of the radiation emitted from the nuclear fuel region occurs at wave numbers where the spectral absorption coefficient of the surrounding transparent walls increases (at wave numbers greater than approximately 5.0×10^4 cm^{-1}, or wavelengths less than 0.2 μ). Thus, the energy incident upon the wall due to radiation from nuclear fuel (i.e., with no seed) would cause unacceptable heating of the transparent wall.

One method for reducing the energy in the ultraviolet region of the spectrum is to add a seed gas to the fuel region. There are several possible candidate gases. At this time, calculations have been made only for 10 atm of hydrogen added to the fuel region. Typical spectral absorption coefficients for the nuclear fuel and hydrogen at the edge-of-fuel conditions are shown in figure 7. The solid curve for case 4 represents the calculated spectral absorption coefficient of 10 atm of hydrogen at the edge-of-fuel temperature of 10 650° R. The sharp peak in the solid curve at a wave number of approximately 82 000 cm^{-1} is due to the Lyman α line of atomic hydrogen. Note that the Lyman α

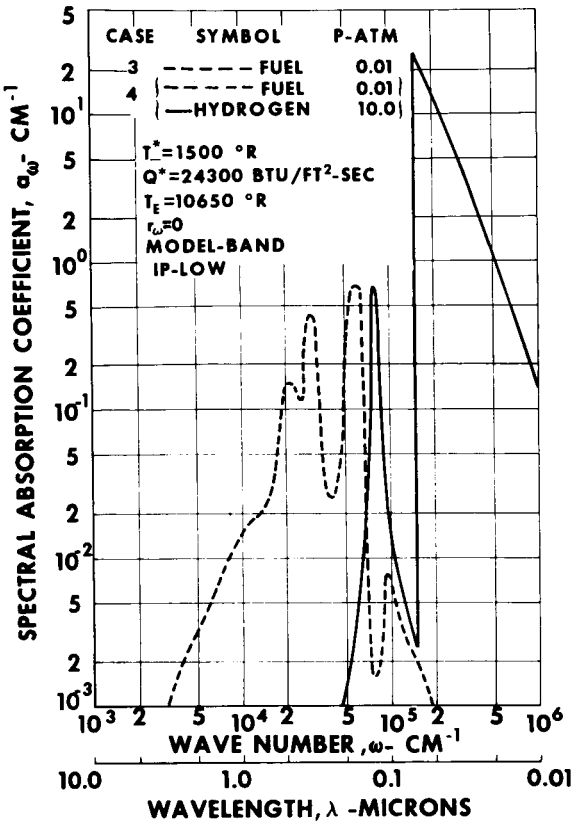

FIGURE 7.—*Spectral absorption coefficients at edge of fuel for cases 3 and 4.*

line partially fills in the valley in the fuel absorption coefficient at a wave number of 0.75×10^4 cm^{-1} (0.13 μ). The continuum at wave numbers greater than 1.0×10^5 cm^{-1} is due to the Lyman bound-free absorption of atomic hydrogen.

Results of the spectral flux analyses are shown in figure 8 for cases 3 and 4 as the relative fractional-flux distribution. The curves in figure 8 indicate the reduction in the relative fractional flux in the ultraviolet spectral region that can be obtained upon addition of 10 atm of hydrogen seed gas.

The results also suggest that seeding with other selected gases would further reduce the quantity of radiation emitted in the critical region at wave numbers beyond approximately 5×10^4 cm^{-1} (wavelengths less than 0.2 μ). Two promising seed materials are diatomic oxygen and water vapor, both of which are very opaque at wavelengths less than 0.2 μ (wave numbers greater than 50 000 cm^{-1}).

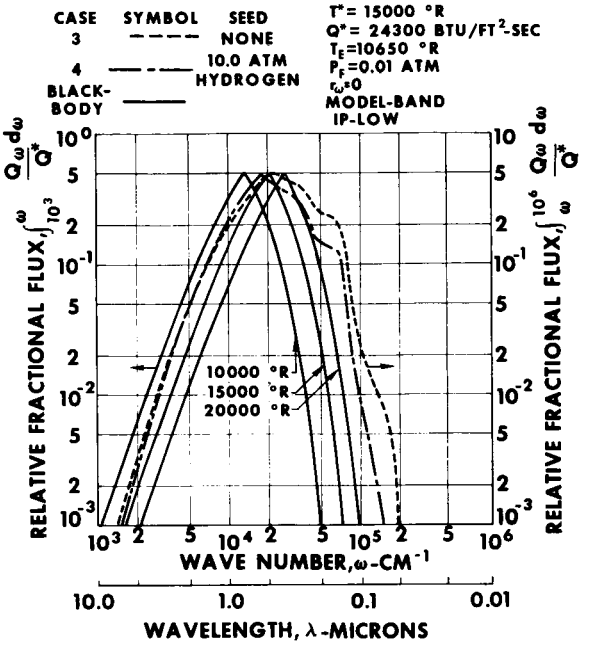

FIGURE 8.—*Relative fractional-flux distributions at edge of fuel for cases 3 and 4.*

Typical spectral absorption coefficients for 10 atm of oxygen at the edge-of-fuel conditions are shown in figure 9. They suggest that oxygen might be effective in reducing the fraction of radiation emitted from the fuel in the critical wave number region above 5×10^4 cm^{-1}. The primary difficulty is that molecular hydrogen and oxygen tend to dissociate at high temperatures, although preliminary calculations indicate that there will be a significant fraction of undissociated molecules at temperatures of interest. Even if these molecules should dissociate at high temperatures, they would provide a protective blanket between the fuel and the wall at lower temperatures to protect the wall from overheating due to absorption of ultraviolet radiation. Additional calculations of the effect of seed addition, including consideration of chemical reactions between the seeds and the nuclear fuel, are being made.

Effects of End-Wall Reflectivity on Axial Fuel Spectrum

In cases 5 and 6 the heavy-atom model configuration of case 1 was used to examine the effects of wall reflectivity on the spectral flux emitted from

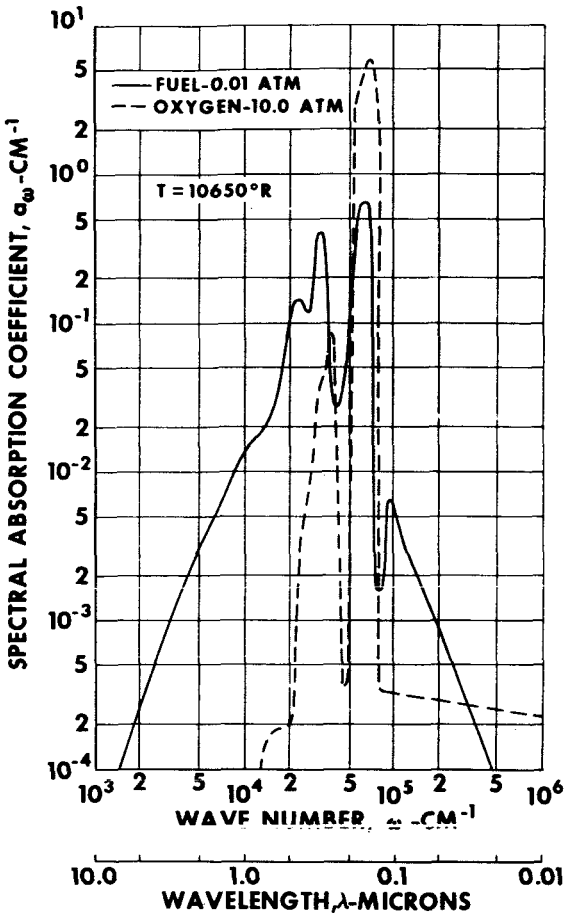

FIGURE 9.—*Comparison of spectral absorption for nuclear fuel and oxygen at edge-of-fuel conditions.*

the fuel region. A uniform reflectivity of 0.5 was used for all wave numbers for case 5, while the spectral reflectivity of aluminum was used for case 6. Relative fractional flux distributions are shown in figure 10 for cases 1, 5, and 6. The results in figure 10 show that the high reflectivity of aluminum in the visible and infrared spectral region shifts the distribution of emitted radiation toward the ultraviolet spectral region.

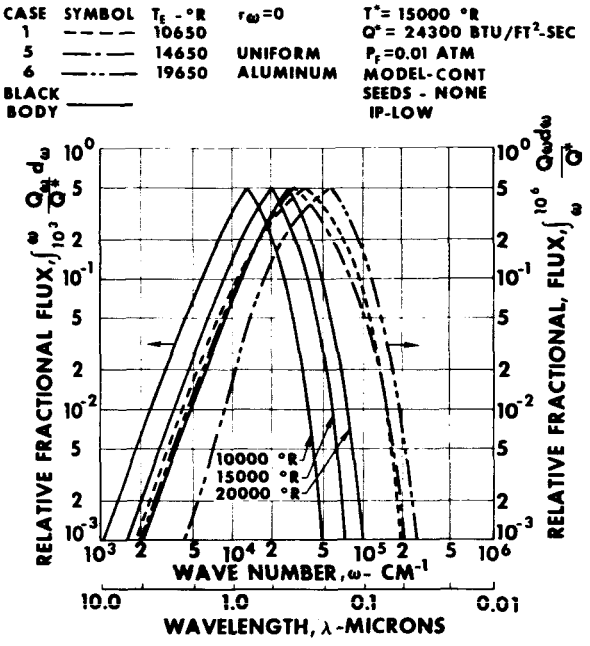

FIGURE 10.—*Relative fractional flux distribution at edge of fuel for cases 1, 5, and 6.*

CONCLUSIONS

The following conclusions can be drawn from an investigation of the spectral radiation emitted from the fuel region of a nuclear light bulb engine:

(1) The spectral distribution of radiative flux emitted from the fuel region of a nuclear light bulb engine differs appreciably from that of a blackbody at a temperature of 15 000° R (8333° K). If no seeds are employed, the spectral distribution from the fuel region is shifted to higher wave numbers (shorter wavelengths).

(2) Addition of a seed gas such as hydrogen tends to attenuate the radiation emitted in the ultraviolet region of the spectrum.

(3) Use of end walls with reflective coatings such as aluminum tends to shift the spectral distribution of radiated energy to higher wave numbers (shorter wavelengths) for a given total flux emitted from the fuel.

REFERENCES

1. KESTEN, A. S.; AND KINNEY, R. B.: Theoretical Effect of Changes in Constituent Opacities on Radiant Heat Transfer in a Vortex-Stabilized Gaseous Nuclear Rocket. Rept. D-910092-5, United Aircraft Res. Lab., Sept. 1965.

2. KESTEN, A. S.; AND KRASCELLA, N. L.: Theoretical Investigation of Radiant Heat Transfer in the Fuel Region of a Gaseous Nuclear Rocket Engine. (Rept. E-910092-9, United Aircraft Res. Lab., Sept. 1966.) NASA CR-695, 1967.

3. KRASCELLA, N. L.: Theoretical Investigation of the Radiant Emission Spectrum From the Fuel Region of a Nuclear Light Bulb Engine. Rept. H-910092-12, United Aircraft Res. Lab., Oct. 1969.
4. DEISSLER, R. G.: Diffusion Approximation for Thermal Radiation in Gases with Jump Boundary Condition. J. Heat Transfer, vol. 7, no. 4, 1967.
5. KRASCELLA, N. L.: Theoretical Investigation of the Spectral Opacities of Hydrogen and Nuclear Fuel. Rept. RTD TDR-63-1101, U.S. Air Force Systems Command, prepared by United Aircraft Res. Lab., Nov. 1963.
6. KRASCELLA, N. L.: Theoretical Investigation of the Opacity of Heavy-Atom Gases. Rept. D-910092-4, United Aircraft Res. Lab., Sept. 1965.
7. WILLIAMSON, H. A.; MICHELS, H. H.; AND SCHNEIDERMAN, S. B.: Theoretical Investigation of the Lowest Five Ionization Potentials of Uranium. Rept. D-910099-2, United Aircraft Res. Lab., Sept. 1965.
8. KRASCELLA, N. L.: Theoretical Investigation of the Absorptive Properties of Small Particles and Heavy-Atom Gases. (Rept. E-910092-7, United Aircraft Res. Lab., Sept. 1966.) NASA CR-693, 1966.
9. BENNETT, H. E.; ET AL.: Infrared Reflectance of Aluminum Evaporated in Ultra-High Vacuum. J. Opt. Soc. Am., vol. 54, no. 9, Sept. 1968, p. 1089.
10. COLE, T. T.; AND OPPENHEIMER, F.: Polarization by Reflection and Some Optical Constants in the Extreme Ultraviolet. Appl. Opt., vol. 1, 1962, p. 709.
11. MADDEN, R. P.; ET AL.: On the Vacuum Ultraviolet Reflectance of Evaporated Aluminum Before and During Oxidation. J. Opt. Soc. Am., vol. 53, no. 5, May 1963, p. 620.
12. HASS, G.; ET AL.: Influence of Purity, Substrate Temperature and Aging Conditions on the Extreme Ultraviolet Reflectance of Evaporated Aluminum. J. Opt. Soc. Am., vol. 47, no. 12, Dec. 1957, p. 1070.

DISCUSSION

Kerrebrock: In the last case you showed, what fraction of the total energy is going into those aluminum walls when you shift the spectrum that much?

Krascella: Offhand I don't know—100 percent of it would be 24 300 Btu.

Park: Could you comment on the line profile, especially in relation to the uncertainty in the pressure broadening such as stark broadening, and how it affects your calculations, especially in the visible range which is important for your radiant energy transfer.

Krascella: Essentially, what we do is to look at intensities or known oscillator strengths. Then we group these into 200-Å intervals.

Park: Then how do you convert that information to emission?

Krascella: We have a distribution of oscillator strength. We also have a model which gives us an energy level scheme.

Park: So you bypass the curve of growth?

Krascella: That is right.

Park: Can you comment on how close this approximation would be to the exact calculation employing the curve of growth?

Krascella: You cannot really because we do not calculate a line profile in the program as such. It is an average spectral absorption coefficient over 200-Å wavelength intervals.

Park: As I understand it, any approximation in radiative transfer programs is notoriously poor and always tends to overestimate the amount of heat transfer. This is an experience in all radiative transport calculations. More typically, these heat transfer calculations would overestimate by a factor of 4 even when you use the exact line-by-line calculation, including the line width.

McLafferty: The width of the lines, because of the high pressure of the neon, is so great that it is much more than the spacing between the lines. Thus, you would never see individual line structure but a completely broadened line, which means that it effectively acts as a continuum with the amount of absorption averaged depending of the oscillator spectrum in that region.

Park: Yes, I understand that in the core region. But the question is, what happens at the interface where the electron density is low and the partial pressure of uranium is low?

Krascella: The total pressure is still 500 atm throughout that region.

Park: Yes; but the absorption is still mainly due to uranium and, in that case, the line would be so thin that there would be a discrepancy between the line-by-line calculation and such an average calculation.

Miller: I have a comment on this question. I do not believe the stark broadening theory as now formulated can be applied to these uranium lines simply because there are inner shell transitions and the theory is not applicable in a direct way to those transitions. We, in our experiments, have tried to get at least a rough estimate of the stark broadening but our limit in detectability would be about 0.1 Å for this broadening and electron densities as high as $10^{17}/cm^3$. We have not been able to detect any broadening.

Park: You probably have to worry about line width.

Krascella: What you are speaking about is undoubtedly very true; nevertheless, I would not like to do this calculation with 300 000 lines of uranium. Undoubtedly you can use a better approximation at lower temperatures. We just have not done it yet.

Patch: You would not have to do such a calculation for 300 000 lines because Parks has a statistical theory that treats all these lines and I have an effective absorption coefficient approximation which is also statistical which is compatible with Parks' theory of uranium opacity.

Bauder: Maybe I misunderstood your model, but isn't it surprising that you had more intensity at the short wavelength than that of a blackbody? In your last figure you

had a blackbody curve and a uranium curve for 20 000° R and at the low-wavelength end the uranium was higher. Is that correct?

Krascella: No, because actually you are looking into the gas at considerably higher temperatures. Effectively what you are seeing is where the holes in the uranium absorption coefficient are at the edge of the fuel with radiation streaming from somewhere in the interior which is at a higher temperature.

Bauder: I see.

Page intentionally left blank

Development of a High-Intensity RF Radiant Energy Source for Simulating the Thermal Environment of the Nuclear Light Bulb Reactor[1]

WARD C. ROMAN

United Aircraft Research Laboratories

Experimental and theoretical investigations are being conducted at the United Aircraft Research Laboratories to obtain information necessary for determining the feasibility of several gaseous-core nuclear rocket engine concepts. The principal results obtained to date from research on the vortex-stabilized nuclear light bulb concept are presented in reference 1. Figure 1(a) shows a cross section

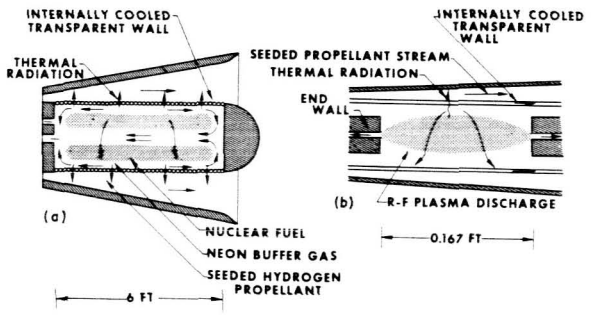

FIGURE 1.—*Nuclear light bulb concept and radiant energy source configuration.* (a) *Cross section of unit cavity.* (b) *Radiant energy source.*

of one of seven unit cavities that would comprise the engine. Heat is transferred by thermal radiation from gaseous nuclear fuel, contained in a radial-inflow vortex, through an internally cooled transparent wall to seeded hydrogen propellant flowing in the annulus surrounding the cavity. The hydrogen is seeded with submicron-sized metal particles to increase its opacity. High-purity fused silica appears suitable for the wall material. Neon buffer gas is injected tangent to the inner surface of the transparent wall to drive the vortex which serves to isolate the gaseous fuel from the transparent wall. A mixture of neon and fuel is withdrawn at the center of one end wall and is processed through a recirculation system. The flow pattern in the region occupied by the nuclear fuel is characterized by well-defined recirculation cells with a radial stagnation surface at a large radius (ref. 2). A relatively laminar flow exists within the central region inside the radial stagnation surface. Because of wall shear and jet mixing, some turbulence may exist close to the peripheral wall. The purpose of the neon buffer gas is to prevent diffusion of the nuclear fuel and fission products to this region.

In the current experiments to develop a non-nuclear radiant energy source capable of producing total radiant energy fluxes within the range expected in nuclear light bulb engines, a high-power, high-pressure, radio-frequency (rf) plasma discharge is used (see fig. 1(b)). The source geometry and flow pattern are similar to those of the engine; i.e., an internally cooled transparent wall, a pair of end walls, and a radial-inflow vortex are used. Figure 1 also shows the significant dimensions for both configurations.

A steady-state source radiating with a total flux equal to that of a blackbody between 8000° and 15 000° R is required. Figure 2 shows these simulation requirements together with the corresponding heat fluxes in various units. The broken curves in figure 2 show the variation of total power radiated

[1] This research was supported by the joint AEC–NASA Space Nuclear Propulsion Office under contracts NASw-847 and SNPC-70.

T*- DEG R	RADIANT HEAT FLUX		
	KW/IN.^{2}	KW/CM^2	BTU/SEC-FT^2
8000	14.4	2.23	1967
15,000	177.8	27.58	24,289

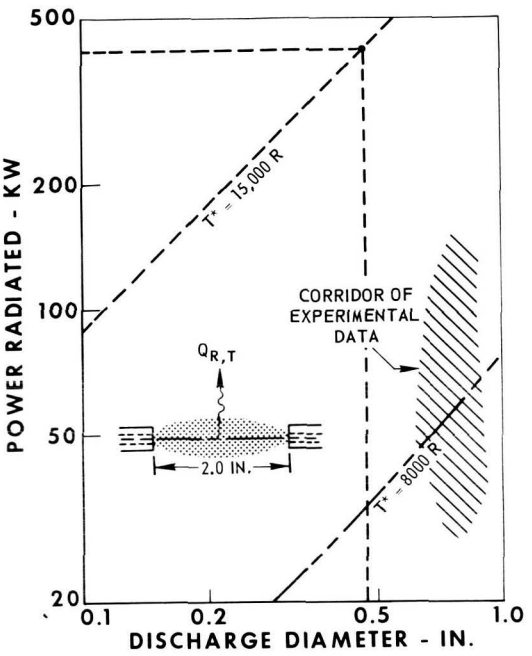

FIGURE 2.—*Radiant energy source requirements.*

from the ellipsoidally shaped rf plasma discharge with discharge diameter (measured at the mid-plane). The upper curve represents the heat flux corresponding to the reference engine described in reference 1, whereas the lower curve represents that of a lower power, derated engine. The source design goal is denoted by the circle in figure 2. For an ellipsoidally shaped plasma source with a major axis of 2 in. and a minor axis of approximately 0.5 in., about 430 kW of radiated power is required to provide a radiant energy flux corresponding to that of a blackbody at 15 000° R. Results obtained to date with the rf plasma radiant energy source are shown by the shaded area in figure 2. A maximum of 156 kW of steady-state power was radiated from the small plasma source.

The purpose of this paper is to describe the major results of the radiant energy source development experiments that have been conducted to date. Further details and discussion are presented in reference 3.

DESCRIPTION OF EQUIPMENT

A specially designed 1.2-MW rf induction heater, developed as part of the United Aircraft Research Laboratories sponsored research program, provides the necessary power input for the radiant energy source. The rf output power is supplied by two power-amplifier tubes which drive a resonant tank circuit of unique design. The resonator section and load are located within a large (approximately 5-ft diam) cylindrical aluminum test tank. The resonator section consists of two arrays of vacuum capacitors; each array is connected to a single-turn work coil.

Figure 3 shows details of the test section. The

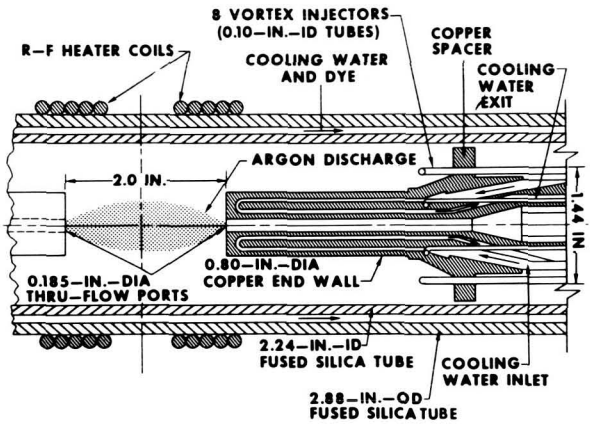

FIGURE 3.—*Details of source test region.*

two single-turn rf heater work coils shown each consist of five water-cooled copper tubes. The i.d. of the coils is 3.06 in. and they are silver plated to reduce heating caused by the high rf coil currents. The operating frequency of the system of approximately 5.5 mHz was chosen to provide high coupling efficiency of the rf power into the plasma discharge. A pair of concentric water-cooled fused silica tubes are located within the rf heater work coils. These tubes form a water-cooled transparent wall through which the plasma discharge radiates. In order to reduce the intense radiation to the components within the test tank, particularly during high-power, high-pressure operation, known concentrations of an organic dye are added to the cooling water. Two cylindrical water-cooled copper end walls spaced 2.0 in. apart provide the end-wall boundary simula-

tion (see fig. 1). These 0.80-in.-diam end walls are concentric with the fused silica tubes. The faces of the end walls were polished to increase their reflectivity. Argon is injected through stainless-steel vortex injectors (fig. 3) to establish the desired radial-inflow vortex flow pattern. The argon is exhausted through ports at the center of each end wall.

A low-power dc arc is used to start the rf discharge. The arc is drawn between two retractable electrodes entering through the through-flow ports. This technique permits moderately high power level rf discharges to be started at pressures between 1.0 and 5.0 atm in less than 40 msec.

Figure 4 shows a side view of the test tank. The

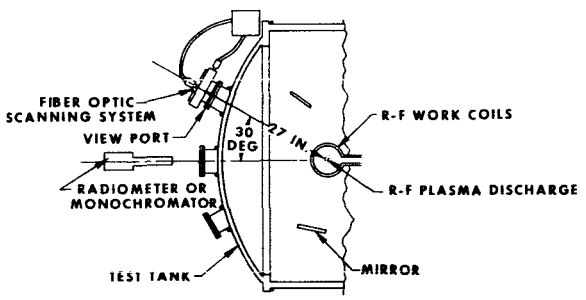

FIGURE 4.—*Schematic of test tank and diagnostic instrumentation.*

front dome of the tank contains five 4-in.-diam windows which allow observation of the test section from different angles. The instrumentation used permits determination of the discharge diameter, shape, and stability using a fiber optic scanning system. Both still and high-speed photography (up to 8000 frames/sec) are used. Mirrors located within the test tank permit observation of the discharge from several angles. The total radiation from the plasma and its distribution within various wavelength bands are determined using a specially constructed radiometer and filter assembly. The radial distribution of temperature within the discharge has been determined in a few tests from measurements using a scanning monochromator. During each test complete calorimetric measurements are taken which allow an energy balance to be made on each water-cooled component of the entire system. The total run time at a given test condition ranges from a few minutes to greater than an hour depending on the test condition.

DISCUSSION OF RESULTS

The effects of varying the power in the discharge on the discharge geometry are shown in figure 5.

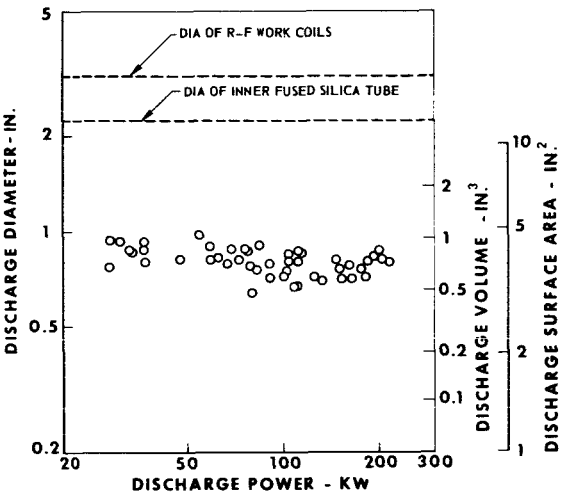

FIGURE 5.—*Geometric characteristics of radiant energy source.* $P_D = 2$ *to 16 atm;* $W_A = 0.010$ *to 0.041 lb/sec.*

The discharge diameter was measured at the axial midplane. Data are shown for the power levels up to 216 kW (the maximum achieved to date). For reference, the two horizontal broken lines in figure 5 indicate the location of the i.d. of the rf heater work coils and the i.d. of the inner fused silica tube. Within the range of the data shown, the 2-in.-long discharge could be maintained in a relatively laminar, stable geometry with diameters ranging between approximately 1.0 and 0.6 in. The corresponding argon weight flow rates and chamber pressures ranged from 0.01 to 0.041 lb/sec and from 2 to 16 atm, respectively. The chamber pressure, argon flow rate, and discharge power were found to be interrelated in determining the most stable operating conditions. For a fixed chamber pressure and power level, the discharge diameter was dependent upon the argon flow rate. In some tests large diameters were obtained by decreasing the argon flow rate until indications of turbulence appeared at the boundary of the plasma. The discharge volume and

surface area were calculated by assuming an ellipsoidally shaped discharge of the diameter and length indicated in figure 5. These volumes and areas were used in computing power densities and radiant energy fluxes.

Figure 6 illustrates typical distributions of temperature within the discharge. These data were obtained using the monochromator, optical system, and test procedures described in reference 3. The temperatures were determined from measurements of the chordal variation of intensity of the argon 4158.59-Å spectral line. The broken curve corresponds to a relatively low-power, low-pressure test condition. The solid curve corresponds to an approximate factor-of-2 increase in both total power deposited and pressure. For these data the argon weight flow was adjusted to keep the discharge diameter approximately constant. The peak temperature in each case occurred off axis at approximately the midradius location. This off-axis peak may be attributed to the mechanism of power deposition into an rf plasma. Calculations were made to estimate the degree of self-absorption present over the test range for the 4158.59-Å line. The results indicate that self-absorption is negligible.

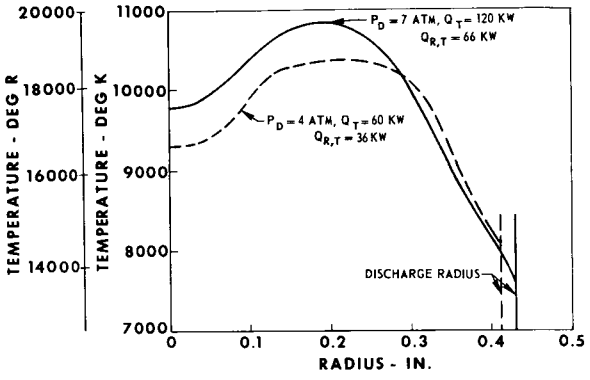

FIGURE 6.—*Typical radial distribution of temperature obtained in rf discharges. Argon 4158.59 Å line.*

Figure 7 shows results of tests to determine the variation of power density with discharge power. For reference, lines of constant discharge volume for two plasma sources with different diameters, each 2 in. long, are shown. The maximum power density achieved was 328 kW/in.^{3} and was limited solely by the operating capability of the 1.2-MW rf induction heater (an overheating problem in the resonator section). From modifications recently completed, future increases in power density can be expected. Comparison of these power densities with results reported in the literature is difficult because of differences in test configurations and flow regimes. However, the maximum power density achieved to date (328 kW/in.^{3}) is more than an order of magnitude greater than any results reported in the literature for a steady-state, rf argon plasma discharge.

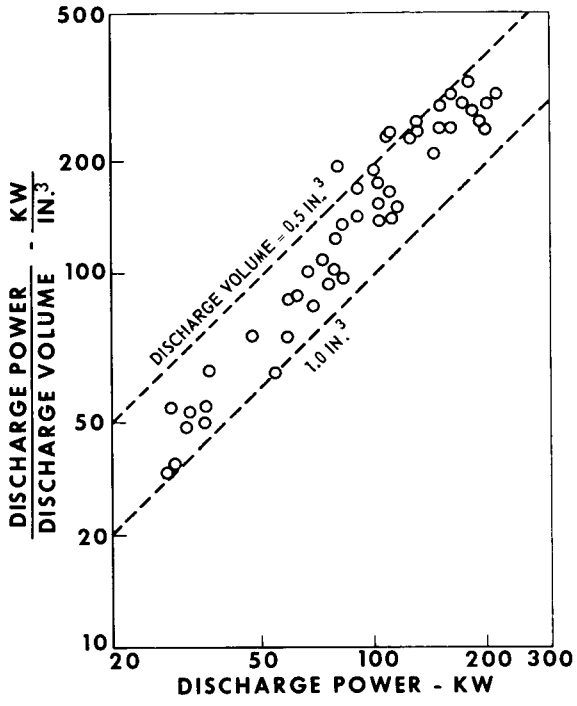

FIGURE 7.—*Variation of discharge power density with discharge power.* $P_D = 2$ *to 16 atm;* $W_A = 0.010$ *to 0.041 lb/sec.*

For each of the data points shown in figure 7, the radiant energy flux at the surface of the discharge was calculated. Estimates were made of the amount of conduction-convection heating of the inner transparent wall (ref. 3). For example, at the highest power input of 216 kW into the plasma discharge, approximately 5 percent of the total energy was transmitted through the inner transparent wall by conduction. Figure 8 shows the vari-

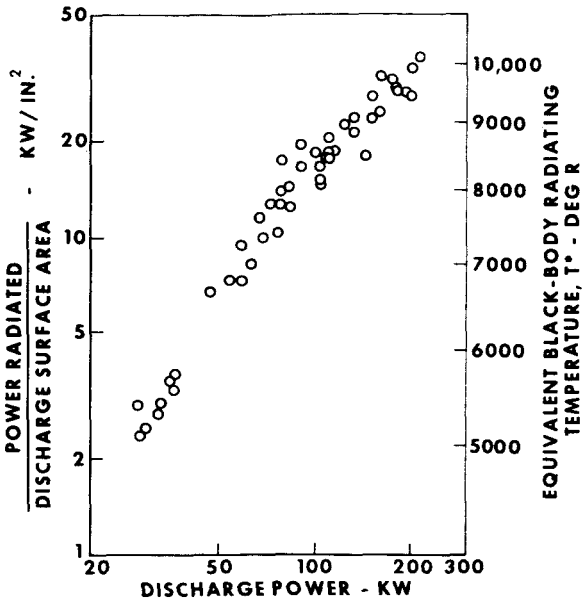

FIGURE 8.—*Variation of radiant energy flux with discharge power.* $P_D = 2$ *to 16 atm;* $W_A = 0.010$ *to 0.041 lb/sec.*

ation of radiant energy flux with discharge power for the data previously shown in figure 7. To aid in comparing the results obtained to date with desired simulation requirements, the equivalent blackbody radiating temperature is shown on the right-hand ordinate of figure 8. Recall that the heat flux in the reference engine design corresponds to 15 000° R and the flux in a derated engine might correspond to as low as 8000° R. The highest level of radiant energy flux achieved in the tests to date was 36.7 kW/in.², which corresponds to an equivalent blackbody radiating temperature of 10 200° R.

Both increased discharge power and increased chamber pressure will be required to achieve higher flux levels. The effect of chamber pressure on the energy radiated was observed by attempting to hold all variables approximately constant except chamber

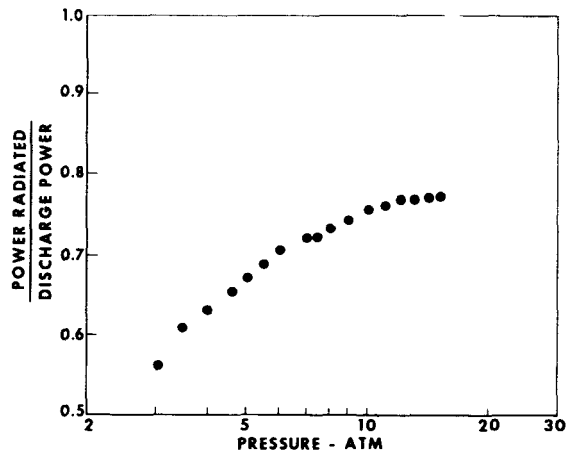

FIGURE 9.—*Effect of chamber pressure on fraction of power radiated.* $Q_T = 50$ *to 116 kW;* $W_A = 0.015$ *lb/sec.*

pressure. Figure 9 shows results for the pressure range from 3 to 15 atm. For the test results shown, the argon weight flow was held constant at 0.015 lb/sec, but the total discharge power increased from 50 to 116 kW. It was not possible to maintain all variables except chamber pressure constant and still maintain a satisfactory discharge except over a limited range. This may be due to the geometric characteristics of the rf plasma discharge in the vortex flow field and is related to the coupling between the discharge and the electrical and magnetic fields producing the discharge. As a result, the thermal and electrical characteristics of an rf plasma depend directly on the combined effects of flow patterns and heat transfer mechanisms within the test chamber. Figure 9 shows that the fraction of power radiated increased significantly with increasing pressure. At 16 atm, which is the maximum pressure level achieved to date, radiation efficiencies approached 80 percent. Tests to increase the pressure further are currently in progress.

REFERENCES

1. McLAFFERTY, G. H.: Investigation of Gaseous Nuclear Rocket Technology—Summary Technical Report. Rept. H-910093-46, United Aircraft Res. Lab., Nov. 1969.
2. CLARK, J. W.; JOHNSON, B. V.; KENDALL, J. S.; MENSING, A. E.; AND TRAVERS, A.: Open-Cycle and Light-Bulb Types of Vortex Stabilized Gaseous Nuclear Rockets. J. Spacecraft Rockets, vol. 5, no. 8, Aug. 1968, pp. 941–947.
3. ROMAN, W. C.; KLEIN, J. F.; AND VOGT, P. G.; Experimental Investigations to Simulate the Thermal Environment, Transparent Walls, and Propellant Heating in a Nuclear Light Bulb Engine. Rept. H-910091-19, United Aircraft Res. Lab., Sept. 1969.

DISCUSSION

Kylstra: Have you experienced any deposits on the inner core cylinder from your electrodes or other materials?

Roman: We did initially because of the dc starting procedure, and this is what was optimized. Concerning our long run time we do, periodically, take out the inner core and examine it quite closely for such things as thermal stress or contamination. This is one of the distinct advantages of the rf source over, for example, a dc source where there is electrode contamination. Our walls are maintained quite clean and true both in the sources shown and in the transparent-wall model tests.

Kylstra: You attribute this mainly to your inward flowing vortex?

Roman: The fluid mechanical pattern is very important in both this and the ellipsoidally shaped plasma.

Park: Have you ever noticed a pressure difference between the outer edge and the center within your cylinder?

Roman: Within the plasma discharge?

Park: While in operation.

Roman: We have not made any pressure measurements except for the chamber pressure.

Park: Yes; I mean that your configuration would afford some confinement, with the plasma acting as a secondary coil and the primary coils being the rf exciting coils. The resulting $\mathbf{J} \times \mathbf{B}$ force would force the plasma to pinch and it would create a higher pressure inside. This is similar to the ordinary pinch device. But the effect will be more dominant than in the pinch device because you have the high particle density, and therefore, if you have chosen the parameters right, you should see increased pressure in the center. This is just the opposite of an MHD centrifuge so that you have an MHD force to create a high pressure region in the center and this may open up a road to confine the plasma in the middle instead of toward the edge.

Roman: The calculations have been made concerning both the fluid mechanical aspect and the magnetic pressure. This has been shown to be negligible for our case. I think that in some of the tests that have been conducted by Arthur Mensing in supporting research more emphasis has been placed on looking at the pressures and the distributions, whereas the goal here has been to develop a very intense source to be used for other test programs and not so much the detailed diagnostics at this time. I think Mr. Mensing has some information pertinent to that since calculations have been carried out.

Bauder: Could you comment on the spectral distribution of your source with respect to the spectral distribution of the previous paper?

Roman: The cutoffs on our filter system are such that we break down into four bands: 0.22 to 0.3, 0.3 to 0.72, 0.72 to 1.0, and 1.0 to 1.3 μ, which is the cutoff at the other end. I calculated the spectral distribution and compared it with that of Nick Krascella. We are significantly higher, as would be expected, in the visible regime of 0.72 to 1 μ; he had a factor of 15 to 20 percent as compared with 40 to 45 percent in our case. There are plans to tailor and shift this spectrum closer to the results of his updated calculations at some future date.

Experiments for Simulating the Absorption of Thermal Radiation in the Propellant Duct of a Nuclear Light Bulb Reactor[1]

JOHN F. KLEIN
United Aircraft Research Laboratories

Experiments are being conducted to simulate the absorption of thermal radiation in the propellant duct of a nuclear light bulb reactor. The objectives of this research are (1) to develop methods for injecting solid particle seeds into a simulated propellant stream, (2) to make effective use of buffer layers to prevent coating of the duct walls, and (3) to absorb a large percentage of incident radiation from a high-intensity light source in a simulated propellant stream.

This paper includes a discussion of the results obtained in initial experiments described in reference 1 and describes experiments that are presently being conducted.

ENGINE CONCEPT

Figure 1 is a sketch showing part of a unit cavity of a full-scale nuclear light bulb engine. The cavity is rotationally symmetric about the centerline. The complete engine is formed by a cluster of seven such cavities. Energy is transferred by thermal radiation from the gaseous nuclear fuel to hydrogen propellant flowing in an annulus surrounding the fuel region. An internally cooled transparent wall separates the fuel region from the propellant region and serves as the inner wall of the propellant duct. The outer wall of the propellant duct has a highly reflecting surface to reduce the heat load to the moderator material.

The hydrogen propellant is essentially transparent to thermal radiation at propellant temperatures below 14 000° R at the engine operating pressure of 500 atm. Therefore, a seed material must be added to the propellant to provide opacity at lower temperatures. Studies reported in references 2 through 7 have shown that the ideal seed material should be submicron-sized particles of a high-melting-point, high-boiling-point metal such as tungsten. Buffer layers of unseeded hydrogen adjacent to each of the propellant duct walls are also required to prevent degradation of the optical properties of the two walls due to coating by the seed material. For the tests discussed herein, argon seeded with carbon was used as the simulated propellant. Carbon was used as the seed because it is readily available and comparatively easy to handle and disperse; moreover, the optical properties of dispersed carbon are known.

[1] This research was supported by the joint AEC–NASA Space Nuclear Propulsion Office under contracts NASw–847 and SNPC–70.

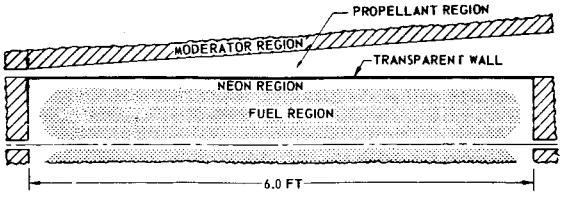

FIGURE 1.—*Sketch of nuclear light bulb unit cavity.*

RESULTS OF INITIAL EXPERIMENTS

Cold Flow Tests

Cold flow tests were conducted to evaluate different methods for introducing the seed flow into

the simulated propellant stream. Figure 2 is a sketch of the seed dispersal system used in the tests. The seed supply was placed in the lower two-thirds

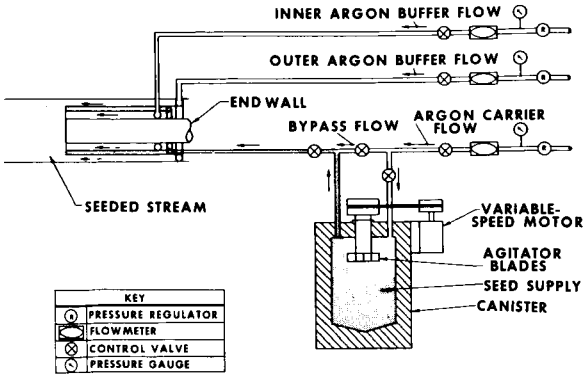

FIGURE 2.—*Sketch of seed dispersal system.*

of the canister. The canister was 11¾ in. deep and 5 in. in diameter. The carbon was dispersed within the canister by means of rotating agitator blades. Argon bled through the canister entrained the carbon and carried it to the test section. The ratio of the carbon-to-argon weight flow was controlled by allowing some of the argon gas to bypass the seed dispersal canister.

A sketch of a two-dimensional configuration in which seeds were introduced into the simulated propellant stream through a slot is shown in figure 3. The simulated propellant duct was formed by two 4.0-in.-long lucite plates spaced 0.273 in. apart. Seeded argon was flowed through a 0.039-in.-wide slot located at the center of the duct. The slot was formed by two aluminum plates which were tapered to a knife edge. Buffer layers of unseeded argon were introduced between the lucite walls and the central seeded stream. The average velocities were matched at the plane of injection in an attempt to minimize turbulence due to the interaction of the three parallel streams.

Tests were conducted with velocities ranging from 5 to 25 ft/sec and with carbon-to-argon weight flow ratios of between 0.1 and 2.0. During each test series the lucite side walls became coated with seeds. The coating level increased at the beginning of each test series and then remained approximately constant. The level of the coating resulted

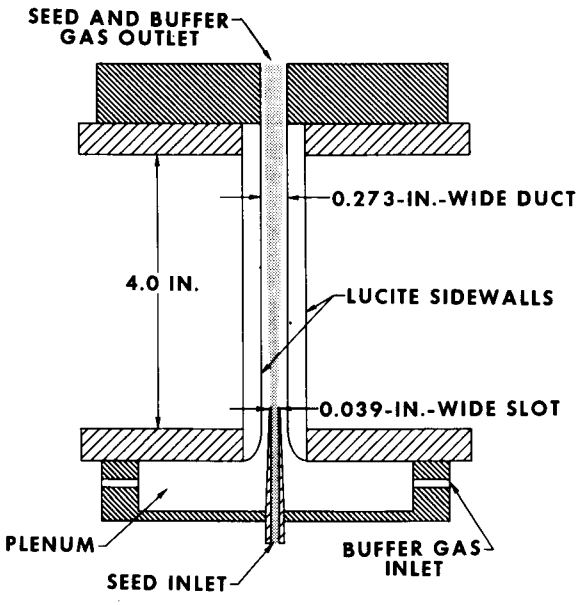

FIGURE 3.—*Two-dimensional configuration for cold flow test.*

in an attenuation of between 40 to 70 percent of the light transmitted through the test section with uncoated walls. Heavier coating occurred for lower velocities and larger carbon-to-argon weight flow ratios. In most cases the level of the coating could be reduced by turning off the seed flow and increasing the buffer flows. In some cases the walls could be cleaned by this technique so that 98 percent of the original transmission was restored. This amount of wall coating would be too great for operation of the nuclear light bulb engine. However, for the purposes of the initial hot flow tests, this amount of coating was considered acceptable.

Hot Flow Tests

Experiments in which the simulated propellant was heated by thermal radiation were conducted using two radiant energy source configurations, the UARL 1.2-MW rf induction heater and a dc arc heater. Figure 4 is a sketch of the configuration used in tests with the dc arc heater. The source geometry was rotationally symmetric about the centerline and consisted of a vortex-stabilized dc arc enclosed within a water-cooled fused silica tube. A complete description of the dc arc is given in reference 1. The simulated propellant duct consisted of the annulus surrounding the source; the test section was 3.0 in. long. Seeded argon was

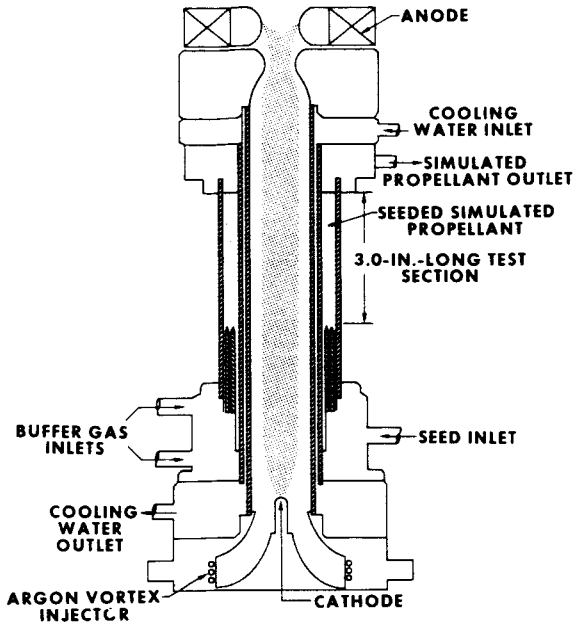

FIGURE 4.—*Propellant heating configuration used with dc arc heater.*

introduced through a 0.039-in.-wide annular slot. Buffer layers of unseeded argon flowed between the central seeded stream and the inner and outer fused silica walls. The buffer layers were each 0.117 in. thick at the injection plane.

The configuration used with the rf radiant energy source is shown in figure 5. The source geometry consisted of a vortex-stabilized rf discharge contained within water-cooled fused silica tubes. The axial boundary of the plasma was formed by two

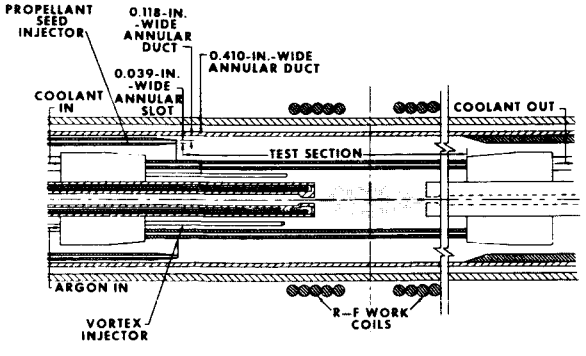

FIGURE 5.—*Propellant heating configuration used with rf radiant energy source.*

water-cooled copper end walls. A complete description of the characteristics of the rf source is also given in reference 1. Seeded argon was introduced through a 0.039-in.-wide annular slot. Buffer layers of unseeded argon flowed between the fused silica walls and the central seeded stream. The outer buffer layer was 0.118 in. thick and the inner buffer layer was 0.253 in. thick at the injection plane.

The argon and carbon flow rates were measured for each test. The average carbon flow rate was determined by measuring the weight change of the carbon in the dispersal canister and the total test time for each test series. Radiation transmitted through the test section before, during, and after each test was measured by a radiometer located outside the test section. The average simulated propellant exit temperature was measured by a chromel-alumel thermocouple located in the simulated propellant exhaust. The thermocouple was located so that it was not exposed to radiation from the source.

During most tests, portions of one or both walls of the simulated propellant duct became coated with carbon seed. The level of coating resulted in a 40 to 60 percent attenuation of the light transmitted through the test section. Generally, the coating was not uniform around the circumference of the test section. As noted during cold flow tests, the coating built up to a certain level early in a test series and then remained approximately constant. In many cases most of the coating could be removed by turning off the seed flow and increasing the buffer flow. For the tests conducted with the dc arc source, both the buffer layers were 0.117 in. wide, and both walls of the propellant duct became coated. For the tests with the rf radiant energy source, the outer buffer layer was 0.118 in. wide and the adjacent wall became coated; the inner buffer layer was 0.253 in. wide and there was no evidence of inner wall coating. Thus, it is apparent that for this configuration the 0.253-in.-thick buffer layer was effective in preventing wall coating. The migration of the seeds to the wall is most likely governed by turbulent diffusion. In these initial tests, no special steps were taken to reduce turbulent mixing other than to match the average velocities at the inlet plane and to taper the seed injection-slot walls to a knife edge.

Figure 6 shows typical time traces of the radia-

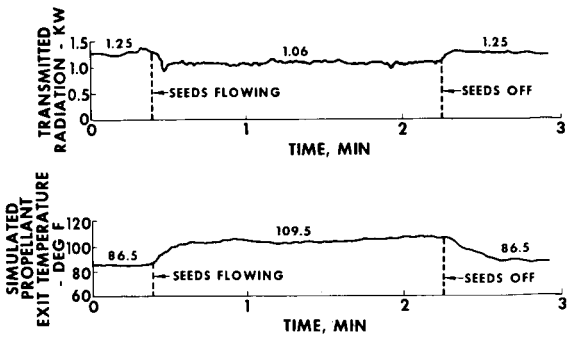

FIGURE 6.—*Typical data from hot flow tests.*

tion transmitted through the test section and the average simulated propellant exit temperature. These data were obtained from a test conducted using the rf radiant energy source. Initially, 1.25 kW of radiation was transmitted through the test section. (This is the radiation transmitted in a test conducted after the initial wall coating has occurred.) The average exhaust temperature was 86.5° F with no seeds flowing. At a time denoted by the first pair of broken lines, the seeds began to flow into the test section. The radiation transmitted decreased and the thermocouple registered a corresponding temperature rise. After about 2 min (denoted by the second set of broken lines), the seed flow was turned off, and the radiation and exhaust temperature returned to their initial values.

Figure 7 shows the fraction of radiation absorbed by the propellant stream η_A versus the attenuation parameter $\rho_s \beta l$. The attenuation parameter is defined as the product of the seed density ρ_s, the mass attenuation coefficient β, and the radiation path length l; it is dimensionless. The maximum value of η_A obtained in the initial experiments was 0.33 as compared with a value required for the reference engine of 0.98 (see ref. 8). The experimental value of the attenuation parameter was 0.41 as compared with a value of 3.0 for the reference engine. Figure 8 shows η_A versus the seed density parameter, defined as the product $\rho_s l$, for several values of mass attenuation coefficient β. The experimentally measured values of the seed density parameter are about the same as those for the reference engine. However, the experimentally achieved values of the mass attenuation coefficient are considerably lower than that of the reference engine. These

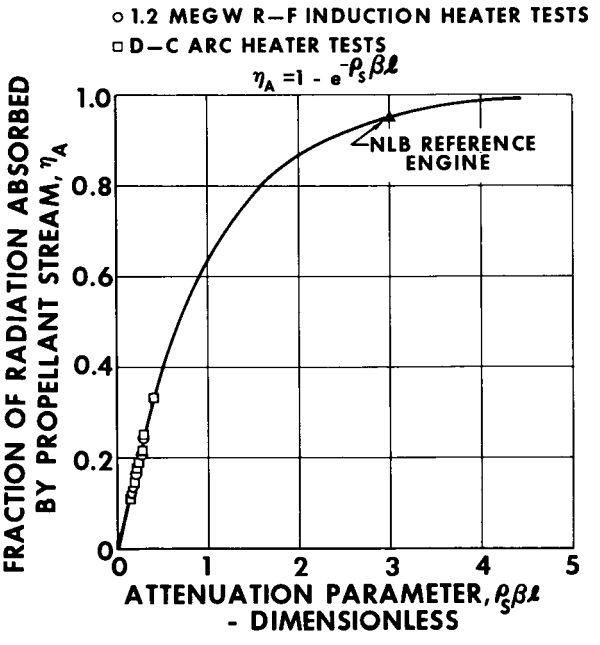

FIGURE 7.—*Variation of radiation absorbed by propellant steam with seed attenuation parameter.*

values of the mass attenuation coefficient also are much lower than those reported in references 6, 7, and 9.

During these initial experiments only small temperature rises were obtained; the maximum

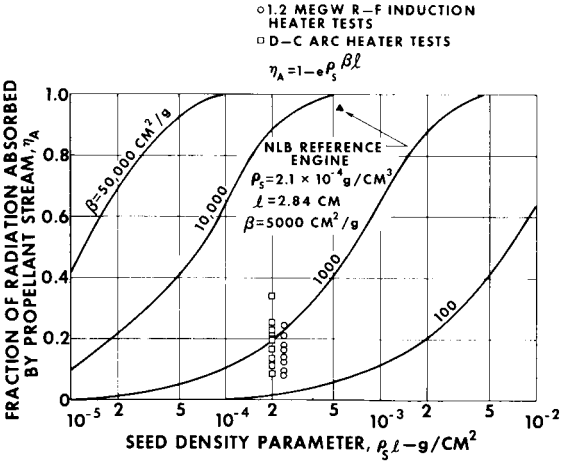

FIGURE 8.—*Variation of radiation absorbed by propellant stream with seed density parameter.*

value for tests where complete data were obtained was 31.4° F. Somewhat larger temperature rises were measured in several tests; however, for these tests the data obtained were incomplete. The maximum measured temperature rise in any test was 223° F.

The temperature rise was limited to low levels for three reasons: (1) Coating of the walls reduced the amount of radiation incident on the propellant stream—elimination of wall coating will provide a moderate increase in the energy available to heat the propellant (approximately 1.5 to 2.5 times that of the initial tests); (2) the mass attenuation coefficient was low (less than 2000 cm^2/g) so that only a small fraction of the incident energy was absorbed in the propellant stream—use of improved dispersal techniques should provide an increased mass attenuation coefficient; and (3) all tests in the initial series were conducted at low radiant power levels because of problems encountered in making the propellant heating configuration compatible with high-power radiant energy sources—tests with the dc arc heater were limited by O-ring seals which were exposed to radiation, and tests with the rf radiant energy source required modifications to the vortex injectors. If the modifications which have recently been made to these configurations are adequate, then it should be possible to increase the radiant energy available to heat the simulated propellant by approximately 50 times that employed in the initial tests.

CURRENT EXPERIMENTS

The current test program incorporates modifications to the test equipment so as to attain considerably higher propellant temperature rises. During the current test program it should be possible, using the available radiant energy sources, to achieve a temperature in excess of 4000° R in the seeded portion of the simulated propellant stream. Figure 9 is a sketch of the inlet of a configuration designed to provide improved performance. It has improved inlet geometry and a better manifold arrangement for the gas feed lines relative to the configuration used in the initial test program. Provisions have been made for changing the seed injection-slot size and the buffer-layer thicknesses. Provision has also been made for the use of porous foam materials (used successfully in the investigation reported in ref. 10) to smooth the velocity profiles and reduce turbulent mixing at the inlet plane.

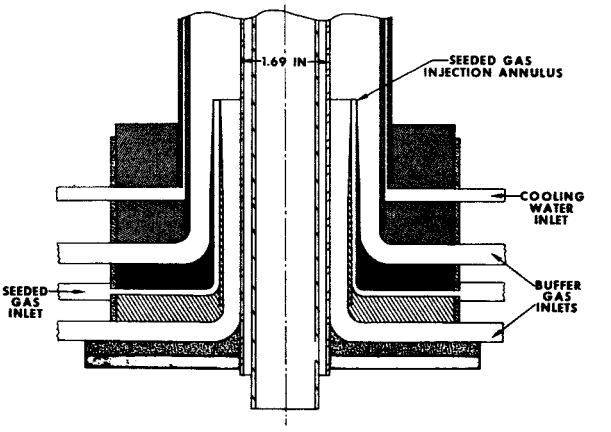

FIGURE 9.—*Sketch of inlet portion of configuration used in current hot flow tests.*

This configuration is compatible with the dc arc heater. The results of tests with this new configuration will provide information for later tests using the 1.2-MW rf heater.

REFERENCES

1. ROMAN, W. C.; KLEIN, J. F.; AND VOGT, P. G.: Experimental Investigations to Simulate the Thermal Environment, Transparent Walls, and Propellant Heating in a Nuclear Light Bulb Engine. Rept. H-910091-19, United Aircraft Res. Lab., Sept. 1969.
2. KRASCELLA, N. L.: Theoretical Investigation of the Absorption and Scattering Characteristics of Small Particles. (Rept. C-910092-1, United Aircraft Res. Lab., Sept. 1964.) NASA CR-210, 1964.
3. KRASCELLA, N. L.: Theoretical Investigation of the Absorptive Properties of Small Particles and Heavy-Atom Gases. (Rept. E-910092-7, United Aircraft Res. Lab., Sept. 1965.) NASA CR-693, 1965.
4. KRASCELLA, N. L.: Tables of the Composition, Opacity, and Thermodynamic Properties of Hydrogen at High Temperatures. (Rept. B-910168-1, United Aircraft Res. Lab., Sept. 1963.) NASA SP-3005, 1963.
5. MARTENEY, P. J.; AND KRASCELLA, N. L.: Theoretical and Experimental Investigations of Spectral Opacities of Mixtures of Hydrogen and Diatomic Gases. Rept. RTD-TDR-63-1102, U.S. Air Force Systems Command, 1963. (United Aircraft Res. Lab., Nov. 1963.)

6. MARTENEY, P. J.: Experimental Investigation of the Opacity of Small Particles. (Rept. C-910092-2, United Aircraft Res. Lab., Sept. 1964.) NASA CR-221, 1964.
7. MARTENEY, P. J.; KRASCELLA, N. L.; AND BURWELL, W. G.: Experimental Refractive Indices and Theoretical Small-Particle Spectral Properties of Selected Metals. Rept. D-910092-6, United Aircraft Res. Lab., Sept. 1965.
8. MCLAFFERTY, G. H.: Investigation of Gaseous Nuclear Rocket Technology—Summary Technical Report. Rept. H-910093-46, United Aircraft Res. Lab., Nov. 1969.
9. WILLIAMS, J. R.; CLEMENT, J. D.; SHENOY, A. S.; AND PARTAIN, W. L.: The Attenuation of Radiant Energy in Hot Seeded Hydrogen—An Experimental Study Related to the Gaseous Core Nuclear Rocket. Quart. Status Rept. 2, Proj. A-1045, Eng. Exp. Sta., Ga. Inst. Tech., Feb. 1969.
10. JOHNSON, B. V.: Exploratory Experimental Study of the Effects of Inlet Flow Conditions on the Flow and Containment Characteristics of Coaxial Flows. Rept. H-910091-21, United Aircraft Res. Lab., Sept. 1969.

DISCUSSION

Soehngen: I wonder if a heat-transfer analysis has been done for the heat transfer through the glass wall of the actual engine case. The glass wall is actually at the lowest temperature in the whole system. Outside, the propellant is at a higher temperature, and, inside, the fuel temperature is higher. How is the cooling situation at this glass wall?

Klein: I have not done the analysis myself. Someone else has done it with the assumptions that the transparent wall is there and is holding up and that it can be cooled in view of the high flux expected in the engine from both the fuel inside and the propellant outside. In other words, the coolant that is envisioned to be used, the size of the passages, etc. result in a heat-transfer coefficient large enough to cool it from the expected heat levels.

Soehngen: Is a report available on this? It is a very interesting problem and a difficult problem.

Klein: I think there is a separate report that has a large section on cooling the transparent walls.

Page intentionally left blank

SESSION VI

MHD POWER GENERATION

Chairman: **H. Hassan**

MHD Power Generation: State of the Art and Prospects for Advanced Nuclear Applications

RICHARD J. ROSA
AVCO Everett Research Laboratory

STATE OF THE ART

The interest in MHD power generation stems from its inherent simplicity. The MHD generator is a heat engine which combines the functions of both a conventional turbine and an electrical generator to directly convert heat into electricity. It requires only that the temperature of the gaseous working fluid be in a range where the gas has an adequate electrical conductivity. The highest operating temperatures are found in the working substance itself. The MHD generator can handle gas conditions which would quickly destroy a conventional turbine, because the MHD generator has no highly stressed, close-tolerance, moving parts. The solid materials from which the generator channel walls are constructed are readily accessible for cooling and MHD generators are accordingly attractive for high-temperature applications where turbine operation is prohibited.

An important feature which distinguishes MHD generators from other heat engines is that the basic conversion is a volume process while losses are proportional to surface area. Thus generators become more attractive as their size increases. It has been pointed out (ref. 1) that an MHD generator combined with a rocket combustion chamber such as a Rocketdyne F–1, 1 500 000-lb-thrust rocket engine could yield 10^4 MW.

The MHD generator also shares with rocket engine technology the ability to start and reach full power very rapidly. This characteristic makes it possible to deliver power of several hundreds of megawatts or more in a few seconds. It is for this type of application that the MHD generator has already achieved its first pilot operation (ref. 2).

During the past 10 years, intensive efforts have been made in the development of MHD generators. These efforts have been international in character (ref. 3) with the major emphasis being placed on commercial application using fossil fuels (refs. 4 and 5). MHD power generation from a hot plasma derived from nuclear heat requires the development of a high-temperature gas-cooled reactor. Reactors of the Nerva type produce a sufficiently high temperature to make coupling to an MHD generator attractive, but still higher temperatures would be still more attractive; that is, temperatures such as are available in principle from the plasma-core reactor. This is especially true in the case of space power applications.

Although the great bulk of the MHD effort has been directed toward fossil-fired commercial applications, it may be helpful to review this work and point out how some of the major problems were solved. This will give at least a partial indication of the feasibility of coupling MHD to the plasma-core reactor as well as an indication of how related problems might be handled in that case.

Generator Development

Very substantial progress had been made in improving both the performance and lifetime of open-cycle generators during the past few years. The linear dimensions of the biggest generators operating or under construction are of the order of several meters and thus it has been possible to obtain high electrical power outputs combined with high power densities (up to 30 MW/m^3). In the United States, the LORHO generator (ref. 2)

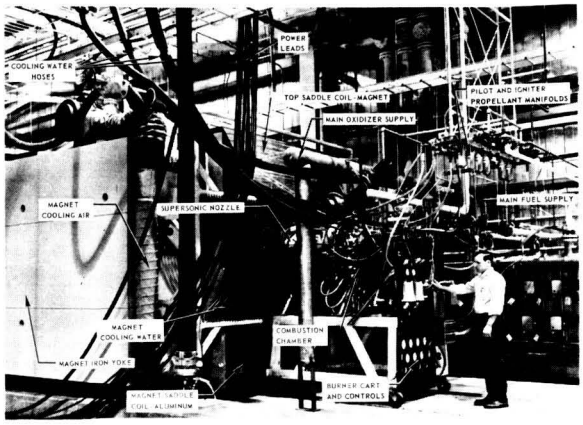

FIGURE 1.—*20-MW LORHO pilot MHD generator for hypersonic-wind-tunnel drive.*

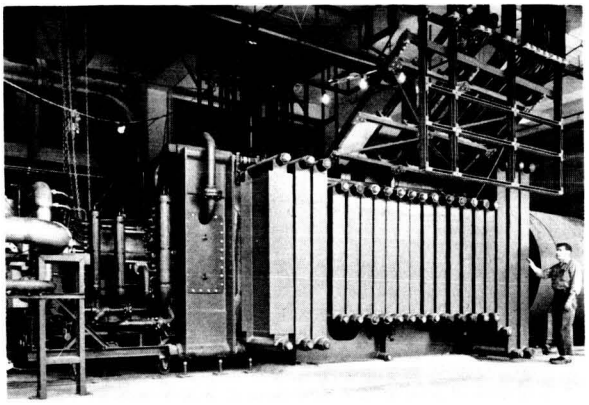

FIGURE 2.—*Mark V self-excited MHD generator with 32-MW gross electric output.*

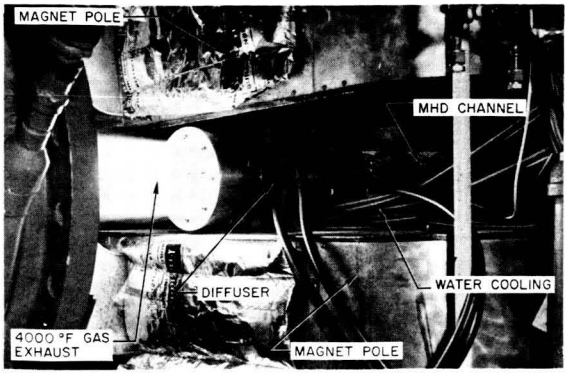

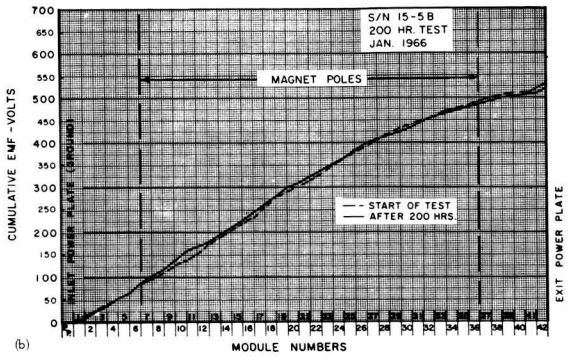

FIGURE 3.—*Long-duration channel test apparatus and performance results from a 200-hr test.* (a) *AVCO long-duration test facility.* (b) *Results from a 200-hour test.*

illustrated in figure 1 has an installed thermal capacity of 430 MW and has delivered electrical outputs of 18 MW for a 3-min run. The Avco Mark V generator (ref. 6), shown in figure 2, has achieved a gross output of 32 MW. The design of these two large installations was based on experience with the Avco Mark II generator facility (ref. 7), which has served as the basic tool for the study of fluid mechanics and channel performance at power outputs of up to 1.5 MW.

Continuous long-term operation of MHD channels at low power levels has been carried out at several facilities. The Avco long-duration test facility illustrated in figure 3(a) has, over a total of several thousand hours of testing, demonstrated that the electrical performance and integrity of electrodes and insulators can be maintained by using the proper level of axial electrical field and proper operating temperature. Test results from a single 200-hr long-duration test of a Hall channel are given in figure 3(b). They confirm that the channel performance was essentially unchanged from the beginning to the end of the test. To achieve this result, a continuous zirconia electrode replenishment technique was employed (ref. 8).

Combustion-driven MHD generator studies have been undertaken in several countries and two approaches have been favored. On the one hand, several small-scale installations which include many of the components required for the complete MHD system have been operated, the most complete example of these being the U–02 installation in Moscow (ref. 9). This has delivered a maximum of 43 kW for a period in excess of 50 hr and is of particular interest in that the power was delivered through a solid-state inverter system to the Moscow grid. Continuous channel operation for a time

period of 100 hr has been reported from a similar type of facility in Japan (ref. 10). In other installations, the facility consists only of a combustor, nozzle, generator duct, and magnet, and the emphasis is on generator studies rather than on long-duration operation. In this category, the Krzhizhanovsky Institute of Power Engineering in Moscow has constructed a large facility known as the ENIN-2 which has an input thermal power of 250 MW and run times of up to 15 min (ref. 11). The Japanese Mark II generator is capable of outputs of 1 MW (ref. 12).

The basic MHD process is simple in principle, and good performance has not, in fact, been particularly difficult to obtain, though several rather complex effects must be dealt with to obtain optimum results. Principal amongst these are the well-known Hall effect and aerodynamic effects due to forces of electromagnetic origin. This situation had led to the study of a wide variety of linear geometries for MHD generators, each optimum for a different set of operating conditions. For example, the LORHO is a circular Hall machine while the Mark V generator channel (fig. 4) was a Faraday

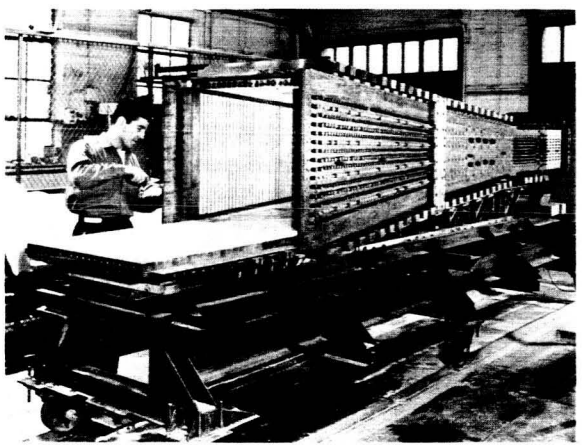

FIGURE 4.—*MHD channel for Mark V generator.*

design which employed a peg wall type of construction for the insulator wall surfaces. New approaches are still being proposed and considered. An example of this is the disk geometry in which either a simple outward radial flow occurs or there is a combination of this flow with swirl (ref. 13).

The construction of high-field-strength superconducting magnets for MHD generators has been shown to be practical as a result of extensive development work in this area of technology. A model superconducting saddle coil magnet with a field strength of 4 T in a 12-in.-diam 5-ft-long bore has been successfully tested (ref. 14). This Avco magnet is illustrated in figure 5.

Baseload Power Generation

The MHD cycles considered for fossil fuel are schematically illustrated in figure 6. They utilize a binary cycle in which the heat energy in the MHD generator exhaust gases is utilized to preheat the combustion air and to generate additional power, either in a steam bottoming plant as indicated by the MHD-Rankine cycle or in a bottoming gas turbine plant as indicated by the MHD-Brayton cycle. The necessary high-temperature combustion conditions are in both cases attained by burning the fuel with compressed air regeneratively heated by the hot MHD exhaust gases. Alternatively, the combustion air may be preheated in separately fired air heaters or the fuel may be burned with oxygen or oxygen-enriched air in order to reach the high flame temperatures required by the MHD generator.

In parallel with the development of the MHD generator itself, a large effort has been devoted to the development of auxiliary equipment for the MHD baseload power system. These efforts have dealt with combustion chambers, high-temperature air heaters, seed recovery systems and pollution control systems. All these items are essential for the practical utilization of MHD for baseload power generation.

The problems related to seeding are perhaps relevant to the subject of this symposium since the methods used to recover and recycle seed may suggest ways in which nuclear fuel could be handled in the case of a nuclear plant. Problems include the introduction and recovery of seed and possible corrosion due to the seed. In practice, seeding is accomplished by adding an alkali salt to the hot combustion products generated in the burner either as solid granules or as a liquid solution (ref. 15). Potassium is most commonly employed for seeding on the basis of economic considerations. Potassium is also present in coal ash which thus constitutes a natural makeup source for seed in coal-fired

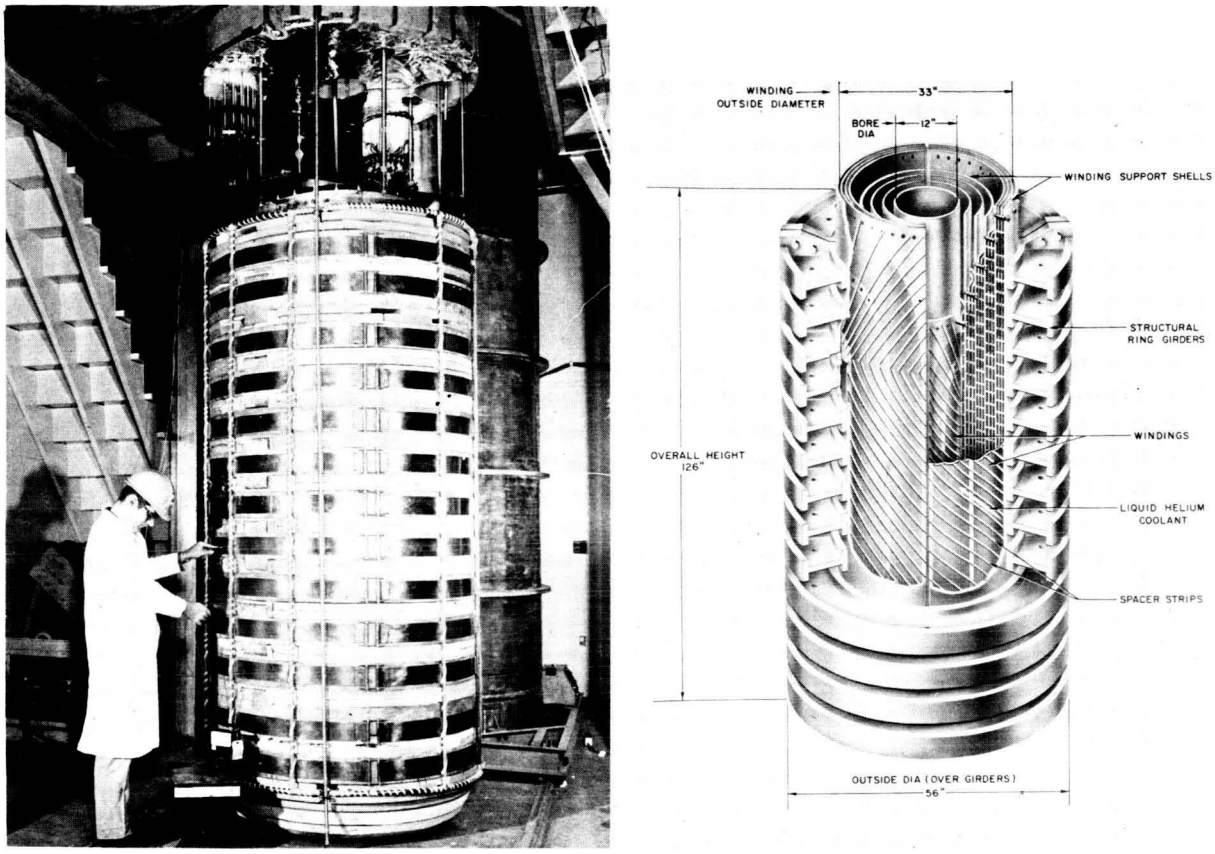

FIGURE 5.—*4-T, 12-in.-bore model superconducting saddle coil magnet.*

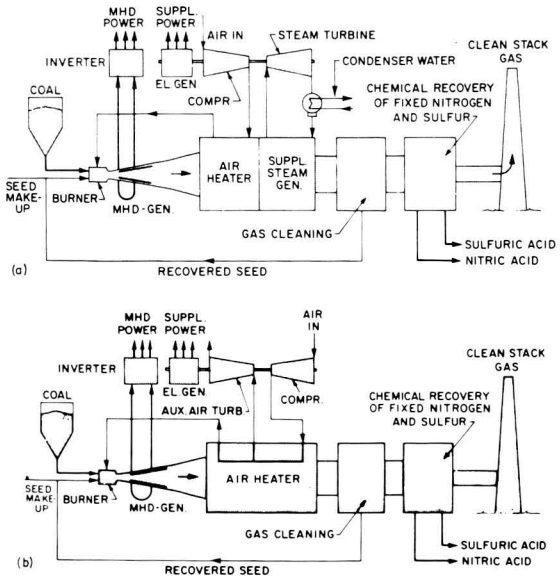

FIGURE 6.—*MHD open power cycles.* (a) *MHD Rankine cycle.* (b) *MHD Brayton cycle.*

plants. However, simple economics necessitates efficient recovery of the seed. It has been demonstrated (ref. 16) that condensed seed particles in the effluent gas can be recovered in electrostatic precipitation equipment at very high efficiencies. Bag filters and scrubbing systems have also been considered (ref. 15). For direct coal-fired systems, it is proposed to separate the bulk of the ash as liquid slag at high gas temperatures before the seed has condensed. This avoids loss of seed in the slag.

The experimental work in seed and ash chemistry has also furnished important information regarding corrosion and the practical use of boilers and high-temperature heat exchangers in seed-laden MHD generator exhaust gases (refs. 15 and 16). The addition of seed does not appear to cause a serious problem for normal boiler operation. However, in the presence of sulfur the use of conventional bare metal tubular heat exchangers for preheating of

the combustion air is limited to about 1500° F because of corrosive attacks from alkali sulfates.

Economic Consideration

The analysis given here covers powerplant designs possible with presently available engineering techniques (first-generation plant designs) and also plants possible with a foreseeable but more advanced state of MHD technology (advanced plant designs). These studies indicate that MHD offers an immediate prospect for raising the overall thermal efficiency to 50 percent and subsequent improvements in the technology can be expected to carry this to at least 60 percent (ref. 17).

Cost estimates for generating electricity in coal-fired MHD powerplants based on 1968 dollars are presented in table I. These are compared with estimates of the cost of generating electricity in conventional coal-fired steam powerplants and also in present nuclear plants.

Although the economics of MHD can be established with a high degree of certainty only after operating experience with large-scale installations has been obtained, the estimates presented here are in substantial agreement with the estimates of others both in the United States and abroad and are considered a reasonable indicator of the economic competitiveness of the MHD process (refs. 17 and 18).

Environmental Effects

It is becoming increasingly evident that a major consideration in the location and operation of large electrical powerplants is the effect which these will have on the environment. The large quantities of particulate matter, sulfur, and nitrogen oxides produced by the combustion of fossil fuel represent a major air pollution problem for fossil-fueled powerplants. In addition, a serious thermal pollution problem exists for all steam-electric powerplants, both fossil fuel and nuclear. The high-temperature MHD energy conversion process provides opportunities for the reduction and control of all these aspects of environmental pollution from powerplants (ref. 19). Most pertinent to a discussion of nuclear MHD plants is thermal pollution.

As a direct consequence of the efficiency increase, an MHD powerplant rejects less heat per unit of electricity generated. The rapid reduction in total heat rejection with increasing plant efficiency is illustrated in figure 7. The fractions of the heat rejected to the condenser and otherwise for different types of thermal powerplants are also indicated.

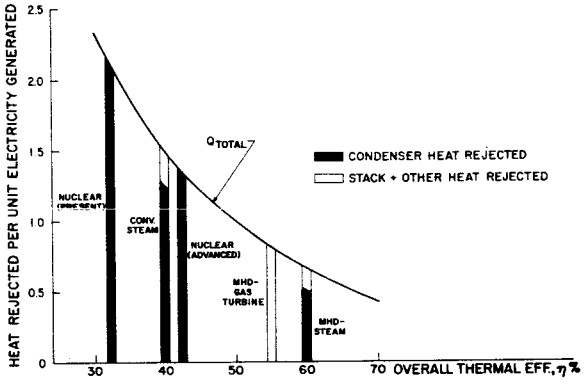

FIGURE 7.—*Comparison of heat rejection from thermal powerplants.* $Q_{Total} = (1 - \eta)/\eta$.

Because of their higher efficiencies, MHD steam powerplants will reduce cooling water requirements to about half the amount needed by conventional fossil-fueled steam powerplants. Compared with present nuclear powerplants which are the least efficient, the amount of cooling water necessary would be reduced to about one-fourth.

TABLE I.—*Comparative Costs of 1000-MW (Nominal) Powerplants*

Item	MHD		Conventional	
	First generator	Advanced	Coal fired	Nuclear
Efficiency, %	50	60	40	32
Capital cost, $/kW	120	90	120	160
Energy cost, mills/kW-hr [a]	4.26	3.34	4.52	5.23

[a] Capitalized at 15 and 80 percent plant capacity factor. Fuel at ($0.20/MBtu).

Even more significant is the fact that the basic nature of the MHD process is such that MHD power systems can be designed without supplementary steam power as indicated by the alternative MHD Brayton cycle previously mentioned. In this case, all the heat can be rejected directly to the atmosphere although the overall thermal efficiency will be somewhat lower than with supplemental steam power generation.

Emergency and Peaking Power Generation

An emergency-peaking MHD plant, as shown in figure 8, is a simple system whose basic components are a combustion chamber, an MHD generator, and an inverter. The fuel, oil or gas, is burned with oxygen or oxygen-enriched air. Air, if used, is supplied at the desired pressure from a compressor driven by a motor or turbine. Regenerative preheating of the air-oxygen mixture may be employed to enhance the economy of operation.

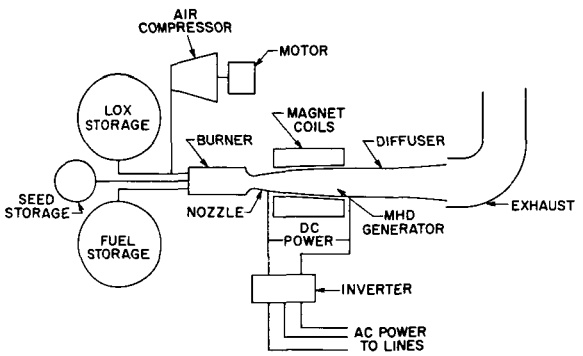

FIGURE 8.—*MHD power system using basic fuel plus liquid oxygen.*

This type of plant can be designed to start in less than 1 sec by maintaining field excitation at all times or by using a superconducting field coil. Because there is no mechanical inertia and because inverters are used, the ac output can be electronically synchronized with the line in millisec. The ability to start and to shift phase rapidly is very valuable for maintaining system stability.

The simplicity of the system leads to low capital cost, in some cases less than one-half of that of other standby power supplies. MHD benefits greatly from economy of scale so the larger the plant, the lower the specific capital cost in dollars per kW. Operating cost for a powerplant of this type is higher than that for a baseload plant because it is designed with the primary objective of obtaining low capital cost. Plants incorporating a spectrum of tradeoffs between capital and operating cost have been studied (ref. 20).

Concluding Comments

In the design of MHD generators the Hall parameter and the internal axial electrical field strength are the two important parameters which establish generator operating conditions. Figure 9 maps out the area which has been explored experimentally and within which good performance has been demonstrated in combustion product gases. The areas within which various types of plants would operate are also shown. It can be seen that present generator experience covers all but advanced baseload plants. It is important to recognize that other developments, such as preheating of the combustion air to very high temperatures, would tend to reduce the parameter requirements for even the most advanced plants.

The successful operation of large experimental generators and the extensive testing of long-duration generator ducts and of auxiliary plant equipment have led to the position where engineering solutions exist for all of the major problems in an open-cycle installation. These developments have made it possible for the U.S.S.R. to undertake the construction of a 75-MW MHD steam pilot powerplant on the outskirts of Moscow. This plant, known as the U–25 (ref. 21), incorporates a 25-MW MHD generator and is scheduled to begin preliminary operation early in 1971. A model of this installation is shown in figure 10.[1]

The research and development work thus far undertaken on MHD generators is depicted in figure 11 with particular reference to the Avco program. In cooperation with a group of utilities [2]

[1] Fig. 10 (U–25 pilot plant) was kindly provided by Dr. V. A. Kirillin, Deputy Premier and Chairman, Committee for Science and Technology, U.S.S.R., and Prof. A. E. Sheindlin, Director, Institute for High Temperatures, Moscow.

[2] Allegheny Power System, Inc., through its subsidiaries; American Electric Power Co., Inc., through its subsidiaries; Boston Edison Electric Co.; Central Illinois Light Co.; the Dayton Power & Light Co.; Illinois Power Co.; Indianapolis Power & Light Co.; Kansas City Power & Light Co.; Louisville Gas & Electric Co.; United Illuminating Co.; and Union Electric Co.

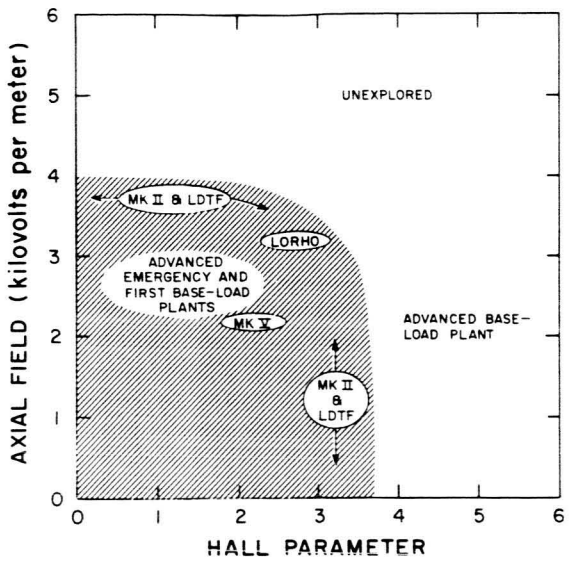

FIGURE 9.—*MHD generator parameters showing present area of operation and future extensions.*

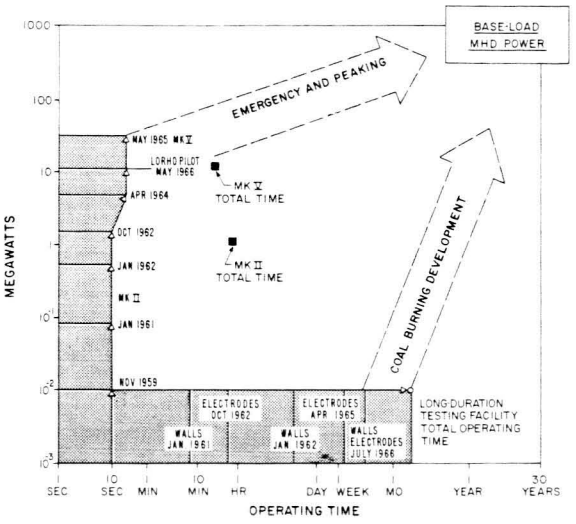

FIGURE 11.—*Past and possible future development of MHD generators.*

and with contract support from the Department of Defense, important experience has been gained with large generators operating at significant power densities. In parallel with this effort, small-scale, long-duration development has yielded important information and experience on the design and construction of all components of an MHD power system. Since the large generators have been operated for quite short times while the long-duration experiments are at a power level of 10 kW, it is appropriate to depict their historical development, respectively, along the ordinate and abscissa of figure 11, in which logarithmic scales are used.

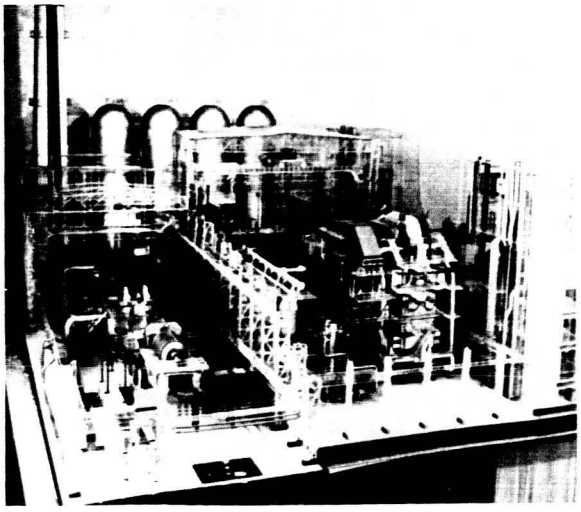

FIGURE 10.—*Model of 75-MW MHD pilot plant under construction in Moscow, U.S.S.R.*

The development of coal-burning generators, as indicate in figure 11, should continue upward from the time axis toward the ultimate goal of a baseload MHD powerplant. This path will concentrate upon the aspects of a baseload plant specifically related to the use of coal, including generator development, combustion, high-temperature regenerative air preheat, seed recovery, and pollution control (ref. 22).

Referring again to figure 11, existing experience with large liquid fuel generators operated with oxygen enrichment provides the basis for an immediate start on the development of MHD generators for emergency and peaking applications. Power output and operating time can be extended in a demonstration peaking unit of between 50- and 200-MW electrical output. In addition to fulfilling the need for emergency and peaking power, this development will complement the work envisaged on coal-fired MHD generators and help to bring central-station baseload plants closer to reality.

NUCLEAR APPLICATIONS

Progress in developing nuclear MHD powerplants is paced by the progress of reactor technology. Whereas the temperature attained by a solid-core rocket reactor of the Nerva type is high enough to be interesting, MHD is capable of handling much more, and nuclear fission is capable of delivering much more. The possibilities inherent in this situation have intrigued the author for many years and some of the speculations arising from this interest are outlined below.

Consider the closed MHD cycle outlined schematically in figure 12. In this kind of system we

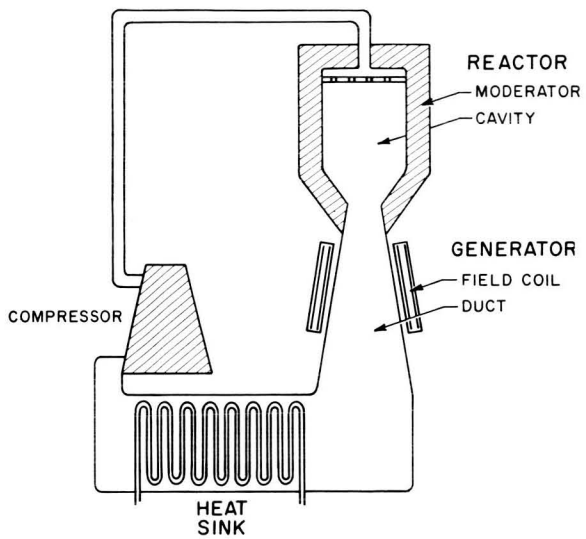

FIGURE *12.—Conceptual nuclear MHD gas cycle.*

may suppose that the nuclear fuel and working gas are mixed together, injected into the cavity where criticality and subsequent heating occur, and then pass out of the reactor and through the MHD generator, still mixed together. Conceivably, they might remain mixed throughout the cycle, but since the vapor pressure of uranium is rather low, and since it is unlikely that a gaseous uranium molecule exists that is stable throughout the temperature range of a cycle, it is more probable that condensation of the nuclear fuel will occur at some point, after which fuel and gas will be handled separately. In any case *the nuclear fuel remains within the system* and is reused.

The fundamental advantage obtained by combining an MHD generator and this type of reactor is a more or less complete removal of any constraint upon the top temperature of the thermodynamic cycle. Going a step further, we can imagine the constraints removed from the bottom temperature as well by using an MHD compressor in place of the conventional compressor and a transparent duct of some sort in place of the conventional radiator.[3] If this were done, then at no point in the cycle would it be necessary for a solid surface to assume the gas temperature. Of course, heating of the containing walls cannot be entirely avoided, so constraints upon temperature are not entirely removed. Nonetheless, a very large gain in top or bottom temperature, or both, is conceivable without postulating specifications for solid materials that are *a priori* unattainable.

The cavity-reactor MHD generator combination might be used in a variety of different kinds of propulsion and/or power-generation systems. These include Brayton and Rankine cycle radiation-cooled space power supplies, some concepts that might be useful for high-thrust propulsion at suborbital velocities and within an atmosphere, and commercial powerplants.

Radiating Powerplants

In a Brayton cycle, if we put aside for this discussion the notion of an MHD compressor, the bottom temperature is limited by compressor-blade strength. As a result, the radiator temperature cannot exceed 600° to 1000° K, with 1500° K as perhaps a reasonable possibility for the future. However, by increasing the top temperature we can obtain high efficiency and an increase in net electric output relative to the heat which must be radiated.

Figure 13 shows estimated values of electric power output per unit radiator area for several values of radiator and peak regenerator temperature. A molecular working gas was assumed in these calculations. Note that an increase of two orders of magnitude over a system employing a turbogenerator might be obtained by the combination of higher efficiency and moderately higher

[3] For example, an early proposal of S. A. Colgate and R. L. Aamodt (ref. 23) for combining MHD with cavity reactors envisioned a double-ended shock-tube arrangement in which compression was done by waves.

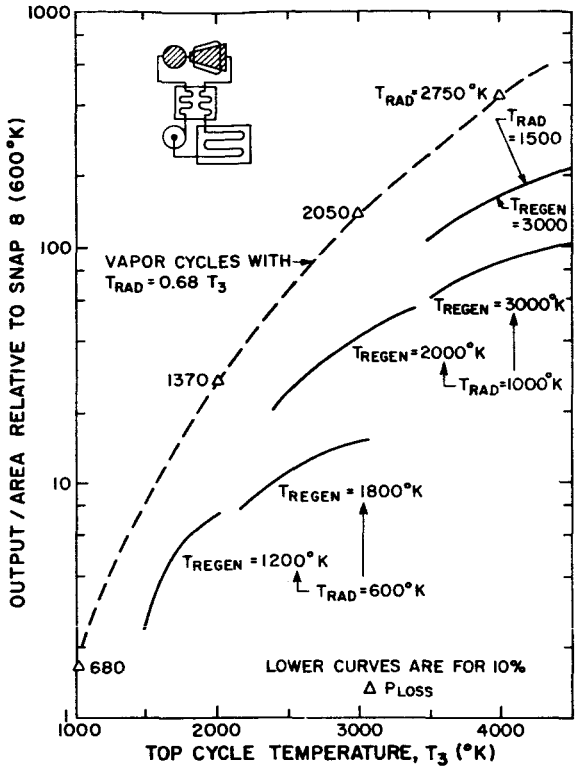

FIGURE 13.—*Performance of Brayton cycles.*

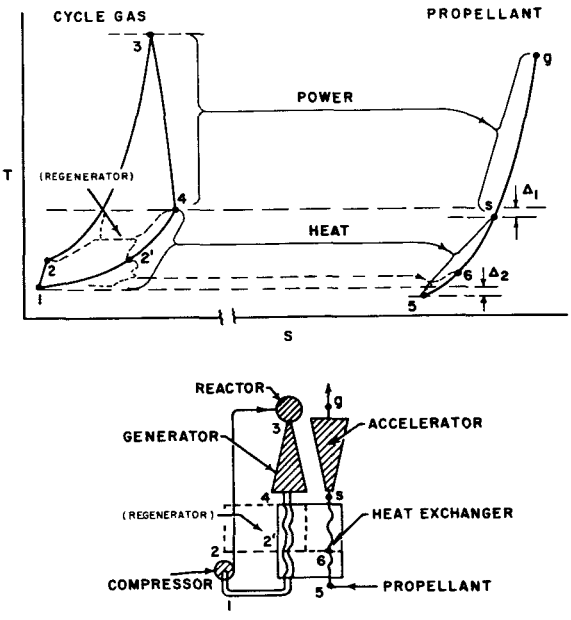

FIGURE 14.—*A propellant-cooled Brayton cycle.*

radiator temperature. Of course, a high W_e/Q_r ratio is not by itself proof of high power per unit mass. For example, a high-temperature radiator is penalized by the fact that the most refractory metals have a high density, and both the MHD generator and the cavity reactor are not likely to have a high specific-power output unless the absolute value of the power is high. However, with these qualifications it is not unreasonable to hope that power output per unit mass can be made to increase in a manner more or less proportional to power output per unit radiator area.

Propellant-Cooled Propulsion Systems

In most propulsion systems the working fluid or the propellant serves, in effect, as a heat sink for the power cycle. This might also be done with a nuclear-MHD system (ref. 24). A possible arrangement is shown in figure 14. While it is not capable of the arbitrarily high specific impulse of a radiating system, it would have the advantage of a higher thrust-to-weight ratio and the possibility of being used within an atmosphere. In effect this arrangement acts as an energy exchanger in which energy is transferred from the cycle gas to the propellant by means of a conventional heat exchanger up to the temperature limit of solids, and thereafter is transferred electrically.

The compressors and heat exchangers needed above are absent in the scheme shown in figure 15

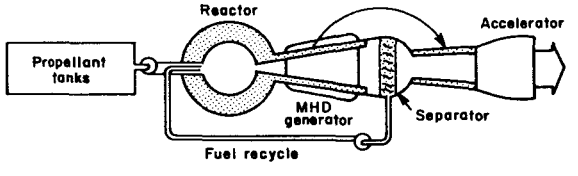

FIGURE 15.—*Open-cycle system.*

(refs. 1 and 25). This open-cycle system depends upon the fact that the vapor pressure of the nuclear fuel will be much less at the exit of an MHD generator than it is at the exit of the reactor so that condensation will occur. For example, if the stagnation temperature after expansion through the generator is 2000° K, the vapor pressure of uranium will have dropped to 10^{-6} atm. Collection of the

vapor droplets might then be accomplished by an array of turning vanes similar to those used for dust and mist collection in various industrial processes. As a result, the working gas would follow an open cycle while the nuclear fuel would follow a closed cycle from reactor to generator to collector, and back again.

When flying in an atmosphere, it might be possible to employ air augmenting advantageously, i.e., the use of some or all of the electric output of the generator to drive an electric ramjet, in both of the cycles described above (and also conceivably in a really high-performance radiating powerplant). Going a step further, the atmosphere could also be used as the heat sink for a closed cycle, obviating the need for any expendable propellant at all. However, materials problems would be likely to restrict this to flight Mach numbers less than about 5.

An attempt to estimate the performance obtainable with these schemes is shown in figure 16. As

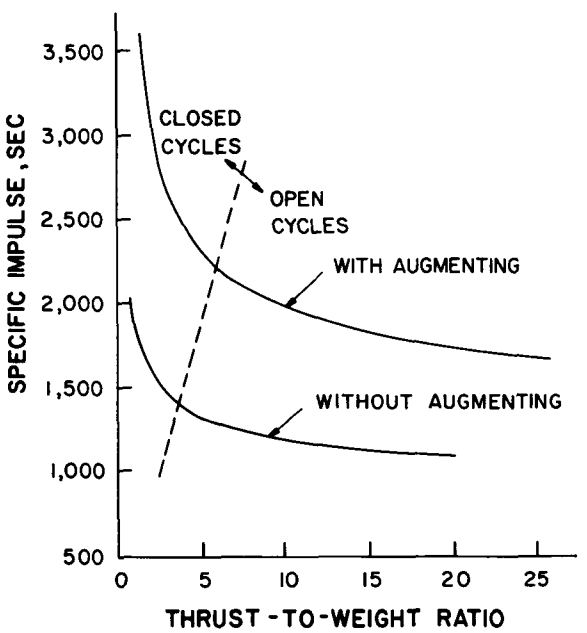

FIGURE *16.—Performance summary.*

with any type of propulsion system, the thrust-to-weight ratio goes down as specific impulses go up, resulting in a more or less hyperbolic curve. Addition of air augmenting can be seen to yield a significant gain. Note that the specific impulse and thrust-to-weight ratio of an air-augmented engine vary with flight velocity, and the values shown here represent effective average values for acceleration from zero to orbital velocity.

Commercial Application

Until recently there did not appear to be a strong incentive for seeking ultrahigh reactor temperatures and ultrahigh cycle efficiency for commercial nuclear power production. Capital cost has been a larger determinant of the bus-bar cost of electricity than has been the cost of fuel, and the containment of fission products within the reactor has been considered essential. Now, however, we observe a growing objection to nuclear power on two counts: Thermal pollution, and the danger of nuclear accident. The former reemphasizes the importance of high efficiency in order to reduce the total quantity of heat rejected and reemphasizes high temperature both for its effect on efficiency and because it facilitates raising the heat rejection temperature which, in turn, facilitates direct rejection of heat to the atmosphere instead of to water.

Concern with nuclear safety suggests that if the chance of serious consequences from a nuclear accident is to be reduced as far as possible fission products should not be allowed to build up in a reactor. This in turn suggests that what presently appears to be one of the greatest drawbacks of a plasma-core reactor may yet come to be regarded as a virtue. Thus it seems clear that the plasma-core reactor, or, for that matter, rocket reactors of the Nerva type, should by no means be excluded from consideration for commercial service. In this connection, an interesting question that should be investigated is whether such reactors are suitable for breeding.

REFERENCES

1. ROSA, R.: Magnetohydrodynamic Energy Conversion. McGraw-Hill Book Co., Inc., 1968.
2. TENO, J.; ET AL.: Studies with a Hall Configuration MHD Generator. Proceedings, 10th Symposium on Engineering Aspects of MHD, Mass. Inst. Tech. (Cambridge, Mass.), 1969.
3. ANON.: MHD Electrical Power Generation—The 1969 Status Report. Joint ENEA/IAEA Int. Liaison Group

on MHD Elec. Power Generation, ENEA (Paris), 1969.
4. SPORN, P.; AND KANTROWITZ, A.: Large Scale Generation of Electric Power by Application of the MHD Concept. Power, vol. 103, 1959.
5. ROSA, R.; ET AL.: MHD for Emergency and Peaking Power Generation. Proceedings, 10th Symposium on Engineering Aspects of MHD, Mass. Inst. Tech. (Cambridge, Mass.), 1969.
6. MATTSSON, A.; ET AL.: Performance of a Self-Excited MHD Generator. Mech. Eng., Nov. 1966, pp. 34–46.
7. LOUIS, J. F; LOTHROP, J.; AND BROGAN, T. R.: Studies of Fluid Mechanics Using a Large Combustion Driven MHD Generator. Phys. Fluids, vol. 7, Mar. 1964, pp. 362–374.
8. TENO, J.; ET AL.: Long Duration Electrodes for Open Cycle MHD Generators. Proceedings, 8th Symposium on Engineering Aspects of MHD. Stanford Univ. (Stanford, Calif.), Mar. 1967.
9. KIRILLIN, V. A.; AND SHEINDLIN, A. E.: Some Data Obtained with an Experimental MHD Power Plant. Proceedings, 8th Symposium on Engineering Aspects of MHD, Stanford Univ. (Stanford, Calif.), 1967.
10. MORI, F.; ET AL.: Long Duration Test of a Combustion-Driven MHD Generator. Electricity from MHD. Vol. 5. Int. Atomic Energy Agency (Vienna), 1968.
11. ZIMMERIN, D.; ET AL.: The ENIN–2 Experimental Open-Cycle MHD Generator Rig. Electricity from MHD. Int. Atomic Energy Agency (Vienna), 1968.
12. MORI, F.; ET AL.; Experiments on MHD Generation with ETL Mark II. Electricity from MHD. Int. Atomic Energy Agency (Vienna), 1968.
13. LOUIS, J. F.: Disk Generator. AIAA J., vol. 6, Sept. 1968, p. 1674.
14. KANTROWITZ, A.; ET AL.: A Model MHD Type Superconducting Magnet. Electricity from MHD. Vol. 3. Int. Atomic Energy Agency (Vienna), 1966.
15. HALS, F. A.: Auxiliary Equipment for MHD Open Cycle Conversion Systems. Electricity from MHD. Vol. 6. Int. Atomic Energy Agency (Vienna), 1968.
16. HALS, F.; KEEFE, L.; AND EL BINDARI, A.: Studies of Seed Recovery and Corrosion in Coal Fired MHD Power Plants. Paper 64–WA/ENER–5, ASME, June 1964.
17. SHEINDLIN, A. E.; ET AL.: Thermal Efficiency of MHD Plants in Terms of Different Methods of Obtaining High Temperature. Proceedings, 10th Symposium on Engineering Aspects of MHD, Mass. Inst. Tech. (Cambridge, Mass.), 1969.
18. HOOVER, D. Q.; ET AL.: Feasibility Study of Coal Burning MHD Generation. R&D Rept. No. 13, Office of Coal Res. (Washington, D.C.), Feb. 1966.
19. HALS, F.; AND JACKSON, W. D.: MHD Power Generation: Economic and Environmental Implications. Proceedings, 10th Symposium on Engineering Aspects of MHD, Mass. Inst. Tech. (Cambridge, Mass.), 1969.
20. ROSA, R.; ET AL.: MHD Power Generation: Status and Prospects for Open-Cycle Systems. IEEE Winter Power Meeting (New York, N.Y.), Jan. 1969.
21. EVANS, R. K.: 75 MW MHD Power Plant Nears Completion. Power, 1969, p. 66.
22. RODDIS, L. H.: MHD for Central Station Power Generation: A Plan for Action. Rept. Prepared for the Executive Office of the President, Off. Sci. and Technol., June 1969.
23. COLGATE, S. A.; AND AAMODT, R. L.: Plasma Reactor Promises Direct Electric Power. Nucleonics, vol. 15, Aug. 1957, pp. 50–55.
24. ROSA, R.: Magnetohydrodynamic Generators and Nuclear Propulsion. Am. Rocket Soc. J., vol. 32, Aug. 1962, pp. 1221–1230.
25. ROSA, R.: A Propulsion System Using a Cavity Reactor and Magnetohydrodynamic Generator. Am. Rocket Soc. J., vol. 31, July 1961, pp. 884–889.

DISCUSSION

Shelton: What is your prediction as to the possible thermal efficiency to be attained in coal-fired MHD powerplants?

Rosa: From 55 to 60 percent. This estimate is based on a system which is bottomed with a steamplant. With one that is bottomed with gas turbines, which looks very desirable these days, 55 percent would be a reasonable expectation.

Thom: I remember one of those beautiful universal-type AVCO charts that showed closed-cycle gas-core reactors in conjunction with an MHD generator and plasma thrusters. That chart had very high temperature figures. I wonder, therefore, why you used a temperature of 6000° K. In this other chart temperatures up to 30 000 ° K were mentioned and they resulted in very nice relations between thrust-to-weight ratios and specific impulse up to 10 000 sec. I used this chart many times to demonstrate the relation of low specific mass with high temperatures.

Rosa: I do not remember that exact chart, but it sounds to me like a chart which was drawn for plasma thrust engines and not for MHD power cycles. For terrestrial power cycles, I am not sure whether temperatures greater than 5000° to 6000° K are really useful. At that temperature the Carnot efficiency is very close to 100 percent, and also a gas conductivity has been achieved which, from an MHD point of view, is entirely adequate.

Miley: There are two parts to my question: (1) Could you comment on the possibility of coupling a high-temperature gas-cooled reactor and other reactors in the cavity concept; and (2) could you comment on the study by Booth of Los Alamos, a couple of years ago, which seemed to be rather conservative in respect to combining MHD and nuclear reactors?

Rosa: There is no reason why it could not be done, and I think Professor Kerrebrock put his finger on an interesting point earlier today when he pointed out that if one is willing to abandon the fission product containment requirement then some of the solid-core reactors, such as the Nerva, could look pretty good for use with an MHD generator. The kind of temperatures they produce (~2500° K) should make possible a very attractive powerplant. Now, as to that Los Alamos

paper which you speak of, for the time when it was written it was a fair assessment. That was the time when interest in water reactors was really booming. I think that was about the time that GE was practically promising to give them away. Things have changed, however. There seemed at that time to be very little incentive for trying to raise the efficiency of a nuclear powerplant, especially since anything nuclear is expensive to develop. I think the picture at the present time is much, much different.

Anonymous: The idea of making MHD power conversion with the gas-core reactor was proposed many years ago by Colgate and Aamodt from Los Alamos. I had a chance to talk to Colgate several years ago about it and he told me that the great problem was always the radiation. According to your calculations the situation has apparently improved. What do you think is really the improvement of your scheme in comparison with older considerations by Colgate and Aamodt?

Rosa: They described a very special system in their paper. It is quite difficult to devise a thermodynamic power cycle in which you do not take the gas out of the reactor, run it through a machine, then through some elaborate heat exchangers, then through a compressor, and then feed it back into the reactor. Their scheme involved, so to speak, one piece of pipe for doing all this. Their difficulty was then to cool the gas off sufficiently, using only radiation through the walls, and still obtain reasonable efficiency. The systems I have described here are, by comparison, more nearly similar to conventional powerplants.

Kinetic Studies of Nuclear-Seeded MHD Plasmas[1]

W. H. Ellis and K. Imani
University of Florida

H. G. Cofer
Westinghouse Nuclear Energy Systems

A new method for studying the electron kinetics in plasmas produced by neutron irradiation of nuclear seeded noble gases is described. Experimentally determined production and loss parameters for plasmas produced by the slowing down of the reaction products of the ^3He $(n,p)t$ reaction is reported for a range of helium gas pressures (1 to 10 atm) that is of interest for reactor coolant and MHD conversion applications.

The voltage output signal amplitude of the pulsed ionization chamber (PIC) is used to measure the steady-state electron density N_e as a function of reactor power and the measured ionization source rate S (ion pairs/sec) for plasmas produced within the ^3He gas filling of the ion chamber during neutron irradiation in the thermal column of the University of Florida Training Reactor. Plasma loss coefficients can then be determined directly and the mechanisms of production and loss can be studied.

Values reported for the second-order plasma loss coefficients obtained with electron densities measured by the PIC technique for steady-state helium plasmas as a function of pressure were in excellent agreement with theoretical predictions and ranged from 5×10^{-8} to 3×10^{-7} cm^3/sec at 300° K.

In evaluating design concepts for MHD conversion of nuclear energy into electrical power, one of the critical factors that must be considered is that of the kinetics of the plasma production and loss involved in such a system. This is true regardless of the method that may be used for producing the converter working medium and is especially true for the lower operating temperatures of solid-core gas-cooled reactors that are or will be available for such applications in the near future. For estimating the levels of ionization that can be produced in the coolant gas in the reactor and the rate at which the plasma will decay during its transport to and through the MHD converter region, it is necessary in all cases to know the value of the plasma loss coefficients precisely and it is most useful to understand the mechanism of plasma production that occurs within the reactor core region.

Thus, when undertaking a study of the feasibility of using the seeding of a nuclear reactor coolant gas with materials with high thermal neutron cross sections such as ^3He for the production of nonequilibrium plasmas for use with MHD converter systems, as suggested by Braun et al. (ref. 1), one of the first problems to be considered was that of the plasma kinetics of such a system. However, it was soon found that most of the conventional methods for plasma density measurements were not applicable for the high-pressure regime (1 to 50 atm) required for such systems and did not lend themselves readily to modifications for high-pressure applications. It therefore became necessary for a new method to be developed. It was desired to have the conditions under which the measurements were to be performed to duplicate those of the actual reactor environment as closely as possible, to involve the use of possible working media, and to be relatively free from high-pressure limitations. The scheme that was developed

[1] Work supported in part by the U.S. Office of Naval Research.

involving the use of an equilibrium or steady-state plasma and the pulsed ionization chamber (PIC) technique for plasma density measurements has all of these desirable characteristics. The technique and its application to the study of the kinetics of nuclear seeded MHD plasmas are the topics of the present paper.

EXPERIMENTAL METHOD

The plasma is generated within the sensitive volume of a ^{3}He filled ionization chamber similar to that shown in figure 1. This is placed in the thermal

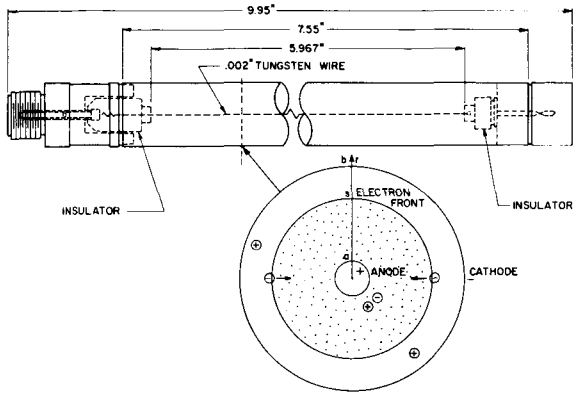

FIGURE 1.—*Ionization chamber configuration.*

column of the University of Florida Training and Research Reactor (UFTR) much in the same manner as would occur in the gas coolant channels of a nuclear seeded reactor–MHD converter coupled system in which the plasma is produced during the slowing down of the charged products of an exoergic nuclear reaction such as

$$^3\text{He}+\text{N} \rightarrow {}^1\text{H}+{}^3\text{H}+764\text{ keV}$$
$$\text{(product kinetic energy)} \qquad (1)$$

The Q of the reaction is partitioned between the two products as kinetic energy. Through the slowing-down process, the kinetic energy is dissipated in the helium gas as ionization and excitation, producing on the average approximately 2 to 3×10^4 ion pairs per interaction with the electrons having sufficient time to slow down to the thermal energies of the gas.

The ionization density is allowed to build up in the gas in a field-free region, which in the case of the ionization chamber is the region between the electrodes of the chamber, where the time rate of change of the plasma density N during growth can be represented by the equation

$$dN/dt=S-\sum_r a_r N^r \qquad (2)$$

where

S external ionizing source term
r order of loss mechanism
a_r recombination or attachment coefficient for the rth-order loss mechanism

Each of the a_r coefficients may be a composite of several possible mechanisms that exhibit a particular order of dependence on the plasma density. It can also be shown that the plasma produced through neutron reactions and slowing-down processes after times long enough for the steady state to be established for sufficiently high source rates will be uniformly distributed throughout the chamber volume, permitting one to use the approximate relationship that $N_e=N_i=N$, the requirement for a neutral plasma.

At steady state the equation reduces to a relationship between the production and loss mechanisms; i.e.,

$$S=\sum_r a_r N^r \qquad (3)$$

this being the condition necessary for the equilibrium-type plasma measurements. The source term S which represents the rate of ionization of the helium gas can be written as

$$S=\phi N_a \sigma \bar{E}/w \qquad (4)$$

where

ϕ thermal neutron flux density, N cm^{-2} sec^{-1}
N_a ^{3}He atom density, atoms cm^{-3}
σ thermal neutron reaction cross section, 5400 b
w average energy required to produce an ion pair, eV/ion pair
$\bar{E}$ average energy deposited in the gas by the (n, p) reaction products
Q the ^{3}He (n,p) ^{3}H reaction energy, 764 keV

For equilibrium or steady-state kinetic studies only two factors need be established, the source rate of ionization S and the steady-state plasma density

N. From these can be determined the level of ionization that can be produced within the reactor coolant and the plasma loss coefficients a_r that have been effective during plasma buildup. The pertinent relationships for the equilibrium measurement scheme are shown pictorially in figure 2 where an idealized

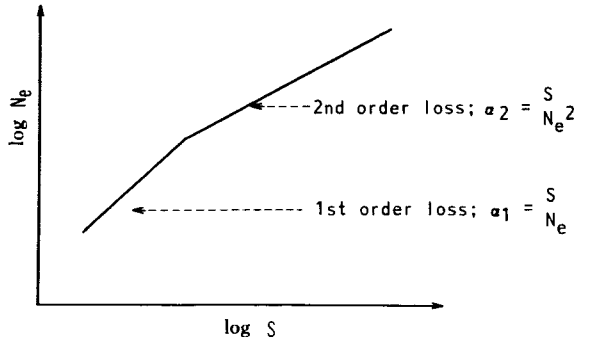

FIGURE 2.—*Summary of equilibrium measurement scheme.* $S = \sum_r a_r N_e^r$; $r = 1, 2$; *log* $S =$ *log* $a_r + r$ *log* N_e; $1/r =$ *Slope of log* N_e *against log* S.

plot of the logarithm of the plasma density versus that of the source rate is given showing regions of linear response characteristic for the case where specific orders of loss predominate over definite regions of plasma density. The order of loss responsible for such linear regions can be obtained from the inverse of their slopes and the loss coefficients can then be determined by applying the appropriate kinetic expressions, as shown in the figure, to the data and solving for the loss coefficients.

The source term S needed in these measurements can be determined experimentally by measuring the steady-state chamber saturation ion current with a constant high voltage potential applied across the chamber electrodes, as shown in figure 3. During

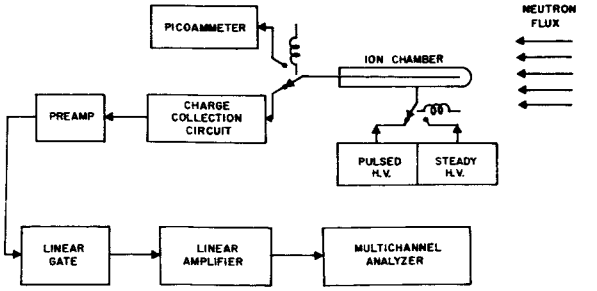

FIGURE 3.—*Block diagram of experimental apparatus used for equilibrium kinetic measurements.*

the measurement, the current is measured with a picoammeter to establish the source ionization rate for each reactor power level for which data are taken. The relationship between the saturated ion current I and the source term S is given by

$$S = I(\mathrm{A})/e(\mathrm{C/ion\ pair})\ U\ (\mathrm{cm^3})$$
$$S = I/eU\ (\mathrm{ion\ pairs/cm^3\ sec}) \qquad (5)$$

where U is the sensitive volume of the chamber.

A measure of the second quantity N, the equilibrium plasma density, can be obtained for a given power level and ion current by use of the PIC technique. A simplified version of the instrumentation used for this purpose is shown in block-diagram form in figure 3. Its operation consists of repetitively applying a pulsed high-voltage collection potential across the electrode system of the ion chamber, represented by the closing of switch S_1 in figure 4, a

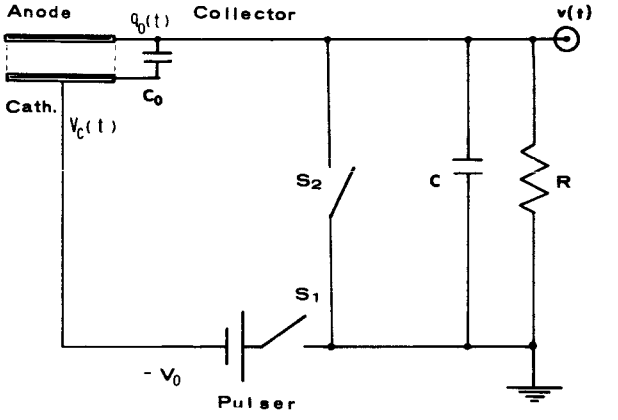

FIGURE 4.—*Schematic diagram of the equivalent circuit for the pulsed ionization chamber circuit.*

schematic of the chamber circuit, and measuring the voltage developed across the ion chamber output circuit load impedance following the rapid charging of the chamber capacitance through an avalanche transistor or biased diode charging network represented by the closing of switch S_2. After the rapid charging of the chamber capacitance, which allows the anode circuit to be returned rapidly to its quiescent condition following the passage of the pulsed high voltage wave front, switch S_2 is opened. The voltage then developed across the anode load impedance as a consequence of electron motion within the chamber and collection at the anode is amplified,

digitized, and stored in a multichannel pulse height analyzer (MCA). The voltage pulse profile can also be observed or photographed with an oscilloscope display unit.

The sequence of events is shown in figure 5. Indicated is the manner in which the electron component of the plasma is rapidly swept from the chamber volume during the application of the high-voltage collection potential and then allowed to recover to its asymptotic steady-state level between pulses. The voltage signal $v(t)$ observed across the anode load has a time profile lying somewhere between the two extreme cases shown in figure 6, which represent the large and small anode circuit resistance-capacitance time constants, respectively.

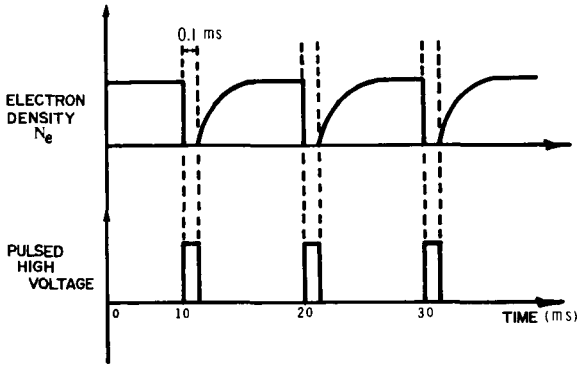

FIGURE 5.—*Ionization chamber pulse sequence characteristics.*

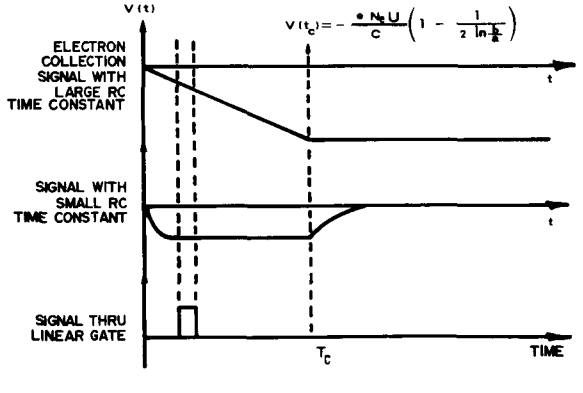

FIGURE 6.—*Time dependence of pulsed ion chamber anode voltage signal.*

RESULTS AND ANALYSIS

A direct plot of the log-log relationship of the two measured quantities, the anode voltage signal amplitude and the ion chamber saturation current for a 1-atm ^{3}He filled chamber, is shown in figure 7 where in the figure the amplitude of the voltage is given as a function of the MCA channel number. The close resemblance between the form of the resulting plot and that shown in figure 2 permits one to determine immediately that the equilibrium kinetics of the plasma buildup involves first- and second-order loss mechanisms for the electrons. Since it has already been shown that the source term S can be obtained directly from the saturated ion current, all that remains to be done prior to obtaining values for the loss coefficients is to establish a relationship between the anode voltage signal amplitude and the initial steady-state plasma density.

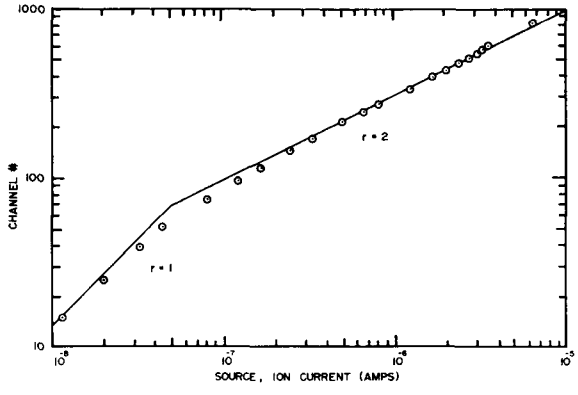

FIGURE 7.—*Typical raw data for equilibrium measurements of a 1 atm ^{3}He chamber.* P = *1 atm.*

For low levels of plasma density of 10^8 cm^{-3} or less where space charge effects are negligible, the densities can be obtained from the anode voltage pulse amplitudes by a system of linear equations for the electron current during collection and by applying Kirchhoff's second law for the response of the anode circuit to the current during that time. In the absence of an appreciable space charge effect and for an ion chamber having cylindrical coaxial electrode geometry where the ratio of the inner to outer electrode radii $a/b \ll 1$, it has been shown, by extending the treatment of Rossi et al. (refs. 2 and 3) to the case of an initial uniformly distributed neutral

plasma, that the electron-ion current is essentially constant during the early times of electron collection t_c and is given by (ref. 4)

$$I(t) = -\frac{eN_eU}{t_c}\left(1+\frac{1}{2\ln(b/a)}\ln\{1-[1-(a^2/b^2)]t/t_c\}\right) \quad (6)$$

where N_e is the initial steady-state electron density. The second term in the large parentheses contributes appreciably only in the latest stages of electron collection.

From Kirchhoff's second law the voltage signal developed across the anode load impedance is given by

$$v(t) = RI(t)\,(1-e^{-t/RC}) \quad (7)$$

where R and C are the shunt resistance and capacitance, respectively, of the anode circuit and $I(t)$ is the electron current that flows into the anode circuit. Two limiting cases are of interest.

(1) *The* RC *time constant is much greater than the time for electron collection,* $RC \gg t_c$.—The leakage of charge through the load resistor R can be neglected during electron collection reducing the problem of the time dependence of the signal voltage $v(t)$ to that of the charging of the anode circuit capacitance C with the chamber current $I(t)$; i.e.,

$$v(t) = 1/C\int_0^t I(t)\,dt \quad (8)$$

which will be an approximately linear function of time throughout most of the time of electron collection. At electron collection t_c equation (8) will be given by

$$v(t_c) = 1/C\int_0^{t_c} I(t)\,dt = -(eN_eU/C)\left[1-\frac{1}{2\ln(b/a)}\right] \quad (9)$$

where the inverse logarithmic term is the fraction of the total signal that is represented by the uncollected positive ion space charge.

(2) *The* RC *time constant is much less than the time for electron collection,* $RC \ll t_c$.—Under this condition the anode capacitance C is rapidly charged to the maximum limiting voltage v_{max} that can be developed across the anode load resistance R for a given value of the ion chamber current $I(t)$ which, until electron collection, will be given by

$$v_{max}(t) = RI(t) = -\frac{ReN_eU}{t_c}\left(1+\frac{1}{2\ln(b/a)}\ln\{1-[1-(a^2/b^2)]t/t_c\}\right) \quad (10)$$

Since during the early stages of electron collection the second term for the ion current can be neglected, $v(t)$ can be expressed directly in terms of the initial electron density N_e and the electron collection time t_c. Thus, the maximum of the signal voltage under these conditions, to a good approximation, is a function of only two variables, the electron density N_e and the electron collection time t_c; i.e.,

$$v_{max}(t) = -ReN_eU/t_c \quad (11)$$

However, for plasma densities of 10^8 cm^{-3} or greater, where space charge effects can no longer be neglected, a more detailed system of analysis must be undertaken in order to relate the plasma density to the anode voltage signal profile. This can be accomplished by the more exact treatment of Kim et al. (ref. 4), where the method of characteristics is used for solving the equation of motion of the electrons of a uniformly distributed neutral plasma in terms of a time-dependent variable $s(t)$ similar to the treatment of Demetriades and Hill (ref. 5), but where the ion chamber is of coaxial electrode geometry. A set of boundary conditions characteristic of a loaded ion chamber output circuit are imposed and $s(t)$ is defined as the radius of the outer boundary of the volume containing electrons and has as its initial value $s(0) = b$. Since the mobility of the ions $k_i \ll k_e$, it is assumed, as it was in the previous treatment, that the ions remain essentially stationary during electron collection. The boundary conditions give a set of four coupled equations with four unknowns with the equations combining to yield an ordinary differential equation in terms of $s(t)^2$ that can be solved numerically with the initial electron density N_e being used as the adjustable parameter. In the case where the RC time constant used for the anode circuit is large ($RC \gg t_c$), the voltage signal pulse profile in terms of $s(t)^2$ is predicted by theory to have the form

$$v(t) = -\frac{eN_eU}{C}\left(1-[s(t)^2/b^2]-\{1-[s(t)^2/b^2]\,[1-(\ln s(t)^2/b^2)]\}/2\ln(b/a)\right) \quad (12)$$

Using this equation and the results of the numerical solutions for $s(t)$ in terms of N_e, a series of theoretical curves can be generated for comparison with experimental voltage pulse profiles measured with the PIC technique as shown in figure 8. From the

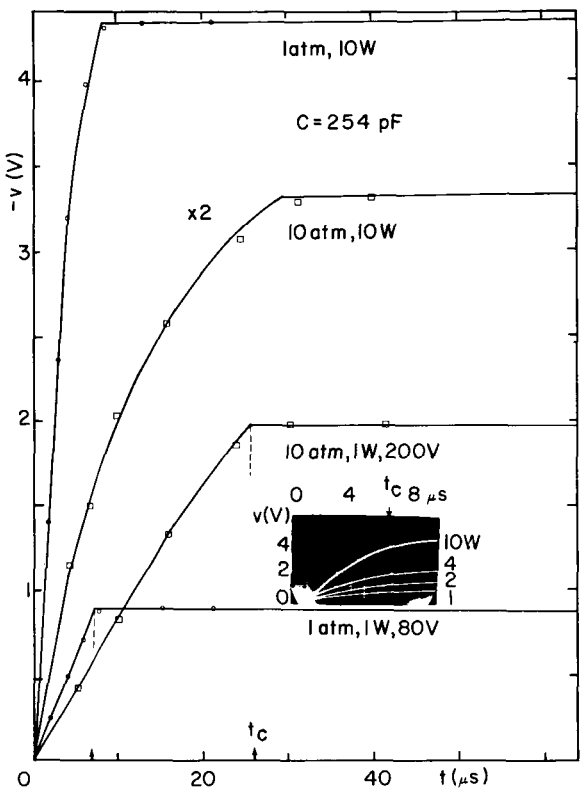

FIGURE 8.—*Anode voltage signal pulse profiles compared with theory.*

best fit of the experimental data, values of the initial electron density N_e can be determined for pulse profiles measured over a wide range of source ionization rates S and initial plasma densities. Since it has been assumed that $N_e=N$ the plasma density, values obtained for the former can be used interchangeably with the latter for high-purity helium support gases.

In figure 8 where are shown four typical sets of experimental data obtained with chambers containing 1 and 10 atm of ^{3}He with the UFTR operated at 1 and 10 W for each chamber, it is seen that the theoretical curves give excellent fits to the experimental data points. It will be noted that for the case having the lowest ionization density (1 atm, 1 W), the pulse profile is quite linear within the period of electron collection; this agrees with the predictions of the linear theory (with negligible space charge effect). However, for the cases of higher ion densities (1 atm, 10 W and 10 atm, 1 and 10 W), there is considerable deviation from linearity with the degree of deviation increasing with plasma density as predicted by the more detailed theory including space charge.

It is interesting to note that, for the case where the electrode radii ratio $a/b \ll 1$ and for an initial value of $s(0)=b$, the anode amplitude at final electron collection $v(t'_c)$, where $s(t'_c)=a$, given by equation (9) reduces to an expression having the same form as that derived from the linear treatment without space charge; i.e.,

$$v(t'_c) = -\frac{eN_eU}{C}\left[1-\frac{1}{2\ln(b/a)}\right]$$

However, in this case t'_c is not necessarily the same as that defined for the linear case. With appreciable space charge the local electric field intensities experienced by the electrons during the latter stages of collection can be modified sufficiently to result in an extension of the period required for observation of full electron collection. This type of characteristic is observed for the data shown in figure 8. Thus, to obtain the proper relationship between the signal voltage amplitude and the initial electron density, one needs merely to measure the voltage amplitude at the respective value of t'_c.

When the logarithm of the values of the steady-state plasma density N, deduced from the initial electron densities N_e determined by numerical fitting of the experimental curves and equating $N=N_e$, are plotted as a function of the logarithm of their respective source ionization rates, one obtains plots in which there are linear regions having slopes that are indicative of the occurrence of first- and second-order loss. Two typical plots of this type are shown in figure 9 where the data presented are for measurements performed with 1- and 10-atm ^{3}He filled chambers at an operating gas temperature of 300° K. The measurements were made over a wide range of ionization source rates $S=10^7-3\times10^{12}$ (ion pairs/cm^3 sec) and plasma densities $N=10^6$ to 10^{10} cm^{-3}. The two-linear-region characteristic predicted from equilibrium theory is quite evident

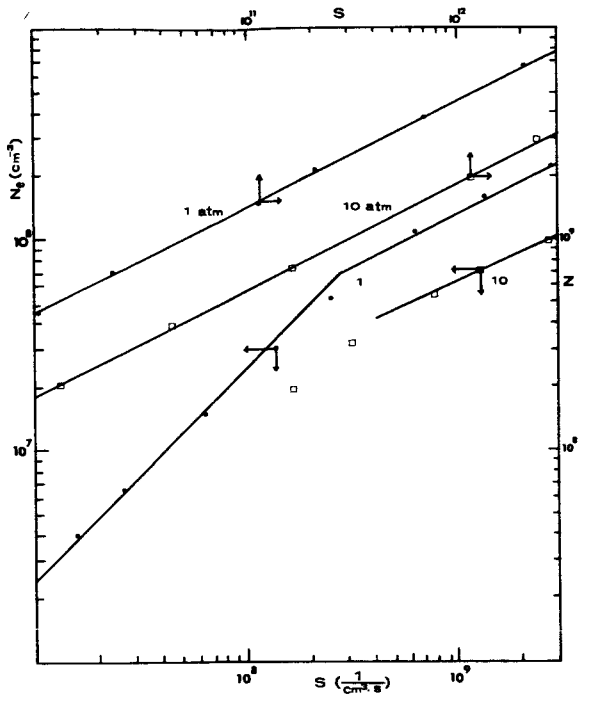

FIGURE *9.—Typical results for equilibrium plasma kinetics measurements of ³He-filled ionization chambers.* $a_1 = S/N_e^2$; $S = I/eU$.

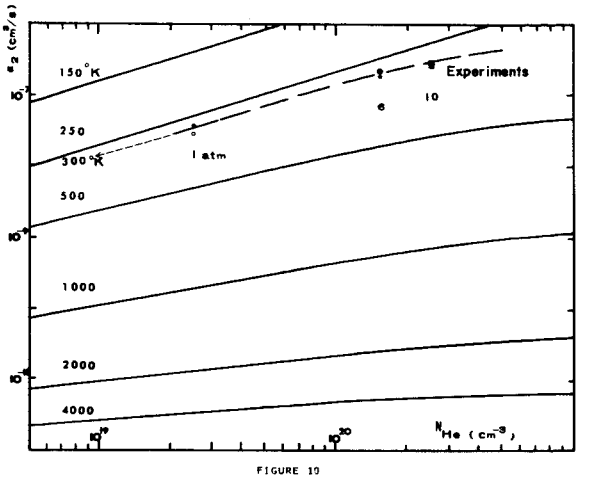

FIGURE *10.—Comparison of equilibrium kinetic measurements with the theory of Bates et al. (ref. 6).*

for each of the two cases plotted and is especially striking for the 1-atm chamber. The solid curves are the result of hand fitting the experimental data points with straight lines of slopes $1/r=1$ and $1/2$ corresponding to regions of first- and second-order loss, respectively. First-order loss coefficients obtained from these measurements ranged from a_1 (1 atm) $\cong 4$ sec^{-1} to a_1 (10 atm) $\cong 10$ sec^{-1}, which yield ambipolar diffusion coefficients corresponding to that of the He^+ ion. The second-order loss coefficients evaluated from the data of the type given in figure 9 range from a_2 (1 atm) $=4.4\times10^{-8}$ cm^3/ sec to a_2 (10 atm) $=3.2\times10^{-7}$ cm^3/sec. These parameters are found to be in excellent agreement with the predictions of the theory of Bates and Khare (ref. 6) for the second-order volume recombination coefficients of helium plasmas. The extent of the agreement is shown in figure 10 where the second-order plasma loss coefficients measured are found to fall on the 300° K constant-temperature curve obtained by interpolating between the curves given by Bates and Khare. The data are also consistent with the extrapolated results of the predictions of Deloche (ref. 7). The calculations of both Bates et al. and Deloche were based on a three-body mechanism of volume recombination in which a neutral helium atom was the third body; i.e.,

$$He^+ + e + He \rightarrow 2\ He \qquad (13)$$

However, it is quite likely that the observed second-order electron kinetics was also due in part to a second-order loss mechanism involving recombination of the electron with the helium molecular ion He_2^+, with a neutral helium atom acting as the third body, i.e.,

$$He_2^+ + e + He \rightarrow He_2^* + He \qquad (14)$$

where the helium molecular ion is rapidly formed at higher pressures by the reaction

$$2He + He^+ \rightarrow He_2^+ + He \qquad (15)$$

CONCLUDING REMARKS

The nature of the results that have been described in this paper for the equilibrium-type measurements of nuclear seeded plasmas has demonstrated that the pulsed ion chamber technique for plasma diagnostics is an effective and significant tool for the study of the kinetics of plasmas in high-pressure gases and is free from the usual limitations to low gas pressures. It has also been demonstrated that measurements can be performed within the environment of an operating reactor with possible reactor

coolant MHD converter working media. The close agreement of the results of these measurements with the findings of other investigators demonstrates that the scheme of investigation is well founded and should be readily extendable to the examination of systems other than ^3He and to the examination of other effects on the plasma such as gas composition and temperature and the electron temperature.

REFERENCES

1. Braun, J.; Nygaard, K.; and Witalis, E.: On Plasma Through Neutron Irradiation. Proc. Symp. Magnetohydrodynamic Elec. Power Generation (Paris, 1964), OECD (Paris), 1964, p. 179.
2. Rossi, B. R.; and Staub, H.: Ionization Chambers and Counters. McGraw-Hill Book Co., Inc., 1949.
3. Bridge, H. S.; Hazen, W. E.; Rossi, B. R.; and Williams, R. W.: Phys. Rev., vol. 74, 1948, p. 1083.
4. Imani, K.; Kim, S. H.; and Ellis, W. H.: Pulsed Ionization Chamber Output Voltage Characteristics. Trans. 1969 Winter Meeting of the Am. Nucl. Soc. (San Francisco, Calif., Dec. 1969).
5. Demetriades, A.; and Hill, J. H.: Transient Motion of Space Charge Through a Neutral Gas. J. Appl. Phys., vol. 36, 1965, p. 147.
6. Bates, D. R.; and Khare, S. P.: Recombination of Positive Ions and Electrons in a Dense Neutral Gas. Proc. Phys. Soc., vol. 85, 1965, p. 231.
7. Deloche, R.: Electron-Ion Recombination in a Dense Neutral Helium Plasma. Eighth Int. Conf. on Ionization Phenomena in Gases (Vienna), 1967.

DISCUSSION

Park: Why do you take the neutral atom as the third body?

Ellis: Electron densities range from 10^7 up to 10^{10} in these measurements. The atom density is quite high. The gas pressure is from 1 to 10 atm. We have a collision-dominated plasma in which the degree of ionization is extremely small.

Park: That would be true after diffusion. However, recombination should take place mainly after the electrons are formed.

Ellis: We allowed the plasma density to build up to an asymptotic limit. In this way we obtained a measure of the effective recombination coefficient. We were not measuring the one that would be effective immediately within the column.

The Performance of Helium Seeded With Uranium in a Magnetohydrodynamic Generator

ALLAN R. BISHOP
NASA Lewis Research Center

The feasibility of using helium seeded with uranium as a working fluid in an MHD generator is discussed. Nonequilibrium ionization of the seed (uranium), including losses due to electrothermal instabilities, is examined over a range of stagnation temperatures (2000° to 4000° K), stagnation pressures (10 to 50 atm), and Mach numbers (0.5 to 1.5).

The optimum mixture (for maximum power density) of helium and uranium is about 6 atoms of uranium/10^5 atoms of helium. The nonequilibrium conductivity, including instability losses, is higher than the equilibrium conductivity for the temperature range considered. The output power of a specific generator configuration is presented as a function of stagnation temperature.

The helium-uranium mixture appears to be a possible working fluid for MHD generators, although the power density is lower than those for more conventional working fluids.

A magnetohydrodynamic (MHD) generator coupled with a nuclear reactor heat source is a possible electric power source for terrestrial and space applications. Most studies of such systems for space power have assumed the use of a solid-core, gas-cooled reactor (ref. 1), but there are a number of papers where the use of liquid- or gas-core reactors is proposed (refs. 2 and 3). In a fluid-core reactor (liquid or gas) a portion of the fission fuel is evaporated or entrained into the working fluid and must pass through the MHD generator. This paper is a study of the effect of this fission fuel on the generator performance.

THE MHD GENERATOR CONCEPT

Most of the interest in liquid- and gas-core reactors is associated with nuclear rockets (ref. 4). The higher operating temperature of these reactors produces higher specific impulse. However, a major concern for such systems is that a portion of the fission fuel mixes with the propellant and is exhausted with the propellant and lost from the system. The proposals for a closed-cycle system overcome this problem by driving an MHD generator to produce electrical power and recirculating the working fluid. The output electric power is used to operate an electric rocket for propulsion. The resulting electric propulsion system, because of its higher reactor temperature, may have lower specific mass than one based on a solid-core reactor.

High reactor operating temperatures tend to make turboalternator systems infeasible and increase the attractiveness of the MHD generator concept. The MHD generator has stationary rather than rotating high-temperature machinery, and consequently has lower stresses in its structural materials. It has a smaller surface contact area with the working fluid, since the power is produced by a volume rather than a surface phenomenon. For space power applications higher permissible operating temperatures permit a higher radiator temperature, with a resulting reduction in radiator area and weight. If an MHD cycle could operate at 3500° K, for example, it would require only half as large a radiator as does the turboalternator Rankine cycle with a boiling temperature at 1365° K discussed in reference 1.

High reactor temperatures are also desirable to improve the conductivity of the gaseous working fluid passing through the generator. Usually a small amount of easily ionized seed material is added to

the working fluid to enhance its conductivity further.

GENERATOR OPERATING CONDITIONS

In this paper the reactor design is not discussed. A source with a specified stagnation temperature T_s, stagnation pressure P_s, and ratio S of seed atoms to working fluid atoms is assumed (fig. 1). The

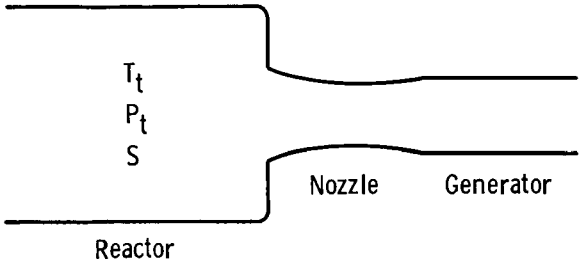

FIGURE 1.—*Reactor, nozzle, and generator configuration.*

mixture is accelerated to specified Mach number with an appropriate nozzle and then enters the generator. The flow at the generator entrance may be subsonic, sonic, or supersonic depending on the nozzle geometry.

The temperature range considered is from $T_s = 2000°$ up to 4000° K. The lower temperature can be reached with solid-core reactors, whereas the upper temperature is approximately the minimum for gas-core reactors.

Working Fluid and Seed

The working fluid is assumed to be helium. This choice is based primarily on the fact that helium is a good neutron moderator. The conductivity is higher if argon or neon is used, but these gases are less satisfactory than helium in the reactor.

Uranium is the fission fuel gas present in the working fluid (helium). Not only is it a typical fission fuel, but its low ionization potential (6.0 eV) makes it an attractive seed material. There are, of course, disadvantages in having a fission fuel seed mixed with the working fluid. The mechanical handling (condensation, pumping, etc.) of radioactive material and the stability of the reactor are only two of the more obvious ones. However, these problems may be present in any case when a liquid- or gas-core reactor is used.

Nonequilibrium Conductivity

The moderate gas temperatures (2000° to 4000° K) and the working fluid (helium) considered in this analysis dictate a need for nonequilibrium conductivity. In this method the temperature of the electrons is raised above that of heavy species. This allows the bulk of the gas to remain at moderate temperatures while significantly increasing its conductivity. The current passing through the generator feeds energy directly to the electrons through Joule heating. The electrons in turn transfer their energy to the rest of the gas by collisions with the heavy species. The temperature of the electrons is determined when these two processes are balanced.

Saha equilibrium at the electron temperature is used to specify the electron number density

$$\frac{n_e^2}{n_n} = \frac{Z_e Z_i}{Z_n}\left(\frac{m_e kTe}{2\pi\hbar^2}\right)^{3/2} \exp\left(-\frac{I}{kTe}\right) \qquad (1)$$

Here n_e and n_n are the number densities of the electrons and seed neutrals, respectively, T_e is the electron temperature, the Z's are the statistical weights of the species, m_e is the electron rest mass, k is the Boltzmann constant, and I is the seed ionization potential.

The electron temperature is determined by a balance between the gain in electron energy from Joule heating and the loss due to collisions between electrons and the heavy species

$$\frac{j^2}{\sigma} = 3\frac{m_e}{\overline{m}}\Delta\nu_e n_e k(Te - T) \qquad (2)$$

Here j is the current density, σ is the conductivity, $\overline{m}$ is the average mass of the heavy species, ν_e is the electron collision frequency, and T is the gas temperature. The symbol Δ denotes a loss factor to account for inelastic collisions between electrons and the heavy species. The Hall current is assumed to be zero, so that the electric current is perpendicular to both the magnetic field and the gas velocity. Radiation and thermal conduction are neglected.

The two previous equations are solved using an iterative technique until consistent values of electron density and electron temperature are determined. The following quantities can then be specified, using the associated expressions:

Conductivity:

$$\sigma = \frac{l^2 n_e}{m_e \nu_e} \qquad (3)$$

Hall parameter:

$$\beta=\frac{lB}{m_e\nu_e} \tag{4}$$

Output power density:

$$P_o=K(1-K)\sigma B^2U^2 \tag{5}$$

Here l is the electron charge, B is the magnetic field, K is the load parameter, and U is the gas velocity.

Electron Uranium Cross Section

The rate of energy transfer from the electrons to the gas atoms is determined by the elastic collision cross section of the electrons with the heavy species. While this quantity is well known for helium, it is unknown for uranium. To this author's knowledge no experimental or theoretical value for this cross section is available in the literature.

A rough estimate for the upper and lower bounds of the electron uranium cross section is given by Kudrin (ref. 5). Those results, after a change in units, are reproduced in figure 2. The curve for the

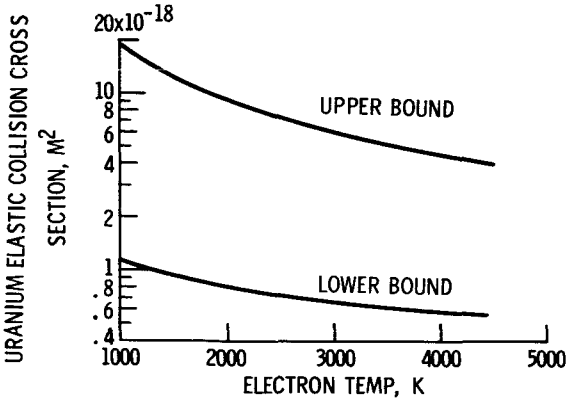

FIGURE 2.—*Uranium elastic collision cross sections as a function of electron temperature (from Kudrin, ref. 5).*

lower bound is computed directly from the equation similar to that given by Kudrin (ref. 5):

$$q_L=3.63\,Te^{-1/2}\times10^{-17}\text{m}^2$$

where q_L is the lower bound of the elastic collision cross section and Te is the electron temperature in °K. The curve for the upper bound q_H was determined by least squares fit to the data in reference 5. The equation for q_H is:

$$q_H=2.73\,Te^{-1.05}\times10^{-14}\text{m}^2$$

These cross sections differ by one order of magnitude in the temperature range of interest. This paper includes calculations at both upper and lower values.

Instabilities

In a nonequilibrium plasma there are many instabilities that can occur. Electrothermal instabilities, where large fluctuations in electron density occur as the Hall parameter is increased, have been observed in several MHD generator experiments (refs. 6 and 7). This type of instability has also been studied analytically by several authors (refs. 8 to 10). The analysis by Dr. Albert Solbes (ref. 11) is used in this paper to predict the losses due to these instabilities.

CALCULATION PROCEDURE

A computer program has been written to calculate the properties and output power density of the plasma. The input parameters to the program are the stagnation temperature and pressure, the Mach number, the seed fraction (ratio of uranium atoms to helium atoms), the magnetic field strength, the appropriate collision cross sections, and a load parameter (ratio of output voltage to generated or U×B voltage). The values of electron number density and electron temperature are determined using equations (1) and (2). The conductivity σ, Hall parameter β, and output power density P_o are then specified from equations (3) to (5). The effects of the instability are included by replacing σ and β by their effective values, as determined from the equations in reference 11. Unless otherwise noted all calculations include the effect of these instabilities.

RESULTS AND DISCUSSION

Conductivity

In figure 3 the conductivity of the working fluid is plotted as a function of uranium (seed) fraction. The stagnation temperature is 3000° K, the stagnation pressure is 1.0×10^6 N/m², the Mach number is 0.5, the magnetic field is 10 T, and the load parameter is 0.5. Unless otherwise specified, these will be the conditions assumed in the rest of this paper.

The height of the shaded area between the curves

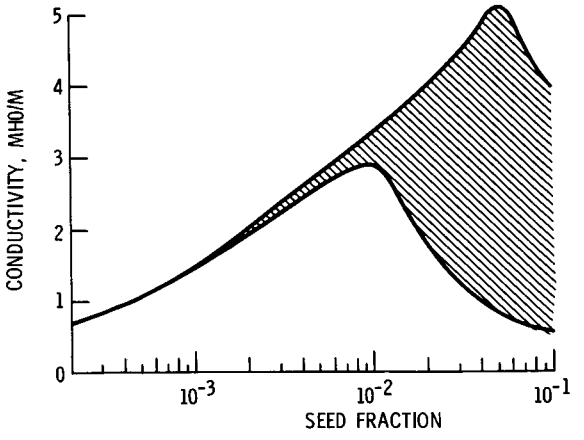

FIGURE 3.—*Helium-uranium plasma conductivity as a function of seed (uranium) fraction. Stagnation temperature, 3000° K; stagnation pressure, 1.0 × 10⁶ N/m²; Mach number, 0.5; magnetic field, 10 T; load parameter, 0.5.*

in figure 3 is the uncertainty in the conductivity, which is due to the uncertainty in the electron uranium elastic cross section. This uncertainty is also present in subsequent figures. The peak in each curve occurs when the rise in electron number density due to an increase in the number of seed atoms is balanced by a drop in electron number density and electron energy due to an increase in collisions between electrons and uranium atoms. Uranium atoms have a larger electron momentum collision cross section than do helium atoms.

The curves in figure 3 indicate that the maximum conductivity occurs between 0.01 and 0.05 seed fraction.

Power Density Variation

Figure 4 shows the variation of output power density with seed fraction. In figure 4(*a*) the Mach

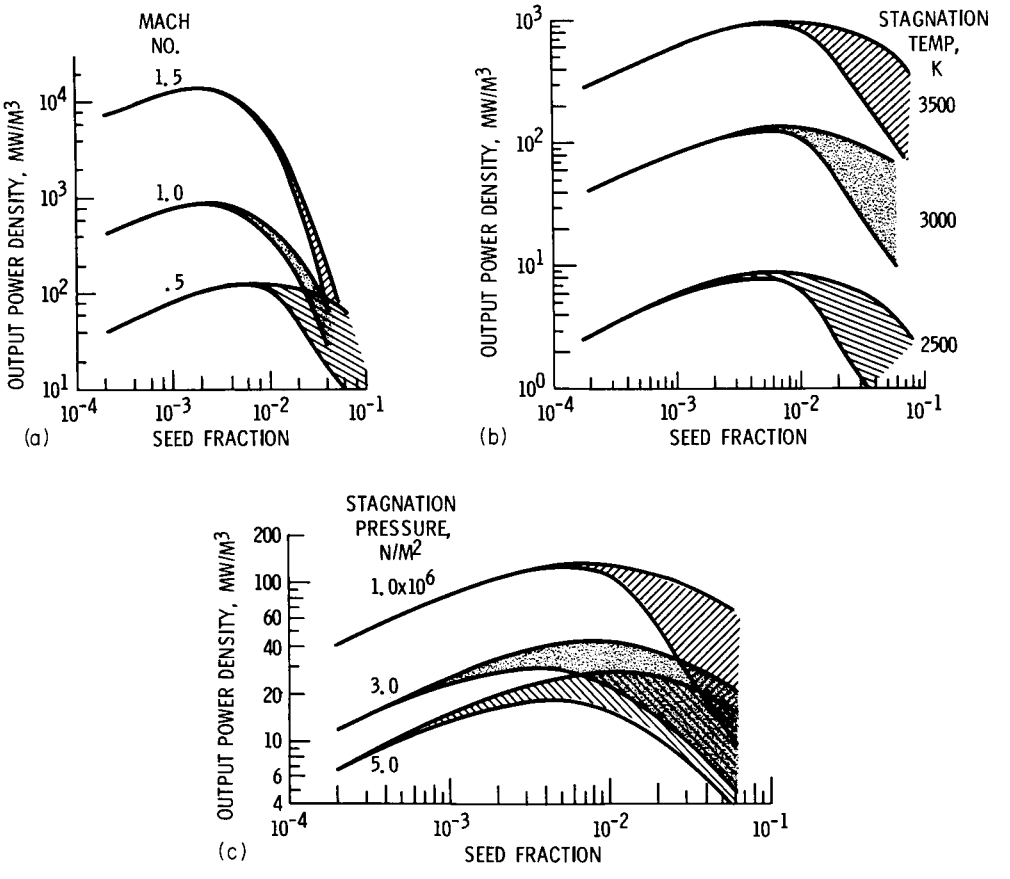

FIGURE 4.—*Output power density versus seed fraction. Unless otherwise noted the parameter values are: Stagnation temperature, 3000° K; stagnation pressure, 1.0 × 10⁶ N/m²; Mach number, 0.5; magnetic field, 10 T; load parameter, 0.5.* (a) *Mach number as a parameter.* (b) *Stagnation temperature as a parameter.* (c) *Stagnation pressure as a parameter.*

number is a parameter. The output power density increases with Mach number. However, the optimum Mach number is a function of the specific generator configuration. A subsonic generator may be more efficient, or have better choking (or "stalling") characteristics.

The initial increase in power density is due to the increase in conductivity. As the proportion of uranium in the working fluid rises, the average molecular weight of the working fluid also increases and the sound velocity decreases. Since a constant Mach number is maintained the fluid velocity also decreases. This lowers the incoming kinetic energy of the working fluid and, as a consequence, the output power density. This effect accounts for the drop in power density at large values of seed fraction.

In figure 4(*b*) the stagnation temperature is the variable parameter. The increase in output power density with stagnation temperature is due to an increase in the conductivity of the working fluid.

In figure 4(*c*) the stagnation pressure is the variable parameter. A high pressure in the working fluid improves heat transfer characteristics in the nuclear reactor but lowers the electron temperature and conductivity through increased collisions between electrons and the heavy species. The lower conductivity shows up in figure 4(*c*) as a reduction in the output power density.

From figure 4 it appears that the optimum seed fraction is about 6×10^{-3}. This value is not critical since the maximums are rather broad. This value of seed fraction will be used for the remainder of this paper.

Effect of Instabilities

The effect that electrothermal instabilities can have on the output power density is illustrated in figure 5. The output power density is plotted as a function of the load parameter. The broken curve is the ideal nonequilibrium case, where the effect of instabilities is neglected. The intermediate solid curve is the result when the instabilities are included. For comparison the power density at equilibrium conductivity, curve *e*, is also plotted. In spite of the 60-percent reduction caused by the instability, the power density is still significantly larger than it is with equilibrium conductivity under these operating conditions. The maximum value of output power density occurs at a load parameter of 0.2.

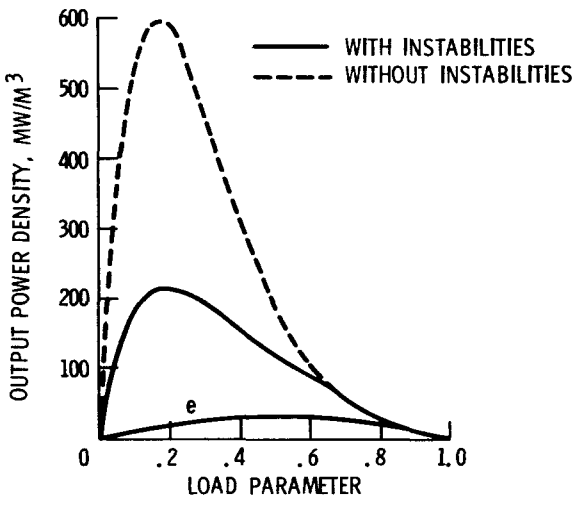

FIGURE 5.—*Output power density as a function of load parameter. Stagnation temperature, 3000° K; stagnation pressure, 1.0×10^6 N/m^2; Mach number, 0.5; magnetic field, 10 T; seed fraction, 0.006.*

Performance of a Specific Generator

The performance of a specific generator design, using helium and uranium as the working fluid, has been analyzed. The generator is one prveiously used by Nichols (ref. 1) in a comparison study of MHD and turboalternator generators. It has uniform Joule dissipation and power generation along the duct, an area variation which minimizes the volume, and a specified length of 0.5 m. A constant generator efficiency (ratio of actual enthalpy change to isentropic enthalpy change) of 46 percent is assumed. This corresponds to a constant load parameter of 0.28. At this value of load parameter the MHD generator with an inlet temperature of 3000° K and a regenerator efficiency of 0.90 has the same cycle efficiency and radiator area (for space power applications) as a turboalternator cycle boiling potassium at 1365° K (ref. 1). In figure 6 the required magnetic field at the entrance of the generator is plotted as a function of the entrance stagnation temperature, with the stagnation pressure as a parameter. The necessary magnetic field (to provide a generator efficiency of 46 percent) increases with increasing pressure and with decreasing temperature.

In figure 7 the entrance magnetic field is fixed at 10 T and the output power per unit inlet area is plotted as a function of entrance stagnation tempera-

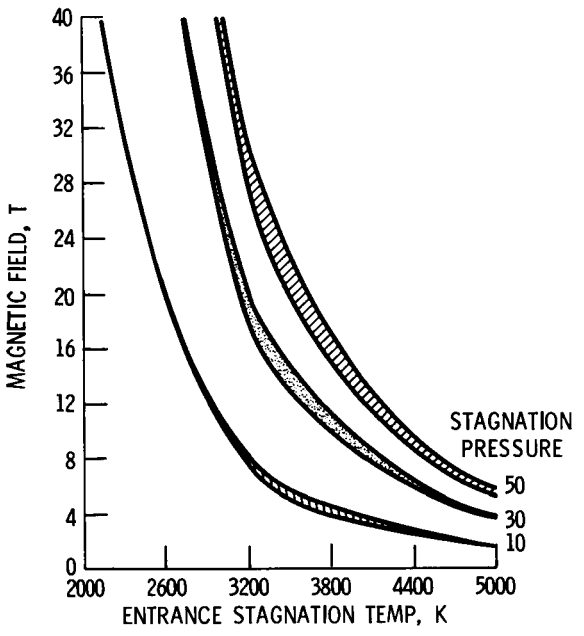

FIGURE 6.—*Magnetic field required to maintain constant generator efficiency of 0.46 as a function of entrance stagnation temperature. Generator from reference 1. Stagnation pressure as a parameter. Mach number, 0.5; seed fraction, 0.006; load parameter, 0.28.*

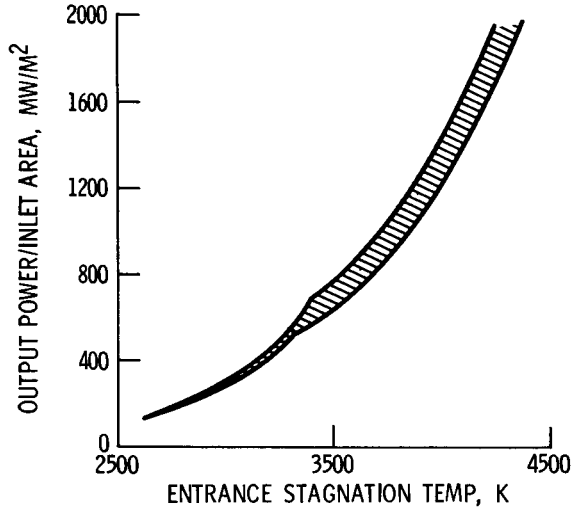

FIGURE 7.—*Output power per unit inlet area as a function of entrance stagnation temperature. Mach number, 0.5; magnetic field, 10 T; load parameter, 0.28; seed fraction 0.006.*

ture. It is clear that the output decreases rapidly as the stagnation temperature is lowered.

Of course the total output power can be increased by increasing the cross-sectional area of the generator, but since the length is fixed in this example, only a limited range of areas is available. Too large an entrance area increases end effects, while too small an entrance area increases friction losses. If the characteristic entrance dimension is one-tenth the generator length, then 1 MW is produced at about 3200° K and 10-atm pressure.

A comparison of the results in figure 7 with the output power of the same generator using neon seeded with cesium indicates a drop in output power when a helium-uranium mixture is used. At an entrance temperature of 2600° K, entrance Mach number of 0.5, and entrance magnetic field of 10 T, Bishop and Nichols (ref. 13) give an output power of 600 MW/m^2 of inlet area for neon seeded with cesium, with an entrance pressure of 30 atm and a load parameter of 0.43. From figure 7, using helium and uranium at identical temperature, Mach number, and magnetic field, the output power is 100 MW/m^2 with an entrance pressure of 3.5 atm and a load parameter of 0.28. Increasing the entrance temperature to 3500° K in figure 7 raises the output power to 700 MW/m^2 with an entrance pressure of 20 atm and a load parameter of 0.28, which is less than that for neon and cesium at the same temperature.

The reduced output power does not completely eliminate the helium-uranium mixture. An increase in the magnetic field or an increase in the volume of the generator can compensate for the power loss. The additional problems of injecting and recovering another seed material may offset the advantages of any power increase from another combination of working fluid and seed. The helium-uranium mixture seems to be a possible working fluid for MHD generators when used in conjunction with liquid- or gas-core reactors.

CONCLUSIONS

A study of the performance of helium seeded with uranium in a magnetohydrodynamic generator shows that—

(1) The helium-uranium mixture is a possible working fluid, although the output power is less than that for conventional working fluids at identical

temperatures, Mach numbers, and magnetic fields.

(2) The optimum uranium atom to helium atom ratio is about 6×10^{-3}, although the maximum is rather broad.

(3) Nonequilibrium conductivity produces more output power in the temperature range considered (2000° to 4000° K) than does equilibrium conductivity, even when electrothermal instabilities are included.

ACKNOWLEDGMENT

The author wishes to acknowledge the assistance of John M. Smith of Lewis Research Center for his advice on the nuclear reactor aspects of this paper.

REFERENCES

1. Nichols, Lester D.: Comparison of Brayton and Rankine Cycle Magnetogasdynamic Space-Power Generation Systems. NASA TN D–5085, 1969.
2. Rosa, R. J.: Radiating Space Power Plants Using the MHD Generator. Res. Rept. AMP–148, AVCO Everett Res. Lab., Feb. 1965.
3. Rosciszewski, J.: Gas Dynamic Calculations of a Power Generator and a Nuclear Rocket with Closed Circulation of a Fissionable Gas. Proceedings of the Sixth International Symposium on Space Technology and Science (Tokyo, 1965), Daikichiro Mori, ed., AGNE Publ. Inc., 1966, pp. 221–230.
4. Rom, Frank E.: Nuclear-Rocket Propulsion. NASA TM X–1685, 1968.
5. Kudrin, L. P.: Estimation of the Conductivity of a Low-Temperature (U-F) Plasma of High Density. Soc. Atomic Energy, vol. 22, no. 4, Apr. 1967, pp. 332–338.
6. Bertolini, E.; Gasparotto, M.; Gay, P.; and Toschi, R.: Subsonic Constant-Area MHD Generator Experiments With the CNEN Blow-Down Loop Facility. Electricity from MHD. Vol. 2. Int. Atomic Energy Agency, 1968, pp. 957–986.
7. Louis, J. F.: High Hall Coefficient Experiments in a Large Disc Generator. Electricity from MHD. Vol. 2. Int. Atomic Energy Agency, 1968, pp. 825–849.
8. Velikchov, E. P.; and Dykhne, A. M.: Plasma Turbulence Due to Ionization Instability in a Strong Magnetic Field. Proceedings of the Sixth International Conference on Ionization Phenomena in Gases. Vol. 4. P. Hubert and E. Cremieu—ALCAN, eds. (Paris), 1963, pp. 511–513.
9. Yoshikawa, S.; and Rose, D. J.: Anomalous Diffusion of a Plasma Across a Magnetic Field. Phys. Fluids, vol. 5, no. 3, Mar. 1962, pp. 334–340.
10. Zampaglione, V.: Effective Conductivity of an MHD Plasma in a Turbulent State. Electricity from MHD. Vol. 1. Int. Atomic Energy Agency, 1968, pp. 593–604.
11. Solbes, Albert: Quasi-Linear Plane Wave Study of Electrothermal Instabilities. Electricity From MHD. Vol. 1. Int. Atomic Energy Agency, 1968, pp. 499–518.
12. Ragsdale, Robert G.; and Lanzo, Chester D.: Summary of Recent Gaseous Reactor Fluid Mechanics Experiments. NASA TM X–1847, 1969.
13. Bishop, Allan R.; and Nichols, Lester D.: Effcet of Electrothermal Instabilities on Brayton- and Rankine-Cycle Magnetohydrodynamic Space-Power Generation Systems. NASA TN D–5461, 1969.

DISCUSSION

Anonymous: Some of the uranium fractions that you mentioned are very high and I wondered if you considered that the vapor pressure of uranium is only 1 atm at 3500° K? This material should condense at most of the temperatures you cited!

Bishop: That is probably true. It was not considered in the analysis.

Shelton: What was the assumed Mach number in the power density calculations?

Bishop: A Mach number of ½, except for the one graph where the Mach number was plotted as a parameter.

Page intentionally left blank

Gas-Core Reactors for MHD Power Systems

J. R. Williams and S. V. Shelton
Georgia Institute of Technology

In recent years much has been said about the thermal pollution, or thermal effects, produced by large electric powerplants. There is increasing concern today about all forms of pollution and the relationship between man and his environment. At the recent American Nuclear Society conference in San Francisco the fears were repeatedly expressed that the electric utilities would not be able to meet the increasing demand for power in the 1970's because of the strong local opposition that has developed to the construction of new generating plants and that, as our power reserves shrink below zero, blackouts and brownouts will become common and rationing of power may even be necessary. Much of the opposition to the new plants is based on their thermal effects, and local governments are being forced to require that these plants adhere to strict limits of the permissible amount of thermal pollution.

For instance, the following notice appeared recently in the *Southeastern Electric Exchange News Review:*

> The Florida Power and Light Co. has until July 1, 1971, to comply with the Dade County thermal pollution law at Turkey Point under another extension granted by the county's Pollution Control Board (Metro). Admitting there is no feasible way to demand immediate compliance from the utility, Metro set the following conditions with the new deadline: FPL must submit a detailed engineering plan to the county pollution control officer by February 1, 1970. A contract to build must be awarded by April 1, 1970, with completion by the 1971 deadline.

The plan includes a 6-mile cooling canal.

The demand for electric power is doubling about every 10 years. What are we going to do? Not provide this power and stifle our economy, or provide this power and vastly increase the already objectional amount of thermal pollution? Fortunately, there is a third alternative.

It may be possible, in the next decade, to build powerplants that will produce twice as much electric power and at the same time only about half as much thermal pollution as today's plants; that is, plants much more efficient than those operating today. Since an electric powerplant is essentially a heat engine operating between two temperature extremes to produce electric power, the maximum possible efficiency of such a plant is increased by increasing the temperature of the heat source or by lowering the temperature of the heat sink. The minimum heat rejection temperature is fixed by the environment, so the only approach to increasing the maximum possible efficiency is increasing the temperature of the heat source.

Unfortunately, most energy conversion devices, such as turbines and thermoelectric elements, cannot operate with source temperatures above about 2500° K. However, there is one energy conversion device that can extract energy from a working fluid at much higher temperatures. In the MHD generator power is extracted from the volume of a fluid moving in a duct where the fluid can be much hotter than the walls of the duct. The rocket engine is an ideal short-term source for such a fluid. Most currently operating MHD powerplants use such a heat source. A 20-MW rocket-driven MHD powerplant has been built by Avco for the Air Force in Tullahoma, Tenn., and a 32-MW generator has also been built by AVCO (ref. 1). These generators, however, can operate for only a few minutes because of fuel consumption. The 20-MW plant is used for powering a hypersonic wind tunnel. The first large fossil-fuel fired MHD powerplant designed for continuous commercial operation is

currently being constructed on the outskirts of Moscow (ref. 2).

The performance of an MHD generator increases with size because of the increasing ratio of volume to surface area. Also, the specific weight of the coil decreases with size and power. There should be no major difficulties in building high-performance MHD devices as large as 10 000 MW. The construction of such a device awaits only the development of a power source which can supply this energy in the form of an extremely hot, rapidly moving gas.

The heat sources for MHD generators which have received essentially all the attention thus far have been either combustion devices or solid-core nuclear reactors. The maximum temperatures in combustion devices are approximately 3000° K and they are even lower for solid-core nuclear reactors. Even when the working fluid is seeded with an easily ionized gas (i.e., cesium or potassium), if the electron temperature is equal to the gas temperature, the electrical conductivity of the fluid is low (refs. 3 to 5), particularly after accelerating the gas through a nozzle. This low electrical conductivity was the initial obstacle to actual operation of an MHD device (ref. 6) and the low conductivity is now the major barrier to the realization of the high efficiencies and power densities of which the MHD generator is theoretically capable (ref. 3).

A solution to the low electrical conductivity problem was thought to be imminent in the earlier 1960's when nonequilibrium ionization was first investigated for MHD devices. By heating the electrons to a temperature higher than that of the gas, the electrical conductivity has been shown to increase by a factor of 10 or more. The proposed method of preferentially heating the electrons is by use of the magnetically induced electric field.

This work on nonequilibrium ionization has been directed toward solid-core nuclear reactor heat sources using noble gases, such as argon, in a closed cycle. Nonequilibrium ionization in combustion devices is not feasible because the very large electron-atom and electron-molecule collision cross sections which exist in combustion products make it virtually impossible to obtain a condition of unequal electron and gas temperatures. The energy transfer from the higher temperature electrons to the gas is much too high.

However, even for the solid-core nuclear reactor using a closed cycle, Brogan states in reference 3, "Indeed, almost the total research effort in generator working fluids for use with a nuclear reactor heat source has been given to the single topic of nonequilibrium ionization. It has proven to be an elusive quarry." Magnetically induced nonequilibrium ionization may still hold the solution to the low electrical conductivity problem, but the most optimistic experimental results so far have failed to produce evidence that the desired values of electrical conductivity ($\sim$100 mho/m) can be produced by this method. Brogan discusses both basic and practical reasons as to why this attainment of useful nonequilibrium ionization is very difficult (ref. 3).

A heat source capable of temperatures higher than the 2500° K which is available from the solid-core nuclear reactor (ref. 7) is seen then to be very desirable and perhaps even essential. These higher temperatures are available by utilizing the concept of the cavity reactor in which the nuclear fuel is a dust (ref. 8), a liquid (ref. 9), or a gas. Since the gaseous reactor concept promises higher temperatures and is somewhat simpler than the dust-bed or liquid-core reactor, this design has received the most attention.

Three gaseous reactor systems that are currently being investigated are the coaxial flow reactor (refs. 10 and 11), the uranium vortex reactor (ref. 12), and the light bulb reactor (refs. 12 to 14 and fig. 1). The coaxial flow system utilizes a slow-moving central stream of very hot gaseous fissioning fuel to heat a fast-moving annular stream of particle-seeded gas by thermal radiation from the core. The vortex concept confines the fissioning fuel in the cavity in a vortex. The coaxial flow and vortex concepts are called open-cycle systems because the fuel becomes mixed with the working fluid and may have to be separated out later. The nuclear light bulb reactor, which confines the fissioning gas inside a transparent partition so that the working fluid is heated by thermal radiation through the partition, is a closed-cycle concept because the fuel does not become mixed with the working fluid. Since the gas used as a working fluid is not opaque to thermal radiation by itself, it

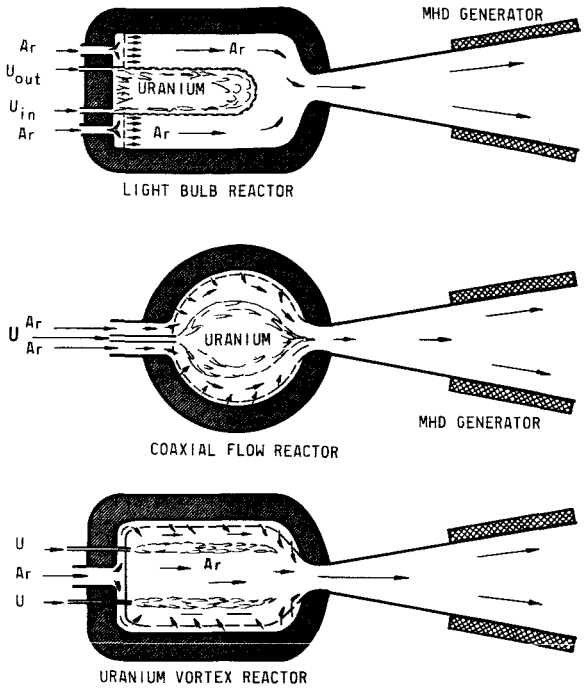

FIGURE 1.—*Gas-core reactor concepts.*

must be seeded with submicron-sized particles to insure maximum heat transfer to the working fluid and minimum heating of the containment vessel and moderator (ref. 15). The moderator, which surrounds the nuclear fuel and working fluid gases, is externally cooled. In the case of open-cycle reactors the fuel which becomes mixed with the working fluid can be condensed out when the fluid temperature drops below 3900° K.

The use of a new heat source for MHD generators in the form of a gaseous-core nuclear reactor appears to offer two solutions to the low electrical conductivity problem which would remove the major obstacle to achieving the high efficiency and power density of which an MHD generator is potentially capable. The first is the very high working fluid temperature (5000° to 7000° K) which may be produced with gaseous reactors and the second is the very high radiation flux which is available in the vicinity of such a reactor. This radiation flux may be extremely effective in ionizing the gas and preferentially heating the electrons. It could overcome many of the difficulties which are encountered with magnetically induced non-equilibrium plasmas. The feasibility of increasing the electrical conductivity by different types of radiation has been analyzed in reference 16 with some encouraging results.

The submicron-sized particles present in the gaseous-core reactor could also enhance the electrical conductivity of the fluid by supplying additional electrons by thermionic emission. This phenomenon has in fact been suggested and briefly studied as a possible substitute for potassium or cesium seeding (refs. 17 and 18). The combination of solid particle seeding and potassium seeding could be a fruitful approach in MHD generators driven by devices other than a gaseous-core nuclear reactor.

The fundamental advantage of combining an MHD generator with a gaseous reactor is a more or less complete removal of any constraint on the top temperature of the thermodynamic cycle. This is particularly important for space power systems which require a high radiator temperature. The gaseous reactor MHD generator may also serve as a topping cycle for large ground-based powerplants to considerably improve their efficiency. The exhaust from the MHD generator could be used to produce steam for conventional turbines before being returned to the reactor. The problem of thermal pollution has been becoming more acute in recent years and points out the need for more efficient nuclear powerplants.

As indicated by Rosa (ref. 19) the gaseous reactor may very well prevent MHD technology from becoming obsolete. It appears to be the best heat source which is capable of allowing the MHD generator to realize its true inherent advantages.

Various design studies (refs. 12 and 20 to 22) of gaseous reactor systems for nuclear rocket propulsion have been completed. The only significant difference between the nuclear rocket reactor and the gas-core reactor for MHD power would be the use of argon instead of hydrogen as the working fluid. Since the neutron absorption cross section of an argon atom is slightly less than that of a hydrogen molecule the operating characteristics would probably be enhanced by the substitution of argon for hydrogen. Also the use of argon should improve uranium containment in the open-cycle systems.

The authors have completed a preliminary design study of a powerplant using a gas-core nuclear

rocket engine as the power source. The working fluid was taken to be argon with a 0.2 percent potassium seed. (The potassium seed may be unnecessary if uranium becomes mixed with the argon.) A reactor pressure of 500 atm was assumed and a 50-to-1 pressure drop was allowed through the MHD duct. A stagnation temperature of 7000° K was assumed at the entrance to the duct. This is a typical exhaust temperature for gas-core reactors currently being proposed. With a loading factor of 0.75, the equilibrium electrical conductivity of the gas entering the generator was calculated to be 300 mho/m at the entrance and 50 at the exit, assuming sonic flow through the duct. The conductivity σ was calculated using the equation

$$\frac{1}{\sigma}=\frac{4}{3}\left(\frac{8kT_e}{\pi m_e}\right)^{1/2}\frac{m_e}{N_e e^2}(N_A Q_{eA}+N_k Q_{ek}) + \frac{65.3}{T_e^{3/2}}\ln\left[\frac{12\pi}{e^3 N_e^{1/2}}(\epsilon_o kT_e)^{3/2}\right] \text{ ohm-m}$$

which sums the resistivities due to electron-argon atom collisions, to electron-potassium atom collisions, and to the interaction of the electrons with the Coulomb fields of the ions. In the above equation T_e is the electron temperature, k is the Boltzmann constant, m_e is the electron mass, N represents number densities, and Q stands for the effective collision cross sections. Collision cross sections variable with respect to temperature were used in these calculations. Also the conservative assumption was made that the electron temperature would be equal to the gas temperature, whereas actually the electron current and nuclear radiation should increase the electron temperature over the gas temperature and thereby enhance the electrical conductivity.

Figure 2 illustrates the resulting plant design. An open-cycle gas-core reactor is shown in conjunction with a fissile fuel separator to remove condensed fuel from the argon for reuse. Separation should be no problem since the uranium would be in the form of small liquid droplets entering the separator. All components of this plant, other than the reactor and fuel separator, can be constructed using present-day technology. Although no MHD generator of this size has yet been built, there are no engineering reasons why one cannot be.

The thermal efficiency of the plant was calculated

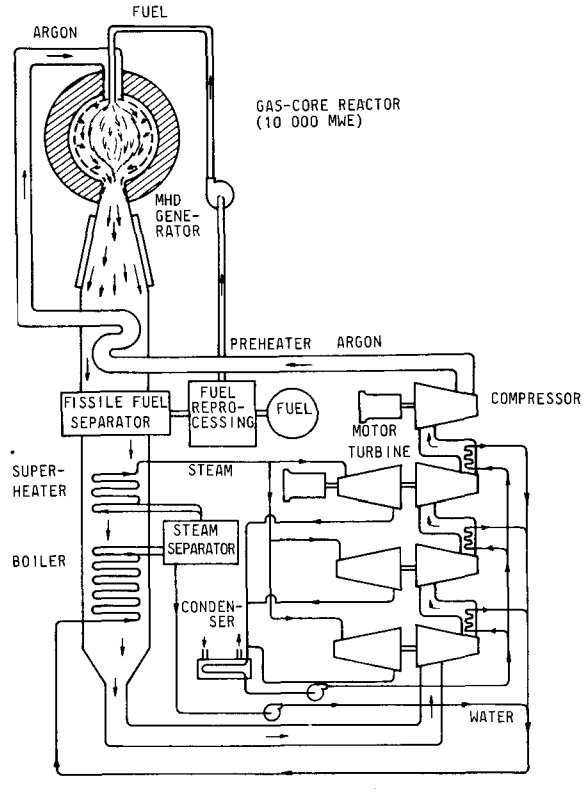

FIGURE 2.—*Preliminary design of gas-core MHD powerplant.*

by dividing the net electrical power output by the heat supplied by the reactor after taking into account pressure losses and losses in the MHD duct, the compressor, and the steam powerplant. A steam plant efficiency of 35 percent was assumed. It was found that the steam plant would not supply enough power to drive the compressor since a 120-psi pressure loss was assumed, so some of the electrical power from the MHD generator would be used to drive the final stages.

The basic equation for the thermal efficiency is

$$\eta_t=\frac{E_{\text{MHD}}+\eta_{spp}Q_{rej}-W_c}{Q_R}$$

where E_{MHD} is the electrical output of the MHD generator, η_{spp} is the efficiency of the steam powerplant, Q_{rej} is the heat rejected from the argon working fluid including intercooling, W_c is the compressor work, and Q_R is the heat supplied by the reactor. Since the heat capacity of argon is constant over a wide range of temperatures and pressures, this equation reduces to

$$\eta_t = \frac{(T_1-T_2)+\eta_{spp}[(T_3-T_4)+3(T_5-T_4)]-4(T_5-T_4)}{T_1-T_6}$$

where the temperatures are as indicated by figure 3. The results of this analysis are presented in table I.

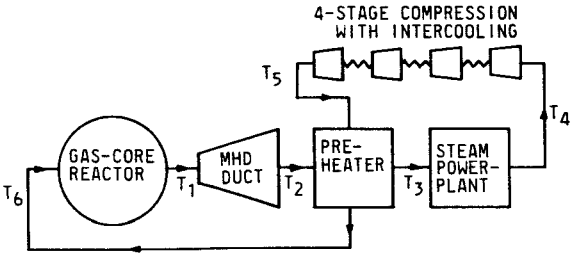

FIGURE 3.—*Block design of gas-core MHD powerplant.*

The authors believe that the assumptions made in this analysis are fairly conservative, and yet a thermal efficiency of 74 percent is predicted. The primary reason for this drastic increase in efficiency over present-day plants is the very high source temperature that is used. The corresponding Carnot efficiency is 94 percent. Obviously, the temperature of the working fluid at the walls of the MHD duct will be cooler than the bulk temperature, but for large generators this has little effect. Thus the gas-core MHD powerplant concept offers a sizeable increase in efficiency over today's plants with a corresponding large reduction in thermal pollution per electrical megawatt.

The system which was considered for this analysis used a nuclear rocket-type reactor in a Brayton cycle with argon as the working fluid. A Rankine cycle system using UF_6 or another suitable uranium- or plutonium-bearing compound may have certain advantages over the Brayton cycle system presented. The pump work would be much less. A Rankine cycle would be more attractive for a space power system if the working fluid were condensed in the radiator and pumped back into the reactor as a liquid. Also, if a uranium or plutonium bearing working fluid is used, there is no longer any need to separate the fissile fuel from the working fluid in the reactor, as must be done in the gas-core nuclear rocket engine since hydrogen would be the propellant. A single-fluid reactor, as illustrated

TABLE I.—*Performance Parameters of a Gas-Core Reactor MHD Commercial Power System*

Parameter	Value
Reactor	
Thermal power input, MW	10 000
Gas pressure, atm	500
Gas inlet temperature, °K	1700
Gas exit temperature, °K	7000
MHD duct	
Length, m	10
Magnetic field, T	4
Isentropic efficiency, percent	80
Electrical conductivity at inlet, mho/m	3000
Inlet pressure, atm	500
Exit pressure, atm	10
Electrical conductivity at exit, mho/m	50
Inlet velocity	Sonic
Inlet area m^2	0.135
Inlet temperature, °K	7000
Exit temperature, °K	2520
Power out, MW	8400
Preheater	
Primary gas inlet temperature, °K	2520
Primary gas exit temperature, °K	1545
Secondary gas inlet temperature, °K	725
Secondary gas exit temperature, °K	1700
Steam powerplant	
Thermal input (including intercooling), MW	4000
Thermal efficiency, percent	35
Argon gas inlet temperature, °K	1545
Argon gas outlet temperature, °K	400
Power out, MW	1400
Compressor	
Number of stages	4
Intercooling (to steam powerplant), MW	1850
Power/stage, MW	610
Compressor isentropic efficiency, percent	85
Inlet temperature, °K	400
Exit temperature, °K	725
Pressure ratio/stage	3.7
System	
Working fluid	Argon
Mass flow rate, kg/sec	3600
Pressure loss (ducts, preheaters, etc.), psi	110
Plant thermal efficiency, percent	74

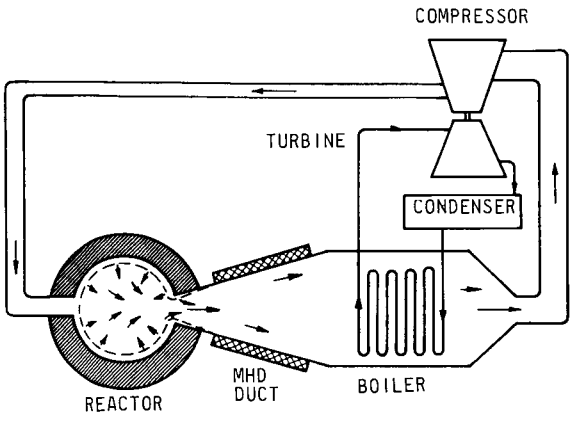

FIGURE 4.—*Concept of single-fluid reactor powerplant.*

by figure 4, would not suffer from the problems of achieving high separation which plague the nuclear rocket concepts and would also require a smaller critical mass of fuel.

In summary, the advantages of the gas-core reactor MHD powerplant are as follows:

(1) High thermal efficiencies of the order of 70 percent

(2) Thermal pollution per electrical megawatt reduced a factor of 3 to 5 over that of today's plants

(3) Very high fuel economy because of the high efficiency and high fuel burnup achieved by recirculating the fissile fuel

(4) The possibility of continuous fuel reprocessing

(5) The continuous removal of xenon and other fission product poisons from the reactor

(6) The absence of fuel elements which may rupture and which have to be replaced

(7) A basically simpler reactor than today's power reactors

It may be said that the gas-core reactor and the MHD generator are relatively new concepts, each with its own problems, and that if you bring the two together, you have twice as many problems. However, that is not the case for the gas-core reactor MHD concept. The big problem with MHD today is achieving high electrical conductivities, but the gas-core reactor solves that problem by providing an extremely hot working fluid. Also, the major problems attributed to the gas-core reactor stem from its use for high specific impulse nuclear rocket propulsion. The constraints on a gas-core reactor for MHD power are much less severe. Thus, bringing the gas-core reactor and the MHD generator together should help to solve the problems of both.

REFERENCES

1. MATTESON, A. C. J.; ET AL.: Energetics 6: Magnetohydrodynamic Power. Mech. Eng., Nov. 1966, pp. 38–41.
2. EVANS, R. K.: 75-MW MHD Power Plant Nears Completion. Power, Jan. 1969, p. 66–67.
3. BROGAN, T. R.: The Plasma MHD Power Generator. Advances in Plasma Physics, Vol. 1. Intersci. Publ., 1968.
4. DOWDY, M. W.: Electrical Conductivity of Seeded Gases at Moderate Temperatures. Ph.D. thesis, Ga. Inst. Technol., Dec. 1968.
5. SHELTON, S. V.; AND CARLSON, W. O.: Variable Collison Cross Section Effects on Electrical Conductivity. AIAA J., vol. 4, no. 9, Sept. 1966, p. 1776.
6. KARLOVITZ, B.; AND HOLASZ, D.: History of the K&H Generator and Conclusions Drawn From the Experimental Results. Proceedings, 3rd Symposium on the Engineering Aspects of MHD. Gordon & Breach, 1963.
7. DURHAM, F. P.: The Nuclear Rocket Program at Los Alamos. Paper No. 69–556, AIAA, June 1969.
8. HATCH, L. P.; REGAN, W. H.; AND POWELL, J. R.: Fluidized Solids as a Nuclear Fuel for Rocket Propulsion. J. Am. Rocket Soc., vol. 31, 1961, p. 547.
9. RAGSDALE, R. G.; KASECK, A. F.; AND DONOVON, L. F.: Performance Potential of a Radiant Heat Transfer Liquid-Core Nuclear Rocket Engine. NASA TN D–4127, 1967.
10. RAGSDALE, R. G.; AND ROM, F. E.: Gas Core Reactor Work at NASA/Lewis. Paper No. 67–499, Third Propulsion Joint Specialist Conf., AIAA, June 1967.
11. RAGSDALE, R. G.; AND LANZO, C. D.: Some Recent Gaseous Reactor Fluid Mechanics Experiments. Paper No. 69–477, AIAA, June 1969.
12. MCLAFFERTY, G. H.; AND BAUER, H. E.: Studies of Specific Nuclear Light Bulb and Open Cycle Vortex-Stabilized Gaseous Nuclear Rocket Engines. Rept. No. F–910093–37, United Aircraft Res. Lab., Sept. 1967.
13. LATHAM, T. S.: Nuclear Studies of the Nuclear Light Bulb Rocket Engine. Rept. No. G–910375–3, United Aircraft Res. Lab., Sept. 1968.
14. KENDALL, J. S.; ROMAN, W. C.; AND VOGT, P. G.: Initial Radio-Frequency Gas Heating Experiments to Simulate the Thermal Environment in a Nuclear Light Bulb Reactor. Rept. No. G–910091–71, United Aircraft Res. Lab., Sept. 1968.
15. WILLIAMS, J. R.; SHENOY, A. S.; AND CLEMENT, J. D.: Radiant Propellant Heating in the Gaseous Core Nuclear Rocket. Paper No. 68–572, AIAA, June 1968.
16. VOSHALL, R.; AND EMMERICH, W.: MHD Power Gen-

eration With Photoionization. IEEE Trans. on Aerospace, vol. 2, no. 2, Apr. 1964, pp. 807–815.

17. Hooper, A. T.; Newby, D.; and Russell, A. H.: Closed-Cycle Nuclear MHD Studies Using Dust Suspensions. Preprint No. SM–74/73, 2d Int. Sym. Magnetohydrodynamic Elec. Power Generation (Salzburg), Int. Atomic Energy Agency (Vienna), 1966.
18. Waldie, B.; and Fells, I.: An Experimental Study of Gas Borne Suspensions of Thermionic Emitters as MHD Working Fluids. Phil. Trans. Roy. Soc. (London), ser. A, vol. 261, July 6, 1967, pp. 490–495.
19. Rosa, R. J.: Magnetohydrodynamic Energy Conversion. McGraw-Hill Book Co., Inc., 1968.
20. Duke, E. E.; and Houghton, W. J.: Gas Core Nuclear Rocket Engine. J. Spacecraft Rockets, vol. 4, Dec. 1967, pp. 1592–1597.
21. Ragsdale, R. G.: No title. Paper presented at the Coaxial Flow Gaseous Core Reactor Workshop (NASA Lewis Res. Center, Aug. 26, 1969).
22. Shelton, S. V.: Rocket Powered MHD Generators. Rept. No. 900–311, Jet Propulsion Lab., Sept. 1969.

DISCUSSION

Winterberg: The temperature in your reactor is 7000° K. In a terrestrial plant, I can imagine that the problem of heat rejection can be solved to some extent, but in a space powerplant the problem arises as to where you get the coolant. What is true for the nozzle is true in the other parts of the whole cycle where the temperatures are excessively high, according to present standards.

Williams: The same problem exists in the gas-core nuclear rocket engine. A few years ago, Howell at NASA Lewis Research Center did a study on the injection of a particle seeded gas in the boundary layer of a nozzle to absorb the radiation. He found that this could help to bring the temperature down and keep the nozzle cool. This is one approach and probably the most promising I have seen to date. In our analysis we took 7000° K because we figured for a gas-core reactor nuclear rocket engine connected with an MHD generator. For the Rankin-cycle system for space power, one may want to use a single fluid. You would have to cool the nozzle in some way, for example, by a sodium coolant going through the nozzle and then through a radiator.

Keyes: I want to reinforce what Dr. Williams has proposed by reminding everyone that ORNL has operated three reactors in which the fuel was circulated outside the core of the reactor, and one of these—the molten salt reactor—has been very successful. The other two had some problems, but not with fission product buildup. Admittedly these were liquid fueled, not gas fueled, but we had continuous chemical processing and fission product removal. I wanted to make this comment in order to show that something similar to Dr. Williams' suggestion has been done. His last concept is particularly appropriate to what we have done at Oak Ridge.

Williams: People think of these systems as being extremely complicated, but I propose that one take a good look at a Westinghouse or GE system if one wants to see something that is really complicated. There one has to replace fuel elements; one has to take them out of the sides and put them in the middle; and one also has to rotate fuel elements. One just does not have that kind of maintenance problem with our kind of system.

Page intentionally left blank

Effects of Columnar Recombination on Conductivities of Nuclear-Seeded Plasmas[1]

D. D. Orvis and G. R. Dalton
University of Florida

The possibility of employing MHD energy conversion with nuclear reactors has received considerable attention in recent years. One plan for such a system would employ a reactor with a cooling gas ionized in the reactor and passed through an MHD generator. To achieve the desired level of electrical conductivity at temperatures which are compatible with the reactor materials, various schemes have been suggested for enhancing the ionization. One method, which is termed nuclear seeding, would employ the isotope ^{3}He in a helium-cooled reactor. The products of the (n,p) reaction are used to ionize the coolant. Another means of achieving the desired ionization would be to release or to generate fission fragments in a suitable coolant gas.

The ionization which is induced by either fission fragments or the products of the (n,p) reaction in ^{3}He is produced in the localized tracks or columns. Such inhomogeneities in the ionization density could reduce the gas conductivity in two ways. First, the ionization columns create localized electrostatic fields which retard homogenization. Second, the high columnar density enhances the recombination.

The phenomenon of columnar recombination has been recognized for many years, generally in connection with unsaturation effects in ion collection. Although such effects are generally small for noble gases, they can be expected to be larger for a system of uranium plasma which is ionized by fission fragments. Furthermore, a recent analytical development by Wilhelm (ref. 1) suggested that even noble gases could exhibit high columnar recombination if the diffusion processes in the column are controlled by the space charge, i.e., where ambipolar diffusion is present. We were concerned that such an effect could be deleterious to the proposed methods of plasma generation. As part of a plan to resolve this matter, we initiated a basic study of the kinetic behavior of columnar ionization. The results of this study were applied to considerations of system conductivities. Although the scope of the study was limited and the main interest was in ^{3}He systems, the results provide some insight into the dynamics of fission-fragment ionization in gases.

DIFFUSION-RECOMBINATION STUDIES

The present study of the kinetics of an ionization column assumes that the columns consist of electrons, one species of singly charged positive ions, and a background of neutral gas atoms. The ionized particles are distributed along a column which is characterized by a very large length-to-diameter ratio. The kinetic behavior of the column is described by a set of coupled nonlinear partial differential equations. These equations are the well-known diffusion-recombination equations for the time rate of change of the particle density:

$$\frac{\partial n_+(r,t)}{\partial t} = D_+\nabla n_+ + e\mu_+\nabla\cdot(n_+\nabla\phi) - an_+n_- \qquad (1)$$

$$\frac{\partial n_-(r,t)}{\partial t} = D_-\nabla^2 n_- - e\mu_-\nabla\cdot(n_-\nabla\phi) - an_+n_- \qquad (2)$$

$$\nabla^2\phi(r,t) = \frac{-e}{\epsilon_0}(n_+ - n_-) \qquad (3)$$

From left to right, the terms on the right-hand side of the first two equations are the diffusion term, the space charge term, and the recombination term. The ion and electron distributions are coupled non-

[1] Work supported in part by the Office of Naval Research and the U.S. Atomic Energy Commission.

linearly through the Poisson equation with the space charge term and through recombination. The equations are quite general until the coefficients, boundary conditions, and initial conditions are specified. For our study, we assumed the background was ^{3}He and inserted appropriate ion and electron diffusion coefficients and mobilities. The recombination coefficient for the three-body ion-electron-neutral process was used for the basic model but was varied parametrically to allow for other processes which might dominate in very dense columns.

The simultaneous solution of the differential equations is obtained by rather standard finite-difference numerical techniques. The details of the method and the treatment of spatial boundary conditions are described elsewhere (ref. 2). For initial conditions, however, both ion and electron species are assumed to have a Gaussian distribution about the column axis. The initial mean-square radius of either distribution is specified by the parameter b_o^2.

The Gaussian distribution function has significance since this is the asymptotic form which develops in the free diffusion of particles away from a line source in an infinite medium. For free diffusion, it can be shown that the mean-square radius grows linearly in time with a slope which is four times the diffusion coefficient. Deviations from pure Gaussians are expected in the presence of space charge and recombination effects. Calculations were carried out with the electron temperature treated as a parameter. Figure 1 is a schematic representation of typical results from the numerical calculations for one electron temperature. The logarithm of the electron density is plotted versus the squared radius at some time greater than zero. The parameter N_o is the specific ionization (ion pairs/cm) in the initial track.

The bottom broken line indicates the shape of the initial distributions of both ions and electrons. For the time t considered, the electrons represented in the bottom curve are diffusing freely.

As the specific ionization increases, more and more of the electronic component becomes retarded by field effects. Near the column axis a certain fraction of the electrons remains to neutralize the space charge. Thus, over that range, the column is exhibiting ambipolar diffusion. This collective fraction increases regularly with increasing initial specific ionization N_o.

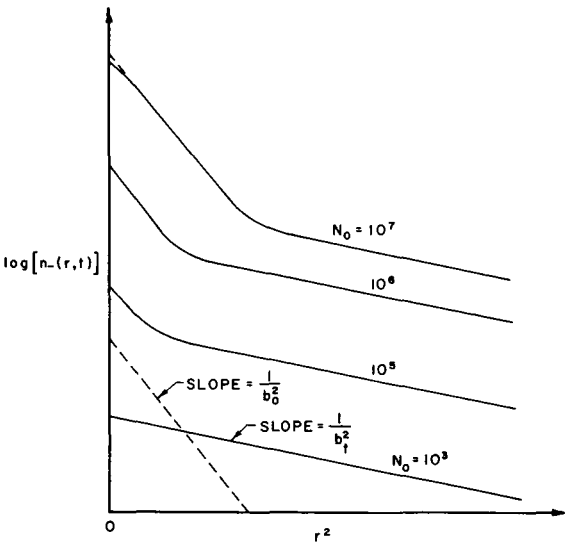

FIGURE 1.—*Columnar electron distribution at time* T. *Gaussian distribution;*

$$\log n = \frac{N}{\pi b_t^2} - \left(\frac{r}{b_t}\right)^2$$

$$b_t^2 = b_o^2 + 4\,Dt$$

The uppermost curves exhibit a depression of both components as indicated by the broken portion of the upper line. This is caused by rapid recombination which is the combined effect of the high density and the slow ambipolar diffusion. This recombination will be more pronounced for the higher recombination coefficients appropriate to uranium systems. The presentation of the density distributions in the form of this figure reveals the presence of a collective region quite readily whereas simple plots of the electron density versus the radius do not.

From considerations of the second spatial moment of the electron distribution, we were able to extract approximate values for the collective fraction of the column. Figure 2 shows this fraction as a function of the ratio $N_o/N_{\min}$ where $N_{\min}$ is the theoretical ion density at which a column of initial radius b_o should behave as a plasma and exhibit collective diffusion. It is seen that only about half of the column is exhibiting collective diffusion even when N_o is 10 times $N_{\min}$. These results suggest that a certain fraction of the columnar ionization will be lost from participating in conduction unless the local space charge is exceeded by external fields or is homogenized.

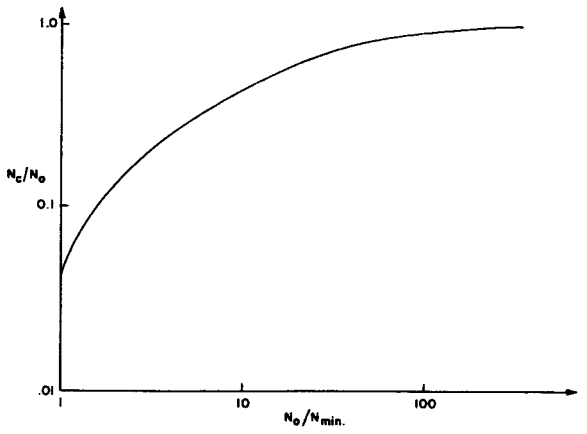

FIGURE 2.—*Collective fraction of electron column.*

Although the recombination during the collective diffusion may be assessed numerically, it is often convenient to use analytic formulas. Thus, in the course of the diffusion-recombination study, we were able to compare numerical calculations with those of two theoretical expressions. The integral ionization density per unit length was calculated as a function of time.

Figure 3 shows a comparison of the remaining

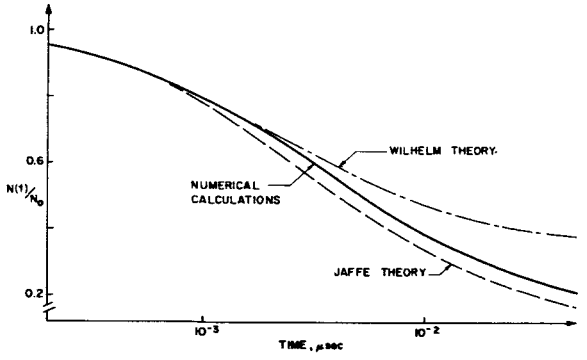

FIGURE 3.—*Comparison of columnar recombination calculations.*

fraction of ion pairs per centimeter at time t for columns which are assumed to have a 100 percent collective fraction. The well-known Jaffe theory (ref. 3) prescribes a diffusion-controlled columnar model in which the distributions remain Gaussian. Because of this, it cannot account for the reduction of the recombination rate for the relative depression near the axis and overestimates the net recombination compared with the numerical results. On the other hand, the Wilhelm theory (ref. 1) is based on a model which emphasizes the central region. It seems to underestimate recombination at late times, but is very good at early times. The numerically calculated densities showed that the late-time distributions are Gaussian. Thus, it seems that the Jaffe theory could be used as an approximate, conservative description of the recombination in the collectively diffusing column.

CONDUCTIVITIES OF IONIZED REACTOR COOLANTS

The conductivity of the reactor coolant is proportional to the mean, homogeneous electron density. Although the ionization is formed in columns, initially if a sufficient number of columns are formed in a pass through the reactor the ionization can be considered as homogeneous. The space-charge field in a single column does not directly affect the overall conductivity. However, each time a new column is formed, there exists the possibility that columnar recombination will reduce the contribution of that column to the conductivity. Columnar recombination will persist until the time when the column becomes homogenized; i.e., when it blends into the background. But the time required to homogenize is a function of the mean background ionization density, the column density, and the ambipolar diffusion coefficient of the column. The diffusion coefficient is a function of the pressure and temperature of the background gas and the electron temperature. The expressions for calculating the homogenization time and the columnar recombination time are described elsewhere (ref. 4).

The variation of conductivity with pressure and temperature for two separate source terms was considered. These correspond to the situations where (1) fission fragments enter the gas from solid fuel regions, or (2) the ionizing particles are generated within the gas.

The results for ionization by fission fragments in ^{3}He when the source is external to the gas are shown in figure 4. Here σ_o is the conductivity at NTP for a nominal neutron flux of 10^{12} N/cm^2 sec. The conversion factor f for flux to columns is based on experiments of Leffert et al. (ref. 5). The straight line indicates the pressure dependence in a homogeneous

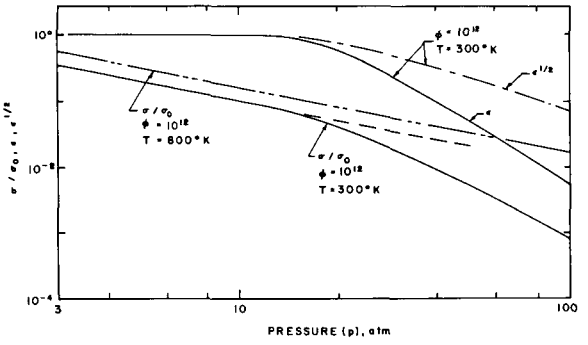

FIGURE 4.—*Ionization by fission fragments in ^{3}He when source is external to gas.*

gas. Deviations from the straight line are due to columnar recombination effects. These were calculated by an application of the Jaffe theory and estimates of homogenization time. It is seen that such effects can occur at moderate pressures but are reduced by increasing temperature and by operating at higher flux levels. Similar calculations were performed for ionization for the (n,p) reaction in ^{3}He. The specific ionization for this reaction is low, however, and columnar recombination does not perturb the homogeneous conductivity for pressures less than about 20 atm at 300° K. These data are not shown here.

CONCLUSIONS

The primary objective of the study was the investigation of the nonlinear effects of recombination and collective diffusion associated with nuclear-seeded ionization. There was very little collective diffusion and practically no recombination above that expected for a homogeneous plasma for the ionization of ^{3}He in a nuclear reactor by the (n,p) reaction. However, high pressures in the range of 20 to 100 atm increase the recombination modestly. The strong influence comes from an increase in temperature, ionization track density (as experienced with fission fragments), and recombination coefficient.

Although the results are not strictly applicable to a fissioning uranium plasma, it is speculated that there may be significant decreases in the charge available to uranium systems due to columnar effects. This can be viewed as an increase in the effective W value for the fission fragments in the gas.

REFERENCES

1. WILHELM, H. E.: Recombination in Columns. J. Chem. Phys., vol. 47, 1967, pp. 4356–4365.
2. ELLIS, W. H.: Study of Nuclear Seeded MHD Plasmas. ONR Yearly Summary Tech. Rept. No. 2, Univ. of Fla., 1967.
3 LOEB, L. B.: Basic Processes of Gaseous Electronics. Univ. of Calif. Press (Berkeley, Calif.), 1955.
4. ORVIS, D. D.: Diffusion-Recombination Kinetics of Columnar Ionization in Gases. Ph.D. thesis, Univ. of Fla., 1970.
5. LEFFERT, C. B.; REES, D. B.; AND JAMERSON, F. E.: Noble Gas Plasma Produced by Fission Fragments. J. Appl. Phys., vol. 37, 1966, pp. 133–142.

DISCUSSION

Ohanian: On what theory do you base the numerical calculations, and why do your results in figure 4 differ from those of the Jaffe and Wilhelm theories?

Orvis: Their theories assume a diffusion-controlled system and that there is always a Gaussian distribution in the system. One integrates over the Gaussians of the ions and electrons and gets their type of curve. My curves result from a similar procedure but allowance is given for local depressions and deviations, and densities are calculated in the integrations.

Miley: In the same figure the time scale is for nanoseconds. In a nanosecond, do you have sufficient time for equilibrium so that your diffusion model will be valid?

Orvis: This is a valid question. The diffusion model we used puts us on the edges of validity. However, we were interested in the initial recombination phenomena in the column. A diffusion time in this column of the order of 10 or so interparticle collision times does not put our diffusion model on too shaky grounds.

Page intentionally left blank

SESSION VII

NUCLEAR LASERS

Chairman: **A. Javan**

On Gas Laser Pumping via Nuclear Radiations[1]

J. C. Guyot, G. H. Miley, J. T. Verdeyen, and T. Ganley
University of Illinois

There are several important reasons for searching for more direct methods of transferring (pumping) energy from isotope or reactor sources into lasers. New pumping techniques may be more efficient, but perhaps more significant is the possibility that the resulting laser may offer unique characteristics, e.g., new frequencies and new methods of modulation and control. Simplified coupling could also offer weight reduction and improved reliability which may be of advantage in space applications. With the increasing "pollution squeeze" on central power stations, it may eventually become attractive to extract simultaneously several energy forms, e.g., laser and electrical power, from a single station.

Possible laser-reactor (or isotope) coupling cycles are illustrated in figure 1. The conventional technique would proceed through a heat cycle, electrical generation via a turbogenerator, and power conditioning (e.g., conversion to high voltage or rf). Two alternate techniques which proceed through a heat cycle, but which are more direct therafter, deserve note. The low-voltage arc laser, originally suggested by Johnson (ref. 1) has been demonstrated experimentally by Herceg and Miley (refs. 2 and 3) for He-Ne. This is essentially equivalent to making a thermionic diode laser, and, if the technique can be extended to cesium, it affords the attractive possibility of simultaneous extraction of electricity and optical emission from a single device.

Another important approach involving a heat cycle utilizes thermal excitation of molecular gases, typically through the expansion of a heated gas stream. This has been discussed extensively by the Russians (refs. 4 through 7); and successful experiments with a CO_2 system have been reported by one of the present authors (refs. 8 and 9) and coworkers.

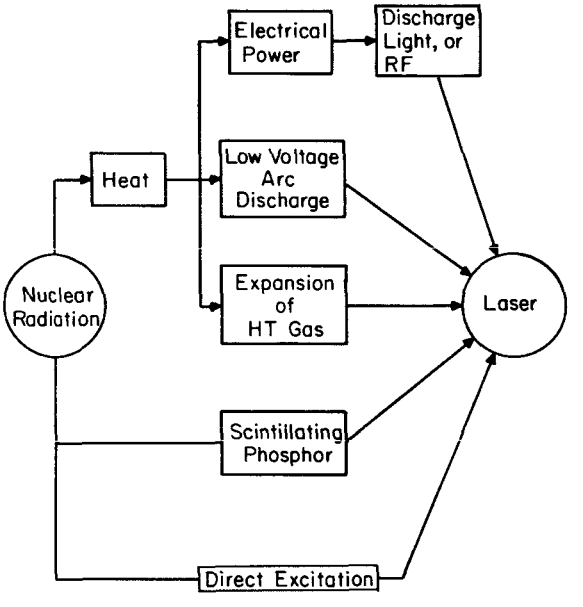

FIGURE 1.—*Various methods for coupling a nuclear reactor (or radioisotope) with gas lasers.*

There are two major approaches which bypass the heat cycle. Sadowski, Held, et al. (refs. 10 and 11) have reported studies using nuclear radiations to cause scintillation in a phosphor which in turn excites a laser, in their case, ruby. The more direct route, the use of radiation to excite the laser itself, is the subject of the present paper.

Because of their high energy, nuclear radiations typically require relatively large volumes of ma-

[1] The University of Illinois research was supported by the Research Division of the U.S. Atomic Energy Commission. Some results reported here represent preliminary studies to be used in theses by the authors.

terials for efficient absorption. A desire to optimize the absorption efficiency lead early workers to concentrate on the direct excitation of solid-state lasers (refs. 12 through 15). As it turns out, this decision proved to be unfortunate in that nuclear radiation was found to suppress, rather than aid, lasing action in solids studied to date. This "cutoff" effect is not clearly understood but is generally attributed to induced currents and effects which, in some respects, can be thought of as a type of radiation damage. While it still may well be found to be possible to avoid this effect in solids, an alternate approach is to look for lasing in liquids or gases. No studies have been reported thus far for liquids, so the present discussion will concentrate on gas lasers. Since prior work in this area has not received wide publication, we shall begin with a brief historical review.

REVIEW OF PREVIOUS STUDIES OF DIRECT EXCITATION OF GAS LASERS

The present review is thought to be complete, but if the reader is aware of additional work on the subject this information would be appreciated by the authors. The workers in this area have been somewhat isolated, and it has been our experience that persons periodically "rediscover" nuclear pumping without realizing the extent of prior studies.

The first comprehensive study of the possibility of nuclear radiation excitation of gas lasers was by Herwig (refs. 16 to 18). He recognized the radiation damage problem associated with solids and demonstrated that threshold requirements for He-Ne mixtures were theoretically within the reach of some reactor and accelerator radiation sources. Among the various advantages cited for this approach, he stressed the important point that a large-diameter He-Ne laser might be possible due to the inherently low electron temperature in the radiation-induced plasma.

Following Herwig's study, DeShong (ref. 19) carried out more detailed calculations for a He-Ne system. He showed that, if a high-pressure large-diameter laser were feasible, direct excitation might be considerably more efficient than a conventional pump cycle. In 1967 DeShong (ref. 20) undertook a series of experiments to verify the feasibility of direct pumping. While his earlier report concentrates on He-Ne, the experiments utilized a CO_2 laser, probably because of the inherent efficiency advantage afforded by it. Results from these experiments will be discussed later, but first it will be noted that during this same period experiments were in progress by Eerkins et al. (refs. 21 to 23) at Northrop Labs. and also by the present group at the University of Illinois (refs. 24 to 28). Both of these groups employed a pulsed TRIGA reactor to obtain high neutron fluxes ($<10^{17}$ thermal neutrons/cm^2-sec peak value) which interacted with boron or uranium coatings, producing charged particles (alphas, fission fragments) which then induced the desired plasma in the laser cavity. The Northrop work involved a variety of noble gases, whereas the Illinois work has, to date, concentrated on He/Ne.

Threshold Estimates

Before the prior experimental results are discussed, it is important to have some indication of threshold requirements available for various systems.

The radiation flux required for threshold depends, of course, on the type of radiation involved and the means used to couple it to the gas. We shall concentrate on reactor neutrons here. Three principal coupling methods are generally considered: Use of a uranium-coated tube, use of a boron-coated tube, or use of a nuclear reaction in the gas volume such as might be induced by a mixture involving ^{3}He or gaseous uranium. The neutron flux requirement generally increases in the same order as the above listing, thus a boron coated tube provides "representative" values and will be used here as the "reference design." Available calculations are summarized in table I. It is interesting that the threshold indicated for CO_2 is quite reasonable and well within the reach of even low-power reactors. The noble gas systems generally require higher fluxes, most conveniently obtainable in a pulsed reactor system such as the TRIGA or PULSTAR where fluxes up to 10^{17} are feasible. Only the argon ion laser calculation exceeds this value, but, as will be pointed out, some experimental data seem to indicate that special ion lines may be attainable at lower fluxes.

These calculations, although quite detailed, should still be considered as only order-of-magni-

TABLE I.—*Some Threshold Estimates*

[Assuming typical pressures: cavities used for electrical pumping]

System	N/cm² sec on ^{10}B	Reference
CO_2-N_2-He (10.8 μ)	1.2×10^9	DeShong, ref. 20.[a]
He-Ne (3.39 μ)	3×10^{12}	Guyot, ref. 25; similar calculations are also found in refs. 17 and 19.
He-Ne (0.63 μ)	5×10^{14}	
Ar (neutral; new lines)	$\approx 10^{15}$	Russell, paper on p. 53.[b]
Ne-O_2 (0.84 μ)	3×10^{16}	Rusk et al., ref. 23.
Ar^+ (ion; uv, blue lines)	$\approx 10^{18}$	Ganley, ref. 26.

[a] Later unpublished studies apparently indicate a somewhat higher value may be required.

[b] Estimate based on Russell's original calculations which assumed fission fragments.

tude estimates. With the exception of Russell's study (paper on page 53) all have generally made the important assumption that, once the energy is deposited in the gas, the subsequent splitting into various states and levels essentially follows the same route as in the conventional electron pumped case. This assumption is open to question and also fails to answer several key questions, namely: Might new lasing lines be attainable? Once normalized to corresponding energy-deposition rates, would pumping via alpha particles, protons, fission fragments, etc. be equivalent? One might instinctively expect that the answers to these questions would be yes and no, respectively. In fact, Russell's calculations which employ explicit solutions of the coupled rate equations for the various levels in argon indicate that, indeed, lines not obtainable in conventional lasers should be possible. Further, Thiess and Miley's calculations (paper on page 369) imply that some differences between alpha particle and fission fragment irradiation should be observed.

In conclusion, the threshold estimates of table I, although instructive, should be viewed with suspicion and considerable more effort in this direction appears to be warranted.

Prior Experimental Status

Results from various experiments reported to date are summarized in table II. Four separate studies of the attractive CO_2 system have been reported. To date, lasing on nuclear radiation alone

TABLE II.—*Experimental Studies of Direct Pumping of Gas Lasers*

Investigator	Source	Gas	Results
DeShong (ref. 20)	Reactor; ^{10}B coating $\geq 2 \times 10^{10}$ N/cm² sec	CO_2-N_2-He	Lower electrical threshold $< 5 \times 10^8$ N/cm² sec; larger above 5×10^9
Andriakhin et al. (ref. 29)	Accelerator; <7 μA, 3-MeV protons	CO_2-N_2-He	Constant electrical threshold; enhanced output power by a factor of 2 to 3
Allario et al. (paper on page 397)	Low-power reactor; ^3He mix; $<10^8$ N/cm² sec	CO_2-N_2-He (Xe)	Output enhancement by several percent
Eerkins, DeJuren, et al. (refs. 21 to 23)	Pulsed thermal reactor; ^{10}B and U coatings; $<10^{17}$ thermal N/cm² sec	Ne-O_2	Possible lasing; 50 W output with ~1 percent efficiency
		Ar; Ne; Kr (plus O_2, He) CO_2-N_2-He	Strong fluorescence or lasing; unusually strong 6684 Å observed in Ar; O_2 ineffective; He increased output somewhat negative
Present authors	Pulsed fast reactor; ^{10}B coating; $<10^{15}$ thermal N/cm² sec and fast N	He-Ne (plus Ar, air)	Strong absorption at 3.39 μ, but gain with air contamination
	Pulsed thermal reactor; ^{10}B coating $<10^{17}$ N/cm² sec	He-Ne; Ne	Various gain-absorption, μ-wave measurements described here

has not been achieved, but various effects on an operating electrical pumped laser have been noted. Most dramatic is the twofold to threefold enhancement of the output reported by Andriakhin et al. (ref. 29) for irradiation by protons from an accelerator. A small enhancement has also been observed by Allario et al. (paper on page 397) using a neutron-^{3}He reaction in the gas volume, despite the quite low neutron fluxes available to them. DeShong's studies (ref. 20), now discontinued, showed an initial decrease in the electrical threshold which, unfortunately, was reversed at higher neutron fluxes. He attributed this problem to effects resulting from radiation-induced dissociation of CO_2. Although Eerkins et al. (ref. 23) failed in their high flux attempts with CO_2, there is some indication that an impurity coating had formed on their mirror, making the cavity losses prohibitive. Unfortunately, their work too has been discontinued, so this experiment has not been repeated.

The only study of noble gas lasers other than that discussed in the present paper is by Eerkins et al. (refs. 21 to 23). They report strong evidence that lasing may have been obtained in several gases, and, because of the importance of this result, we will discuss it in a little more detail. A sketch of their apparatus is shown in figure 2; the lower canister section which housed the coated-tube section (boron or uranium coating) was designed for insertion directly in a TRIGA fuel element position. Elaborate supporting systems included provision for continuous gas flow and remote mirror adjustment. The optical output traveled through the 20-ft pipe section which was submerged in the reactor pool water, and then, at the water surface, was deflected 90° to the various detectors, spectrometers, etc. Their conclusions were based on the diagnostics and observations summarized in table III.

Several points should be noted. The evidence of lasing, while impressive, is all indirect. It centers around the fact that emission at wavelengths which are known to lase in electrical discharges were favored relative to normally strong fluorescent lines. The laser output was observed to require a minimum or threshold reactor power (this point was not checked for all gases, however) as well as a shift in its peak relative to the reactor peak power,

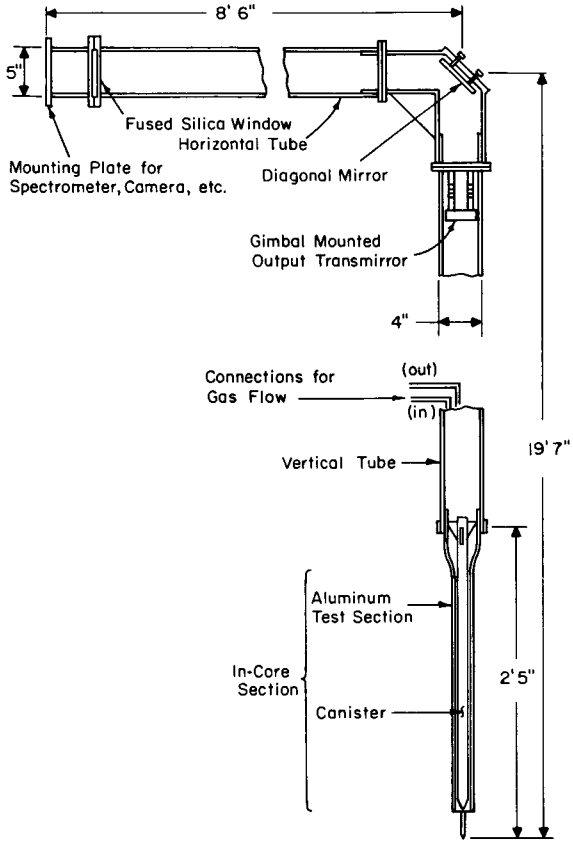

FIGURE 2.—*Sketch of confinement tube used in Northrop Corp.'s in-core experiments (adapted from ref. 23).*

and both of these characteristics might be expected for a lasing system. These features are evident from figure 3, which shows typical traces of the laser output (xenon in this instance) and the reactor power. The addition of various additives to the gases, e.g., O_2 and Ar, was not found to have a strong effect other than in the Ne-O_2 case studied in early experiments. The latter system in fact produced one of the largest light outputs, corresponding to an average power of about 50 W over the time of the reactor pulse. The observation of an unusually strong 6684-Å line from argon is perhaps one of the most startling results noted. This line is not favored in a normal argon laser, and, if confirmed, this observation supports the earlier arguments that unique lines may be possible via nuclear pumping.

In conclusion, the Northrop studies provide

TABLE III.—*Northrop Observations and Diagnostics*

Equipment	Observations and diagnostics
Early $Ne-O_2$ experiments	
Polaroid photos	Extended emission over 0.1 to 1 sec
Photomultiplier (0.3–1.2 μ)	Threshold behavior
Lead-selenide detector (1.2–5 μ)	2-mrad spot, delayed 4 to 5 msec
	Apparent Ne lines
Later experiments	
Polaroid photos	Strong "lasing" lines vs. absence of fluorescent lines
Spectrograph	Threshold behavior
PIN detector (0.3–1.1 μ)	Time delay $\approx$ 3 msec
Time resolved spectrograms	Strong 6684-Å line in Ar observed despite very low mirror reflectivity and low film sensitivity at this wavelength

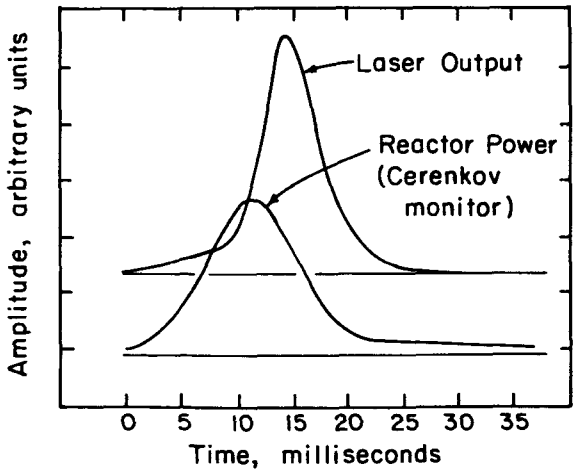

FIGURE 3.—*Laser cavity output obtained in Northrop experiments for 200-torr xenon (ref. 3).*

tantalizing, although incomplete, evidence that lasing in a variety of systems is possible with an in-core laser. It is indeed unfortunate that these experiments were not continued so that more definitive, quantitative data could be available.

IN-CORE LASER STUDIES AT UNIVERSITY OF ILLINOIS

The planning for this work was based on several philosophical points. It was thought that a comprehensive study of the characteristics of a single system would provide the best insight into the various ramifications of nuclear pumping. A He-Ne system was selected for this study, mainly because the data necessary for a detailed study were readily available. Since the threshold for the 3.39-μ line is lowest, this wavelength was singled out for the initial attempts. Because this work is still in progress and hence incomplete, the following presentation is given in historical order. First, in-core laser experiments using the Illinois TRIGA are described; then, interim gain experiments using the Oak Ridge health physics research reactor (HPRR) pulsed reactor (necessitated by a temporary shutdown of the Illinois TRIGA for upgrading in power level); and, finally, recent gain-absorption studies using the advanced TRIGA at Illinois.

Initial Studies at the University of Illinois

The laser tube shown in figure 4 was used in the initial experiments. (Although it is similar in some respects to the Northrop design of figure 2, this tube is much simpler, not having a flow system, remote adjustments, etc. Furthermore, the basic cavity dimensions and optics are entirely different.) The radiation pumping section employed an alu-

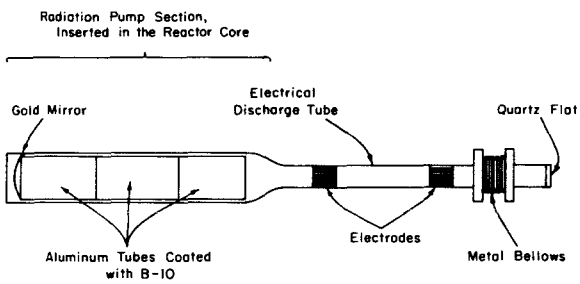

FIGURE 4.—*Design of incore laser tube used in initial Illinois experiments. The active volume (B-10 section) had about a 0.75-in. diam and was about 24 in. long. The electrical discharge-laser section, used for alinement purposes, was normally off during a reactor pulse. Several pulses were run with it on, however, to demonstrate that alinement was maintained throughout the pulse.*

minum tube (20-mm bore, 24 in. long) with its internal surface coated with a boron-10 layer roughly 450 μ thick. The smaller diameter (5-mm bore, 12 in. long) discharge tube connected above the boron section was used with conventional electrical pumping in order to aline the system prior to the experiment. The electrical power was turned off during the actual reactor pulse. The laser was intended for operation on the 3.39-μ transition so a gold-coated mirror (reflection coefficient $\approx$ 96 percent, focal length, 45 in.) was fused onto one end of the tube, and a quartz flat (reflection coefficient $\approx$ 3 percent) mounted on a metal bellows was used on the other. This allowed easy alinement, yet provided a rugged system that would maintain adjustment while being positioned in the nuclear reactor.

In order to submerge the laser in the water of the TRIGA reactor tank, it was placed in a 20-ft aluminum tube sealed at the lower end. A front surface mirror was placed at the top of the aluminum tube in order to deflect the light output into an indium-arsenide infrared detector, with a spectral response ranging from 1 to 3.8 μ.

The tube was filled with a He-Ne mixture (9-to-1 pressure ratio), and, although several pressures were studied, the following results were obtained at 5 torr. A typical reactor pulse and the corresponding light signal output are shown in figure 5.[2] Although the systems are different, note the striking similarity between this result and the Northrop data in figure 3. Specifically, both outputs are asymmetric and the peak is delayed by several milliseconds relative to the reactor pulse. The asymmetry of the light signal is characteristic of a threshold behavior. However, the significance of the delay in the peak of the laser signal is not fully understood. As already noted, the atomic lifetimes involved in the He-Ne lasing levels are quite short relative to the times involved here. Hence, this cannot account for the delay. However, assuming that the output is due to lasing, a possible explanation is that the highest excitation rate occurs near the tube walls so that a diffusion time enters while the distribution of excited states shifts to a fundamental mode with a maximum at the centerline along the active lasing volume. Also, as pointed out later, an alternate explanation in terms of a nonlasing light output is possible.

Although the light intensity is fairly low, in the microwatt range, this is roughly comparable to the output observed at the same position when the electrical pumping was used.

The threshold character of this output is further illustrated in figure 6 where the peak detector out-

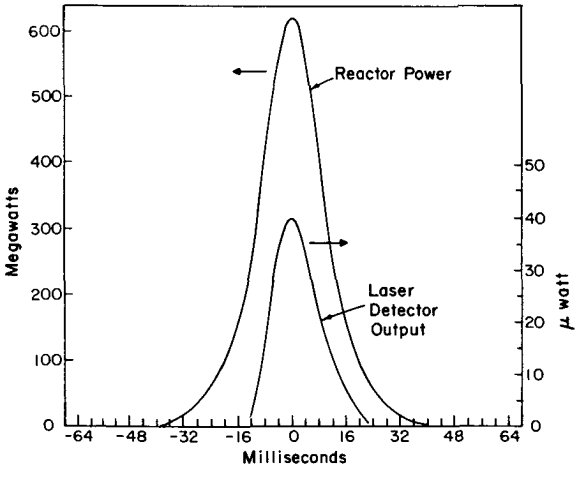

FIGURE 5.—*Traces of light output and reactor power for 5 torr of 9-to-1 He-Ne. The optics were arranged here so that radiation between only 2 and 3.5 was recorded.*

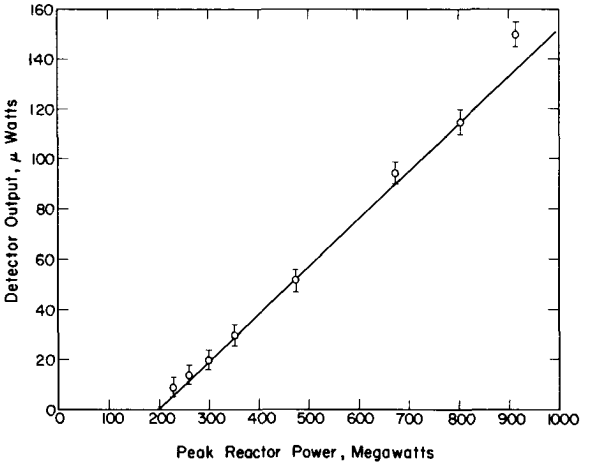

FIGURE 6.—*Plot of peak light output against peak reactor power. The threshold of 200-MW reactor power corresponds to a thermal neutron flux of* 2×10^{15} *N/cm²-sec.*

[2] Since the time scale associated with the reactor pulse is large compared with the atomic lifetimes involved in the laser cycle, the laser output and reactor fluxes can be assumed to be in a state of "quasi-equilibrium"; i.e., although a reactor pulse is used for pumping, the laser should not be viewed as a pulsed laser in the traditional sense.

put is plotted as a function of the peak reactor power. The neutron flux corresponding to the threshold shown here is roughly 2×10^{15} N/cm^2 sec. Although these results appear to indicate lasing, several discomforting facts emerged. Spectral filter measurements showed that about 90 percent of the output detected here fell in the 2- to 2.5-μ range rather than at 3.39 μ as expected. Instrumentation limitations prevented a positive identification of the wavelength(s) involved. Also, a change in the mirror alinement did not strongly affect the output. Further tests with a completely evacuated tube and with a quartz tubing containing a boron-10 coated aluminum tube showed that a large portion of the output could likely be attributed to simple thermal radiation created by the high temperature of the boron coating during the pulse, as well as fluorescence due to the quartz. In fact, these radiations also exhibit a threshold behavior and a delay time. The former apparently is related to the lower limit of sensitivity of the infrared detector, while the delay time occurs because the spectral response of the detector is shifted toward the shorter wavelength with respect to the emitted radiation spectrum. Since the wall temperature and also transmission of the radiation are affected by the introduction of a gas into the tube, it is difficult to subtract out this background accurately from the desired signal, and in view of these difficulties the interpretation of these results remains ambiguous and it is doubtful that lasing was obtained.

Unfortunately, before these questions could be resolved, the Illinois reactor was shut down for an extended period for some major changes required to allow upgrading to higher power levels. During this period, the Oak Ridge experiments described in the next section were undertaken.

Experiments Using the Oak Ridge Fast-Burst Reactor

The Oak Ridge fast-burst reactor (alternately known as the health physics research reactor or HPRR) is an unshielded fast reactor designed for pulsed operation. The experimental arrangement used with this reactor is shown in figure 7. Because of the difficulties in interpretation encountered in the previous in-core laser study, a new type of experiment employing a gain cell was designed. A ^{10}B lined-quartz tube was fitted with Brewster angle-end windows, and the beam from a 3.39-μ He-Ne

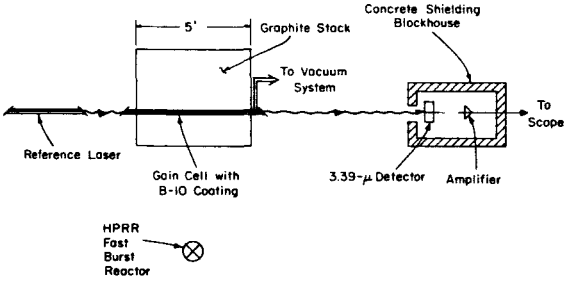

FIGURE 7.—*Schematic illustration of the arrangement for the Oak Ridge HPRR experiments (top view).*

laser was passed through this cell and then focused on a liquid-nitrogen-cooled indium-antimonide infrared detector. If a population inversion occurs in the nuclear-radiation-induced plasma inside the cell, the reference laser beam is amplified. If sufficient amplification is obtained, the construction of a nuclear pumped laser is assured since this requires only the addition of mirrors to form a cavity around the gain cell.

Fast neutrons from the reactor were utilized by moderating them in a large (5- by 5- by 5.5-ft) graphite stack as indicated in figure 7. This afforded a peak thermal flux at the gain cell of roughly 2×10^{15} N/cm^2 sec for the pulse sizes used in this work. The width (FWHM) of the neutron pulse was about 0.1 msec as opposed to about 30 msec for the earlier TRIGA studies. Extensive shielding was built up around the detector and reference laser in order to prevent a background signal due to radiations coming directly from the reactor. This, in fact, represented the major problem area of the experiment and several shield designs were tried before a reasonably successful one was found. Some change in detector sensitivity was still encountered during the pulse, but the results were corrected for this by using a calibration obtained from pulses with a reference thermal source in front of the detector. The detector was placed far enough from the gain cell (approximately 40 ft) so that spontaneous light from the gas in the gain cell would be greatly attenuated because of its random direction. Thus, the coherent beam from the reference laser was the dominant signal detected, so that any gain obtained could be attributed to the 3.39-μ line, and this eliminated many of the wavelength problems encountered in the earlier incore laser

study. (This was verified experimentally by measuring the actual background using pulses with the reference laser turned off. Additional background measurements were made with the reference laser on but with the gain cell evacuated in order to check on possible fluorescence of the cell window, changes in transmission, and radiation effects on the reference laser itself.)

Results from two separate series of measurements taken several months apart are shown in figure 8.

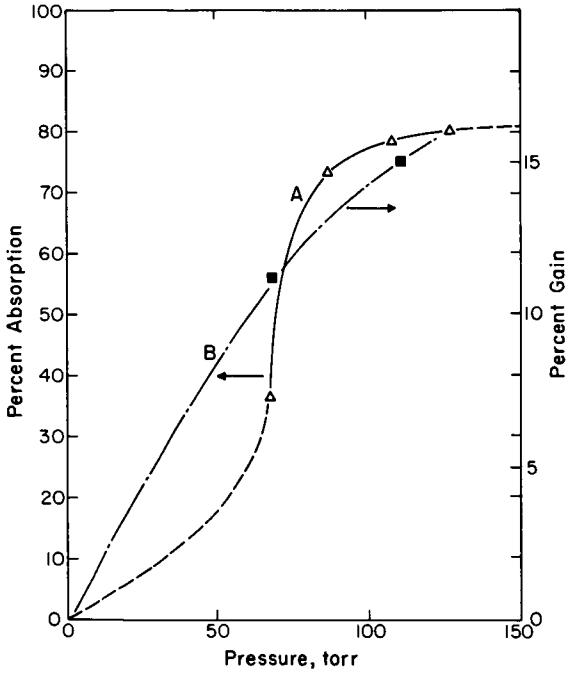

FIGURE 8.—*Absorption and gain curves measured for the 3.39 line. Curve A is for He-Ne while curve B is for He-Ne contaminated with air.*

Curve *A* was obtained first, using a mixture of 9/1 helium to neon. As indicated, instead of a gain, a surprisingly large absorption of almost 80 percent was obtained above 100 torr. This is unusual since the lower level of the 3.39 transition, the $3p_4$ level in figure 9, has such a short lifetime that its population density, i.e., absorption, would be normally very small. One possible explanation for this result is illustrated in figure 9 where it is noted that electronic excitation back into the $3p_4$ level from the 1*s* metastable level in neon might occur. The 1*s* level is metastable because the transition to ground

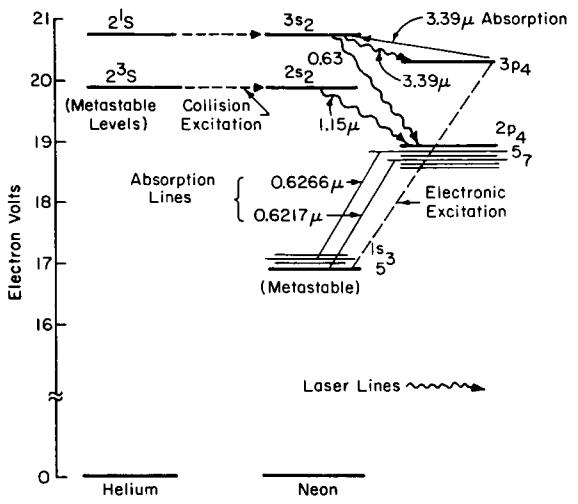

FIGURE 9.—*Level diagram for He-Ne. Only levels of importance to the discussion are shown, and sublevels are omitted unless needed.*

is optically forbidden, thus deexcitation must occur through collisions or diffusion to the wall. This is, in fact, the commonly accepted explanation for the observation that an optimum pressure-diameter product of about 5 mm-torr occurs in the conventional electrical laser. In the present case, the large diameter of the gain cell (approximately 1 in.) coupled with the high pressures could well have resulted in sufficient 1*s* concentration to cause a significant back-reaction via electron collision.

Curve *B* of figure 8 was obtained at a later date when, by accident, air leaked into the gain cell with the He-Ne. The exact air content is not known, but it is thought to have been considerably less than the Ne partial pressure. Time limitations at the HPRR combined with equipment problems prevented removal of the air, and since experiments using O_2 as an additive had been planned anyway, the work was continued. This turned out to be quite fortunate, since, as shown, up to 15 percent gain was observed. The explanation for this is not entirely clear. In fact, the effect may have been due to water vapor in the air or other uncontrolled parameters. However, one possibility is that the O_2 in the air acted as a scavenger, removing the neon metastables via collision and thus reducing the possibility of a back-excitation into the lower 3.39 level. This would, in fact, be analogous to the Ne-O_2 experiments by Northrop discussed earlier where

a strong laserlike signal was observed. (The $1s$ neon state has sufficient energy to dissociate the oxygen molecule upon collision, and this process is a basic step in the Ne-O_2 laser which involves a 0.84-μ oscillation in the excited O.)

Although few data points are shown in figure 8, it might be noted that each one represents considerable time and effort in preparation of the gain cell as well as in preparation of the reactor for pulsing. Also each represents several pulses plus several background pulse measurements. While the precise value of the gain might be questioned, the presence of air must have had a large effect on the system since there is almost a 100-percent difference between this measurement and the earlier ones which lead to absorption. In view of the significance of these results, it is hoped that continued studies of this nature will be possible in the near future as scheduling at the HPRR permits.

In summary, some evidence was obtained that population inversion for the 3.39-μ level could be obtained by adding small amounts of air to the He-Ne system. Without this additive a strong absorption is obtained. This absorption effect is consistent with the earlier failure to obtain a 3.39-μ output with the in-core laser at Illinois.

Recent Experiments With the Illinois Advanced TRIGA

Two different types of experiments have been initiated with the Illinois Advanced TRIGA to obtain a better understanding of the Oak Ridge results. One is aimed at the measurement of metastable concentrations for Ne as well as for He; the other is designed to characterize the thermalized electron density and temperature in the plasma. Both experimental arrangements are shown in figure 10, but we will consider the metastable measurements first. The principle of the measurement is best understood by reference to figure 9. The absorption coefficient for the line connecting two excited states (say the 6217-Å line between the $1s_5$ and $2p_7$) is proportional to the difference of population between these two states. It is a reasonable assumption to neglect the population density of the upper state ($2p_7$), which has a short lifetime, relative to the population of the metastable state ($1s_5$). Thus a measure of the absorption of a beam of 6217-Å light passing through an excited Ne gas

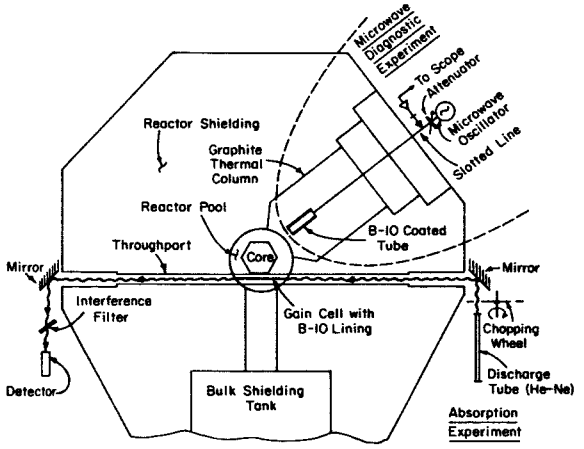

FIGURE *10.—Schematical arrangement of optical absorption and also microwave experiments at Illinois Advanced TRIGA.*

provides a measurement of the $1s_5$ metastable density. The population density of the $1s_3$ state can be measured by a similar method, using the 6266-Å line.

The concept has been carried out using the arrangement shown in figure 10. The incoherent light from a He-Ne discharge tube is passed through a fast chopping wheel (900 cps) and sent through the boron-coated "test" or "gain" cell which is positioned next to the reactor core in the throughport. The intensity of the transmitted light is measured by a photomultiplier located at the opposite end of the throughport, using a narrow band detection technique. The output from the photomultiplier is sent through a high-pass filter, then through a tuned amplifier with its bandwidth centered around 900 cps, and is finally recorded on an oscilloscope. This grants a minimum background light; i.e., the plasma glow from the gain cell is essentially eliminated. Finally, only that wavelength of interest (e.g., 6217-Å) is selected by placing a narrow-band interference filter in front of the photomultiplier. The position of the photomultiplier with respect to the throughport is such as to insure no background due to nuclear radiations coming from the core of the reactor.

A typical measurement is shown in figure 11, and a plot of the absorption due to the two lines in pure neon is shown in figure 12 as a function of pressure. The oscillatory effect in the transmitted signal of figure 11 is due to the chopping wheel. The ampli-

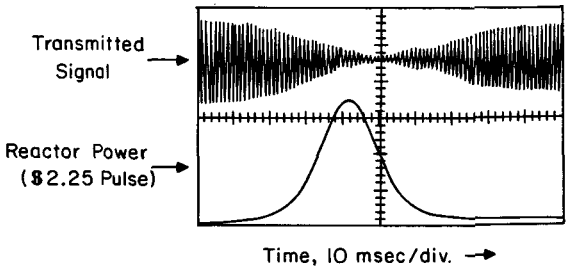

FIGURE 11.—*Typical absorption measurement for 6226 Å line in 9-to-1 He-Ne at 400 torr.*

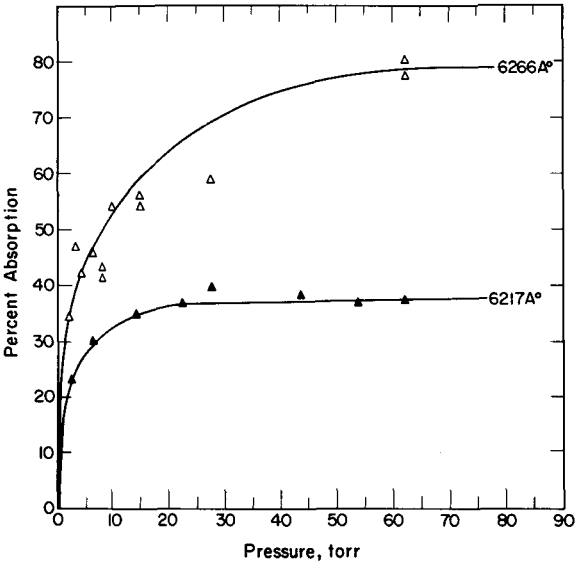

FIGURE 12.—*Absorption against pressure for 6266 and 6217 Å lines in pure neon. Curves correspond to the maximum absorption point. Peak reactor flux for these measurements is approximately 10^{15} N/cm²-sec.*

tude of this oscillation is a measure of the transmission, i.e., the narrow portion which occurs at about 8 msec, after the peak of the reactor pulse represents the point of maximum absorption. (It is estimated that a peak neutron flux of about 10^{14} to 10^{15} N/cm² sec was obtained over a 4-ft section of the test cell for the data in figs. 11 and 12.)

Similar measurements are now in progress for He-Ne mixtures, as is a measurement of He metastable densities in pure He and mixtures.

The back calculation of the metastable population densities is not straightforward since the absorption coefficient depends on both the line shape of the emission and the absorption spectra. However, with an assumption of pure Doppler broadening with equal widths for both spectra the following results would be obtained: A 35-percent absorption of the 6217-Å line would correspond to a $1s_5$ density of 10^{10} atoms/cm³. An absorption of 75 percent of the 6266-Å line would correspond to a $1s_3$ density of 3×10^9 atoms/cm³. Similar measurements in electrically excited He-Ne lasers have yielded values which are one or two orders of magnitude higher (refs. 30 and 31).

The experimental setup for the second general type of experiment—the measurement of electron densities and temperatures—is also shown schematically in figure 10. This represents an extension of the microwave methods originally utilized by Bhattacharya et al. (ref. 32) for measuring the Illinois TRIGA dynamic behavior. However, their work was restricted to uncoated tubes (gamma-induced plasmas), whereas the present study uses boron tubes similar to those in the optical gain cell. So that these measurements can be run simultaneously with the gain cell, the microwave tube is inserted in a position near the core in the graphite thermal column. This work has just begun, and one of the early results from the slotted-line apparatus is shown in figure 13. A shift in the standing wave pattern in the waveguide results in the fringe effect in the slotted-line output, and the degree of shift (number of fringes) is a measure of the electron density. As seen, about 2.1 fringes occurred on either side of the peak of the reactor pulse. This

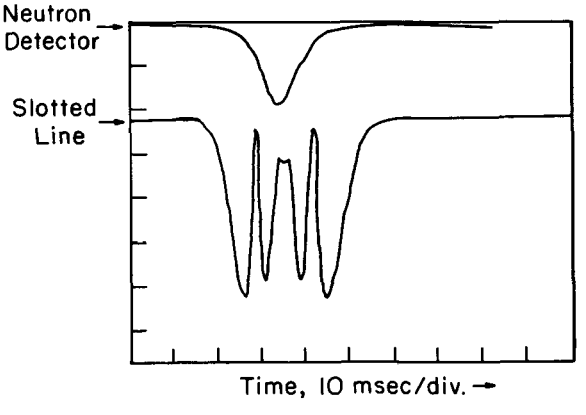

FIGURE 13.—*Typical fringe pattern from microwave study for 10 torr of pure neon and a peak reactor flux at the tube of about 10^{15} N/cm²-sec.*

was for 9.6 GHz and from standard relations an electron density of 1.4×10^{11} electrons/cm^3 is readily found. This value is in reasonable agreement with the estimated density. These same data can be used to calculate a collision frequency for momentum transfer and this in turn can be used to infer the electron temperature. However, a direct measurement of the electron temperature will require a different technique and it is planned to use the standard method of balancing the microwave noise radiated by the plasma against a known noise source.

The significance of these electron measurements is perhaps best understood by reference to Russell's calculations (paper by G. R. Russell on p. 53). He assumed that collisional-radiative recombination is a dominant recombination process, and variations in the rate of recombination from one level to another may control which levels are inverted and by how much. A knowledge of the electron density and temperature then allows a prediction of these recombination rates. Further, such information is vital if the back-excitation theory mentioned earlier is to be tested.

CONCLUSIONS

Both the Northrop and the Illinois studies indicate that direct nuclear radiation pumping of certain gas lasers is feasible in the high fluxes provided by a pulsed nuclear reactor. This is perhaps not too surprising since it might be expected that if enough energy can be "pumped into" the gas, whether by nuclear radiations or by electrical discharge, lasing must be possible with at least some systems. The key question is the one raised in the introduction: Will the resulting laser have any important new characteristics? Certainly no answer is yet clear; the experimental data are simply too skimpy. However, the Illinois studies do demonstrate that there are indeed significant differences between nuclear radiation pumping and normal electrical excitation. Recall that 3.39 μ was not obtained from He-Ne, but, instead, an anomalous absorption was found at this wavelength; observation of a 15-percent gain at the HPRR could be interpreted as the effect of an impurity like air on the He-Ne mixture; and neon-metastable density measurements do not appear to be entirely consistent with values for electrical discharges. All of these points taken together indicate that same major differences exist between the radiation-induced plasma and an electrical discharge. The task remaining, then, is to obtain a clear understanding of the mechanisms involved, and this may in turn show the way to techniques for capitalizing on the differences. It is with this objective in mind that the rather basic optical absorption and electron density-temperature measurements described here have been undertaken.

REFERENCES

1. Johnson, F. M.: Laser Excited by Nuclear Heat. Nucleonics, vol. 22, 1964, p. 57.
2. Herceg, J. E.; and Miley, G. H.: A Laser Utilizing a Low-Voltage Arc Discharge in Helium-Neon. J. Appl. Phys., vol. 39, 1968, p. 2147.
3. Herceg, J. E.; and Miley, G. H.: Characteristics of a Low-Voltage Helium-Neon Laser. J. Appl. Phys., vol. 40, 1969, p. 465.
4. Basov, N. G.; Oraevskii, A. N.; and Shcheglov, V. A.: Thermal Methods for Laser Excitation. Sov. Phys.-Tech. Phys., vol. 12, 1967, p. 243.
5. Makhov, G.; and Wieder, I.: Vibrational Excitation of CO_2 by Transfer From Thermally Excited Nitrogen. IEEE J. Quant. Electron., vol. QE 3, 1967, p. 378.
6. Basov, N. G.; Mikhailov, V. G.; Oraevskii, A. N.; and Shcheglov, V. A.: Molecular Population Inversion in the Supersonic Flow of a Binary Gas in a Laval Nozzle. Sov. Phys.-Tech. Phys., vol. 13, 1969, p. 1630.
7. Gol'dfarb, V. M.; and Luk'yanov, G. A.: Use of a Plasma Jet to Amplify Radiation. Sov. Phys.-Tech. Phys., vol. 13, 1969, p. 1365.
8. Wisniewski, E. E.; Fein, M. E.; Verdeyen, J. T.; and Cherrington, B. E.: Thermal Production of a Population Inversion in Carbon Dioxide. Appl. Phys. Letters, vol. 12, 1968, p. 257.
9. Fein, M. E.; Verdeyen, J. T.: and Cherrington, B. E.: A Thermally Pumped CO_2 Laser. Appl. Phys. Letters, vol. 14, 1969, p. 337.
10. Sadowski, H.; Kopelman, D.; and Held, K.: Nuclear Pumped Laser Feasibility Experiment. Rept. 000152-1, Kollsman Instr. Corp., Sept. 1964.
11. Held, K.; Jericho; and Solon, L. R.: Phosphor Transducer Means for Pumping Coherent Light Generators by Nuclear Energy Sources. U.S. Patent No. 3,470,490, Sept. 30, 1969.
12. Derr, V. E.; McNice, G. T.; and Rushworth, P. M.: Application of Nuclear Radiation to the Pumping of Lasers. Radioisotopes for Aerospace; Pt. 2, Systems

and Applications. Plenum Press (New York, N.Y.), 1966, p. 309.

13. COMPTON, D. M. J.; AND CESEUA, R. A.: Effects of Pulsed Irradiation on an Operating Laser. GA-6247, Gen. Atomics, Inc., Apr. 20, 1965.
14. COMPTON, D. M. J.; AND CESEUA, R. A.: Radiation Effects on Lasers. GA-7274, Gen. Atomics, Inc., Sept. 21, 1966.
15. TITTEL, F.; AND KAMEL, N.: Radiation Effects in Glass Lasers. In: Interaction of Radiation With Solids, A. Bishay, ed., Plenum Press (New York, N.Y.), 1967, p. 261.
16. HERWIG, L. O.: Bulletin Am. Phys. Soc., vol. 9, no. 2, 1964, p. 160.
17. HERWIG, L. O.: Summary of Preliminary Studies Concerning Nuclear-Pumping of Gas Laser Systems. Rept. C-110053-5, United Aircraft Corp., Feb. 1964.
18. HERWIG, L. O.: Concepts for Direct Conversion of Stored Nuclear Energy to Laser Beam Power. Trans. Am. Nucl. Soc., vol. 7, no. 1, 1964, p. 131.
19. DESHONG, J. A., JR.: Optimum Design of High-Pressure, Large-Diameter, Direct-Nuclear-Pumped, Gas Lasers. ANL-7030, Argonne Natl. Lab., June 1965.
20. DESHONG, J. A., JR.: Summary of Model I Nuclear Pumped Gas Laser Experiments. Intern. Argonne Natl. Lab. Rept., Apr. 29, 1967.
21. EERKINS, J. W.: Research on Direct Nuclear Pumping of Gas Lasers (DNPGL). Rept. NSL-66-144-1, Northrop Space Lab., Sept. 1966.
22. DAVIS, B. I.; AND DEJUREN, J. A.: Nuclear-Pumped Noble-Gas Ion-Laser Experiments. Rept. NCL-68-13R, Northrop Corp. Lab.
23. RUSK, J. R.; COOK, R. D.; EERKINS, J. W.; DEJUREN, J. A.; AND DAVIS, B. T.: Research on Direct Nuclear Pumping of Gas Lasers (DNPGL). Rept. AFAL-TR-68-256, Northrop Lab., Dec. 1968.
24. GUYOT, J. C.; HERCEG, J.; MILEY, G. H.; AND VERDEYEN, J. T.: Advanced Methods for Reactor-Laser Coupling. Proc. Ann. Rev. Electron., Univ. of Ill., Nov. 1967.
25. GUYOT, J. C.: Nuclear Radiation Pumped Gas Laser. Intern. Rept., Nucl. Eng. Prog., Univ. of Ill., Aug. 3, 1966.
26. GANLEY, T: Nuclear Radiation Pumped Ion Laser. Intern. Rept., Nucl. Eng. Prog., Univ. of Ill., Aug. 1, 1969.
27. MILEY, G. H.: Direct Energy Conversion Involving Nuclear Radiations. Proc. Special Topics in Nucl. Eng. (Gatlinburg, Tenn.), Aug. 1967.
28. MILEY, G. H.; AND VERDEYEN, J. T.: Advanced Methods for Nuclear Reactor-Gas Laser Coupling. Tech. Prog. Rept. AT(11-1)-2007, U.S. At. Energy Comm. and Univ. of Ill., Oct. 1969.
29. ANDRIAKHIN, V. M.; VELIKHOV, E. P.; GOLUBEV, S. A.; KRASIL'NIKOV, S. S.; PROKHOROV, A. M.; PIS'MENNYI, V. D.; AND RAKHIMIOV, A. T.: Increase of CO_2 Laser Power Under the Influence of a Beam of Fast Protons. JETP Letters, vol. 8, 1968, pp. 214-216.
30. SCHLIE, L. A.; AND VERDEYEN, J. T.: Radial Profile of Neon $1s_5$ Atoms in a He-Ne Active Discharge and Their Lens Effect on Lasing at 6401 Å. IEEE J. Quant. Electron., vol. QE 5, 1969, p. 21.
31. WHILE, A. D.; AND GORDON, E. I.: Excitation Mechanisms and Current Dependence of Population Inversion in He-Ne Lasers. Appl. Phys. Letters, vol. 3, 1963, p. 197.
32. BHATTACHARYA, ASHOK; GOLDSTEIN, L.; ADLER, F. T.; VERDEYEN, J. T.; AND BIALECKE, E. P.: Microwave Measurement of Dynamic Reactor Response. Appl. Phys. Letters, vol. 5, 1964, p. 242.

DISCUSSION

Javan: The 15-percent gain is for how long a tube?

Miley: It is about 3 ft.

Javan: Is the boron coating on the inside of the tube?

Miley: Yes; so that the alpha particles which are directed out of the boron end up in the gas. In these tubes the alpha particle ranges are much larger than the tube diameter and only a fraction of their energy is deposited in the gas.

Javan: Presumably you expected that the helium metastable would be excited by alpha particles. The behavior is so strange that one would expect the impurities would influence the population density of metastables. I would worry about the boron, but on the other hand you said you introduced air and you obtained different results. It is not quite clear what is going on.

Miley: Certainly we do not have a clear understanding of the mechanisms involved. However, experience with electrical lasers shows that the He-Ne system is very sensitive to impurities so it is not too surprising that air had a strong effect.

Javan: In the beginning you mentioned that you had operated at pressures as high as 150 torr; what was the lowest pressure?

Miley: It was about 3 to 4 torr.

Calculations of Ionization-Excitation Source Rates in Gaseous Media Irradiated by Fission Fragments and Alpha Particles[1]

P. E. THIESS AND G. H. MILEY
University of Illinois

Experimental data for the slowing and charge loss of high-energy heavy ions in gaseous and solid media are reviewed with special emphasis on fission fragments and alpha particles. These data are interpreted in terms of a semiempirical slowing law of the form $T/T_o = \{1 - [s/\lambda(T_o)]\}^{1/(n+1)}$ where T is the energy of the ion after traveling a distance s, $\lambda(T_o)$ is the ion range corresponding to the initial energy T_o, and the parameter n is primarily a function of the type of ion involved with a weak dependence on the target material. The charge on the ion or charge fraction after it has slowed to an energy T is also interpreted by a semiempirical relation.

The problem of predicting the spatial distribution of primary ionization-excitation source rates in a fluid being irradiated by ions from an adjoining solid fuel layer is considered. The slowing and charge loss law is used along with a transmission function previously developed by the authors (ref. 1) to predict the energy spectra of the flux of charged particles at any plane in the fluid slab.

Excitation cross sections for direct impact and secondary effects due to high-energy secondary electrons (δ-rays) and recoil atoms are surveyed. A δ-ray recoil atom pseudo cross section is derived to include these secondary effects in the calculations. The flux spectra and cross sections are used to compute the spatial variation in the production rate of ionization or excitation. Detailed results are presented for the irradiation of helium in a channel bounded by fuel plates on either side. In addition to the spatial variation in the source rate of excited states produced, the total excitation produced in the channel is obtained as well as its variation with gas pressure for the case of low gas pressures.

One of the frequently proposed methods for the creation of a plasma by nuclear radiation separates the fuel region in which nuclear particles are born from the plasma volume. In this manner it is possible to obtain higher rates of ionization in the gas than are achievable with a fuel-gas mixture. Such concepts introduce an important class of "two-region" ionization-excitation density calculations of interest in research related to nuclear MHD (see paper by Tang, Stefanko, and Dickson on p. 29; that by Ellis, Imani, and Cofer on p. 327; that by Rosa on p. 315; that by Sherman on p. 47; that by Bishop on p. 335; and ref. 2), nuclear light bulb rockets (see paper by Schwenk and Franklin on p. 3), and nuclear radiation pumped gas lasers (see paper by Guyot, Miley, Verdeyen, and Ganley on p. 357). The calculations are also of practical importance to the design of chemonuclear reactors (ref. 3). In all of these applications, high-energy, heavy ions are born via nuclear reactions in a very thin solid fuel layer and escape at the surface to irradiate a process fluid, and the ionization and excitation which is created in the gas forms a plasma. This plasma, being created by high-energy, heavy ion impact, should differ significantly from those plasmas which are created in the laboratory by electron discharges.

In nature, radiation-produced plasmas are com-

[1] These studies were supported by the Research Division of the U.S. Atomic Energy Commission under contract AT(11-1)2007. Parts of this paper include results to be used in sections of a Ph.D. thesis by author P. E. Thiess.

monplace. For example, the aurora (ref. 4) is created by the bombardment of the upper atmosphere at the poles by trapped high-energy solar protons. This process has received considerable attention in the literature; however, the literature is peculiarly devoid of calculations for laboratory nuclear-radiation-produced plasmas. In the present study an engineering model for the calculation of the ionization and excitation source term for the plasma kinetic model is derived for an infinite flat plate fuel element surrounded by a process fluid as illustrated in figure 1. Although this geometry excludes the

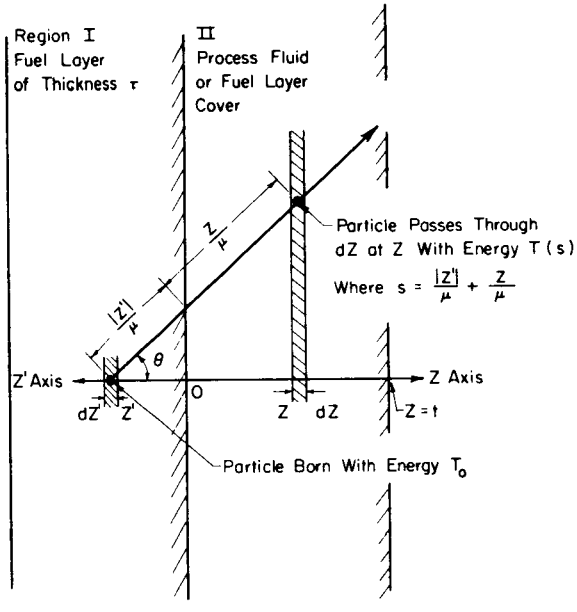

FIGURE 1.—*Planar geometry for the two-region problem.*

case of a homogeneous fuel-plasma mixture, the methods which are developed can easily be extended to such cases.

PREVIOUS STUDIES AND THE MODEL

In an earlier publication (ref. 1), Miley and Thiess reviewed methods reported prior to 1968 for the prediction of the plasma number density. They proposed a new model which offers a unified approach to such calculations. This model is easily adapted to different types of nuclear radiation and introduces a method for calculating the energy spectra of the charged particle flux at any plane Z in the gas volume. Use of this flux with energy-dependent cross sections for ionization and excitation permits detailed calculation of the source of ionization and excitation in the gas. Such predictions could not be obtained from the older models since they did not allow the transformation of variables necessary to obtain an energy spectra.

Figure 2 summarizes the calculations for nuclear-

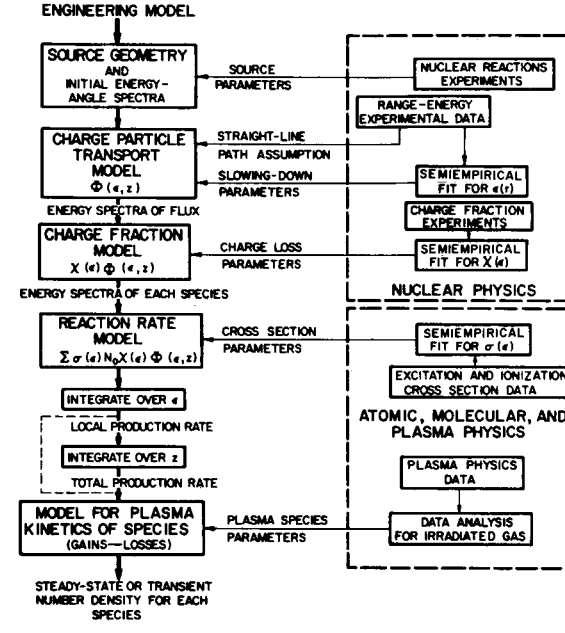

FIGURE 2.—*Flow diagram for plasma specie number calculations for plasmas which are generated by radiation.*

radiation-produced plasma by use of a flow diagram to illustrate the key stages and shows the data required from nuclear physics, atomic and molecular physics, and plasma physics. The following sections will discuss each of the components in the flow diagram and the appendixes will present the experimental data reductions outlined in the flow diagram.

Source Geometry and Reaction Rate Model

Complicated source geometries and sources which have an initial energy and angle spectra are often encountered in practical applications. However, in order to reduce the complexity of the model and to make clear the physical processes, Miley and Thiess originally assumed the source geometry to be an infinite slab (ref. 1). The charged particles are born uniformly with position Z' with a single energy T_o

and have an isotropic angular distribution. These assumptions will also be made in this paper. Fortunately, fission fragment and alpha sources closely approximate the assumptions of this model for the following reasons:

(1) The neutron flux depression is negligible in the fuel layer. Solid fuel sources must be made very thin in order for fragments to escape since the range of fragments and alphas in metallic foils is very small.

(2) Decay processes are isotropic as is the production of charged particles by thermal neutron reactions. In the latter case the energy and incident angle of the neutron can be neglected in the reaction equation.

(3) Decay alpha sources are monoenergetic, while initial estimates of the effects of fission fragments have traditionally used two average fragment groups, one group for the light fragments and a second group for the heavy fragments. Likewise, boron-10 n-α sources can be treated using two groups, one for the alpha and one for the lithium ion. In the case of uncovered alpha sources, the recoil atom must also be included as a second group.

Charged Particle Transport and Flux Model

In order to derive a transmission function for charged particle transport, it is assumed that the path of the particle is a straight line. This assumption is confirmed by cloud chamber photographs of alpha particle (ref. 5) and fission fragment (ref. 6) tracks. It is only during the last 5 percent of the particle track that nuclear collisions of the neutralized ion with the target give rise to scattering at large angles. Since this portion of the track contributes only a small amount to the total ionization and excitation, we neglected these scattering effects. Large-angle scattering which produces high-energy recoil atoms becomes more important when the target has roughly the same mass as the ion; e.g., alpha particles irradiating helium. Fortunately, even then such events have a very low probability and within the approximations made in the model can also be neglected.

The charged particle transport model proposed is also based on a semiempirical slowing-down law of the form:

$$\epsilon=\frac{T(s)}{T_o}=\left[1-\frac{s}{\lambda(T_o)}\right]^{\frac{1}{n+1}} \tag{1}$$

The justification for use of this form was given in the paper by Guyot et al. (page 357). Experimental data presented in figures A1 to A4 in appendix A for alpha particles and fission fragments confirm that this energy-range relation is a reasonable approximation to the actual slowing process for most of the track of the charged particle.

Using the above assumptions, the authors derived the following expression for the energy spectra of the charged particle flux at plane Z in the plasma as shown in figure 1 (eqs. (10) and (12) in ref. 1):

$$\frac{d\Phi(z,\epsilon)}{\tau S(T_o)}=\frac{n_{\mathrm{I}}+1}{Z\tau/\lambda_{\mathrm{I}}(T_o)}\epsilon^{n_{\mathrm{II}}}\int_{\mu_{\min}(\epsilon)}^{\mu_{\max}(\epsilon)}\left[\epsilon^{n_{\mathrm{II}}+1}+\frac{z}{\mu}\right]^{\frac{n_{\mathrm{I}}-n_{\mathrm{II}}}{n_{\mathrm{II}}+1}}d\mu \tag{2}$$

where

ϵ	reduced energy, T/T_o
μ	direction cosine of charged particle path
$\tau/\lambda_{\mathrm{I}}(T_o)$	reduced source thickness
τ	source region thickness
$\lambda_{\mathrm{I}}(T_o)$	range of ion at energy T_o in fuel region
z	reduced coordinate in process fluid, $Z/\lambda_{\mathrm{II}}(T_o)$
$\lambda_{\mathrm{II}}(T_o)$	range of ion at energy T_o in process fluid
$S(T_o)$	source rate of charged particles per unit volume
n_{I}	slowing law fitting parameter in fuel region
n_{II}	slowing law fitting parameter in process fluid

and where $\mu_{\max}(\epsilon)$ and $\mu_{\min}(\epsilon)$ are given in table III of reference 1 or by equations (19) and (15), respectively. Where n_{I} and n_{II} are not equal, the integral must be evaluated by numerical integration. However, for equal values of n_{I} and n_{II} the flux spectra reduce to an analytical expression:

$$\frac{d\Phi(z,\epsilon)}{\tau S(T_o)}=\frac{n_{\mathrm{I}}+1}{Z\tau/\lambda_{\mathrm{I}}(T_o)}\epsilon^{n_{\mathrm{II}}}\left[\mu_{\max}(\epsilon)-\mu_{\min}(\epsilon)\right] \tag{3}$$

Typical flux spectra predicted by this model at various planes in the gas volume are shown in figures 3 and 4 for a source foil of thickness one-quarter the range of the charged particle in the fuel media. The peak of the flux spectra shifts to lower and lower energies as one proceeds to planes farther

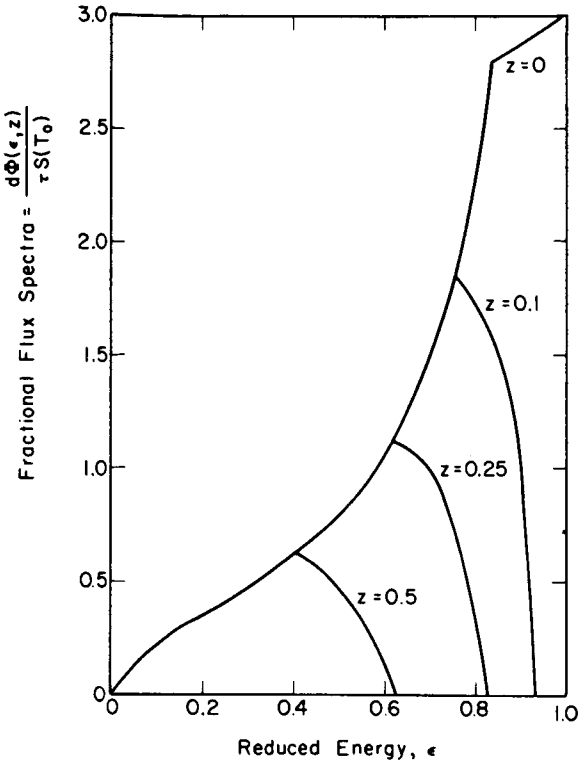

FIGURE 3.—*Energy spectra of the flux of alpha particles at various gas planes.* $n_I = n_{II} = 0.5$; $\tau/\lambda_I = 0.25$.

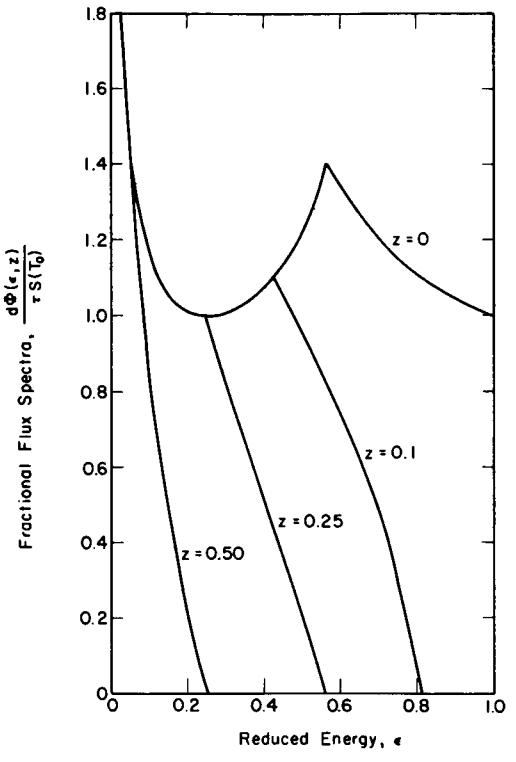

FIGURE 4.—*Energy spectra of the flux of fission fragments at various gas planes.* $n_I = n_{II} = -1/2$; $\tau/\lambda_I = 0.25$.

from the interface of the fuel layer and gas and fewer and fewer charged particles are able to reach the plane because they are stopped in the gas volume. One also notes that there is a maximum ion energy at each plane in the gas which corresponds to the energy a particle born at the fuel surface traveling perpendicular to the layer has as it crosses the plane.

The difference in the flux spectra for alpha particle and fission fragment sources is clearly evident from the figures and should be expected since the slowing-down mechanisms of the two are different. Because of their mass and electronic charge, fragments lose much more of their energy in the initial part of their track via electronic interactions; thus, in contrast to fission fragments, the alpha particle energy spectrum is more heavily weighted toward high energies.

Note that, because of the use of a single value of the slowing-down fitting parameter n over the entire track, the low-energy portion of both figures is not accurately predicted by this model. Experimental data presented in appendix A for slowing over two decades in energy require at least two energy regions with different n-values for an accurate fit. However, the low-energy portion of the spectra does not contribute a large fraction of the ionization-excitation created for planes in the gas less than $Z/\lambda_{II}(T_o) \cong 0.5$, and hence a single n-value is a reasonable approximation.

In summary, the model uses the energy-range relation and straight line path approximation to predict the flux spectra at a point of interest in the process fluid without inquiry into the details of the slowing process. Thus the model is an engineering approximation to a multicollisional slowing which, to be handled precisely, would require a much more elaborate technique, e.g., Monte Carlo. However, once the approximate flux spectra have been calculated by this method, the results can then be used to probe the effects of single collisions at the point of interest. This method avoids the use of the w-value for computing the spatial dependence of the ioniza-

tion rate and allows a direct calculation of excited-state production rates. As shown in the paper by Guyot et al. (p. 357), the assumption of a constant value of w in the gas volume, as done in many previous calculations, does introduce some error in prediction of spatial variations. Even in some cases where the spatial variation is small, e.g., a gas channel of spacing much less than the charged particle range, the use of w is erroneous since by definition w is the average over the entire track of the particle.

Charge Fraction Model

It is a well-known fact that as high-energy, heavy ions lose energy their average electronic charge slowly decreases and at any instant a quasi-equilibrium charge state exists due to the continual capture and loss of electrons (ref. 7). This is an important phenomenon in some reaction rate calculations, and there are two ways to represent it. One method, applicable to light ions such as alpha particles, finds the fraction $\chi(\epsilon)$ of each ion species present in a beam of particles at a given energy. This is manageable for light ions which have three, four, or five possible ionized states but soon becomes cumbersome for situations with charge states greater than five. In the latter case it is more convenient to perform a statistical average over the ionized states at a given energy and find the average charge in the beam as a function of energy. This method is particularly useful in treating fission fragments which are initially born with as many as 20 to 24 electrons missing and capture electrons as they slow down until they become neutralized. It requires, however, that the product of the cross section and the charge fraction be averaged for each energy in order to account correctly for the effects of charge loss. That is, $\Sigma\ \sigma(\epsilon)\ \chi(\epsilon)$ is replaced by $<\sigma\chi>$ as discussed in appendix C.

In appendix B the available experimental data on alpha particle and fission fragment charge loss are analyzed and a semiempirical model is developed for the fraction of each of the three charge states of the alpha particle vs its energy. This model can be used in the spirit of the semiempirical slowing-down law to obtain estimates of the flux spectra of a particular ion species.

The models suggested by the data presented in figure B1 for alpha particles are (see appendix B for the derivation):

Doubly ionized helium ion:

$$\chi_{He^{++}}(\epsilon)=\frac{1}{1+\frac{1}{A_2}\epsilon_b^{-m_2}+\frac{1}{A_1A_2}\epsilon_b^{-(m_1+m_2)}} \tag{4}$$

Singly ionized helium ion:

$$\chi_{He^{+}}(\epsilon)=\frac{1}{1+A_2\epsilon_b^{m_2}+\frac{1}{A_1}\epsilon_b^{-m_1}} \tag{5}$$

Fast neutral helium atom:

$$\chi_{He^{0}}(\epsilon)=\frac{1}{1+A_1\epsilon_b^{m_1}+A_1A_2\epsilon_b^{(m_1+m_2)}} \tag{6}$$

Here $\chi_{He^{++}}(\epsilon)$, $\chi_{He^{+}}(\epsilon)$, and $\chi_{He^{0}}(\epsilon)$ represent the fractions of the various charge states in a beam of alpha particles, e.g., the doubly ionized, singly ionized, or neutralized helium atom, respectively. The ion energy in these equations is normalized by T_b, the energy which corresponds to the velocity of the outermost electron (Bohr orbit) and is equal to 99.2 keV for an alpha particle. This reduced energy can be related to the reduced ion energy ϵ by the following expression

$$\epsilon_b=\frac{T}{T_b}=\epsilon\frac{T_o}{T_b}$$

where T_o is the initial energy of the ion (5.3 MeV for a polonium-210 alpha particle). In the above equations, A_1 and A_2 are fitting constants for the magnitude of the charge fraction and m_1 and m_2 are fitting exponents for the energy dependence of the charge fraction.

Values for the above parameters for a beam of alpha particles irradiating a helium target are given in table I and $\chi_{He^{++}}(\epsilon)$, $\chi_{He^{+}}(\epsilon)$, and $\chi_{He^{0}}(\epsilon)$ are shown in figure 5 for this case. The calculation shows that inclusion of the charge on the helium ion is important for polonium-210 alpha sources (T_o= 5.3 MeV) if the alpha energy drops below 2 MeV anywhere in the plasma region. The figure also illustrates that for a boron-10 source foil (T_o=1.47 MeV) the ion charge is quite important since much of the track of the helium and lithium fragments lies in an energy range where the charge fraction changes rapidly; e.g., note the rapid growth of He^+ below approximately 680 keV.

The model suggested by the data presented in figure B2 for fission fragments is a power law fit in fragment energy:

$$q(\epsilon)=q_o\epsilon^{m/2}=q_o\left(\frac{V}{V_o}\right)^m \tag{7}$$

TABLE I.—*Parameters Used in Excitation Rate Calculations for Helium Being Irradiated by 5.3-MeV Alphas From Polonium-210*

Slowing parameters
$n_I = n_{II} = 0.5 \qquad T_o = 5.3$ MeV
$\rho_I \lambda_I(T_o) = \begin{cases} 16.7 \text{ mg/cm}^2 \text{ in Po} \\ 16.2 \text{ mg/cm}^2 \text{ in Au} \end{cases}$
or
$\lambda_I(T_o) = \begin{cases} 0.0018 \text{ cm in Po} \\ 0.00084 \text{ cm in Au} \end{cases}$
$\rho_{II}\lambda_{II}(T_o) = 2.3 \text{ mg/cm}^2 \text{ in He}$
or
$\lambda_{II}(T_o) = 19.6$ cm at STP

Charge loss parameters		
$T>250$ keV:	$n_1 = 3.13$	$n_2 = 2.21$
	$A_1 = 0.074$	$A_2 = 0.00921$
$T<250$ keV:	$n_1 = 1.05$	$n_2 = 1.00$
	$A_1 = 0.496$	$A_2 = 0.0280$

Density
$\frac{N_o}{\rho} = 1.505 \times 10^{20} \text{ mg}^{-1}$

Delta-ray constants
$T^{\delta}_{max} = 2.9$ keV
$\sigma_p^{*\delta} = \begin{cases} 24.6 \times 10^{-20} \text{ cm}^2 & \text{for } He^{++} \text{ ions} \\ 12.3 \times 10^{-20} \text{ cm}^2 & \text{for } He^{+} \text{ ions} \end{cases}$
$\rho\lambda^{\delta}(T^{\delta}_{max}) = 9.3 \times 10^{-3} \text{ mg/cm}^2$
$\frac{\rho\lambda^{\delta}(T^{\delta}_{max})}{\rho\lambda_{II}(T_o)} = 4.0 \times 10^{-3}$

Here $q(\epsilon)$ and q_o are the average charge at energy ϵ and the initial charge at energy T_o, respectively; and V and V_o are the velocity and initial velocity. Table II lists the values for q_o and m for light and heavy fission fragment groups. In general, m is nearly equal to 1.0. As will be discussed in the next section, proper accounting of the charge loss for fission fragments is especially important in excitation rate calculations.

Reaction Rate Model

For low-density plasmas the local production of ionization and excitation should be calculated using cross-sectional data in a manner analogous to reactor calculations for neutron populations (ref. 8). Using the flux spectra predicted by the slowing-down model and the charge loss model, the rate of formation of a species j in the volume dZ at z is:

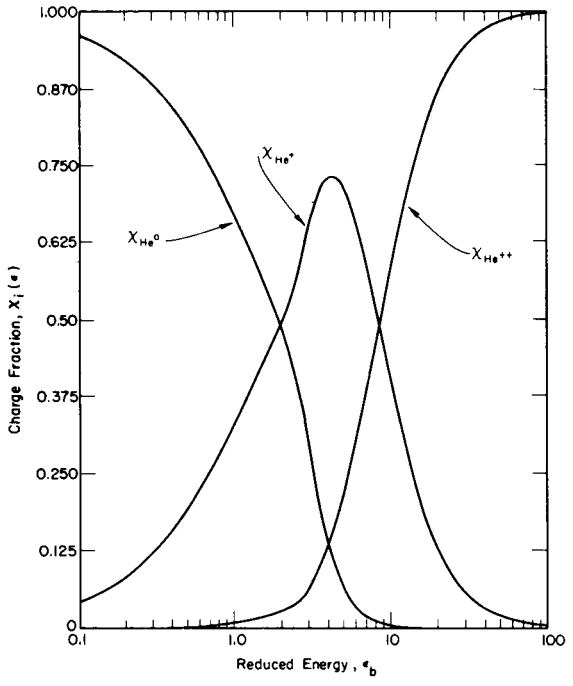

FIGURE 5.—*Equilibrium charge fraction for a beam of alpha particles irradiating a helium target. Use was made of equations (4), (5), and (6) and data from figure B1.*

$$R_j(z) = \sum_i \int_{\epsilon_{min}}^{\epsilon_{max}} N_i(z) \left\{ \sum_m \left[\underbrace{\sigma_{ij}^{m}(\epsilon)\, \chi_m(\epsilon)}_{\text{Direct impact}} + \underbrace{\sigma_{ij}^{\delta m}(\epsilon)\, \chi_m(\epsilon)}_{\text{Recoil effects}} \right] \right\} d\Phi(z,\epsilon)\, d\epsilon \qquad (8)$$

where

$\sigma_{ij}^{m}(\epsilon)$ is the probability for formation of species j from species i per unit track length of an ion of energy ϵ and electronic charge m

$\sigma_{ij}^{\delta m}(\epsilon)$ pseudo cross section to account for the contribution of recoil ions and electrons (delta rays) in the production of species j at z

N_i number density of species i at z in the plasma

$d\Phi(z,\epsilon)$ flux spectra at plane Z as defined by equation (2)

Equation (8) includes the effect of direct impact excitation as well as excitation created by recoil particles such as delta-ray electrons. The latter often have such short ranges that their effects can

TABLE II.—*Parameters Used in Excitation Rate Calculations for Helium Being Irradiated by Fission Fragments*

Parameter	Light fission fragment group	Heavy fission fragment group
Slowing parameters:		
$n_I = n_{II}$	—0.50	—0.50
T_o, MeV	98	67
$\rho_I\lambda_I\ (T_o)$		
U, mg/cm²	13.0	9.7
UO_2, mg/cm²	9.4	6.8
$\rho_{II}\lambda_{II}(T_o)$, He, mg/cm²	0.495	0.406
or		
$\lambda_{II}(T_o)$, He, cm	2.80	2.30
Charge loss parameters:		
q_o	+20e	+22e
m_{II}	0.95	0.95
Density:		
$\frac{N_o}{\rho}$, mg⁻¹	1.5×10^{20}	1.5×10^{20}
Delta-ray constants:		
M^{ff}, amu	96	140
T^{δ}_{max}, keV	2.2	1.05
$\sigma^{*\delta}_{ff}$, cm²	3.18×10^{-18}	8.20×10^{-18}
$\rho_{II}\lambda^{\delta}(T^{\delta}_{max})$, mg/cm²	11.65×10^{-3}	2.16×10^{-3}
$\frac{\rho_{II}\lambda^{\delta}(T^{\delta}_{max})}{\rho_{II}\lambda_{II}(T_o)}$	0.024	0.0053

be lumped at the point of origin by using a pseudo cross section as derived in appendix D.

Because of the general lack of cross-sectional data at MeV ion energies and for highly charged ions, it is frequently necessary to estimate the cross section for a particular state from proton data. Also, it is often necessary to use the dependence of experimental data on the principal quantum number to estimate the cross section for excitation. For example, the 2^1P, 2^1S, and 3^1S states in helium have not been measured for heavy ion impact and hence must be calculated from cross sections for higher levels. More cross-section data are presently available for hydrogen and helium targets than for all the other gases. Helium was selected as the example in this paper because of our interest in the He-Ne laser and because data are available for proton excitation in helium.

Figure 6 and table III present the available experimental data for the excitation of helium n^1S, n^1P, and n^1D states (ref. 9) by heavy ions and the level diagram for these states. At energies above 100 keV, all of these data seem to fit the Bethe-Born cross section well (refs. 10 and 11). Therefore we used this analytic cross section in our

TABLE III.—*Parameters Used in Calculating the Rate of Formation of Excited States in Helium Using a Bethe-Born Cross Section*

Excited state in helium	$\sigma_{of}{}^{*p}$, cm²	5.3 MeV alpha		^{235}U fission fragment			
				Direct impact		Delta rays	
		Direct impact, ϵ^*	Delta rays, $\epsilon^{\delta*}$	Light, ϵ^*	Heavy, ϵ^*	Light, $\epsilon^{*\delta}$	Heavy, $\epsilon^{*\delta}$
2^1S	[a] 24.0×10^{-19}	0.04	0.0097	0.0490	0.0145	0.0125	0.01465
3^1S	[a] 7.0	.04	.0097	.0490	.0145	.0125	.01465
4^1S	3.0	.04	.0097	.0490	.0145	.0125	.01465
5^1S	1.8	.04	.0097	.0490	.0145	.0125	.01465
6^1S	1.2	.04	.0097	.0490	.0145	.0125	.01465
7^1S	.8	.04	.0097	.0490	.0145	.0125	.01465
2^1P	[a] 108	.10	.0259	.130	.277	.0335	.0392
3^1P	32	.10	.0259	.130	.277	.0335	.0392
4^1P	6	.10	.0259	.130	.277	.0335	.0392
5^1P	4	.10	.0259	.130	.277	.0335	.0392
6^1P	2.8	.10	.0259	.130	.277	.0335	.0392
4^1D	.8	.04	.0097	.0490	.0145	.0125	.01465

[a] Fit by n^{-3} rule.

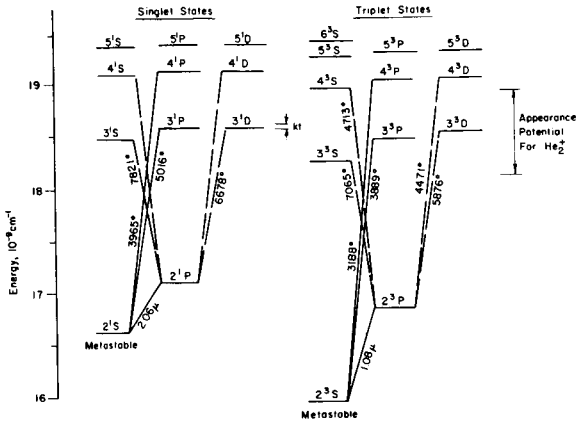

(a) *Energy level diagram.*

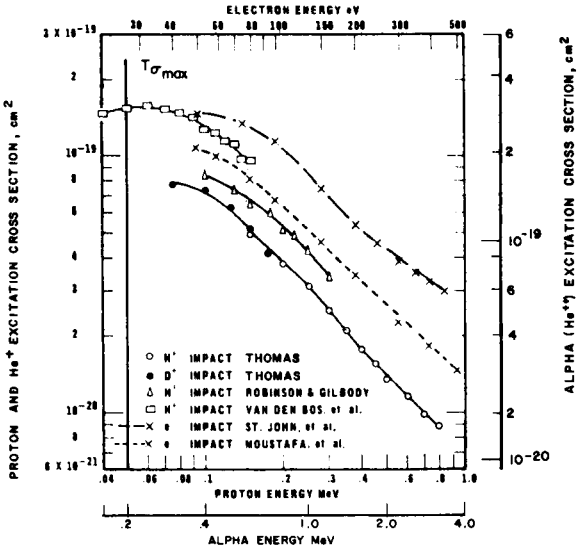

(b) *Experimental measurement of* n^1S *excited state.*

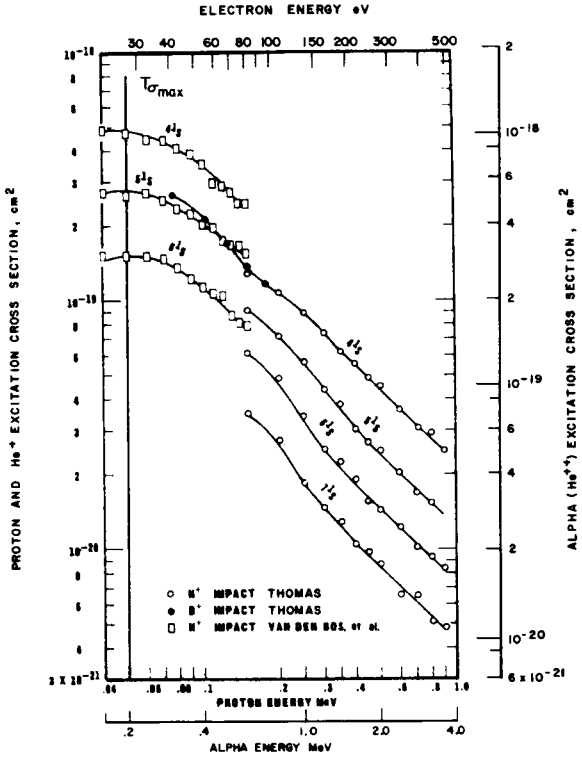

(c) *Experimental measurement of* n^1P *excited state.*

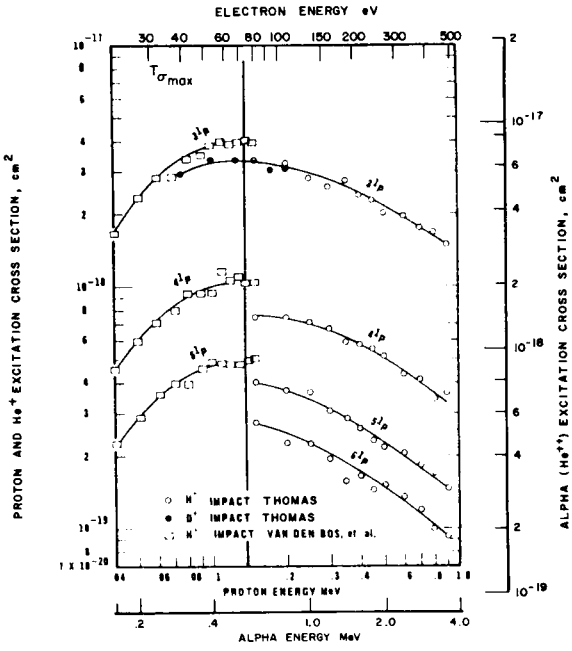

(d) *Experimental measurement of* 4^1D *excited state.*

FIGURE 6.—*Energy-level diagrams of the excited states in helium and experimental measurements of the excitation cross sections.*

calculations but normalized it to the experimental data. This was done by writing the Bethe-Born cross section in terms of the maximum cross section value and the energy at which this maximum occurs. This gives

$$\sigma_{ij}^{m}(\epsilon)=\begin{cases}\sigma_{ij}^{*p}\dfrac{\epsilon^*}{\epsilon}q^2\log\left(\dfrac{2.718\,\epsilon}{\epsilon^*}\right) & \text{for } \epsilon>\dfrac{\epsilon^*}{2.718}\\ 0 & \text{for } \epsilon<\dfrac{\epsilon^*}{2.718}\end{cases} \tag{9}$$

The term σ_{ij}^{*p} in equation (9) is the maximum value of the cross section for proton excitation of state j from state i, while ϵ^* is equal to $\frac{T_{\sigma,\max}}{T}$, where $T_{\sigma,\max}$ is the ion energy at which the cross section is a maximum and q is the charge state on the ion. Table III lists the maximum value of the helium excitation cross section and the reduced energy at which the cross section is a maximum.

This cross-section representation breaks down for the fast neutral as $q=0$. Experimental data on excitation by fast neutrals are very limited. For the present calculations equation (9) was used for neutral impact with q^2 in the above equation replaced by $\frac{\sigma^{*\text{ neutral}}}{\sigma^{*\text{ proton}}}$. As a rough estimate, this ratio was taken to be 0.35 for the n^1S states and 0.28 for the n^1P states on the basis of the very limited data presented in the review article by De Herr (ref. 12). No neutral excitation experimental data have been abstracted for helium impact, therefore the meager data for hydrogen impact had to be used. Table IV lists some of these data.

The use of the Bethe-Born cross section also is dubious for those states such as the triplets in helium whose excitation is forbidden by the Wigner spin rule for heavy ion impact. Data on triplet excitation by protons and He^+ ions were also reviewed by De Herr (ref. 12). Although "shell effects" are seen in the measured cross sections, it would appear that a first estimate of the triple excitation by heavy ion impact could be made using the Bethe-Born cross section fit to experimental data. Table IV also gives some of the available data on the excitation of triplet states in helium by both protons and He^+ ions.

Figure 7 shows a pseudo cross section for the excitation created by delta rays (high-energy scattered electrons) produced by both alpha particles and fission fragments. This cross section is derived in appendix D. The model is based on the assumption that all the effects of the delta ray can be lumped at its point of origin. This is reasonably valid for most gas pressures and gas volumes of interest here. Since delta electrons are born with energies up to 2 keV for fission fragments and alpha particles irradiating a helium target, then

TABLE IV.—*Excitation of Helium by Neutral Hydrogen Atoms and Singly Charged Helium Ions as Reported by De Herr (ref. 12)*

Hydrogen atom excitation measurements by Van Eck (1964)			Singly ionized helium measurements by De Herr and Van den Bos (1965)		
State	Maximum value of cross section, cm^2	Energy at which maximum occurs, keV	State	Maximum value of cross section, cm^2	Energy at which maximum occurs, keV
4^1S	1.8×10^{-19}	25	4^3S	1.43×10^{-19}	70
5^1S	.8	22	5^3S	.67	70
3^1P	>3.0	>35	6^3S	.42	90
4^1P	>2.2	35	3^3P	7.78	50
4^1D	.38	20	4^3P	2.64	55
5^1D	.21	20	5^3P	.944	60
4^3S	5.6	20	3^3D	15.0	20
5^3S	2.0	17.5	4^3D	3.16	30
3^3P	4.6	15	5^3D	1.33	35
4^3P	2.26	15			
3^3D	1.70	12.5			
4^3D	.76	12.5			

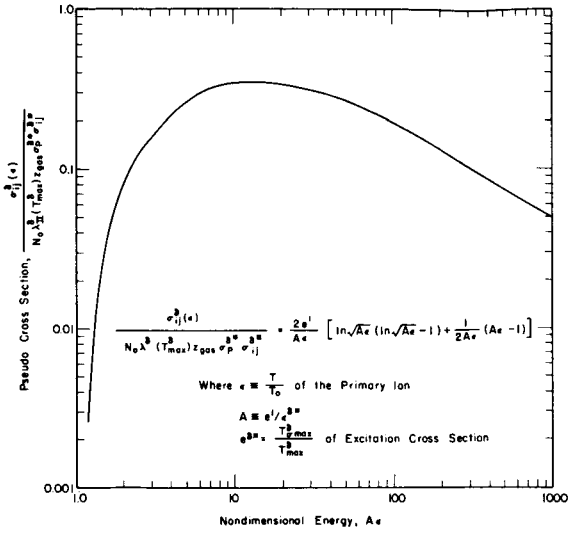

FIGURE 7.—*Pseudo cross section for the production of excited states by delta rays scattered by alpha rays. Rutherford scattering, the Thomas-Widdington slowing-down law, and a Bethe-Born cross excitation were assumed.*

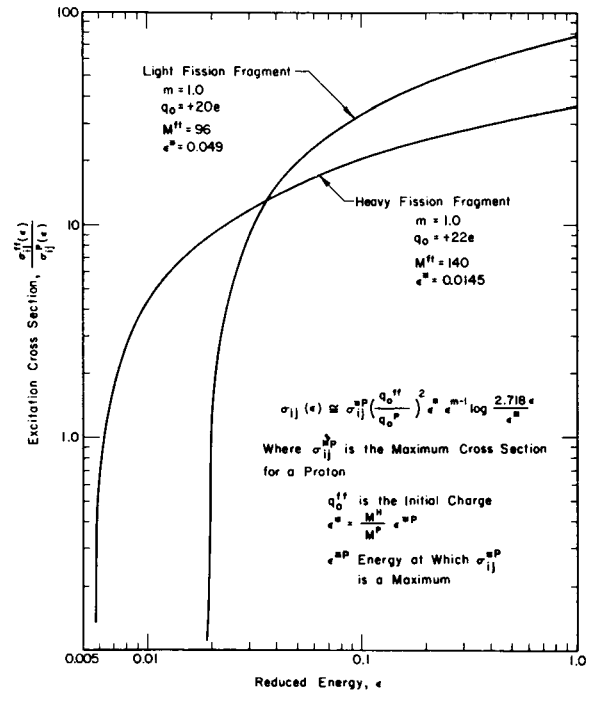

FIGURE 8.—*Calculated fission fragment excitation cross section of n¹S and n¹D states in helium using proton and charge loss data.*

both the Bethe-Born cross section and the slowing model used are reasonable approximations to use in the model. If more accuracy is necessary at low energies, the pseudo cross section could be rederived using another approximation such as the Gryzinski cross section (refs. 13 and 14) or experimental values. Because of Rutherford scattering and slowing-down effects, the pseudo cross section has a maximum at some 10^4 times the energy of the maximum in the electron impact cross section and therefore is important only for ion energies above 100 keV.

The pseudo cross section for a fission fragment has a different shape because of the variation of the fragment electronic charge as it slows down. Its form is approximately ϵ times that for an alpha. Because of charge loss on a fragment, the pseudo cross section is a maximum at the initial energy of the fragment.

Since there exist no excitation data for heavy, highly charged, high-energy ions such as fission fragments, it is again necessary to extrapolate using proton data. The Bethe-Born cross section was again used and, as derived in appendix C, proton data and charge loss data were used to predict the energy variation and magnitude. Figure 8 shows the results for light and heavy fission fragment groups exciting n^1S and n^1D states in helium. The charge variation on the fragment gives rise to an excitation cross section which has a maximum at the initial energy of the fragment rather than at some lower energy. Also, the larger initial charge of the fragment $(+20$ to $+22e)$ results in an initial magnitude for the cross section some 30 to 70 times that of a proton or an electron. The difference between light and heavy fragment masses shows up in the cutoff energy for the cross section. This difference arises because the Bethe-Born cross section scales linearly in velocity between various ions, and not in energy.

The slowing of fission fragments and alpha particles also produces recoil atoms which can contribute to the excitation and ionization source. Recoil effects will be particularly important near the end of the charged particle track after the ion itself has been neutralized. It can be argued that the ionization and excitation created in this part of the track is small compared with the portion where electronic interaction predominates. Therefore, recoil effects will be neglected. (Some low-energy

recoils are created by *small*-angle scattering in the electronic slowing region of a fission fragment track (ref. 15). The effects of these recoils could be included by the use of a pseudo cross section just as for delta rays since the range of the recoil atom is small compared with that of the primary ion. Irradiation of light gases with neutrons, protons, and alphas, however, does produce an occasional *large*-angle scattering event which cannot be handled by the present model. The problem has been tackled in auroral physics and has been investigated in nuclear physics (ref. 5). The present model can be used to set up a source term for the recoils and then a transmission function can be derived for the recoil atom. However, this involves two additional integration variables which introduce needless complexity since such events have very small cross sections (ref. 5).)

Plasma Kinetic Model

In order to evaluate the steady-state or transient number density of a species in the plasma, it is necessary to formulate a model for the plasma kinetics of each species which includes the production term predicted in the previous section, other sources due to collisions between species, and the loss mechanisms for each species. Since this aspect of nuclear-generated plasma calculations depends on the particular problem of interest, it will not be treated in this paper and the reader is referred to the few existing studies which appear in the literature. The papers by Leffert, Rees, and Jamerson (ref. 16) and Rees, Leffert, and Rose (ref. 17) discuss the plasma kinetics of the electron-ion density for Ne-Ar plasmas created by fission fragments. The thesis and papers by Bennett (ref. 18) discuss the excited-state populations in He, Ne, Ar, and N_2 created by alpha particles. Russell in a paper on page 53 discussed the excited-state kinetics in argon being irradiated by fission fragments. Research is underway by the authors using a 1-Ci alpha source to study a variety of gases spectroscopically and later reports will include a plasma kinetic model applicable to this work. The purpose of the remaining section of this paper is to illustrate how the source term is found for a nuclear-generated plasma and some of the interesting features of the production of excited states in helium.

RESULTS FOR HELIUM IRRADIATION IN A GAS CHANNEL BETWEEN TWO INFINITE SOURCE FOILS

The techniques described in the previous sections can be used to predict ionization or excitation source rates in either an infinite gas medium or a finite-width gas channel irradiated from both walls by charged particles. The model not only predicts the spatial variation of production of ionization or excitation but by integration over the gas volume predicts the total amount of ionization or excitation produced and the pressure variation for each species in the gas. The model thus is very versatile in its application to practical problems which arise in studies of nuclear-generated plasmas and radiation chemistry.

As an example of the technique, calculations were made for the irradiation of pure helium by a polonium-210 source and by a uranium-235 foil. We selected to study only the excited states produced by direct impact and delta-ray recoil impact and did not, at this time, calculate ionization rates. Since we did not include the plasma kinetics of the "thermal" electron-ion plasma, the results do not include the additional excitation rate due to the electrons and ions in the thermalized plasma. Our study is thus limited to a low-temperature, weakly ionized helium plasma where the major source of excitation comes from direct impact or from high-energy recoils. Tables I and II list the parameters used in the calculations. Numerical integration of equation (8) was performed on an IBM–360 computer using standard techniques. Wherever possible the results were first obtained in nondimensional form and then combined with parameters listed in tables I and II to obtain numerical answers. In this manner the computer results could be used for many special cases without rerunning the integration.

Spatial Variation of the Production of Excited States

Figure 9 shows the spatial variation in the gas of the production rate of n^1P states in helium for various source thicknesses of polonium-210. The magnitude represents an efficiency for the production of excited states since it is normalized to the maximum rate. For thin sources the large initial energy loss near the source foil interface causes

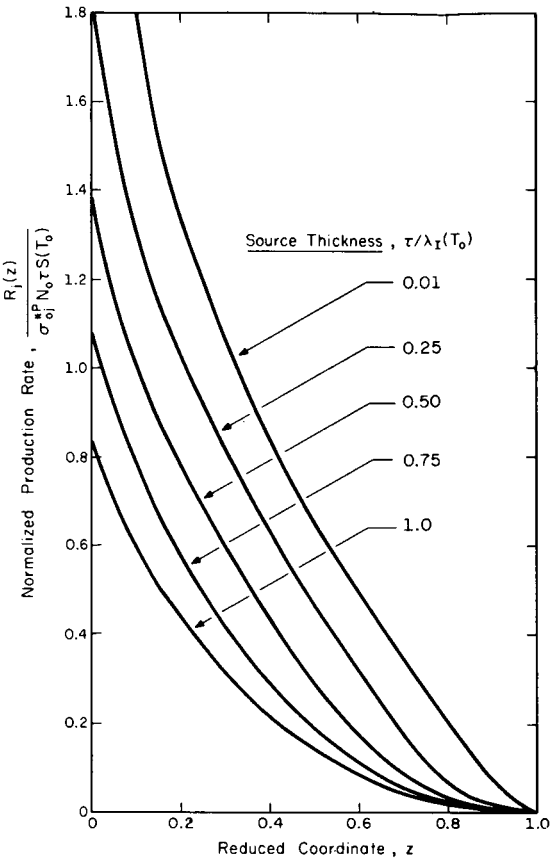

FIGURE 9.—*Spatial variation of the production of n^1P excited states in helium by polonium-210 alphas.*

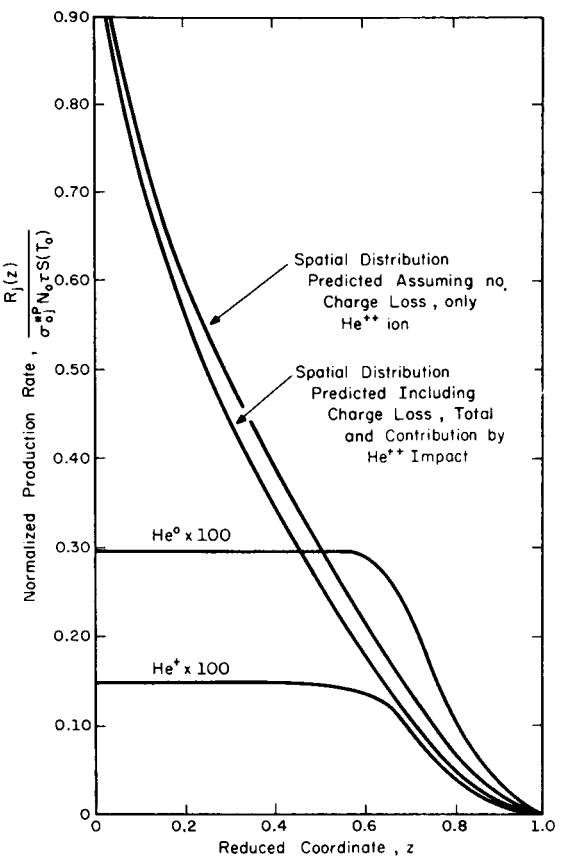

FIGURE 10.—*Contributions to the excitation of helium of the various charge states of 5.3 MeV polonium-210 alpha particles for a source thickness of τ/λ_I (T_o) = 0.25.*

a rapid decrease in the rate of production of excited states in the gas region. Energy losses in the fuel layer itself account for the decrease in efficiency with increasing source thickness. Although the efficiency is smaller, the total excitation rate for a thick source is larger due to the larger source rate $\tau S(T_o)$.

Figure 10 shows the contribution to the local source rate of n^1S and n^1D states in helium by the various charge states of the alpha particles for a polonium foil with thickness $\tau/\lambda_I(T_o) = 0.25$. For this foil thickness the He^{2+} ion creates more than 99 percent of the excitation produced up to the $Z = 0.75$ plane. It is only for planes near the value of the alpha's range that the He^+ and He^0 ions contribute significantly to the production of excited states. This result is not surprising. Several factors heavily weight the contribution of the He^{2+} ion. Figure 5 shows that the charge fraction of He^+ does not become significant until the alpha has had its energy reduced to about 20 percent of its initial value. However, the alpha particle flux spectra in figure 3 for this foil thickness show that there are relatively few alphas which have energies below this value. Also, the cross section for the He^{2+} charge state is 4 times larger than for the singly ionized state and more than 10 times larger than for the neutral state.

One is tempted to conclude from such a plot that the He^+ and He^0 states can be neglected. For thin source foils and thin gas slabs such a conclusion may be justified. However, it is not so good for thicker source foils where more alphas are emerging from the source at lower energies.

Figure 10 also shows that if He^{2+} is assumed to be the only ion species (charge fraction is 1.0), the result is overestimated by about 5 percent. Plots

for the spatial variation of the number of n^1S and n^1D excited states produced have shapes similar to those shown in figure 9 but are smaller in magnitude because of the cross section.

Similar results are shown in figures 11 and 12

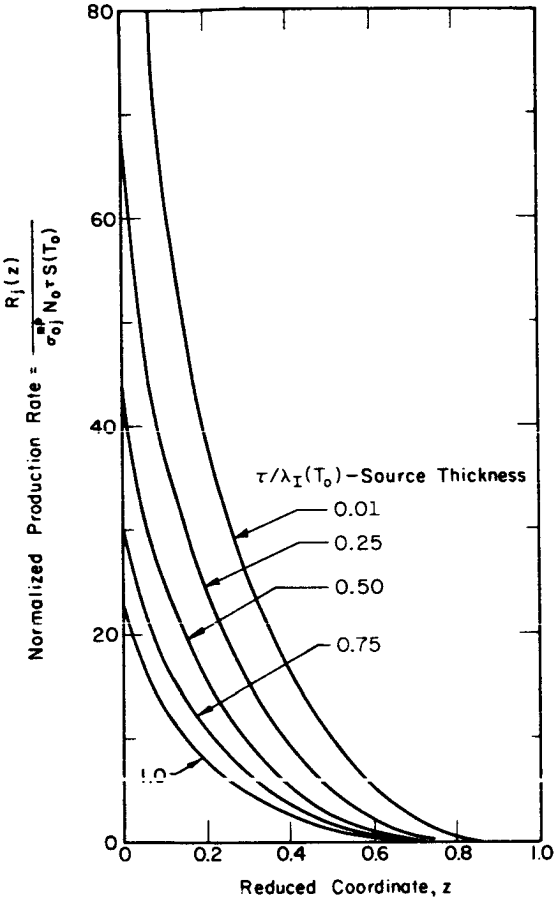

FIGURE 11.—*Spatial variation of the production of* n^1S *and* n^1D *excited states in helium by light fission fragments.* $n_I = n_{II} = -0.50$; $m_{II} = 0.95$; $M^{ff} = 96$ *amu*; $T_0 = 98$ *MeV.*

for the spatial variation of the excitation produced in helium by direct impact of light fission fragments. Because of the peculiar variation of the cross section for fission fragment excitation and the rapid energy loss of the fragment, the number of excited states produced and the "efficiency" drop quite rapidly as one moves away from the source foil boundary into the gas region. The excitation produced at the wall, however, is large compared with that for an alpha particle because of the higher

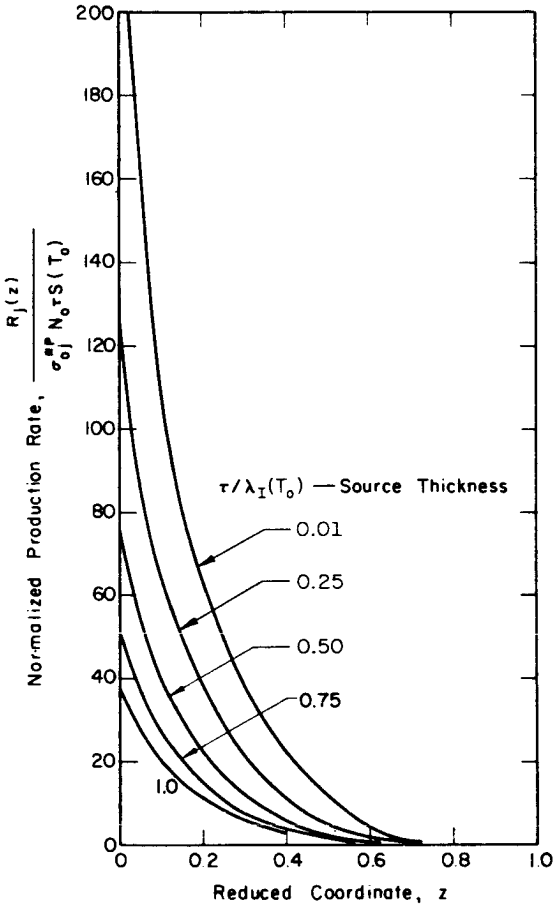

FIGURE 12.—*Spatial variation of the production of* n^1P *excited states in helium by light fission fragments.* $n_I = n_{II} = -0.50$; $m_{II} = 0.95$; $M^{ff} = 96$ *amu*; $T_0 = 98$ *MeV*; $\epsilon^* = 0.130$.

fragment energy and cross section. Also because of the mass of the fragment there is a region in the gas in which no excitation is produced by direct impact. The threshold energy for light fragment excitation shown in figure 8 is roughly 2 MeV. Below this energy the fragment is probably neutralized and undergoes only nuclear collision, thus giving rise to the "dark" region beyond planes eight-tenths of the fragment range into the gas volume.

The spatial variation of the production of the singlet states in helium does not differ much with the type of state but each of the states differs in magnitude. More n^1P states are created not only because of the magnitude of their cross section but

also because they are optically allowed transitions so that the maximum in the excitation cross section occurs at a higher energy than for forbidden transitions such as n^1S and n^1D.

Turning now to the contribution of the delta rays to the production of excited states in helium, similar spatial variation plots were obtained for each state, source thickness, and type of charge particle. Figure 13 compares the ratio of the number of excited states produced per unit volume by delta rays to the number produced by direct impact. Near the polonium source foil 5 to 6 percent of the total excitation is created by the delta rays. This fraction increases as one moves into the gas volume. This effect is due to the shift in the flux spectra which increases the weight of lower energies where more deltas are produced by Rutherford scattering. The fact that the deltas have a lower initial energy does not outweigh this effect since they are born with energies well above the peak in the cross section. Depending on the accuracy desired, one can decide from these plots whether to make the additional calculations needed to include the effects of delta rays.

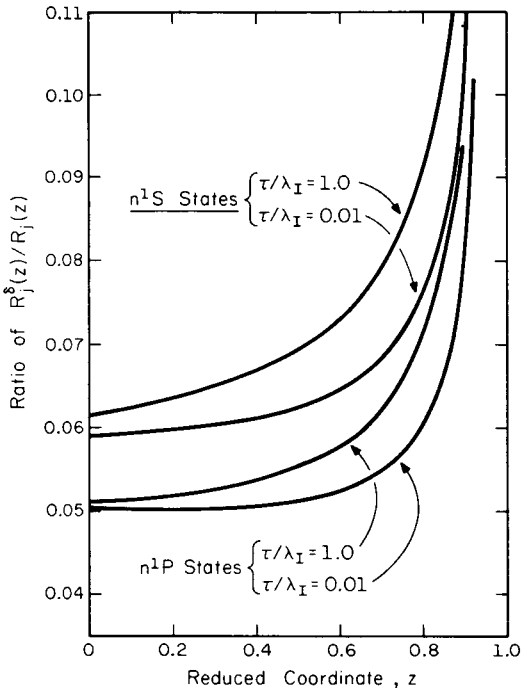

FIGURE 13.—*The spatial variation of the production of excited states by delta rays scattered by alpha particles from a polonium-210 source.*

Figure 14 shows similar results for fission fragment irradiation of helium. Here some 13 to 15 percent of the production of excited states near the source foil is by the delta rays. However, rather than increasing as one moves away from the foil, this percentage decreases until the point is reached that direct impact excitation is no longer energetically possible and all the excitation produced is by the delta as shown by the light fragment curves.

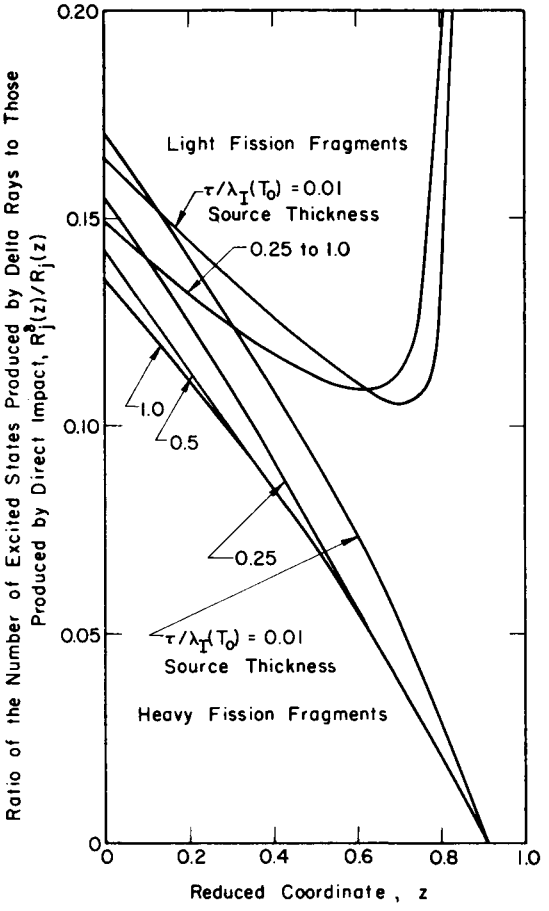

FIGURE 14.—*The spatial variation of the production of excited states of* n^1S *and* n^1D *helium by delta rays scattered by fission fragments.*

Total Production Rate

The total production rate in a gas channel irradiated by source foils on either side can be easily obtained by integration of the local production rate over the gas volume. For high gas pressures where the gas volume thickness t is greater than the range of the charged particle, all of the particles are stopped in the gas volume and none reenter the fuel plate. Hence all of the excitation and ionization they create are deposited in the gas. Integration over the gas volume therefore is over z between 0 and 1.0 and the result is multiplied by two for the two fuel plates which irradiate the channel. If the gas pressure is high enough so that $\lambda_{II}(T_o) < t/2$, there will be a source-free region at the center of the channel which does not contribute to the production of ionized or excited species.

The results of the integration for a dense helium gas slab irradiated by various source thicknesses of polonium-210 and uranium-235 are shown in figures 15 and 16. Most of the excitation produced goes into the 2^1P, 3^1P, and 2^1S states with smaller amounts going into higher P levels and the S levels. For a polonium source ($S(T_o) = 1.5 \times 10^{15}$ alphas/cm^3 sec) roughly 3300 2^1P states are created per alpha for a thin source which decrease to about 880 for a thick source because of energy losses in the source itself. For a polonium source of thickness equal to the alpha particle range (1.8×10^{-3} cm) about 4×10^{15} 2^1S metastables are produced in the

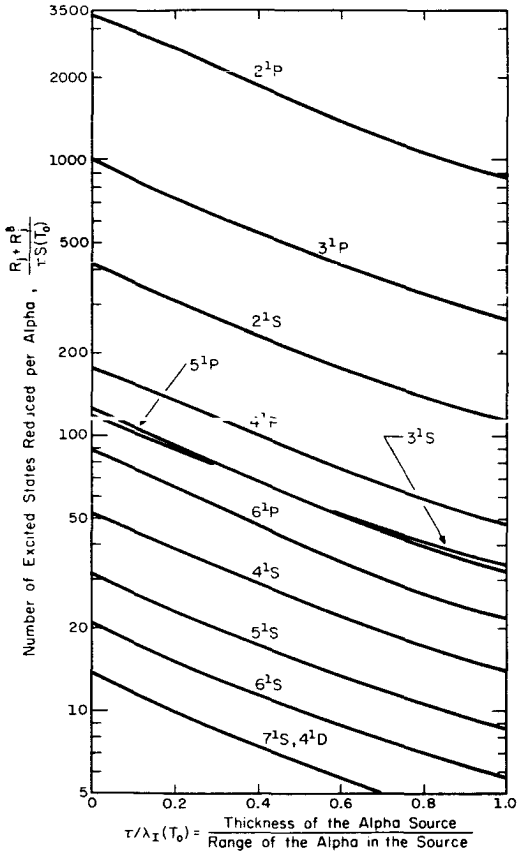

FIGURE 15.—*Effect of the source thickness on the production of excited states in a dense helium slab irradiated by two polonium-210 source foils. Helium thickness* $t > \lambda_{II}(T_o)$; $T_o = 5.3$ *MeV including charge loss and delta-ray effects.*

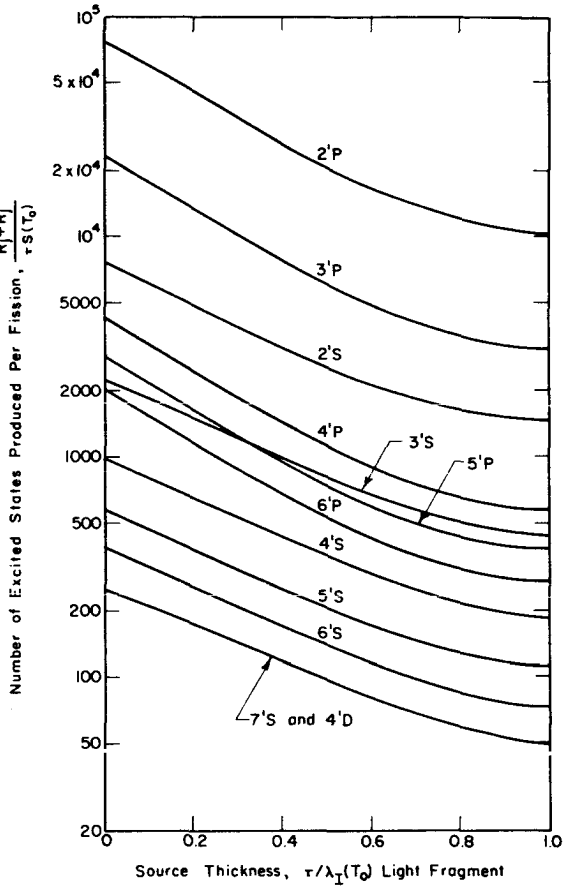

FIGURE 16.—*Effect of the source thickness on the production of excited states in a dense helium slab by two uranium-235 foils. Helium thickness* $t > \lambda_{II}(T_o)$.

channel per square centimeter of channel wall per second (assuming there are no losses to impurity atoms or to ionized states and there is complete trapping of the vacuum ultraviolet). For a 1-Ci source the number of metastables produced is estimated to be 2×10^{14}/sec.

The effect of the energy loss in the source foil is also evident for a uranium-235 fission fragment source where the decrease of excited states produced is larger for thicker source foils. Figure 16 shows that about 80 000 2^1P states are formed per fission for a thin source while some 10 000 2^1P states are formed per fission for a thick source. The different production rate caused by the energy dependence of the cross section is observable in comparing 3^1S and 5^1P production in the figure.

In order to produce the same amount of excitation from a thick fission source as that obtainable from a thick polonium-210 source, a thermal neutron flux of 1.5×10^{13} N/cm² sec is needed. This flux is reduced to 7×10^{9} N/cm² sec if the alpha source can be made to a strength of only 10 mCi/cm² corresponding to the current limit which can withstand a vacuum. Unfortunately, large polonium sources must also be manufactured with a cover material to keep the contamination within AEC regulations. Radiation damage to this cover limits the maximum source strength which can be safely contained.

However, for spectroscopic studies, a polonium source has the advantage that little radiation shielding is needed. Thus a much larger solid angle of the optical emission from the plasma can be focused onto a spectrometer slit than is possible when the plasma is generated in a reactor core where shielding requires that the spectrometer be remotely located. (It was for this reason, as well as the shutdown for conversion of our reactor, that we switched from in-core spectroscopy experiments to a polonium source. The University of Illinois Alpha Irradiation Facility, scheduled for delivery in February 1970, will be the largest vacuum radiation chemistry alpha source yet manufactured (1 to 5 Ci).)

A comparison can also be made here between use of a boron-10 foil and a uranium-235 foil if we assume they both have a thickness equal to the fragment range and are placed in equal neutron fluxes. (The results for a boron-10 foil are about the same as those presented for a polonium-210 source.) Because of its larger thermal neutron cross section and atom density for boron-10, it produces a charged particle source rate 10 times that for a uranium-235 foil. However, the fission fragments from a thin uranium foil still produce about 2.5 times the number of excited states produced by "fragments" from a thin boron-10 foil because of the differences in initial energy and cross section. The production rate, however, is not the only consideration in the selection of a source. One important point to note is that both boron-10 and uranium-235 sources introduce impurities into the gas but boron products are less offensive.

The discussion to this point has assumed that the pressure times the channel width is sufficiently large that all charge particles are stopped in the gas. However, it is often desirable to operate at low gas pressures or with a narrow channel. Then particles leaving the fuel on one side may cross the channel and reenter the fuel on the other side. We have carried out calculations for such cases, again assuming that the channel has fuel plates on either side. Excitation rates were again found by integration over the channel volume, taking care to account for the fact that some of the charged particles with angles near the normal reenter the fuel region on the opposite side of the channel. Figure 17 shows the results of the integration as the pressure variation of the number of 2^1P states excited in the helium channel per alpha particle for various thicknesses of the polonium-210 source foils. Energy loss in the source foil causes fewer states per alpha to be formed in the gas region for thicker sources, although the total production rate is still larger for a thick source than for a thin source. Linearization of the spatial rate of production of excited states near the fuel-gas interface leads to the following expression for the total excitation produced in the channel:

$$R_j+R_j^{\delta}=(a+bP^*)P^*\tau S(T_o) \qquad \text{for } P^*<0.1 \tag{10}$$

where

$$P^*=\frac{p}{760\text{ torr}}\times\frac{t}{\lambda_{II}(T_o,1\text{ atm})_{\text{light fission fragment}}}$$

This expression predicts that at low gas pressures the rate of formation of excited states is quadratic in pressure and not linear as assumed by Bennett

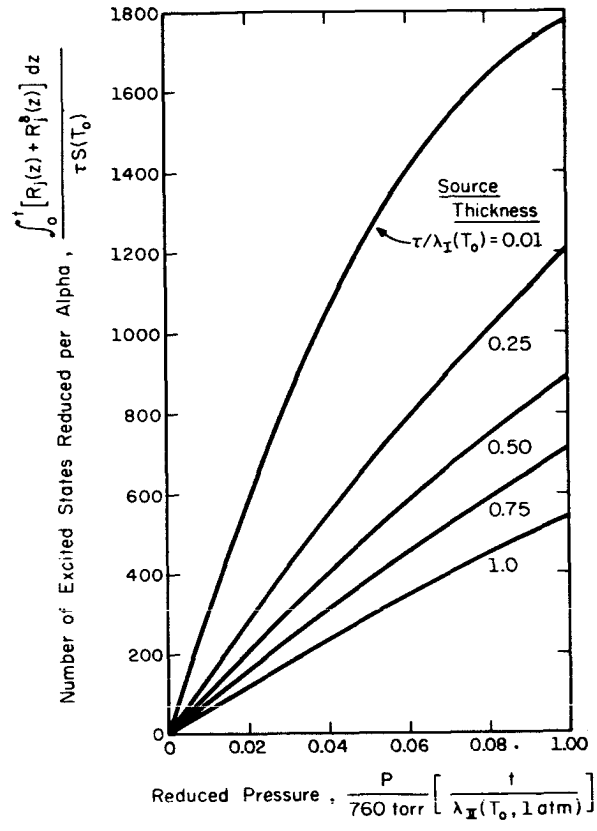

FIGURE 17.—*Pressure variation of the production of the helium 2¹P excited state in a low-pressure channel irradiated by two polonium-210 source foils.*

(ref. 18), although at very low pressures the linear term does dominate. Values for a and b for fission fragment and polonium alpha particle excitation of helium 2^1S and 2^1P states are listed in table V. Values for the production of other singlet states in helium can be found by multiplying the values in the table by the ratio of the cross section of that state to either the 2^1S or 2^1P cross section as listed in table III. The value of b is negative because the highest source rate occurs at the wall of the gas channel and decreases as one moves toward the channel centerline because of the energy and charge loss of the charged particles in the gas.

Again a comparison of polonium, boron-10, and uranium sources can be made. Since at low pressures the early part of the charged particle track is favored, somewhat different results are obtained from those discussed earlier for high pressure. A neutron flux of about 4×10^{13} N/cm² sec is needed for the excitation rate of a thick fission foil to surpass that of a thick polonium source. However, a flux of only about 7×10^{10} N/cm² sec is needed to make a thick fission foil surpass the strength of a 10 mCi/cm² polonium source. A thick boron-10 source produces about twice the excitation produced by a thick uranium source, but as the thickness of the source decreases fission fragments ultimately can produce slightly larger excitation in the gas.

CONCLUSIONS

The model for the production of ionization and excitation in a nuclear-radiation-produced plasma using a charged particle flux and cross section has been demonstrated to give a fairly detailed description for the complex excitation rates in the plasma. Both the spatial variation of the source of ionization and excitation and the total volume rate and its pressure dependence are obtained from the model. The calculations for a polonium-210 alpha source and a uranium-235 fission fragment source indicate that for high gas pressures a polonium source of 10 mCi/cm² will produce more excitation unless a

TABLE V.—*Comparison of Excitation of Helium at Low Gas Pressures by Fission Fragments and Polonium-210 Alpha Particles*

Source foil thickness, $\tau/\lambda_I(T_o)$	2^1S state				2^1P state			
	Fission fragment		^{210}Po alpha		Fission fragment		^{210}Po alpha	
	a	b	a	b	a	b	a	b
1.00	1.4×10^4	-4.7×10^4	0.58×10^4	-6.7×10^4	2.1×10^5	-7.9×10^5	0.47×10^5	-5.9×10^5
.75	1.9	−5.5	.74	−8.2	2.8	−10.4	.60	−7.0
.50	2.7	−8.0	.94	−10.5	4.1	−15.6	.75	−9.1
.75	4.4	−13.6	1.25	−16.3	7.4	−52.2	1.05	−14.1
.01	9.2	−68.0	2.59	−79.4	25.8	−109.0	2.20	−68.0

neutron flux greater than 7×10^{10} N/cm^2 sec is available. At low gas pressures this flux is also 7×10^{10} N/cm^2 sec. For low gas pressures a thick boron-10 source produces more excitation than a thick fission source while at high gas pressures the calculations show a fission fragment source produces slightly more excitation than does a boron-10 source.

For flat plate channels at low pressures the production of excited states is shown to be quadratic in pressure when the pressure-channel width product is in the range of 200 to 300 torr-cm for a fission source and 1500 to 3000 torr-cm for a polonium source. This may be an important fact in the interpretation of spectroscopic data. At very low gas pressures (0 to 50 or 0 to 500 torr-cm for fission or polonium sources, respectively), the linear behavior of the source term with pressure is approximately valid, as assumed by previous workers.

ACKNOWLEDGMENTS

Danny Weidenfeld did some of the numerical coding for the alpha particle charge fraction. The calculations for the production rate of excited states utilized numerical double integration techniques developed several years ago by Miss Patricia Squires. Ronnie Lo and Enno Nomm assisted in some of the hand calculations.

APPENDIX A

ANALYSIS OF AVAILABLE EXPERIMENTAL DATA ON SLOWING DOWN OF ALPHA PARTICLES AND FISSION FRAGMENTS

The model presented in this paper rests primarily on the use of a two-parameter semiempirical relation for the energy of a charged particle after traveling a distance s given in equation (1). The precedence for adopting this relation was enumerated in the previous article by the authors (ref. 1). The purpose of this appendix is to bring together all available data for alpha particles and fission fragments and to obtain appropriate parameters to use in the calculations for each particle.

Data on slowing appear in the literature in several forms. One form shows experiments in which the energy of a charged particle is measured for various distances traversed in a medium. For the purposes of our model such data are ideal since a log-log plot of ϵ vs $(1-s/\lambda)$ yields the value of $1/(n+1)$ as the slope. However, very few data have been presented in this form.

A second form, widely used in older papers, shows the total range of the charged particle vs the initial ion energy. Equation (1) can be rewritten to obtain the following relation for the range of an ion starting at energy T as compared with one starting at T_o:

$$\frac{\lambda(T)}{\lambda(T_o)}=\epsilon^{n+1} \tag{A1}$$

Thus a log-log plot of $\lambda(T)$ vs T has a slope of $n+1$.

The final form in which data appear most frequently in recent literature is as an atomic or molecular stopping cross section vs the energy of the particle. By definition the stopping cross section is

$$\mathrm{E}\equiv\frac{1}{N_o}\frac{dT}{dS} \tag{A2}$$

where N_o is the number density of the target atoms. Using equation (1) this has the form

$$\mathrm{E}=\frac{T_o^{n+1}}{(n+1)N_o\lambda(T_o)}T^{-n} \tag{A3}$$

and therefore a log-log plot of E vs T has a slope of $-n$.

All three of these forms had to be used to obtain values of n for alpha particles and fission fragments.

Alpha Particles

Older range-energy data for alpha particles were obtained from decay sources or from n and alpha reactions. Almost all of the data were published as the total alpha range for a given energy. Unfortunately, many of the materials of interest today have not been restudied under more controlled conditions. Jesse and Sadauskis reviewed the data obtained prior to 1950 for air and argon (ref. 19). Figure A1 plots the values of λ (T) vs T they report as sug-

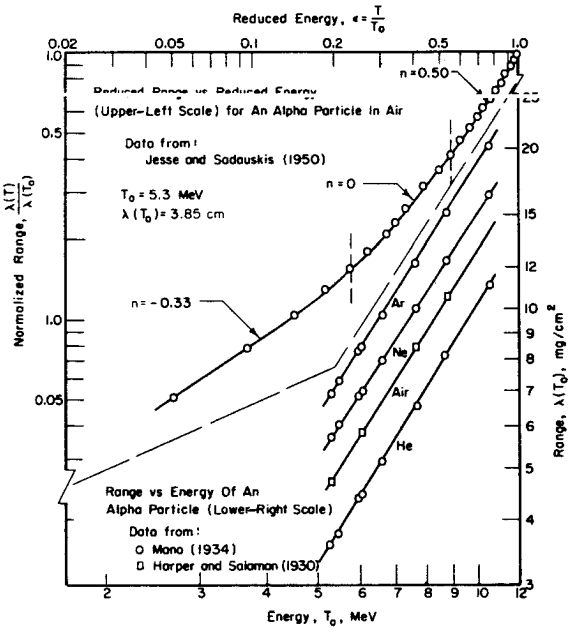

FIGURE *A1.—Data on range versus energy for alpha particles in gases.*

gested by equation (A1). Other older data on alpha particle ranges in H_2, He, N_2, O_2, Ne, Ar, Kr, Xe, and CO_2 were reviewed by Bogaardt and Kondijs (ref. 20). Rosenblum (ref. 21) made similar measurements in solids such as Li, Al, Ni, Cu, and Au.

More recent alpha slowing data have been reported by Kerr et al. (ref. 22) and Weyl (ref. 23) for gases while Northcliffe (ref. 24) has summarized the available data for metal foils. The values of atomic stopping cross sections they reported are plotted in figure A2. In both figures A1 and A2 at

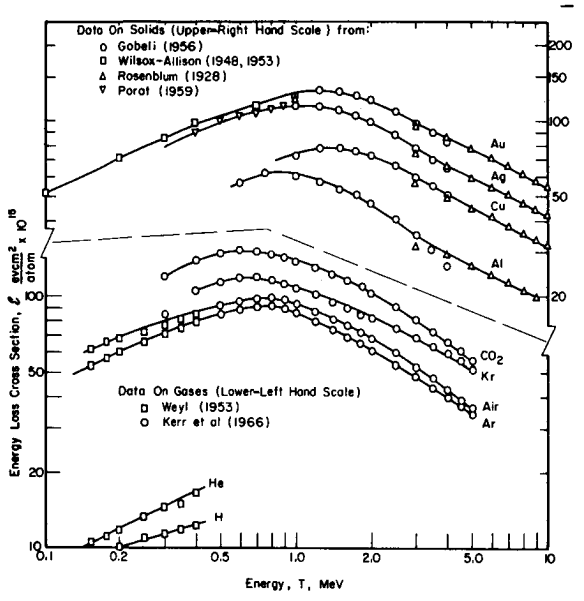

FIGURE *A2.—Energy loss cross section measurements versus energy for alpha particles in gases and solids.*

least two energy regions with values of n with different signs are needed. The dividing energy between these two energy regions is about 600 keV, which is roughly the energy at which half of the alphas are singly ionized. The use of a single value of the fitting parameter n is justified if the alpha energies of interest all lie in one region or the other. For a 5.3-MeV polonium-210 alpha a single positive value of n may be a reasonable approximation. However, a 1.47-MeV boron-10 alpha should have its energy loss broken into two or preferably three energy groups, one with a negative n, one with n equal to zero, and one with a positive value of n.

Fission Fragments

Older data on the slowing down of fission fragments were reviewed by the authors in an earlier paper (ref. 25). The data presented in that paper were based on experiments by Fulmer (ref. 26), but his work has since been found to contain an error because it was not corrected for the gas density used (ref. 27). Newer data on fragment slowing down are now available. Axtman and his students have studied slowing in N_2 (refs. 28 and 29); Moore and Miller (ref. 30) have studied H_2, He, Ar, Kr, and Xe; Kahn and Forgue (refs. 31 and 32) studied Ag, Al, Au, Ni, CO_2, and Xe; and Albrecht and Muenzl (ref. 33) recently reported data for Al, Ag, and Au.

Figures A3 and A4 show a fit of equation (1) to Kahn and Forgue's data. Light fission fragments can be represented by a single value of n over nearly a decade in energy loss. It is necessary, however, for the heavy fragment passing through metallic foils to use two values of n, one for energies above $\epsilon = 0.4$ and a second for those below $\epsilon =$

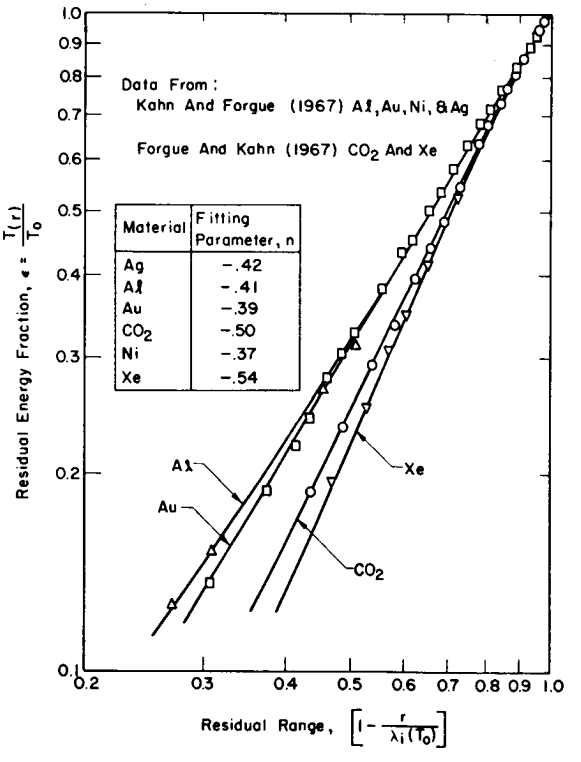

FIGURE *A3.—Residual energy fraction versus residual range for light fission fragments in various materials.*

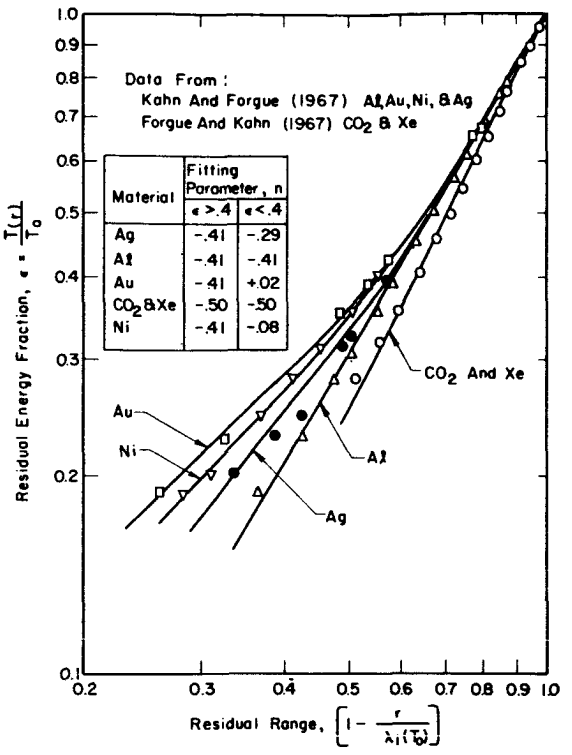

FIGURE *A4.—Residual energy fraction versus residual range for heavy fission fragments in various materials.*

0.4. Unfortunately, data on CO_2 and Xe were not taken for low enough energies to see this breakpoint. Moore and Miller observed this to occur at 57 MeV, which is the energy of an electron corresponding to the *N*-shell. The change in slope is probably due to the change in the electron capture and loss process for the ionized fragments above and below this energy. Moore, Miller, Kahn, and Forgue chose to present their data using the nondimensional energy and range suggested by the Lindhard-Scharff-Schiøtt (LSS) theory (refs. 34, 35, and 36), which predicted a slowing relation of the form

$$\frac{d\epsilon^{\ddagger}}{d\rho} = k(\epsilon^{\ddagger})^{1/2} \qquad \text{(A4)}$$

where

$$\epsilon^{\ddagger} = \frac{TaM_2}{Z_1 Z_2 e^2 (M_1+M_2)}$$

$$\rho = \lambda N_0 M_2 (4\pi a^2) M_1/(M_1+M_2)^2$$

and

$$k \cong \frac{0.0793\, Z_1^{1/6}(Z_1Z_2)^{1/2}(M_1+M_2)^{3/2}}{(Z_1^{2/3}+Z_2^{2/3})^{3/4}\, M_1^{3/2} M_2^{3/2}}$$

with the Thomas-Fermi penetration constant a given by

$$a = 0.8853\, a_0 (Z_1^{2/3}+Z_2^{2/3})^{-1/2}$$

where a_0 is the first Bohr orbit radius.

In their relations the subscript 1 refers to the projectile and 2, to the target. This form is equivalent to equation (1) if the value of n is taken to be $-\frac{1}{2}$. Data obtained by Kahn and Forgue (ref. 31) and Moore and Miller (ref. 30), however, did not entirely fit this theoretical model.[2] Whether one chooses to use equation (1) in a piecewise fit as already suggested for alpha particles, to use a least-squares fitting of $\epsilon^{\ddagger}$ vs ρ to some function to obtain a single range-energy relation as suggested by both Kahn and Forgue and Albrecht and Muenzl, or to allow k to be a function of energy as suggested by Moore and Miller is a matter of personal choice. The form chosen, however, does affect the complexity of the model for the charge particle flux and equation (1) does lead to a straightforward answer for the flux. Hence we feel its use represents a reasonable compromise between complexity and accuracy.

[2] A recent review of the LSS theory (ref. 37) indicates that in many practical applications where experimental data are not known the theory can be used to give fairly accurate answers for single-specie, heavy ions in solids. It does not work, however, for a high-energy alpha particle above 600 keV for the same reason that it does not predict fission fragment behavior. Most authors feel that the LSS theory does not fit experimental data because it incorrectly treats the energy loss due to electronic interactions.

APPENDIX B

ANALYSIS OF AVAILABLE EXPERIMENTAL DATA ON CHARGE LOSS FOR ALPHA PARTICLES AND FISSION FRAGMENTS

Two methods of treating the charge loss of a high-energy heavy ion were discussed earlier. The charge fraction approach was suggested by Northcliffe (ref. 24) based on Bohr's original analysis of capture and loss cross sections for protons and alpha particles (ref. 38). On the basis of the available data for ions heavier than helium, Northcliffe found a universal relationship for the charge fraction in terms of the ion velocity v

$$\frac{\chi_Z(z)}{\chi_{Z-1}(z)}=\begin{cases}0.365z^4 & \text{for } z>2.5\\ 0.3z^{4.35} & \text{for } z<2.5\end{cases} \tag{B1}$$

$$\frac{\chi_{Z-1}(z)}{\chi_{Z-2}(z)}=1.6z^4 \tag{B2}$$

$$\frac{\chi_{Z-2}(z)}{\chi_{Z-3}(z)}=12z^4 \tag{B3}$$

where $z=\dfrac{v}{v_1}=v/cZ/137$ and v_1 is the velocity of an electron in the innermost Bohr orbit. However, he did not analyze the data for alpha particles. Figure B1 shows the available data for the charge fraction ratios $\chi_{He^{++}}/\chi_{He^{+}}$ and $\chi_{He^{+}}/\chi_{He^{0}}$. The power law suggested by Northcliffe also appears to be valid for alpha particles with different values of the slope and constant. Like the slowing law it is a two-parameter, semiempirical law of the form

$$\frac{\chi_{He^{++}}}{\chi_{He^{+}}}=A_2\epsilon_b^{n_2} \tag{B4}$$

$$\frac{\chi_{He^{+}}}{\chi_{He^{+0}}}=A_1\epsilon_b^{n_1} \tag{B5}$$

Using these relations and the fact that

$$\chi_{He^{++}}+\chi_{He^{+}}+\chi_{He^{0}}=1.0 \tag{B6}$$

equations (4), (5), and (6) for $\chi_{He^{++}}(\epsilon)$, $\chi_{He^{+}}(\epsilon)$, and $\chi_{He^{0}}(\epsilon)$ can be found. Values for A_2, A_1, n_1, and n_2 are given in table I for the data plotted in figure B1.

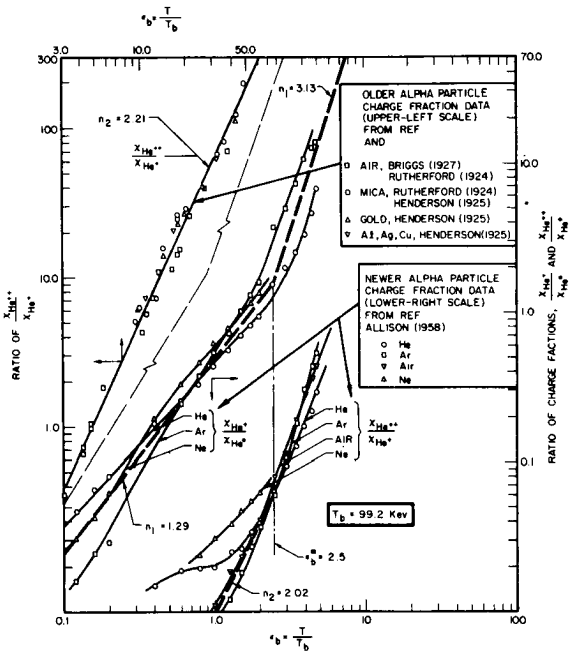

FIGURE *B1.—Charge fraction data versus energy for alpha particle.*

Before we pass on to the charge on a fission fragment, it is interesting to note a few things about the data plotted in figure B1. The older measurements by Briggs (ref. 39), Rutherford (ref. 40), and Henderson (refs. 41 and 42) for alphas above 600 keV have not been repeated in the past 30 years. Although the slope of their data seems to agree with the newer data below 600 keV reported by Allison (ref. 43), Barnett and Stier (ref. 44), and Snitzer (ref. 45), the two curves are discontinuous in magnitude. Such differences are often due to problems in calibrating the detector as were found for Snitzer's results or due to neglect of the He^0 fraction. In the case of the older data, visual observation of scintillations was used, and this

could explain the discrepancy. While most physicists have left this area for high-energy physics, perhaps it would be well to repeat the experiments done by Rutherford et al. using modern techniques. There is also a lack of data on alpha charge loss in noble gases at these higher energies.

The availability of experimental data for fission fragment charge loss is not good. Only three studies have been made, of which only the work by Fulmer and Cohen (ref. 46) can be classed as a fairly complete study. Lassen (ref. 47) in 1945, under Bohr's direction, made the first measurements of the electronic charge on a fission fragment slowing in mica, and he continued his research into the early 1950's with other targets. Recently the question of the effect of the charge on a fission fragment was studied by Linnerud (ref. 48) for uranium foils.

The data taken by Fulmer shown in figure B2 also suggest a semiempirical two-parameter power law for the average charge of the form given by equation (7). Values of m read from the slope of the curves in figure B2 all lie between 0.9 and 1.05. A somewhat different value might be expected at energies below Fulmer's measurements. Neufeld (ref. 49) has studied this theoretically and predicts changes in slope as the various shells in the ion are progressively filled; however, such effects have not shown up in experiments because the low-energy region of fragment slowing and charge loss remains unexplored. In an attempt to probe these effects, ^{79}Br and ^{127}I were used to simulate fission fragments in the range of 15 to 160 MeV. This work was reported by Moak et al. (ref. 50) using a carbon target and a tandem Van de Graff accelerator. They did not find that their data would fit the power law and suggested instead an exponential law. Much research is needed in this area before accurate calculations can be made. For the purposes of the present paper the charge loss model for the high-energy region as measured by Fulmer will be used. It is hoped that any error this introduces in estimates of ionization and excitation at low energies will be small.

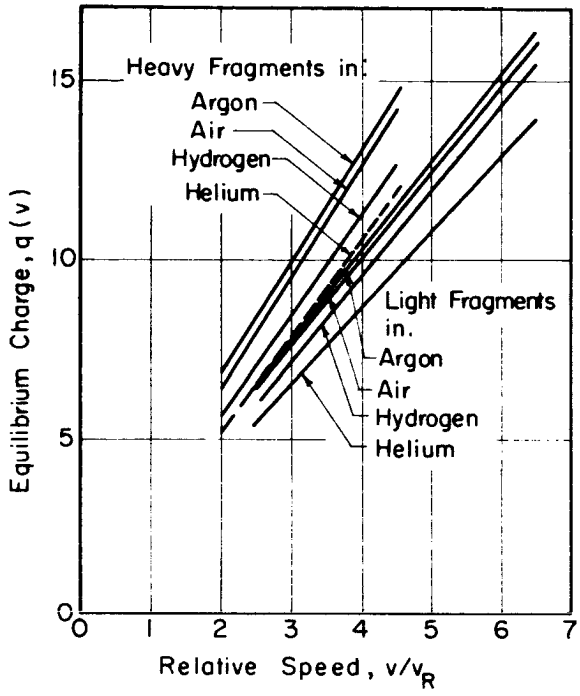

FIGURE *B2.—Fulmer's data (ref. 44) on the average equilibrium charge on a fission fragment against its energy.*

APPENDIX C

DERIVATION OF THE EXCITATION CROSS SECTION FOR FISSION FRAGMENT IMPACT

Since there have been no measurements for the excitation cross section for fission fragment impact on a gaseous target, and because we are forced to adopt an average charge loss model, the excitation cross section for a fragment must be estimated by fitting proton data and charge loss data to the Bethe-Born cross section. Theoretical treatment of excitation using the Born approximation leads to the expression for the cross section (ref. 10)

$$\sigma_{oj}=\frac{16\pi q^2 e^4}{m_e v}\left|Z_{oj}\right|^2 \log\left(\frac{2\,m_e v^2}{E_j-I}\right) \qquad \text{(C1)}$$

where

E_j	energy of excited state of target atom
I	ionization energy of target atom
q	number of electronic charge units on projectile
v	velocity of projectile
m_e	mass of an electron
$\lvert Z_{oj}\rvert^2$	transition probability

Thus the Born approximation indicates that particles having equal charges and equal velocities will have the same excitation probability per unit track length. This makes it possible to use high-energy electron and proton data to predict the cross section for He^{2+}, He^{+}, Li^{3+}, Li^{2+}, and Li^{+} ions where no measurements may exist. The validity of this is demonstrated in figure 6 where electron, H^{+}, and D^{+} data have been brought together along with the alpha particle cross section prediction. For velocities equal to those of a proton, the energy of a heavy ion is

$$T^i=\frac{M^i}{M^p}T^p \qquad \text{(C2)}$$

Thus, in order to have the same cross section value the alpha particle must have an energy four times that of a proton. In addition, because of the charge difference, the alpha cross section is four times that of a proton, while that of the He^{+} ion has the same magnitude.

In the case of a fission fragment the average charge decreases with energy in accordance with the semiempirical law of equation (7). When the form of the Bethe-Born cross section normalized to the maximum cross section value for a proton and the energy at which it occurs given by equation (9) is used, the cross section for fission fragment excitation becomes:

$$\sigma_{oj}^{ff}(\epsilon)=\sigma_{oj}^{*p}(q_o^{ff})^2\,\epsilon^{*ff}\,\epsilon^{m-1}\log\left(\frac{2.718\,\epsilon}{\epsilon^{*ff}}\right) \qquad \text{(C3)}$$

where

σ_{oj}^{*p}	maximum value of proton cross section occurring at ϵ^{*p}
q_o^{ff}	initial charge on the fragment
m	fragment charge loss fitting parameter
$\epsilon^{*ff}=\frac{M^{ff}}{M^p}\epsilon^{*p}$	
M^{ff}	mass of the fragment
M^p	mass of the proton

This cross section is shown in figure 8 for $m=1.0$ for excitation of the n^1S and n^1D states in helium. A similar cross section is predicted for the n^1P states.

APPENDIX D

DERIVATION OF THE PSEUDO CROSS SECTION FOR THE PRODUCTION OF EXCITED STATES BY DELTA RAYS SCATTERED BY THE PRIMARY ION IN SLOWING DOWN

The effects of recoil particles produced by high-energy, heavy ions are important in some nuclear-radiation-produced plasmas. Delta-ray and recoil atom tracks have been observed in cloud chamber photographs to produce small branches to either side of the primary ion track (refs. 5 and 6). Although these cascade effects are contained in w (the energy to produce an ion pair), when one uses a single collision model such as equation 8 it is necessary to derive a collisional model for the recoil particles.

Fortunately, at reasonable gas pressures the range of the delta-ray electrons and recoil atoms created by small-angle nuclear scattering is very small in comparison with the range of the primary ion. For example, in tables I and II the maximum ratios of the range of the delta to the primary ion are 0.004, 0.024, and 0.0053 for polonium-210 alphas (5.3 MeV), light fission fragments, and heavy fission fragments, respectively. Therefore a reasonable estimate of the excitation or ionization produced by the delta-ray and small-angle recoil atoms is to lump their effects at the point of origin and to introduce a pseudo cross section to represent the interaction. It is derived by summing up over all scattering angles along the entire track of the recoil particles.

Let us assume that the recoil electrons or atoms are created by classical Rutherford scattering (ref. 5). Thus the initial energy of the recoil scattered with direction cosine μ_δ in figure D1 by an ion of mass M, charge q, and reduced energy ϵ is

$$T_o^{\delta}(\mu_\delta, \epsilon) = 4\frac{m_e}{M}T_o\epsilon\mu_\delta \qquad \text{(D1)}$$

The Rutherford cross section for production of recoils in the solid angle $d\mu_\delta$ is

$$d\sigma_p^{\delta}(\mu_\delta, \epsilon) = \left(\frac{M}{m_e}\right)^2 \frac{\pi e^4 q^2}{2T_o{}^2\epsilon^2\mu_\delta{}^3}d\mu_\delta$$

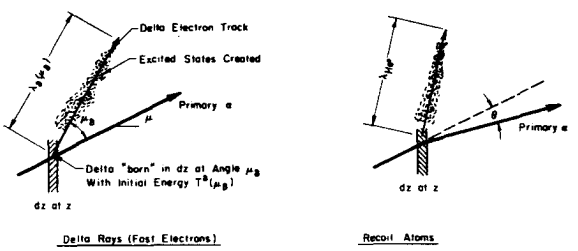

FIGURE *D1.—Excitation and ionization by secondary currents.*

or

$$d\sigma_p^{\delta}(\mu_\delta, \epsilon) = \sigma_p{}^{\delta *}\frac{1}{\epsilon^2\mu_\delta{}^3}d\mu_\delta \qquad \text{(D2)}$$

where

$$\sigma_p{}^{\delta *} \equiv \left(\frac{M}{m_e}\right)^2 \frac{\pi e^4 q^2}{2T_o{}^2}$$

which is the maximum value of the scattering cross section as given in table I for a He^{++} and a He^{+} ion.

Setting ϵ and μ_δ equal to 1 in equation (D1) gives the maximum recoil energy that can be imparted to an electron, namely

$$T^{\delta}{}_{\max} \equiv \frac{m_e}{M}T_o \qquad \text{(D3)}$$

The values of $T^{\delta}{}_{\max}$ for a 5.3 MeV alpha and light and heavy fission fragments as listed in tables I and II are 2.9, 2.2, and 1.05 keV, respectively. With initial electron energies of these magnitudes the Thomas-Whiddington slowing law for electrons can be used ($n=1.0$ in eq. (1)), and the energy of the electron after traveling a distance s becomes

$$T^{\delta}(s, \mu_\delta, \epsilon) = T_o^{\delta}(\mu, \epsilon)\left\{1 - \frac{s}{\lambda^{\delta}[T_o^{\delta}(\mu_\delta, \epsilon)]}\right\} \qquad \text{(D4)}$$

Using equation (D1) for the initial energy of the electron and the relationship for $\lambda_\delta(T^\delta)$ given by

equation (A1), this can be written as

$$T^{\delta}(s, \mu_{\delta}, \epsilon) = T^{\delta}_{\max}\, \epsilon\, \mu \left[1 - \frac{s}{\lambda^{\delta}(T^{\delta}_{\max})\, \epsilon^2 \mu_{\delta}^4} \right] \quad \text{(D5)}$$

Also the Bethe-Born cross section for excitation can be used for electron impact because of the magnitude of the initial energy. Equation (9) can be rewritten for the scattered electron, normalizing the energy either to $T^{\delta}_{\max}$ or to $T_o^{\delta}(\mu_{\delta}\epsilon)$ as

$$\sigma_{ij}(\epsilon'') = \frac{\sigma_{oj}{}^{\delta *}\, \epsilon^{\delta *}}{\epsilon \mu_{\delta}{}^2 \epsilon''} \log \left(\frac{2.718 \epsilon \mu_{\delta}{}^2 \epsilon''}{\epsilon^{\delta *}} \right) \quad \text{(D6)}$$

where $\sigma_{oj}{}^{\delta *}$ is the maximum value of the electron excitation cross section occurring at $T_{\sigma}{}^{\delta}{}_{\max}$ and

$$\epsilon^{\delta *} \equiv \frac{T_{\sigma}{}^{\delta}{}_{\max}}{T^{\delta}_{\max}}$$

The number of excited states produced per electron scattered into the solid angle $d\mu_{\delta}$ by an ion of energy ϵ therefore is

$$\int_0^{\lambda \delta(\mu \delta,\, \epsilon)} \sigma_{ij}{}^{\delta}(\epsilon'')\, N_o\, ds \quad \text{(D7)}$$

By use of the slowing law given by equation (D4) this integral can be converted into a summation over energy, with recognition that the electron excitation cross section goes to zero at

$$\epsilon'' = \frac{\epsilon^{\delta *}}{2.718\, \epsilon \mu_{\delta}{}^2}$$

The result is

$$2N_o \lambda^{\delta}(T^{\delta}_{\max})\, \epsilon \mu_{\delta}{}^2 \sigma_{ij}{}^{\delta *} \epsilon^{\delta *} \int_{\epsilon^{\delta *}/2.718 \epsilon \mu_{\delta}{}^2}^{1.0} \log \left(\frac{2.718 \epsilon \mu_{\delta}{}^2 \epsilon''}{\epsilon^{\delta *}} \right) d\epsilon''$$

or

$$2N_o \lambda^{\delta}(T^{\delta}_{\max})\, \sigma_{ij}{}^{\delta *} \epsilon^{\delta *} \epsilon \mu_{\delta}{}^2 \left[\log \left(\frac{2.178 \epsilon \mu_{\delta}{}^2}{\epsilon^{\delta *}} \right) - 1 + \frac{\epsilon^{\delta *}}{2.718 \epsilon \mu_{\delta}{}^2} \right] \quad \text{(D8)}$$

Multiplying this result by the probability of scattering over all solid angles give the pseudo cross section. Before writing the integral, however, we note from equation (D1) that there is a direction cosine corresponding to an initial delta energy below the threshold energy for optical excitation. Therefore integration over the solid angles is cut off at this angle, and this, in turn, avoids the problem of the integral blowing up as $\mu_{\delta} \to 0$. This minimum direction cosine is

$$\mu_{\delta \min} = \sqrt{\frac{\epsilon^{\delta *}}{2.718 \epsilon}} \quad \text{(D9)}$$

Defining

$$A \equiv \frac{2.718}{\epsilon^{\delta *}} \quad \text{(D10)}$$

we find that the total number of excited states produced per unit track length by a primary ion of energy ϵ in a gas having Z_{gas} electrons per atom is

$$2N_o{}^2 \lambda^{\delta}(T^{\delta}_{\max})\, Z_{\text{gas}} \sigma_p{}^{\delta *} \sigma_{ij}{}^{\delta *} \epsilon^{\delta *} \int_{\sqrt{1/A\epsilon}}^{1.0} \frac{1}{\epsilon \mu_{\delta}} \left[\log (A \epsilon \mu_{\delta}{}^2) - 1 + \frac{1}{A \epsilon \mu_{\delta}{}^2} \right] d\mu_{\delta} \quad \text{(D11)}$$

Then, after integration, the pseudo cross section has the form

$$\frac{\sigma_{ij}{}^{\delta}(\epsilon)}{N_o \lambda^{\delta}(T^{\delta}_{\max})\, Z_{\text{gas}} \sigma_p{}^{\delta *} \sigma_{ij}{}^{\delta *}} = \frac{5.436}{A\epsilon} \left[\log \sqrt{A\epsilon} (\log \sqrt{A\epsilon} - 1) + \frac{1}{2A\epsilon} (A\epsilon - 1) \right] \quad \text{(D12)}$$

which is shown plotted vs $A\epsilon$ in figure 7 for an alpha particle.

The pseudo cross section for the effects of delta rays scattered by fission fragments has a slightly different form because of the charge loss which is given by equation (7). If we retain $\sigma_p{}^{\delta *}$ (equation (D2)) as the appropriate value for an alpha particle, the pseudo cross section for a fission fragment is simply $(M^{ff})^2 \epsilon^m/16$ times equation (D12).

REFERENCES

1. Miley, George H.; and Thiess, Paul E.: A Unified Approach to Two-Region Ionization-Excitation Density Calculations. Nucl. Appl., vol. 6, 1969, p. 434.
2. Braun, J.; Nygaard, K.; and Witalis, E.: On Plasma Through Neutron Irradiation. Vol. 1, Int. Symp. on MHD (Paris), European At. Energy Agency, 1964, p. 179.
3. Steinberg, M.: Chemonuclear Reactions and Chemical Processing. Vol. 1 of Advances in Nuclear Science and Engineering, ch. 7, Academic Press (New York, N.Y.), 1962.
4. Chamberlain, J. W.: Physics of the Aurora and Airglow. Academic Press (New York, N.Y.), 1961.
5. Rutherford, E.; Chadwick, J.; and Ellis, C. D.: Radiations From Radioactive Substances. Cambridge Univ. Press (Cambridge, England), 1930.

6. BOGGILD, J. K.; BROSTROM, K. J.; AND LAURITSEN, T.: Range and Straggling of Fission Fragments. Phys. Rev., vol. 59, 1941, p. 275.
7. EVANS, R. D.: The Atomic Nucleus. McGraw-Hill Book Co., Inc., 1955, pp. 633–637.
8. MECHREBLIAN, R. V.; AND HOLMES, D. K.: Reactor Analysis. McGraw-Hill Book Co., Inc., 1960, p. 63.
9. THOMAS, E. W.; AND BENT, G. D.: Formation of Excited States in a Helium Target by the Impact of 0.15 to 1.0 MeV Protons and Deuterons. I. Experimental. Phys. Rev., vol. 164, 1967, p. 143.
10. MOTT, N. F.; AND MASSEY, H. S. W.: The Theory of Atomic Collisions. Oxford Univ. Press (London), 1965, pp. 497 and 613.
11. THOMAS, E. W.: Cross Sections for the Formation of Excited States in a Helium Target by the Impact of 0.15 to 1.0 MeV Protons and Deutron. II. Comparison With Theory. Phys. Rev., vol. 164, 1967, p. 151.
12. DE HERR, F. J.: Experimental Studies of Excitation in Collisions Between Atomic and Ionic Systems. Advances in Atomic and Molecular Physics, vol. 2, D. R. Bates and I. Estermann, eds., Academic Press (New York, N.Y.), 1966, pp. 327–384.
13. GRYZINSKI, M.: Two-Particle Collisions. I. General Relations for Collisions in the Laboratory System. II. Coulomb Collisions in the Laboratory System of Coordinates. Phys. Rev., vol. A138, 1965, p. 305.
14. GRYZINSKI, M.: Classical Theory of Atomic Collisions. I. Theory of Inelastic Collisions. Phys. Rev., vol. A138, 1965, p. 336.
15. ENGELKEMEIR, D.: Fission-Fragment Scattering. Phys. Rev., vol. 146, 1966, p. 304.
16. LEFFERT, C. B.; REES, D. B.; AND JAMERSON, F. E.: Noble Gas Plasma Produced by Fission Fragments. J. Appl. Phys., vol. 37, 1966, p. 133.
17. REES, D. B.; LEFFERT, C. B.; AND ROSE, D. J.: Electron Density in Mixed Gas Plasmas Generated by Fission Fragments. J. Appl. Phys., vol. 40, 1969, p. 1884.
18. BENNETT, W. R., JR.: Optical Spectra Excited in High Pressure Noble Gases by Alpha Impact. Ann. Phys., vol. 18, 1962, p. 367.
19. JESSE, W. P.; AND SADAUSKIS, J.: The Range-Energy Curves for Alpha-Particles and Protons. Phys. Rev., vol. 78, 1950, p. 1.
20. BOGAARDT, M.; AND KONDIJS, B.: Sur les potentiels moyers d'excitation et les relations energie-parcours dans les elements legens. Physica, vol. 18, 1952, p. 249.
21. ROSENBLUM, S.: Recherches experimentales sur le passage des rayons a travers la matrere. Ann. Phys. (Paris), vol. 10, 1928, p. 408.
22. KERR, G. D.; HAIRR, L. M.; UNDERWOOD, N.; AND WALTNERS, A. A.: Molecular Stopping Cross Sections of Air, N_2, Kr, CO_2 and CH_4 for Alpha Particles. Health Phys., vol. 12, 1966, pp. 1475–1480.
23. WEYL, P. K.: The Energy Loss of Hydrogen, Helium, Nitrogen, and Neon Ions in Gases. Phys. Rev., vol. 91, 1953, p. 289.
24. NORTHCLIFFE, L. C.: Passage of Heavy Ions Through Matter. In: Annual Review of Nuclear Science, Vol. 13. Annual Reviews, Inc. (Palo Alto, Calif.), 1963, p. 67.
25. MILEY, G. H.: Fission-Fragment Transport Effects as Related to Fission-Electric-Cell Efficiencies. Nucl. Sci. & Eng., vol. 24, 1966, p. 322.
26. FULMER, C. B.: Scintillation Response of CsI (Tl) Crystals to Fission Fragments and Energy versus Range in Various Materials for Light and Heavy Fission Fragments. Phys. Rev., vol. 108, 1957, p. 113.
27. FULMER, C. B.: Density Effect on Energy versus Range of Fission Fragments in Gases. Phys. Rev., vol. 139, 1965, p. B54.
28. MULAS, P. M.; AND AXTMAN, R. C.: Energy Loss of Fission Fragments in Light Materials. Phys. Rev., vol. 146, 1966, p. 296.
29. AXTMAN, R. C.; AND SEARS, J. J.: Excitation of Nitrogen Gas by Alpha Particles and Fission Fragments. J. Chem. Phys., vol. 44, 1966, p. 3279.
30. MOORE, M. S.; AND MILLER, L. G.: Slowing of Fission Fragments in Noble Gases. Phys. Rev., vol. 157, 1967, p. 1049.
31. KAHN, S.; AND FORGUE, V.: Range-Energy Relation and Energy Loss of Fission Fragments in Solids. Phys. Rev., vol. 163, 1967, p. 290.
32. FORGUE, V.; AND KAHN, S.: Determination of Fission Fragment Energies Using Solid-State Detectors. Nucl. Instr. and Methods, vol. 48, 1967, p. 93.
33. ALBRECHT, H.; AND MUENZL, H.: Specific Energy Loss of Heavy Ions in Al, Ag, and Au. E. Phys., vol. 220, 1969, p. 381.
34. LINDHARD, J.; NIELSEN, V.; AND SCHARFF, M.: Approximation Method in Classical Scattering by Screened Coulomb Fields. Mat. Fys. Medd. Dan. Vid. Selsk., vol. 36, no. 10, 1968.
35. LINDHARD, J.; SCHARFF, M.; AND SCHIØTT, H. E.: Range Concepts and Heavy Ion Ranges. Mat. Fys. Medd. Dan. Vid. Selsk., vol. 33, no. 14, 1963.
36. LINDHARD, J.; NIELSEN, V.; SCHARFF, M.; AND THOMSEN, P. V.: Integral Equations Governing Radiation Effects. Mat. Fys. Medd. Dan. Vid. Selsk., vol. 33, no. 10, 1963.
37. CARTER, G.; AND COLLIGON, J. S.: The Penetration in Ions. In: Ion Bombardment of Solids, ch. 5, American Elsevier (New York, N.Y.), 1968.
38. BOHR, N.: The Penetration of Atomic Particles Through Matter. Mat. Fys. Medd. Dan. Vid. Selsk., vol. 18, no. 8, 1948.
39. BRIGGS, G. H.: The Decrease in Velocity of α Particles from Radium C. Proc. Roy. Soc. (London), ser. A, vol. 114, 1927, p. 341.
40. RUTHERFORD, E.: The Capture and Loss of Electrons by α Particles. Phil. Mag., vol. 47, 1924, p. 277.
41. HENDERSON, G. H.: Changes in the Charge of an α-Particle Passing Through Matter. Proc. Roy. Soc. (London), ser. A, vol. 102, 1922, p. 496.
42. HENDERSON, G. H.: The Capture and Loss of Electrons by α-Particles. Proc. Roy. Soc. (London), ser. A, vol. 109, 1923, p. 157.

43. ALLISON, S. K.: Experimental Results on Charge-Changing Collisions of Hydrogen and Helium Atoms and Ions at Kinetic Energies Above 0.2 KeV. Rev. Mod. Phys., vol. 30, 1958, p. 1137.

44. BARNETT, C. F.; AND STIER, P. M.: Charge Exchange Cross Sections for Helium Ions in Gases. Phys. Rev., vol. 109, 1958, p. 385.

45. SNITZER, E.: Charge States of a Helium Beam in Hydrogen, Helium, Air, and Argon. Phys. Rev., vol. 89, 1953, p. 1237.

46. FULMER, C. B.; AND COHEN, B. L.: Equilibrium Charges of Fission Fragments in Gases. Phys. Rev., vol. 109, 1958, p. 94.

47. LASSEN, N. O.: On the Variation Along Range of the $H\rho$-Distribution and the Charge of Fission Fragment of the Light Group. Phys. Rev., vol. 69, 1946, p. 137.

48. LINNERUD, H. J.; CONNOLLY, T. J.; SHER, R.; AND SAFANOV, G.: A Measurement of Average Fission-Fragment Electronic Charge Dependence on Source Thickness. Trans. Am. Nucl. Soc., vol. 10, no. 1, 1967, p. 70.

49. NEUFELD, J.: On the Relationship Between the Charge of Ion and Its Velocity. Health Phys., vol. 1, 1958, p. 315.

50. MOAK, C. D.; LUTZ, H. O.; BRIDWELL, L. B.; NORTHCLIFFE, L. C.; AND DATZ, S.: Evidence of Shell Effects and the Approach to Equilibrium in the Charge-State Distributions for 15-160 MeV ^{79}Br and ^{127}I Ions in Carbon. Phys. Rev. Letters, vol. 18, no. 2, 1967, p. 41.

Enhancement of Laser Output by Nuclear Reactions

F. ALLARIO
NASA Langley Research Center

R. T. SCHNEIDER
University of Florida

R. A. LUCHT AND R. V. HESS
NASA Langley Research Center

The possibility of producing population inversion in gas lasers using the high-energy products of nuclear reactions has been considered by several groups (refs. 1 to 4) with the He-Ne laser primarily considered. In reference 3, the influence of neutron irradiation on a He-Ne laser using the isotope $_2{}^3He$ in the mixture was considered. The isotope $_2{}^3He$ has a large cross section for neutron capture, resulting in the reaction $_2{}^3He(n,p)_1{}^3H$ with 760 keV of kinetic energy available to the reaction products. In reference 4, an experiment which simulates these high-energy products with a high-energy proton beam was reported, and substantial enhancement of laser power was observed in an electric-discharge-excited CO_2 laser using mixtures of CO_2-N_2-He. However, the authors are not aware of any experiments performed with $_2{}^3He$ in a CO_2 laser using electric discharge excitation and neutron irradiation.

A joint research program is in progress between the Plasma Physics and Gas Laser Branch at NASA Langley Research Center and the Department of Nuclear Engineering Sciences of the University of Florida to study the effect of nuclear reaction products (including light and heavy particles and gamma rays) on the population inversion of gas lasers with emphasis on molecular and ionic systems. Preliminary experimental results are presented in this paper on the enhancement of the output power of a CO_2 laser excited by an electric discharge using mixtures of CO_2-N_2-$_2{}^3He$ and irradiated by neutrons obtained from a nuclear reactor. In this preliminary work, the enhancement of power was small, typically less than 10 percent, and is attributed to the low neutron flux available from the reactor. The low neutron flux should result in a considerably smaller proton flux than that simulated in the experiments of reference 4 where more than 100 percent enhancement was observed. However, both experiments show that the use of high-energy particles introduces an additional source of ionization in addition to that due to the electrical discharge and offers a possibility for operation of laser tubes with larger volumes and higher pressures without transition from glow to arc filaments which in some cases limit the available output power of an electric-discharge-excited CO_2 laser.

EXPERIMENTAL APPARATUS

The laser which was used in the experiment is shown in figure 1. The active discharge region was approximately 75 cm long, with a tube diameter of 2.5 cm. The discharge region was cooled by a water jacket. A 20-kV, 100-mA dc power supply was used to excite the discharge. The optical cavity employed a long radius cavity configuration with internal, di-

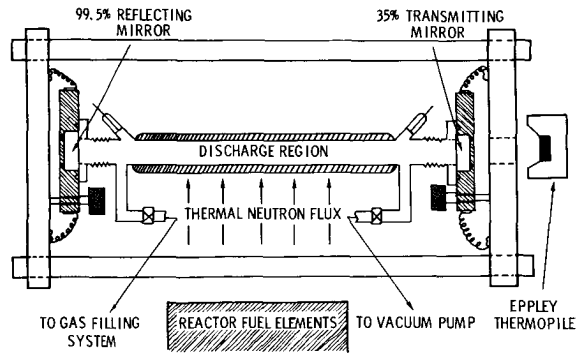

FIGURE 1.—*Static fill CO_2 laser discharge.*

electrically coated Ge mirrors. The mirror radius was 10 m; the totally reflecting mirror was better than 99 percent reflecting and the partially reflecting mirror was 35 percent transmitting. The output of an Eppley thermopile recorded with a Keithley microvoltmeter was used to measure the laser power. Maximum power was obtained with a mixture ratio of 3.5 $_2{}^3$He, 1.5 CO_2, and 1.5 N_2 at a total pressure of 14.1 torr.

To irradiate the discharge region, neutron leakage from an experimental reactor was used with neutron fluxes at the center of the discharge tube not exceeding 10^7 to 10^8 N/cm^2/sec with only half the discharge tube length exposed to any significant neutron irradiation (shown schematically in fig. 1). During the experiment, the laser was operated at power levels below 1 W since small changes in laser power were expected because of the small neutron flux. When the experiment was performed, the system was first made to lase, the neutron flux was raised to its maximum level and then decreased abruptly to an insignificantly small level. Readings on the microvoltmeter were taken before and after the abrupt change in neutron flux.

EXPERIMENTAL RESULTS

Some of the preliminary results obtained are summarized in table I. The laser power is given in microvolts, with 400 μV corresponding to 0.50 W. For some of the measurements, a small amount of H_2 or Xe was added to the mixture to increase the stability of the output power. Typically, fluctuations in output power were less than 1 percent.

Results in the top part of table I were obtained with a small amount of H_2. In this case, a decrease of 5 μV was observed when the neutron flux was turned off in the range of laser power between 135 and 35 μV. This represents a fractional change in power of 4 and 13 percent, respectively, and indicates that the change in power depends upon only the partial pressure of $_2{}^3$He and not upon laser power. No changes in the input electrical power were observed due to the neutron irradiation using this mixture; however, with only $_2{}^3$He in the discharge at the same partial pressure as in the mixture, a 25-percent decrease in current was observed when the neutron flux was turned off while changes in the voltage drop across the tube were less than 20 percent.

In order better to understand the mechanism involved in the observed enhancement, a calculation was performed to determine the neutron flux required to produce threshold laser oscillation using $_2{}^3$He and neutron irradiation. The results indicated that the available neutron flux was several orders of magnitude too small to sustain threshold laser

TABLE I. *Preliminary Experimental Results*

Total pressure, torr	Mixture ratio	CW laser output, μV	
		Neutrons on	Neutrons off
14.1	3.5 $_2{}^3$He 1.5 N_2 1.5 CO_2 1.0 H_2	 135 35	 130 30
14.1	3.5 $_2{}^3$He 1.0 N_2 1.0 CO_2 1.0 Xe	100	97.5

oscillation. Therefore, in this experiment, direct nuclear pumping of the lower vibrational levels of N_2 or the upper laser level of CO_2 seems unlikely. Rather, the power enhancement appears to arise from a tailoring of the electron temperature *Te*, as was discussed in the simulation experiment of reference 4. A lowering of *Te* is beneficial to a CO_2 laser using mixtures of CO_2-N_2-He in an electric discharge since, in these mixtures, *Te* is generally higher than that value corresponding to the maximum in the excitation cross section $Q(\max)$ for the first eight vibrational levels of N_2 (ref. 5); and a lowering of *Te* toward this maximum value (2.3 eV) will increase the excitation cross section of N_2 and thus the preferential pumping of the upper CO_2 laser level (ref. 6). In the lower part of table I the results of a test using a small amount of Xe instead of H_2 are shown which indicate that the effect of neutron irradiation is probably to lower *Te* in the discharge.[1] The Xe is known to increase the efficiency of a static fill CO_2 laser because it brings *Te* closer toward $Q(\max)$ (ref. 7), so that with Xe replacing H_2 in this mixture it is expected that *Te* is nearer $Q(\max)$ without neutron irradiation and the effect of neutron irradiation should be smaller. This, in fact, was observed; in the lower part of table I the change in power was only 2.5 μV even though the partial pressure of $_2{}^3$He was higher in the mixture containing Xe than in that containing H_2.

[1] Research grade Xe was used and the percentage of the isotope ^{135}Xe was sufficiently small so that neutron poisoning by ^{135}Xe is expected to be small.

CONCLUDING REMARKS

Enhancement of laser power using neutron irradiation in a CO_2-N_2-$_2{}^3$He electric-discharge-excited gas mixture has been observed. The observed enhancement, although small in this experiment because of a low neutron flux and limited irradiated volume of the discharge tube, is expected to increase with the larger neutron fluxes available at the University of Florida reactor facilities (10^{13} to 10^{14} N/cm^2/sec). It is believed that the increase in laser power coincided with an increase in ionization and lowering of *Te* in the discharge which leads to enhanced electronic excitation of the lower vibrational levels of N_2, and thus to an increase in preferential pumping of the upper CO_2 laser level. The increased level of ionization and lowering of *Te* suggests that neutron irradiation of a $_2{}^3$He mixture might serve to delay filamentation from a glow to arc discharge in an electric discharge CO_2 laser to higher pressures, thus increasing the available output power from such systems. Future experiments are planned to explore this possibility, using the larger available neutron fluxes in comparatively large volume tubes and at relatively high pressures.

REFERENCES

1. DeShong, J. A., Jr.: Optimum Design of High-Pressure, Large-Diameter, Direct Nuclear-Pumped, Gas Laser. ANL–7030, Argonne Natl. Lab., June 1965.
2. Guyot, J. C., Verdeyn, J. T.; and Miley, G. H.: Experiments Using Nuclear Radiation to Pump a He-Ne Laser. Proc. Fifth Ann. Rev. Electron., Univ. of Ill., Nov. 1967.
3. Herwig, L. O.: Summary of Preliminary Studies Concerning Nuclear Pumping of Gas Laser Systems. Rept. No. C–11053–5, United Aircraft Res. Lab., Feb. 1964.
4. Andriahkin, V. M.; et al.: Increase of CO_2 Laser Power Under the Influence of a Beam of Fast Protons. JETP Letters, vol. 8, no. 7, 1968, pp. 214–216.
5. Carswell, A. I.; and Wood, J. I.: Plasma Properties of a CO_2 Laser Discharge. J. Appl. Phys., vol. 38, no. 7, 1967, pp. 3028–3030.
6. Schulz, G. J.: Vibrational Excitation of Nitrogen by Electron Impact. Phys. Rev., vol. 125, no. 1, 1962, p. 229.
7. Clark, P. O.; and Wada, J. Y.: J. Quantum Electron., vol. QE–4, May 1968, pp. 263–266.

DISCUSSION

Javan: Did you observe change of voltage and current when you switched the reactor on?

Allario: No; when we were operating with the gas mixture we did not observe any change in current, possibly because we had some rather crude voltmeters. However, in another experiment, $_2{}^3$He was put into the tube alone and the discharge was operated at about 2 kV and 20 mA. We saw a change of 5 mA but no change in voltage, which was a little surprising, but again the instruments were not ideal. I suspect that if we look more closely with more sensitive instruments we will probably see a change.

Williams: What was the neutron flux?

Allario: I was told that the flux was probably no more than 10^8 N/cm^2/sec, which is rather low.

Javan: In experiments of this kind (I am completely ignorant of what is involved in experimental layout as far as the reactor is concerned) is it readily possible to run experiments and change the gas pressure? How long does it take, for instance?

Allario: This run took about 2 hr. The experiment and the operator's panel are in different rooms. The laser instrumentation was remotely controlled from a separate room. The laser was alined before the run. This is a static fill system. There must be a really good vacuum system if one is to be able to walk out of the room and 2 hr later turn the discharge on and expect to see a lasing action. Therefore, we do have difficulties.

Javan: It looks as if this is just the beginning of many to come.

Allario: Yes, we foresee many difficulties with these systems.

Javan: There aren't many lasers that you can really manipulate. One has a variety of possibilities; e.g., one can vary the gas pressure. Somehow, the high pressure systems come to mind. There are so many possibilities that you can have a rapid rate of excitation of excited levels at pressures higher than 1 or 2 atm. You would have sufficient gain at many interesting transitions and those might also offer some new possibilities.

Allario: I am excited about this program because it gives us the means of producing the inversion really from the top of the energy level diagram and not from the bottom. Electron excitation starts from the ground state. Here you can envision that all your excitations start from upper levels and trickle down, and, in a sense, that is a completely different mechanism.

Kascak: What is the maximum gain you could obtain from a flux with 10^8 if you had perfect coupling and perfect inversion?

Allario: I haven't made that calculation because it is very difficult to make. The tube is only 1 in. in diameter and the question is, how many collisions go on and what is the coupling? I haven't analyzed this system yet. We decided to look at it experimentally first to see whether it was worthwhile to actually analyze it. The Russians give a good indication of the potential. They obtained an increase in laser power output of a factor of 2 or 3. They had a relatively weak proton beam, 7 μA. We should be able to generate more protons than they did in the Van de Graaff accelerator. Going to higher pressures is also very interesting.

Javan: I haven't seen the Russian work.

Allario: It was a conventional flowing CO_2 discharge. They just put a hole in one of the mirrors and shot the proton beam down along the axis of the laser.

PANEL DISCUSSION

Direction and Needs for Future Research

Chairman: R. E. UHRIG

R. E. Uhrig

The topic of the Panel Discussion is "Direction and Needs for Future Research." The format we shall follow for this discussion is that each of the participants in the panel will spend about 10 minutes giving his own views on the subject. In my letter to the participants I suggested that they might use the following order in their presentation: First, the definition of their own particular field of interest; second, the future needs for basic and applied research; and, third, possible applications for and benefits to be derived from this research. I think the latter item is particularly important today in view of the prevalent atmosphere which promotes the inquiry, "What do we need research for and what is its application?" I hope that our panelists will try to cover this latter general item as well as the need for specific items or specific research.

We shall start with Frank Rom. I am sure all of you know him as Chief of the Advanced Nuclear Concepts Branch of the NASA Lewis Research Center. He is a graduate of Cornell University and has been with NASA and its predecessor, NACA, since 1948. He has worked in all phases and with all kinds of nuclear propulsion for aircraft, rockets, and space since 1950.

Frank E. Rom

My particular field of interest in gas-core reactor work is nuclear rocket propulsion. That does not mean, however, that I have let my mind be channeled into only that particular area. I would like us to discuss other uses for the gas-core reactor in order to determine what can be gained by so doing. I have found that there should probably be more interest in the gas core for other applications than for rocket propulsion.

The gas-core concept that we have been working on at Lewis is shown in figure 1. I would like to review very briefly how it works by referring to this figure. This figure shows a spherical-cavity reactor. In this particular concept we inject propellant through a porous wall that surrounds the cavity. The propellant may be introduced at any particular angle and perhaps causes some swirl. The propellant then flows around the hot fissioning uranium plasma. It is heated by thermal radiation from the plasma; then it passes through the nozzle to produce thrust. The power level of the reactor is determined by the thrust and the specific impulse we desire. In other words, if the gas contains a certain amount of energy and if there is a certain flow of gas to obtain the desired thrust, the power level is determined. This means that the uranium plasma must generate and radiate that required

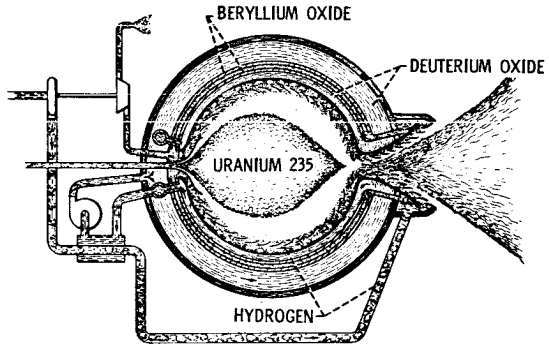

FIGURE 1.—*Concept of gas-core reactor engine.*

amount of energy. In order for the uranium to radiate this amount of energy, its temperature level must come up to whatever level is needed. This is a simple way of undrestanding the gas-core concept.

We do not want the uranium to mix with the hydrogen as the hydrogen flows around the uranium plasma. We have tried to arrange this configuration so that the uranium would tend to remain within the cavity, but we do recognize that there would be mixing between the two streams and some uranium would be lost. In order to compensate for the uranium that is lost, we must inject makeup uranium into the core. I have indicated the insertion of the makeup uranium by means of a solid rod which vaporizes as it enters the high neutron flux within the cavity. The uranium rod is shielded from neutrons as it passes through the reflector-moderator by means of a neutron absorber such as cadmium.

Inasmuch as cold hydrogen is transparent to thermal radiation, it must be rendered opaque in order to prevent excessive heat loads on the wall. The hydrogen is therefore seeded by smokelike particles as it is introduced into the cavity. Enough seeding is used so that the amount of heat that goes into the wall is reduced to about ¼ percent of the energy that is radiated by the uranium plasma. I wish to emphasize that point to show that only a very small fraction of the energy is allowed to get to the wall compared with the amount of energy that is generated.

Before we proceed, I would like to quote Dr. Von Ohain, to whom we described this concept several years ago. He was quite taken with the concept because, he said, "It had to work." Perhaps it would not produce so much power as or it would allow much more uranium to escape than we would like, but it would work. This is the major virtue that we see for this particular concept: If it is built, it would work and be a starting point for solving the real problems of making a useful gas-core reactor engine.

Let me now discuss some other kinds of gas-core reactors that we have envisioned. First of all, for nuclear rocket gas cores we have always attempted to minimize the weight of the system, maximize the flow of hydrogen, and minimize the amount of uranium that escapes. We have chosen hydrogen as the reactor coolant because it is a good propellant, although, actually, any gas could be used as the coolant. Solid material could be introduced into the gases since it would become gaseous at the temperatures of gas cores. This fact should stimulate the imagination of those in the field of physical chemistry to utilize the environment that is produced by the high fissioning rate in the uranium plasma. High photon fluxes, high neutron and gamma fluxes, high electron densities, and high-energy fission fragments are all made available. Perhaps a chemist, recognizing that a gas-core reactor might be possible, could conceive of new processes not possible before. For example, he might fix nitrogen at efficiencies much higher than those presently possible. I am not a chemist, but I am sure there are many reactions which have been considered, but not seriously, or have never been considered because it has not been recognized that they could be produced. The important point is that any element, mixture, or compound can be exposed to heretofore unattainable environments and this may open up whole new fields of interest and applications.

Some of the characteristics that could be obtained in gas-core reactors are given in table I. Temperatures can range from 1000° to 100 000° K, the level depending on the location in the reactor and the desired operating power level. Pressures are in the range of up to 1000 atm. Power levels can be anywhere in the range of 10 to 1 million MW. I do not know whether there is any limit on the upper power level because the cavity could be any diameter (I do not see why there should be any

TABLE I.—*Characteristics of Gas-Core Reactors*

Characteristic	Range
Temperature, °K	1000 to 100 000
Pressure, atm	10 to 1000
Power, MW	10 to 1 000 000
Cavity diam, m	1 to 100
Neutron flux, N/sec/cm^2	10^{14} to 10^{18}
Gamma flux, photons/sec/cm^2	10^{14} to 10^{18}
Energy flux (few eV range), photons/sec/cm^2	10^{22} to 10^{25}
Radiant heat flux, kW/cm^2	1 to 1000
Uranium density, atoms/cm^3	10^{18} to 10^{21}
Electron density, N/cm^3	10^{17} to 10^{22}
Neutron density, N/cm^3	10^{9} to 10^{13}
Fission density, fissions/sec/cm^3	10^{11} to 10^{15}
Fission product energy, MeV	0 to 100

particular limit on the size of the reactor). The reactor could be less than 1 m in diam or it could be 100 m or larger. Neutron fluxes can be in the range of 10^{14} to 10^{18} N/cm^2/sec, the rate depending on the particular configuration and power level, size, or reflector material. Such high neutron fluxes should be of particular interest to people who like to make new elements in quantity. I am referring to transuramic elements, for example, where high neutron fluxes are needed to increase the atomic number of elements that are being irradiated. Gamma flux of the order of 10^{14} to 10^{18} is possible and energy fluxes in the range of 10^{22} to 10^{25} photons/cm^2/sec are available (the energy level would be in the few-eV range). In terms of radiated heat flux, this becomes about 1 to 1000 kW/cm^2. Uranium density in the core is of the order of 10^{18} to 10^{21} atoms/cm^3. Electron density is in about the same range (10^{17} to 10^{22}). There is a high neutron density possible, of the order of 10^9 to 10^{13} N/cm^3. This is far from a continuum but nevertheless it is still a high density, should it be of interest. Fission density is of the order of 10^{11} to 10^{15} fissions/sec/cm^3. The energy of the fission products which varies from over 100 MeV down to thermal energy could be deposited in any atoms that happen to be in the uranium core. I might add that one could introduce any elements, combinations of elements, or any number of them into the uranium core to produce ordinary compounds or entirely new compounds that heretofore were never thought possible.

The purpose of going through this list is to try to indicate to people with all types of backgrounds and fields of interest the environmental conditions possible in gas-core reactors, with the hope that new avenues of thought will be stimulated. New environments most probably will uncover various laws of natural behavior that we do not know exist because we have never before been able to make observations of behavior in them.

Let me digress for a moment to make the following reflection. We tend to be inhibited in our thinking of what can be done with gas-core environments because we don't really believe that a gas core can be built. This automatically puts a bias in our thinking processes so that we do not look ahead or use imagination. I say we scientists in particular must think a little differently. Scientists tend to be proud that they can predict things that will occur, but the problem is that most discoveries are usually not predicted. Even though scientists like to make predictions, it is very rare when a discovery is predicted. I think we should recognize this fact of life and let our minds wander a little, so that we can imagine things and invent theories. We should not be so badly inhibited by what is extrapolated from known observations. We should recognize that most theory is merely a shorthand or symbolic way of stating what we have already observed in nature. Extrapolation of a theory beyond the range of observed data is at best an educated guess and surely does not preclude the discovery of entirely new phenomena in this new range.

I am reminded of the story of Marconi when he invented wireless communication. Maxwell's equations, which related electrical fields to electrical magnetic radiation, were well known at that time. Anybody could determine that electromagnetic waves could be radiated and detected at some other point, but the scientists, with their known facts, said the amount of energy required to radiate a detectable signal at a distance would be enormous because of the inverse square attenuation factor. Furthermore, they said that electromagnetic radiation traveled in straight lines and therefore could not go beyond the horizon even if high power were used to generate the signals. Marconi listened to all of this advice, but it didn't stop him. He proceeded to build his wireless and it was a dramatic success; the thin unknown layers of ionized atmosphere caused the electromagnetic radiation to be reflected. He truly transmitted messages long distances even though the scientists would have been perfectly correct in their pessimism if only the facts they knew were operative. With their known facts they reached correct conclusions; unfortunately, lack of knowledge of some of the facts that had not yet been discovered inhibited the scientists to the point that the wireless would not have been discovered if it had been up to them. The point that I am trying to make is that discoveries do not come by theoretical extrapolation from regions of known observations. They are made by carrying out experiments in the regions where observations have not previously been made.

The idea of carrying out experiments in unknown regions leads to the point that we should start

building a gas-core reactor tomorrow. It should be a much simpler concept than that we are discussing for rocket propulsion so that construction could begin with a minimum of delay. The startup sequence for a particular gas-core reactor, which I call the hole-in-the-ground gas-core reactor, is shown in figure 2. This reactor is basically a big cavity

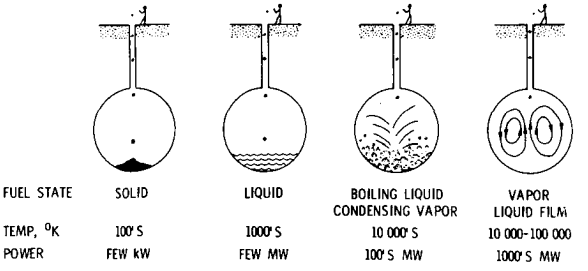

FIGURE 2.—*Hole-in-the-ground gas-core reactor startup sequence.*

that is excavated underground with a shaft extending to the surface. Uranium is dropped down into this hole piece by piece. Only very small pieces of uranium-235 are used. Each piece has a minimal amount of reactivity, so that there is no possible danger of a nuclear excursion. Soon there is sufficient uranium so that the mass becomes critical. It will then start generating power at an increasing rate until its temperature coefficient levels off at the power which will maintain that temperature for which the assembly is just critical. Another small piece is dropped in and the power and temperature levels go up. Soon, as more and more uranium is added, the mass of uranium begins to melt. The reactor can never go prompt critical because there is never enough material introduced at one time to allow this.

The mass eventually becomes liquid. The liquid temperature continues to rise with each piece of uranium added. The power level will increase to maintain that temperature level for which the assembly is just critical as the boiling point is reached or when the vapor pressures start becoming appreciable. The vaporization and subsequent condensation of the fuel on the cavity walls will now be the power leveling mechanism. As still more fuel is added, the rate of vaporization will increase. A great deal of uranium is vaporized and condensed on the wall. Then the walls themselves become a contributor to the reactivity so that the liquid level or amount of uranium in the liquid state at the bottom will be reduced. Soon most of the uranium will be deposited on the walls. There will be a little boiling liquid on the bottom, and the vapors from the boiling liquid will condense on the walls. Now, because there is fissioning occurring in the layer of solid material on the wall, it becomes hotter and hotter. As the process continues and as the power level increases, the inner surface of the uranium deposited on the wall will reach the melting point and begin to run down into the boiling pool at the bottom. This is a kind of refluxing action, and, eventually, as more and more fuel is added and as the power level continues to increase, all of the uranium will be on the wall, in liquid droplets running down the wall and evaporating, or in the form of vapor in the large cavity volume. Finally, at high power levels, there is only a very thin uranium film on the wall and a large fraction of the uranium is in the gaseous state in the cavity volume. This gas probably sets up convection cells where high-temperature vapor rises up in the center. Some gas condenses on the wall and forms runlets or droplets on the wall. These runlets or droplets cannot last very long because they are generating heat internally. This occurs because the local fuel thickness in the wall is greater where the droplets are, so that the droplets evaporate because of the local high-heat generation. As the liquid droplets form, they also evaporate as they flow down toward the bottom. The result is a large gaseous plasma fission uranium reactor. In this discussion I have assumed that all the heat generated is removed by cooling the outer wall of the cavity.

Figure 3 shows the practical application of the foregoing procedure. The obvious thing, as shown in the figure, is to place a spherical containing shell in the hole in the ground and back it up with a coolant such as water. The water then will act as the coolant on the outside of the containment vessel which holds the gaseous uranium. The gaseous and liquid uranium is contained by a "crucible" of chilled uranium metal. Any other fissionable material or compound can be used to form a similar condensed layer on the cold containing vessel walls to act as a crucible for the very high temperature fissioning gas.

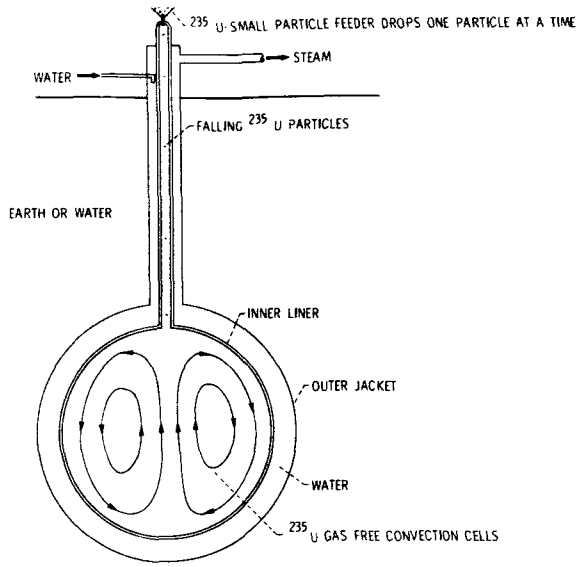

FIGURE 3.—*Hole-in-the-ground gas-core reactor.*

The rate of increase in power level of the reactor is determined by the rate at which fuel is introduced into the cavity. The more fuel the operator puts in, the greater will be the increase in power of the reactor. When he reaches some particular power level such as that limited by the ability to cool the containing vessel, the operator no longer adds fuel except to compensate for the uranium burnup and poisoning and any other effects that occur because of fission product buildup. The operator can run this reactor at any desired power level by adjusting the rate at which he introduces new fuel.

I can see no reason why this reactor would not work. The biggest problem would be in trying to predict in detail what happens in the core, but this should not stop one from building the reactor. Our vanity, which might make us wish to be able to predict exactly what goes on in the cavity, should not inhibit us. The reactor will work according to the laws of nature even if it is too complicated for our understanding and predictions. A good prediction would be nice, but it would be an almost impossible task and very approximate at best. We have been working on the gas core for many years—on the various aspects of heat transfer, fluid mechanics, and neutronics. We have treated these phenomena independently of each other and have only begun to really attack the problem of understanding the effects of their mutual coupling. It is doubtful that we will ever understand more than the idealized effects of these couplings.

Therefore, I say that we could now build this reactor which I believe will work. I further believe that this would be the safest reactor that could be built. It would be as safe as, if not safer than, any reactor that is now running, because of the almost instantaneous vaporization or dispersion of any local high concentration of fuel. For example, if a piece of uranium fell off the wall, it would instantly vaporize because the reactor is operating at such a high neutron flux. Without attachment to the cold wall the piece would have no means for heat absorption or removal except by vaporization. The vaporization would be extremely rapid and therefore prevent nonequilibrium concentrations from causing any reactor instability. The rate of temperature rise of this material would be measured in the order of many millions of degrees per second. A prompt critical arrangement, therefore, could not occur in the reactor. Any material concentrations out of equilibrium would immediately disassemble because of vaporization.

We should build this reactor tomorrow. The successful demonstration of the gas core would then be the biggest impetus we could have to carry out and expand the worthwhile research that is now going on in trying to understand the gas core and finding applications which we have only begun to envision. I think that we should build it so that we can determine the most important problems in using the gas core for more complex applications. We would open a "Pandora's box"; a whole new regime of environments would be available to us. Environments like this have not been produced on Earth, and new discoveries will come from generating and using them. What they are I do not know, but I am sure they are there to be uncovered. The sooner we proceed to build one of these reactors, the sooner we will start to uncover more of Mother Nature's secrets, and the sooner we will be able to benefit from their discovery.

R. E. Uhrig

I am reminded by Frank Rom's comments of a lecture we heard many years ago, about 1950 to be specific, dealing with gaseous diffusion plant operation. The lecturer listed 17 disadvantages on one side of the board and on the other side he put all

the advantages: 1. It works! Well, as a word of encouragement here, the gaseous diffusion plant has been very successful, Frank.

Our next speaker is Dr. John Morfitt, who was educated at Northeastern University and the University of Tennessee. He worked at Oak Ridge in isotope separation and chemical processing development and in the critical mass laboratory. From 1955 to 1969 he was manager of the Nucleonics Development Laboratories of the General Electric Co. in Cincinnati, Ohio; then he became manager of GE's test station on the National Reactor Testing Station. He is presently Assistant General Manager for Research and Engineering, Idaho Nuclear Corp., Idaho Falls. Idaho Nuclear is performing nuclear measurements on a chain-reacting uranium gas. Perhaps you can tell us a bit about that operation, John.

J. W. Morfitt

Thank you. I'll begin by telling you what we are doing now. We are working on Frank Rom's famous cavity reactor. At the moment, we have an aluminum sphere, 4 ft in diam, filled with uranium-235 hexafluoride gas. We have taken this device critical, thus establishing a self-sustained chain reaction in it. The 4-ft tank containing the gas is surrounded, in turn, by an empty 6-ft-diam tank in which there is a 1-ft gap between the walls of the two tanks. Outside that 6-ft-diam tank are 3 ft of D_2O. That configuration has been taken critical with about 8.4 kg of uranium-235, and we are now making the first nuclear measurements in it.

Since I believe the other speakers will take up specific applications, I would like to continue for a few minutes the thought which Frank Rom propounded.

Dr. Robert Brugger of our organization, Idaho Nuclear Corp., makes an interesting analogy. He has said: "Suppose we were meeting here to discuss the development of light and the experiments you could do with it. The first thing we would consider is building the biggest light bulb we could afford. Then we would pump as much power into it as we could without burning out the filament. Next, somebody might have the idea of pulsing this source to reduce the heat load. Next, we would investigate aspects such as reflecting and focusing; then someone would consider monochromatic light so we could divide the source into energy pieces. Finally, with a lot of brain power and hard work, and a large amount of luck, we might stumble across something that would accomplish all of these things simultaneously, and we might name it a laser, or something like that."

If we scan the situation in the nuclear field today, we are already building research reactors as big as we can afford; we are already operating them just below the power levels that keep the filaments, or the fuel elements, from burning out; and we can pulse reactors only under certain conditions. The nearest things we have to focusing are big tanks of moderator called flux traps, and they are good only for "focusing" factors of 2 to 5. Compare that with the factors that Rom put on the board. As for monochromatic neutrons (neutrons of single energy), except in very special cases, we are severely handicapped in both quantity and quality. Now I do not intend to take the position at this time—that will be for the next meeting, not this one—that the cavity reactor is going to do for neutron physics and engineering what the laser did for optics. Nevertheless, I think that we must consider the cavity reactor as a new device that has new properties, new opportunities, and new applications, and not as just another reactor. It is a new kind of reactor. You have heard, or you will hear, of applications in rocketry, in magnetohydrodynamics, and in lasers. You have heard Rom indicate that we may be able to develop a terrestrial source in which we can produce temperatures of 10 000° to 50 000° C in a volume about the size of a walk-in refrigerator. Give scientists that kind of research tool and they will find some very interesting things to do with it. Note that the neutron and gamma fluxes (the number of neutrons crossing a square centimeter per second) are up by 2 to 4 orders of magnitude, factors of 100 to 10 000; this opens a whole new regime. Frank mentioned the irradiation of transuranic elements and elements with very low cross sections. Remember, when we talk about factors of 100, we are talking about carrying out irradiation experiments in a period of 1 month that, with present devices, would take 8 years. So there is a whole new kind of opportunity here.

To return to the fixed-energy neutrons for a moment, I believe that we are not now much better provided with available sources of monochromatic

neutrons, with a few notable exceptions, than we were with light when we had the kerosene lamp for a monochromatic light source. Of course, I cannot prove this mathematically.

In Europe, there are many so-called "hot sources" operating. A beam can be taken from a reactor of thermal neutrons and passed through some heated material such as pyrolytic graphite or beryllium oxide. With luck the source can be operated at 1200° C, and then, hopefully, the neutrons can be warmed up to higher energies. In this country we have no such hot source operating anywhere. Many chemists in this country need hot sources. For example, they can be used to study the vibrational modes of molecules, a technique which has applications in solid-state physics.

The hot neutrons of Europe are not hot enough for many purposes. Ideally in these experiments one would like higher energy neutrons. Then, by use of a small scattering angle there will be minimum momentum transfer to the molecule under study. It becomes possible to use neutrons for nondestructive tests on living tissues of animals, for example.

Even with present technologies if the source were intense enough so that one could afford to throw neutrons away, it would often be possible to choose the energy range desired. And, with temperatures that the cavity reactor could supply, neutrons could be obtained with energies up in the electron volt region, energies which would be comparable with the vibrational energies of, and the binding energies of, complex molecules. To take another example, we are trying to develop a Plowshare program in this country in which we plan to explode nuclear devices in air so as to create big canals or harbors, but we cannot test these devices in the air. That is the dilemma. With neutron beams of the intensity that a cavity reactor provides, we could take small samples to destruction. By blasting such a small sample with a beam of this high power we would learn a great deal about the design, behavior, and consequences of the proposed test, not only in terms of performance, but in terms of its effect on the environment. High-energy, high-flux gamma sources are used now in weapons and Plowshare development, but available neutron sources have too low a flux to take the uranium to destruction.

As a matter of fact, when Frank Rom and I were talking last night, it occurred to us that, even though the subject of weapons development is highly classified, there may be some peripheral observations that are not classified. Several people have said, "If only we had some plasma." Well, there is some fine plasma in the bomb burst or in its corona. I am sure that all kinds of spectroscopes have been turned on it. Undoubtedly all kinds of spectral measurements and energy line determinations have been made and the recombination of various lines have been very carefully studied. Some of that information obtained as a byproduct could indeed be unclassified and therefore obtainable. I think we ought to investigate if any unclassified data from the weapons field could help us develop the cavity reactor concept.

When Frank Rom mentioned the story about Marconi, I thought of Faraday. Faraday (in about 1830) was the first man I know of to try to obtain money from a government for research and development. A scientific group was sent from the Royal Society to see him, along with some members of the Office of the Exchequer. They asked, "What is your experiment good for, Dr. Faraday?" And he answered, "I'm not quite sure, but I'm sure of one thing. Fifty years from now you gentlemen will put a tax on it." It turned out that he was right.

The moral of this story is that we have in the cavity reactor a source of heat, a source of gamma rays, a source of X-rays, and a source of neutrons, but when we finally have a source of money for the Internal Revenue Service, we will truly be successful.

R. E. Uhrig

Our next speaker is Carl Schwenk of the Space Nuclear Propulsion Office, which is jointly operated by the Atomic Energy Commission and NASA. Carl was educated at Pennsylvania State and the University of Illinois. He was at the NASA Lewis Research Center from 1951 to 1959, moved to NASA Headquarters in 1959, and has been with SNPO since 1960. He is presently an assistant manager with the responsibility for vehicles and technology.

F. C. Schwenk

We in the Space Nuclear Propulsion Office (SNPO) have considered applications of uranium plasma only insofar as they relate to propulsion

systems in space. Also, as most of you who have been associated with me know, we have done very few mission analysis or application studies of the gas-core-reactor propulsion systems such as Frank Rom and the United Aircraft Research Center people have described. We have more or less accepted as an article of faith the belief that if we could achieve an engine that had a specific impulse of 1500 sec or more with a thrust-to-weight ratio of 1 or more we would have an extremely useful propulsion system for some vague distant future time. Associated with this belief were some vague notions of interplanetary travel.

Our support for the research that was prompted by these vague notions has been surprisingly steadfast. I believe that we can look back over the last 9 years or so and see that, in general, we have maintained a fairly constant support of research in this activity. Actually, however, our total budget for the development of nuclear propulsion, which includes the solid-core-reactor technology and the NERVA engine as well, has decreased somewhat in the last several years. It is interesting, at least to me, that the people for whom I work have generally viewed this area of technology as being one that should receive support. They have not been overly generous, but at least their support has been steadfast and has been based on the belief that ultimately something will result from research of this nature which is stimulated by the drive for work at very high temperatures, very high pressures, high neutron fluxes, and so on.

The fact that we may not be any closer to the development of a workable propulsion system after these many years is not particularly discouraging to me. I think that we are learning much and shall learn more as we continue working in this area. One of the reasons for this is that our programs have always attempted to emphasize the fundamentals; we have tried not to be trapped into gadgetry, into thinking piecemeal of large-scale hardware programs before we are ready to do so. In speaking to one of the points that Dr. Uhrig mentioned in his letter, we would like to continue work toward understanding the basic phenomena as they apply to uranium plasma so that we will be better able to predict pressure-temperature relationships, critical masses, and stability. I am speaking primarily in the sense of applications in the propulsion area.

The Space Task Group, which was established by President Nixon, recognized that economy of spaceflight was essential; otherwise, the future of man's exploration of space would be very, very limited. This emphasis on economy has now made us think for the first time in practical ways about reusable systems for space. There is a corollary to that: The importance of a fission propulsion system becomes underlined and we need to continue pursuing our programs to obtain better and better propulsion systems which will give us the economy that we need in order to make spaceflight attractive. We must forget the era in which we threw space systems away and go into an era in which we can discuss space systems which can operate as airliners are operated for transportation on Earth.

Several items become important in reusable systems. At one time we worried quite a bit about initial cost, but I think that with reusable systems the investment cost is less important if we can consider systems that have many, many hours of usability in a space environment. I am introducing these points to stimulate thought about new kinds of applications for advanced propulsion systems such as gas-core reactors. It is time we did so, because it might put us into another framework of operating environments and would better guide our research.

As to applications other than spaceflight, it would seem clear that the development of a gas-core reactor for a ground-based powerplant should be significantly easier than the development of one that would be useful for spaceflight because many of the size, weight, and volume restrictions for spaceflight could be removed. If a gas-core reactor can provide a great increase in the efficiency of our power-producing systems, this in itself should be considered as we think of the long-term future. I recently heard a commentator say that by the year 2000 our population growth would be such that in the few years between now and then the United States must produce as many new jobs and housing units as we have produced in the previous few hundred years of our existence. Of course, as we all know, that implies a tremendous increase in power requirements. The concerns over the building of a powerplant on the shores of the Chesapeake Bay indicate a great worry about thermal pollution, which will increase as power demands increase. The only way we can solve that problem with heat

engines is to attain higher efficiency. If this is possible with the gas-core reactor, it certainly would be a strong reason for pursuing research in this area to provide highly efficient ground-based power stations.

There are some other factors that might be interesting in connection with a ground-based powerplant based on a gas-core reactor. One is that there would be no worry about a limitation of fuel element lifetime. The lifetime of the system would be restricted by factors other than the metallurgy of the fuel. There would be continuous removal of fission products from the system, and this certainly would be attractive to those who analyze safety of systems. In the long term, the maintainability of such systems might be considerably easier than that of a system which contains all the fission products within it; that is, a system which could discharge the greatest source of radioactivity from itself could be worked on and repaired. This also has some advantages.

R. E. Uhrig

Our next speaker is George McLafferty. I am sure that all of you are aware of his involvement with the gaseous nuclear rocket program, specifically the light bulb concept at the United Aircraft Research Laboratories. George was educated at the Massachusetts Institute of Technology at both the undergraduate and graduate levels. He initially worked in the area of supersonic and hypersonic inlets in the aerodynamics area; then he entered the gaseous-core reactor field and has been there for about the last 10 years.

G. H. McLafferty

The future problems that we should attack in this business are those which we see as limiting the performance of one or another advanced engine concept. If we of the United Aircraft Corp. have done our job in the last few days, we should have reiterated a number of times the problem areas that are associated with the nuclear light bulb engine. I hope we have done that, even though we have not formally categorized the problems up to this point; this is what I would like to do now.

I shall divide the nuclear light bulb problem areas into three categories. The first category includes the problems which, if we cannot solve them, "kill" the nuclear light-bulb concept entirely, so that it will not work in any remotely attractive fashion. The second category deals with technical areas which have a major influence on the final engineering of the light bulb engine but which do not basically influence its feasibility. These problem areas may require that many millions of dollars of engineering effort be devoted to their solution, but they do not basically influence whether the device will work. The third category involves problems of the philosophical type that we would like to know more about, but which are not of vital interest in the mechanics of the engine. Such philosophical problems are in the province of the universities, and we in industry, with our need for directing our effort toward a specific objective, must avoid them at this time. I shall now delineate each part of our light bulb engine concept and fit each problem into one or another of these categories.

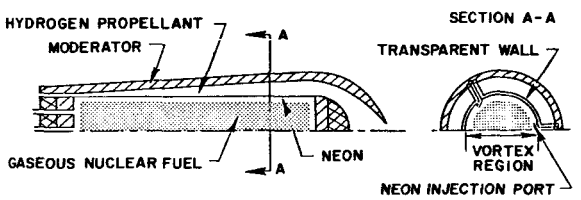

FIGURE 4.—*Nuclear light bulb unit cavity.*

Using figure 4, I will start from the centerline and work outward. As you know, we envision that the gaseous nuclear fuel near the centerline will be at a very high temperature; hence we are concerned with the fuel ionization potentials and the fuel spectral absorption coefficients at these high temperatures. However, at this point in time, such worries are problems in the third category, because there are so many photon mean free paths between the centerline and the edge of the fuel that the situation at the centerline does not influence the output spectrum. Also, changing the average fuel opacity near the centerline by a factor of 2 has only a very small influence on the centerline temperature.

As we go outward through the fuel region, we reach the edge of the fuel, where the temperatures

are between 10 000° and 25 000° R. Under these conditions the characteristics of the fuel greatly influence the radiant energy spectrum emitted from the fuel region. As Nick Krascella has demonstrated, this influence is very important. It appears that the fuel near the edge of the fuel cloud is so transparent in the ultraviolet that we can "see" a long way into the fuel; this means that a large amount of the ultraviolet energy is emitted in this portion of the spectrum, thereby forcing us to put some kind of a seed in the fuel or buffer regions. Therefore, unless it can be shown that there is much more opacity in the fuel in the ultraviolet than we now believe to be present, seeds will be necessary. Furthermore, the details of the fuel opacity spectrum will not be important in either the ultraviolet or the visible range (i.e., both are philosophical problems). They are the kinds of problems which should be studied but are not the kind that will influence the feasibility of the engine. However, the seed that must be added near the edge of the fuel region to control the energy spectrum is obviously a problem in the first category. We must learn to control the radiant energy spectrum coming out of the fuel in order to make this engine work.

Going further out from the centerline, we envision a neon region between the edge of the fuel and the internally cooled transparent wall. We must keep the concentration of fuel near the wall extremely low to prevent the fuel from condensing on the wall. In all of our vortex tests, we encounter turbulence just inside the wall because the flow in this region is basically unstable, since the gradient in angular momentum in this region violates the Rayleigh and Taylor-Goertler criteria for flow stability. However, in much of our vortex flow work, we find that this turbulence is limited to a small region near the wall and that we observe very laminar flow near the edge of the fuel-containment region, either because of stabilizing radial gradients in density or circulation. Our work in this technical area must lead to as large a region as possible of low-turbulence, essentially laminar flow in order to keep the nuclear fuel from diffusing radially outward. This is a problem in the first category.

Going further outward, we encounter a transparent wall. One of the problems associated with the wall is the development of fabrication techniques for providing assemblies of thin-wall tubes. James Clark has shown pictures of transparent-wall structures with 0.005-in.-thick walls. We have learned to build these structures in model scale. Although we have not yet built them in the size that will be required for the full-scale engine, we are sure that it can be done. Therefore, we shall designate transparent-wall fabrication as a problem in the second category; much work will be involved, but there is nothing that cannot be solved by the application of a concerted engineering effort.

Another problem is the transmission characteristics of the transparent wall. Although we have not discussed it much during this conference, nuclear radiation causes the transparent wall to "color" in a manner which is characterized primarily by an absorption band centered at a wavelength of approximately 0.21 μ. This color can be annealed by operating the transparent wall at a relatively high temperature, or it can be bleached by photons. It appears from our present knowledge that this radiation-induced absorption will cause us to reduce the thickness of the wall so that the wall can be cooled, but it will not interfere with the feasibility of the concept. Therefore, we also put radiation damage to fused silica walls under the second category.

We also periodically propose substituting beryllium oxide for fused silica as a transparent-wall material. Beryllium oxide has two advantages: First, the ultraviolet "cutoff" wavelength is down around 0.11 μ and, second, it has a very high thermal conductivity. However, we have never been able to acquire a sufficiently pure specimen of single-crystal BeO to be able to make accurate measurements of its transmission characteristics. At the present time we consider the development of BeO to be a problem in the third category. However, if we should encounter difficulties in blocking the ultraviolet thermal radiation by the introduction of seeds, then BeO will become a problem in the first category. This might be an excellent technical area in which university people could work, that is, the development of high-quality, single-crystal, BeO to be used in the nuclear light bulb engine.

As we go farther outward, we encounter the propellant region. As John Klein has discussed, we must keep the seed particles off the wall to prevent wall overheating. To do this we must minimize the turbulence in the stream that tends to diffuse the particles to the wall. We believe that control of pro-

pellant stream turbulence is a problem of the first category. As a result, we are interested in the fluid mechanics work that is being carried out on the coaxial-flow reactor, since we employ coaxial streams of seeded and unseeded propellant gas. However, we tend to be interested more in nearly equal stream velocities, which tend to minimize turbulence, than in the large velocity differences required in the coaxial-flow reactor. We also must employ deagglomerated particles; this requires shear and turbulence upstream of the entrance to the propellant region. This turbulence must die out before the flow enters the cavity, and this leads to the requirement for screens at the cavity entrance. Control of the relative stream turbulence in the propellant stream upstream and downstream of the cavity entrance is a problem in the first category.

If we now follow the propellant flow in a downstream direction, we reach the exhaust nozzle. We have performed many calculations on the design of the transparent cooling system for the nozzle. According to these calculations, the flow required to keep the nozzle cool is about 12 percent of the main flow, which results in approximately a 6-percent loss in specific impulse. Such a loss is certainly acceptable; therefore, we call this a problem of the second category.

In addition, there are an entire series of other problems that deal with the pressure shell, the pressure control system, the turbopumps, the fuel recycle system, etc. Right now, we consider all these problems to be in the second category. The studies we have carried out so far indicate that we can solve these problems, but we are not so confident in that statement that we are avoiding these problems completely. We are working on them, as you heard from Richard Rodgers, and we are trying to discover whether any parts of these problems will fall into the first category.

Where are we in solving these problems, particularly those in the first category? We believe that now we have the tools available from the work that has been supported by SNPO to provide the answers. We think that in a period of 1 to 3 years we shall have investigated all of these problems and shown either that the light bulb is feasible or, unhappily, that it does not work. If it does not work, there are two possible directions in which to go: Either we can quit or we can look for some other concept that will avoid the otherwise unsolvable problems that are encountered. However, we believe that a positive attitude is desirable, and we are working on the basis that we are going to make the nuclear light bulb work. Therefore, let us continue the discussion as if that has happened.

Suppose that 2 years from now we have investigated all of the problems in the first category and have solutions to them that appear to work and will satisfy reasonably skeptical people. (I am sure we shall never satisfy everybody.) What shall we do then? We believe that we should then install a nuclear light bulb model in a nuclear reactor and conduct a test very similar to the rf heated tests that are now being conducted. In such a nuclear test, the driving neutrons would be provided by a solid-core reactor, such as NERVA or PEWEE. After successful completion of such a test, the way would be open to test a complete engine.

Figure 5 shows the reference nuclear light bulb

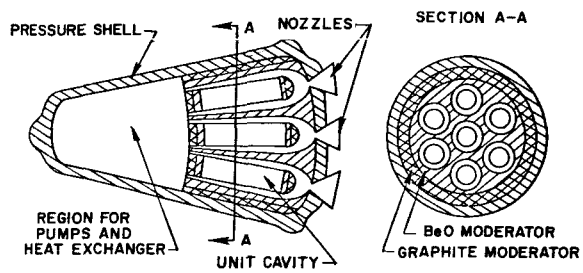

FIGURE 5.—*Nuclear light bulb engine.*

engine. This engine would have a weight of about 70 000 lb and a thrust of about 90 000 lb and would produce a specific impulse of about 1800 sec at a power level of 4600 MW. Such an engine would be a very interesting device for space travel. It would have some of the characteristics of other possible gaseous nuclear rockets, in that it would have a very high specific impulse and the fission products could be thrown away at the end of each operating period (i.e., the engine would be reusable, which is very important). The nuclear light bulb engine also has the potential of providing perfect containment of the gaseous nuclear fuel and appears to be somewhat smaller than some other concepts. The ability to provide near-perfect fuel containment will become more important with the passage of time,

particularly with the advent of the space shuttle which NASA is now planning to develop. Such a shuttle would place payloads in orbit at a relatively low cost per pound; therefore, the cost savings due to a large decrease in required initial weight in Earth orbit resulting from the use of advanced nuclear rockets will be much less than if the payloads were placed in orbit by using Saturn V launch vehicles. Because of this, we cannot afford to lose much nuclear fuel and still have an economically attractive system. However, even with less-than-perfect containment, gas-core nuclear rockets will be very advantageous for use in ambitious missions with velocity increments which are higher than those that can be provided economically by chemical or solid-core nuclear rockets. In addition, it is also very desirable for the gas-core rocket to be good enough to compete with these other systems in the space between the Earth and the Moon, where the velocity increments are not so great that gas-core rockets are necessary, but where the economic advantages obtainable from a high-performance gas-core rocket will be substantial for many mission situations. For this reason, we should aim for a very good gas-core rocket.

In summary, we have the faith that we can make a nuclear light bulb work, but this faith is tempered with an appreciation of the magnitude of the problems to be overcome. We also have a logical program that can progress to the point where we can prove that it will or will not work. Finally, the nuclear light bulb engine has the performance potential to make it a very attractive device for use in the Nation's future space explorations.

R. E. Uhrig

Our next panelist is Jack Kerrebrock, who is currently professor of aeronautics and astronautics at Massachusetts Institute of Technology and Director of the Space Propulsion and Gas Turbine Laboratories. His undergraduate work was taken at Oregon State and his graduate work at Yale and California Institute of Technology. He was at the Oak Ridge National Laboratory from 1956 to 1958 working on gaseous nuclear rockets; from 1958 to 1960 he was at CalTech; and he has been at MIT since 1960.

Jack Kerrebrock

My interest in gaseous reactors is centered around space propulsion (i.e., gaseous nuclear rockets), although I have a parallel interest in MHD power generation which leads me to be concerned also with some of the gaseous reactor generator coupling schemes that have been proposed.

I would like to review the gaseous nuclear rocket field over the years and then, on that basis, to try to make some suggestions as to what we should do, that is, what the critical research topics are. We began intensive work on gaseous nuclear rockets around 1957 with studies of vortex containment, diffusion-type nuclear rockets in which uranium and hydrogen were intimately mixed and the uranium was contained in the reactor by a centripetal force field which resulted from swirling flow inside a tube. This concept was one that involved near-thermal equilibrium between the uranium and the hydrogen everywhere in the reactor. It was recognized very early that the critical question in this type of reactor was whether one could realize this containment mechanism by fluid mechanical means. This was researched very intensively by people at Oak Ridge, Aerospace Corp., United Aircraft Corp., JPL, and elsewhere. The conclusion was that it will not work. The reason for this conclusion is clear; it is that you cannot make a high enough tangential velocity by injecting fluid tangentially into a vortex tube to centrifuge out the uranium. So for the moment this concept has been abandoned.

A parallel effort on a different concept was begun at Lewis Research Center and other places. This involves separating the uranium and the propellant into two distinct regions and transferring the energy from the uranium to the propellant by radiant transfer. This concept minimizes the problem of containment. It makes the containment much less critical because it does not require mixing between the fuel region and the propellant region. On the other hand, it introduces an entirely new feature, which is the radiant energy transfer from the region of extremely high temperature to one of lower temperature at unprecedentedly high flux rates.

It is my opinion that this is the critical problem for the gaseous nuclear rocket concepts presently under study, that is, the problem of radiant transfer

between the fuel region and the propellant region. It is further my opinion that the critical experiment has yet to be performed which will demonstrate the feasibility of these systems. My reasons for this are the following. First, there is a general trend in all types of high-power, high-performance energy conversion system such as this that, as you deviate further and further from equilibrium, the system becomes less practical. It becomes less predictable, more subject to instabilities, and, in general, much more difficult to realize. As an extreme example of this, consider fusion reactors, which must operate about as far from equilibrium as is imaginable.

To be more specific, two problems worry me. One is that of limiting the energy flux to the walls to a tiny fraction of the energy which is radiated from the core. Frank Rom quoted a wall energy flux which is ¼ percent of the total energy which leaves the core. I think that George McLafferty is not quite so optimistic, but, on the other hand, in his rf heated experiment one-fourth of the energy from the plasma goes into the walls. It is quite possible that one can design systems that will, in principle, control the energy transfer from the hot plasma to the walls of the reactor, but there are mechanisms which can disrupt this enterprise, such as instabilities, turbulence, and various other factors which are very difficult to take account of now; in fact, one cannot really resolve these difficulties until one has performed a critical feasibility experiment.

The second problem that worries me about this energy transfer mechanism is the possibility of a fundamental instability in the energy transfer process itself between the hot gas and the propellant. An example of the kind of thing that can happen was presented by Dr. Monsler in a paper earlier in this symposium. This calculation, which is an idealized one, certainly does not show that the nuclear light bulb engine or any other gaseous nuclear rocket will be unstable. It does quantitatively examine a mechanism which leads to an instability and which one cannot be sure will not exist in a nuclear reactor of this type. I think that more investigation is needed in this general area of instabilities because this is a completely uncharted region of energy transfer and we cannot be sure that these systems will behave as well and as systematically as predicted from relatively simple theories.

In the final analysis, we need a series of critical experiments on this particular energy transfer mechanism in which the real energy transfer rates and the real plasma properties are simulated, so that we can answer the question of whether, in fact, some type of bulk instability does arise.

I do not know how to do this experiment; if I did, I would do it. But I suggest that we should examine shock-tube techniques, which have proven to be so valuable for other purposes in that they permit a simulation of very high-power, high-temperature experiments on a short time scale which would not be possible with a reasonable budget on a steady-state basis.

Finally, in regard to the gaseous nuclear reactor, MHD concept, I would like to register enthusiasm, because I think that this is potentially a very useful and viable scheme. However, I would like to make the following statement. At the present time the limitation on nuclear MHD power-generation schemes is really in fission fragment containment. If one relaxes the requirement that fission fragments be retained in the reactor, then solid-core nuclear reactors are capable of attaining such high temperatures that the performance of a solid-core nuclear reactor coupled to an MHD generator is very attractive. Gaseous nuclear reactor MHD enthusiasts must be aware of this competition.

R. E. Uhrig

Our next participant in the discussion is Dr. Richard Schneider with whom, I am sure, you are all familiar. Dr. Schneider was educated at the University of Stuttgart at both the undergraduate and graduate levels. He was a staff member of the University of Stuttgart following graduation and in the early 1960's came to the United States with the Allison Division of General Motors. In 1964 he came to the University of Florida and has been a member of the faculty of the Nuclear Engineering Sciences Department since that time.

R. T. Schneider

I am a spectroscopist and my interest is diagnostics of plasmas. A spectroscopist needs a light source; uranium plasmas are a new type of light

source—a nuclear light source. This very fact is extremely exciting for each spectroscopist.

First, I would like to discuss the feelings of a physicist confronted with this new field of uranium plasmas. Ordinarily one is accustomed to talk about temperatures in the electron-volt region, and now suddenly there is a plasma having particles of a hundred million eV interacting with the plasma. Obviously a whole host of new problems will appear which are very much worth investigating and which should be very challenging to any scientist.

Now, how would an engineer feel as he looks at this new field? Engineers are looking for power density. If one looks at the development of civilization, one finds that it was a straight function of the power density people could make. Now the power density of a uranium plasma, nuclear energy, is in the true sense, as other speakers have already pointed out, astronomical. And therefore the rewards for an engineer working in this field will sooner or later (maybe a hundred years from now, maybe sooner) be astronomical as well.

I believe that is really all that needs to be said; how the final application will look, we cannot now say. The potential is there; nuclear energy is here and we have only to learn how to harness it. As soon as it is admitted that a fuel can be in the plasma state power density will be limited only by one's ability to harness it.

Look at the fine papers presented at this conference and the excellent people attending it, and look at the panel members. They all felt it was worth their while to come here. That in itself will entice other people to look into this subject.

Nuclear energy is here to stay and uranium plasmas are part of it and will be exploited in the near or distant future in one form or another.

ADDENDUM

Comments on the Colloid-Core Reactor

W. JACKOMIS AND H. VON OHAIN

Aerospace Research Laboratories

The following comments are intended to serve as an addendum to the panel discussion of the Symposium on Research on Uranium Plasmas and Their Technological Applications held at the University of Florida in January 1970. Since the panel discussion provided a comprehensive review of the many scientific aspects of uranium plasmas and their potential applications to reactor power and propulsion systems, it is felt that comments relating to the current status of the colloidal-core nuclear reactor rocket engine (CCNRRE) investigations are of interest. These comments seem appropriate, particularly in view of the fact that the CCNRRE concept is considered by many to be a possible steppingstone to future plasma reactors. (See refs. 1, 2, and 3.)

As indicated in references 4, 5, and 6, and the paper by Tang, Stefanko, and Dickson on page 29, the CCNRRE operates at temperatures below plasma-state conditions. Furthermore, the CCNRRE concept is a hybrid concept, combining many of the best features of both the solid-core reactor (NERVA) and the gaseous-core reactor. As with the gaseous-core reactor, isolation of fuel from the cavity walls allows high operating temperatures, in the range from about 3400° to 5000° K, with correspondingly high specific impulse (I_{sp}) values ($\approx$ 1000 to 1500 sec). At the same time, most of the extremely difficult fuel confinement problems associated with the gaseous-core reactor are circumvented by the use of colloid-size nuclear fuel particles. The CCNRRE concept possesses the inherent advantage of covering a broad range of cavity reactor types capable of using solid colloids, liquid colloids (refs. 7 and 8), or a hybrid gaseous-liquid mixture. The latter implies a uranium vapor-condensation cycle. In the liquid colloid type, fissioning submicroscopic droplets are suspended in the propellant gas within the cavity. The solid colloid type is basically a special type of dust-core reactor without, however, employing rotating drums.

In principle, the CCNRRE concept is similar to the Kerrebrock reactor concept (ref. 9) but offers two potential advantages. These are: (1) Fuel containment of particles by inertial separation and (2) the achievement of criticality in a small reactor cavity through high fuel particle concentrations. These advantages are possible because the CCNRRE concept uses solid or liquid colloids as a fissioning substance rather than a fissioning vapor as employed in the Kerrebrock reactor.

In order to achieve the maximum performance potential of the CCNRRE, a number of aeromechanical conditions must be fulfilled. These are:

(1) Obtain a cavity in which the ratio of fissionable mass to the mass of the propellant gas is of the order of 100:1. This ratio is required to achieve criticality in a cavity less than about 1 m in diam.

(2) Demonstrate effective inertial separation of fuel particles from the propellant gas. The fuel loss rate must be maintained below about 1 part per million of the propellant mass flow.

(3) Prevent local overheating, excessive erosion, and damaging particle-wall interactions in the cavity. These can be prevented by avoiding the deposition of fuel particles or surface condensation of uranium vapor at the cavity walls.

(4) Prevent formation of overheated gas zones

in the cavity which could result in the decomposition of fuel particles. This decomposition can be prevented by regenerative and film cooling techniques, i.e., by injecting almost the entire mass of the propellant gas into the cavity and through the fissioning cloud to serve as a coolant.

Engineering attempts to satisfy each of these conditions are exemplified by recalling the well-known dust-core reactor concept. This concept proposes to use a rotating drum inside the cavity reactor (ref. 10). However, many of the engineering problems associated with rotating machine elements inside the reactor cavity may be difficult to solve.

Recent research efforts at the Aerospace Research Laboratories (ARL) have shown that the aeromechanic conditions specified for the CCNRRE can be fulfilled without resorting to rotating machine elements. Investigations with multicomponent flows having extremely high particle concentrations have resulted in the development of unique techniques which admit the propellant gas at the periphery of the cavity and at the side walls. This technique minimizes particle-wall interactions and gives rise to an internal reversed meridian flow pattern. It should be noted that in using these techniques it becomes necessary to depart from conventional designs of cylindrical cavity configurations.

Essentially, three significant design characteristics of the new cavity configuration must be controlled. First, the ratio of cavity diameter to axial length at the periphery must be relatively large, e.g., of the order of about 3 to 1. Secondly, the following ratios must be large: (1) Cavity length at axis of symmetry to exhaust thrust diameter, and (2) outer cavity diameter to exhaust throat diameter. Lastly, the configuration of the cavity side walls must be made compatible with the meridian flow pattern. This is an important feature because the fuel particles must be prevented from depositing on the side walls. With cavities designed in this manner, a number of aeromechanical characteristics have already been demonstrated. These are:

(1) The effectiveness of secondary flow control by sidewall injection and the minimization of particle loss through boundary layers (ref. 11).

(2) Inertial separation and containment of submicroscopic particles, including particles of the order of 0.25 μ (ref. 11).

(3) Extremely high particle concentrations in the carrier gas without particle deposition at the cavity walls. The ratio of the particle mass to the mass of the carrier gas is of the order of 100 to 1. A detailed ARL report of this work is currently being prepared.

(4) Gas admission that allows most of the propellant gas to pass through the particle cloud and also to form a cooling film over the cavity surface. A detailed ARL report of this work is also currently in preparation.

As a result of these efforts, ARL's future research program is aimed at demonstrating feasibility of the CCNRRE concept. This effort will include the following studies:

(1) Fuel colloid materials, colloid size, and aeromechanical simulation techniques. It should be noted that the amount of erosion occurring in the cavity decreases with a decrease in particle size. Furthermore, it should be noted that with small particles the fission product attenuation in the propellant gas increases.

(2) Multicomponent flows having extremely high particle concentrations in strong inertial fields. These efforts will include investigations on particle-wall interaction phenomena associated with those factors which influence the transfer of momentum, energy, and heat; erosion; and flow instabilities at the interface between the particle laden gas and the pure gas in the inertial fields. In addition, studies relating to the phenomena of particle heat release will be undertaken.

(3) Diagnostics and special instrumentation for multicomponent flows having extremely high concentrations of particles.

Concurrent with ARL's in-house aeromechanical studies, the Astronuclear Division of Westinghouse conducted studies relating to the nucleonics feasibility of the CCNRRE concept. A report of their studies is listed as reference 12. Their efforts included studies on materials, fuel loading requirements for reactor criticality as a function of the geometric parameters of the cavity, reactor testing requirements, and a conceptual reactor design. For the latter, consideration is given to the use of additional solid fuel elements within the moderator.

Both ARL and Westinghouse have come to a number of significant conclusions with regard to the CCNRRE concept. These may be summarized as follows:

(1) By solving the complex aeromechanics problems of multicomponent flows having extremely high particle concentrations, several significant payoffs for advancing cavity reactor technology are possible. These payoffs lend themselves to the development of reactors having high specific impulse, simplicity, reliability, and long endurance. Furthermore, the reactor would have no rotating elements and would operate with moderate wall temperatures. The reactor would be compact and have thrust-to-weight ratios of the order of 5 to 1, even for thrust levels as low as 20 000 lb. The combined effects of low fuel loss rate, high specific impulse, high thrust-to-weight ratio, and low thrust values result in a drastic reduction of the cost of space operations. Because of these potential performance characteristics, the CCNRRE concept appears to be uniquely suited to cislunar space missions where fast orbital plane changes (up to 45°) and high incremental velocities are required.

(2) Testing of the colloidal core reactor is possible with existing facilities. Fundamental reactor investigations can be conducted with low pressure levels in simple structures by substituting a gas of higher molecular weight, such as nitrogen, for the hydrogen used as the propellant gas. Furthermore, the working medium need not be heated prior to starting the reactor. Hence, without difficult or costly preheating techniques, the reactor can be operated at low power levels.[1] This would enable investigations of fuel loading requirements and fuel particle distributions to be conducted under actual flow conditions. In addition, characteristics such as starting, control, stability phenomena, and the effects of colloid heat release could be determined.

On the basis of the results of their recent study, investigators at Westinghouse concluded that the solid colloid cavity reactor is nearest to feasibility and is a most logical follow-on to the NERVA reactor. In addition to the advantages already mentioned, this concept offers a potential specific impulse increase of over 20 percent of that which solid-core reactors are able to achieve. These combined features make the CCNRRE concept very attractive for cislunar space operations. Furthermore, the liquid colloid core and the condensation cycle reactor represent important growth potentials for future reactor development.

[1] Private communication with Dr. R. Ragsdale, NASA Lewis Research Center, dated January 8, 1970.

REFERENCES

1. ROM, F.: Comments on the Feasibility of Developing Gas Core Nuclear Reactors. NASA TM X-52644, 1969.
2. RAGSDALE, R.: Relationships between Engine Parameters and Fuel Mass Containment in an Open Cycle Gas Core Reactor. NASA TM X-52733, 1969.
3. MCLAFFERTY, G.: Investigation of Gaseous Nuclear Technology. United Aircraft Res. Lab. (NASA Contract H910093-46), Nov. 1969.
4. KELLER, R.; AND VON OHAIN, H.: Research Relevant to Gas Core Reactor. Rept. 64-189, Aerospace Res. Lab., Aug. 1964. (Classified paper.)
5. POPLAWSKY, R.; AND PINCHACK, A.: Aerodynamics Performance of Reversed Flow Vortex Chambers. Rept. 65-219, Aerospace Res. Lab., Oct. 1965.
6. KELLER, M.: A Colloid Core Reactor Concept. 4th Symp. on Advanced Propulsion Concepts (Palo Alto, Calif., Apr. 26, 1965), Aerospace Res. Lab., 1965. (Classified paper.)
7. GREY, J.: Where the Carrot Does Not Improve Vision—Nuclear Energy for Space. Astronaut. Aeron., Mar. 1966.
8. NELSON, S.; GREY, J.; AND WILLIAMS, P.: Conceptual Study of Liquid Core Nuclear Reactor. J. Spacecraft Rockets, May 1965, pp. 381-384.
9. KERREBROCK, J.; AND MEGHREBLIAN, R.: Vortex Confinement for the Gaseous Fission Rocket. J. Aerospace Sci., vol. 28, no. 9, Sept. 1961, pp. 710-724.
10. HATCH, L.; REGAN, W.; AND POWELL, J.: Fluidized Solids as a Nuclear Fuel for Rocket Propulsion. J. Am. Rocket Soc., vol. 31, 1961, p. 547.
11. FLETCHER, E.; GYARMATHY, G.; AND HASINGER, S.: Separation of Submicron Condensate Particles in a Vortex Chamber. Rept. 66-0218, Aerospace Res. Lab., Nov. 1965.
12. ANON.: Engineering Study of Colloid Fueled Nuclear Rocket. Rept. 69-0215, Aerospace Res. Lab., Dec. 1969.
13. ANON.: The Utility of Colloid Core Nuclear Reactors for Space Propulsion. Rept. 66-0001, Off. Res. Analysis, June 1966. (Classified paper.)

Page intentionally left blank

ATTENDEES

ALLARIO, F.
NASA Langley Research Center
ALMENAS, K.
University of Maryland
BAUDER, U.
Aerospace Research Laboratory
BETTENHAUSEN, L. H.
University of Virginia
BISHOP, A. R.
NASA Lewis Research Center
BOSTICK, W. H.
Stevens Institute of Technology
CAMPBELL, H. D.
University of Florida
CARROLL, E. E.
University of Florida
CHAKOFF, H. E.
University of Florida
CLARK, J. W.
United Aircraft Corp.
CLARKSON, M. H.
University of Florida
CLEMENT, J. D.
Georgia Institute of Technology
COTTER, T. P.
Los Alamos Scientific Laboratory
DALTON, G. R.
University of Florida
DAVIDSON, J. N.
University of Michigan
DIAZ, N. J.
University of Florida
DELMER, T. N.
Gulf General Atomic, Inc.
DUINK, S.
University of Florida
EDWARDS, L. J.
AFRPL
ELLIOTT, F.
University of Florida
ELLIS, W. H.
University of Florida
ENGLEHART, R. W.
University of Florida
EVANS, D.
University of Florida
FEICHTNER, J.
Westinghouse Electric Corp.
FLEMING, J.
University of Florida
FRANKLIN, C. E.
NASA Space Nuclear Propulsion Office
FRINK, R. O.
University of Florida
GREATHOUSE, G.
Greathouse Consulting Service
GREEN, D.
University of Florida
GRITTON, E. C.
Rand Corp.
GROSS, P.
University of Florida
HANLIN, J.
Auburn University
HASSAN, H. A.
North Carolina State University
HO, C.
Columbia University
HOLLIS, J.
University of Florida
IMANI, K.
University of Florida
IQBAL, M.
University of Florida
JACOBS, W. R.
Georgia Institute of Technology
JAKOMIS, W.
Aerospace Research Laboratory
JAVAN, A.
Massachusetts Institute of Technology
JEFFREYS, H.
University of Florida
JOHNSON, B. V.
United Aircraft Corp.
KASCAK, A. F.
NASA Langley Research Center
KEEFER, D.
University of Florida
KELM, S.
DVL Stuttgart, Germany
KELLER, M. R.
Westinghouse Electric Corp.
KENDALL, J.
United Aircraft Corp.
KENG, E. Y. H.
Georgia Institute of Technology
KERREBROCK, J. L.
Massachusetts Institute of Technology
KEYES, J. J., JR.
Oak Ridge National Laboratory

KIM, S. H.
University of Florida
KLEIN, J. F.
United Aircraft Corp.
KRASCELLA, N. L.
United Aircraft Corp.
KURZWEG, U. H.
University of Florida
KYLSTRA, C. D.
University of Florida
LATHAM, T. S.
United Aircraft Corp.
LEWELLEN, W. S.
Massachusetts Institute of Technology
LOCKEY, M.
University of Florida
LOHNERT, G. H.
University of Florida
MCLAFFERTY, G. H.
United Aircraft Corp.
MACHADO, R. E.
University of Florida
MACK, J. M.
University of Florida
MARKWELL, F.
University of Florida
MASSER, C. C.
NASA Lewis Research Center
MENSING, A. E.
United Aircraft Corp.
MILEY, G. H.
University of Illinois
MILLER, B. E.
University of Florida
MILLER, M. H.
University of Maryland
MONSLER, M.
AVCO Corp.
MOORE, F. K.
Cornell University
MORFITT, J. W.
Idaho Nuclear Corp.
MYERS, O. E.
University of Florida
OHANIAN, M. J.
University of Florida
OLIVER, C.
University of Florida
ORTABASI, U.
University of Florida
ORVIS, D. D.
University of Florida
OVERMAN, C. H.
University of Florida
PARK, C.
NASA Ames Research Center
PARTAIN, W. L.
Georgia Institute of Technology
PATCH, R. W.
NASA Lewis Research Center
PELL, K. M.
Auburn University
PEREZ, F.
University of Florida
PIKE, W. J.
University of Florida
PODNEY, W. N.
Institute for Defense Analyses
PUTNAM, J.
University of Florida
RADZIEMSKI, L. J.
Los Alamos Scientific Laboratory
RAGSDALE, R. G.
NASA Lewis Research Laboratory
RAMM, H. J.
ARO Corp.
RANDOL, A. G., III
Nuclear Fuel Service, Inc.
REINMANN, J. J.
NASA Lewis Research Center
RENNER, D. W.
University of Florida
RHOADS, H.
University of Florida
RODGERS, R. J.
United Aircraft Corp.
ROM, F.
NASA Lewis Research Center
ROMAN, W. C.
United Aircraft Corp.
ROSA, R. J.
AVCO Corp.
RUSSELL, G.
Jet Propulsion Laboratory
SCHIKORR, W. M.
University of Florida
SCHNEIDER, R. T.
University of Florida
SCHNITZLER, B. E.
University of Florida
SCHRADE, H.
Aerospace Research Laboratory
SCHULTZ, K. R.
University of Florida
SCHWENK, C.
NASA Space Nuclear Propulsion Office
SHELTON, S. V.
Georgia Institute of Technology
SHERMAN, A.
Computer and Applied Sciences, Inc.
SHOBER, R. A.
University of Florida
SHUMAKER, D. E.
University of Florida
SMITH, N. A.
University of Florida
SOEHNGEN, A.
Aerospace Research Laboratory

SOKELAND, W. P.
University of Florida
SOUTHWARD, F.
University of Florida
SPECTOR, S.
University of Florida
SPIELMANN, G.
University of Florida
STERRITT, D.
University of Florida
STILES, P. L.
University of Florida
STRATTON, T. F.
Los Alamos Scientific Laboratory
STROBEL, D. J.
Cornell University
SWANDER, J. E.
University of Florida
TANG, Y. S.
Westinghouse Electric Corp.
THEISS, P. E.
University of Illinois
THOM, K.
NASA Space Nuclear Propulsion Office
TIDMAN, D.
University of Maryland
TIMMONS, D. H.
University of Missouri
TURMAN, B.
Aerospace Research Laboratory
UHRIG, R. E.
University of Florida
UNGER, H. E.
Northwestern University
USHER, J.
University of Florida
VERSLUIS, R. M.
University of Florida
VON OHAIN, H.
Aerospace Research Laboratory
WALTERS, R.
University of Florida
WETHINGTON, J. A.
University of Florida
WILKERSON, T. D.
University of Maryland
WILLIAMS, J. R.
Georgia Institute of Technology
WINTERBERG, F.
University of Nevada

☆ U.S. GOVERNMENT PRINTING OFFICE: 1971 0—404-527